Prediction and Measurement of Special Core Analysis Petrophysical Parameters in the Nubian Sandstone of the North Africa

Hassan M. Sbiga

Submitted for the degree **of Doctor of Philosophy**

Heriot-Watt University
Institute of Petroleum Engineering
Edinburgh-Scotland, UK

November, 2013

Abstract

One of the main objectives of this work was to investigate the applicability and accuracy of artificial neural networks for estimating special core analysis (SCAL) parameters from minimal core training data and wireline logs. The SCAL data was obtained from measurements on core plugs undertaken at the Libyan Petroleum Institute (L.P.I). Previous neural network studies have attempted to predict routine core analysis parameters, such as permeability, but not SCAL parameters such as true formation resistivity (R_t), resistivity index (RI), water saturation (S_w), saturation exponent (n) and Amott-Harvey Wettability Index ($I_{A/H}$). Different combinations of wireline logs were used to train a variety of neural network predictors. Some of the predictors were trained using a large dataset from the entire cored interval of the training well. Other genetically focused neural network (GFNN) predictors were trained just from one short representative genetic unit (RGU) in the training well. The predictors were then tested in an adjacent well in the same oil field and also in another well in a different oil field. Significantly the performance of the GFNN predictors was as good (and in most cases better) than the predictors trained on the much larger dataset. This demonstrated the useful of the GFNN approach, which is very cost effective in terms of the minimal core that is required, and the reduced computer processing time. Moreover, this is the first time that these GFNN predictors have been used to predict SCAL parameters in the studied area, the Nubian Sandstone Formation in North Africa. These neural network predictors are particularly useful in this area due to the limited amount of SCAL data that is currently available.

Quantitative statistical measures of heterogeneity were also examined on the reservoir samples, followed by a comparative analysis of hydraulic units (HUs) with a newer approach of global hydraulic elements (GHEs) to characterize the reservoir units in the studied area. The GHEs were then applied to select minimal representative core training data to train the genetically focused neural networks (GFNNs) to predict the SCAL parameters.

The thesis also describes the factors affecting SCAL resistivity parameters. Laboratory measurements on the Nubian Sandstone reservoir rock samples showed changes in the formation resistivity factor (F) and cementation exponent (m) between ambient conditions and at overburden pressures. Changes were also observed in the saturation exponent (n) before and after wettability measurement. The experimental results also showed that there was a good relation between resistivity and the type of pore system which is consistent with study result from Swanson (1985) confirming earlier work.

Dedication

This thesis is dedicated to my parents, my wife, my sons Abdussalam and Mohamed, and all my family members.

Acknowledgments

I would like to express my heartfelt thanks to my supervisor, Professor David K. Potter, for his support and valuable advice and encouragement during my study. Also many thanks go to Professor Patrick Corbett for his guidance. I would like to thank Mr. Fateh Elhakimi for his enthusiasm and help during the early stages of this study. I also wish to thank Dr. Arfan Ali for his advice and support during this research. Many thanks also to all the staff and students of the Institute of Petroleum Engineering (IPE) who I met, who helped me and who made my visits to the Institute very comfortable and satisfying. Special thanks go to all my Libyan friends over the years in IPE. Special thanks also go to Mr. Rashid Toumi, Abulgasem Abousef, Ramadan Aboaisha, Khalid Al-Ruwaili and all my friends for their endless support.

The financial support from the Libyan Petroleum Institute (LPI) is also highly appreciated.

ACADEMIC REGISTRY
Research Thesis Submission

Name*:*	HASSAN MASAOUD SBIGA		
School/PGI:	INSTITUTE OF PETROLEUM ENGINEERING		
Version: *(i.e. First, Resubmission, Final)*	Final	Degree Sought (Award **and** Subject area)	PhD

Declaration

In accordance with the appropriate regulations I hereby submit my thesis and I declare that:

1) The thesis embodies the results of my own work and has been composed by myself
2) Where appropriate, I have made acknowledgement of the work of others and have made reference to work carried out in collaboration with other persons
3) the thesis is the correct version of the thesis for submission and is the same version as any electronic versions submitted*.
4) my thesis for the award referred to, deposited in the Heriot-Watt University Library, should be made available for loan or photocopying and be available via the Institutional Repository, subject to such conditions as the Librarian may require
5) I understand that as a student of the University I am required to abide by the Regulations of the University and to conform to its discipline.

* *Please note that it is the responsibility of the candidate to ensure that the correct version of the thesis is submitted.*

Signature of Candidate*:*		Date:	

Submission

Submitted By *(name in capitals):*	
Signature of Individual Submitting:	
Date Submitted:	

For Completion in the Student Service Centre (SSC)

Received in the SSC by *(name in capitals):*			
Method of Submission *(Handed in to SSC; posted through internal/external mail):*			
*E-thesis Submitted (**mandatory for final theses)***			
Signature:		Date:	

Contents

List of Tables

List of Figures

Nomenclature

a	Archie's constant
A	Cross-Sectional area Perpendicular to the direction of flow, cm^2
BOPD	Barrels of Oil per Day
BPNN	Back Propagation Neural Network
CALI	Caliper log
C_j	Storage capacity, dimensionless
C_V	Coefficient of variation
DT	Sonic Log
FF	Formation resistivity factor, dimensionless
F_g	Shape factor
F_j	Flow Capacity, dimensionless
FZI	Flow Zone Indicator, dimensionless
GFNN	Genetic Focused Neural Network
GHE	Global Hydraulic Element
GR	Gamma Ray, API
HU	Hydraulic Unit
I_w	Displacement by water ratio
I_o	Displacement by oil ratio
$I_{A/H}$	Amott Harvey Wettability Index
ILD	Deep Induction log, ohm-m
ILM	Medium Induction log, ohm.m
K	Permeability, mD
Kg	Gas Permeability, mD
Lc	Lorenz Coefficient
LP	Lorenz Plot
LPI	Libyan Petroleum Institute
L	Length of sample, cm
m	Cementation factor, dimensionless
MICP	Mercury Injection Capillary Pressure, psi
n	Archie's saturation exponent, dimensionless
N_i	Normalised wireline log or core parameter at depth i .

NN	Neural Network
NPHI	Neutron Porosity Log
O_i	The output from neuron in the Prior layer
O.B.P	Overburden Pressure, psi
P1& P2	Upstream and downstream pressures, atm
P*a*	Atmospheric Pressure, atm
ΔP	Pressure differential, atm
PUC	Pre-Upper-Cretaceous
Qg	Gas flow rate, cc/sec
r	Resistance, ohm
r	Radius of capillary tube
rp	Pore thought radius, micron
R	Resistivity, ohm.m
RCA	Routine Core Analysis
REV	Representative Elementary Volume
RFT	Repeated Formation Test
RGU	Representative Genetic Unit
RHOB	Bulk density, gm/cc
RI	Resistivity Index, dimensionless
r_{mh}	Mean hydraulic radius
R_t	True resistivity of the partially saturated rocks, ohm.m
R_o	Resistivity of fully saturated rock, ohm.m
RQI	Reservoir Quality Index
R_w	Water resistivity, ohm.m
SCAL	Special Core Analysis Laboratory
SD	Standard deviation
SEM	Scanning Electron Microscope
SGHE	Storage capacity
SGR	Spectral Gamma Ray, API
S_g	Surface area per unit grain volume
SHg	Cumulative mercury saturation, percentage
Sor	residual oil saturation, fraction

S_w	Water saturation, fraction
Sw_{irr}	Irreducible water saturation, fraction
TGHE	Flow capacity (Transmissive GHE)
V_b	Bulk volume, cc
V_{Dp}	Dykstra-Parson coefficient, dimensionless
V_g	Grain volume, cc
Vo,s	Volume of oil Spontaneously imbibed, cc
Vo,d	Volume of oil dynamically imbibed, cc
V_p	Pore volume, cc
V_w	Water Volume, cc
Vw,s	Volume of water Spontaneously imbibed, cc
Vw,d	Volume of water dynamically imbibed, cc
W_{ij}	Connection weight from neuron i to neuron j
ΔW_{ij}	The weight change
X_i	Value of wireline log or core parameter
X_{min}	Minimum value
X_{max}	Maximum value

Greek Letters

Ø	Fractional Porosity
μ_g	Gas viscosity, cp
τ	Tourtosity
$Ø_e$	Effective porosity
$Ø_z$	Normalised Porosity, fraction
η	Is the learning rate
θ	Contact angle, degree
δ_j	Is the error of neuron j
σ	Interfacial tension, dyne/cm

Conference Papers

Part of this work is presented in the following conferences:

- Sbiga, H., (2010). "Prediction of True Resistivity and Resistivity Index by Using Genetically Focused Neural Networks Approach (GFNN's)" Presented at 11th meditation of conference and Exhibition held in Tripoli-Libya from **23-25** Feb., 2010

- Sbiga, H., (2012). "Electric Properties and Its Effect on Micro-porosity Rocks" Presented at the SPE International Production and Operations Conference and Exhibition held in Doha Qatar, 14-16 May 2012, SPE 154349

- Sbiga, H., (2012). "Prediction of Resistivity Parameters by Using Genetically Focused Neural Networks Approach (GFNN's)" Presented at 12th meditation of conference and Exhibition held in Tripoli-Libya from 20-22 Nov., 2012

CHAPTER ONE

Introduction

Reservoir description plays an important role in the petroleum industry. The understanding of reservoir rock properties such as porosity, permeability, water saturation, and resistivity assists engineers to improve the characterisation of the reservoir. In recent years, new developments in computer science, especially in neural network techniques, have contributed to the success of many diverse research areas in the science. This thesis firstly looks at statistical measures of heterogeneity in the Nubian Sandstone of North Africa using conventional core analysis data. This is followed by a comparative study, using data from six wells, of classical hydraulic flow units (HUs) with the newer approach of global hydraulic elements (GHEs) in the Nubian Sandstone. Then an analysis of the factors affecting special core analysis (SCAL) resistivity parameters is presented, involving experimental laboratory measurements. The rest of the thesis is devoted to neural network prediction from wireline logs of various SCAL petrophysical parameters. These included true formation resistivity, resistivity index, water saturation, saturation exponent, and wettability index. Part of the latter work involved training neural networks using minimal training data from genetically focussed neural nets (GFNN). The aim was to integrate a "Genetic Petrophysics" approach and neural network techniques to develop methodologies for reliable prediction using minimal representative training data. The methodologies were desired to possess the following characteristics:

1. Rapidity
2. Reliability
3. Cost–effectiveness
4. Applicability to diverse parameters in reservoir characterisation

The thesis has implications for cost-effective exploration approaches that limit the number of wireline logs economically in early exploration wells, and limit the coring interval to a minimum. The thesis shows how minimal representative SCAL plugs can initially be selected using the global hydraulic element template, and demonstrates that prediction of

SCAL parameters in large intervals can be made by training neural nets on data from these few selected representative core plugs in conjunction with wireline log data.

1.1 Neural Networks

Neural networks have a long history, going back at least to the early 1940's. Neural networks have been applied in a wide variety of fields. One of the principle advantages of a neural network is its ability to discover patterns in data, which may be imperceptible to the human brain or standard statistical methods. The most frequently used type of neural network is a feed forward neural network using a back-propagation learning algorithm, due to it is popularity and simplicity. In a typical neural data processing procedure, the database is divided into two separate portions called training and test datasets. The training dataset is used to develop the desired network. In this process (depending on the paradigm that is being used) the desired output in the training set is used to help the network learn by adjusting the weights between its neurons or processing elements.

Neural networks can help engineers and researchers by addressing some fundamental petroleum engineering problems that conventional computing has been unable to solve. Petroleum engineering may benefit from neural networks on occasions when engineering data for design and interpretations are less than adequate, such as old fields. Lack of adequate data may also be encountered because of the high cost of coring, well testing, and so on. Neural networks have proved to be valuable pattern–recognition tools. They are capable of finding highly complex patterns within large amounts of data. A relevant example is well log interpretation. It is generally accepted that there is more information embedded in well logs than meets the eye. Determining, predicting, or estimating formation permeability without actual laboratory measurement of the cores (or minimal cores) or interruption in production for well test data collection has been a fundamental problem for petroleum engineers. Neural networks can potentially help predict reservoir parameters using minimal training data.

A neural network is a generalised numerical tool which enables the correlation or linking of one set of data called the 'input' to another set called the 'output'. It is assumed that the input and output may be related in some way, although it is not necessary to know this relationship. Rather a known set of data, called the 'training dataset', containing both input

and output for a number of different cases is used to teach the neural network to recognise any association which may exist. Therefore, the training dataset is said to comprise a number of 'patterns' each of which is a list of the inputs and outputs. The values of the input data are applied into an array of 'input neurons'. Each of these is connected to a variable number of neurons in a 'hidden layer' and the value of each input is transmitted through a connection into these hidden neurons where they are combined. In turn each neuron in the hidden layer communicates a signal to an 'output neuron' which represents a specific output value. In fact, there may be more than one hidden layer of neurons and the number of neurons in each layer may be different, although they will all be inter-connected to the neurons of adjacent layers. Importantly, the signals which are transferred between neurons in a network are modified by multiplying the value by a 'weight' which is associated with each connection. The different connections have different weights and these, therefore, determine the influence a particular neuron has on a particular output of the network. During training both input and output are known. With the input data, the connection weights are adjusted so that the neural network will give output values which match as closely as possible the real output values in the training dataset. When this training process is complete, the values of the weights are fixed. At this point these weights have essentially encoded the intelligence of the training dataset into the neural network. The neural network is then able to predict further outputs on the basis of information supplied as input along with the weights that were determined in the training process.

Osborne (1992) first introduced back-propagation neural networks for permeability prediction from wireline logs. Following this several other studies have been published (Mohaghegh et al., 1995; Wong et al., 1997; Arpat et al., 1998; Jamialahmadi and Javadpour, 2000; Helle et al., 2001). All previous studies have used wireline logs in conjunction with core plug data to train the neural network. In the present study some SCAL parameters on core plugs were measured in the laboratory in the Libyan Petroleum Institute (LPI). Part of the data was used for the neural network training datasets, and part of it was used to test the neural predictions in the test datasets. The work presented is new as very few previous studies have attempted to predict SCAL parameters such as true resistivity, resistivity index, saturation exponent, water saturation, and Amott-Harvey Index from neural networks using minimal core training data.

1.2 Fundamental Reservoir Rock Properties

For any reservoir rock there are two key petrophysical parameters. The first is the capacity of the rock to store fluid, namely porosity. The second is connectivity of the pore space, which allows fluid to flow through the rock, namely permeability. Routine core analysis defines the porosity and permeability magnitude and distribution. SCAL complements this routine data, and furnishes information that allows calculation of static fluid distribution as well as dynamic flow performance of a well or reservoir. Moreover, a special core analysis program can assist in defining the most favourable recovery technique to maximize oil recovery and profitability. Downhole log interpretation is considerably enhanced by a SCAL program through the measurement of electrical and acoustic properties of reservoir rocks and fluid saturations from displacement experiments (capillary pressure and relative permeability data). The objectives of performing a SCAL program are to achieve an accurate representation of the reservoir rock characteristics, information that is necessary for reliable reservoir engineering calculations and modelling.

The amount of hydrocarbon reserves is one of the most important parameters in the decision making process in developing a reservoir. The estimation of hydrocarbon reserve is strongly dependent of electric log data and on the value of saturation exponent (n) used.[3] The interpretation of the electrical (resistivity) logging data is based on Archie's law. Resistivity logging is the most widely used method of identifying hydrocarbon intervals in the wellbore. The standard method of relating oil saturation in clay-free reservoirs to electrical resistivity is based on Archie's saturation equation (Archie 1942):

$$RI = \frac{R_t}{Ro} = S_w^{-n} \quad \text{---------- (1.1)}$$

where the resistivity index, RI , is equal to the ratio of the resistivity of the sample (R_t) at brine saturation (S_w) over the resistivity of the sample at one hundred percent brine saturation (R_o). The resistivity index is related to the saturation of the sample and the saturation exponent (n). The saturation exponent must be determined by experimental core analysis. The standard technique for determining the saturation exponent involves measurments on cleaned cores, usually with air as the non-wetting phase and brine as wetting phase. This air/brine system is only representative of the drainage conditions in

strongly water wet situations. When oil displaced by water, for instance during water flooding, different distributions of fluid may prevail at the pore scale due to hysteresis effects controlled by pore geometries, initial saturation and wettability distribution at the pore scale. When the rock is compacted as a result of overburden pressure, the matrix is under stress and porosity decreases as a result of compaction, and the cementation factor will change.

Rocks can be classified based on their pore geometry as intergranular or non intergranular. Pore size and pore throat size varies regularly through the rock. Rasmus (1987) studied the effect of pore geometry on reservoir rock resistivity. He modelled mathematically the effect of vuggy pore geometry on rock resistivity. His model results showed that the resistivity of the fully saturated rock is relatively insensitive to the secondary vuggy porosity. In partially saturated rocks, the resistivity of partially saturated rocks is insensitive to the vuggy pore system if the vugs are oil wet. The Archie saturation exponent tends to increase as a result of increasing water saturation caused by a vuggy pore system, since the water occupies the middle of the vugs in an oil-wet vuggy system forming discontinuous droplets. These isolated water droplets do not contribute to the electrical conduction but give rise to water saturation, and, in turn, the saturation exponent will increase. In water-wet systems, as oil continuous to invade the pore system, the water volume decreases dramatically compared to the increase in resistivity, resulting in a lower water saturation and saturation exponent.

Wettability plays a major role in controlling the distribution of fluids within the pore space inside a rock. Keller (1953) presented evidence that the saturation exponent could be substantially different from the usually assumed value of 2.0. He found that Archie's saturation exponent (n) varies from 1.5 to 11.7 for the same rock, depending on how the cores were treated. For the same water saturation, the resistivity of an oil reservoir can vary by a thousand times for different wetting conditions. The wettability of sandstone cores was altered from water-wet to oil-wet conditions by using various chemical treatments. Keller concluded that the wettability played a great role in the fluid distribution within the rock space. By changing the relative position of the conducting fluid with respect to the rock surface, the electric behaviour of the fluid-filled sandstone would also change.

1.3 Hydraulic Units and Global Hydraulic Elements in Heterogeneous Reservoirs

In reservoir characterization heterogeneity specifically applies to variability that affects flow. Heterogeneity is the property of the medium that causes the flood front, the boundary between the displacing and displaced fluids, to distort and spread as the displacement proceeds (Jensen et al, 2000). Reservoir heterogeneity is defined as a variation in reservoir properties as a function of the spatial continuity. The relation between reservoir heterogeneity and dynamic field parameters is one of the key issues of an integrated study, since it determines the details and accuracy to be attained by the geological description (Cosentino, 2001).

Amaefule et al (1993) detailed a methodology for determining hydraulic flow unit in wells by working out the flow zone indicator (FZI) and the reservoir quality index (RQI) using the core plug porosity and permeability data. The disadvantages of this approach are that, firstly, one has to calculate the HUs for each well, which involves employing a de-clustering technique, and is very time consuming. Secondly, the results from one well can't easily be compared with the results from another well (HU1 in well 1 may not necessarily be the same as HU1 in well 2). Therefore, a new approach by Corbett et al (2003) and Corbett and Potter (2004) have been introduced involving global hydraulic elements (GHEs) in order to combat the disadvantages of the HU approach. This GHE approach involved the construction of a GHE template, with zones representing different FZI values, on the porosity-permeability crossplot. Corbett et al (2003) and Corbett and Potter (2004) split the porosity-permeability space into 10 manageable GHEs. A major advantage of this approach are that there is no need to subsequently calculate anything thus saving time (one merely plots one's porosity-permeability data on the template and can count the number of GHEs that it occupies). Also data from any reservoir worldwide can be compared on exactly the same reference frame (unlike the classical HU approach). The purpose of the study in this thesis was to compare both the HU and GHE approaches in six different wells of three fields in the Nubian Sandstone in North Africa, in order to determine whether the predetermined GHE template provided comparable information (in terms of number of GHEs) to the number of HUs determined from the classical analysis. If the number of GHEs in any particular well was close to the number of determined HUs then this would

confirm the GHE approach as a comparable, but, quicker and more useful way of comparing data between different wells in a field and between different fields.

1.4 Genetic Petrophysics

Another recent innovation in neural network prediction was extended in this thesis. The concept of "genetic petrophysics" was proposed by Corbett et al (1998). They recognised that there are representative elements within reservoirs (genetic units) that may repeat several times (for example, shoreface coarsening upwards parasequences). These repeating units can be exploited for prediction purposes. By studying one of the representative genetic units (RGUs) in detail, the properties of the others in the rest of the well or in adjacent wells can be predicted. Le and Potter (2003) and Potter et al (2003) subsequently used this idea to train genetically focused neural nets (GFNNS) to predict permeability and other important petrophysical parameters. This involved training the neural net predictors merely on data from a short RGU instead of from data from a larger interval. They showed that those GFNN predictors performed almost as well as predictors trained on the entire cored interval of a well. The obvious advantage of the GFNN approach is that it provides a very cost effective (in terms of minimal core measurements and computer processing time) and rapid way of making predictions. The present study applies the GFNN approach to the North Africa oil fields of the Nubian Sandstone, and also for the first time used this technique to predict SCAL parameters.

1.5 Location and Geology of the Oilfields in this study

This study has been undertaken in three oil fields: A-Libya, B-Libya, and C-Libya (Figure 1.2) in the Sirt Basin located in Libya. The Nubian Sandstone Formation is the main reservoir in these oil fields.

1.5.1 Sirt Basin

The Sirt Basin is the youngest of the Libyan basins (Figure 1.1). It has the largest petroleum reserves in Libya and is ranked the 13th among the world's petroleum basins. The basin's recoverable reserves are about 45 billion barrels of oil and 33 trillion cubic feet of gas. Generally the origin of the Sirt Basin is attributed to the collapse of the Sirt Arch during Late Jurassic to Early Cretaceous times. Massa and Delort (1984) reported that the Sirt Basin was a permanent high from the Middle Paleozoic until the Early Mesozoic. In the Early Paleozoic the basin was the site of siliciclastic deposition, and clastics accumulated all over North Africa. In the Cretaceous and Tertiary, large quantities of organic-rich shales and other terrigenous clastic materials accumulated in the basinal area.

The Sirt Basin contains some sixteen giant oil fields with about 117 billion barrels of proven oil-in-place.[4] The two principal source rocks in the Sirt Province are the Upper Cretaceous Rachmat Shale and the Sirt Shale. Hydrocarbon distribution in the Sirt Basin has been controlled by major tectonic events. This is particularly true of reservoirs related to Cretaceous and Eocene to Miocene rift structures. These reservoirs in the Sirt Basin are composed of 58% clastics, mostly of Mesozoic age and 42% of carbonate rocks mostly of Tertiary age.

1.5.2 Nubian Sandstone Formation, Sirt Basin

The Nubian Formation of the eastern Sirt Basin, Libya, comprises mainly sandstones and shale resting unconformably on a basement of igneous and metamorphic rocks. The Nubian Formation has been subdivided into three members. Member 1 forms the uppermost part of the formation, and comprises mainly sandstones with intercalation of siltstones and shale of variable thickness, and has a maximum known thickness of about 1099ft. Member 2

represents the middle part of the Nubian Formation, and consists of shale and silty shale, with a maximum known thickness of 2362ft. Member 3 is the basal part of the formation, and rests directly on the crystalline basement. It comprises sandstones with subordinate intercalations of siltstones and shale, and exceeds 3002ft in thickness.

The sandstones tend to be fine to coarse grained, quartzitic, tan-grey coloured and are usually poorly sorted with a clay matrix. The finer sandstones are more poorly sorted, but the coarser sandstones have very little in terms of matrix and are thus very porous. The shale tends to be red, maroon, green, micaceous and laminated. There are also conglomerates containing rounded quartz pebbles within a sandstone and claystone matrix (Barr and Weegar, 1972). Much of the Nubian Formation was probably deposited in fluvial depositional systems (Barr and Weegar, 1972).

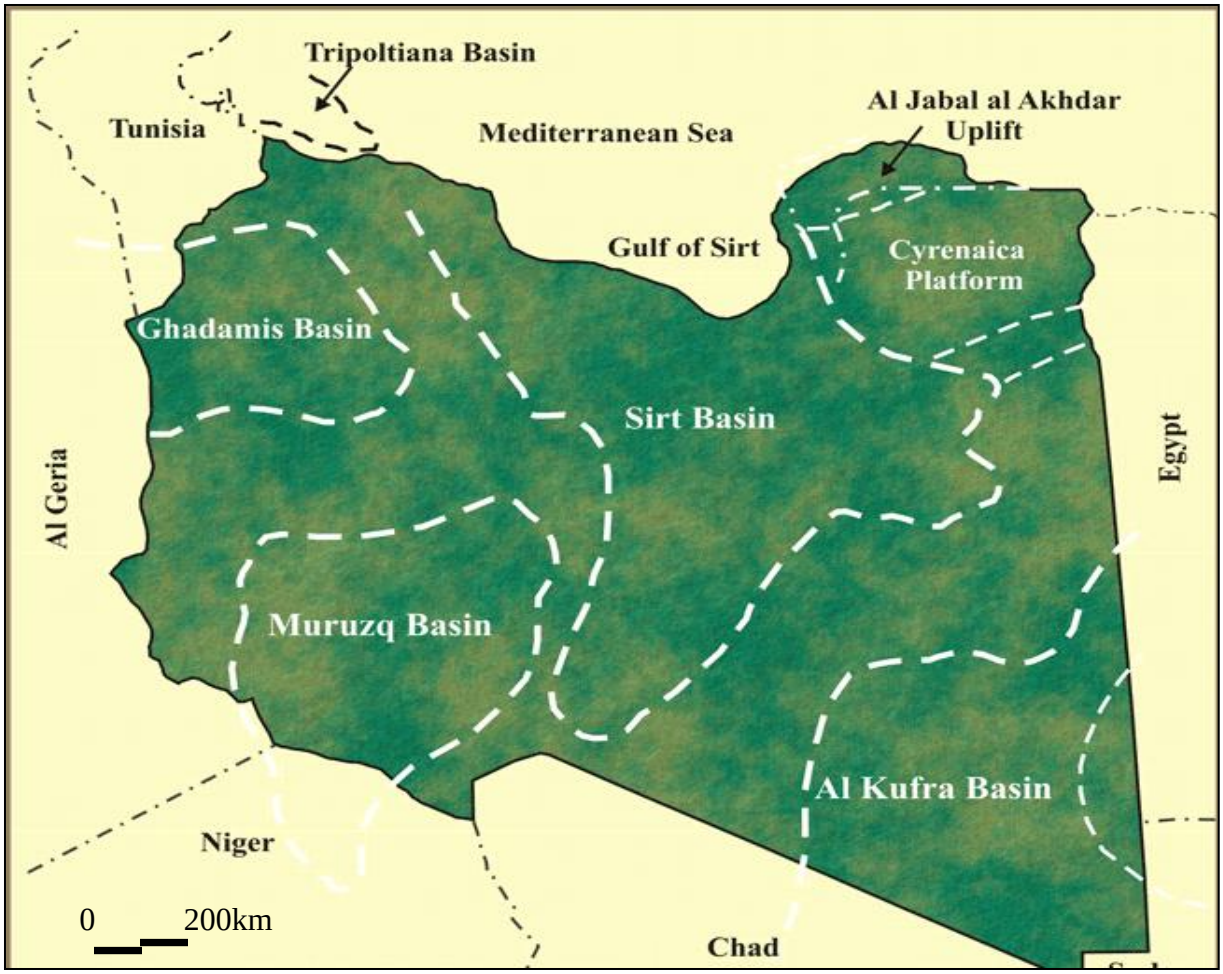

Figure 1.1. Location of major sedimentary basins of Libya.(Hassan S.Hassan, 2009)

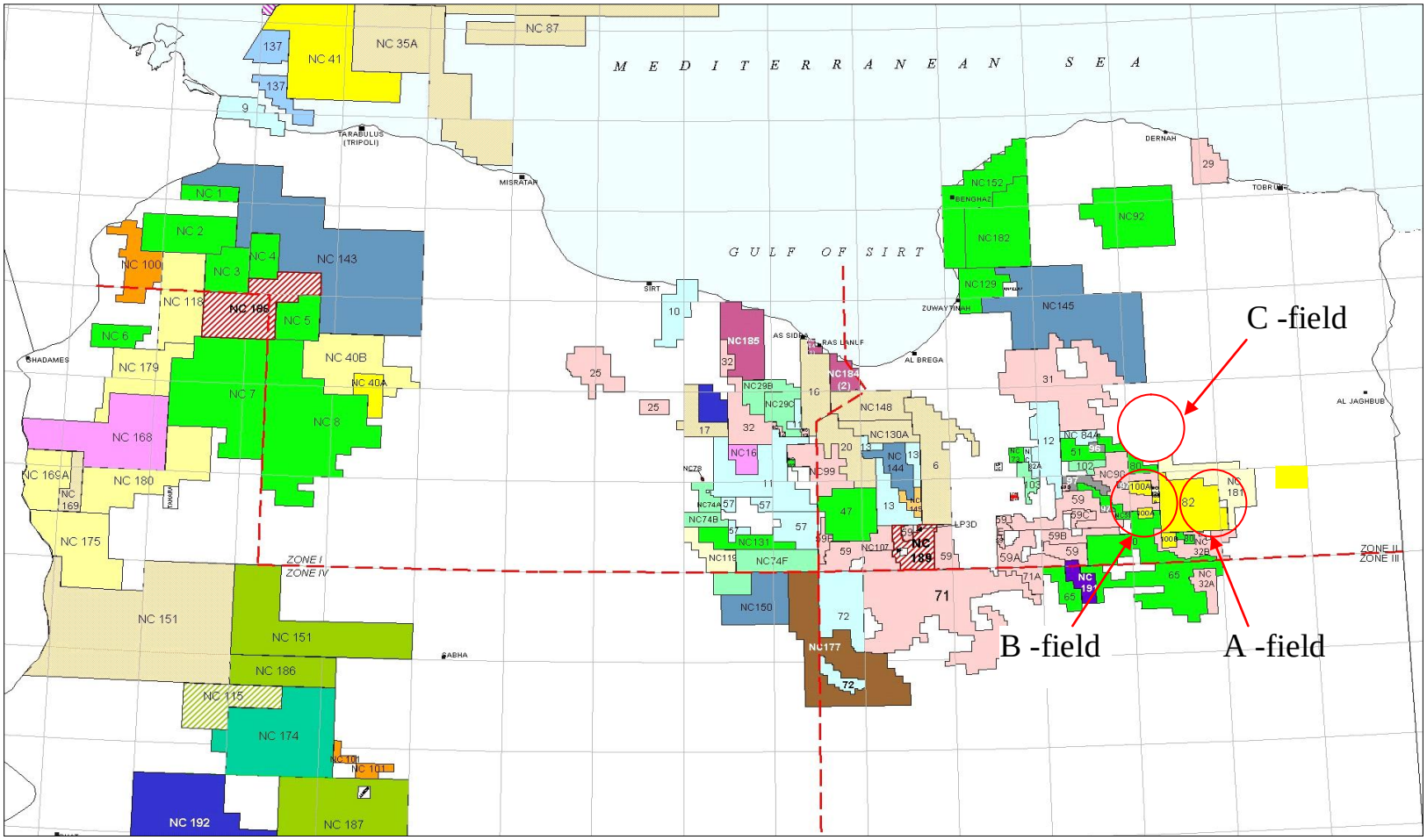

Figure 1.2. Location of the oil the fields used in this study.

1.5.3. Field A-Libya

Field A-Libya is one of the largest fields in the Sirt Basin (Figure 1.3). The exploration of this field began in the early 1980's. Well A-02-Libya was planned as an appraisal well for the eastern flank of the A structure. It is located about 8530 ft ESE from the A-01 discovery well. Well A-01 has total oil initial in place (OIIP) of about 61.86 MMSTB while A-02 has an (OIIP) of about 42.38 MMSTB.

Two additional wells A-04 and A-05 were drilled after the (OIIP) estimate in February 1993. The top reservoir was found lower than expected in both of these wells. The reservoir pressure from RFT indicates both A-04 and A-05 are hydraulically isolated from the reservoir block being depleted by A-01 and A-02. From log analysis and RFT results it is possible to speculate that the porosity- permeability relation in the A-reservoir could be different from the other reservoirs in this area. The zones of this field have relatively good porosity, moreover the average porosity of well A-04 is 11.5% in the interval of 15382-15524 ft, while in A-05 it is 9.5% in the interval of 15560-15565 ft and the water saturation averages are 30% and 38% respectively in the same intervals. The Upper Nubian Sandstone reservoir member 1 of well A-02 consists of 482 ft (15398-15880 ft) of quartzose sandstone with interlayers of shale. The reservoir can be divided into four intervals as shown in Table 1.1.

Table 1.1. Petrophysical parameters of well A-02.

Zone	Depth interval(ft)	Average Ø %	Average Sw%	Net pay(ft)	Net Gross%
Zone 1	15366-15418	11	26	26	50.5
Zone 2	15418-15574	11	25	110	70.3
Zone 3	15574-15670	9.2	31	40	41.5
Zone 4	15670-15806	10.7	41	24	17.6

The formation mostly consists of fine-medium to coarse sandstone, friable to compact, moderately to well cemented, white, greyish, and occasionally yellowish. It is composed of quartz grains, poorly sorted, sub angular, sub-rounded, in a siliceous or argillaceous (mostly kaolinitic) matrix. It is interbedded with shale, moderately hard, red-brick to brown and light-dark grey, subfissile, silty grading to siltstone. Good oil is seen (from the bottom hole cores) at 15833 ft.

The Upper Nubian Sandstone reservoir member 1 of well A-01 (15120-15859 ft) consists of quartzose sandstone with interlayers of shale. The reservoir can be divided into five zonations as shown in Table 1.2.

Table 1.2. Petrophysical parameters of well A-01.

Zone	Depth interval (ft)	Average Ø %	Average Sw %	Net pay(ft)	Net Gross%
Zone 1	15120-15190	11	26	23	33
Zone 2	15190-15363	11	39	81	18
Zone 3	15363-15562	12	27	157	79
Zone 4	15562-15664	12	34	42	41
Zone 5	15664-15859	10	27	6	32

The upper part in well A-03, 15160-15525 ft, has good porosity. The net pay is 277ft, N/G is 79%, Sw is 20%. The lower part, 15525-15865 ft, has very poor lithological characteristics. The net pay is 68 ft, N/G is 20%, Sw is 30-50%. The oil-water contact is not evident. The "Upper Nubian Sandstone" reservoir consists of 705 ft (15160-15865 ft) of quartz sandstone with interbedded shale. (7)

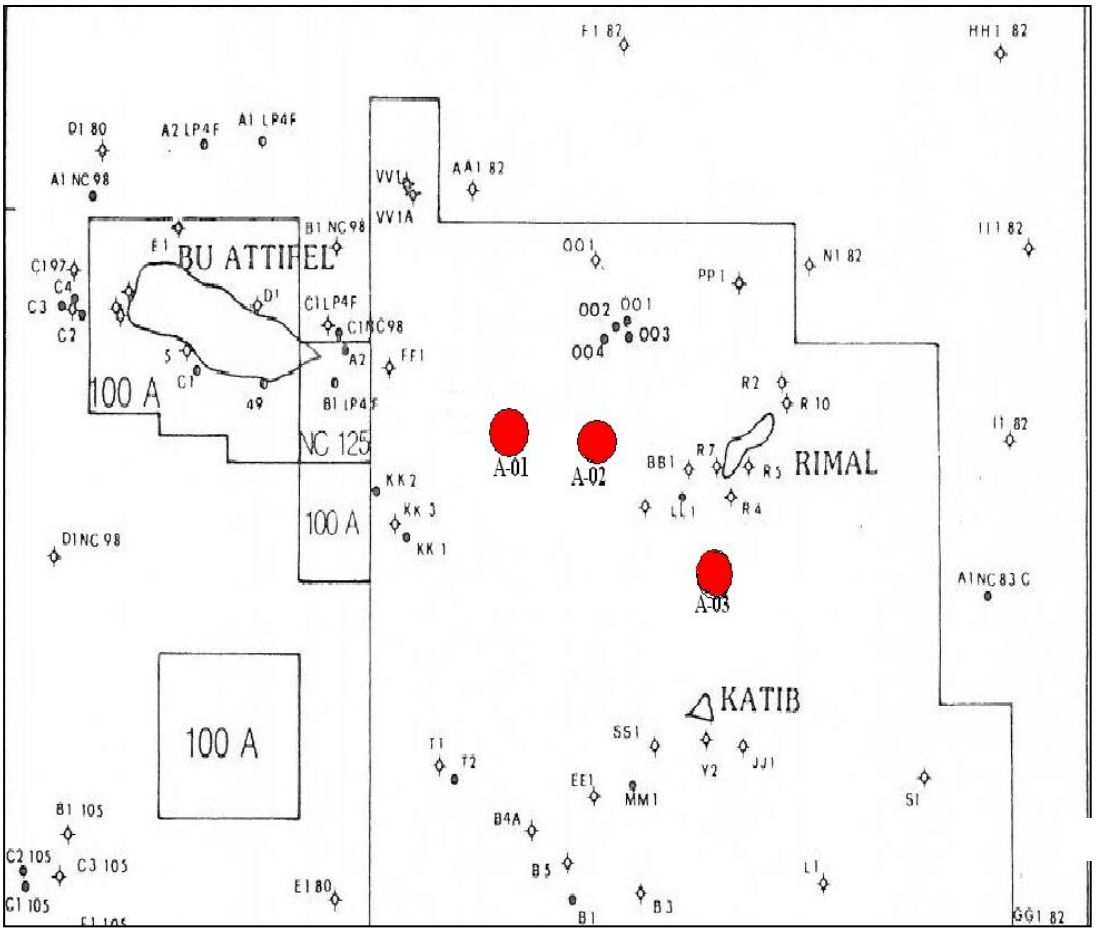

Figure 1.3. Location map of field A.

1.5.4. Field B-Libya

Field B is located at the south-western edge of the Sirt Basin. Field B–Libya mainly produces from the Nubian Sandstone (Upper and Lower) and also from the Socna "C" Formation.

1.5.5. Socna Formation (Upper Cretaceous)

The Socna Formation marks the beginning of the Upper Cretaceous marine sedimentation, which developed concurrently with a tectonic or sinking distension phase. The consequent formation of horsts and grabens led to the formation of structural highs, one of which is part of the B-Field reservoir. The beginning of the Socna Formation sedimentation occurred in an evaporitic hypersaline lagoon environment, with deposition of salt and chalk layers a few metres thick.

1.5.6. Upper Nubian Sandstone Formation (Lower Cretaceous)

The Upper Nubian Sandstone Formation is a thick sequence of continental sandstones of a fluvial environment, with thick intercalations of lacustrine shales at the bottom. The analysis of continuous well coring in the reservoir led to the identification of four lithofacies:

1- Micro-conglomerates
2- Sandstones
3- Shaly siltstone
4- Shales

1.5.7. Lower Nubian Sandstone Formation (Lower Cretaceous)

The Lower Nubian Sandstone Formation consists of well sorted medium-grained to fine-grained sandstones of a fluvial depositional environment, rich in argillaceous silty layers of a lacustrine origin. The Lower Nubian Sandstone features a higher clay content and finer grain size than the Upper Nubian Sandstone, so the average porosity and permeability values are considerably lower in the Lower Nubian Formation.

Well B0-1 is one of the wells in the B-Field used in this study. This well was planned as a development well and it is located about 3280 ft ENE of B-57 and 2560 ft N of B-62 (Figure 1.4). Structurally it is in the eastern area of the E-W elongated horst bounded southward by a south dipping fault and northward by a secondary fault dipping in the opposite direction. No particular differences in the fluid content have been observed from log data. The RFT gradient changes from 0.21 psi/ft in the upper part of the reservoir to 0.26 psi/ft in the lower part, suggesting the presence of light oil in the reservoir. The main reservoir petrophysical parameters for different perforated intervals are represented in Figure 1.5 and Table 1.3.

Table 1.3. Petrophysical parameters of well B-01.

Zone	Depth interval (ft)	Average Ø%	Average Sw%	Net pay(ft)	Net Gross%
Zone 1	13876-14245	13.1	20.2	284	77.1
Zone 2	14176-14210	14.3	16.3	32	94.1
Zone 3	14152-14166	14.0	18.4	14	100
Zone 4	14137-14146	13.9	18	9	100
Zone 5	14110-14128	12.9	20	18	100

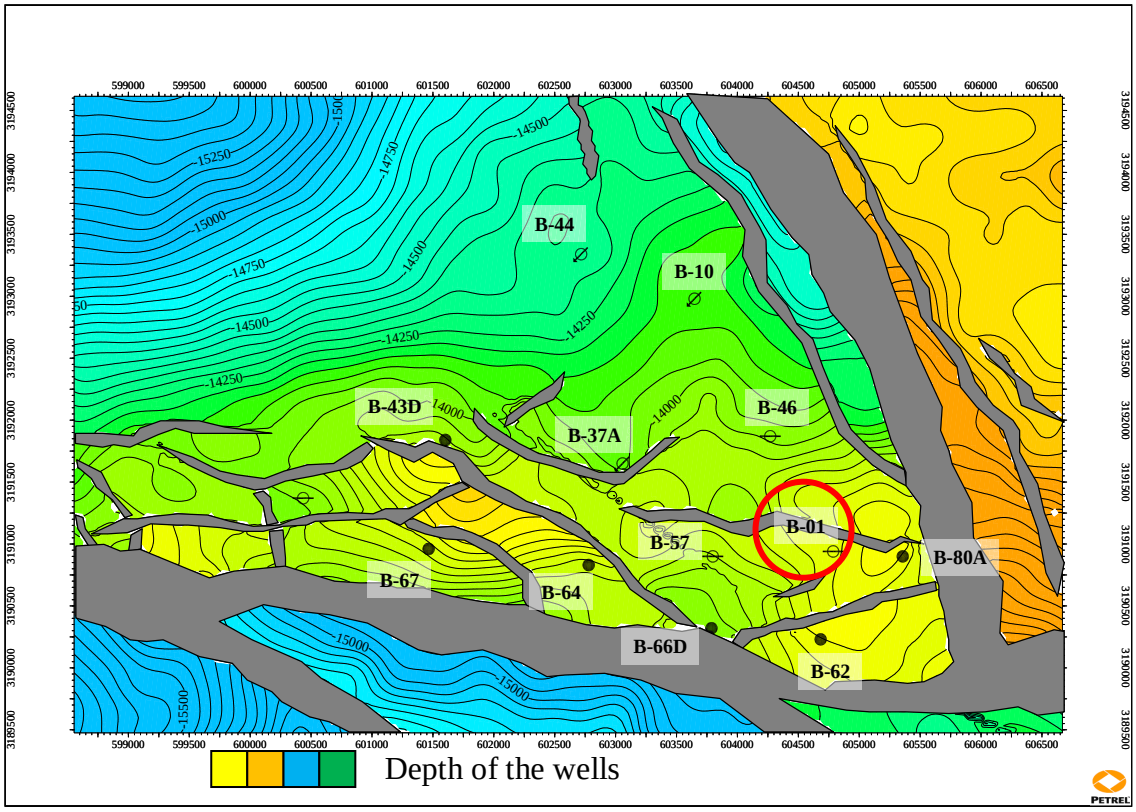

Figure 1.4. Location map of well B-01.

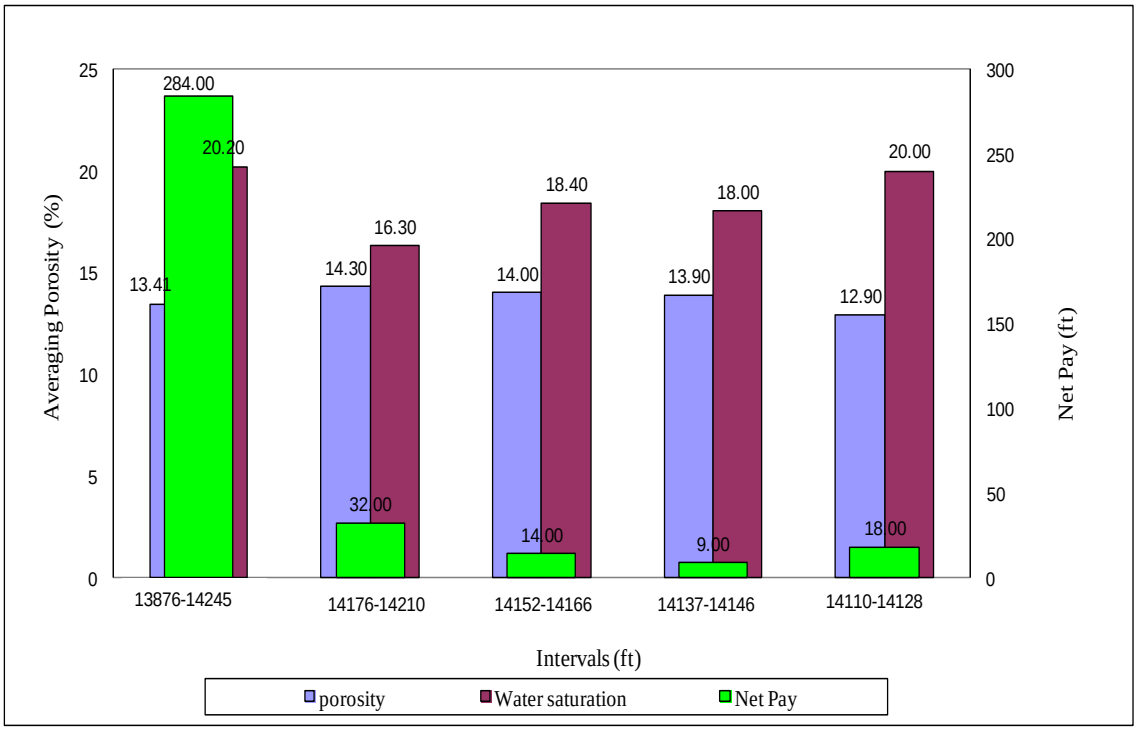

Figure 1.5. The main reservoir parameters of well B-01 in B-Field.

1.5.8. Field C-Libya

The production well C-02 is located in the eastern part of the As Sarah structure (Figure 1.6). The total depth reached was 13260 ft. The well encountered 665.5ft net pay of oil bearing sandstone in the Pre-Upper-Cretaceous (PUC). A "Three-Rate" test yielded an average rate of 11218 barrels oil per day (BOPD) through 48/64" choke. Well C-02 is completed as an oil well. The well was designed in accordance with the current geological and reservoir engineering conception (simulation study) in order to realize the scheduled well pattern and to increase production capacity within the seismically covered area of the oil field. The sandstone is mainly fine to coarse-grained, generally fair to good porosity, with locally some thin layers of siltstone. The petrophysical parameters of well C-02 are presented in Table 1.4.

Table 1.4. Petrophysical parameters of well C-02.

Zone	Depth interval (ft)	Thickness(ft)	Net pay (ft)	Average Ø %	Average Sw%
Oil bearing zone	11506-12266	760	665.5	11.3	5
Transition zone	12266-12332	66	28	10.9	28

The second well in this field used in this study is C-01, which is located in the south-eastern sector of the As Sarah structure. The total depth reached was 12920 ft. The well encountered 283 ft net pay of oil bearing sandstone of the (PUC) B reservoir. A "Three-Rate test yielded an average rate of 4919 (BOPD) through 48/64"choke, and it is completed as an oil well. The sandstone is grey-brown, hard, friable, mainly medium to coarse-grained, very poorly cemented, moderate to well sorted, angular to subangular. The petrophysical parameters of well C-01 are presented in Table 1.5.

Table 1.5. Petrophysical parameters of well C-01.

Zone	Depth interval (ft)	Thickness(ft)	Net pay (ft)	Average Ø %	Average Sw%
Oil bearing zone	11912-12265	353	283	14.8	5.5
Transition zone	12265-12294	29	29	12.5	10

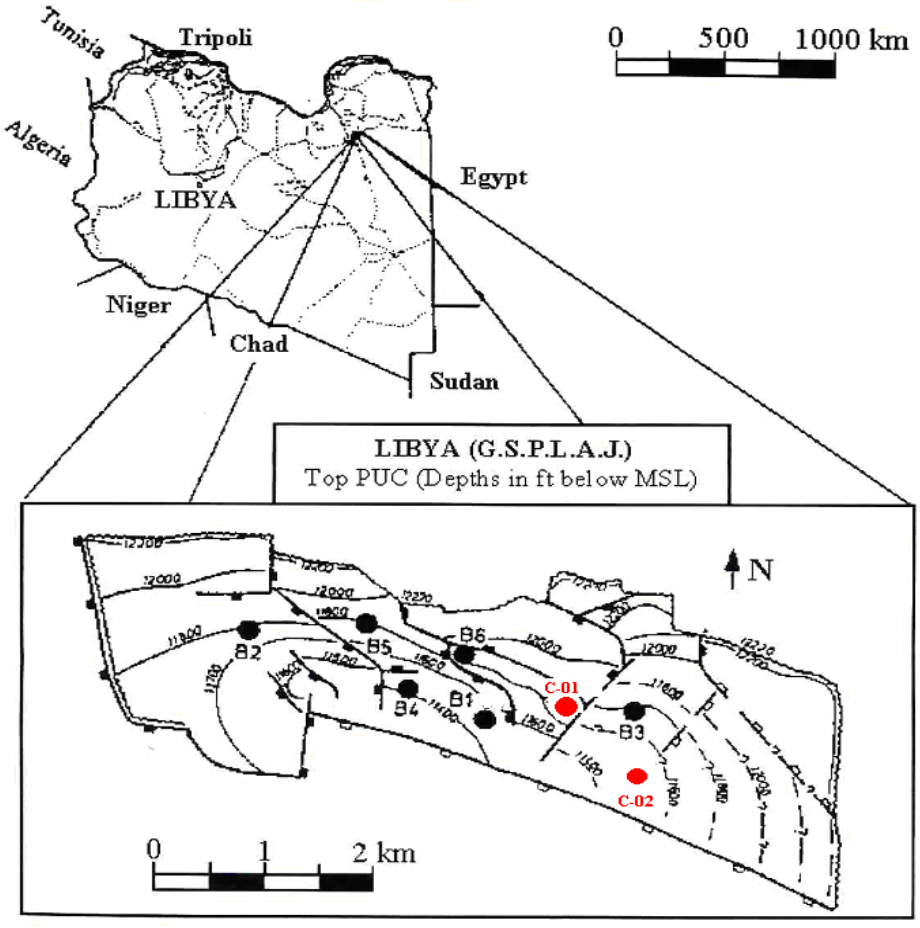

Figure 1.6. Location map of Field C.

1.6 Layout of the Thesis

The rest of the thesis consists of 5 further chapters:

Chapter 2. This chapter details a statistical analysis of the conventional core data for the six studied wells in Fields A, B and C in the Nubian Sandstone in North Africa. Also the global hydraulic elements (GHEs) approach was applied for the first time in these Nubian Sandstone reservoirs. The classical hydraulic unit approach of Amaefule et al (1993) was also compared with the new global hydraulic elements approach of Corbett and Potter (2004).

Chapter 3. This chapter describes some of the factors affecting SCAL resistivity parameters from experimental laboratory measurements. It includes the effect of overburden pressure on the formation resistivity factor and cementation exponent, and the effect of wettability measurement on the saturation exponent. It also looks at the relation between resistivity index and pore type.

Chapter 4. The main SCAL parameters are introduced and neural network predictors were trained using the SCAL data from an entire cored interval from a training well well A-02 along with associated combinations of different wireline logs. These predictors were then applied to an adjacent well in the same oil field well A-01, and to a test well in a different oil field well B-01.

Chapter 5. The genetically focused neural network (GFNN) approach was tested by training predictors on a short representative genetic unit (RGU). Various predictors were trained using different combinations of wireline logs as input and a back propagation algorithm. The results were compared with predictors based on a substantially larger dataset comprising the entire cored interval of the training well. The GFNN approach was validated in test intervals of the training well A-02, an adjacent well A-01 in the same oil field and in a test well B-01 in a different oil field.

Chapter 6. This chapter draws the general conclusions from the entire thesis.

CHAPTER TWO

Measures of Heterogeneity and a Comparison of Hydraulic Units and Global Hydraulic Elements in Heterogeneous Reservoirs in the Nubian Sandstone

2.1 Introduction and Objectives

In reservoir characterization, heterogeneity specifically applies to variability that affects flow. Heterogeneity is the property of the medium that causes the flood front, the boundary between the displacing and displaced fluids, to distort and spread as the displacement proceeds (Jensen et al, 2000). The reservoir heterogeneity is then defined as a variation in reservoir properties as a function of the spatial continuity. The relation between reservoir heterogeneity and dynamic field parameters is one of the key issues of an integrated study, since it determines the degree of details and accuracy to be attained by the geological description (Cosentino, 2001).

Geostatistical methods are used extensively in the petroleum industry to quantitatively describe the reservoir heterogeneity. The reservoir may be non-uniform in important properties such as porosity, permeability, wettability, and connate water saturation (Ahmed, 2001). However permeability varies far more than the other properties that effect flow and displacement. Performance models have been developed to show how permeability heterogeneity will influence a particular recovery process (Lake, 1989). A formation is said to have a uniformity coefficient of zero in a specified property when that property is constant throughout the formation thickness.

Hydraulic Units (HUs) are defined as “the units of reservoir rock that have similar averages of rock properties, which affect fluid and electric flow” (Amaefule et al, 1993). The concept of petrophysical hydraulic units is used to classify the rocks based on their pore size attributes. For the application of this approach, it is preferable to use stressed porosity and permeability data.

Amaefule et al. (1993) detailed a methodology for determining hydraulic flow units in wells by working out the flow zone indicator (FZI) and the reservoir quality index (RQI) using the core plug porosity and permeability data. The disadvantages of this approach are that, firstly, one has to calculate the HUs for each well, which involves employing de-clustering technique, and is very time consuming. Secondly, the results from one well can't easily be compared with results from another well (HU1 in well 1 may not necessarily be the same as HU1 in well 2). Therefore, a new approach by Corbett et al. (2003) and Corbett and Potter (2004) have been introduced involving global hydraulic elements (GHEs) in order to combat the disadvantages of the HU approach. This GHE approach involved the construction of a GHE template, with zones representing different FZI values on the porosity-permeability crossplot.

There are two main objectives of this chapter:

1. To undertake a detailed statistical analysis of the conventional core data for all the studied wells describe the heterogeneity.
2. To apply the global hydraulic elements (GHE) approach for the first time in the Nubian Sandstone reservoirs in six representative wells in Fields A, B and C in North Africa. The classical hydraulic unit approach of Amaefule et al. (1993) was also compared with the new global hydraulic elements approach of Corbett and Potter (2004).

Subsequently the GHE approach was then used later in this thesis (see Chapter 5) to select minimal representative core plugs to train genetically focused neural network (GFNN) predictors.

2.2 Measures of Heterogeneity

Since permeability varies far more than the other properties that affect flow and displacement, measures of heterogeneity are almost exclusively applied to permeability data. Heterogeneity measures are useful for a number of purposes. Since heterogeneity influences the performance of many flow processes, it is helpful to have a single statistic that will convey the permeability variation (Lake,1989). Heterogeneity measures are also helpful when comparing the performance of two or more fields. Whatever the reservoir properties involved, heterogeneity measures can be classified

into two groups, static and dynamic. (Lake,1989). *Static measures* are based on measured samples from the formation and require some flow model to be used to interpret the effect of variability on flow. *Dynamic measures* use a flow experiment and are, therefore, a direct measure of how the heterogeneity affects the flow. Each type has advantages and disadvantages. An advantage of dynamic measures is that, if the process used during the flow experiment closely parallels the process that is expected to be applied to the reservoir, the results are more directly applicable with a minimum of interpretation. Disadvantages include the cost, the complexity, and the selection of "representative" elements of the reservoir for conducting the flow experiments at the appropriate scale.

2.3 The Coefficient of Variation

A static measure often used in describing the amount of variation in a population is the coefficient of variation, C_v,

$$SD = \left(\sum \frac{(k - \bar{k})^2}{n - 1} \right)^{0.5} \quad \text{---------- (2.1)}$$

$$CV = \frac{SD}{\bar{K}} \quad \text{---------- (2.2)}$$

The coefficient of variation normalizes the standard deviation so that comparisons between samples can be made. The coefficient of variation has become more widely encountered in reservoir description and has been used to define the level of heterogeneity (Corbett & Jensen, 1991):

$0.0 < C_v < 0.5$ Homogeneous

$0.5 < C_v < 1.0$ Heterogeneous

$1.0 < C_v$ Very Heterogeneous

For data from different populations or sources, the mean and standard deviation often tend to change together such that C_v remains relatively constant. Any large changes in C_v between two samples would indicate a dramatic difference in the populations

associated with those samples. The coefficient of variation is being increasingly applied in geological and engineering studies as an assessment of permeability heterogeneity. C_v has been used in a study of the effects of heterogeneity and structure upon unstable miscible displacements (Moissis and Wheeler, 1990). It is also useful when comparing variability of different facies, particularly when there can be competing causes for permeability variation. Corbett and Jensen (1991) for example, used C_v to assess the relative affects of grain size variation and mica content upon permeability variation.

2.3.1 Statistical analysis and C_v in the Nubian Sandstone: (Fields A, B and C)

It is important to recognize that the estimates of the core population parameters (i.e., average horizontal permeability or porosity) should be based on sufficient samples (in number and size) taken from that core. If the core properties are poorly estimated, one can expect the reservoir properties to be poorly modelled. The more variable a parameter is, the more samples are required to estimate it. Permeability is commonly very variable and therefore difficult to estimate. Conventional core analysis data including porosity, permeability, and grain density from six wells A-01, A-02, A-03, B-01, C-01, and C-02 were undertaken from laboratory measurements performed at the Libyan Petroleum Institute (L.P.I.). The statistical parameters of conventional core analysis data are calculated based on representative depth intervals. The averages of conventional core analysis data are calculated as follows:

Arithmetic mean of porosity:

$$\bar{\phi} = \frac{\sum (h_i \times \phi_i)}{\sum h_i} \quad \text{---------- (2.3)}$$

$$\text{Porosity capacity} = h_i \times \phi_i \quad \text{---------- (2.4)}$$

$$\text{Cumulative porosity capacity} = \sum h_i \times \varphi_i \quad \text{---------- (2.5)}$$

Arithmetic mean of permeability:

$$\bar{k} = \frac{\sum (h_i \times k_i)}{\sum h_i} \quad \text{---------- (2.6)}$$

Geometric mean of permeability:

$$\bar{k} = 10^{\frac{\sum(h_i \times \log k_i)}{\sum h_i}} \text{ ----------(2.7)}$$

Harmonic mean of permeability:

$$\bar{k} = \frac{\sum h_i}{\sum \frac{h_i}{k_i}} \text{ ----------(2.8)}$$

$$\text{Permeability capacity} = h_i \times k_i \text{ (mD.ft) ---------- (2.9)}$$

$$\text{Cumulative permeability capacity} = \sum h_i \times k_i \text{ (mD.ft) ---------- (2.10)}$$

$$\text{Frequency} = \frac{\text{number of samples in a range}}{\text{total number of samples}} \text{ ---------- (2.11)}$$

Table 2.1 illustrates the results and degree of heterogeneity according to coefficient of variation for the six wells. Tables 2.2 and 2.3 show the data interpretation of permeability and porosity analysis while Figures 2.1 and 2.2 are show the frequency distribution for the same parameters for well A-02 as an example. The rest of the tables and figures for the other wells are available in Appendix-B.

2.3.2 Graphical representation of conventional core analysis

Conventional core analysis parameters are graphically displayed to maximize information content and to ease their interpretation. Graphic representation of core analysis data in log histograms and frequency distribution permit direct visual comparison of core data in multi-well reservoir studies. Graphical and statistical analysis may also reveal trends in reservoir quality which are not readily extracted from only the numerical core data.

2.3.2.1 Histograms

Frequency distribution histogram plots allow visual inspection of the variability of a petrophysical parameter. In common frequency distribution analysis, an incremental value of a petrophysical parameter is plotted on the x-axis, vertical bars on the y-axis represent the percentage or the number of the petrophysical parameter falling within the increment. Cumulative frequency curves indicated by ascending order are also presented in Figures 2.1 and 2.2. Frequency distribution histogram plots are is

particularly useful for comparing petrophysical parameters from different core intervals or different wells.

Table 2.1. The results of statistical analysis data for the studied wells.

Well Number	A-01	A-02	A-03	B-01	C-01	C-02
Number of samples	51	463	86	253	140	94
Minimum value of permeability	0.02	0.001	0.020	0.020	3.10	0.24
Maximum value of permeability	838.0	960	991.39	2434	1979	1520
Arithmetic average	62.85	28.01	58.27	336.82	505.7	241
Harmonic average	0.523	0.062	0.292	1.191	70.09	3.40
Geometric average	7.850	0.973	4.77	59.991	327.4	44.82
SD (standard deviation)	151	103.35	158.13	438.53	379. 7	315
C_v (coefficient of variation)	**2.4**	**3.69**	**2.71**	**1.30**	**0.75**	**1.31**

Table 2.2. Statistical analysis of horizontal plug permeability for well A-02.

Permeability Range (mD)	**Samples in range**	**Mean Permeability(mD) (Arithmetic Average)**	**Frequency (%)**	**Cumulative Frequency (%)**
<0.01	11	0.01	2.44	2.44
0.01-0.02	16	0.01	3.55	5.99
0.02-0.04	31	0.03	6.87	12.86
0.04-0.08	31	0.06	6.87	19.73
0.08-0.16	38	0.12	8.43	28.16
0.16-0.32	46	0.24	10.20	38.36
0.32-0.64	46	0.45	10.20	48.56
0.64-1.25	41	0.92	9.09	57.65
1.25-2.50	33	1.74	7.32	64.97
2.50-5.00	30	3.49	6.65	71.62
5- 10	27	6.77	5.99	77.61
10- 20	28	14.83	6.21	83.81
20- 40	21	28.74	4.66	88.47
40- 80	19	64.95	4.21	92.68
80- 160	11	119.36	2.44	95.12
160- 320	9	236.49	2.00	97.12
320- 640	9	456.26	2.00	99.11
640-1280	4	792.71	0.89	100.00

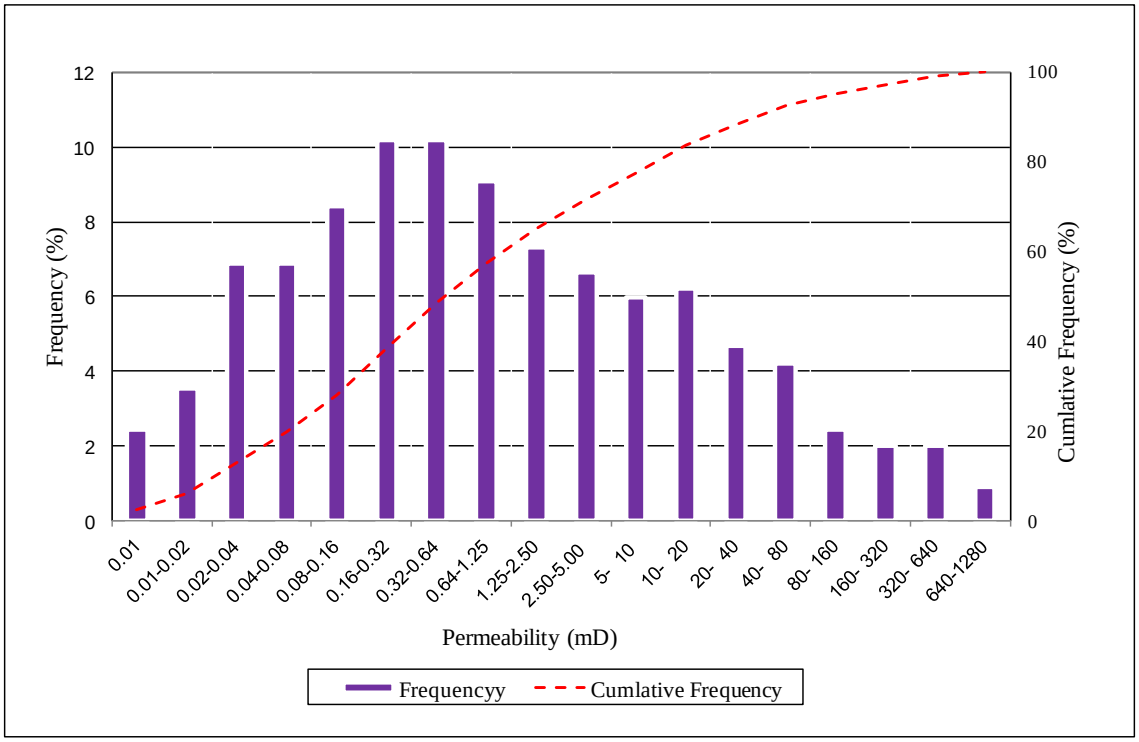

Figure 2.1. Horizontal permeability frequency distribution of well A-02.

Table 2.3. Statistical analysis of porosity for well A-02.

Porosity Range (%)	Samples in range	Mean Porosity (%)	Frequency (%)	Cumulative Frequency (%)
0-2	25	1.10	5.34	5.34
2-4	57	2.98	12.18	17.52
4-6	54	4.93	11.54	29.06
6-8	73	6.91	15.60	44.66
8-10	95	8.98	20.30	64.96
10-12	79	10.92	16.88	81.84
12-14	48	12.86	10.26	92.09
14-16	26	14.83	5.56	97.65
16-18	8	16.76	1.71	99.36
18-20	3	18.34	0.64	100.00

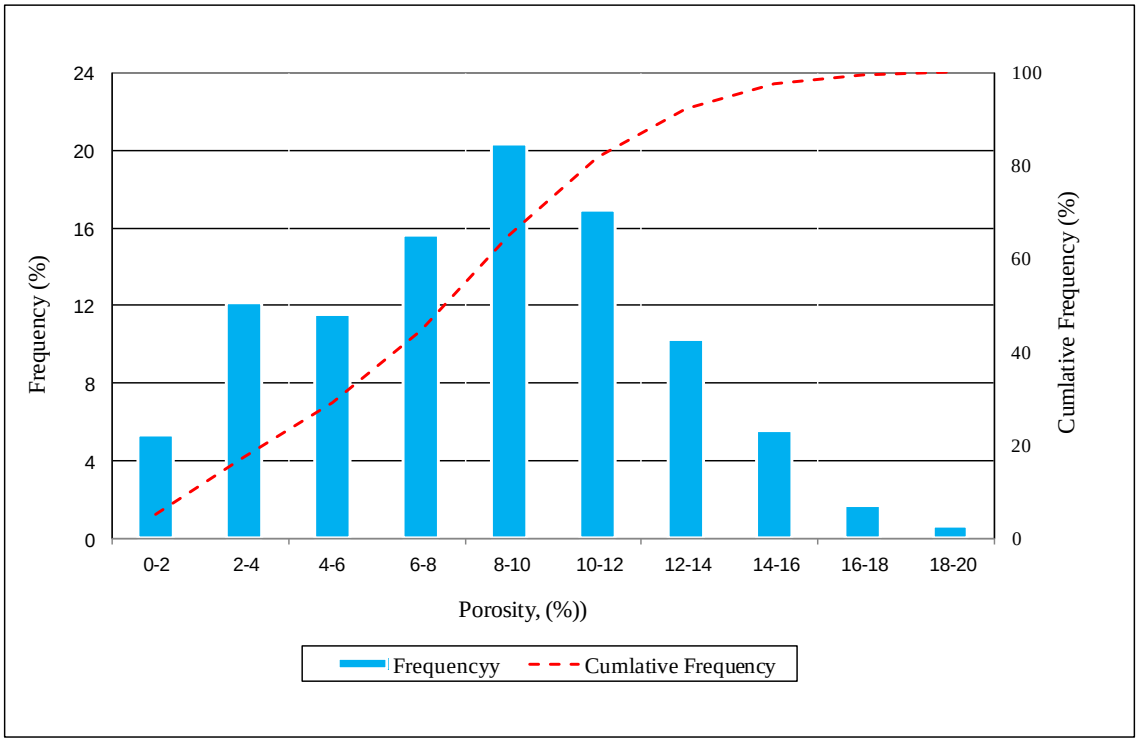

Figure 2.2. Porosity frequency distribution of well A-02.

2.4 Dykstra-Parsons Coefficient

The most common measure of permeability variation used in the petroleum industry is $V_{DP,}$ the Dykstra-Parsons coefficient (Dykstra and Parsons, 1950):

$$V_{DP} = \frac{k_{50} - k_{84.1}}{k_{50}} \quad \text{---------- (2.12)}$$

The Dykstra-Parsons permeability variation is a measure of the uniformity of permeability distribution throughout a zone. It is predicted on the finding that permeability usually has a log normal distribution. That is, when the number of samples within a permeability range is plotted against the values of log permeability, this usually yields a bell-shaped curve. This relationship allows the calculation of the permeability variation by arranging the permeability values in a descending order and plotting each permeability value against the percentage of the total number of values that exceed that permeability value. The plot is done on probability paper. A best-fit straight line (Figure 2.3) is then drawn through the points. Permeability values at 50% and 84.1% are read and used in the calculation. The 50% value is related to the mean permeability and 84.1% value is related to the standard deviation in a normal distribution. The values of

permeability variation can range from zero to 1, with an exactly uniform set of data having a value of zero.

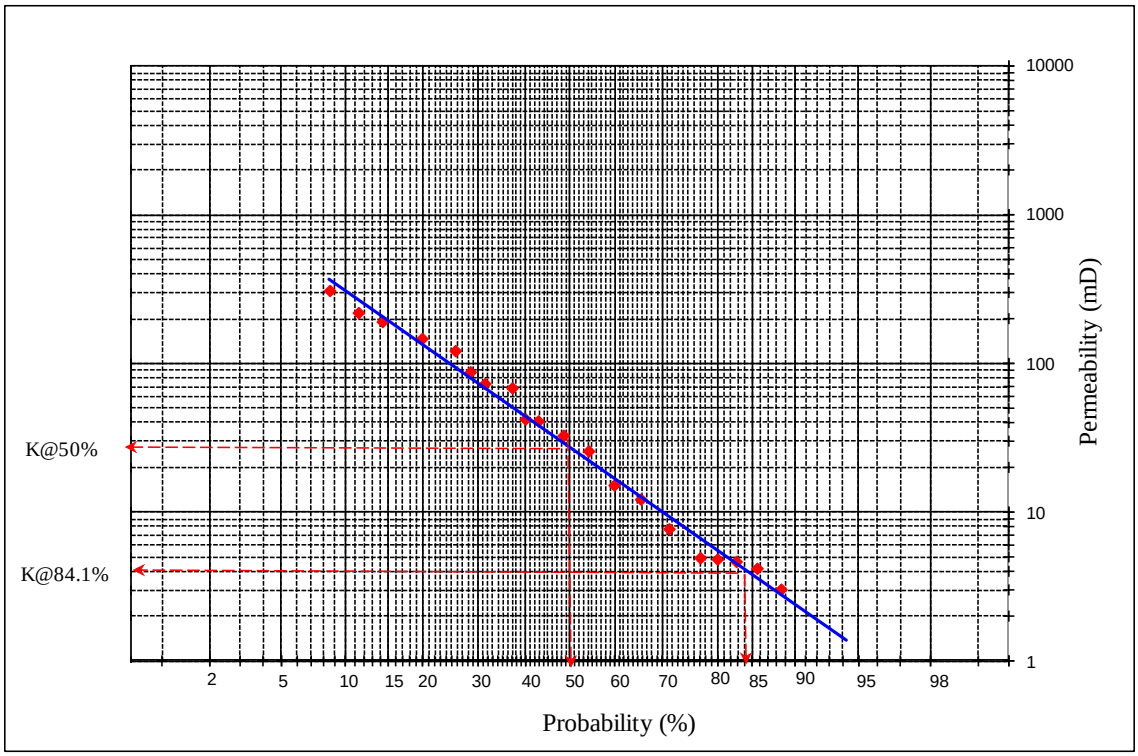

Figure 2.3. Probability plot for Dykstra-Parsons permeability variation determination.

2.4.1 Application of Dykstra-Parsons Coefficient in the Studied Area

The Dykstra-Parsons coefficient was computed from the permeability data for the six wells in fields A, B and C in North Africa. The probability associated with each data point is the thickness of the interval represented by the data point. $K_{0.50}$ and $K_{0.841}$ are taken from a "best fit" line through the data when they are plotted on a logarithmic probability plot. Figures 2.4-2.9 show the best fit line for each well and Table 2.4 shows the summarised results for Dykstra-Parson coefficient (V_{DP}) describing the degree of heterogeneity for each well.

Table 2.4. The degree of heterogeneity (Dykstra-Parsons method) for the studied wells.

Well Number	**A-01**	**A-02**	**A-03**	**B-01**	**C-01**	**C-02**
Number of samples.	35	155	69	197	142	84
K @ 50%	28.4	25	15.49	135	366	73
K @ 84.1%	5.104	6	2.3	20	149	9
V_{DP}	**0.82**	**0.76**	**0.85**	**0.85**	**0.59**	**0.87**

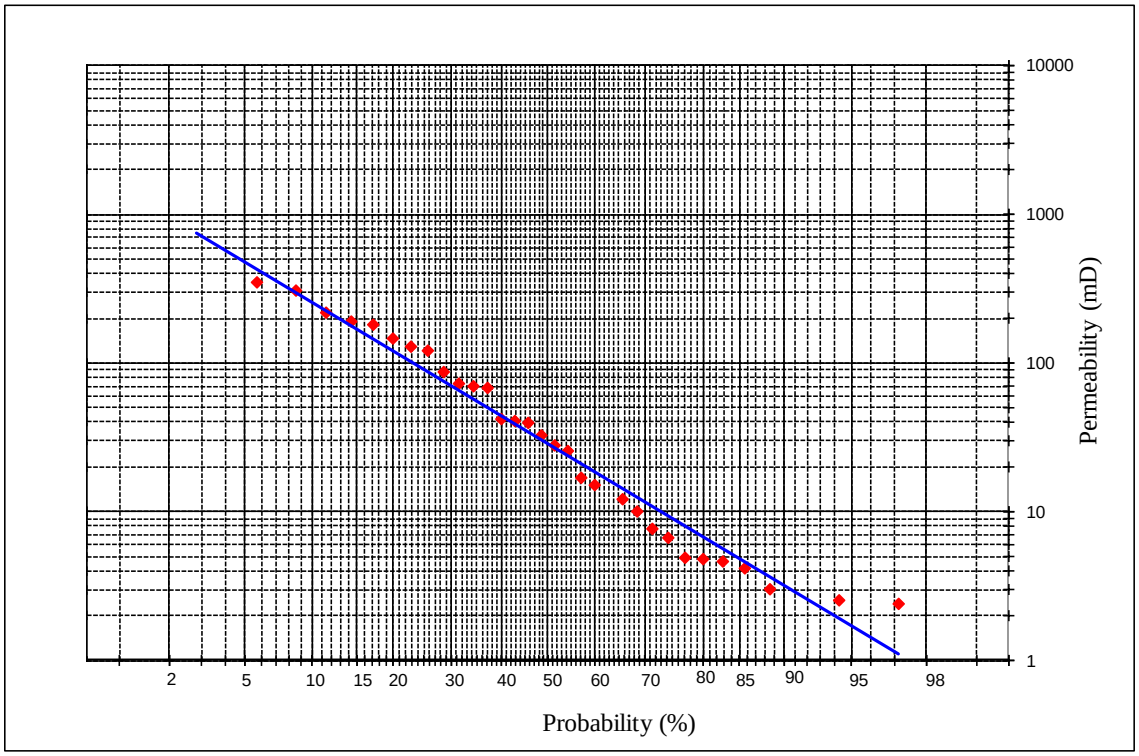

Figure 2.4. Dykstra-Parsons coefficient of permeability variation for well A-01.

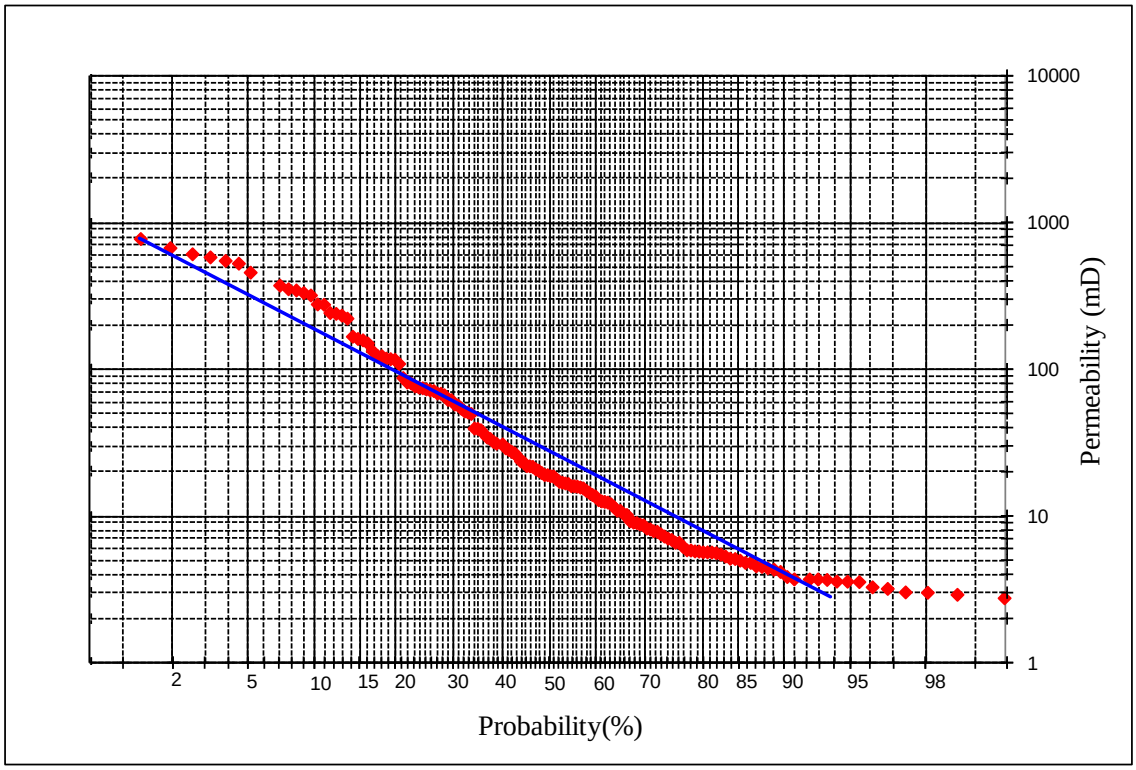

Figure 2.5. Dykstra-Parsons coefficient of permeability variation for well A-02.

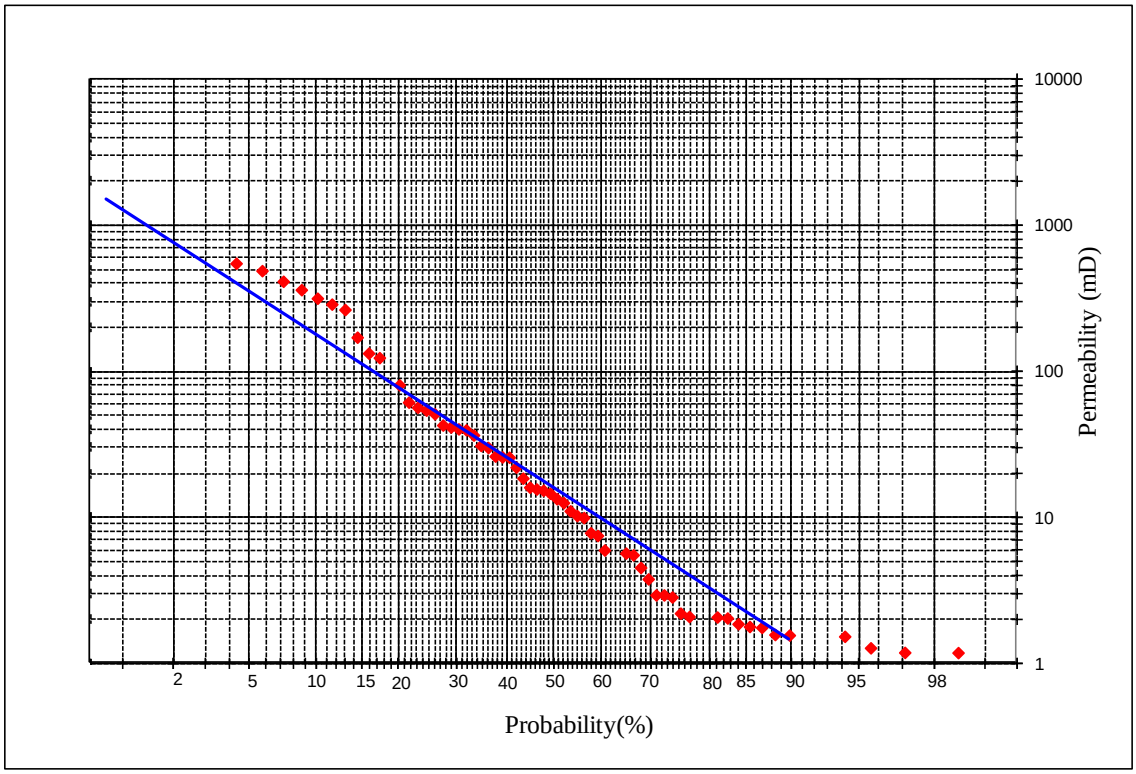

Figure 2.6. Dykstra-Parsons coefficient of permeability variation for well A-03.

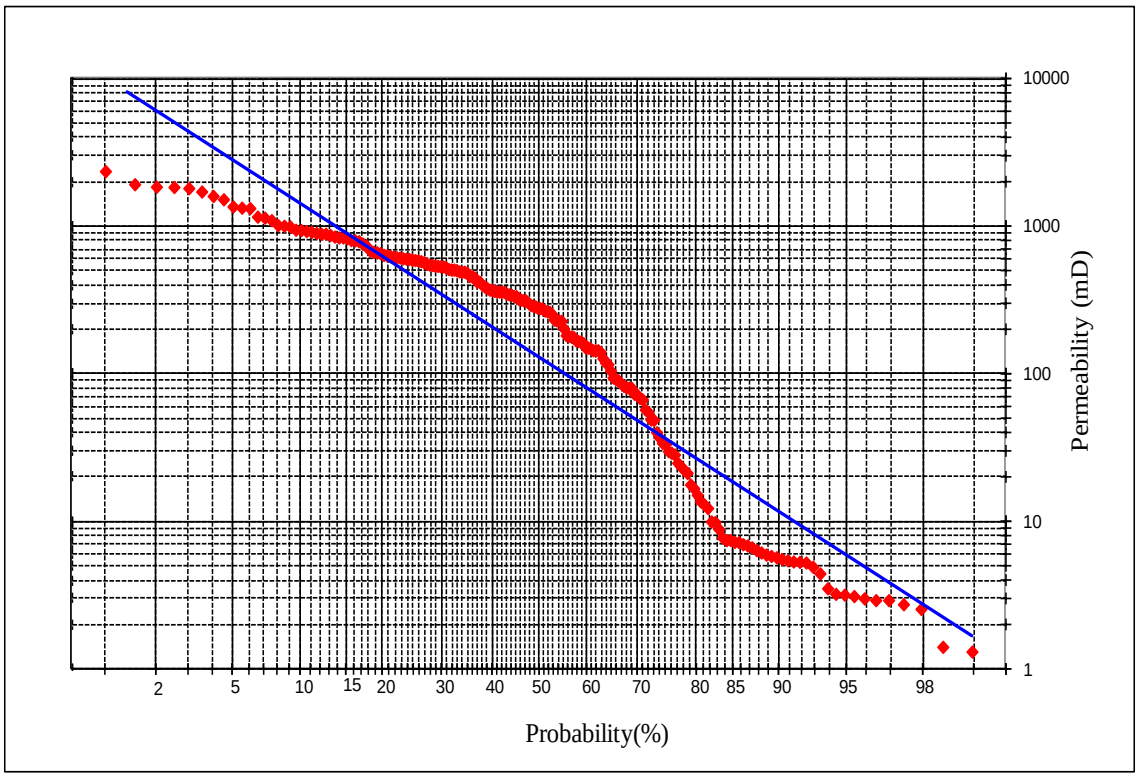

Figure 2.7. Dykstra-Parsons coefficient of permeability variation for well B-01.

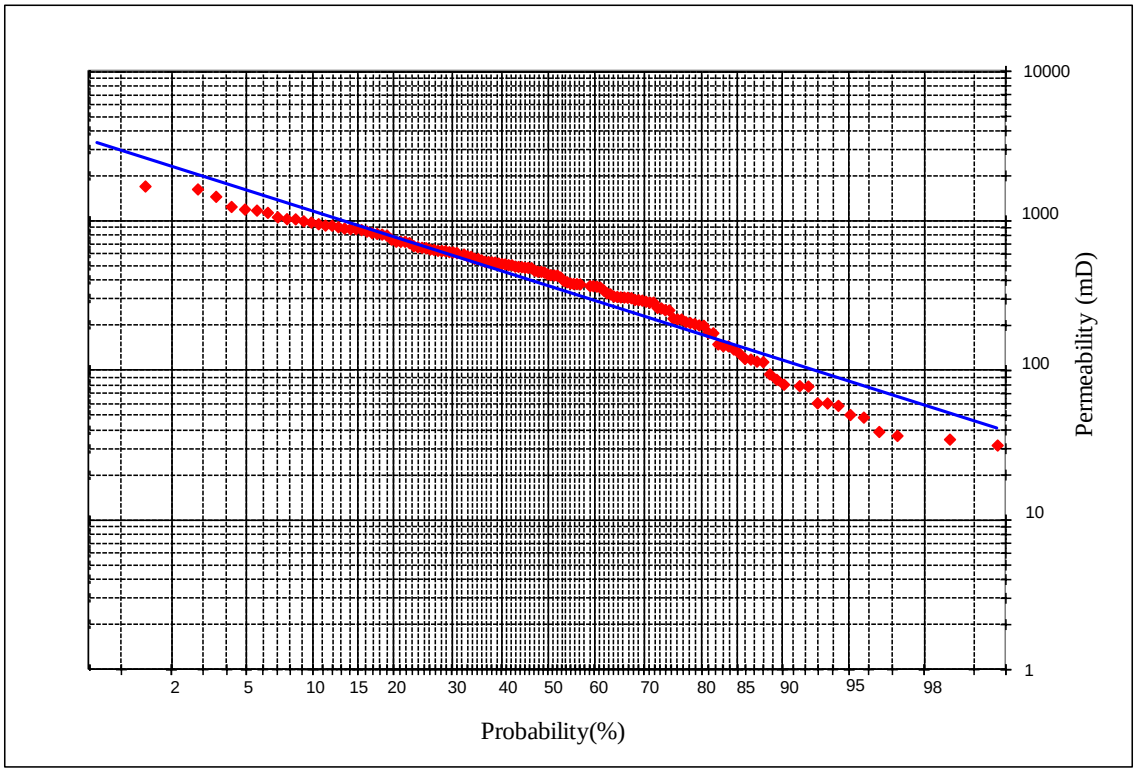

Figure 2.8. Dykstra-Parsons coefficient of permeability variation for well C-01.

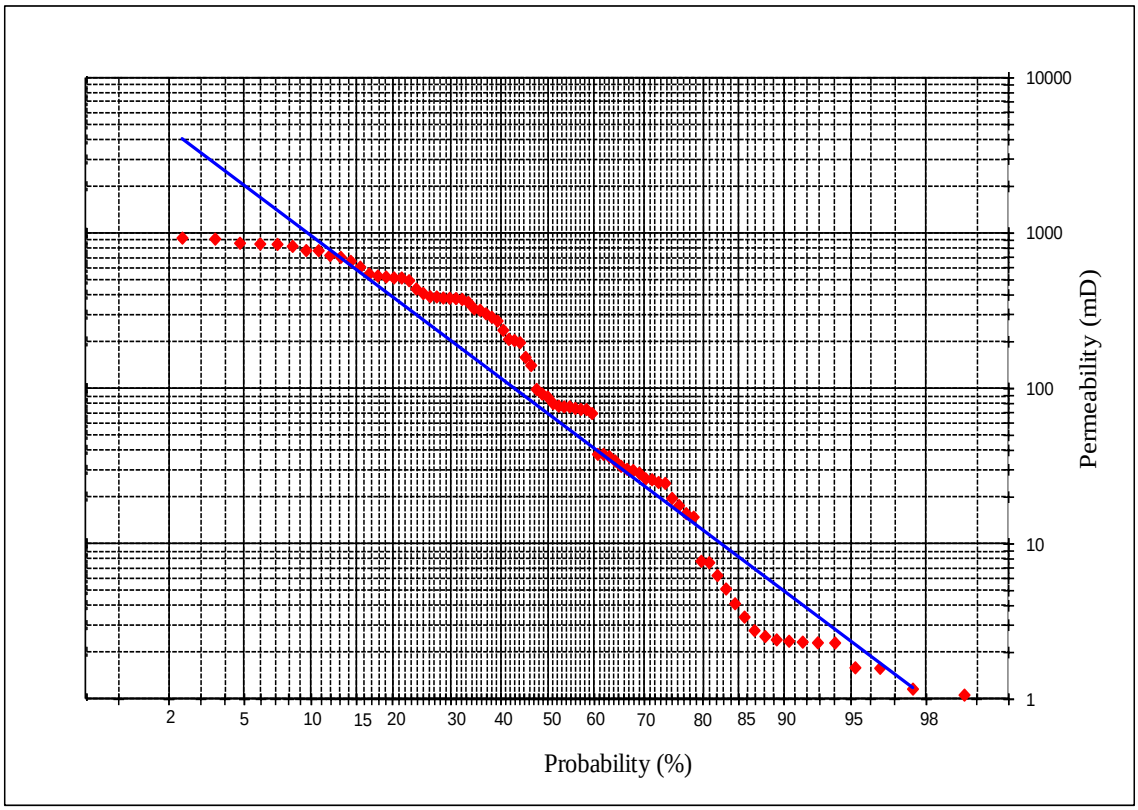

Figure 2.9. Dykstra-Parsons coefficient of permeability variation for well C-02.

2.5 Lorenz Plot (LP)

M. O. Lorenz (1905) first conceived the Lorenz Plot (LP), which, as a statistical tool, was used to accurately describe the unequal distribution of wealth in society, where a few people owned a large portion of the wealth. Lake and Jensen (1991), in their review of heterogeneity measures used in reservoir characterization, described the Lorenz procedure to include porosity variations. Also if the elements in the Lorenz coefficient are uniform continuous layers between the inlet and outlet of the medium, the Lorenz Plot becomes identical to the fractional flow curve used in immiscible displacement calculations. In broad terms, the Lorenz curve relates the static core data and the dynamic flow properties (i.e. the fluid flow characteristics) at the well bore. The LP provides a graphical means of representing the balance of flow and storage elements in reservoirs (Pinisetti, 2000).

2.5.1 Lorenz Plot construction

To construct a Lorenz Plot, first arrange the permeability values in descending order of K/Ø and then calculate the partial sum.

(i) The cumulative permeability-thickness, Σkh, and the cumulative reservoir thickness, Σh, are calculated.

(ii) The permeability-thickness data is arranged in a descending order.

(iii) The flow capacity (F_j) and storage capacity (C_j) are calculated as follows (Jensen et al., 1997):

$$\mathbf{F_j} = \frac{\sum_{j=1}^{J} \mathbf{k_j h_j}}{\sum_{i=1}^{I} \mathbf{k_i h_i}} \quad \text{---------- (2.13)}$$

$$\mathbf{C_j} = \frac{\sum_{j=1}^{J} \boldsymbol{\phi}_j \mathbf{h_j}}{\sum_{i=1}^{I} \boldsymbol{\phi}_i \mathbf{h_i}} \quad \text{---------- (2.14)}$$

Where $1 \leq J \leq I$ and there are I datasets.

iv) The calculated Fj and Cj are plotted in a linear graph scale from 0 to 1 on each axis (Figure 2.10).

2.5.2 Lorenz Coefficient (Lc)

The Lorenz coefficient is a value used to describe the degree of heterogeneity by which any permeability distribution is characterised. Schmalz and Rahme (1950) introduced a single parameter that describes the degree of heterogeneity within a pay zone section. This term is called the Lorenz Coefficient (Lc) and varies between zero, for a completely homogenous system, to one for a completely heterogeneous system. Figure 2.11 shows an illustration of the flow capacity distribution. A completely uniform system would have all permeabilities and porosities equal, and a plot of the normalised ∑kh versus ∑Øh would be a straight line. It indicates that as the degree of contrast between high and low values of permeability increases the plot exhibits greater concavity towards the upper left corner. This would indicate more heterogeneity, i.e., the severity of deviation from a straight line is an indication of heterogeneity (Ahmed, 2001).

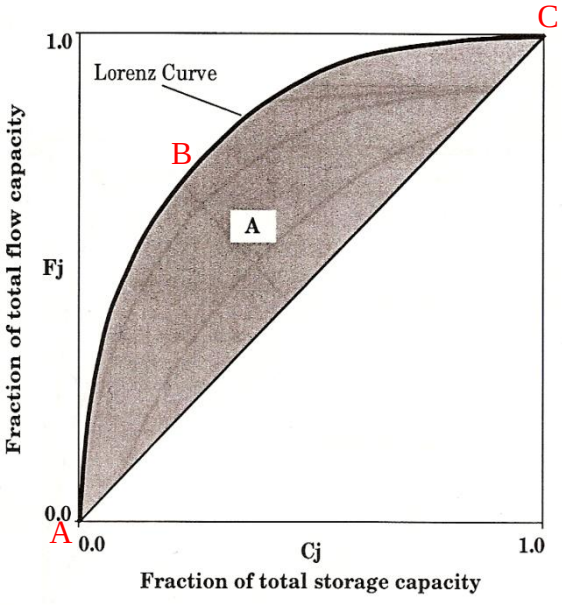

Figure 2.10. Determination of the Lorenz coefficient.

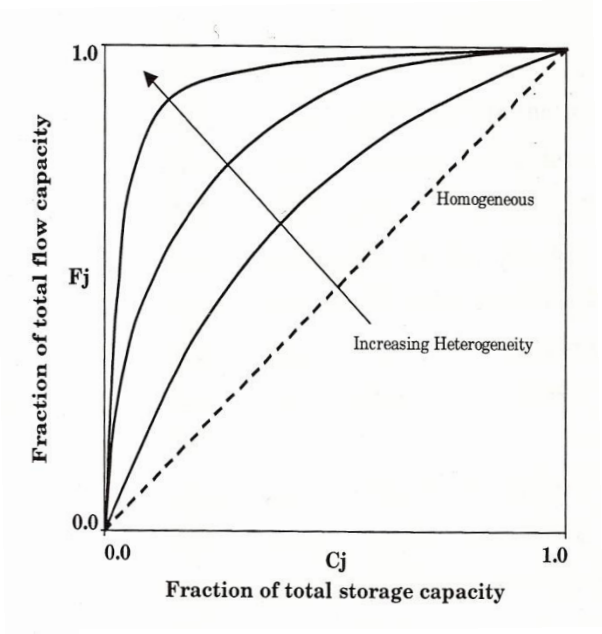

Figure 2.11. The Lorenz plot shows an illustration of the flow capacity range of increasing heterogeneity.

It is instructive to review the computation of the Lorenz coefficient from porosity and permeability data. If A represent the area between the curve and the diagonal line (the shaded region in Figure 2.10) the Lorenz coefficient (Lc) is defined as Lc=2A. The Lorenz coefficient,Lc, is given by twice the area (the shaded region in Fig2.10) between the Lorenz curve ABC and the diagonal AC (Lake, 1989).Using the trapezoidal integration rule (Lake and Jensen, 1991; Jensen et al. 2000) then:

$$Lc = \frac{1}{2I\sum_{i=1}^{I}\frac{k_i}{\phi_i}} \sum_{i=1}^{I}\sum_{J=1}^{J}\left|\frac{k_i}{\phi_i} - \frac{k_j}{\phi_j}\right| \quad \text{---------- (2.15)}$$

The Lorenz coefficient has several advantages over the Dykstra-Parsons coefficient:

1. It can be calculated with good accuracy for any distribution. Lc is, however, still not a unique measure of variability.

2. It does not rely on best-fit procedures. In fact, being essentially a numerical integration, there is typically less calculation error in Lc than in V_{DP}.

2.6 Transmissive and Storage Dominated Global Hydraulic Elements (GHEs) in the studied area

The transmissivity (flow) capacity and storability (storage) capacity can be estimated for the Global Hydraulic Elements GHE by using a Lorenz plot. It is useful to identify the storage capacity and flow capacity of the reservoir formation and it's very useful to use this information in a petrography to see what is the difference between the GHEs dominating storage capacity and GHEs which are dominating flow capacity. The properties transmissivity and storativity are important in well test analysis and the identification of flow intervals, they will affect the thickness assigned in the determination of predominant flow interval indicated. (Zheng et al. 2000). Transmissive (TGHE) and storage (SGHE) dominated are defined by the intercept of the tangent with a unit slop of the Lorenz curve.

Cores recovered from the reservoir sections of six wells (A-01, A-02, A-03, B-01, C-01, and C-02) from the three fields (A, B and C) of the Nubian Sandstone in North Africa were available for this study. A static description was carried out using the Lorenz Plot

(LP) in order to estimate the reservoir heterogeneity and describe the permeability variation. The flow and storage characteristics are described in terms of Global Hydraulic Elements (GHEs) on the Lorenz plots. GHEs are defined and described in more detail in section 2.8. Essentially they are like hydraulic flow units, but are plotted on a pre-determined template (Corbett and Potter, 2004) so that data from any reservoir can readily be split into GHEs and be compared to any other reservoir in an identical fashion. For well A-01 (Figure 2.12) the Lorenz plot shows that approximately 75% of the flow would be coming from global hydraulic elements (GHEs) 7 and 8, which provide only 25% of the storage. The proportion of the flow capacity of these GHEs is more than their proportion of storage capacity, thus they are transmissive- dominated GHEs (TGHE). The core plug data also indicate that a zone of high permeability exists (Figure 2.13). Only 25% of the total flow is coming from GHEs 4, 5, and 6, which provide 75% of the storage capacity. The storage capacity of these is more than their flow capacity, therefore they are storage-dominated GHEs (SGHE) (Corbett et al., 2001). The Lorenz Coefficient (Lc) as a measure of heterogeneity was calculated to be 0.662.

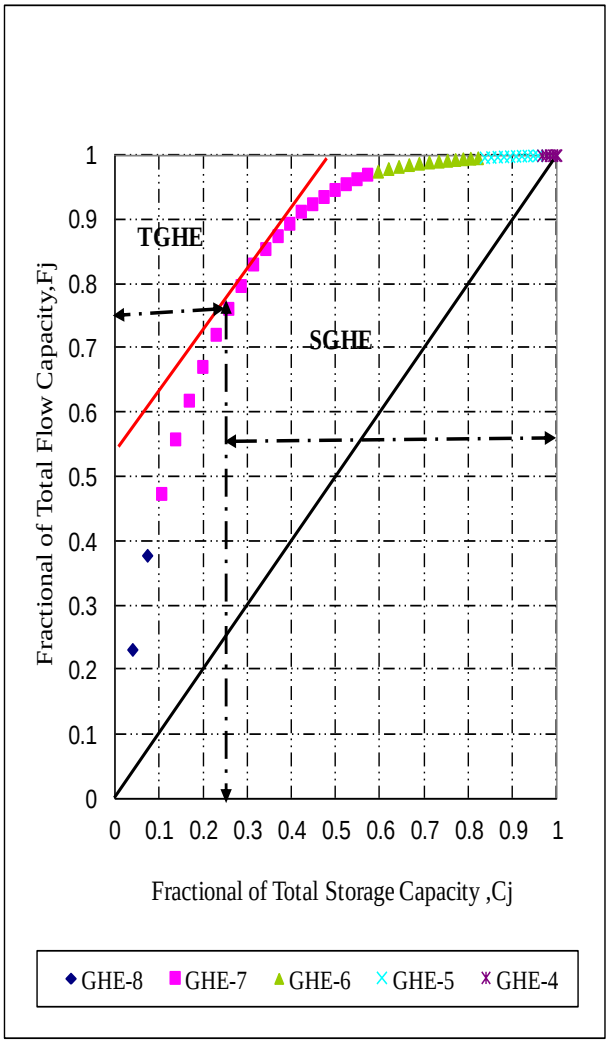

Figure 2.12. The Lorenz Plot for well A-01 showing the flow and storage contribution. Transmissive-dominated GHEs (TGHE) and storage-dominated GHEs (SGHE) are indicated. Global hydraulic elements (GHEs) 7 and 8 are transmissive-dominated, which provide almost 75% of the flow capacity. Global hydraulic elements (GHEs) 4, 5 and 6 are more storage-dominated, which provide almost 75% of the total storage capacity.

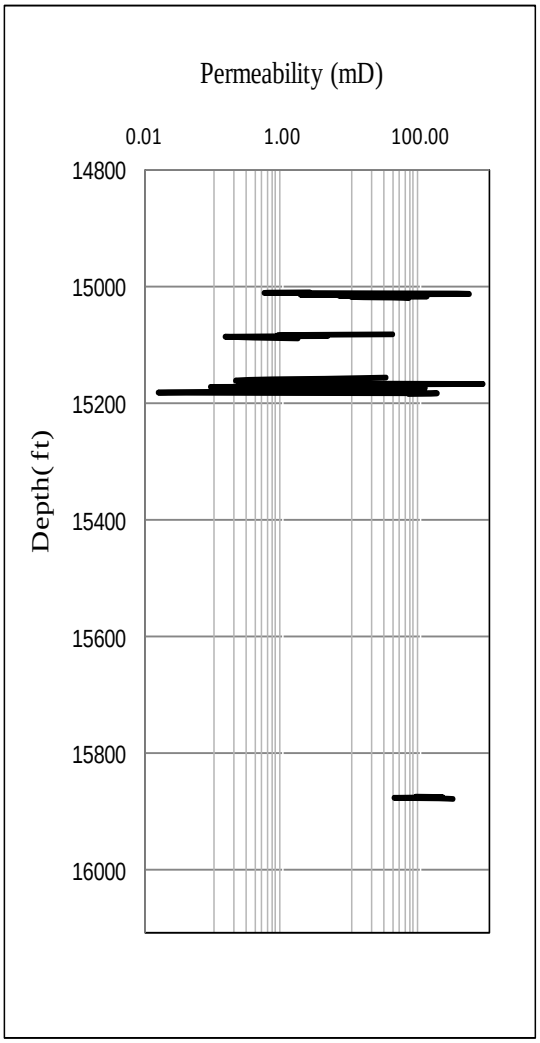

Figure 2.13. Core plug permeability for well A-01.

The Lorenz Plot for well A-02 (Figure 2.14) shows that approximately 83% of the total flow is coming from GHEs 7 and 8 (transmissive-dominated GHEs), which provide 17% of the storage. The core plug data clearly show high permeability zones (Figure 2.15). Only 17% of the total flow is coming from GHEs 2, 3, 4, 5 and 6, which provide 83% of the storage capacity (storage-dominated GHEs). The Lorenz Coefficient (Lc) was calculated to be 0.80.

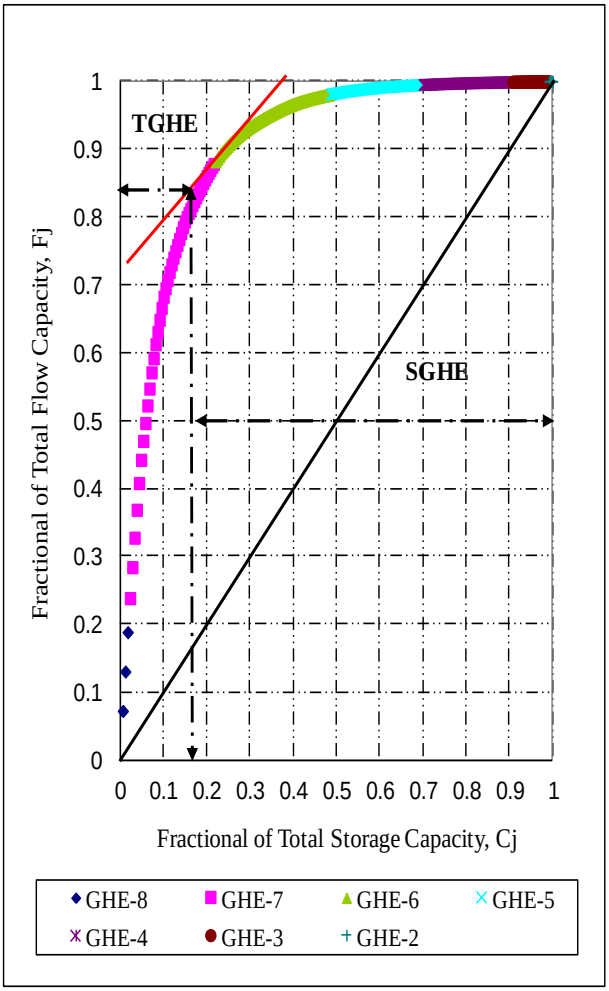

Figure 2.14. The Lorenz Plot for well A-02 showing the flow and storage contribution. Transmissive-dominated GHEs (TGHE) and storage-dominated GHEs (SGHE) are indicated.

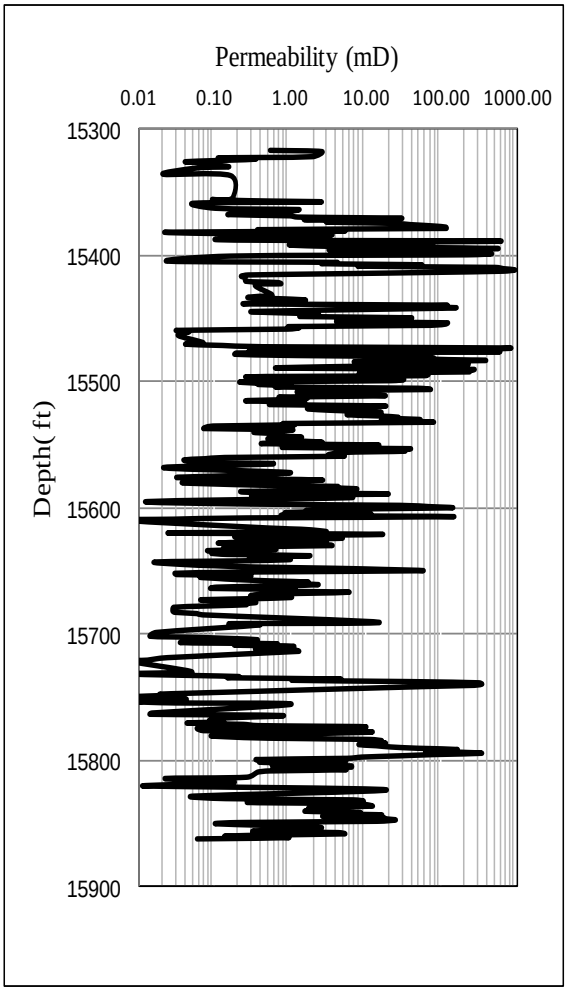

Figure 2.15. Core plug permeability for well A-02.

The Lorenz plot for well A-03 (Figure 2.16) shows that 80% of the total flow is coming from GHE 8 and 7 (transmissive-dominated GHEs), which provide 18% of the storage. Only 20% of the total flow is coming from GHEs 3, 4, 5 and 6, which provide 82% of the storage capacity (storage-dominated GHEs). The Lorenz coefficient (Lc) as a measure of heterogeneity was calculated to be 0.765. Also in well A-03 core plug permeability data shows low, medium and high values of permeability (Figure 2.17).

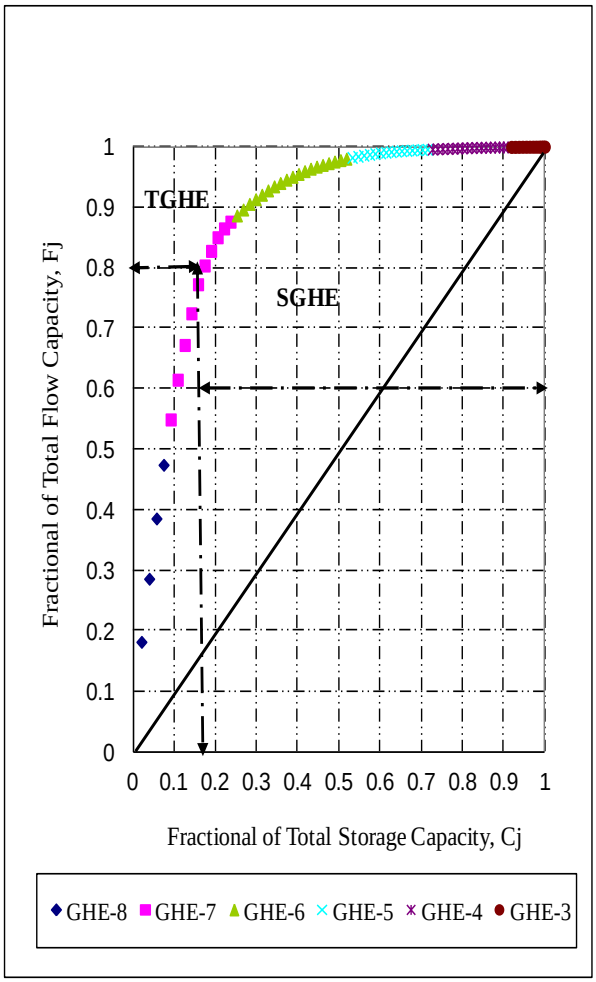

Figure 2.16. The Lorenz Plot for well A-03 showing the flow and storage contribution. Transmissive-dominated GHEs (TGHE) and storage-dominated GHEs (SGHE) are indicated.

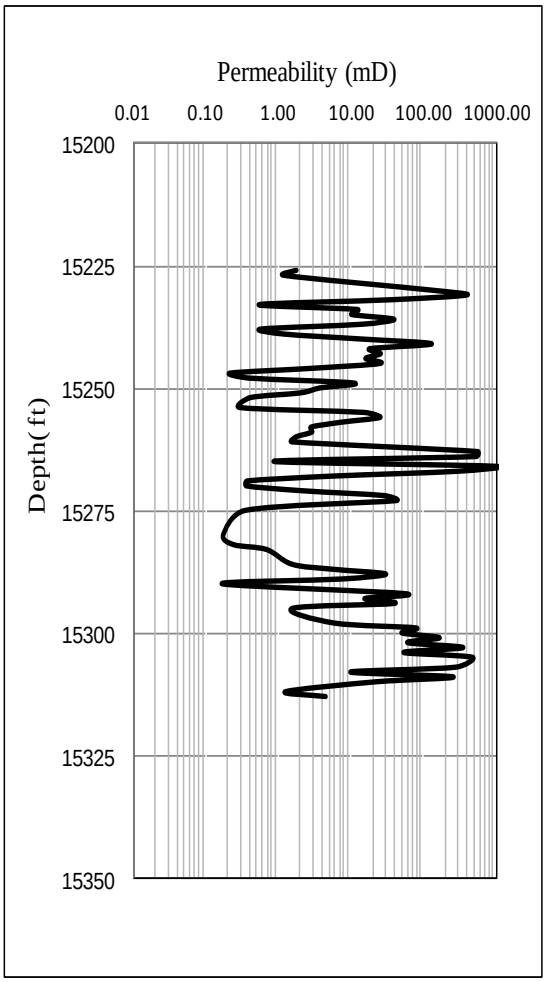

Figure 2.17. Core plug permeability for well A-03.

The Lorenz plot for well B-01 (Figure 2.18) shows that 78% of the total flow is coming from GHEs 7 and 8 (transmissive-dominated GHEs), which provide only 40% of the storage. Only 22% of the total flow is coming from GHEs 4, 5, and 6, which represent 60% of the storage capacity (storage-dominated GHEs). The Lorenz Coefficient (Lc) as a measure of heterogeneity was calculated to be 0.51. This value is the lowest one in the studied wells and this well appears to be moderately heterogeneous. Also in well B-01 the core plug permeability data shows a range of permeability, with a large proportion in the high zone (Figure 2.19).

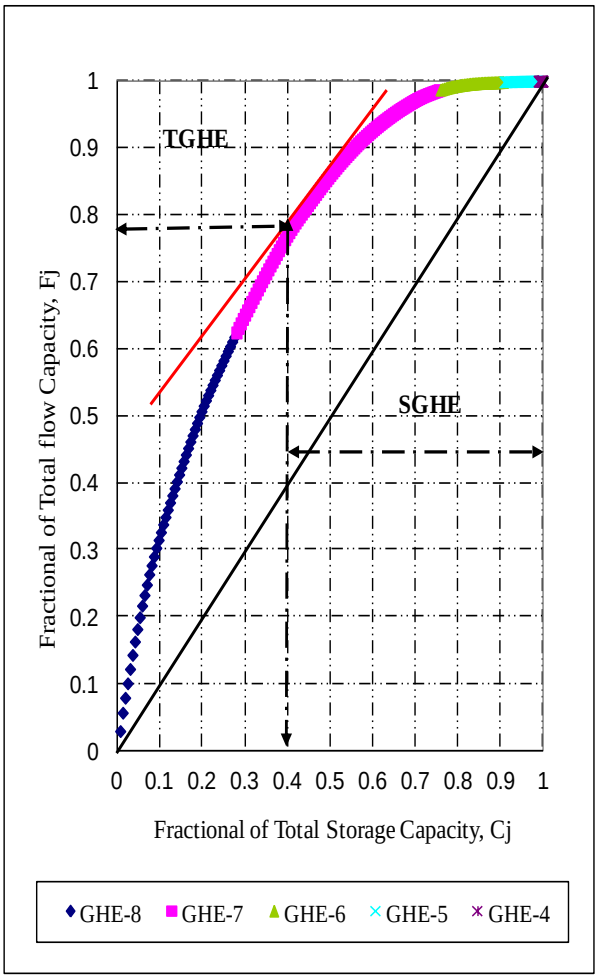

Figure 2.18. The Lorenz Plot for well B-01 showing the flow and storage contribution. Transmissive-dominated GHEs (TGHE) and storage-dominated GHEs (SGHE) are indicated.

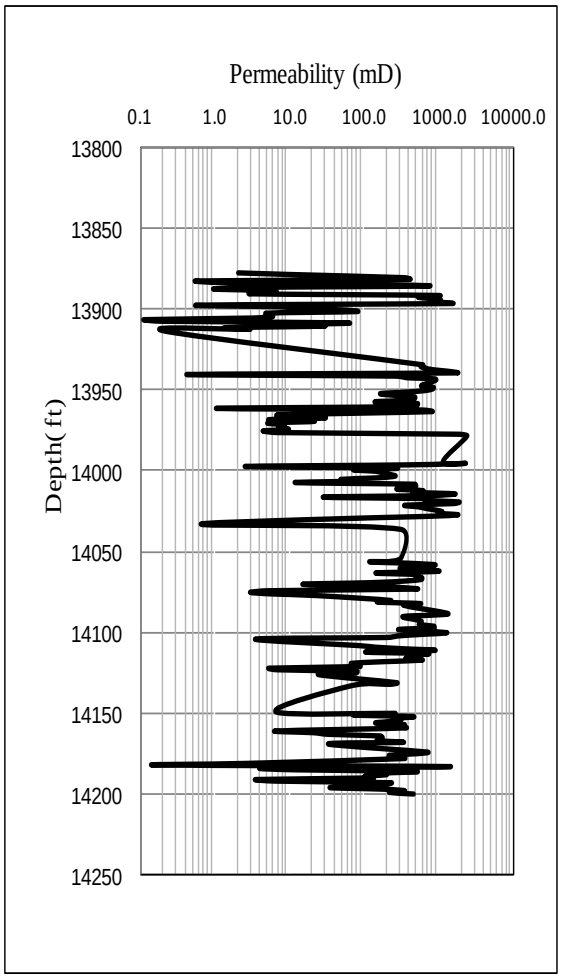

Figure 2.19. Core plug permeability for well B-01.

The Lorenz plot for well C-01 (Figure 2.20) shows that 68% of the total flow is coming from GHEs 7 and 8 (transmissive-dominated GHEs), which provide only 40% of the storage. Only 32% of the total flow is coming from GHEs 6, which represent 60% of the storage capacity (storage-dominated GHEs). The Lorenz coefficient (Lc) was calculated to be 0.48, and this well appears to be less heterogeneous because the formation is mainly medium to coarse-grained, very poorly cemented, moderate to well sorted, angular to subangular. In well C-01 core plug permeability data generally show medium to high permeability values (Figure 2.21).

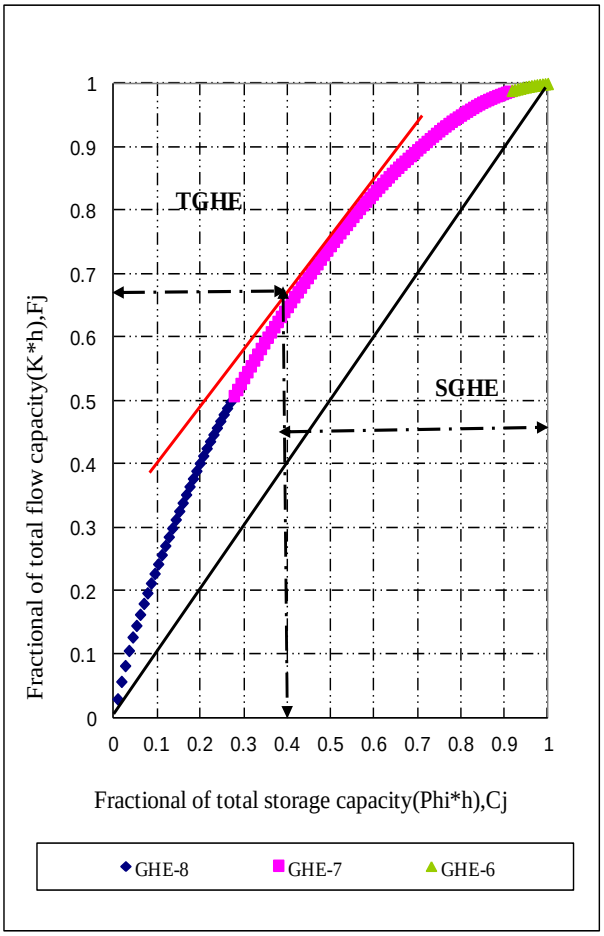

Figure 2.20. The Lorenz Plot for well C-01 showing the flow and storage contribution. Transmissive-dominated GHEs (TGHE) and storage-dominated GHEs (SGHE) are indicated.

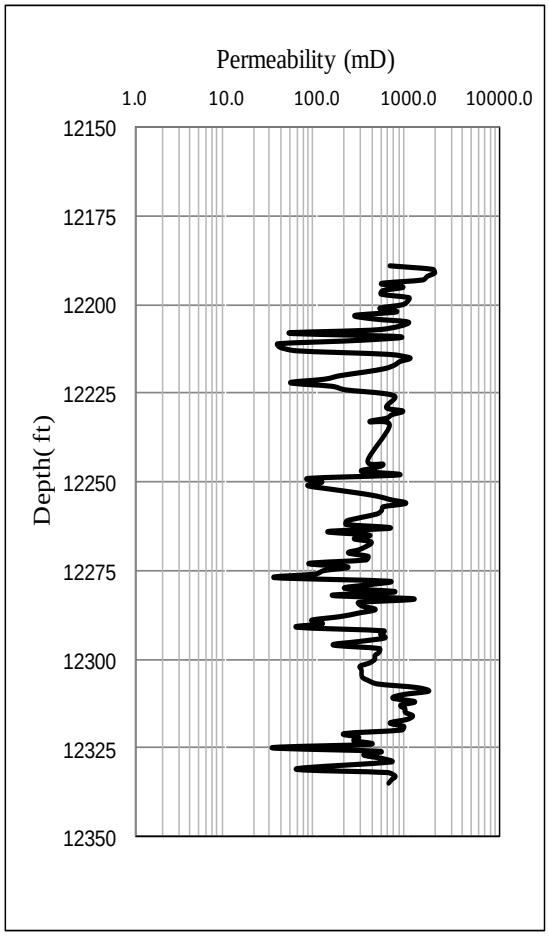

Figure 2.21. Core plug permeability for well C-01.

In well C-02, the sandstone is mainly fine to coarse-grained, generally fair to good porosity, with locally some thin layers of siltstone. The Lorenz plot for well C-02 (Figure 2.22) shows that 88% of the total flow is coming from GHEs 7 and 8 (transmissive-dominated GHEs), which provide only 42% of the storage. Only 12% of the total flow is coming from GHEs 3, 4, 5, and 6, which represent 58% of the storage capacity (storage-dominated GHEs). The Lorenz coefficient (Lc) was calculated to be 0.54, and this well appears to be moderately heterogeneous. In well C-02 core plug permeability data generally show medium to high permeability values (Figure 2.23).

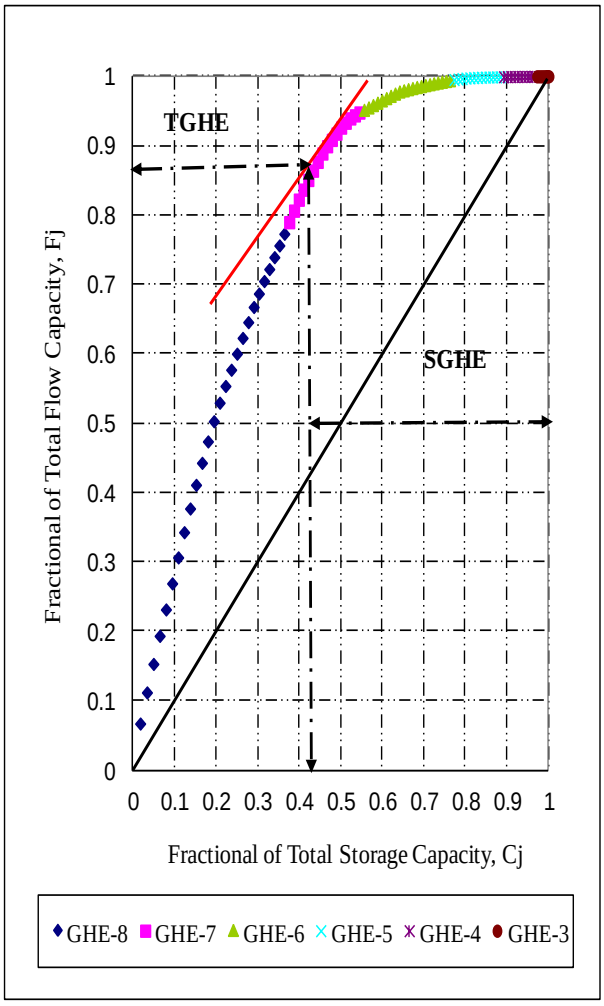

Figure 2.22. The Lorenz Plot for well C-02 showing the flow and storage contribution. Transmissive-dominated GHEs (TGHE) and storage-dominated GHEs (SGHE) are indicated.

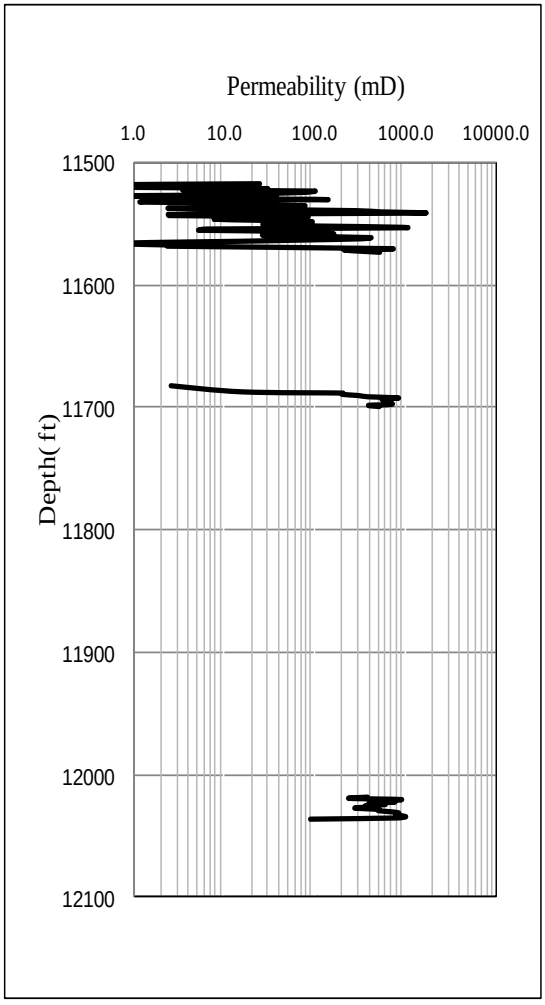

Figure 2.23. Core plug permeability for well C-02.

Table 2.5. The results of the Lorenz coefficient values of the studied wells.

Well Number	**A-01**	**A-02**	**A-03**	**B-01**	**C-01**	**C-02**
Number of samples	48.0	353.0	77.0	244.0	142	92.0
Lorenz coefficient (Lc)	**0.662**	**0.80**	**0.767**	**0.51**	**0.48**	**0.54**

2.7 Hydraulic Units

The concept of hydraulic flow units has been used in the oil industry with a good deal of success during the past few years. Amaefule et al. (1993) defined a hydraulic flow unit (HU) as the representative elementary volume (REV) of the total reservoir rock within which geological attributes of texture, mineralogy, sedimentary structure, bedding contacts and petrophysical properties (porosity, permeability and capillary pressure) that affect fluid flow are internally consistent and predictably different from properties of another rock volume. Based on the Kozeny-Carman equation (Kozeny, 1927; Carmen, 1937) and the concept of mean hydraulic radius, Amaefule et al. (1993) proposed a method for identification of hydraulic units. For a circular and cylindrical capillary tube, the mean hydraulic radius is defined as the ratio of the volume open to flow to the internal surface area, r_{mh} , as follows:

$$r_{mh} = \frac{\pi r^2 L}{2\pi r L} = \frac{r}{2} \quad \text{---------- (2.16)}$$

where r is the radius of the capillary tube and L is the capillary tube length. The Kozeny-Carman equation relates permeability, effective porosity, mean hydraulic radius and tortuosity as follows:

$$k = \frac{\phi_e}{2\tau^2}\left(\frac{r}{2}\right)^2 = \frac{\phi_e}{2\tau^2}\left(r_{mh}\right)^2 \quad \text{---------- (2.17)}$$

where k is the permeability, ϕ_e is the effective porosity and τ is tortuosity.

The mean hydraulic radius is related to surface area per unit grain volume S_{gr} and effective porosity as follows:

$$r_{mh} = \frac{1}{S_{gr}}\left(\frac{\phi_e}{1-\phi_e}\right) \quad \text{---------- (2.18)}$$

Substituting Equation 2.18 for the mean hydraulic radius in Equation 2.17, the Kozeny-Carman equation becomes:

$$k = \frac{\phi_e^{\,3}}{(1-\phi_e)^2}\left(\frac{1}{F_g \tau^2 S_{gr}^2}\right) \quad \text{---------- (2.19)}$$

where F_g is the shape factor. The term $F_g\tau^2$ is referred to as the Kozeny constant and usually varies from 5-100 in real reservoir rocks.

2.7.1 Flow zone indicator (FZI) and reservoir quality index (RQI)

Due to the difficulty of estimating an exact value for the Kozeny constant, $F_g\tau^2$, the computation of permeability from Equation 2.19 was often difficult. Amaefule et al. (1993) came to the conclusion that the Kozeny constant is a variable "constant", which varies between hydraulic units, but is constant within a given unit. Tiab and Donaldson (1996) suggest that the Kozeny constant reflects the effect of grain shape, grain size, pore shape and tortuosity. Therefore this constant is more likely to be a constant for a given rock type (rock with similar hydraulic properties) and different for another rock type.

The issue of the variability of the Kozeny constant was addressed by Amaefule et al. (1993). Dividing both sides of equation 2.19 by the effective porosity ϕ_e and taking the square root of both sides gives:

$$0.0314\sqrt{\frac{k}{\phi}} = \frac{\phi_e}{(1-\phi_e)}\left(\frac{1}{\sqrt{F_g}\,\tau\, S_g}\right) \quad \text{---------- (2.20)}$$

where 0.0314 is the permeability conversion factor from μm^2 to mD. Equation 2.20 defines what Amaefule et al. (1993) termed the reservoir quality index (RQI).

$$RQI = 0.0314\sqrt{\frac{k}{\phi_e}} \quad \text{---------- (2.21)}$$

Amaefule et al. (1993) introduced another key parameter, which they called the flow zone indicator (FZI) given by:

$$\mathbf{FZI} = \frac{1}{\sqrt{\mathbf{F_g}}\tau^2 \mathbf{S_g}} = \frac{\mathbf{RQI}}{\phi_z} \quad \text{---------- (2.22)}$$

$$\phi_z = \frac{\phi_e}{1-\phi_e} \quad \text{---------- (2.23)}$$

where ϕz is defined as the ratio of pore volume to grain volume. FZI is a parameter that incorporates the geological attributes of texture and mineralogy to discriminate distinct facies. Taking the logarithm of both sides of Equation 2.22 yields:

$$\text{Log}(\text{RQI}) = \text{Log}(\text{FZI}) + \text{Log}(\phi_z) \quad \text{---------- (2.24)}$$

On a log-log plot of RQI versus ϕz, all samples with similar pore and grain size attributes will lie on a straight line with unit slope. Samples with different FZI will lie on other parallel lines. The flow zone indicator (FZI) of each group of samples can be determined from the intercept of the unit slope line at ϕz equal 1. Samples that lie on the same straight line have similar pore-size attributes and, therefore, constitute a hydraulic unit (HU) according to Amaefule et al. (1993). The basis of the hydraulic unit classification is to identify groups of data that form unit-slope straight lines on the log-log plot of RQI versus ϕz. The permeability of a sample within a HU is then calculated using the mean FZI value and the corresponding sample porosity using the following equation:

$$\text{K} = 1014 \times \overline{\text{FZI}}^2 \frac{\phi_e{}^3}{(1-\phi_e)^2} \quad \text{---------- (2.25)}$$

where $\overline{\text{FZI}}$ is the mean FZI value for a given HU.

2.8 Global Hydraulic Element (GHE) Template

Petrophysicists have long attempted to split hydrocarbon-bearing reservoirs into a limited number of elements, each with their own unique characteristics. The first approach was the Hydraulic Flow Unit (HU) concept as discussed in section 2.7. This method was successful in determining different regimes in a single dataset, such as a cored well, but this method has two major limitations. Firstly, it is very time consuming since one has to work out the hydraulic flow units for each well. Secondly, it doesn't allow one to compare hydraulic flow units from different wells (HU1 from well 1 may not be the same as HU1 from well 2). These limitations are litted by a new concept named "global hydraulic elements (GHEs)" which was developed by Corbett et al. (2003) and Corbett and Potter (2004). This approach is also based on the flow zone indicator (FZI), and has the same underlying theory as the hydraulic flow unit concept. Using Equation 2.25 a GHE template for different values of FZI can be constructed (Figure 2.24). Corbett and Potter (2004) defined ten GHEs (Table 2.6 and Figure 2.24). The number of GHEs and their boundaries were arbitrarily chosen in order to obtain a wide enough range of possible combinations of porosity and permeability in a manageable number of GHEs. The advantages of the GHE template are that one merely has to plot the porosity and permeability data on the template (and therefore one doesn't need to make any time consuming calculations as in the HU approach), and that different reservoirs from anywhere in the world can be compared on exactly the same universal plot.

Clusters of plugs with similar GHE values form physical elements in a reservoir. Corbett and Potter (2004) pointed out that the plotting of plug data on the GHE "basemap" (Figure 2.24) allows trends to be easily determined. They demonstrated that shallow marine reservoirs show clear progressions across GHEs as the sandstone coarsens and cleans upwards. The GHE template can also be potentially applied to core data for identification of other significant trends in a wide range of crossplots for different parameters (Corbett and Potter, 2004). In the present study the GHE approach will be applied in the reservoirs of three fields (A, B and C) of the Nubian Sandstone in North Africa for the first time.

2.8.1 Geological Understanding of GHE

The first group (GHE2-3) represent sandstone gray color, fine to very fine grained, containing coarse grained sand, ripple cross laminated, horizontal burrows in parts with thin mudstone bands, dark gray with few scattered sand grains.

The second group (GHE3-4) represent sandstone, moderately to dark gray color, medium grained, followed by mudstone. The sandstone display parallel horizontal lamination to current and wave ripple cross-lamination and bidirectional cross-stratification. The group (GHE5-8) Filling upward sequence comprising coarse to very coarse sandstones interbedded with mudstone bounded by lowering scoured surfaces. The sandstone dark gray and brownish mostly coarse to very coarse grained. It is well sorted, medium to coarse grained sandstone with minor detrital clays. It contains quartz overgrowth and traces of non ferroan dolomite and anhydrite. Kaolinite pore-filling is the dominant authigenic clay phase. The permeability is excellent where porosity is moderate due to well sorting of sandstone and minor amounts of cement.

Table 2.6. Ten global hydraulic elements and the FZI values as proposed by Corbett and Potter (2004).

FZI	48	24	12	6	3	1.5	0.75	0.375	0.1875	0.0938
GHE	10	9	8	7	6	5	4	3	2	1

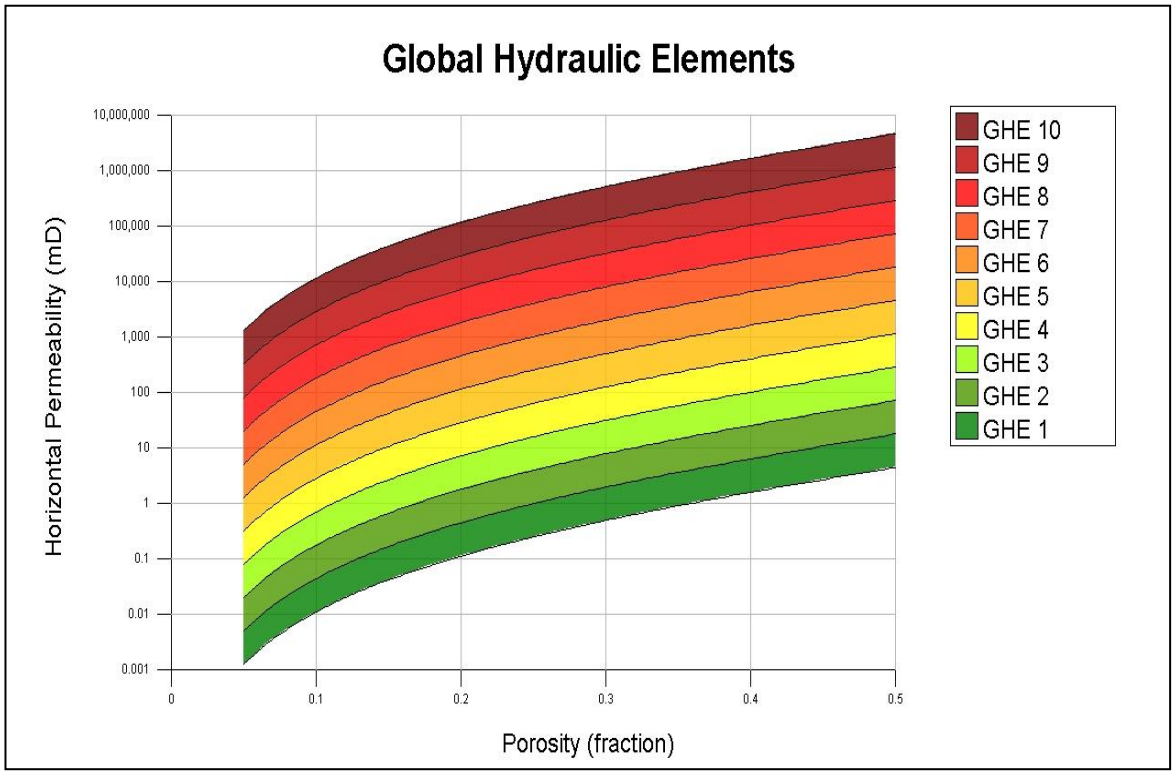

Figure 2.24. Global hydraulic elements template showing GHE 1 at the base to GHE 10 at the top (Corbett and Potter, 2004).

2.9 Conventional Hydraulic Unit Determination and Comparison with Global Hydraulic Elements in the studied area of the Nubian Sandstone

The conventional hydraulic unit (HU) classification in the six studied wells was performed. For this conventional classification, it is necessary to use all the available core plug data for each well. For example, for well A-02 the permeability and porosity data of 463 horizontal core plugs were used to calculate the FZI values for each core plug using Equation 2.22. Five distinct lines were recognized. Therefore, it was decided to group the core plug data into five clusters, corresponding to 5 appropriate HUs. The HU number was labelled from HU1 to HU5 according to the cluster number. In this way, the HU of each core plug was identified and plotted on the permeability–porosity plot in Figure 2.25.

Based on the HU classification, a plot of Φz vs. RQI for each HU was constructed. The unit slope lines were drawn for each HU through their data clusters and their mean value of FZI that was calculated for each hydraulic unit at the intercept with Φ_z equal 1. The mean FZI values were then used to construct the porosity-permeability relationship within each hydraulic unit using Equation 2.22. Figure 2.26 shows the Φz versus RQI crossplot for well A-02 along with the mean FZI value for all the classic HUs. Figure 2.27 shows the porosity–permeability crossplot combined with the HUs for all the well A-02 core data. The porosity–permeability crossplots with the conventional HUs for the other wells A-03, A-01, B-01, C-01 and C-02 are shown in Figures 2.29, 2.31, 2.33, 2.35 and 2.37 respectively.

The rapid and more straightforward approach (compared to the conventional HU approach) is to plot the porosity and permeability data on the pre-determined global hydraulic element (GHE) template of Corbett and Potter (2004). The GHE approach avoids the need to do any lengthy calculations or cluster analysis associated with the conventional HU approach. In the present study the porosity-permeability plug data plotted on the GHE template for well A-02 is shown in Figure 2.28. The porosity-permeability plug data plotted on the GHE template for the other wells A-03, A-01, B-01, C-01 and C-02 are shown in Figures 2.30, 2.32, 2.34, 2.36 and 2.38. To make clear the comparison between the methodology of the old approach (HU) and the new approach (GHE) a workflow chart for each is shown in Figure 2.43.

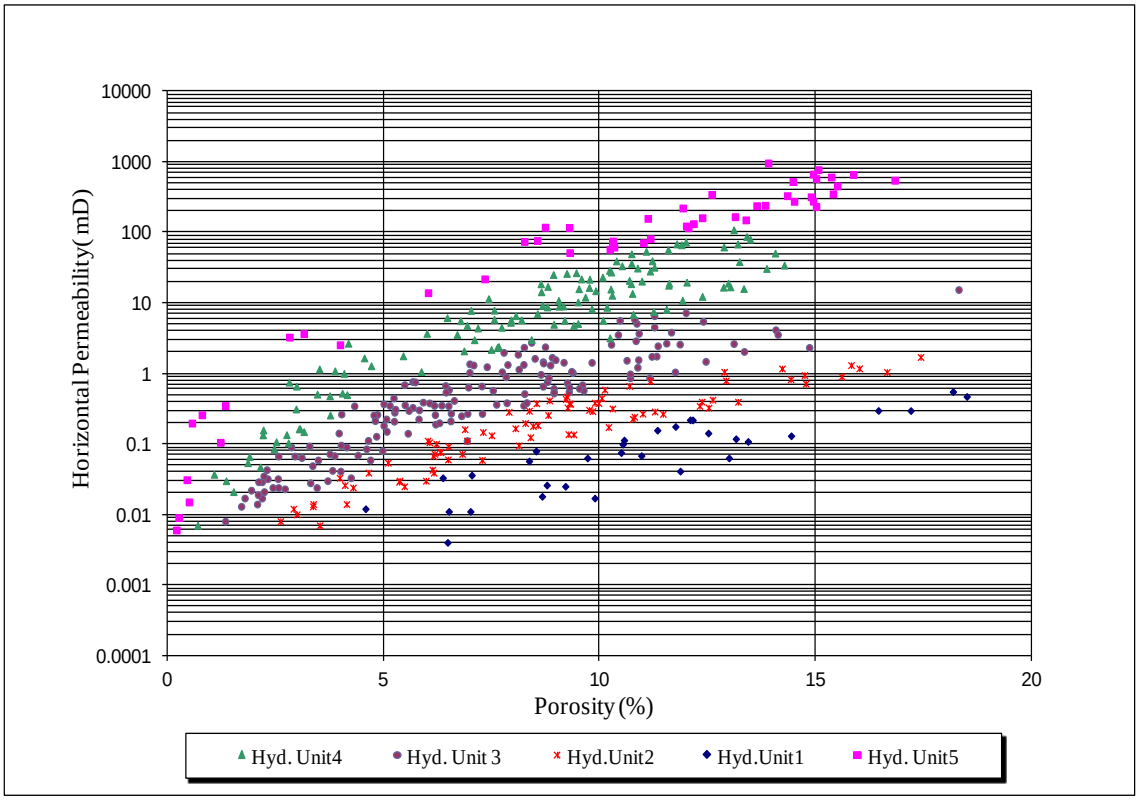

Figurre 2.25. Porosity-permeability crossplot and the conventional hydraulic unit classification of all core plugs in well A-02.

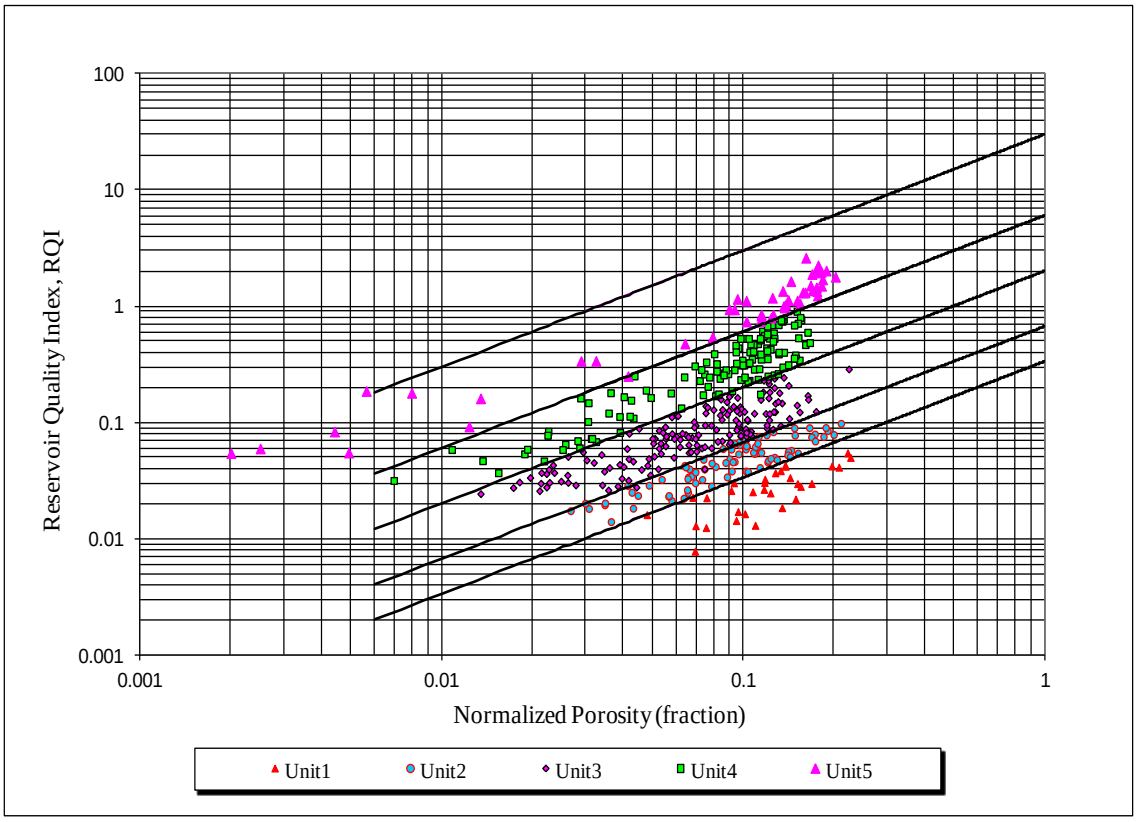

Figure 2.26. Φz.vs.RQI crossplot for all hydraulic units in well A-02. The mean FZI values for each hydraulic unit are given by the intercept of straight lines at Φ_z equal 1.

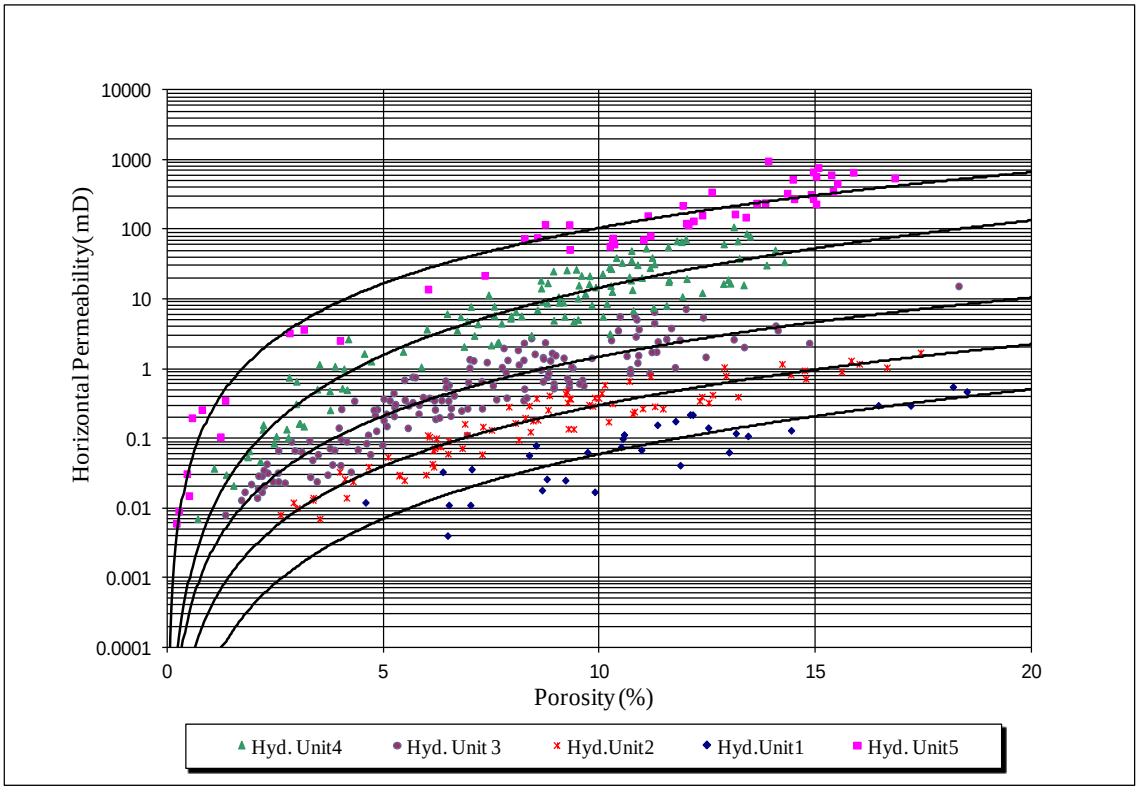

Figure 2.27. Conventional hydraulic units in well A-02. The curves represent the porosity-permeability relationship for each hydraulic unit.

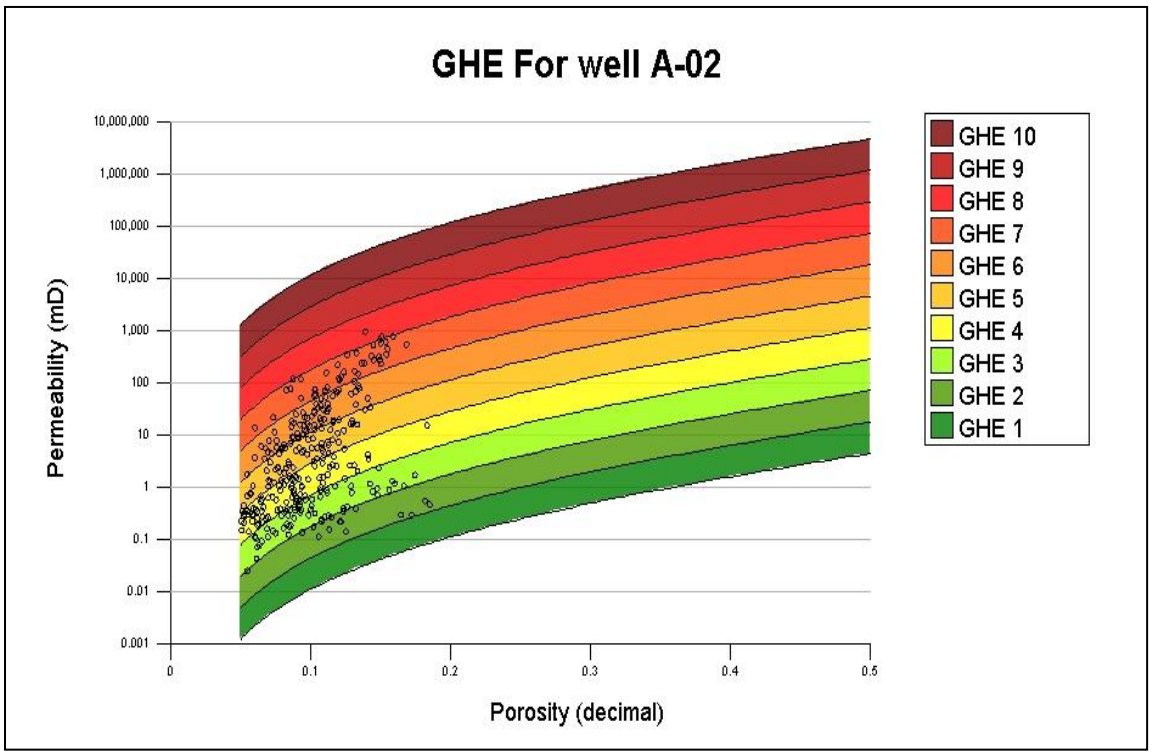

Figure 2.28. Global hydraulic elements in well A-02 (all data) using the template of Corbett et al. (2003) and Corbett and Potter (2004).

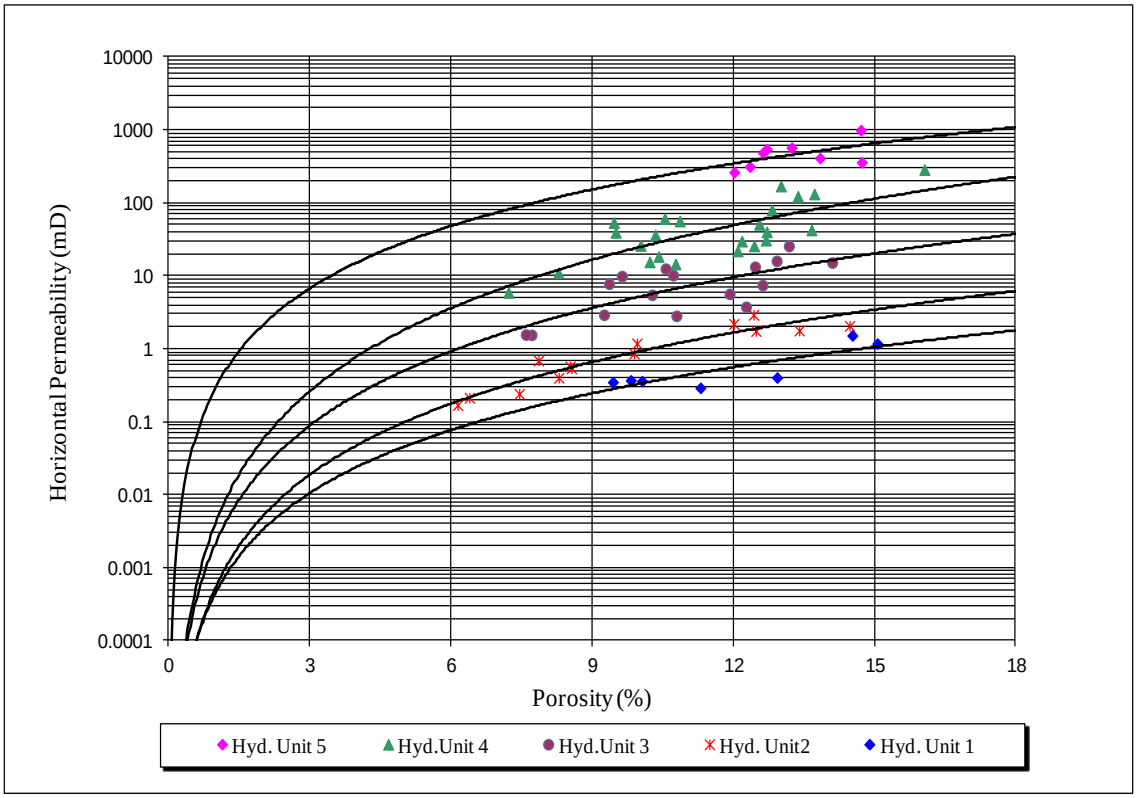

Figure 2.29. Conventional hydraulic units in well A-03. The curves represent the porosity-permeability relationship for each hydraulic unit.

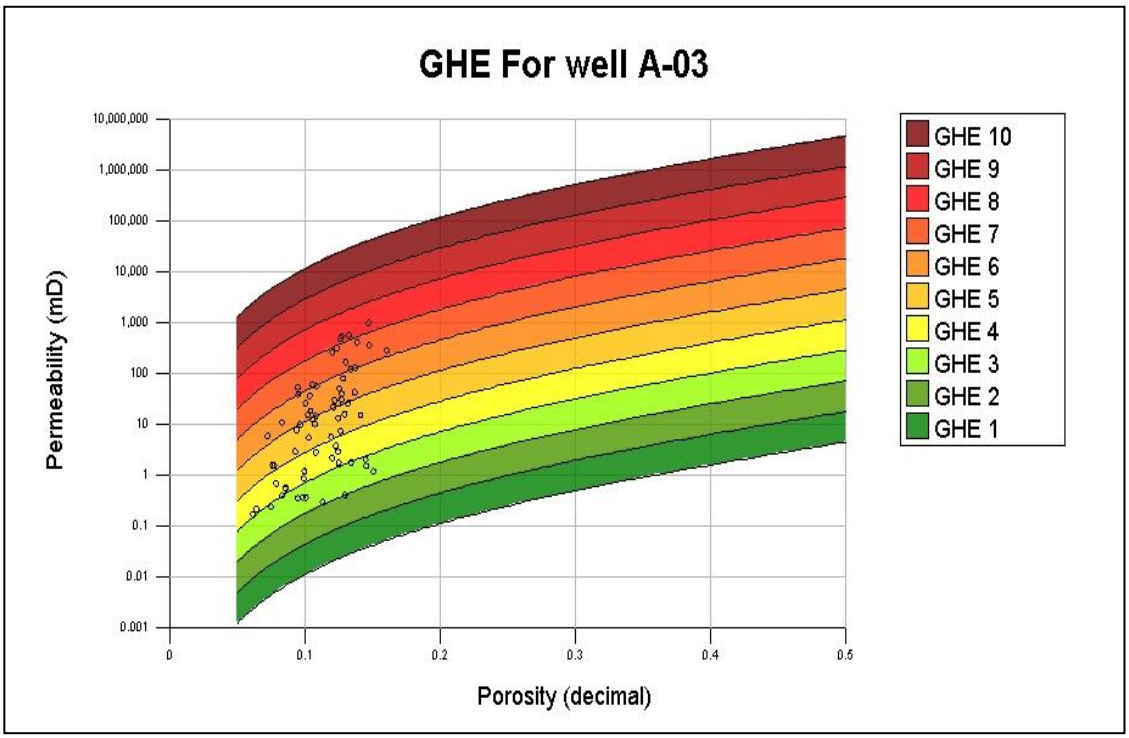

Figure 2.30. Global hydraulic elements in well A-03 (all data) using the template of Corbett et al. (2003) and Corbett and Potter (2004).

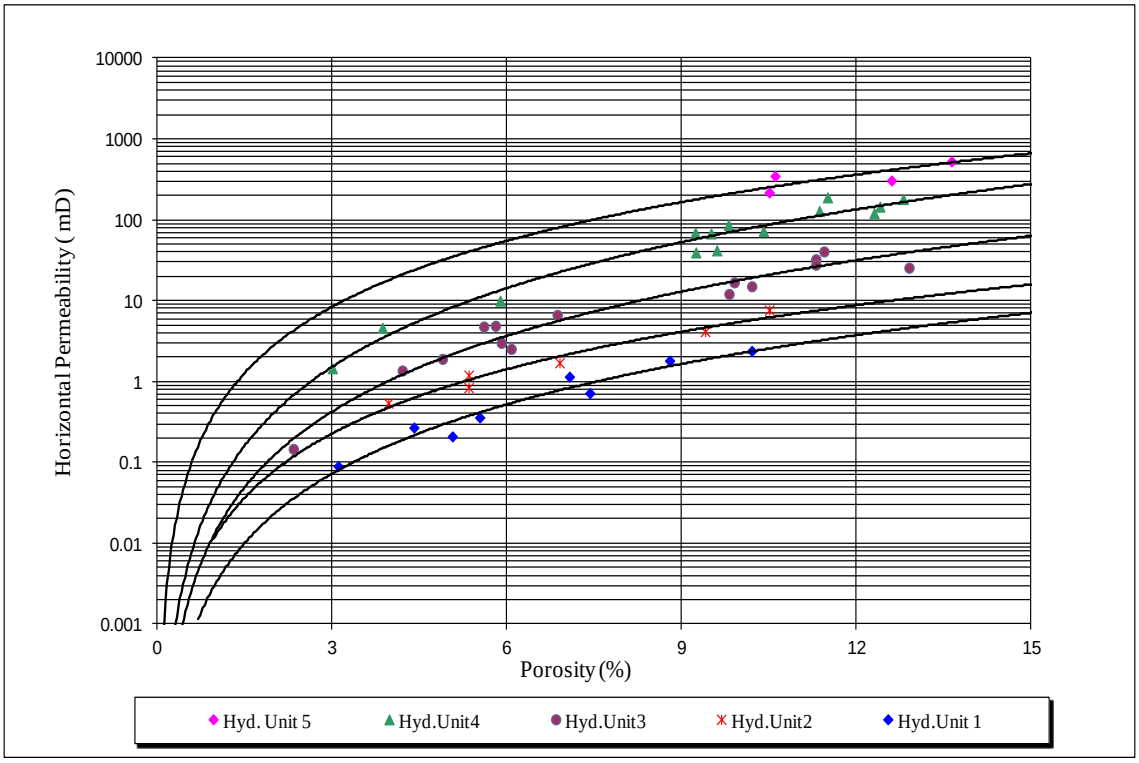

Figure 2.31. Conventional hydraulic units in well A-01. The curves represent the porosity-permeability relationship for each hydraulic unit.

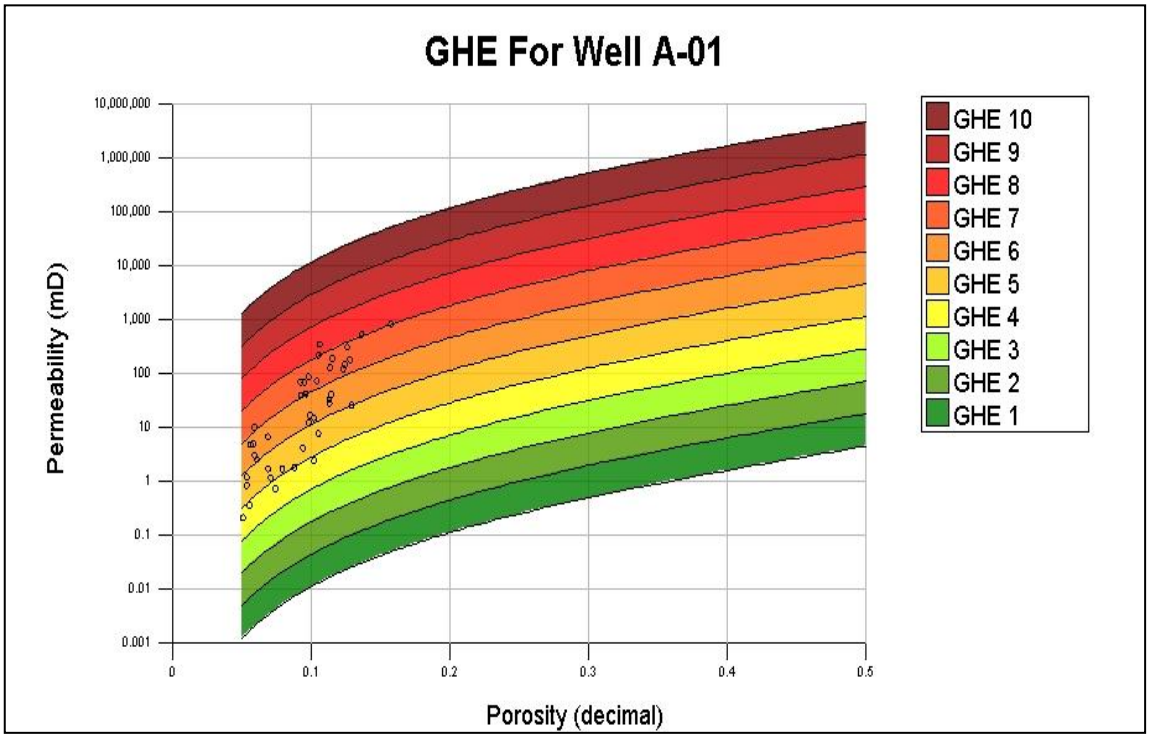

Figure 2.32. Global hydraulic elements in well A-01 (all data) using the template of Corbett et al. (2003) and Corbett and Potter (2004).

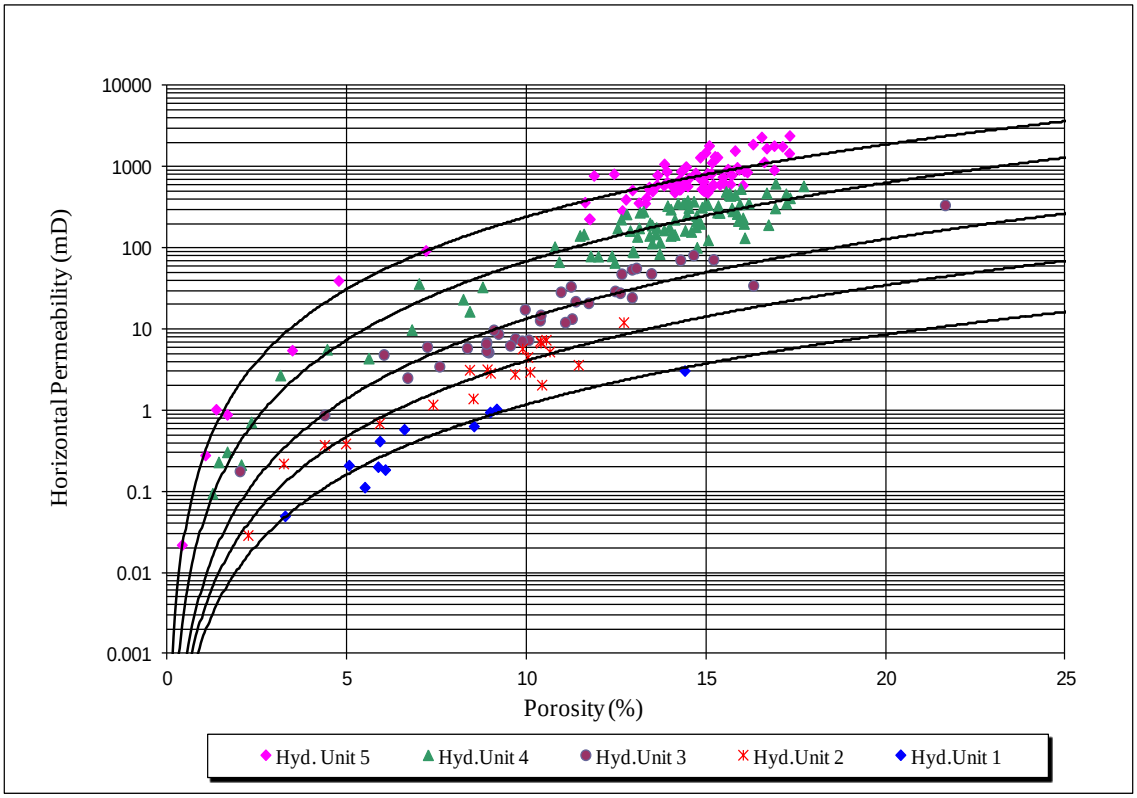

Figure 2.33. Conventional hydraulic units in well B-01. The curves represent the porosity-permeability relationship for each hydraulic unit.

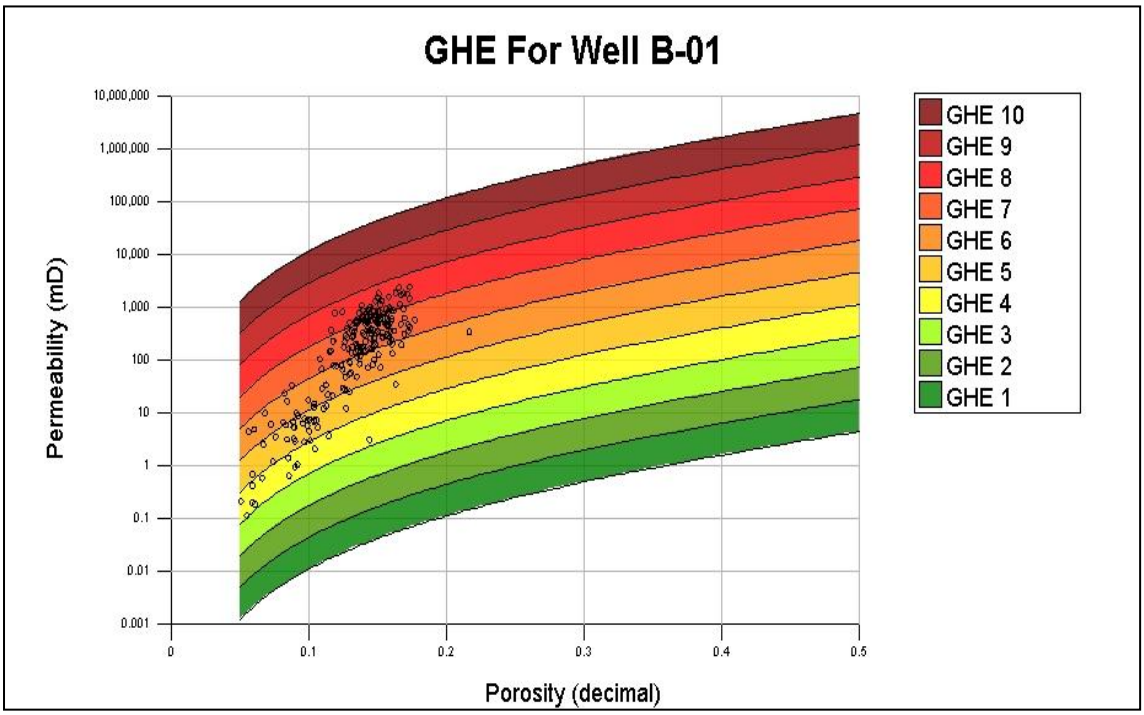

Figure 2.34. Global hydraulic elements in well B-01 (all data) using the template of Corbett et al. (2003) and Corbett and Potter (2004).

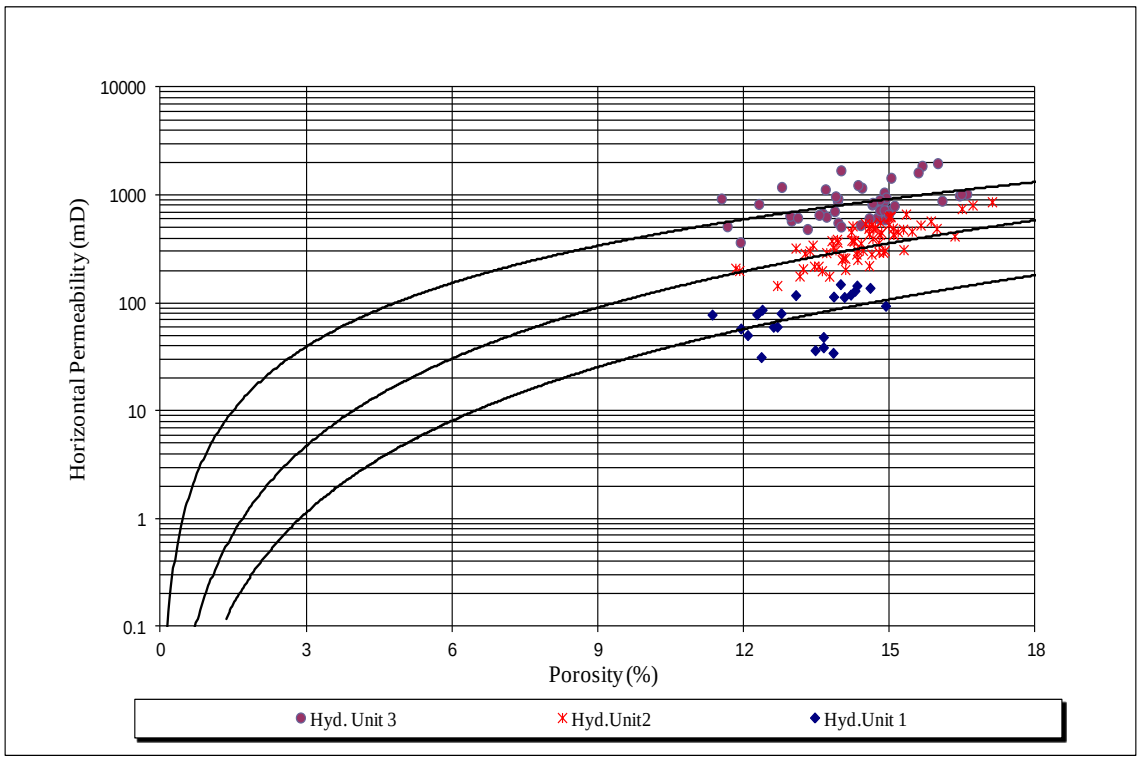

Figure 2.35. Conventional hydraulic units in well C-01. The curves represent the porosity-permeability relationship for each hydraulic unit.

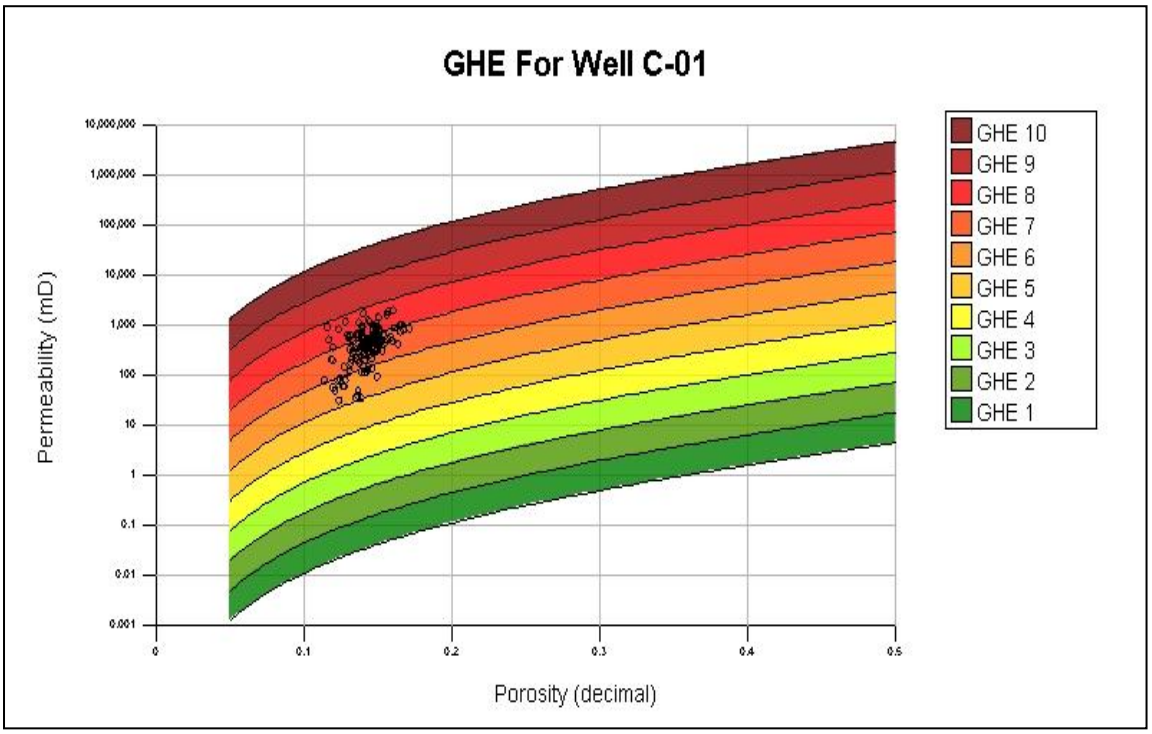

Figure 2.36. Global hydraulic elements in well C-01 (all data) using the template of Corbett et al. (2003) and Corbett and Potter (2004).

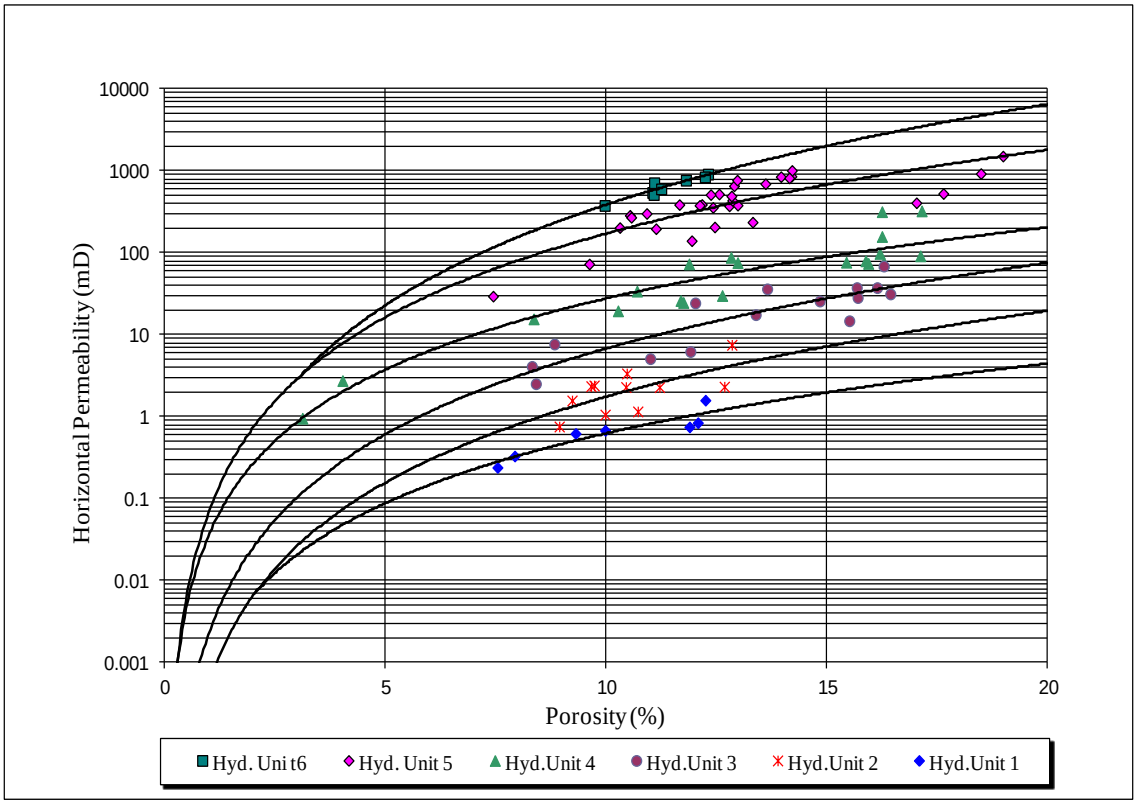

Figure 2.37. Conventional hydraulic units in well C-02. The curves represent porosity-permeability relationship for each hydraulic unit.

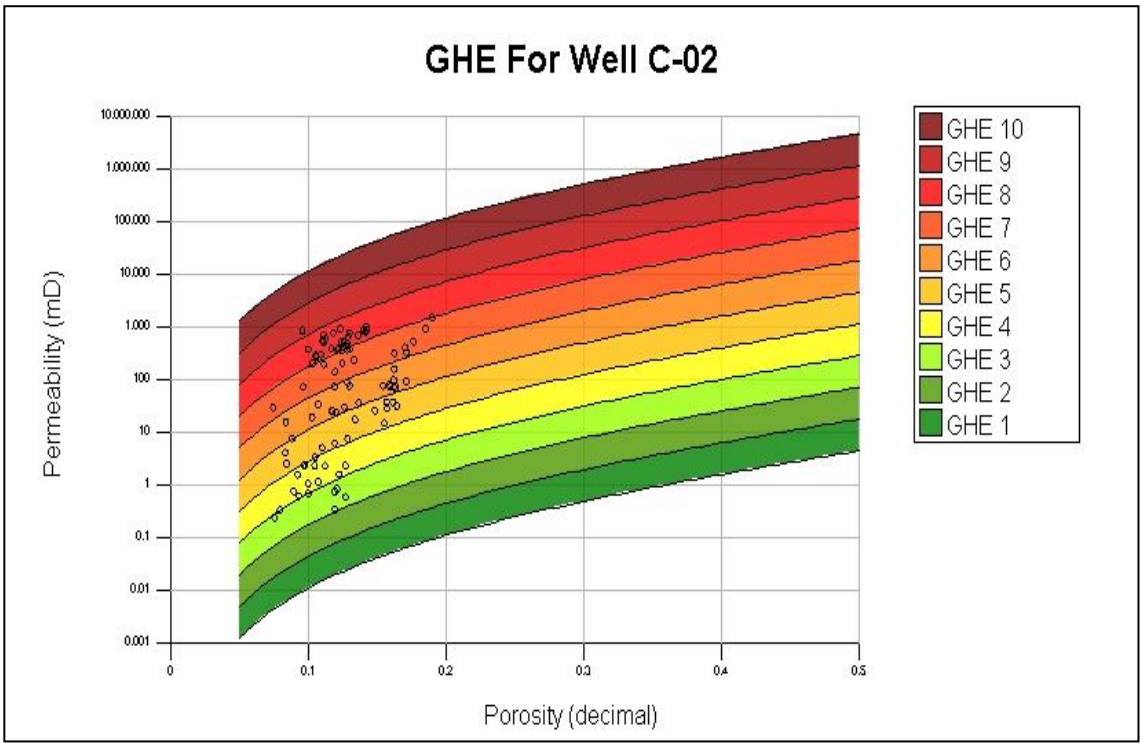

Figure 2.38. Global hydraulic elements in well C-02 (all data) using the template of Corbett et al. (2003) and Corbett and Potter (2004).

Table 2.7. Summary of the number of HUs and GHEs determined in the studied wells.

Well no.	HU	GHE
A-01	5	5
A-02	5	7
A-03	5	6
B-01	5	5
C-01	3	3
C-02	6	6

Table 2.8. Summary of the number of plugs and their GHEs.

Number of plugs	Well Name	GHE
03	A1-Libya	8
10	A1-Libya	7
15	A3-Libya	5
18	B1-Libya	8
24	A3-Libya	6
29	C2-Libya	5
41	C1-Libya	7
42	A3-Libya	5
47	C2-Libya	6
53	A1-Libya	8
83	A2-Libya	6
123	A2-Libya	7

2.10 Other Rock Typing Methods:

2.10.1 Winland method

Winland of Amoco (Spreaing et al., 2001) established an empirical relationship between porosity, permeability, and pore throat radius from mercury injection capillary pressure (MICP) measurements in order to obtain net pay cut-off values in some clastic reservoirs.

Winland correlated porosity and permeability to pore throat radius corresponding to different mercury saturations and found that the 35^{th} percentile (R35) gave the best correlation. R35 was defined empirically by Winland as the pore throat radius where the pore network becomes interconnected, forming a continues fluid path through the sample. Winland rock typing is based on samples with similar R35belonging to the same rock type. Essentially, Winland rock typing and HU rock typing give a consistent (in terms of numbers of flow units in a data set) breakdown of porosity-permeability data. An R35 value can be determined for the same clusters of rock types as determined by an FZI value, and vice versa. The analogy between using an "effective" pore radius to determine GHEs is even more consistent with the grain size classification approach used by sedimentologists. The FZI value is easier to calculate than R35 value, requiring only single porosity and permeability value, but GHE concept could be expanded to also include an R35 value classification (this is already used by some workers).

A porosity-permeability relationship can be constructed for the different rock types based on their group R35 value. R35 ports correspond to calculated pore throat radius (microns) at 35% mercury saturation from mercury injection capillary pressure test. They can be calculated directly from Winland's equation (equation 2.26) based on permeability and porosity. In equation 1, permeability is input in millidarcies and porosity in percent. The R35 was calculated then used to perform rock typing (Figure 2.40), again this reservoir (A-02) has been classified into five rock types are appropriate.

$$\text{Log } R35 = 0.732 + 0.588 * \text{Log}(k) - 0.864 * \text{Log}(Ø) \quad (2.26)$$

2.10.2Unordered Lorenz Plot (ULP)

The Unordered Lorenz Plot (**ULP**), Pinisetti in (2000), is also known in the literature as Stratigraphically Modified Lorenz Plot (**MLP**), (Gunter et al; 1997). Unordered Lorenz Plot (**ULP**) can be constructed with the same procedures as Lorenz Plot, but without any ordering for the data (i.e. keeping the natural depth order). This will preserve the stratigraphic information, and shows layers with increased permeability. The unordered plot shows which layer is likely to contribute more to the fluid flow into the well bore. The modified Lorenz was constructed and used to perform rock typing (Figure 2.41), a gain five rock types are appropriate based on inflection points.

From all the methods above, this demonstrates the usefulness of the GHE approach and gave more flow units about 7 units in this well A-02, this it appears that the arbitrary of GHEs proposed by Corbett and Potter (2004) on the pre-determined template is about right.

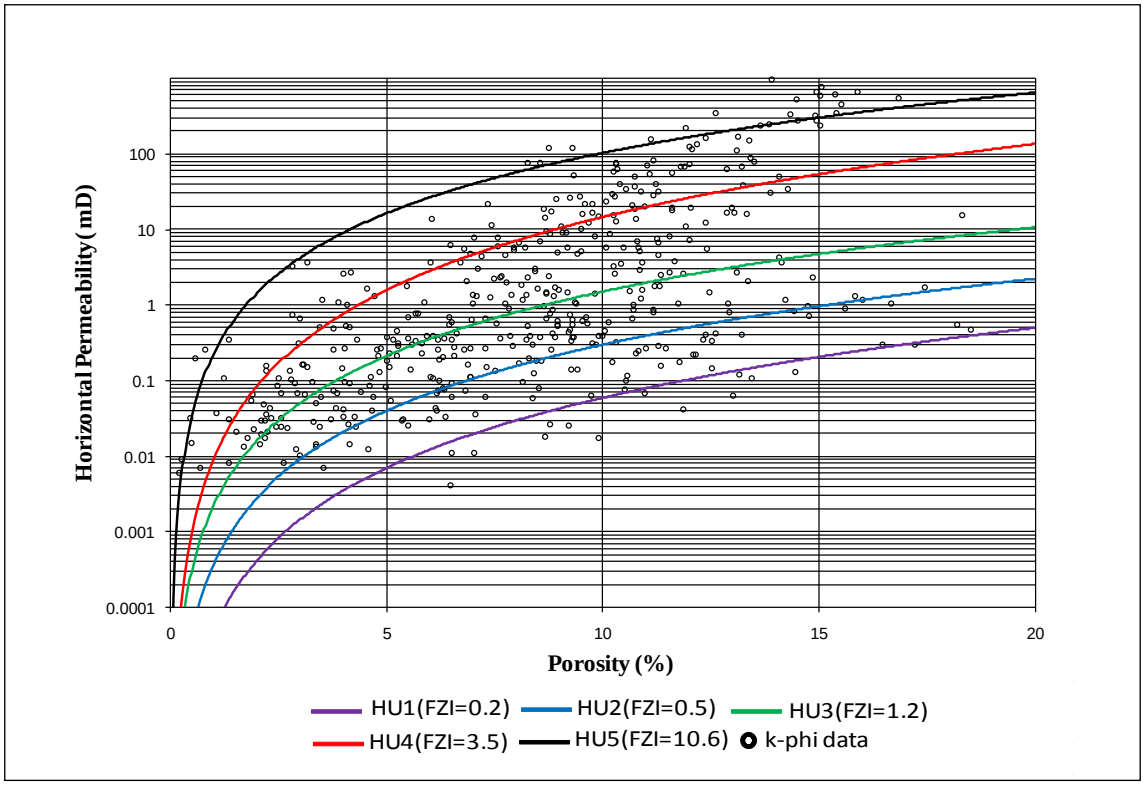

Figure 2.39. Well A-02 K-phi crossplot using HU.

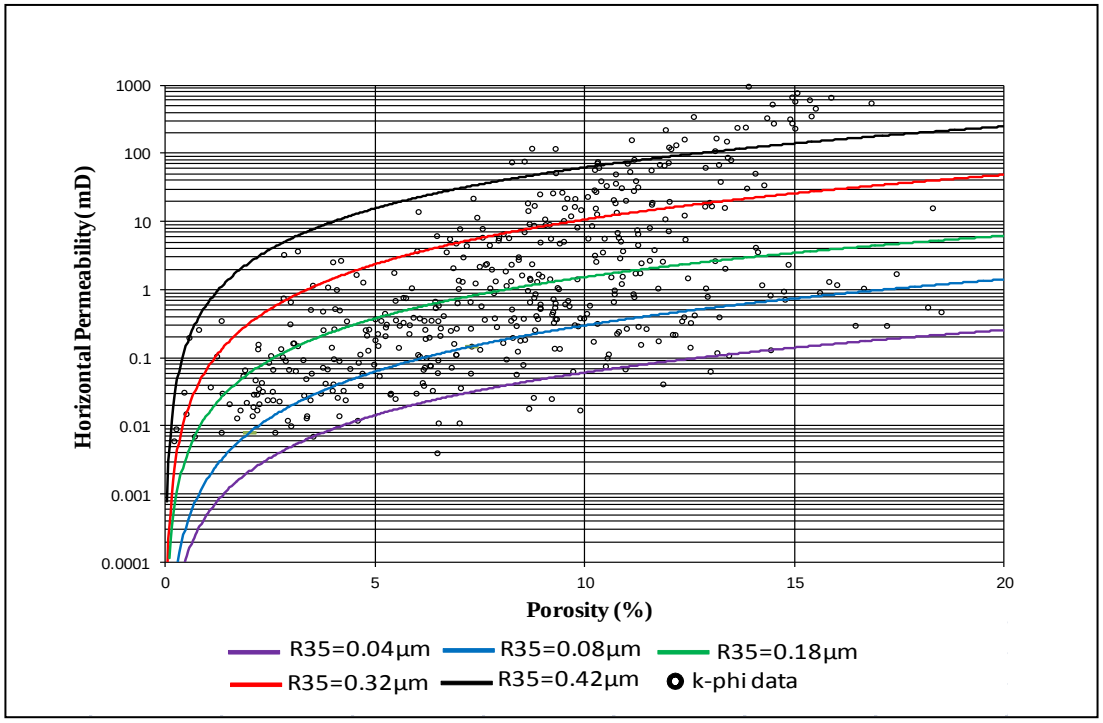

Figure 2.40. Well A-02 K-phi crossplot using Winland equation.

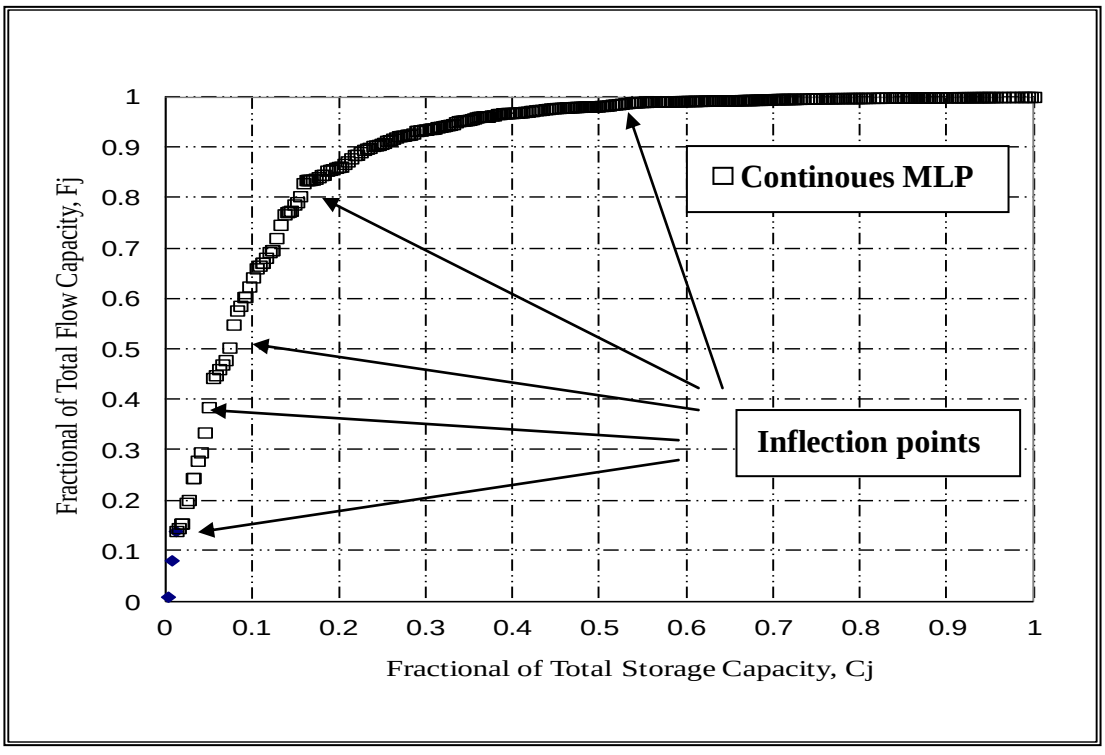

Figure 2.41. The flow units for well A-02 based on inflection points.

Hydraulic units are identified based on the flow zone indicator (FZI) values. For multiple hydraulic units, FZI distribution function is superposition of the individual (FZI) distributions around their means. Desuperposition process can be carried out using probability plot to identify the number of hydraulic units and their mean (Abbaszadeh et al. 1996). To identify the number of hydraulic units using probability technique, FZI values are calculated from core data by using equations 2.22. A plot of cumulative probability versus FZI produces a probability plot. The points from a normally distributed will fall on approximately a straight line. The points on a straight line form a hydraulic unit. The probability plot (Figure 2.42) shows five trends of well A-02. Based on this graphical analysis is made and is shown in Figure 2.26.

The increase of number of clusters above five does not lead to any considerable reduction of the estimated error in calculations and predictions, this fact is clear in GHEs approach which demonstrated that the number of GHEs and their boundaries were arbitrarily chosen in order to obtain a wide enough range of possible combinations of porosity and permeability in a manageable number of GHEs.

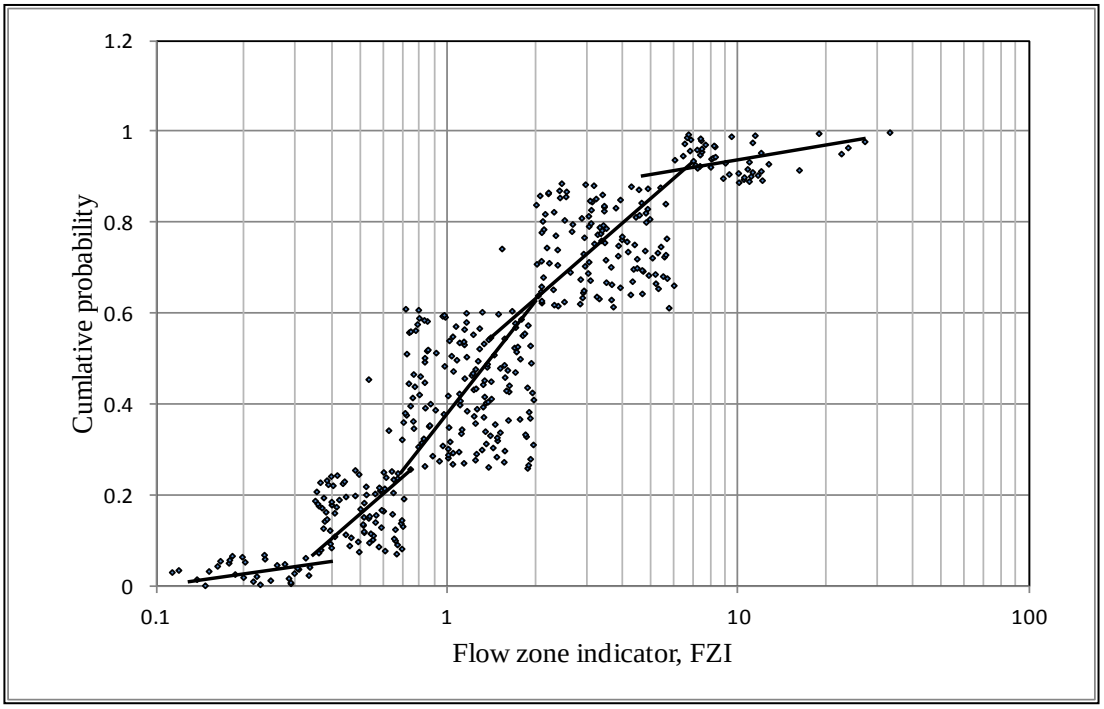

Figure 2.42.Determination of the number of hydraulic units and their boundaries using probability plot.

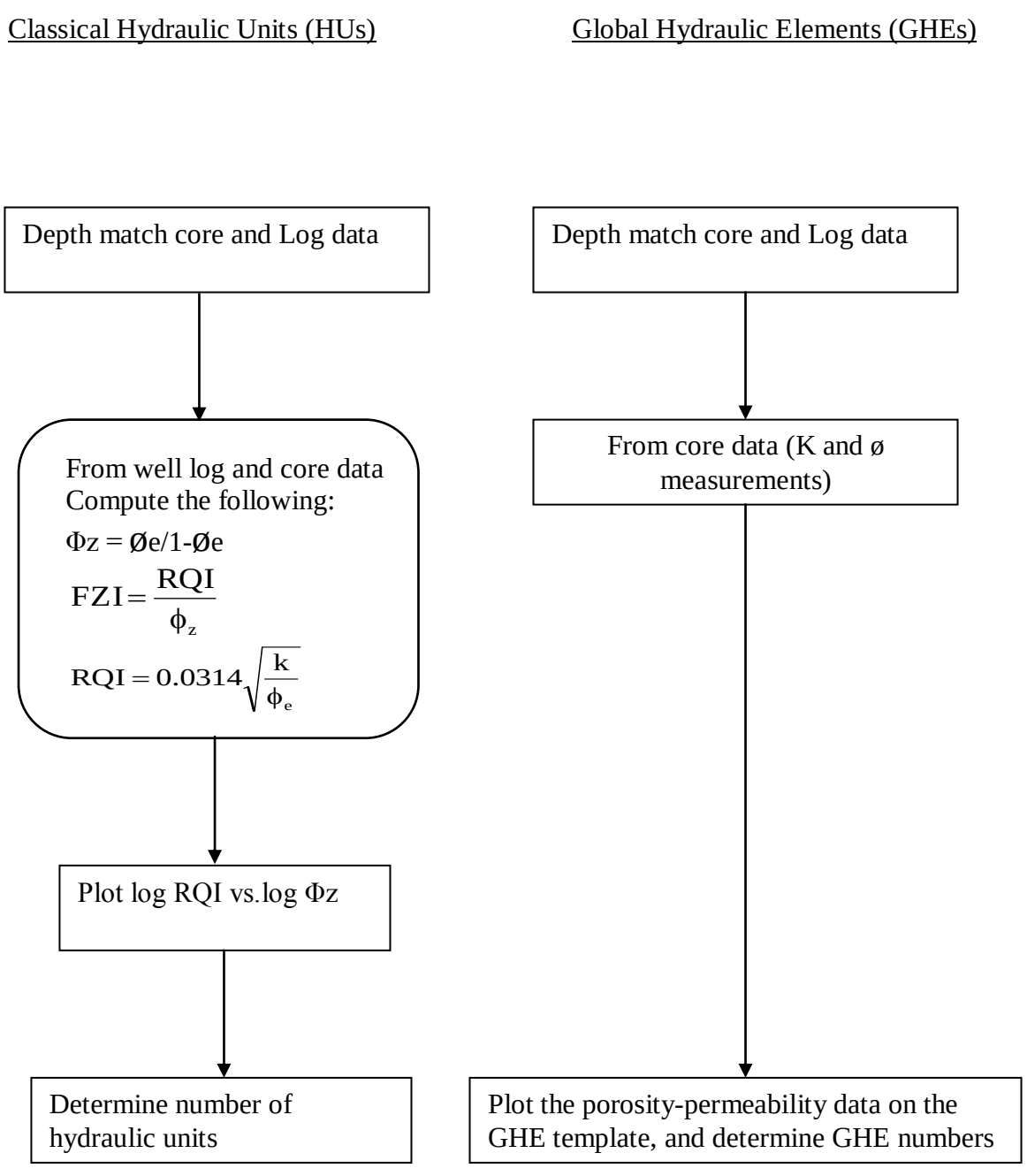

Figure 2.43. Flow chart of the workflow associated with the classic hydraulic units approach (Amaefule et al., 1993) and the global hydraulic elements approach (Corbett et al., 2003 and Corbett and Potter, 2004).

2.11 Discussion of Results

2.11.1 Heterogeneity Parameters in the Nubian Sandstone in the studied area

The histogram for porosity for well A-02 (Figure 2.2) shows a slightly more symmetrical distribution than that for permeability (Figure 2.1). A petrophysical parameter may be normally distributed (often porosity, grain density and fluid saturations) or log-normally distributed (usually pore geometry, grain size and permeability). In the former, the parameter is normally distributed around its mean and shows a bell type frequency distribution histogram. In the latter, the frequency distribution of the logarithm of the parameter shows a normal distribution. In general, Tables 2.2 and 2.3 and Figures 2.1 and 2.2 shows that the distributions are skewed towards slightly low to medium porosity and permeability values.

The statistical analysis of permeability for the six wells and in this study showed that most of the reservoirs are very heterogeneous. The values of C_V (Table 2.1) are greater than 1 for five of the wells (A-01, A-02, A-03, B-01 and C-02) meaning they are very heterogeneous, whilst the remaining well (C-01) is heterogeneous having a C_v of 0.75. In terms of the Dykstra-Parsons coefficient V_{DP} (Table 2.4) the values are again high for the same five wells (A-01, A-02, A-03, B-01 and C-02) supporting the Cv results in showing that these wells are very heterogeneous. Well C-01 has a lower value of V_{DP} than the others consistent with its lower value of Cv. A study by Lambert (1981) shows that V_{DP} estimated from vertical wells ranges between 0.65 and 0.99. Our results (Table 2.4) show most results of the studied wells give different degree of heterogeneity, ranges from 0.59-0.87 for six vertical wells.

Table 2.5 shows the results for the Lorenz Coefficient (Lc) as a measure of the degree of heterogeneity. The values for the six wells studied are all relatively high, with wells A-02 and A-03 having the highest values. For the six wells studied most of the flow was in the higher permeability zones (GHEs 7 and 8), whereas most of the storage was in the lower GHEs 2-6.

2.11.2 Comparison between Conventional Hydraulic Units and Global Hydraulic Elements in the Nubian Sandstone

A comparison of the GHE and HU results for all the studied wells is shown in Table 2.7 (and the total number of plugs and their GHE affiliation is shown in Table 2.8). The GHE results gave approximately the same number of GHEs as the number of conventional HUs. Therefore it appears that the number of arbitrary GHEs on the template is about right. As will be shown in Chapter 5 the GHE approach can be used to select minimal representative plugs to train genetically focussed neural nets.

2.12 Conclusions

- Statistical analysis determining the widely used coefficients for measuring heterogeneity C_v, V_{DP} and Lc showed that most of the wells studied in the Nubian Sandstone contain very heterogeneous reservoirs.

- Reservoir heterogeneity measurements by Cv, Vdp and Lc are all consistent.

- From the Lorenz plots all the wells showed that 75-90% of the total flow is coming from GHEs 7 and 8, whilst most of the storage is in GHEs 2-6.

- A comparative study of six wells in the Nubian Sandstone in three North African fields showed that for each well the number of global hydraulic elements (GHEs), using the template Corbett and Potter (2004), was almost the same as the number of hydraulic units (HUs) using the classical methodology of Amaefule et al. (1993). This demonstrates the usefulness of the GHE approach (which allows one to compare porosity-permeability data from any reservoir on the same template without the need to make any calculations), since it appears that the arbitrary number of GHEs proposed by Corbett and Potter (2004) on the pre-determined template is about right.

CHAPTER THREE

Factors Affecting Special Core Analysis Resistivity Parameters

3.1 Introduction and Objectives

This chapter describes the main reservoir rock properties including porosity, permeability, resistivity, wettability, and mercury injection capillary pressure. Laboratory measurements methods were undertaken on core samples selected from three different fields (A, B, and C) from the Nubian Sandstone Formation of the central graben. These measurements were conducted in order to determine the factors which affect resistivity parameters, and to investigate the effect of rock heterogeneity and wettability on these parameters. This included determining the saturation exponent (n) in the laboratory at two stages. The first stage was before wettability measurements were conducted on the samples, and the second stage was after the wettability measurements in order to find any effect on the saturation exponent.

Another objective of this chapter was to quantify experimentally pores and porosity types (macro- and micro-porosity), which have an affect on the electrical properties, by integrating capillary pressure curves with other routine and special core analysis. These experiments were made for the first time to obtain a relation between pore size distribution and saturation exponent n. The experimental results indicate that there is a good relation between resistivity and pore type depending on the pore size. When oil begins to penetrate micro-pore systems in measurements of resistivity index versus brine saturation (after wettability measurement), a significant change in slope of the resistivity index relationship occurs.

3.2 Factors affecting reservoir rock resistivity

3.2.1 Effect of overburden pressure on resistivity of reservoir rocks

In performing laboratory measurements, changes have been observed in the resistivity of fluid filled reservoir rocks as a result of changing overburden pressure conditions. These changes may result from changing the internal pore structure and an increase in tortuosity and decrease in the effective cross-sectional area that is available for the flow of electric current, Wyble(1958). Glanville (1959) showed that an increase in rock resistivity and formation factor increased as overburden pressure was applied, to a maximum increase of 51 % in resistivity for a sample of 9.9% porosity. Most of the samples studied by Glanville (1959) showed that samples with lower intrinsic porosity exhibited larger percentage increases in formation factor and resistivity after overburden pressure was appied than samples with higher porosity. Glanville attributed the increase in resistivity to the change in pore geometry. All the formations studied by Glanville showed an increase in cementation factor. Sandstone formations underwent a greater increase (13.0 to 81.0%) than carbonate formations (2.0 to 7.1%).

3.2.2 Effect of wettability on resistivity

Wettability plays a great role in the fluid distribution within the rock pore space by changing the relative position of the conducting fluid with respect to the rock surface, which affect the electric behaviour of fluid filled rocks (Anderson 1986 a). In hydrocarbon reservoirs there is generally more than one fluid in contact with another phase. The distribution of fluid within the rock pore space is not controlled by pore geometry alone. The interaction between the fluids and the rock surface has a role too. When two immiscible fluids are in contact with the rock pore surface, one of them may spread onto the surface of the solid more strongly than the other fluid. The fluid which is more attracted to the solid surface is known as the wetting phase, while the other fluid that is not attracted by the solid surface is known as the non-wetting phase. Therefore, the wettability is defined as “the tendency of one fluid to spread on or adhere to a solid surface in the presence of other immiscible fluids.” Wettability may change from place to place within the rock framework. In water-wet rocks, water occupies the smaller pores and spreads over the majority of the pore surface area of the grains which contact water, while oil is located in

the middle of the pores. Similarly in an oil-wet system, the rock is preferentially in contact with the oil and the location of the two fluids is reversed from the water- wet case, and oil will occupy the small pores and contact the majority of the rock surface. The wettability of a system can range from strongly water-wet to strongly oil-wet. When the rock has no strong preference for either oil or water, the system is said to be of neutral (or intermediate) wettability. The wettability of hydrocarbon bearing rocks can be altered from its original water-wet state to oil-wet by adsorption of polar compounds or by adsorption of organic materials originally in the crude oil. Wettability is also easily altered as a result of coring fluid. In coring operations, the core is partially penetrated by the drilling fluid, which, if it contains surface active materials, may change the wettability of the rock. Core handling during storage and testing (Anderson, 1986) may change the native wettability due to evaporation of fluids and exposure to surface active agents.

Generally, reservoir rocks are often assumed to be water wet and their saturation exponent (n) is generally assumed to be close to 2. However, it is substantially affected by wettability as well as the pore geometry and often no longer equals 2. Keller (1953) presented evidence that the saturation exponent could be substantially different from 2. He found that Archie's saturation exponent (n) varies from 1.5 to 11.7 for the same rock (Figure 3.1), depending on how cores were treated. For the same water saturation, the resistivity of an oil reservoir can vary by three orders of magnitude for different wetting conditions. The wettability played a significant role in the fluid distribution within the rock pore space by changing the relative position of the conducting fluid with respect to the rock surface, which affected the electric behaviour of fluid-filled rocks.

Sweeny and Jennings (1960) found that the resistivity of hydrocarbon bearing rocks is strongly affected by the wettability. Their data showed that the resistivity is greater when the wetting conditions are changed from water-wet to oil-wet. They concluded that the conducting fluid (water) exists in discrete non-connected globules when the rock is oil-wet, which are unable to conduct electric current. Archie's saturation exponent varies from 1.6 to almost 8.0 for water-wet and oil-wet carbonate cores respectively (Figure 3.2).

Mungan and Moore (1968) pointed out that an Archie's saturation exponent as high as 9.0 can be calculated when the conductive liquid is non-wetting. For strongly water-wet rocks, a unique relationship exists between Archie's saturation exponent and resistivity as described by Archie's law. At lower saturation, Archie's saturation exponent becomes larger and more saturation dependent. They attributed the change of saturation exponent (n) to higher values at lower water saturation to the fact that water is becoming discontinuous and not contributing to the flow of current. For the same core specimen, cleaning may have some impact on the wettability conditions of the rock. Archie's saturation exponent varied from 1.91 to 2.71 for extracted and non-extracted cores respectively (Figure 3.3).

Donaldson and Siddiqui (1989) found a linear relationship between the U. S. Bureau of Mines (USBM) wettability index and Archie's saturation exponent n. Archie's saturation exponent increases with decreasing wettability index because the saturation exponent increases as the rock becomes more oil-wet (Figure 3.4).

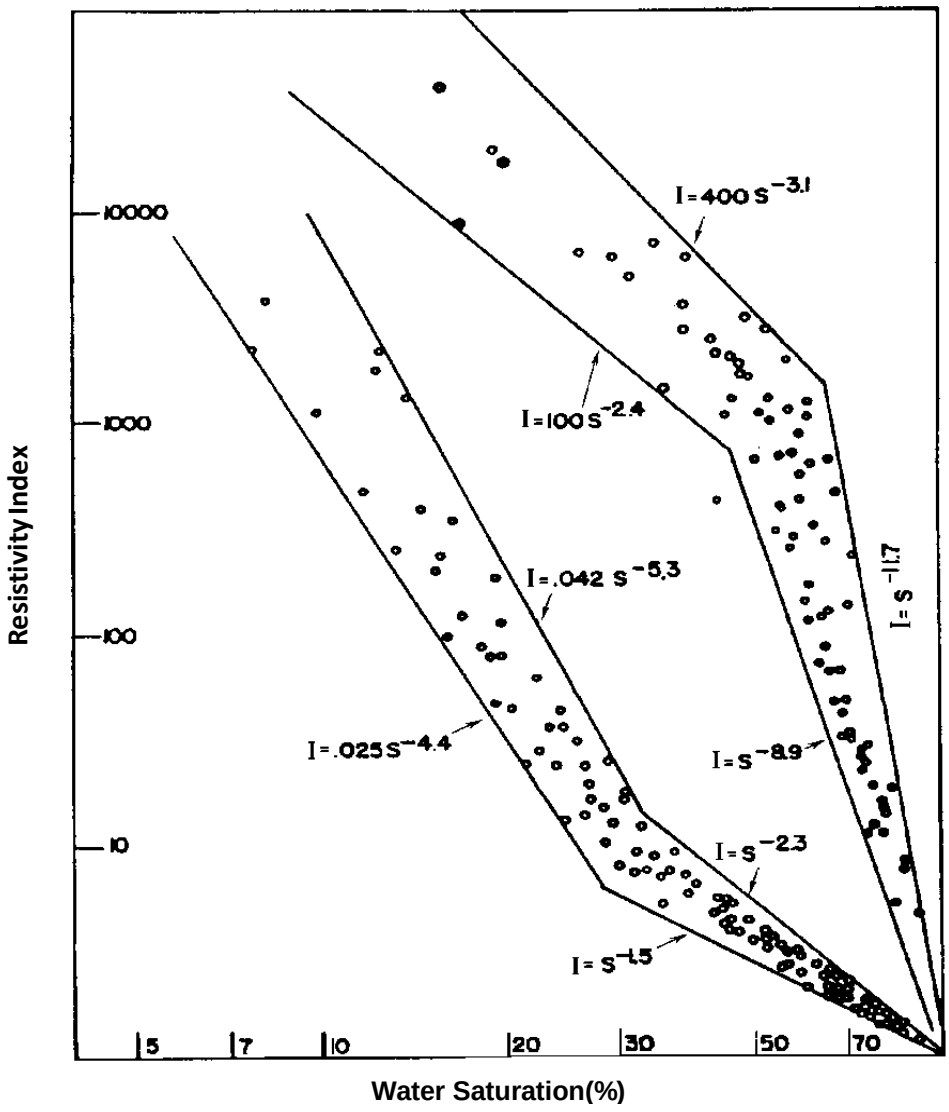

Figure 3.1. Resistivity index versus water saturation for oil-wet and water-wet rocks. From Keller (1953).

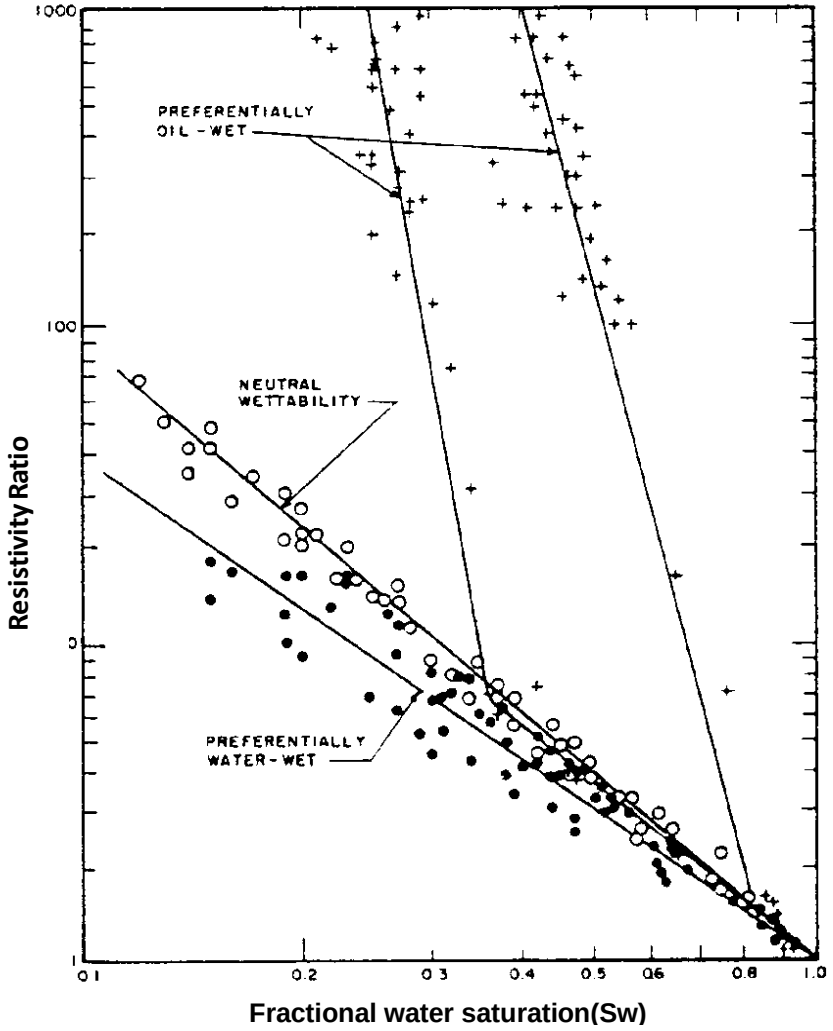

Figure 3.2. Resistivity index water saturation relation for oil-wet and water-wet carbonate cores. From Sweeney and Jennings (1960).

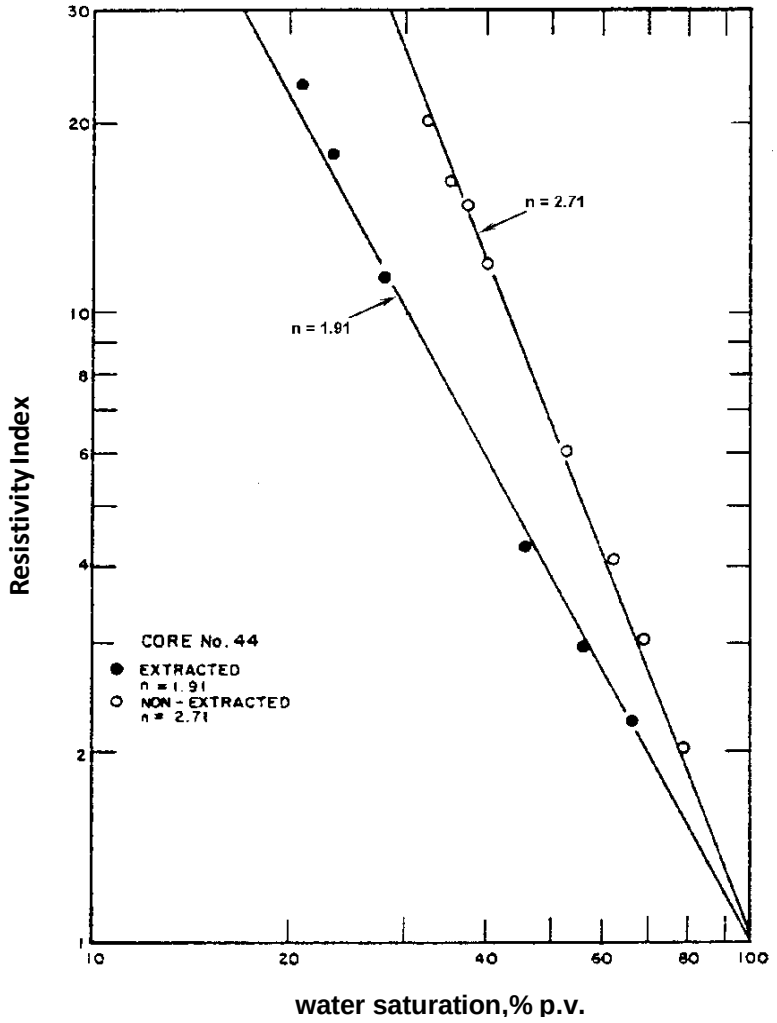

Figure 3.3. Effect of sample cleaning on Archie's saturation exponent. From Mungan and Moore (1986).

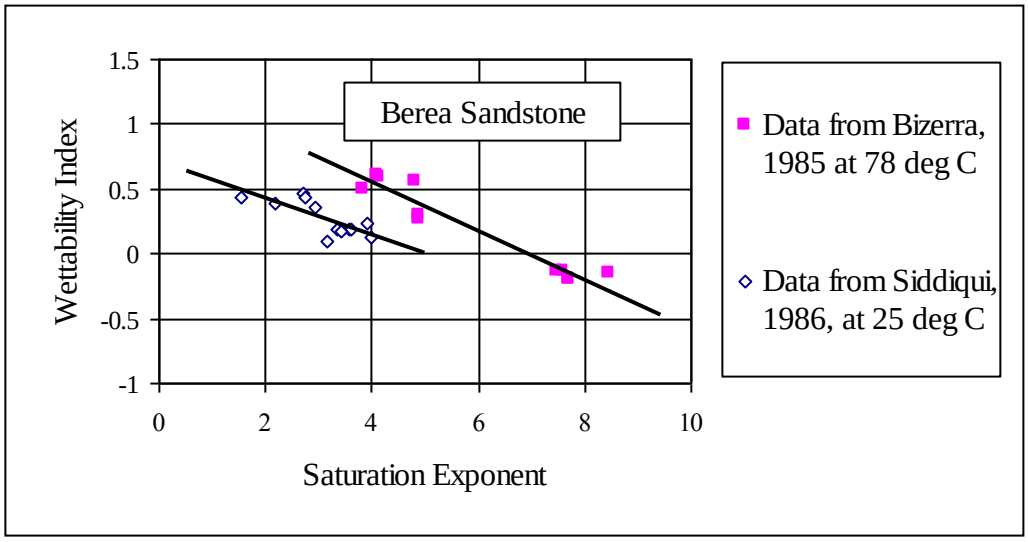

(a)

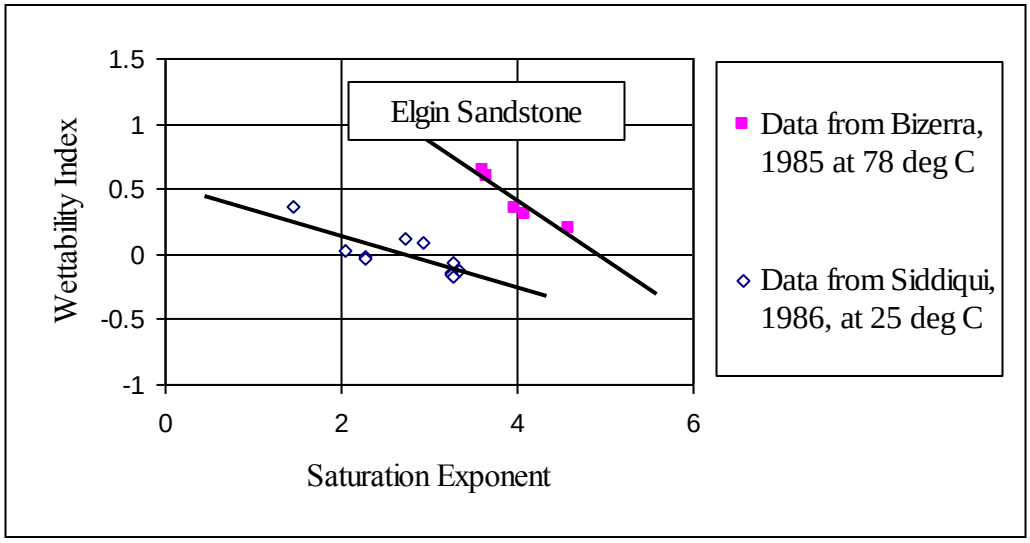

(b)

Figure 3.4. Archie's saturation exponent as a function of wettability index for (a) Berea and (b) Elgin sandstones. Donaldson and Siddiqui (1989).

3.2.3 Effect of temperature on resistivity

When the temperature of a conductor rises, its resistivity may increase or decrease depending on the type of the conductor. The resistivity of some metallic conductors increases with increasing temperature because the nuclei in a metal are exited at higher temperature slowing down the movement of the electrons responsible for the electric conduction. The resistivity of dry granite and olivine increases with increasing temperature (Schon, 1996). On the contrary, the resistivity of ionic conductors (electrolytes) decreases with increasing temperature because the mobility of ions increases with increasing temperature and as a result of the decrease in liquid viscosity. Therefore, the resistivity of brine saturated rocks decreases with increasing temperature.

3.2.4 Effect of the type of pore system on resistivity

Whenever two immiscible fluids such as oil and water in a reservoir exist in equilibrium in capillary-like pore geometry, there is a difference in the pressure across their interface. This pressure difference is called "Capillary Pressure" which is caused by the preferential wetting of the capillary wall by one of the fluids and gives rise to wetting fluid into the capillary tube. Capillary pressure characteristics of reservoir rocks affect the flow and distribution of fluids within the reservoir. It is one of the most important reservoir rock properties that relate reservoir rock and fluid properties. The magnitude of capillary pressure is related to the height above the free-water level in the reservoir. Capillary pressure characteristics of reservoir rocks are dependent on grain size, grain shape, packing, sorting and environment of deposition and diagenesis. These geological parameters affect the pore throat radius, often referred to as the pore size distribution within the rock.

The arrangement of the grains constituting sedimentary rocks generally leaves pores and channels for oil, gas and water to accumulate and to flow. Under SEM (Scanning Electron Microscope) the narrower constrictions connecting the pore bodies are referred to as pore throats, which control the permeability of reservoir rocks. Depending on their size, pores can be micro- or macro-pores. In partially saturated rocks, the effect of vuggy porosity on the resistivity depends on the wettability of the vuggy pore space. If the vugs are oil-wet the resistivity is insensitive to the vuggy pore system. Archie's saturation exponent tends to

increase as a result of increasing water saturation caused by a vuggy pore system, since the water occupies the middle of the vugs in an oil-wet vuggy system forming discontinuous droplets. These isolated water droplets do not contribute to the electrical conduction but give rise to water saturation, and, in turn, the saturation exponent will increase. If the vuggy pore system is water-wet, oil occupies the middle of the pores and the water forms a continuous path on the wall of vugs and intergranular pores, which connect vuggy pores together. As oil continues to invade the pore system, water volume decreases dramatically compared with the increase in resistivity resulting in lower water saturation and saturation exponent.

The mercury injection method entails injecting mercury into a clean, dry sample and monitoring the injection pressure and the amount of mercury injected into the rock sample. Drainage and imbibition capillary pressure curves can be obtained. Modern mercury injection capillary pressure apparatus enables injecting mercury into a rock sample at high pressure. An injection pressure of up to 60,000 psi can be achieved. This high pressure injection can penetrate pores down to 0.003 microns in diameter, which will yield a detailed pore size distribution.

3.3 Petrophysical Parameters of the Studied Area

3.3.1 Porosity and Permeability

In this study the controls on porosity and permeability of Nubian Sandstones Formation in North Africa Oil Field, Sirt Basin, are considered with respect to their texture and cementation, their petrophysical classification and the effect of subdivision of the petrophysical rock types. The main controls on hydraulic properties and hence the fluid in the porous reservoir media is of major importance for reservoir description. In this study the porosity and permeability of Nubian sandstone Formation which are determined from the laboratory are highly variable across the whole volume of the reservoir being moderate to good in the some intervals and poor in other intervals.

The most important and emerging challenge for geoscientist and engineering's is to improve the reservoir description programs, which though detailed, have not always included description at the pore throat scale (Amaefule et al., 1993).

For this reason the Global Hydraulic Elements have been used in this study to improve the description of Nubian Sandstone Formation, to identify the rock types in this formation, and to distinguish between rock types using the Global Hydraulic Elements approach.

The twelve representative samples were selected from ninety four samples based on GHEs boundaries due to Flow Zone Indicator (FZI) values for ten GHE which is gives in the Table (2.6) chapter 2. Four Global Hydraulic Elements are identified for six wells GHE,5,6,7,8 as shown in a Figure 3.5 and Table 3.1. Three samples were selected from each global hydraulic element and in the Nubian Sandstone Formation permeability values of less than 2 mD are not regarded as good reservoir material.

Core data of porosity and permeability plot as permeability versus porosity of Nubian Sandstone Formation (6 wells, A-01, A-02, A-03, B-01, C-01, and C-02) are shown in Figure 3.5 and the values are presented in Table 3.1. The twelve representative sandstone core samples used had porosities between 8.01% and 17.91% and permeabilities between 4.9 mD and 1146 mD. These core plugs show a distinct trend in texture contrast where the fine to medium grained and poorly to moderate sorted sands are associated with GHE-4 while the coarse grained and well sorted sands are associated with GHE-7 and GHE-8 with the best reservoir rock quality.

Core samples were selected to study the petrophysical parameters and their effect on resistivity. One and a half inch diameter core plugs were cut from full diameter core in the horizontal direction using a diamond core bit with water as the bit coolant and lubricant. The samples were extracted of hydrocarbons using toluene, leached of salt using methanol, and oven dried at 80 ^{o}C for a period of 48 to 72 hours, and then left to cool to room temperature before conventional core analysis commenced.

Routine core analysis porosity and permeability measurements were first conducted on the plugs and the results shown in Table 3.1 and Figure 3.5. The measurements of porosity and permeability were already explained in detail in Appendix D.

Table 3.1. Porosity and permeability values of the selected representative samples.

Samples#	Well Name	Ø (%)	K(mD)	GHE
03	A1-Libya	10.39	337.5	8
10	A1-Libya	9.01	34.11	7
15	A3-Libya	12.17	12.55	5
18	B1-Libya	14.59	1146	8
24	A3-Libya	8.01	9.910	6
29	C2-Libya	17.38	69.86	5
41	C1-Libya	15.34	660.4	7
42	A3-Libya	11.71	4.901	5
47	C2-Libya	17.91	279.7	6
53	A1-Libya	11.16	297.7	8
83	A2-Libya	9.56	27.73	6
123	A2-Libya	12.76	118.1	7

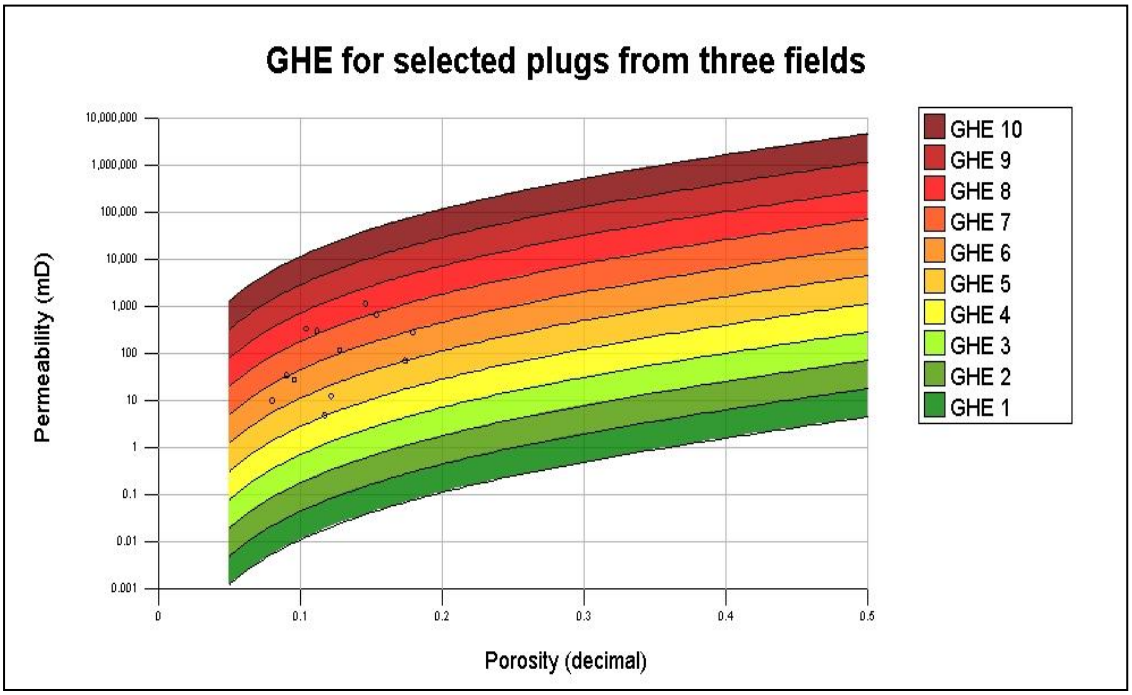

Figure 3.5. Global hydraulic element porosity-permeability crossplot for the twelve selected representative samples.

3.3.2 Formation resistivity factor at ambient conditions

Formation factor measurements were made on 100 % brine saturated rock sample either at ambient conditions or elevated reservoir overburden pressure. Sample resistance was measured and converted to resistivity using the sample cross-sectional area and length. Formation resistivity factor was calculated as the ratio of the sample resistivity to the resistivity of the water saturating it. The formation resistivity factor of a group of samples was plotted versus their porosities on log-log graph paper. The slope of the best fit line is the value of the cementation factor (m) and the intercept is the value of rock consolidation factor "a"

The twelve representative sandstone core samples used had porosities between 8.01% and 17.91% and permeabilities between 4.9 mD and 1146 mD. The porosity, formation resistivity factor and cementation exponent of the twelve samples at ambient conditions were measured and are presented in Table 3.2. Figure 3.6 shows the formation resistivity factor versus porosity measured at ambient conditions. In the measured cores a well defined relationship exists between formation resistivity factor and porosity. The formation resistivity factor was a best fit to Archie's equation (assuming the coefficient "a" was equal to 1) so that the cementation factor (m) was calculated for each sample. The average cementation factor for all core samples was calculated from the slope of the best fit straight line through the points and was found to be 1.69 and the correlation coefficient R^2 was 0.99. The following equation represents the relation between formation resistivity factor (FF) and porosity (ø):

$$FF = \frac{1}{\phi^{1.69}} \quad \text{---------- (3.1)}$$

Where:

FF Formation resistivity factor

Ø Porosity (fraction)

The formation factor has been calculated for each Global hydraulic Elements using Equation 3.1. The cementation exponent decreases from GHE-5 to GHE-8 and this decrease is related to the texture and overburden pressure. This fact is clear in Table 3.2 the cementation factor is 1.74 in sample # 42 (GHE-5) which is fine to medium grained and moderately sorted. In sample #24(GHE-6) which is fine to medium grained and moderately sorted and less cemented, the cementation factor is 1.72. In sample # 10 (GHE-7) which is good reservoir quality, medium to coarse grained and well sorted, the cementation factor is 1.65. In sample # 53 (GHE-8) which is best reservoir quality medium to coarse grained and well sorted, the cementation factor is 1.64.

From table 3.2, with increasing porosity, formation factor decrease and cementation factor changes. The reason for the observed variation in cementation factor has been attributed to a number of factors such as

- Degree of cementation.
- Shape, sorting and packing of particles system
- Type of pore system (intergranular, fractured, vuggy and microporous system)
- Tortuosity
- Constrictions existing in the porous system
- Conductive solids and clay minerals
- Compaction due to overburden pressure

Table 3.2. Porosity, formation resistivity factor and cementation exponent values for the Nubian Sandstone core samples at ambient conditions.

Sample #	Porosity (%)	Formation resistivity Factor (F.F)	Cementation exponent "m"	GHE
03	10.39	41.6	1.65	8
10	9.01	52.8	1.65	7
15	12.17	44.6	1.80	5
18	14.59	23.9	1.65	8
24	8.01	60.4	1.72	6
29	17.38	20.3	1.72	5
41	15.34	23.3	1.68	7
42	11.71	41.8	1.74	5
47	17.91	20.0	1.74	6
53	11.16	36.8	1.64	8
83	9.56	59.0	1.74	6
123	12.76	33.5	1.71	7

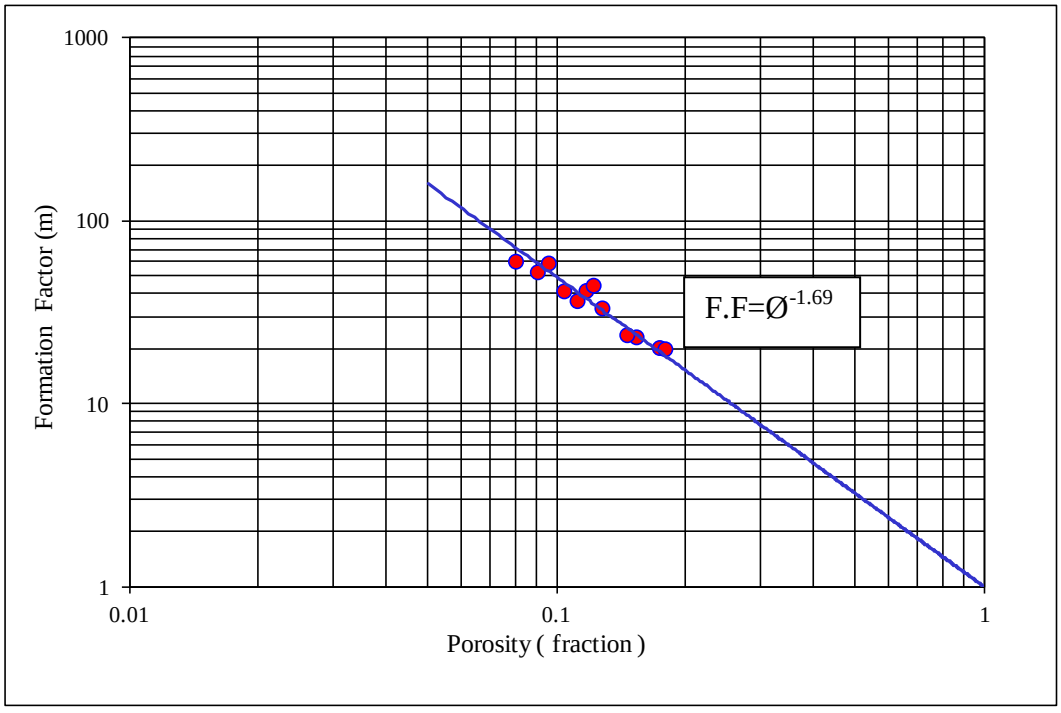

Figure 3.6. Formation factor versus porosity at ambient conditions.

3.3.3 Formation resistivity factor and cementation exponent at overburden pressure

The Archie's cementation factor (m) has been found to vary from 1.3 to approximately 2.2 for unconsolidated and consolidated sands respectively (Amyx et al., 1960). Most previous studies showed that the formation resistivity factor and cementation exponent increase with overburden pressure. In this work, both formation resistivity factor (FF) and cementation exponent (m) were found to increase with confining pressure for the Nubian Sandstone samples. Table 3.3 and Figure 3.7 show the experimental results of the effect of overburden pressure on the cementation exponent and formation factor for the selected twelve plugs. The average value for the twelve plugs at each pressure stage is shown. Table 3.4 shows the individual results for porosity, formation resistivity factor and cementation exponent at different overburden pressures for one of the samples.

Table 3.3. Average cementation exponent for the twelve core samples at different values of overburden pressure.

Overburden Pressure (psi)	Cementation exponent (m)
1000	1.71
2000	1.72
3000	1.74
4000	1.75
5000	1.76

Table 3.4. Porosity, formation resistivity factor and cementation exponent for sample # 3 at different values of overburden pressure.

Pressure (Psi)	Porosity (%)	Formation Factor (F.F)	Cementation exponent (m)
0	10.39	41.6	1.65
1000	10.11	44.6	1.66
2000	9.92	47.09	1.67
3000	9.82	49.21	1.68
4000	9.73	52.02	1.70
5000	9.68	54.52	1.71

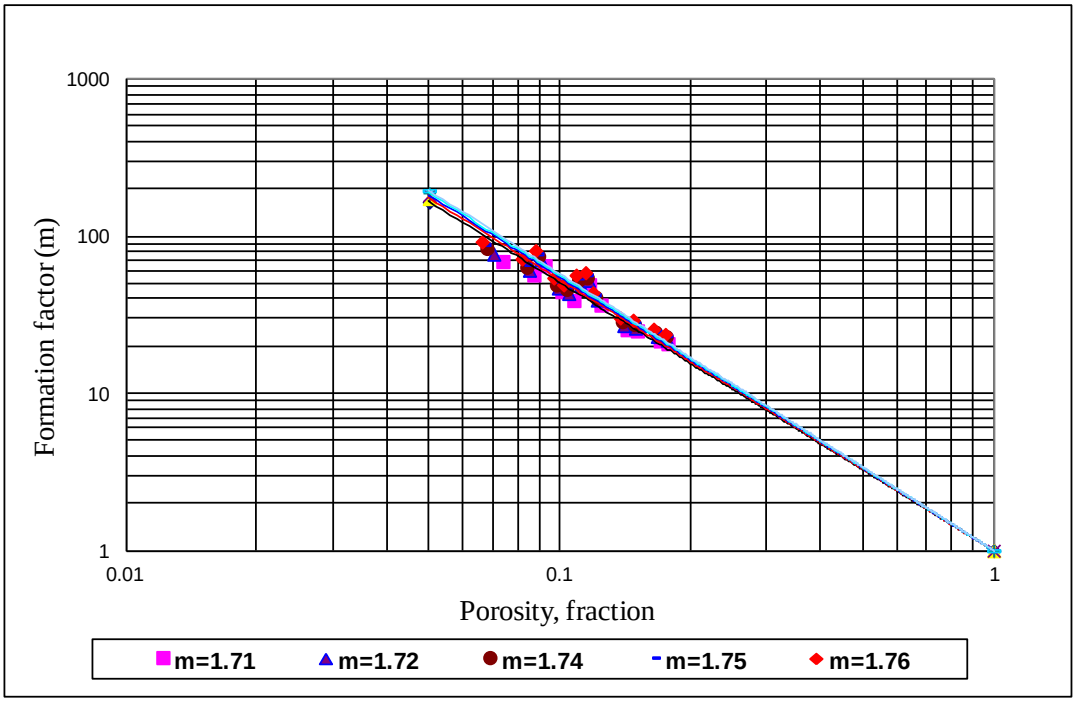

Figure3.7. Formation factor versus porosity at different overburden pressure. The different values of the cementation factor m refer to the different overburden pressures as given in Table 3.3.

3.3.4 Saturation exponent, capillary pressure and resistivity index before and after wettability measurement

Saturation exponent (n) values are normally determined experimentally in the laboratory on core samples of the actual formation under consideration. Due to the fact that the saturation exponent varies with both lithology and wettability a suite of saturation exponent value measurements is often conducted on samples with a range of porosity, permeability and lithology which may be present in the formation (Bennion et al., 1996). Saturation exponent values were determined on the twelve representative core samples from porous plate capillary pressure measurements in the laboratory. The global hydraulic element (GHE) template (Figure 3.5) was used to select three representative plugs from each GHE. The selected plugs were taken from six wells from the Nubian Sandstone Formation. The samples were cleaned in hot solvents, dried and then mounted into the core holder. All the samples were saturated with the brine (salinity 135,000 ppm). Powder was used between the samples and the porous plate to maintain hydraulic contact during the test. The resistivity of 100% saturated samples (R_o) and the brine resistivity (R_w) were measured on

consecutive days until the results were stabilized. The equilibrium brine saturation was measured at an air-brine capillary pressure of 1, 2, 4, 8, 15, 35, 60 and 120 psi. The resistance was used to calculate the sample resistivity, and the partial resistivity (R_t) was divided by the sample resistivity at hundred percent liquid saturation (R_o) which yielded resistivity index. During the measurement, the pressure was increased in steps and the final equilibrium produced volumes of the wetting phase were recorded for each step. The measurement procedures were described (see Appendix D). In the present work, the output data of capillary pressure for sample #3 before and after wettability measurement is displayed in Table 3.5 and in Figures 3.8 and 3.9. Because the wettability affects waterflood performance, Amott wettability measurements were made on the same samples.

The saturation exponent for sample # 3 before wettability measurement was 1.39. When the wettability measurement was conducted on the sample, the sample imbibed oil (tendency to be oil-wet), and the saturation exponent increased to 2.39 as shown in Table 3.6 and in Figure 3.10.

Table 3.5. Resistivity index and water saturation for sample#3 from porous plate capillary pressure measurement.

Capillary pressure at ambient. (Psi)	Capillary pressure at reservoir. (Psi)	Water Saturation Before Wettability Measurement (fraction)	Water Saturation After Wettability Measurement (fraction)	Resistivity Index (RI) Before Wettability Measurement	Resistivity Index (RI) After Wettability Measurement
1	0.36	0.7214	0.7873	1.451	3.997
2	0.72	0.4612	0.6843	1.460	3.327
4	1.44	0.3414	0.5300	1.407	3.099
8	2.89	0.2410	0.4000	1.371	2.799
15	5.42	0.2014	0.3018	1.387	2.475
35	12.6	0.1536	0.2315	1.382	2.223
60	21.7	0.1368	0.1935	1.371	2.072
120	43.3	0.1174	0.1832	1.400	2.047

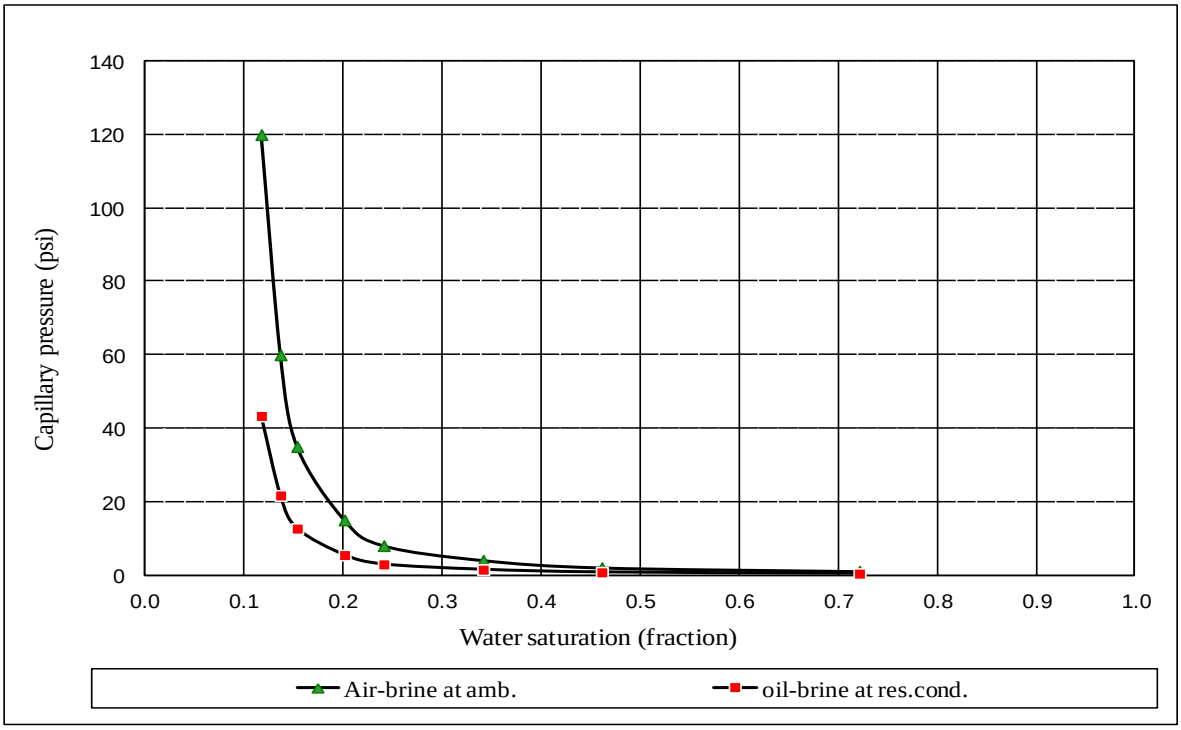

Figure 3.8. Capillary pressure curves for sample # 3 before wettability measurement.

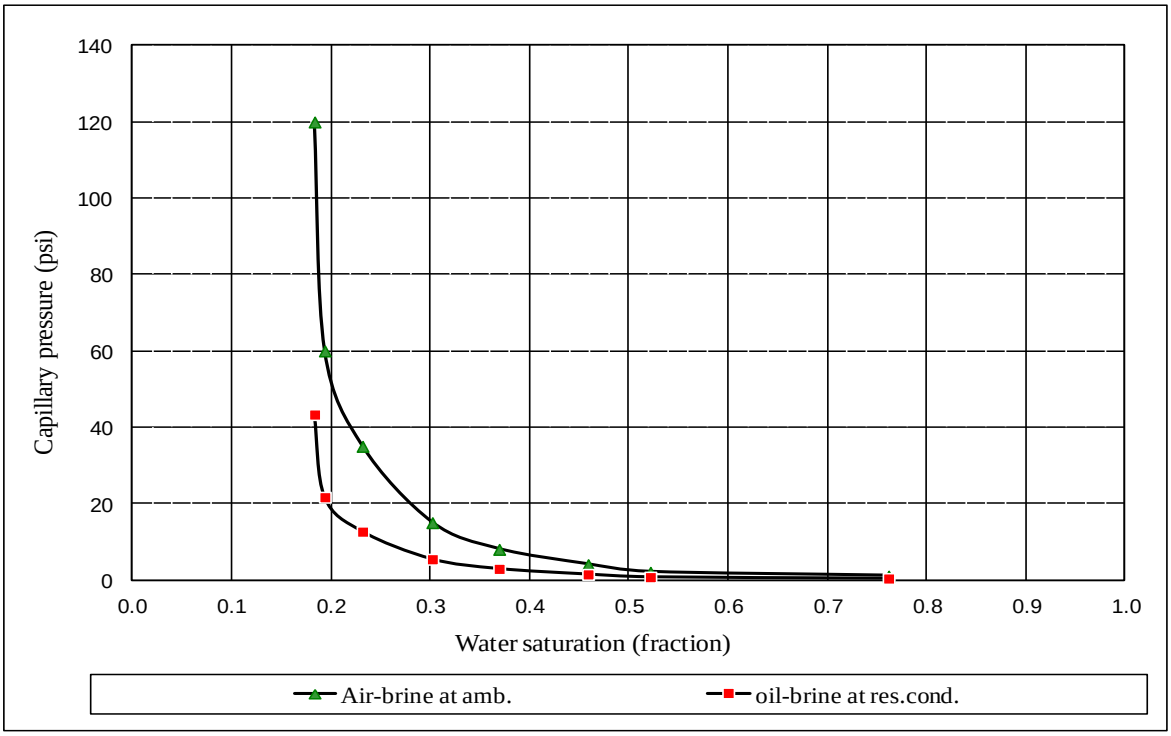

Figure 3.9. Capillary pressure curves for sample # 3 after wettability measurement.

Table 3.6. Saturation exponent values before and after wettability measurement.

Sample #	Well Name	Saturation Exponent (n) Before Wettability Measurement	Saturation Exponent (n) After Wettability Measurement
03	A1-Libya	1.39	2.39
10	A1-Libya	1.75	2.60
15	A3-Libya	2.06	2.79
18	B1-Libya	1.76	2.65
24	A3-Libya	1.93	2.18
29	C2-Libya	1.79	2.59
41	C1-Libya	1.87	2.50
42	A3-Libya	2.18	2.86
47	C2-Libya	1.91	2.65
53	A1-Libya	1.78	2.43
83	A2-Libya	1.97	2.49
123	A2-Libya	1.73	2.22

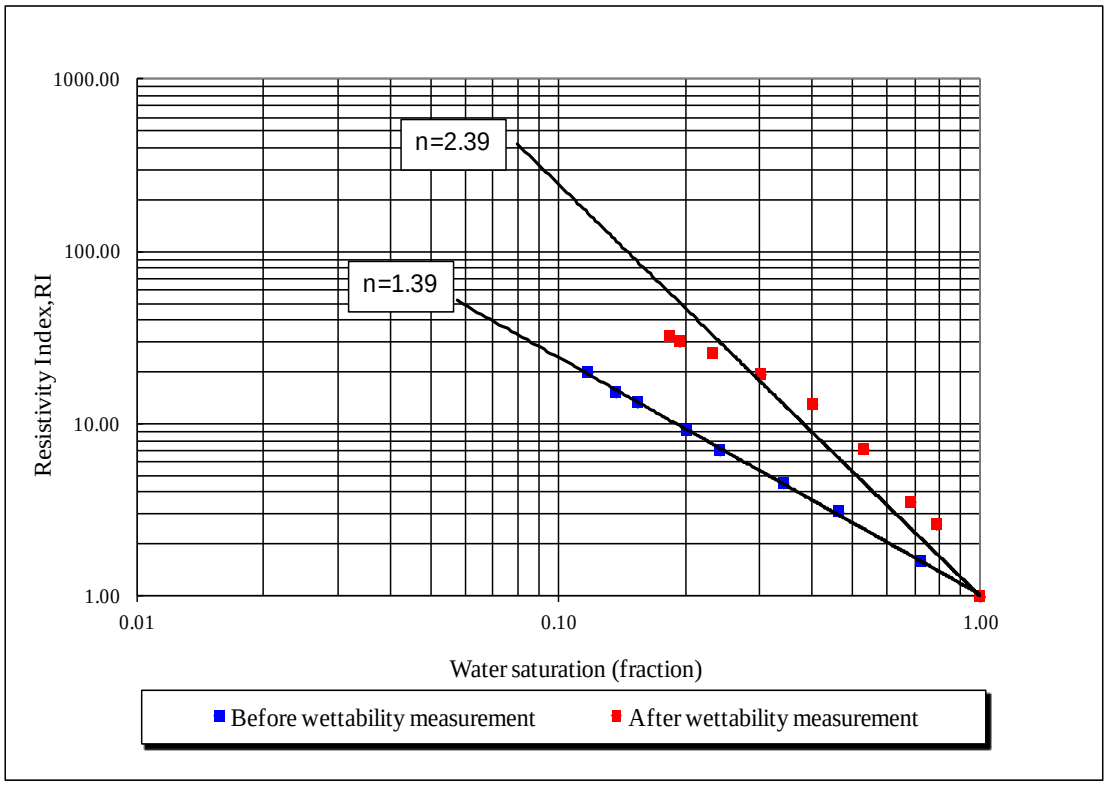

Figure 3.10. Resistivity index versus water saturation before and after wettability measurement for sample # 3.

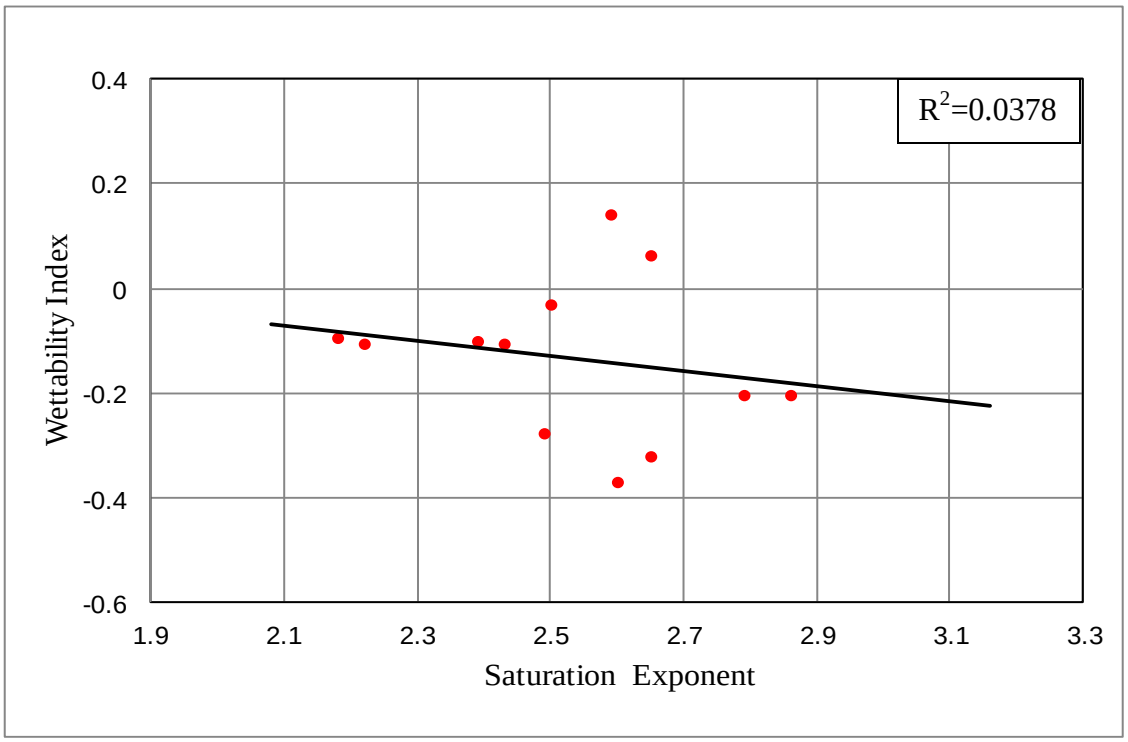

Figure 3.11. Saturation exponent as a function of wettability index for the twelve selected representative samples.

3.3.5 Pore size distribution from mercury injection capillary pressure measurements

After the measurements core pore volume, injection pressure and mercury volume, pressure is plotted versus mercury saturation to generate a capillary pressure curve. The analysis is very rapid allowing up to 8 samples to be analysed in 24 hours. The analysis can provide high resolution data. Irregular and small samples can be used. However, the test is destructive. Samples cannot be used for subsequent core testing and cannot be confined. Using capillary pressure curves as a means of determining pore size distribution was first suggested by Washburn (1921). Most pore size distribution measurements have been determined by the mercury injection procedure. Capillary pressure, pore size and pore size distribution are closely related to the rock and fluid properties, and consequently have an effect on oil recovery of a reservoir. Pore size distribution can be calculated from mercury injection capillary pressure data; however, a broad range of pore size and type is covered by mercury injection capillary pressure. The pore throat radius is calculated as:

$$r = \frac{2\sigma\cos\theta}{P_C} \quad \text{---------- (3.2)}$$

In an air-mercury system where σ= 480 dyn/cm, θ=140^o and pressure in psi, the pore entry radius in microns can be determined as follows:

$$r_p(\text{micron}) = \frac{106}{P_c(\text{psi})} \quad \text{---------- (3.3)}$$

The different fluids are usually used in the laboratory; the measurements of laboratory capillary pressure must be corrected before use in reservoir calculations. Given the contact angle for the fluids in the laboratory and the interfacial tension, we can write as a following:

$$P_{CL} = \frac{2(\sigma\cos\theta)_L}{r} \quad \text{---------- (3.4)}$$

For the reservoir capillary pressure:

$$P_{CR} = \frac{2(\sigma\cos\theta)_R}{r} \quad \text{---------- (3.5)}$$

By dividing this equation and solve for reservoir capillary pressure then:

$$P_{CR} = P_{CL}\,\frac{(\sigma\cos\theta)_R}{(\sigma\cos\theta)_L} \quad \text{---------- (3.6)}$$

Where:

P_{CR} = Reservoir capillary pressure (psi).

P_{CL} = Laboratory capillary pressure (psi).

σ_L = Laboratory interfacial tension (dynes/cm

σ_R = Reservoir interfacial tension (dynes/cm).

θ_R = Reservoir contact angle (degree).

θ_L = Laboratory contact angle (degree).

The laboratory capillary pressure transported from mercury injection and has been converted to the reservoir capillary pressure using equation 3.5 for more detail see Table A23 in appendix A.

The twelve core samples underwent mercury injection capillary pressure measurements using a Micromeritics Auto pore IV 9510 mercury porosimeter with windows software. A mercury injection capillary pressure measurement was explained in detail (see Appendix D). Mercury volumes are expressed in cubic centimetres mercury per gram dry weight of rock sample, and the output data of sample # 3 is displayed in Table 3.7 and in Figures 3.12 - 3.14. These figures are discussed in more detail in the next discussion section.

Table 3.7. Interpretation of air-mercury capillary pressure data and calculation of pore size distribution for sample # 3 during Drainage (D) and imbibtion (I) cycles.

Pore volume (C.C) : 0.159				Threshold pressure (psi) : 5.498	
Porosity (%) : 10.28				Dry Weight (gm) : 3.69	
Permeability (mD) : 337.5				sample Depth (ft) : 15012	
Pressure Psia	Cycle	Cum. Hg Sat. Pore Vol. (%)	Wetting Phase, Sw Pore Vol. (%)	Incr. Hg Sat. Pore Vol.(%)	r_p microns
5.498	D	0.000	100.000	0.000	19.401
6.000	D	7.471	92.529	7.471	17.778
7.488	D	20.037	79.963	12.566	14.245
8.494	D	24.919	75.081	4.882	12.557
10.484	D	30.739	69.261	5.820	10.173
12.985	D	34.813	65.187	4.074	8.215
15.966	D	37.651	62.349	2.839	6.681
19.952	D	40.324	59.676	2.672	5.346
24.997	D	42.877	57.123	2.554	4.267
29.975	D	43.497	56.503	0.620	3.558
36.364	D	44.299	55.701	0.802	2.933
47.293	D	45.417	54.583	1.118	2.255
57.895	D	45.880	54.120	0.463	1.842
72.603	D	46.553	53.447	0.672	1.469
86.736	D	47.238	52.762	0.685	1.230
110.521	D	48.938	51.062	1.700	0.965
136.744	D	50.372	49.628	1.434	0.780
170.515	D	51.922	48.078	1.551	0.626
217.089	D	53.373	46.627	1.450	0.491
266.742	D	54.565	45.435	1.192	0.400
327.014	D	55.467	44.533	0.902	0.326
416.542	D	56.394	43.606	0.927	0.256
516.246	D	57.040	42.960	0.646	0.207
636.984	D	57.672	42.328	0.632	0.167
800.615	D	58.329	41.671	0.657	0.133

Pressure (Psia)	Cycle	Cum. Hg Sat. Pore Vol. (%)	Wetting Phase (Sw) Pore Vol. (%)	Incr. Hg Sat. Pore Vol. (%)	r_p microns
987.492	D	58.932	41.068	0.604	0.108
1199.091	D	59.621	40.379	0.689	0.089
1495.970	D	60.429	39.571	0.808	0.0713
1894.701	D	61.555	38.445	1.126	0.0563
2345.765	D	62.374	37.626	0.820	0.0455
2894.696	D	62.973	37.027	0.599	0.0368
3592.163	D	63.796	36.204	0.823	0.0297
4480.783	D	64.205	35.795	0.409	0.0238
5582.575	D	64.637	35.363	0.431	0.0191
6882.724	D	64.932	35.068	0.295	0.0155
8580.083	D	65.151	34.849	0.219	0.0124
10581.297	D	65.278	34.722	0.126	0.0101
13181.535	D	65.281	34.719	0.004	0.0081
14781.165	D	65.318	34.682	0.037	0.0072
16379.425	D	65.418	34.582	0.099	0.0065
19979.568	D	65.536	34.464	0.118	0.0053
24991.703	D	65.603	34.397	0.068	0.0043
29993.539	D	65.971	34.029	0.368	0.0036
34990.906	D	65.971	34.029	0.000	0.0030
39993.086	D	65.971	34.029	0.000	0.0027
44990.063	D	65.971	34.029	0.000	0.0024
49987.453	D	65.971	34.029	0.000	0.0021
54993.406	D	65.971	34.029	0.000	0.0019
59855.215	D	65.971	34.029	0.000	0.0018
46107.730	I	65.657	34.343		
35502.543	I	65.657	34.343		
27307.168	I	65.657	34.343		
21009.095	I	65.657	34.343		
16006.950	I	65.657	34.343		
12411.234	I	65.657	34.343		
9611.0830	I	65.657	34.343		
7314.6650	I	65.657	34.343		
5712.2275	I	65.657	34.343		
4303.4785	I	65.657	34.343		
3304.1771	I	65.657	34.343		
2603.4155	I	65.657	34.343		
1996.2829	I	65.657	34.343		
1506.6490	I	65.657	34.343		
1205.2506	I	64.908	35.092		
901.18908	I	64.501	35.499		
701.61450	I	64.501	35.499		
501.99649	I	64.501	35.499		

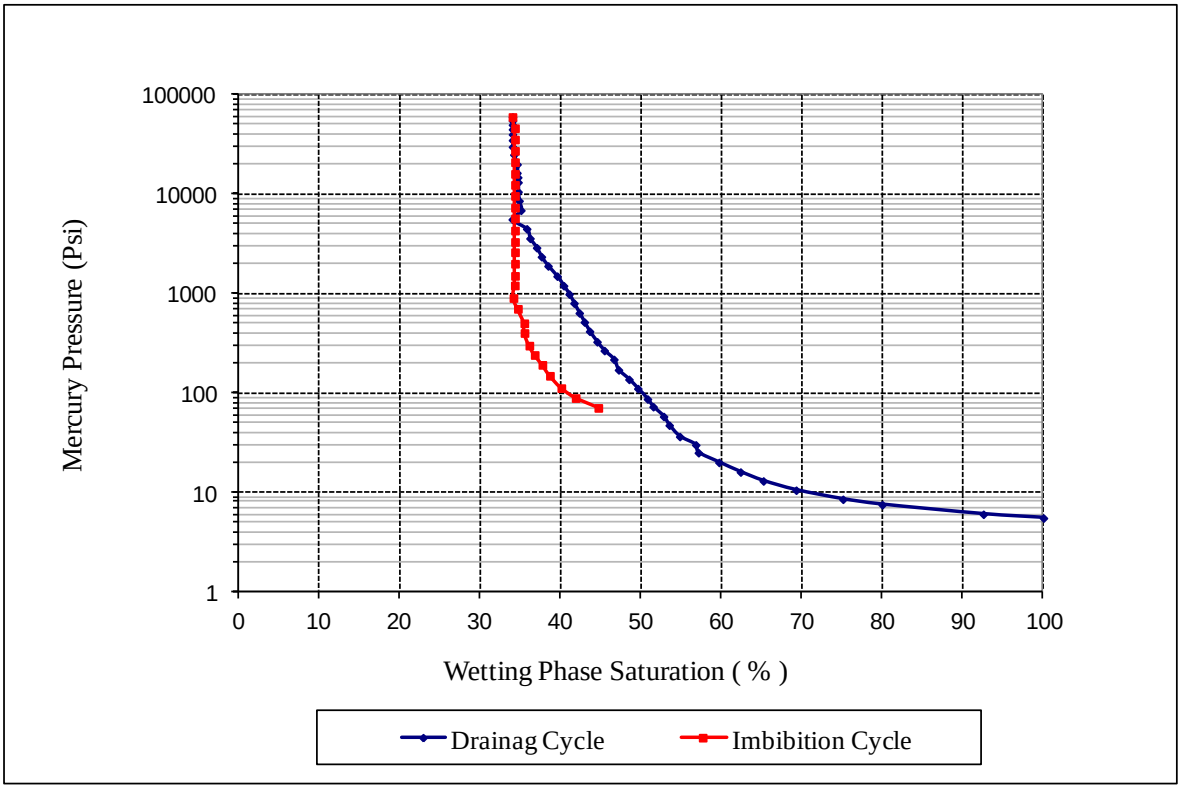

Figure 3.12. Drainage and imbibition cycles.

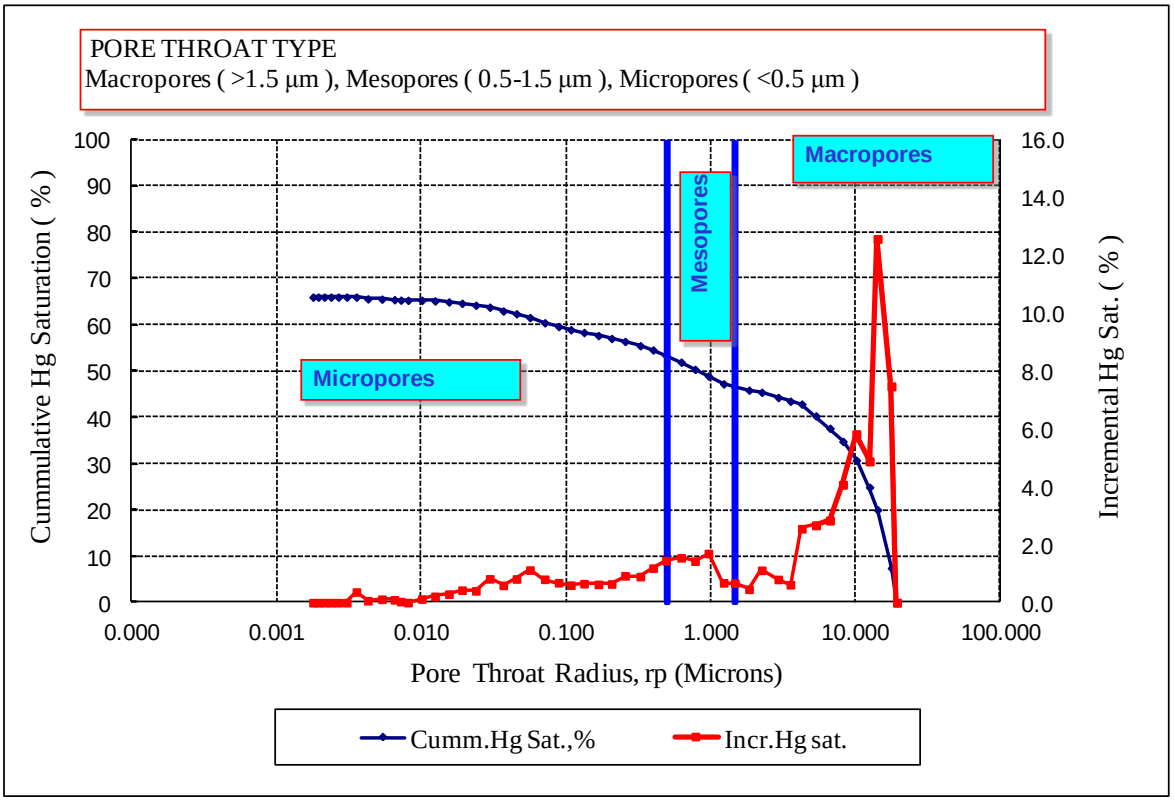

Figure 3.13. Pore size distribution for sample # 3.

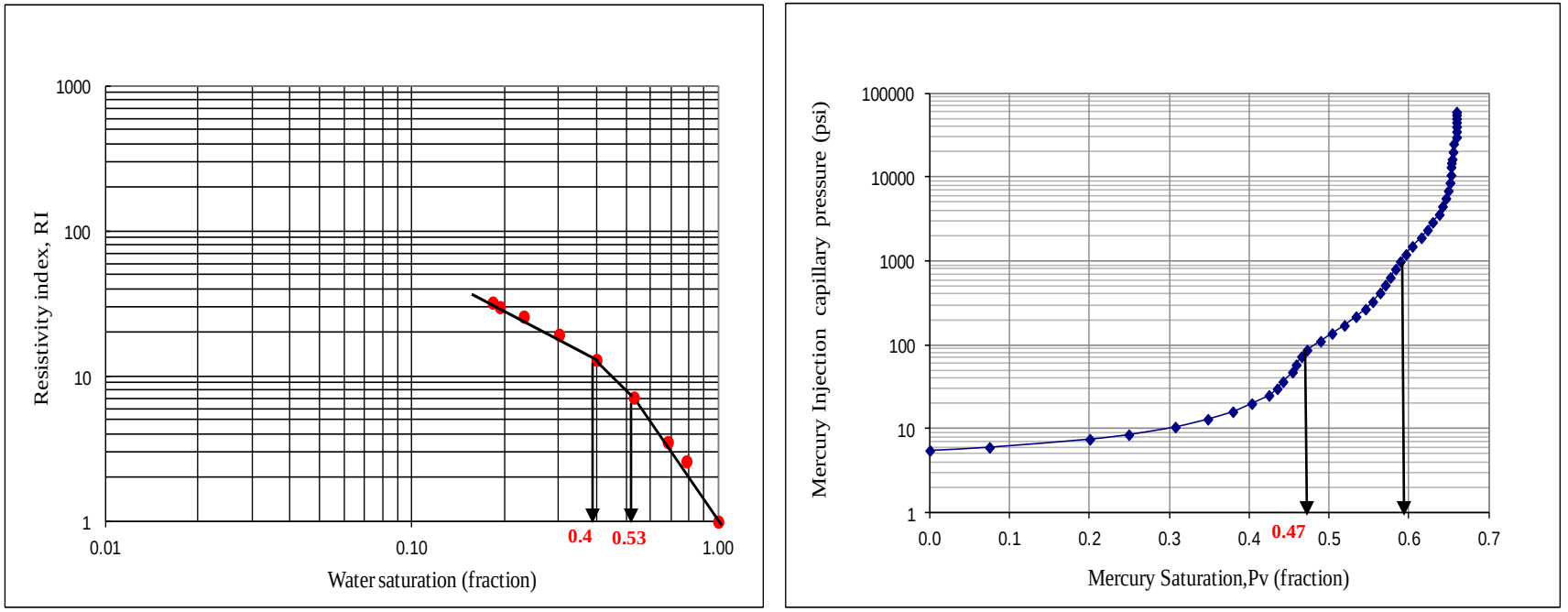

(a) (b)

Figure 3.14. Resistivity index versus water saturation and mercury capillary pressure versus mercury saturation for sample # 3.

3.4 Discussion of Results

3.4.1 Effect of overburden pressure on formation factor and cementation exponent

In performing laboratory measurements, changes have been observed in the resistivity of fluid filled reservoir rocks as a result of changing overburden pressure conditions. These changes may result from changing the internal pore structure and an increase in tortuosity and decrease in the effective cross-sectional area that is available for the flow of electric current. In fact this relation is very clear in this study in Table 3.3 and Figure 3.7. Table 3.4 summarises the experimental results of the effect of overburden pressure and cementation exponent for sample # 3. A systematic decrease in rock conductivity and increase in formation factor as the overburden pressure increased over the range of 1000 to 5000 psi was seen. The overburden pressure was started from 1000 psi because during lab measurements the reduction effect of pore volume starts with pressure greater than 800 psi, and the ended with 5000 psi because the reservoir pressure is 5500 psi. The cementation exponent of sample #3 was increased from 1.66 to 1.71 (+3.0%) as a result of increasing the pressure up to 5000 psi. Wyble (1958) showed that the cementation exponent (m) of one of the samples studied was increased from 1.87 to 2.04 (+9.1%) as a result of increasing the pressure up to 5000 psi . For sample #3 the original value of porosity was 10.39% at zero overburden pressure, and formation factor 41.6. When the initial overburden pressure was applied (1000 psi) to the sample, the porosity decreased to 10.11% and the formation factor became 44.6. As the pressure was increased up to 5000 psi, porosity decreased to 9.68% and formation factor increased to 54.52. Overburden pressure will reduce the bulk volume. At low overburden pressures, fissures start to close with small compression in mineral grains. As the overburden pressure increases, the rock undergoes bulk compression resulting from pore and grain deformation. As the pressure is depleted in a reservoir, the effective overburden pressure increases causing a reduction in pore volume. The results indicate the rock is compacted as a result of overburden pressure, the matrix is under stress and porosity decreases, and therefore the cementation exponent will change. This change may result from changing the internal pore structure and a decrease in the effective cross-sectional area that is available to flow the electric current.

The relation between cementation exponent and global hydraulic elements (GHEs) was also observed. This relation is very clear in Table 3.2. The cementation factor is 1.74 in sample # 42 (GHE-5) which is fine to medium grained and moderately sorted. In sample #24(GHE-6) which is fine to medium grained and moderately sorted and less cemented, the cementation factor is 1.72. In sample # 10 (GHE-7) which is good reservoir quality, medium to coarse grained and well sorted, the cementation factor is 1.65. In sample # 53 (GHE-8) which is best reservoir quality medium to coarse grained and well sorted, the cementation factor is 1.64. The cementation exponent decreases from GHE-5 to GHE-8 and this decrease is related to the texture and overburden pressure.

3.4.2 Water saturation, saturation exponent and the effect of wettability measurement

In section 3.3.4 the water saturation for sample # 3 after wettability measurement (Figure 3.9) is slightly higher than the water saturation before wettability measurement (Figure 3.8). The reason is that the sample imbibed oil, so the resistivity increases because of the decrease of cross-sectional area and a fraction of the non-wetting phase becomes disconnected and surrounded by oil which acts as an insulator to the flow of electric current. Figure 3.10 shows the relation between resistivity index and water saturation before and after wettability measurement for sample # 3.

Estimation of hydrocarbon reserves is strongly dependent of electric log data and on the value of saturation exponent (n) used. The saturation exponent is usually either assumed to be 2.0 regardless of reservoir wettability or is derived from laboratory measurement of electrical properties of the cores. It can vary between 1.2 to 2.2 (Serra, 1984) for water-wet rocks, and can have a value from 2.2 or higher when the rock wettability changes towards oil-wet (Anderson, 1986a). For sample #3 the saturation exponent before wettability measurement was 1.39, and when the wettability test was conducted the sample imbibed oil (tendency to be oil wet), and the saturation exponent increased to 2.39. In water-wet rock, the brine occupies the small pores and forms a continuous film on the rock surface. In an oil-wet rock, the brine is located in the centres of the large pores. This difference in brine distribution caused by the wettability becomes very important as the brine saturation is lowered. Generally, almost all of the brine in the water-wet rock remains continuous, so the resistivity increases because of the decrease in cross- sectional area that can conduct flow. In oil-wet rock, a portion of the brine will

lose electrical continuity, so the saturation exponent will increase at a faster rate. In oil-wet rock, a fraction of the non-wetting phase (specially at low brine saturation) which is located in the middle becomes disconnected and surrounded by oil which acts as an insulator to the flow of electric current. The insulation of this portion of brine prevents it from contributing to the flow of electric current and hence leads to higher values of saturation exponent. Finally, in Figure 3.11 Archie's saturation exponent increases as the rock becomes more oil wet.

3.4.3 Mercury injection capillary pressure and pore size distribution

Drainage and imbibition capillary pressure curves were obtained (Figure 3.12). Pressure is introduced into the apparatus, which allows the mercury to enter the rock sample. The pressure is introduced at a series of increasing pressure increments. The magnitude of pressure and the incremental volume of mercury injected into the sample are monitored and recorded after equilibrium. As the pressure increases, mercury moves into the sample's pores, vacating the stem (Drainage or Intrusion). The greater the pressure, the smaller the pore diameter in to which the mercury can be forced. An imbibition curve can be produced by incrementally decreasing of the pressure gradually in steps to withdraw the mercury from the pores in pressure steps from 60,000 psi to 14 psi (Imbibition or Extrusion).

Pore throat radius can be determined from mercury injection tests and may be used to categorize the rock by pore type (Figure 3.13): macro, meso, and micro. Micro-porosity in reservoir rocks has been described as the pore system whose average pore diameter is less than 0.0625mm **(**Pittman, 1971). Micro-pores can be in communication with larger pores or can be isolated and separate from the macro-porosity. Porosity logs see micro-porosity as part of the total porosity, but resistivity logs are affected to a large extent by the water contained in a micro-porous system. If micro-porosity is abundant enough and contains high immobile water, calculation of water saturation using conventional methods will erroneously yield high water saturation and the interval analysed can be regarded as a water-bearing zone. The relationship between resistivity index and brine saturation of rocks containing micro-porosity is not linear, but the slope decreases towards the lower water saturation end. The reason is that, as oil saturation increases, first the larger pores dominate the resistivity. At this stage, water saturation is still high because micro-pores hold up a large water volume, which causes a high saturation

exponent. As the oil starts to drain water from micro-pores, water saturation decreases sharply with little influence on resistivity and causes saturation exponent (n) to decrease with decreasing water saturation (Swanson, 1985).

From the mercury injection capillary pressure data for sandstone sample # 3 the pore size distribution (rp) was calculated from Equation (3.2) and the values shown in Table 3.7 are the pore throat size at which maximum intrusion of the non-wetting phase occurs. From the mercury capillary pressure curve (Figure 3.14, b), the micropore system is arbitrarily defined as pores with entry pressures greater than that found at the inflection point in the first steeply rising region of the capillary pressure curve. The macropores are those entered by mercury below this pressure. The latter contribute to the hydrocarbon oil storage volume and permeability. Note that the inflection point occurs at about 100 psi mercury pressures in this example and is thus visible in the standard 1000 psi capillary pressure curves. Figure 3.13 shows that the macropores contain about 80% of the total pore space, the mesopores about 12% and the micropores are less than 10%. The ranges of the values of the pore throats radius according to the Core Laboratories Company Manual are as follows: macropores are greater than 1.5 µm, mesopores are 0.5-1.5 µm, and micropores are less than 0.5 µm. It is clear from Figures 3.14 (a) and (b) a good relation between resistivity and type of pores (macro- and micropore system) was observed. Note that at the saturation where mercury penetration into micro-porosity occurs, there is also a significant change in slope (saturation exponent, n,) between resistivity index and water saturation after wettability measurement. The reason for this change in slope (saturation exponent) may be due to micro-pores / irregular surfaces through this sample which also affect the low mercury saturation portion of the MICP curve. The reason behind this phenomenon is that, as the oil saturation increases, first the resistivity is dominated by the large pore network. Water saturation is still high because micro-pores hold a large water volume, and lead to high apparent saturation exponent. Then as capillary effects increase sufficiently to penetrate the micro-pores, water drains from micro-pores with very little influence on resistivity, causing the saturation exponent to decrease. The difference between these results and Swanson results that Swanson in his work didn't use the wettability measurement.

The original wettability of a formation and altered wettability during and after hydrocarbon migration influence the profile of initial water saturation, Swi, and production characteristics in the formation. The distribution of fluid in the rocks is determined by the buoyancy based pressure difference between the oil and water phases, which is termed the capillary pressure, Pc. This wetting heterogeneity can affect recovery. Under waterflood, water penetrates the water-wet layers more readily than the oil-wet layers because of capillary effects. As mercury is a non-wetting fluid, pressure must be built up before it displaces the wetting phase. At a sample specific pressure, which is dependent on the pore-throat size, the percentage of mercury intruded increases rapidly. This is the threshold/displacement pressure and graphically corresponds to an upward convex inflection point on the mercury injection curve

For sandstone samples containing micro-porosity, a mercury capillary pressure curve such as in Figure 3.14 b is found. The micropore system is arbitrarily defined as pores with entry pressure greater than found at the inflection point in the first steeply rising region of the capillary pressure curve. The macropores are those entered by mercury below this pressure (Swanson 1985). The latter contribute to hydrocarbon oil storage volume and permeability.

The Amott wettability test was performed on plug samples from Nubian Sandstone Formation before porous plate capillary pressure test. By integrating of mercury injection capillary pressure curves and porous plate capillary pressure technique, the types of pore system were classified.

Initially, the mercury starts with low pressure injection until the macropores was saturated. The inflection point from this region was observed at about 100 psi, and the mercury saturation was 0.47 as shown in Figure (3.14b). From porous plate capillary pressure test, the macropores region was observed during air injection at constant slope (n) until the sample reaches 0.53 water saturation as shown in Figure (3.14 a).The slope start to changes at 4 psi, at this point the oil starts to displace the water from the large pores and the inflection point in the mercury injection capillary pressure curve was observed.

The mercury injection capillary pressure increases and the mercury start to enter small poree (mesopores). A second inflection point was seen at pressure about 1000 psi, and

the mercury saturation was 0.6. The pressure continues to increase until the mercury fills the micropores as shown in Figure 3.14 b. In Figure 3.14 a, the slope (n) decrease toward lower water saturation when the pressure increases from 4 to 8 psi until the mesopores was saturated at water saturation equal 0.4.

A comparison was made between the mercury injection capillary pressure curve and resistivity index versus water saturation relationship, this indicates the second inflection point where the mesopores was saturated. The remaining pores in the sample represent the micro-porosity at constant slope (n) and the relative volume of these micropores is a major factor controlling water saturation in oil and gas reservoirs.

From above a good relationship between the type of pore system and resistivity was obtained in order to classify rock porosity type.

Petrophysical characteristics such as porosity, recovery efficiency, irreducible water saturation, pore-throat size, pore-throat size distribution and threshold pressure are determined using mercury porosimetry. These characteristics determine the shape, slopes and plateau of the capillary-pressure curve. Analysis of the MICP curve is, therefore, important for various phases of reservoir production, especially secondary and tertiary recovery. These data may be evaluated in conjunction with additional SCAL and routine core petrophysical data in order to provide an accurate assessment of reservoir and/or seal potential.

3.5 Reserve estimation

The saturation exponent value is a function of pore system geometry and formation wettability, although a value 2.0 is commonly assumed. This value can vary considerably from formation to formation and may result in over or under estimation of water saturation in many situations (Bennion et al., 1996), and the error in the estimation can subsequently lead to inaccurate estimates of the hydrocarbon in place.

The effect of overburden pressure on core samples changes pore size and pore throat size distribution, and this may increase irreducible water saturation and affects oil recovery. If the influence of micro-porosity on resistivity parameters (m and n) is ignored, significant errors in the estimation of hydrocarbon volume can occur. Since the

micro-porosity leads to a decrease in the cementation factor and saturation exponent, the use of higher values of m and n leads to overestimation of water saturation and underestimation of hydrocarbon in place. Capillary pressure, pore size and pore size distribution are closely related to the rock and fluid properties, and consequently effect the oil recovery within a reservoir.

3.6 Conclusions

1. Changes were observed in the formation resistivity factor and cementation exponent due to ambient conditions and changes of overburden pressure. The cementation exponent also decreased from GHE-5 to GHE-8.

2. Changes were also observed in the saturation exponent (n) and water saturation (S_w) before and after wettability measurement. Samples with an oil-wet tendency have higher irreducible brine saturation and higher Archie saturation exponent values than samples with an uniform water-wet surface.

3. Mercury injection capillary pressure and resistivity index measurements demonstrated a good relation between resistivity and type of pores (macro- and micro-pore system). When oil begins to penetrate micro-pore systems in measurements of resistivity index versus brine saturation, a significant change in slope of the curve occurs.

CHAPTER FOUR

Prediction of Special Core Analysis (SCAL) Parameters using Neural Networks with Different Combinations of Wireline Logs

4.1 Introduction and Objectives

Laboratory resistivity, water saturation and wettability measurements were explained in detail (see Appendix D). Acquiring representative core samples from a large number of wells can prove to be very expensive and time consuming. The majority of wells, however, are logged and the use of wireline log data in conjunction with some core data has been proposed as a rapid, cheap, and alternative to predict some special core analysis (SCAL) parameters instead of collecting extensive core or performing SCAL measurements in all wells. Neural network predictors are potentially very useful in the present study due to the limited SCAL data for the studied well. In this chapter a number of SCAL parameters were predicted using neural networks based on different combinations of wireline logs. The procedure firstly involved training the neural network predictors using data in a training well. These predictors were then applied to an adjacent test well in the same oil field, and to another test well in a different oil field. The most frequently used type of neural network is a feed forward neural network using a back-propagation learning algorithm, due to its popularity and simplicity.

Osborne (1992) first introduced back-propagation neural networks for permeability prediction from wireline logs. Subsequently, several other studies have been published where neural networks have been used to predict conventional core petrophysical properties, primarily permeability (Mohaghegh et al., 1995; Malik et al., 1996; Wong et al., 1997; Arpat et al., 1998; Jamialahmadi and Javadpour, 2000; Helle et al., 2001; Bhatt and Helle, 2002; Le, 2004). All previous studies have used wireline logs in conjunction with core plug data to train the neural networks. In the present study some SCAL properties data (true formation resistivity, resistivity index, water saturation, saturation exponent, and Amott-Harvey Wettability Index) have been predicted using neural networks. The

predictors were trained with data from a series of representative SCAL plugs, chosen from the global hydraulic elements in the training well (Figure 4.1), in conjunction with the corresponding wireline log data. The SCAL measurements were undertaken at the Libyan Petroleum Institute (LPI). Java neural network software (Java NNS version 1.1) was used to train the predictors.

4.2 Neural Networks

4.2.1 Introduction to Neural Networks

A neural network is a generalised numerical tool, which enables the correlation or linking of one set of data, called the input dataset, to another called the output dataset. It is assumed that the input and output data may be related in some way, although it is not necessary to know this relationship. A known set of data, called the training dataset, containing both inputs and outputs, is used to teach the neural network to recognise any association which may exist. The input data are applied to an array of input neurons. Each of these is connected to a variable number of neurons in a hidden layer. In turn each neuron in the hidden layer communicates to the output neuron, giving a specific output value. In fact, there may be more than one hidden layer of neurons and the number of neurons in each layer may be different, although they will all be interconnected to the neurons of adjacent layers. Importantly, the signals transferred between neurons in a network are modified by multiplying the value of a weight, which is associated with each connection. The different connections have different weights and these, therefore, determine the influence a particular neuron has on a particular output of the network. During training both the input and output data are known. Using the input data, the connection weights are adjusted automatically so that the neural network gives output values which match as closely as possible the real output values in the training dataset. The neural network is then able to predict further outputs on the basis of information supplied as input along with the weights that were determined in the training process.

4.2.2 Back Propagation Artificial Neural Networks

Back propagation artificial neural networks (**BPANNs**), used in the present study, are the most common type of feed –forward multi-layered neural network, consisting of an input

layer, hidden layers and output layer. The neurons from each layer are connected to the neurons in the next layer, and the connections between neurons are weighted. Each neuron receives a net input (net_j) that is computed from weighted outputs from prior neurons connected to this neuron:

$$net_j = \sum_{i=1}^{n} W_{ij} \; O_i \quad \text{---------- (4.1)}$$

where:

W_{ij} is the connection weight from neuron i to neuron j
O_i is the output from neuron i in the prior layer

The output from each neuron is dictated by its activation function, a mathematical function, which calculates the neuron's output based on the input to this neuron. The most commonly used activation function in back-propagation neural networks is the sigmoid activation function, which produces an output in the range 0 to 1 and is a continuous function. The sigmoid activation function has the mathematical formula as follows:

$$f(x) = \frac{1}{1+e^{-x}} \quad \text{----------(4.2)}$$

The desired performance of a neural network is achieved through the training process. Given input and output patterns to the neural networks, it will adjust the connection weight between neurons as mentioned earlier until the predicted output is close to the desired output. An input pattern is presented to the network. This input is then propagated forward in the network until activation reaches the output layer. This constitutes the so-called forward propagation phase. The output of the layer is then compared with the output pattern. The error, that is the difference between the output O_j and the teaching input t_j of a target output neuron j, is then used together with the output of the source neuron i to compute the necessary changes of the weight W_{ij}. To compute the errors of inner neurons for which no teaching input is available (neurons of hidden layers), the errors of the following layer, which are already computed, are used. In this way the errors are propagated backward, so this phase is called backward propagation. The most commonly

used back-propagation update rule is the generalised delta rule, which is mathematically expressed as follows:

$$\Delta W_{ij} = \eta \delta_j O_i \quad \text{---------- (4.3)}$$

Where:

ΔW_{ij} is the weight change

η is the learning rate

δ_j is the error of neuron j

O_j is the output from neurons

The first step is to define the network architecture, which includes the number of input, hidden and output layers and the number of neurons in each layer. This is usually done by "trial and error". Wong et al. (1995 and 1997) used one hidden layer with 5 neurons; Huang et al. (1996) used 12 neurons in a single hidden layer; Arpat et al. (1998) used one hidden layer with 15, 18 and 30 neurons; Du et al. (2003) have indicated that the neural network can be improved by adding more hidden layers.

Determination of the appropriate number of nodes for the hidden layer is difficult, and often also done by trial and error. Le (2004) suggested a simple rule of thumb as follows:

$$\text{Number of neurons (hidden layer)} = 2\sqrt{\text{number of input neurons} + 1} \quad \text{---------- (4.4)}$$

The important feature of the back-propagation neural network is that it learns to reproduce the outputs not by just remembering that output appropriate for every input, but by learning the patterns contained within the data. Once trained, the network can make predictions from novel sets of input data.

There are four major concerns to be considered in order to predict SCAL parameters using back-propagation neural networks. They are: the number of input wireline logs, the number of core plugs in the training dataset, the network architecture, and the number of predictions.

The first concern is the number of wireline logs being used as input to the neural network. For instance, Helle et al. (2001) used a different combination of 4 wireline logs (GR, RHOB, DT, NPHI) to predict permeability in some North Sea reservoir wells. In this study, the number of input is 4, 5, 6, and 7 corresponding to 4, 5, 6, and 7 keys wireline logs to predict SCAL parameters (Figure 4.2). The second concern is the amount of core data in the training dataset and it's important because it plays a crucial role in terms of time and cost. The less cores that is needed, the lower would be the costs. In all published case studies to date, the number of core plugs in the training dataset was generally substantial. For instance, the lower published number of samples in a training dataset, which was called "limited", was 45 core plugs (Arpat et al., 1998). In this study 55 core plugs were used "limited". The third concern is the number of hidden layers and number of hidden neurons in each hidden layer. This task is usually done by "trial and error". Arpat et al. (1998) used one hidden layer with 15, 18, and 30 neurons. In this study, 5, 6, 7, and 8 hidden layers (Figure 4.2) with 24, 34, 46, and 60 neurons were used. The last concern is the number of predictions to be used, and single prediction was used (Figure 4.2). In order to choose the most suitable learning rate, its firstly set to 0.2 and then is gradually reduced to 0. The right learning rate was then selected as the 0.2 giving the minimal error in the training dataset.

The neural network classifies new patterns and predicts on output based on the learned patterns. Neural networks often have application when relationships of parameters are too complicated or require too much time to solve via conventional methods. The most frequently used type of neural network is a feed forward neural network using a back-propagation learning algorithm, due to its popularity and simplicity

Learning backpropagation algorithm is consider as an optimization problem because before any mathematical derivation it helps to develop some intuitions about the relationship between the actual output of a neuron and the correct output for a particular training case.

The advantage of network, the connection weights are adjusted automatically by using input data and gave output values which match as closely as possible the real output values in the training dataset. The neural network will converge to the correct SCAL parameter

values by backpropagation the error between its prediction and actual parameter value. In this particular case study, the application of the GFNNs approach to predict SCAL parameters to be a worthwhile technique for improved prediction and has potential for a wider scope of application such as full field review or asset evaluation where data, costs and time are normally limited.

The previous investigations (Mohaghegh et al.1996) have revealed that neural network is a powerful tool for identifying the complex relationship among permeability, porosity, fluid saturations, depositional environments, lithology, and well log data.

4.3 Resistivity Predictions using Neural Networks

4.3.1 Introduction to Resistivity

Electrical resistivity was the earliest and still the most frequently measured physical property of rocks to locate oil and gas reservoirs. Electrical resistivity methods involve the measurement of the apparent resistivity of soils and rock as a function of depth or position. The electrical resistivity of a material is its ability to resist or impede the flow of electric current. The resistivity of rocks is a complicated function of porosity, permeability, ionic content of the pore water, and clay mineralization. Dry rocks are poor conductors, therefore they normally exhibit extremely high resistivity (Keller, 1989). Reservoir rocks are porous and their pores are generally saturated with water, oil and gas. Formation water normally has resistivity of 0.04 to 10 ohm-m at 70° F, which is much lower than that of the rock grains. As a result, they are moderate conductors when they are saturated with water. The electrical resistivity of a material can be defined by the following equation:

$$R = r\frac{A}{L} \quad \text{---------- (4.5)}$$

Where:

R Resistivity

r Resistance

A Cross-sectional area of the conductor available to current flow

L Length of the conductor

In hydrocarbon bearing rocks, water often coexists with oil or gas or both. Hydrocarbons are non-conductors and their resistivity is equivalent to the resistivity of rock grains. Therefore, the electric conduction is only through the pore water if the rock does not contain conductive minerals. The resistivity of hydrocarbon bearing rock can be related to the resistivity of the same rock when it is initially entirely saturated with water (R_o) by the following relationship:

$$R_o = R_t S_w^{\,n} \quad \text{---------- (4.6)}$$

where R_t is the true formation resistivity, S_w is the water saturation and n is the saturation exponent. Archie (1942) defined the resistivity index (RI) as the ratio R_t/R_o.

4.3.2 Neural Network Predictions of R_t and RI

4.3.2.1 Available Datasets

The predictors were trained using 55 SCAL plug resistivity measurements (R_t and RI), in conjunction with the corresponding wireline log data at the same depths. The SCAL plug measurements were performed in the laboratory in the Libyan Petroleum Institute (LPI). The SCAL plugs were 1.5 inch in diameter from well A-02 in Field A-Libya. The predictors were then tested on an adjacent well in the same oil field (well A-01, which is located about 8,530 ft WNW of well A-02) and in a different oil field (well B-01, Field B-Libya). All these wells are producing from the same formation (Nubian Sandstone). The first data requirement is the wireline logs used as input to train neural networks. In the present study the following wireline logs were available in each of wells A-02, A-01 and B-01: spectral gamma ray (SGR), computed gamma ray (CGR), calliper (CALI), bulk density (RHOB), neutron porosity (NPHI), deep induction log (ILD), medium induction log (ILM) and *p*-wave sonic transit time (SONIC). Different combinations of wireline logs were used to train the neural networks. The wireline logs and core data were depth matched before training the neural networks. In the Nubian Sandstone Formation permeability values of less than 2mD are not regarded as good reservoir material. Therefore for this study only

plugs whose permeability was greater than 2 mD were selected as the training dataset from well A-02 (Figure 4.1 and Table 4.1).

4.3.2.2 Data Normalization

The wireline log and SCAL plug resistivity data from all wells were normalised, since the neural network program processes data ranging from zero to one. It was decided to normalise most wireline logs based on the usual maximum and minimum values given in the log headers (Tables 4.2-4.4). The resistivity logs and all SCAL plug resistivity values were normalised based on the logarithm of their minimum and maximum values, due to the large range of resistivity values. Each wireline log data point and SCAL plug resistivity parameter (R_t and RI) value at the corresponding depth was normalised via the following equation:

$$N_i = \frac{X_i - X_{min}}{X_{max} - X_{min}} \quad \text{----------} \quad (4.7)$$

where:

N_i Normalised wireline log or core parameter at depth i.

X_i Value of wireline log or core parameter.

X_{min} Minimum value.

X_{max} Maximum value.

Table 4.1. Summary of the petrophysical parameters used in study area from training well A-02 and its GHEs.

Sample #	Log depth (ft)	Core depth (ft)	K(mD)	Ø(fraction)	RQI	$Ø_z$	FZI	GHE
30	15385	15373	3.01	0.0842	0.1877	0.0919	2.0420	5
33	15388	15376	76.3	0.0856	0.9375	0.0936	10.0142	7
34	15389	15377	117	0.0930	1.1137	0.1025	10.8619	7
35	15390	15378	118	0.0874	1.1538	0.0958	12.0471	7
44	15401	15389	34.2	0.1428	0.4859	0.1666	2.9170	5
45	15402	15390	74.1	0.0826	0.9405	0.0900	10.4455	7
48	15405	15393	19.6	0.1202	0.4010	0.1366	2.9348	5
51	15410	15398	455	0.1551	1.7007	0.1836	9.2645	7
52	15411	15399	221	0.1193	1.3515	0.1355	9.9768	7
57	15419	15407	56.5	0.1159	0.6933	0.1311	5.2885	6
59	15421	15409	524	0.1448	1.8889	0.1693	11.1560	7
61	15423	15411	960	0.1391	2.6086	0.1616	16.1446	8
62	15424	15412	771	0.1588	2.1879	0.1888	11.5899	8
64	15426	15414	4.53	0.1127	0.1991	0.1270	1.5673	5
80	15452	15439	108.54	0.1311	0.9035	0.1509	5.9881	6
83	15455	15442	15.913	0.0924	0.4121	0.1018	4.0475	6
86	15459	15446	2.341	0.0825	0.1673	0.0899	1.8602	5
89	15462	15449	38.362	0.1324	0.5345	0.1526	3.5024	6
95	15468	15455	72.833	0.1200	0.7736	0.1364	5.6729	6
111	15486	15473	772.31	0.1507	2.2479	0.1774	12.6683	8
114	15489	15476	607.125	0.1537	1.9735	0.1816	10.8663	7
118	15493	15480	66.43	0.1190	0.7419	0.1351	5.4925	6
119	15494	15481	79.873	0.1349	0.7641	0.1559	4.8998	6
121	15496	15483	371.063	0.1328	1.6598	0.1531	10.8387	7
122	15497	15484	7.001	0.0856	0.2840	0.0936	3.0334	6
124	15499	15486	231.88	0.1502	1.2337	0.1767	6.9803	7
127	15503	15490	274.752	0.1451	1.3664	0.1697	8.0503	7

Sample #	Log depth (ft)	Core depth (ft)	K(mD)	Ø(fraction)	RQI	Øz	FZI	GHE
131	15507	15494	68.044	0.1320	0.7129	0.1521	4.6880	6
132	15508	15495	61.771	0.1288	0.6876	0.1478	4.6512	6
134	15511	15498	31.068	0.1088	0.5306	0.1221	4.3463	6
142	15519	15506	70.956	0.1102	0.7968	0.1238	6.4335	7
155	15532	15519	16.833	0.1303	0.3569	0.1498	2.3821	5
156	15533	15520	7.493	0.1125	0.2563	0.1268	2.0216	5
160	15537	15524	15.932	0.1334	0.3432	0.1539	2.2292	5
186	15563	15550	13.583	0.1076	0.3528	0.1206	2.9260	5
190	15567	15554	31.916	0.1127	0.5284	0.1270	4.1602	6
192	15569	15556	4.953	0.0894	0.2337	0.0982	2.3806	5
223	15602	15589	20.291	0.1098	0.4269	0.1233	3.4607	6
226	15605	15592	5.829	0.0756	0.2757	0.0818	3.3714	6
235	15614	15601	5.728	0.0819	0.2626	0.0892	2.9437	5
241	15620	15607	149.809	0.1339	1.0503	0.1546	6.7935	7
279	15663	15650	51.44	0.0931	0.7381	0.1027	7.1897	7
353	15752	15738	36.166	0.1074	0.5762	0.1203	4.7888	6
394	15798	15784	11.46	0.0743	0.3899	0.0803	4.8575	6
395	15799	15785	16.51	0.0976	0.4084	0.1082	3.7760	6
396	15800	15786	10.81	0.0905	0.3432	0.0995	3.4490	6
400	15804	15790	21.83	0.0734	0.5415	0.0792	6.8365	7
404	15808	15794	157.27	0.1112	1.1808	0.1251	9.4383	7
406	15810	15796	81.02	0.1118	0.8453	0.1259	6.7153	7
408	15812	15798	8.94	0.0906	0.3119	0.0996	3.1308	6
439	15846	15832	6.86	0.1078	0.2504	0.1208	2.0728	5
444	15851	15837	12.32	0.1238	0.3132	0.1413	2.2167	5
454	15861	15847	18.57	0.0864	0.4604	0.0946	4.8682	6
455	15862	15848	25.19	0.0893	0.5273	0.0981	5.3777	6
456	15863	15849	14.33	0.0865	0.4041	0.0947	4.2680	6

Table 4.2. The range of wireline log and resistivity values for normalisation purposes in the BPNN for the **training well A-02** at **1.0** ft spacing.

	SGR (API)	CGR (API)	CALI (in)	RHOB (g/cc)	NPHI (fraction)	Log ILD (Ohm.m)	Log ILM (Ohm.m)	DT (µs/ft)	Log R_t (Ohm.m)	Log RI (Ohm.m)
Min.	11.85	4.50	5.78	2.36	0.042	0.127	0.29	59.4	1.256	0.71
Max	157.94	63.20	6.344	2.66	0.2109	1.95	2.07	78.6	1.60	1.21

Table 4.3. The range of wireline log and resistivity values for normalisation purposes in the BPNN for adjacent test well **A-01** in the same oil field at **0.5** ft spacing.

	SGR (API)	CGR (API)	CALI (in)	RHOB (g/cc)	NPHI (Fraction)	Log ILD (Ohm.m)	Log ILM (Ohm.m)	DT (µs/ft)	Log RT (Ohm.m)	Log RI (Ohm.m)
Min.	10.09	7.21	5.53	2.38	0.035	0.238	0.302	56.8	1.31	0.76
Max.	121.25	86.47	7.17	2.75	0.239	1.78	1.85	73.6	1.59	1.16

Table 4.4. The range of wireline log and resistivity values for normalisation purposes in the BPNN for test well **B-01** in a different oil field at **0.5** ft spacing.

	SGR (API)	CGR (API)	CALI (in)	RHOB (g/cc)	NPHI (fraction)	Log ILD (Ohm.m)	Log ILM (Ohm.m)	DT (µs/ft)	Log RT (Ohm.m)	Log RI (Ohm.m)
Min.	23.04	20.44	5.89	2.37	0.057	0.67	0.37	60.9	1.31	0.76
Max.	81.69	58.73	6.47	2.59	0.112	1.94	1.62	83.2	1.59	1.16

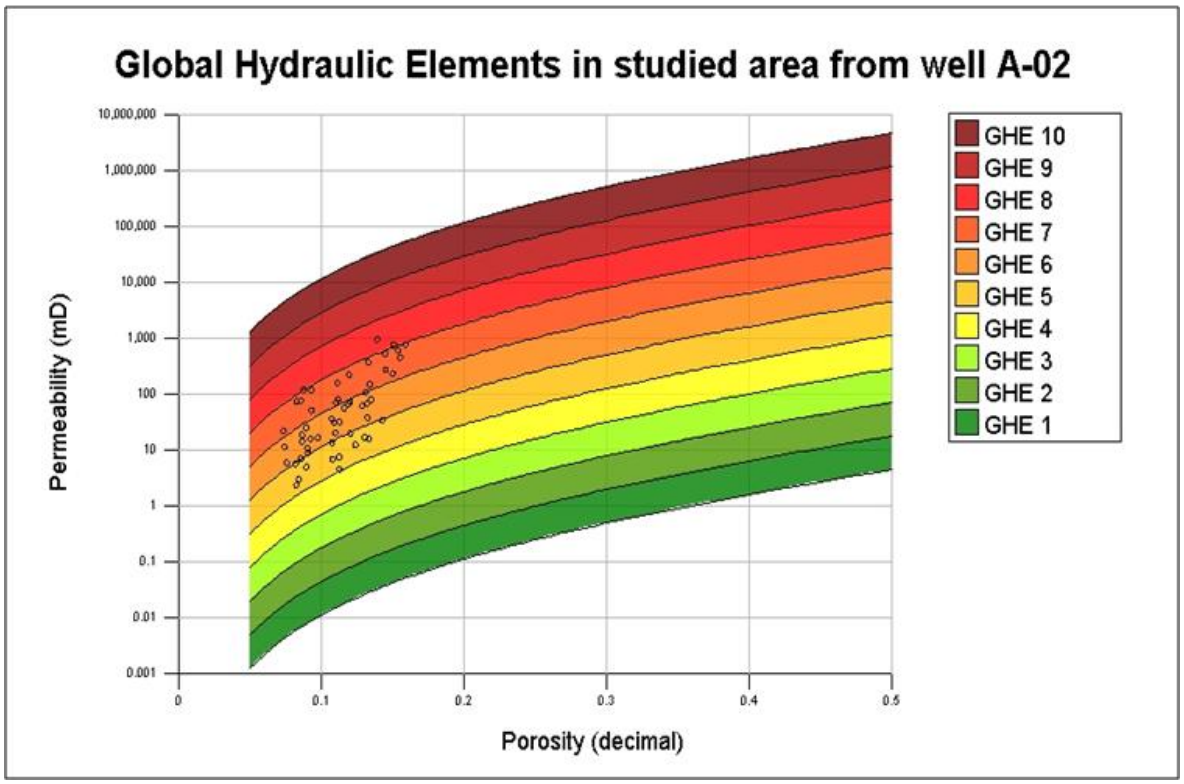

Figure 4.1. Global hydraulic element porosity-permeability crossplot for the 55 SCAL samples.

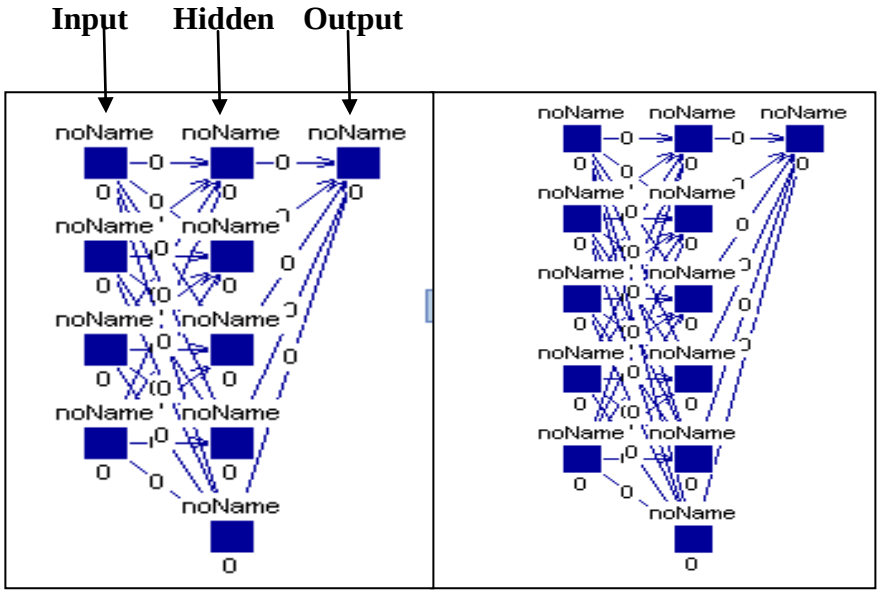

Figure 4.2. The structure of a typical back propagation neural network (BPNN) .

4.4 Results

4.4.1. True resistivity (R_t) and resistivity index (RI) predictors from training well A-02

The results from the training process in well A-02 were tabulated, together with crossplots of the measured resistivity parameters versus predicted resistivity parameters, and plots of the predictions with depth. Tables 4.5 and 4.6 show the performance of various predictors (using different input wireline logs at 1.0 ft depth spacing) in terms of the coefficient of determination (R^2) between the measured and predicted values of R_t and RI for the training well for prediction at 1.0 ft depth spacing. The results show that the coefficients of determination between measured and predicted values are relatively high in all cases for the training dataset. Crossplots of the measured versus predicted values are shown in Figures 4.3 and 4.4. The coefficient of determination for R_t is very similar for cases 1, 3 and 4 (Table 4.5). Likewise the coefficient of determination for RI is very similar for cases 1, 3 and 4 (Table 4.6). For both parameters case 2 gives a slightly lower value of R^2. The only difference between case 2 and the other three cases is that case 2 does not contain bulk density (RHOB) as one of the input wireline logs. Crossplot of predicted true resistivity and true restivity from wire line logs is shown in Figure 4.5.

The measured and predicted values of R_t and RI along the depth for case 4 are shown in Figures 4.6 and 4.7. There are similar profiles for the measured and predicted curves, which is expected since this is the training data.

The results of the predictors from the training well at 0.5 ft depth spacing are shown in Appendix C. Tables C5 and C6 show the performance of various predictors (using different input wireline logs) in terms of the coefficient of determination (R^2) between the measured and predicted values of R_t and RI for the training well for prediction at 0.5 ft depth spacing. Crossplots of the measured versus predicted values are shown in Figures C2 and C3. The predictors at this smaller depth spacing were still very good, but their R^2 values were slightly lower that the predictors at 1.0 ft spacing.

Table 4.5. Summary results of true resistivity (R_t) predictors trained on the entire cored interval (containing 55 SCAL plugs) in training well **A-02** at **1.0 ft** spacing.

Input	**Output**	**Coefficient of determination (R^2) in training well A-02**
Case 1 (RHOB,NPHI,ILD &ILM)	R_t	0.8232
Case 2 (SGR,CGR,NPHI,ILD &ILM)	R_t	0.7507
Case 3 (SGR,CGR,RHOB,NPHI,ILD &ILM)	R_t	0.8230
Case 4 (SGR,CGR,RHOB,NPHI,ILD , ILM, & DT)	R_t	0.8320

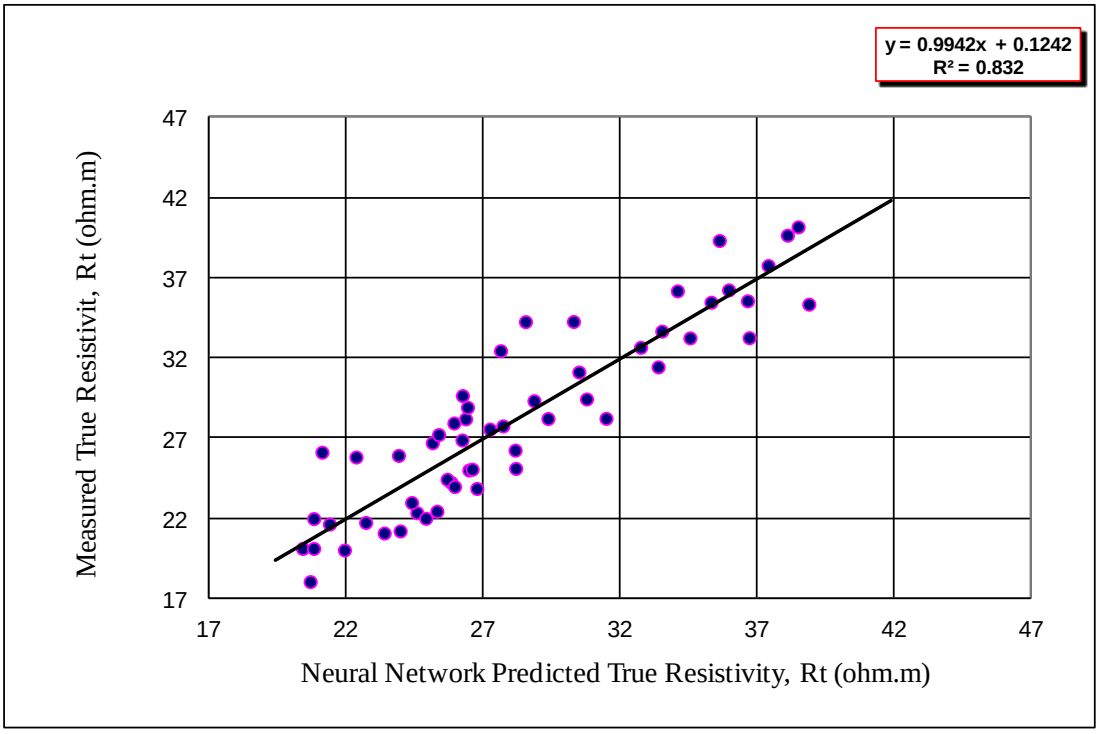

Figure 4.3. Crossplot of measured true resistivity versus BPNN predicted true resistivity for the case 4 predictor trained on the entire cored interval using **7** wireline logs for training well **A-02** at **1.0 ft**.spacing

Table 4.6. Summary results of resistivity index (RI) predictors trained on all entire cored interval in training well A-02 at 1.0 ft spacing.

Input	Output	Coefficient of determination (R^2) in training well A-02
Case 1 (RHOB,NPHI,ILD &ILM)	RI	0.9061
Case 2 (SGR,CGR,NPHI,ILD &ILM)	RI	0.8260
Case 3 (SGR,CGR,RHOB,NPHI,ILD &ILM)	RI	0.9070
Case 4 (SGR,CGR,RHOB,NPHI,ILD , ILM, & DT)	RI	0.9078

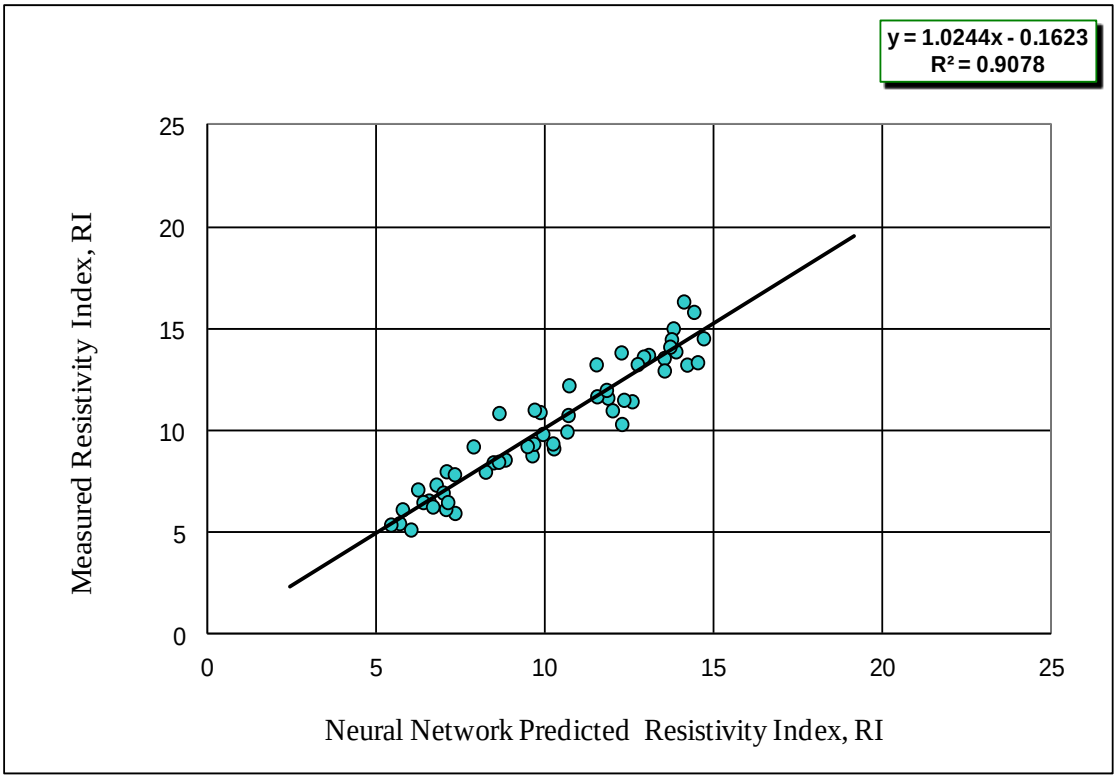

Figure 4.4. Crossplot of measured resistivity index versus BPNN predicted resistivity index for the case 4 predictor trained on the entire cored interval using **7** wireline logs for training well **A-02** at **1.0 ft** spacing.

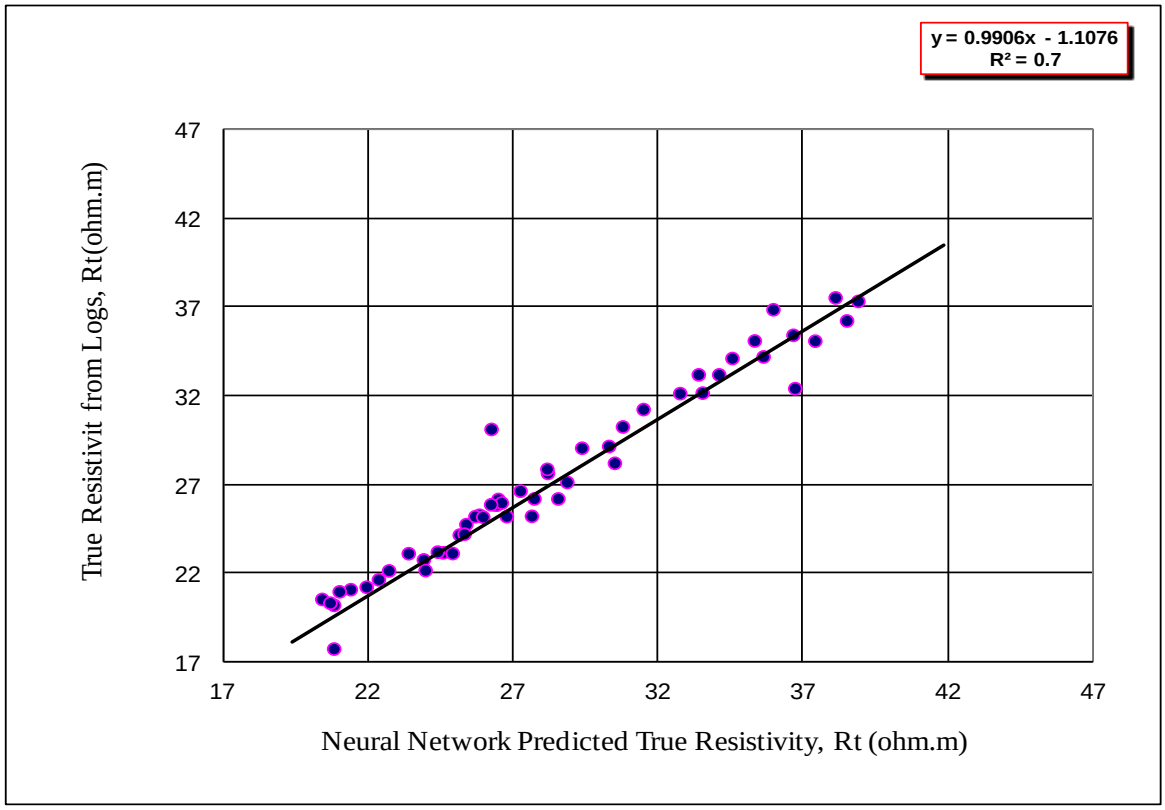

Figure 4.5.Crossplot of true resistivity from wireline logs versus.BPNN predicted true resistivity for the predictor trained on the entire cored interval using 6 wireline logs for training well A-02 at 1.0 ft depth spacing.

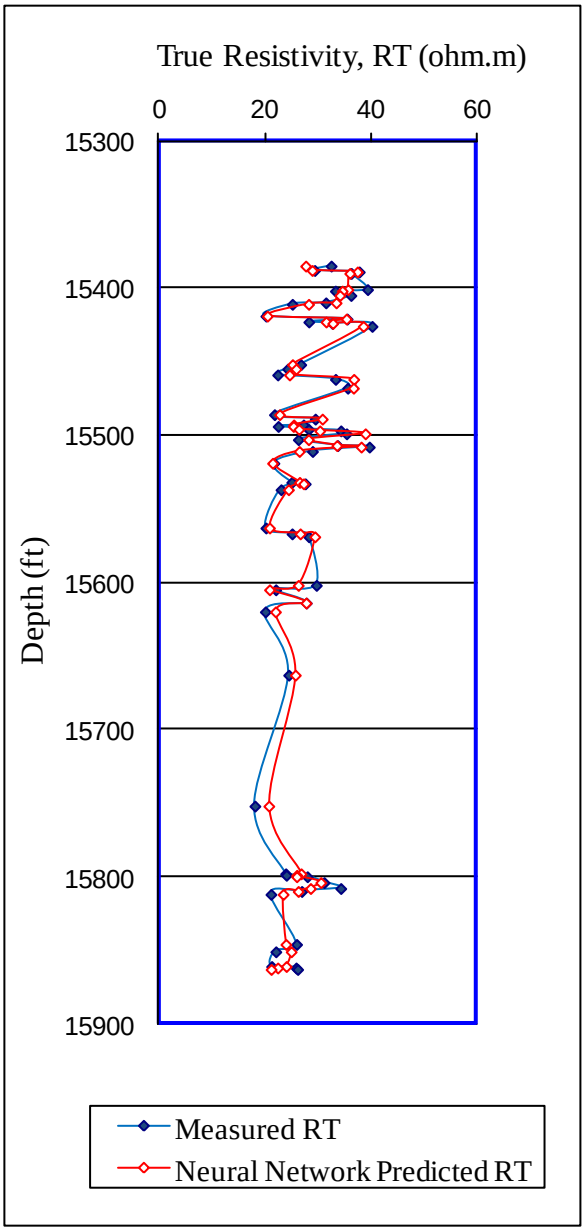

Figure 4.6. Measured R_t and BPNN predicted R_t along the depth for case 4 in the training well **A-02** using 7 conventional wireline logs at **1.0 ft** spacing.

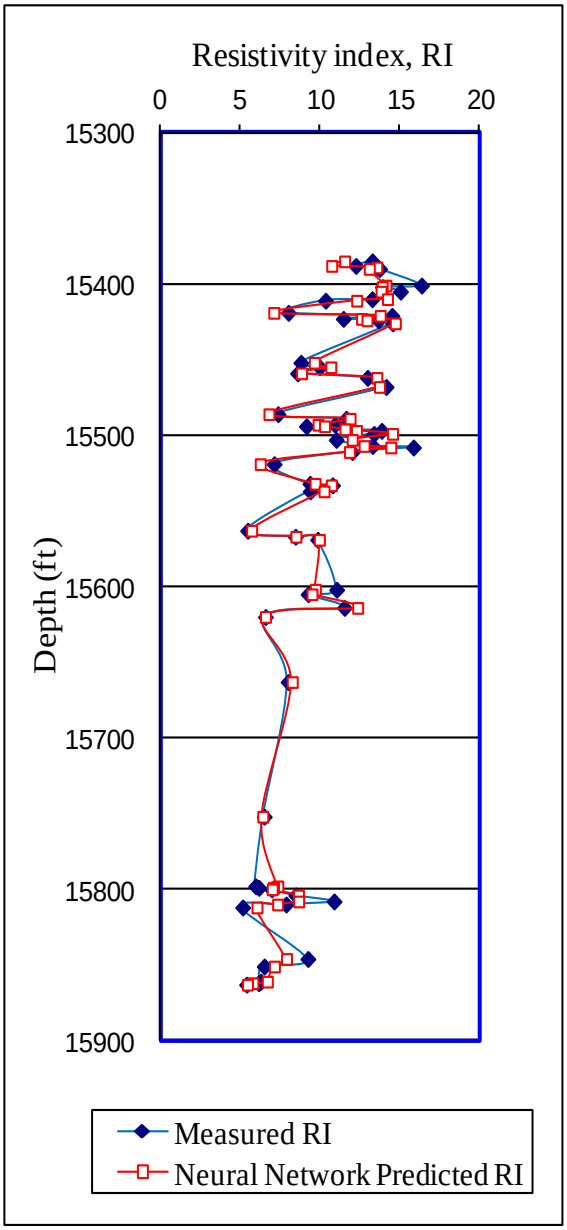

Figure 4.7. Measured RI and BPNN predicted RI along the depth for case 4 in the training well **A-02** using 7 conventional wireline logs at **1.0 ft** spacing.

4.4.2 *Test 1: testing predictions of R_t and RI in an adjacent well (A-01) in the same oilfield using the training well (A-02) predictors*

After the training process in well A-02, the predictors were first tested on the cored interval in adjacent well A-01 in the same oil field. Tables 4.7 and 4.8 summarise the performance, in terms of the coefficient of determination (R^2) between the predicted and measured values, of various predictors based on different wireline log combinations. The predictors were trained from well A-02 at 0.5 ft spacing and tested in adjacent well A-01 at 0.5 ft spacing. The values of R^2 are close to 0.6 for resistivity index (RI) from cases 3 and 4 suggesting that the predictors are doing a reasonable job. The R^2 value for case 2 without the RHOB data is slightly lower, which might be expected since the performance of case 2 in the training well (Table 4.6) was a bit worse. The R^2 values between the measured and predicted values of R_t at 0.5 ft spacing in well A-01 are relatively low (Table 4.7). However, it is clear from crossplots of measured versus predicted R_t (Figure 4.9) and RI (Figure 4.11) that the predictions are still relatively good (r^2=0.5,average error=0.11). The crossplots for these two figures are for case 4. In both crossplots the regression line is very close to the 1:1 line, and the points are well distributed around this line. Figures 4.8 and 4.10 show the corresponding plots for the training data in each case.

Figures 4.13 and 4.15 show the R_t and RI predictions in well A-01 at 0.5 ft spacing along the depth (the corresponding training data plots from well A-02 are shown in Figures 4.12 and 4.14). The predictions largely match the measured values.

The results of predictions at 1.0 ft depth spacing are available in Appendix C. Tables C7 and C8 summarise the performance, in terms of the coefficient of determination (R^2) between the predicted and measured values, of various predictors based on different wireline log combinations. Crossplots of the measured versus predicted values are shown in Figures C4 and C5. The predictors were trained from well A-02 at 0.5 ft spacing and tested in adjacent well A-01 at 1.0 ft spacing. These predictions were not quite as good as the predictions at 0.5 ft spacing.

Table 4.7. Summary results of true resistivity predictors (trained on the entire cored interval in well **A-02**) when tested in adjacent well **A-01** in the same oil field at **0.5** ft spacing.

Input	**Output**	**Coefficient of determination (R^2) in adjacent well A-01**
Case 2 (SGR,CGR,NPHI,ILD &ILM)	R_t	0.4232
Case 3 (SGR,CGR,RHOB,NPHI,ILD &ILM)	R_t	0.4340
Case 4 (SGR,CGR,RHOB,NPHI,ILD ,ILM,& DT)	R_t	0.4580

Table 4.8. Summary results of resistivity index predictors (trained on the entire cored interval in well **A-02**) when tested in adjacent well **A-01** in the same oil field at **0.5** ft spacing.

Input	**Output**	**Coefficient of determination (R^2) in adjacent well A-01**
Case 2 (SGR,CGR,NPHI,ILD &ILM)	RI	0.5403
Case 3 (SGR,CGR,RHOB,NPHI,ILD &ILM)	RI	0.5875
Case 4 (SGR,CGR,RHOB,NPHI,ILD ,ILM,& DT)	RI	0.5872

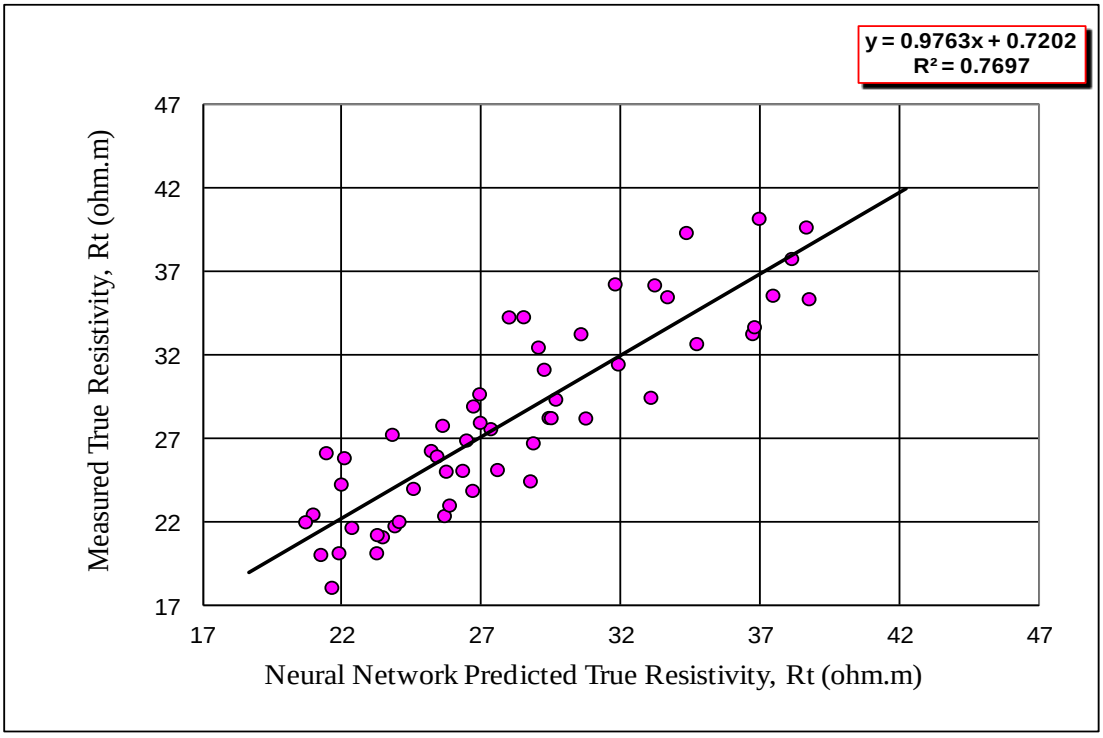

Figure 4.8. Crossplot of training data: measured true resistivity versus BPNN predicted true resistivity for the case 4 predictor trained on the entire cored interval using **7** wireline logs for training well **A-02** at **0.5** ft spacing.

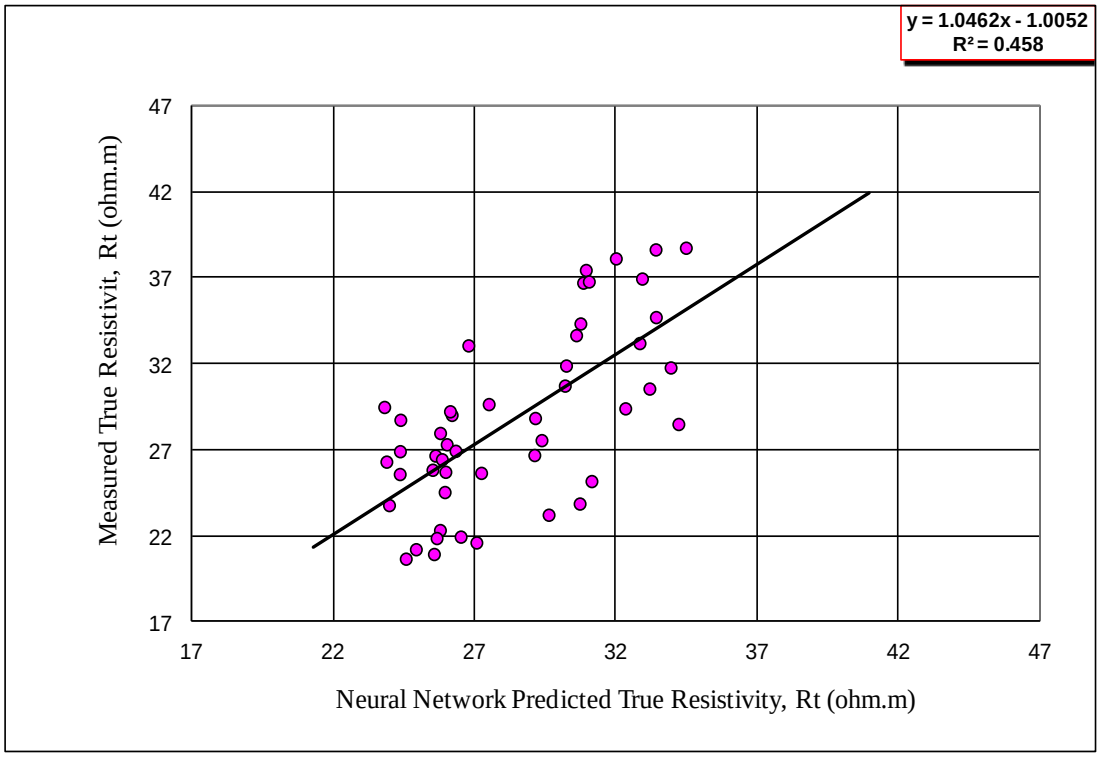

Figure 4.9. Crossplot of test data: measured true resistivity versus BPNN predicted true resistivity when tested in adjacent well **A-01** for the case 4 predictor trained on the entire cored interval using **7** wireline logs from training well **A-02** at **0.5** ft spacing.

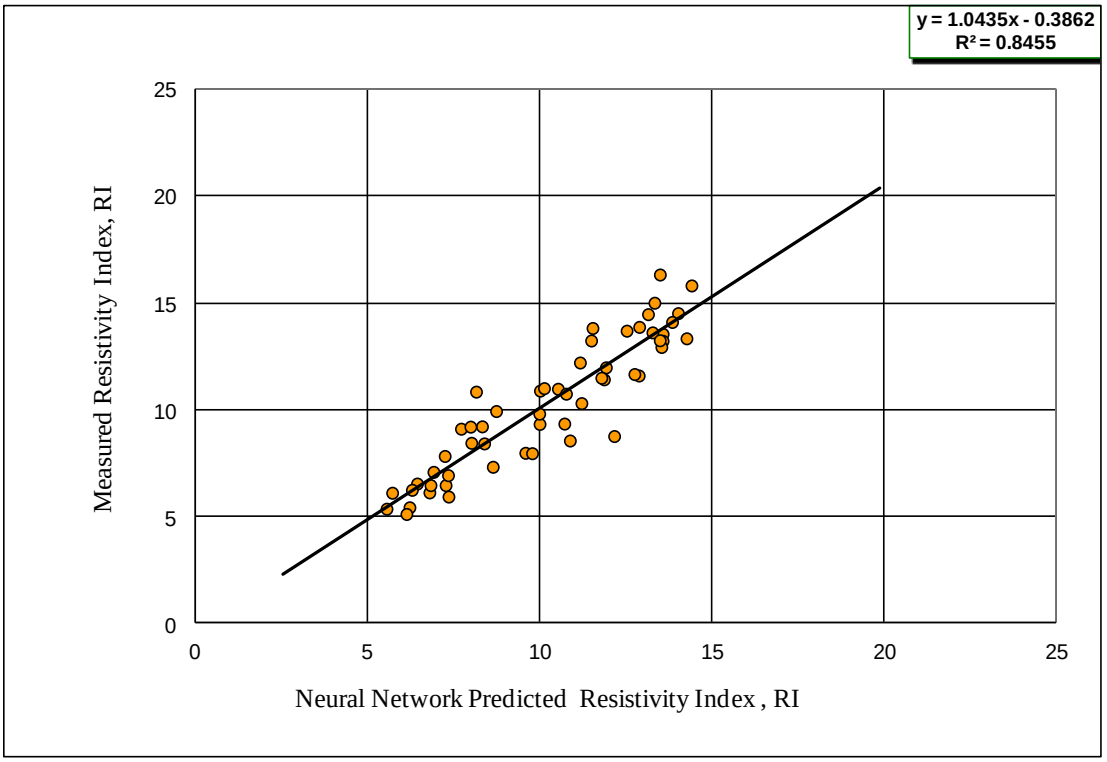

Figure 4.10. Crossplot of training data: measured resistivity index versus BPNN predicted resistivity index for the case 4 predictor trained on the entire cored interval using **7** wireline logs for training well **A-02** at **0.5** ft spacing.

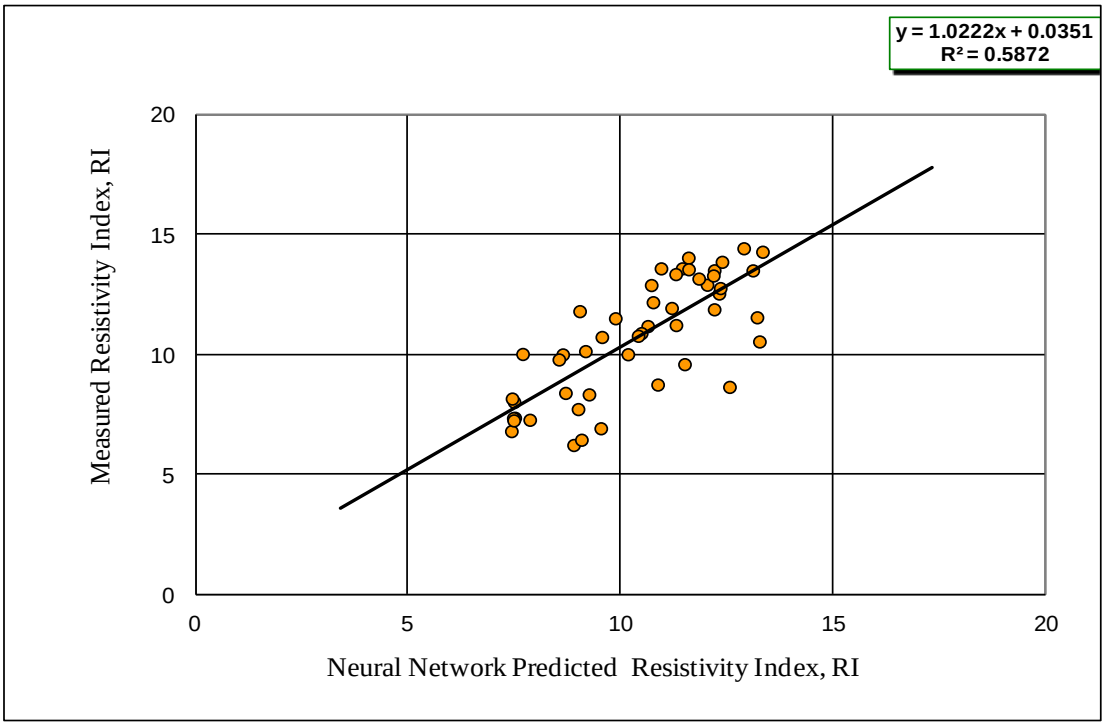

Figure 4.11. Crossplot of test data: measured resistivity index versus BPNN predicted resistivity index when tested in adjacent well **A-01** for the case 4 predictor trained on the entire cored interval using **7** wireline logs from training well **A-02** at **0.5** ft spacing.

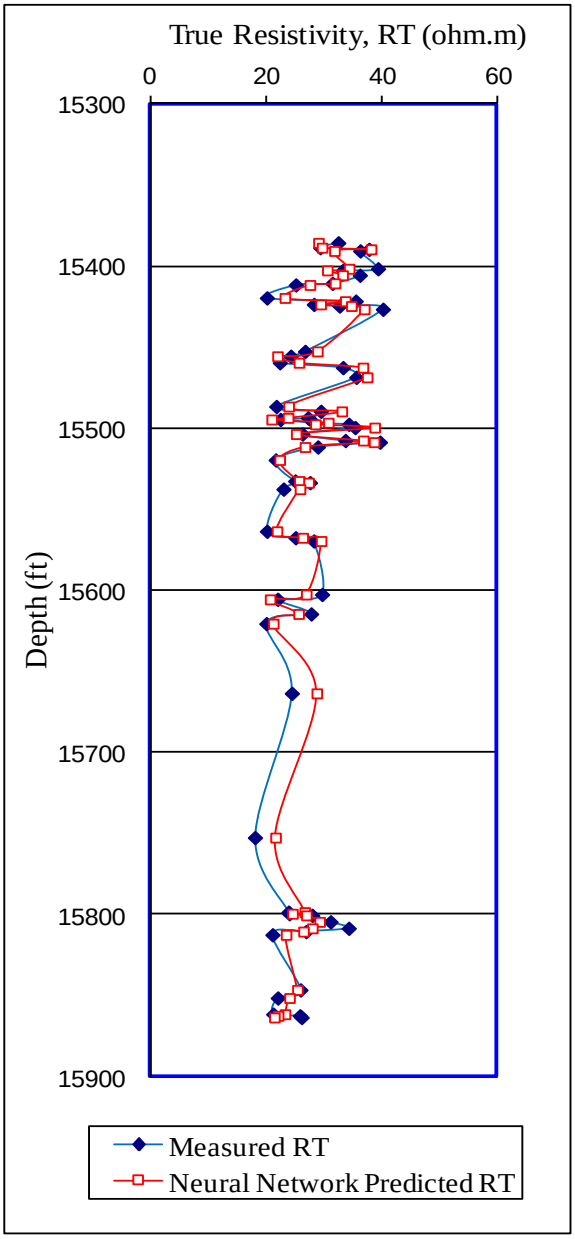

Figure 4.12. Measured R_t and BPNN predicted R_t along the depth for case 4 in training well **A-02** using **7** conventional wireline logs at **0.5** ft spacing.

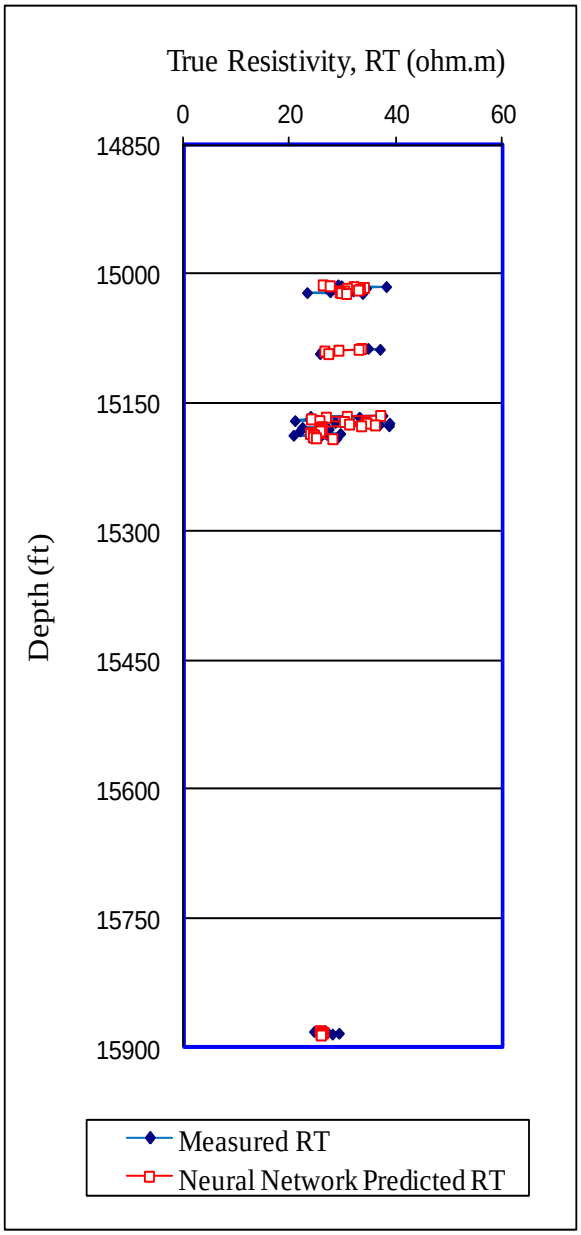

Figure4.13. Measured R_t and BPNN predicted R_t along the depth in adjacent test well **A-01** for the case 4 predictor trained on the entire core dataset from the training well at **0.5** ft spacing.

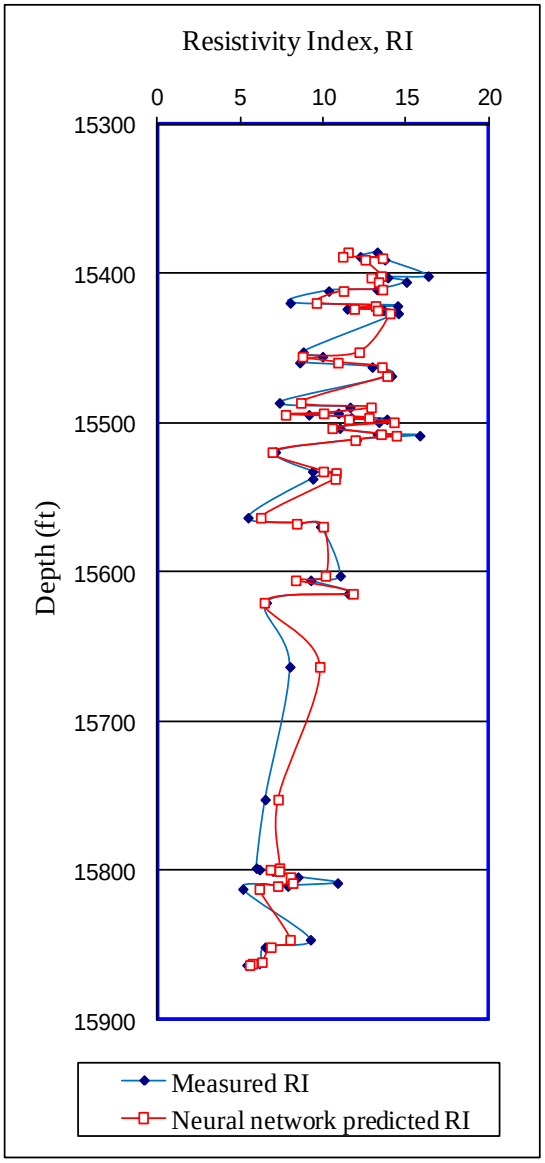

Figure 4.14. Measured RI and BPNN predicted RI along the depth for case 4 in training well **A-02** using **7** conventional wireline logs at **0.5** ft spacing.

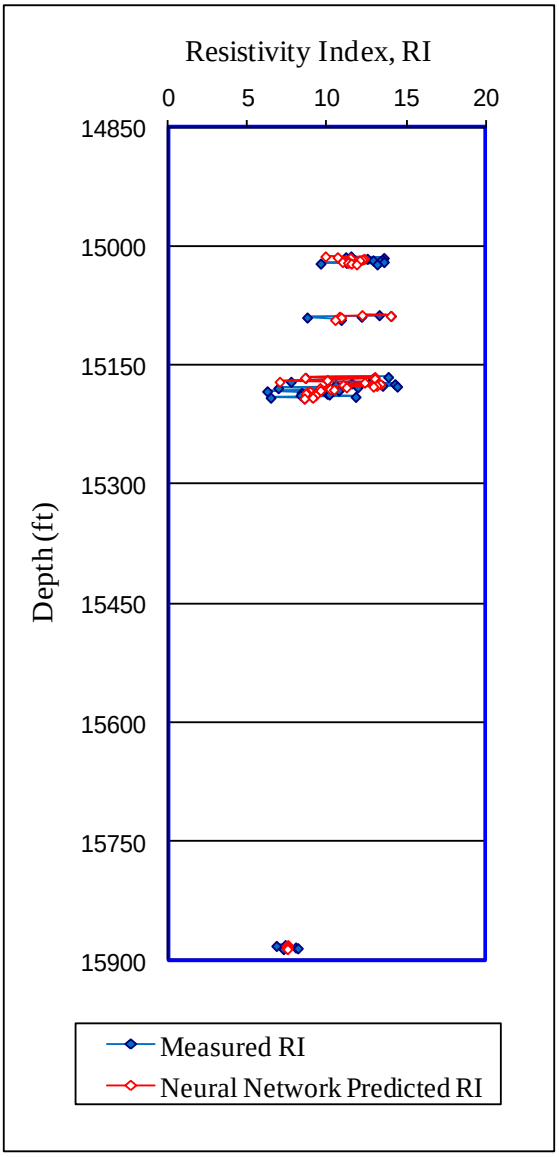

Figure 4.15. Measured RI and BPNN predicted RI along the depth in adjacent test well **A-01** for the case 4 predictor trained on the entire core dataset from the training well at **0.5** ft spacing.

4.4.3 *Test 2: testing predictions of R_t and RI in another well (B-01) in a different oilfield using the training well (A-02) predictors*

The training well predictors for R_t and RI were then tested on an interval in a different oil field in Field B – Libya. The predictors were trained from well A-02 at 0.5 ft spacing and tested in well B-01 at 0.5 ft spacing as well. Tables 4.9 and 4.10 summarise the performance, in terms of the coefficient of determination (R^2) between the predicted and measured values, of various predictors based on different wireline log combinations at 0.5 ft depth spacing. Whilst the R^2 values are quite low, the regression lines for the crossplots of measured versus predicted R_t (Figure 4.17) and RI (Figure 4.19) are still quite close to the 1:1 line, even though there is a spread of data points around this line. Figures 4.16 and 4.18 show the corresponding plots for the training data in each case.

Figures 4.21 and 4.23 show the R_t and RI predictions in well B-01 at 0.5 ft spacing along the depth (the corresponding training data plots from well A-02 are shown in Figures 4.20 and 4.22). Despite the low R^2 values in Tables 4.9 and 4.10 the general profile along the depth of the predictions shown in Figures 4.21 and 4.23 follow the measured values reasonably well.

The results of predictions at 1.0 ft depth spacing are available in Appendix C. Tables C9 and C10 summarise the performance, in terms of the coefficient of determination (R^2) between the predicted and measured values, of various predictors based on different wireline log combinations. Crossplots of the measured versus predicted values are shown in Figures C6 and C7. The predictors were trained from well A-02 at 0.5 ft spacing and tested in well B-01 at 1.0 ft spacing. These predictions were not quite as good as the predictions at 0.5 ft spacing.

Table 4.9. Summary results of true resistivity predictors (trained on the entire cored interval in well **A-02**) when applied in test well **B-01** in a different oil field at **0.5** ft spacing.

Input	**Output**	**Coefficient of determination (R^2) in test well B-01**
Case 2 (SGR,CGR,NPHI,ILD &ILM)	R_t	0.269
Case 3 (SGR,CGR,RHOB,NPHI,ILD &ILM)	R_t	0.315
Case 4 (SGR,CGR,RHOB,NPHI,ILD ,ILM,& DT)	R_t	0.343

Table 4.10. Summary results of resistivity index predictors (trained on the entire cored interval in well **A-02**) when applied in test well **B-01** in a different oil field at **0.5 ft** spacing.

Input	**Output**	**Coefficient of determination (R^2) in test well B-01**
Case 2 (SGR,CGR,NPHI,ILD &ILM)	RI	0. 4223
Case 3 (SGR,CGR,RHOB,NPHI,ILD &ILM)	RI	0.3565
Case 4 (SGR,CGR,RHOB,NPHI,ILD, ILM,& DT)	RI	0.3589

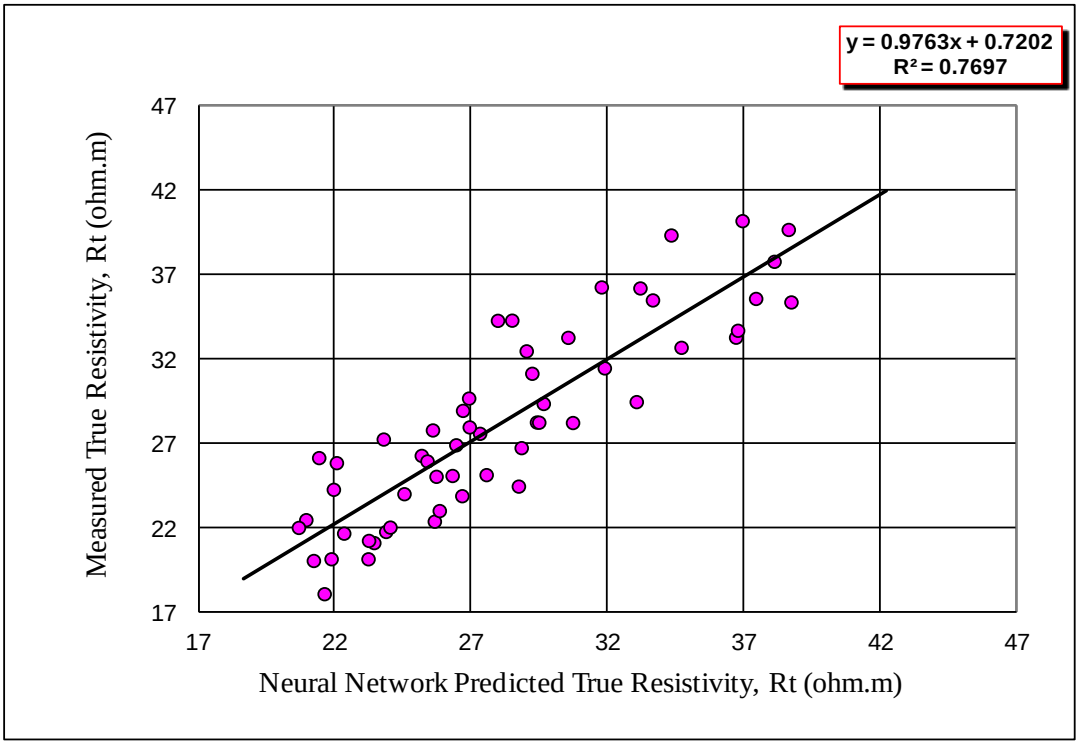

Figure 4.16 Crossplot of training data: measured true resistivity versus BPNN predicted true resistivity for the case 4 predictor trained on the entire cored interval using **7** wireline logs for training well **A-02** at **0.5** ft spacing.

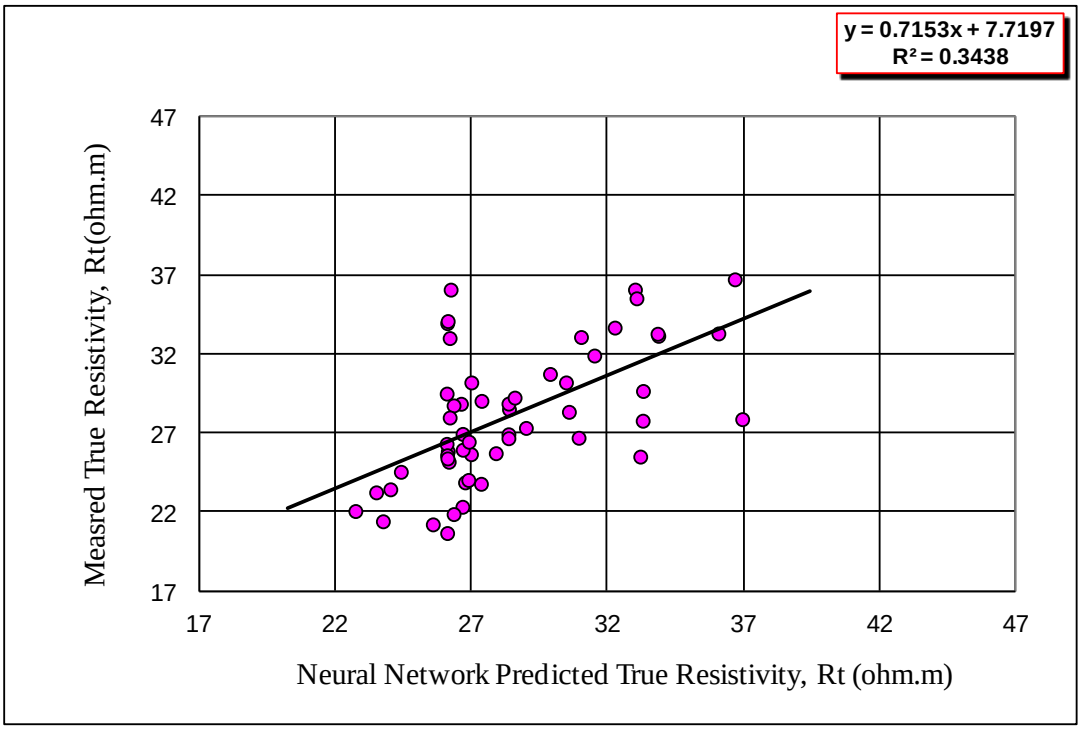

Figure 4.17 Crossplot of test data: measured true resistivity versus BPNN predicted true resistivity when tested in well **B-01** in a different oil field for the case 4 predictor trained on the entire cored interval using **7** wireline logs from training well **A-02** at **0.5** ft spacing.

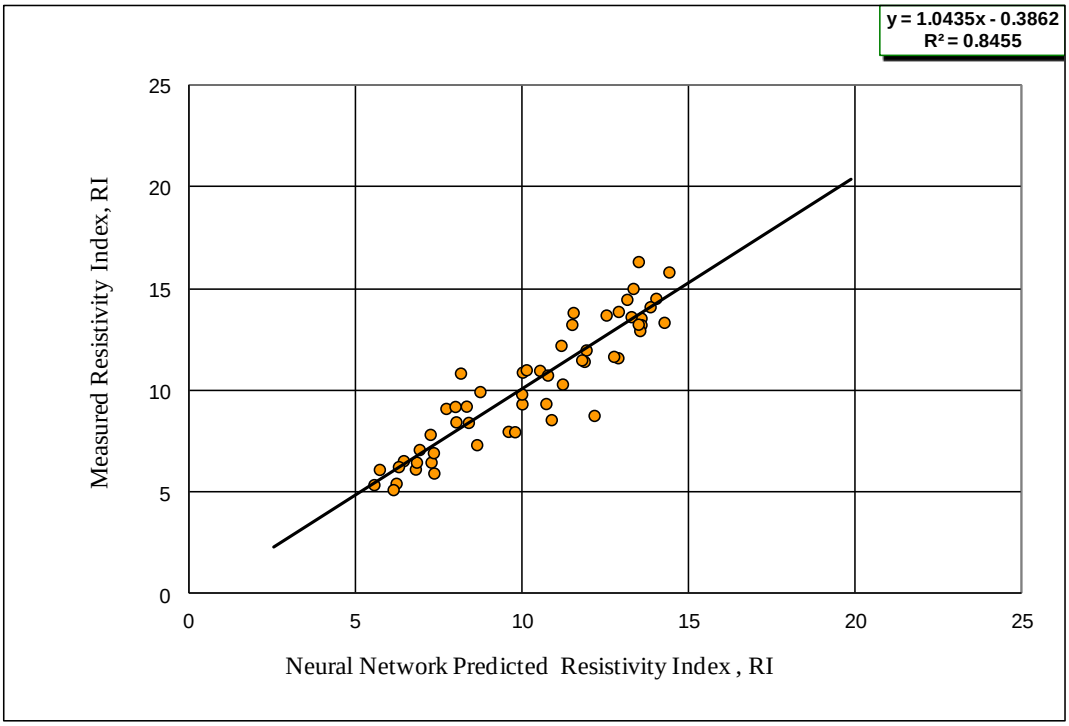

Figure 4.18. Crossplot of training data: measured resistivity index versus BPNN predicted resistivity index for the case 4 predictor trained on the entire cored interval using **7** wireline logs for training well **A-02** at **0.5** ft spacing.

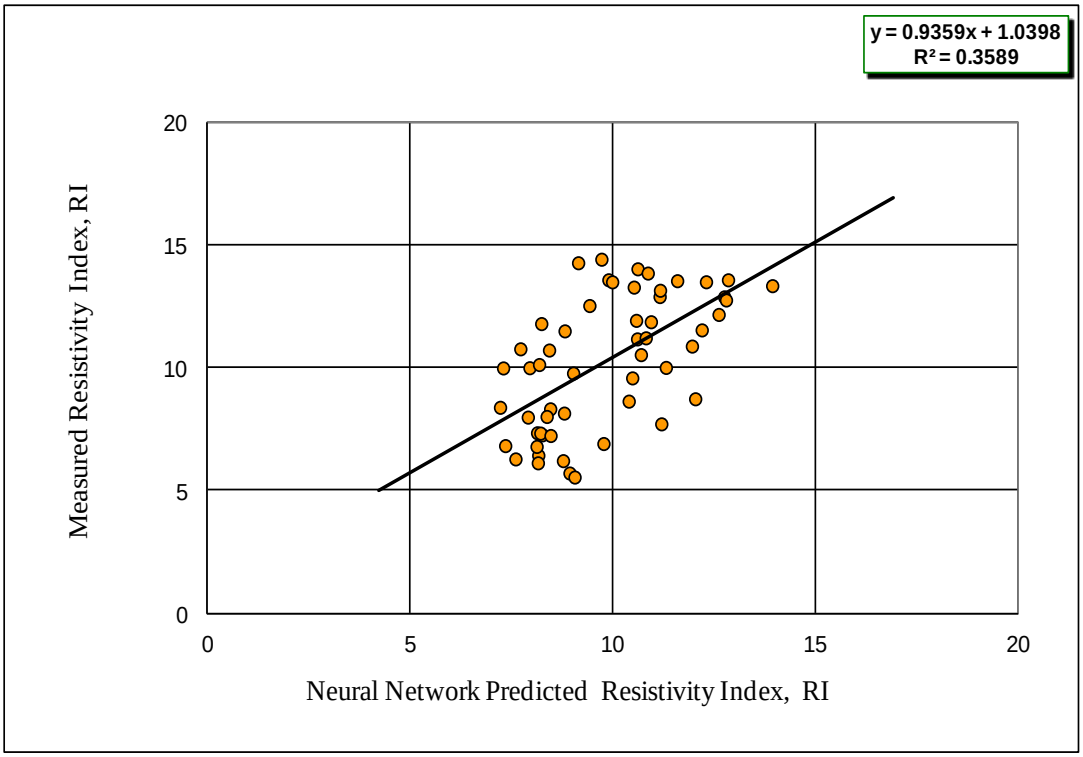

Figure 4.19. Crossplot of test data: measured resistivity index versus BPNN predicted resistivity index when tested in well **B-01** in a different oil field for the case 4 predictor trained on the entire cored interval using **7** wireline logs from training well **A-02** at **0.5** ft spacing.

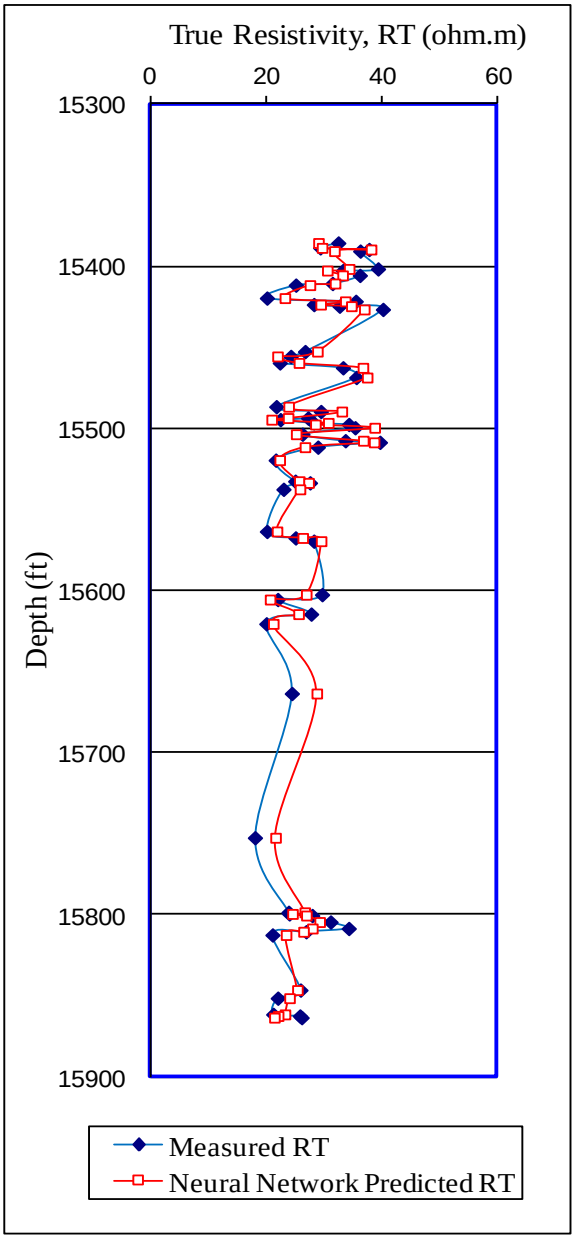

Figure 4.20. Measured R_t and BPNN predicted R_t along the depth for case 4 in training well **A-02** using **7** conventional wireline logs at **0.5** ft spacing.

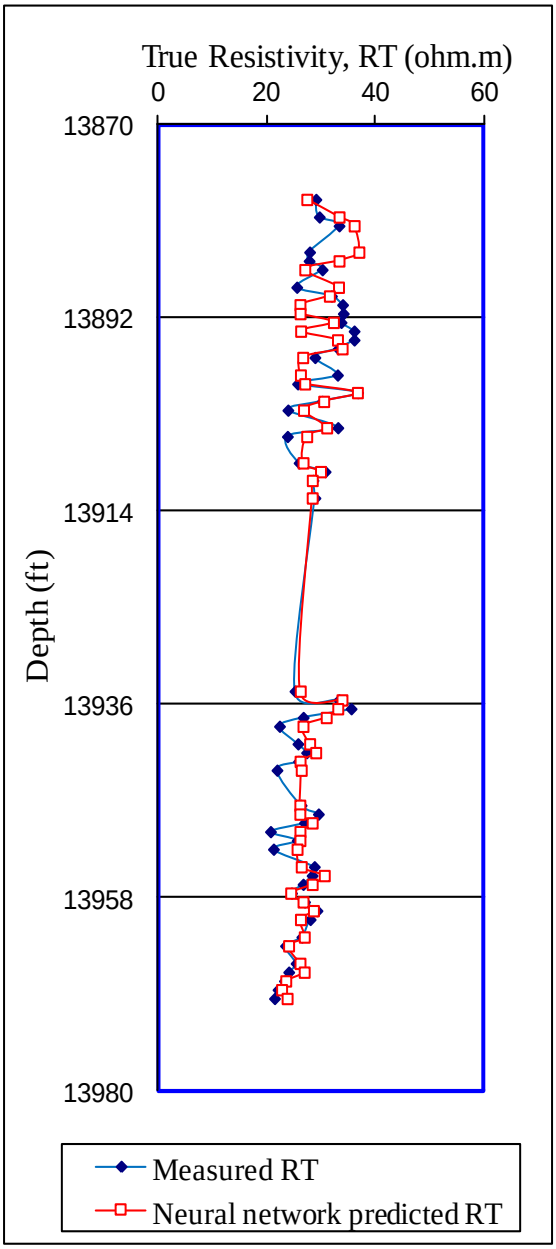

Figure 4.21 Measured R_t and BPNN predicted R_t along the depth in test well **B-01** in a different oil field for the case 4 predictor trained on the entire core dataset from the training well at **0.5** ft spacing.

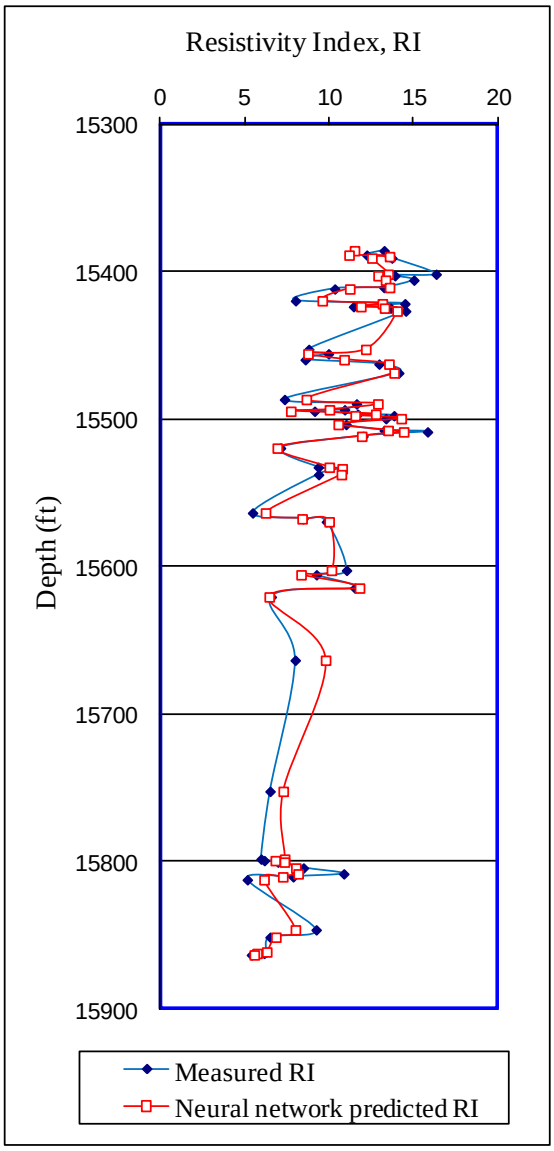

Figure 4.22. Measured RI and BPNN predicted RI along the depth for case 4 in training well **A-02** using **7** conventional wireline logs at **0.5** ft spacing.

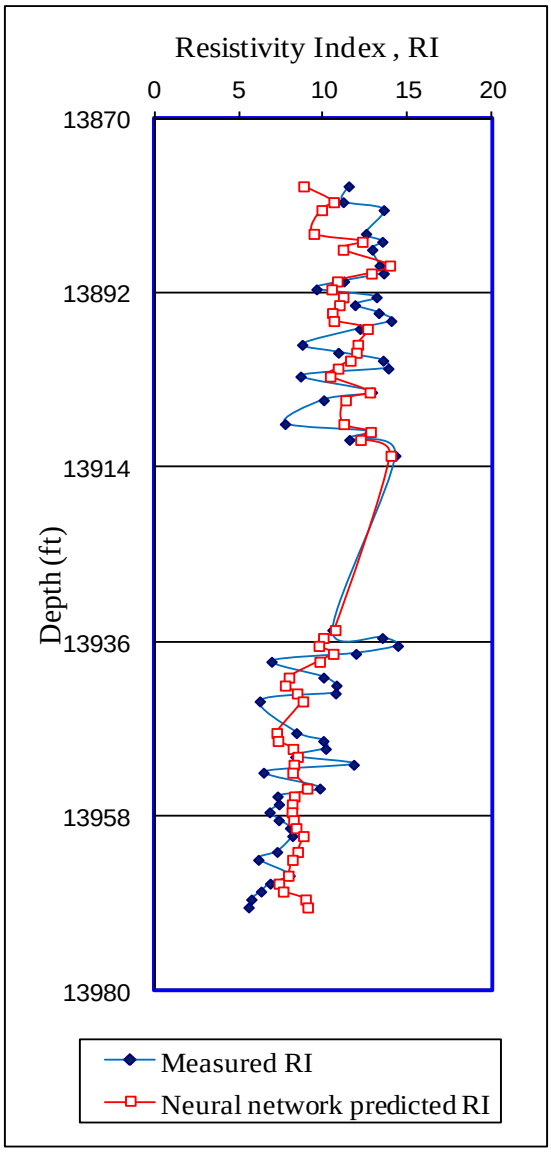

Figure 4.23. Measured RI and BPNN predicted RI along the depth in test well **B-01** in a different oil field for the case 4 predictor trained on the entire core dataset from the training well at **0.5** ft spacing.

4.5 Water Saturation (S_w) and Saturation Exponent (n)

The arrangement of the grains constituting sedimentary rocks leaves pores and channels for oil, gas and water to coexist. The volume of the fluids within sedimentary rocks depends on the pore space. The volume of a particular fluid relative to the pore volume is called the fluid saturation, which is the ratio of the volume of that fluid to the total pore volume of the rock. In other words, it is the fraction of porosity which is occupied by that particular fluid. The water saturation, S_w, is given by:

$$S_w = \frac{V_w}{V_p} \quad \text{---------- (4.8)}$$

where V_w is the volume occupied by water and and V_p is the total pore volume. Saturation is a dimensionless quantity. It is expressed in either fraction ($0<S_w<1$) or in percentage ($0<S_w<100$). Since pores in petroleum reservoirs are completely saturated with fluids, the summation of all fluid saturation in a reservoir must make a total of 100%. A log-log plot of resistivity index (RI) versus water saturation (S_w) yields a straight line with a slope equal to n

$$n = -\frac{\log RI}{\log S_w} \quad \text{---------- (4.9)}$$

The parameter n is a numerical constant known as Archie's saturation exponent and varies between 1.2 to 2.2 (Serra, 1984) for water-wet rocks. Archie's saturation exponent is strongly dependent on the geometric distribution and continuity of the conductive fluid (water) within the rock pore space. It can have a value of 2.2 or higher when the rock wettability changes towards oil-wet (Anderson, 1986a).

Water saturation (S_w) is an important parameter in reservoir evaluation and management. Knowing the water saturation, the fraction of hydrocarbon in the reservoir ($1-S_w$) can be determined. In this thesis water saturation (S_w) was calculated using Equation 4.6 from resistivity index and saturation exponent, which were obtained from measurements of

capillary pressure by the porous plate technique as one of the SCAL tests performed at the Libyan Petroleum Institute (LPI). In experimental measurement of the determination of water saturation was detailed in Appendix D.

4.6 Neural Network Prediction of Water Saturation (S_w) and Saturation Exponent (n)

4.6.1 Available Data

The predictors were trained using water saturation (S_w) and saturation exponent (n) values, determined from the 55 SCAL plugs, in conjunction with the corresponding wireline log data at the same depths. The wireline log and core data were depth matched before training the neural networks. The wireline logs, water saturation, and saturation exponent values from all wells were normalised using Equation 4.7, and the values are shown in Tables 4.11-4.13. Most of the wireline logs were normalised based on the usual maximum and minimum values given in the log headers. The resistivity wireline log values were normalised based on the logarithm of their minimum and maximum values.

Table 4.11. The range of wireline log, water saturation (S_w), and saturation exponent (n) values f or normalisation purposes in the BPNN for training well **A-02** at **1.0 ft** spacing.

	SGR (API)	CGR (API)	CALI (in)	RHOB (g/cc)	NPHI (fraction)	Log ILD (Ohm.m)	Log ILM (Ohm.m)	DT (µs/ft)	S_w (Fraction)	n
Min.	11.85	4.50	5.78	2.36	0.042	0.127	0.29	59.4	0.2444	1.92
Max	157.94	63.20	6.344	2.66	0.2109	1.95	2.07	78.6	0.4521	2.14

Table 4.12. The range of wireline log, water saturation (S_w), and saturation exponent (n) values for normalisation purposes in the BPNN for adjacent test well **A-01** in the same oil field at **0.5 ft** spacing.

	SGR (API)	CGR (API)	CALI (in)	RHOB (g/cc)	NPHI (fraction)	Log ILD (Ohm.m)	Log ILM (Ohm.m)	DT (µs/ft)	S_w (Fraction)	n
Min.	10.09	7.21	5.53	2.38	0.035	0.238	0.302	56.8	0.2576	1.95
Max	121.25	86.47	7.17	2.75	0.239	1.78	1.85	73.6	0.4178	2.13

Table 4.13. The range of wireline log, water saturation (S_w), and saturation exponent (n) values for normalisation purposes in the BPNN for test well **B-01** in different oil field at **0.5 ft** spacing.

	SGR (API)	CGR (API)	CALI (in)	RHOB (g/cc)	NPHI (fraction)	Log ILD (Ohm.m)	Log ILM (Ohm.m)	DT (µs/ft)	S_w (Fraction)	n
Min.	23.04	20.44	5.89	2.37	0.057	0.67	0.37	60.9	0.2576	1.95
Max	81.69	58.73	6.47	2.59	0.112	1.94	1.62	83.2	0.4178	2.13

4.7 Results

4.7.1 Water saturation and saturation exponent predictors from training well A-02

Table 4.14 shows the performance of the water saturation predictors trained in well A-02 from different combinations of wireline logs at 1.0 ft depth spacing in terms of the coefficient of determination (R^2) between the measured and predicted values. The predictors in Table 4.14 were trained on data at 1.0 ft spacing. Cases 1, 3 and 4 gave the best predictors in terms of the R^2 values, as was the case for the resistivity predictors in section 4.4. All these predictors contained the bulk density (RHOB) wireline log, whereas case 2 did not. Figure 4.24 shows the crossplot of predicted versus measured values for case 3 and the small scatter of points around the 1:1 regression line.

Table 4.15 shows the performance of the saturation exponent predictors trained in well A-02 on (core and logs) data 1.0 ft spacing. All the predictors in this case give very similar good results. Figure 4.25 shows the crossplot of predicted versus measured values for case 3. Measured and predicted S_w and n values are shown along the depth for case 3 in Figures 4.26 and 4.27.

The results of the predictors from the training well that were trained on data at 0.5 ft depth spacing are shown in Appendix C. Tables C14 and C15 show the performance of various predictors (using different input wireline logs) in terms of the coefficient of determination (R^2) between the measured and predicted values of S_w and n for the training well for prediction at 0.5 ft depth spacing. Crossplots of the measured versus predicted values are shown in Figures C8 and C9. The predictors at this smaller depth spacing were still very good, but their R^2 values were slightly lower that the predictors at 1.0 ft spacing.

Table 4.14. Summary results of water saturation (S_w) predictors trained on the entire cored interval in the training well **A-02** at **1.0** ft spacing.

Input	**Output**	**Coefficient of determination (R^2) in training well A-02**
Case 1 (RHOB,NPHI,ILD &ILM)	S_w	0.9040
Case 2 (SGR,CGR,NPHI,ILD &ILM)	S_w	0.8342
Case 3 (SGR,CGR,RHOB,NPHI,ILD &ILM)	S_w	0.9056
Case 4 (SGR,CGR,RHOB,NPHI,ILD ,ILM,& DT)	S_w	0.9063

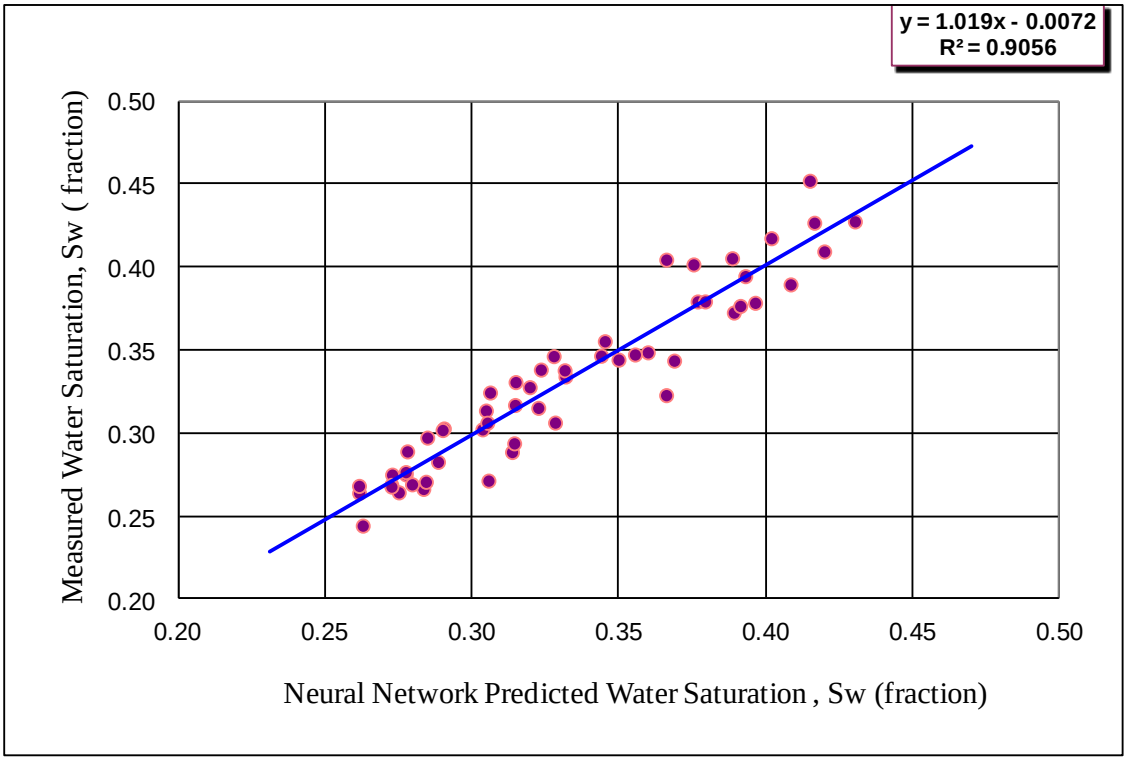

Figure 4.24 Crossplot of measured water saturation (S_w) versus BPNN predicted water saturation for the case 3 predictor trained on the entire cored interval using 6 wireline logs for training well **A-02** at **1.0** ft spacing.

Table 4.15. Summary results of saturation exponent (n) predictors trained on the entire cored interval in the training well **A-02** at **1.0** ft spacing.

Input	**Output**	**Coefficient of determination (R^2) in training well A-02**
Case 1 (RHOB,NPHI,ILD &ILM)	n	0.8535
Case 2 (SGR,CGR,NPHI,ILD &ILM)	n	0.8532
Case 3 (SGR,CGR,RHOB,NPHI,ILD &ILM)	n	0.8525
Case 4 (SGR,CGR,RHOB,NPHI,ILD ,ILM,& DT)	n	0.8529

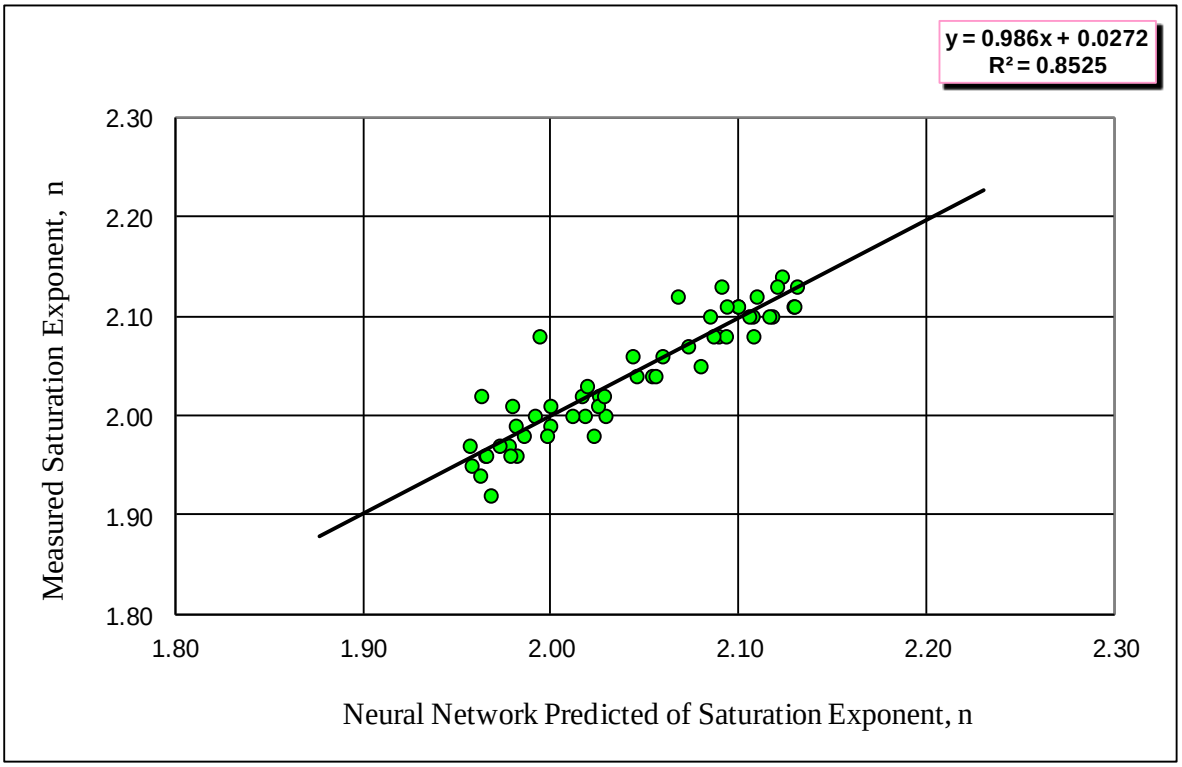

Figure 4.25. Crossplot of measured saturation exponent (n) versus BPNN predicted saturation exponent for the case 3 predictor trained on the entire cored interval using 6 wireline logs for training well **A-02** at **1.0** ft spacing.

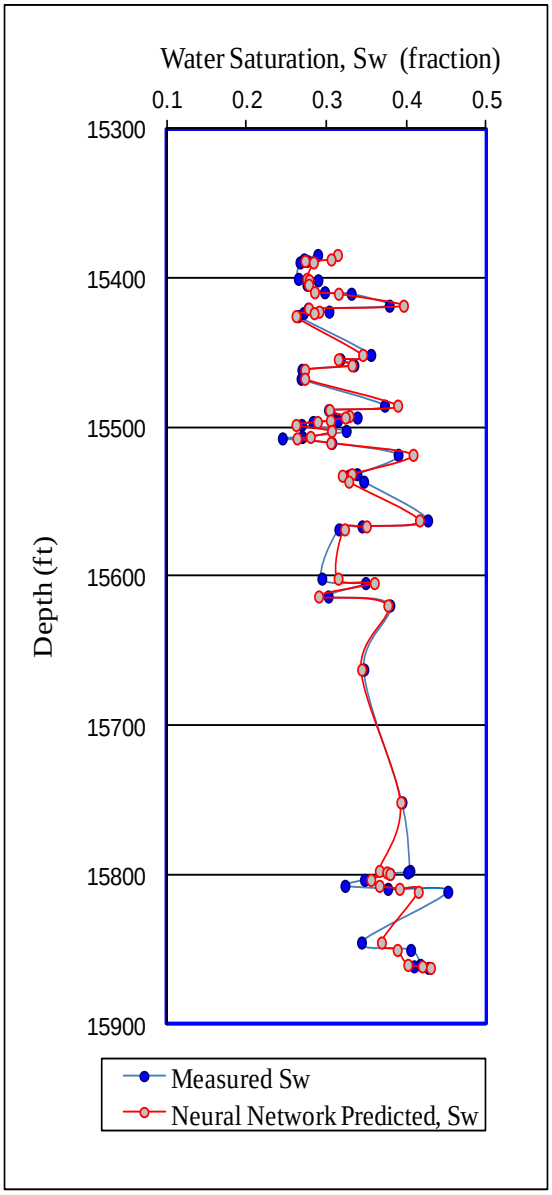

Figure 4.26 Measured S_w and neural network predicted S_w along the depth for case 3 in the training well **A-02** using **6** conventional wireline logs at **1.0** ft spacing.

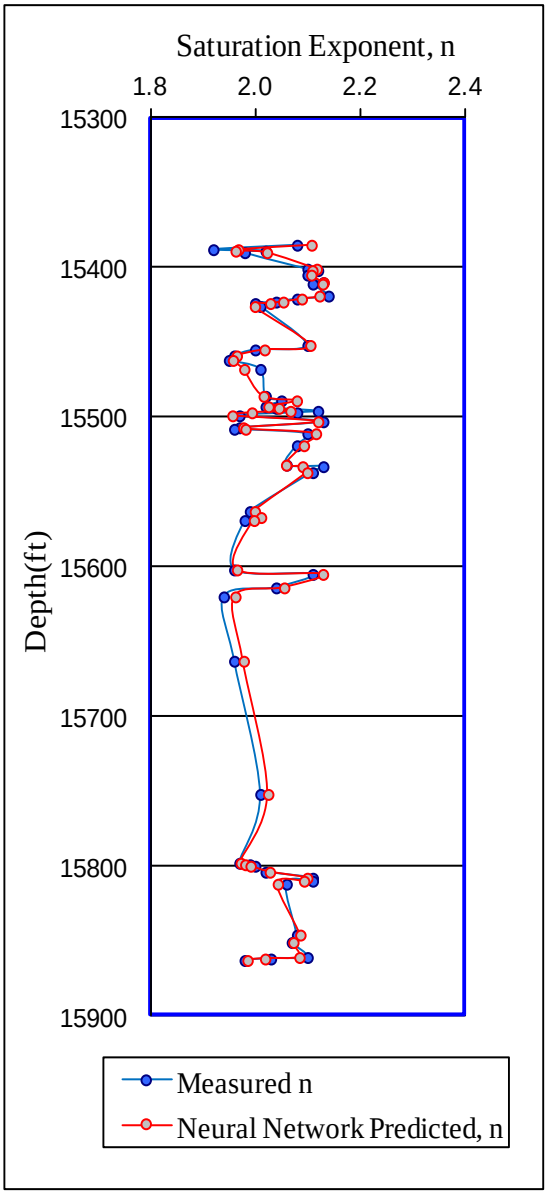

Figure 4.27. Measured n and BPNN predicted n along the depth for case 3 in the training well **A-02** using **6** conventional wireline logs at **1.0** ft

4.7.2 Test 3: testing predictions of water saturation and saturation exponent in an adjacent well (A-01) in the same oilfield using the training well (A-02) predictors

After the training process in well A-02, the water saturation and saturation exponent predictors were first tested on the cored interval in adjacent well A-01 in the same oil field. Tables 4.16 and 4.17 summarise the performance, in terms of the coefficient of determination (R^2) between the predicted and measured values, of various predictors based on different wireline log combinations at 0.5 ft depth spacing. The values of R^2 are 0.56 and 0.55 for water saturation (Table 4.16) from cases 3 and 4 suggesting that the predictors are doing a reasonable job. The crossplot for case 3 (Figure 4.29 for the test data, along with the training data in Figure 4.28) confirms this, where the regression line goes through the 1:1 line between the predicted and measured values. The R^2 value for case 2 without the RHOB data is slightly lower, as was the situation for the resistivity parameters in section 4.4.

The R^2 values between the measured and predicted values of saturation exponent trained on data at 0.5 ft spacing in well A-01 are relatively low (Table 4.17). However, the crossplot of measured versus predicted saturation exponent (Figure 4.31 for the case 3 predictor) still gives a regression line through the 1:1 line (the training data is shown in Figure 4.30).

Figures 4.33 and 4.35 show the water saturation and saturation exponent predictions in well A-01 from data trained at 0.5 ft spacing along the depth (the corresponding training data plots from well A-02 are shown in Figures 4.32 and 4.34). The predictions largely match the measured values.

The results of predictions at 1.0 ft depth spacing are available in Appendix C. Tables C16 and C17 summarise the performance, in terms of the coefficient of determination (R^2) between the predicted and measured values, of various predictors based on different wireline log combinations. Crossplots of the measured versus predicted values are shown in Figures C10 and C11. The predictors were trained from well A-02 at 0.5 ft spacing and tested in adjacent well A-01 at 1.0 ft spacing. These predictions were not quite as good as the predictions at 0.5 ft spacing.

Table 4.16. Summary results of, water saturation (S_w) predictors (trained on the entire cored interval of well **A-02**) when tested in adjacent well **A-01** in the same oil field at **0.5** ft spacing.

Input	**Output**	**Coefficient of determination (R^2) in adjacent well A-01**
Case 2 (SGR,CGR,NPHI,ILD &ILM)	S_w	0.4532
Case 3 (SGR,CGR,RHOB,NPHI,ILD &ILM)	S_w	0.5595
Case 4 (SGR,CGR,RHOB,NPHI,ILD, ILM,& DT)	S_w	0.5530

Table 4.17. Summary results of the saturation exponent (n) predictors (trained on the entire cored interval of well **A-02**) when applied in adjacent well **A-01** in the same oil field at **0.5** ft spacing.

Input	**Output**	**Coefficient of determination (R^2) in adjacent well A-01**
Case 2 (SGR,CGR,NPHI,ILD &ILM)	n	0.2546
Case 3 (SGR,CGR,RHOB,NPHI,ILD &ILM)	n	0.2436
Case 4 (SGR,CGR,RHOB,NPHI,ILD ,ILM,& DT)	n	0.2620

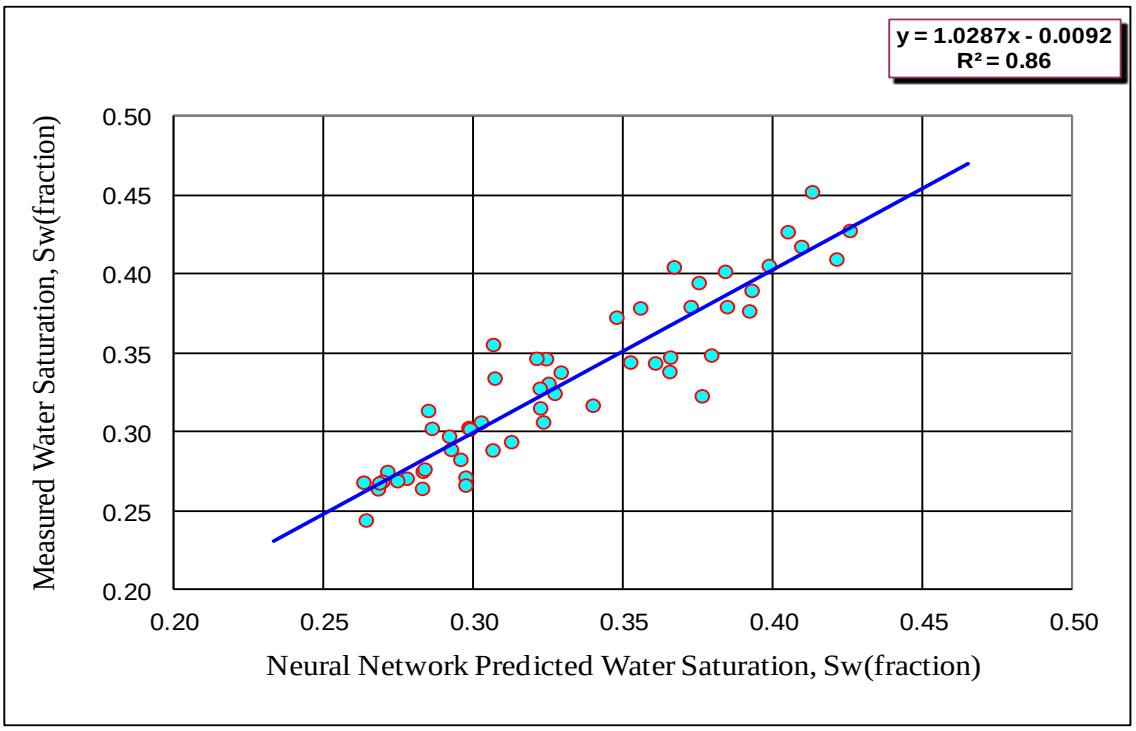

Figure 4.28. Crossplot of training data: measured water saturation (S_w) versus BPNN predicted water saturation for the case 3 predictor trained on the entire cored interval using 6 wireline logs for training well **A-02** at **0.5** ft spacing.

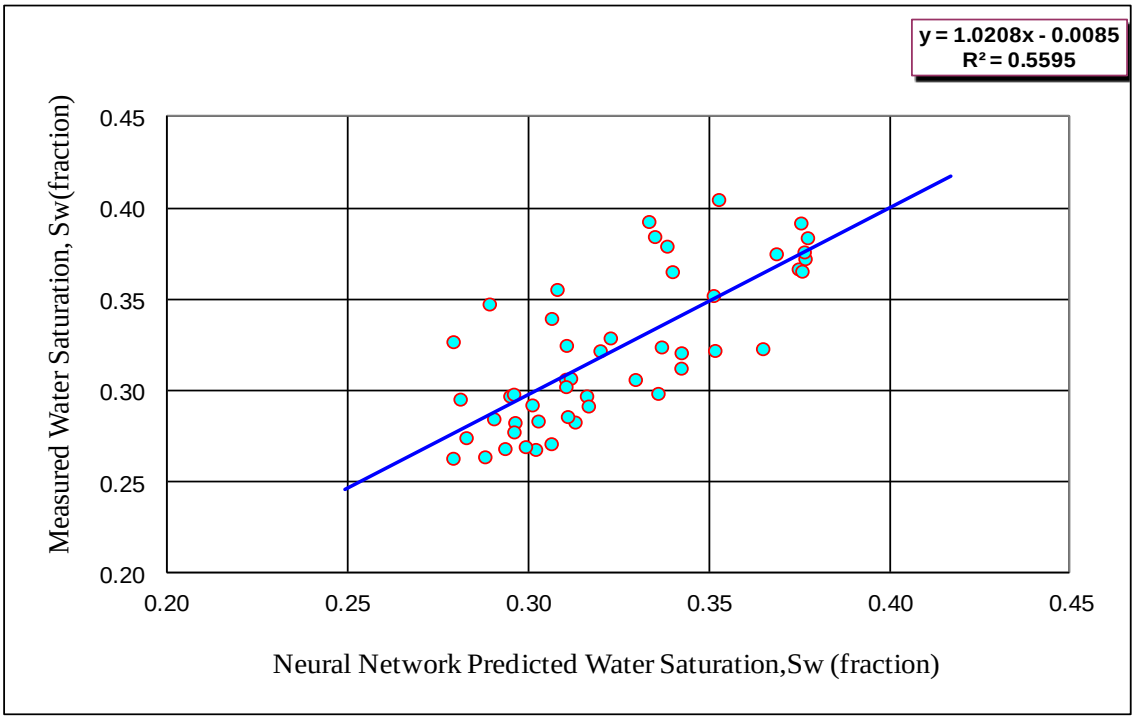

Figure 4.29. Crossplot of test data: measured water saturation (S_w) versus BPNN predicted water saturation when tested in adjacent well **A-01** for the case 3 predictor trained on the entire cored interval using 6 wireline logs from training well **A-02** at **0.5** ft spacing.

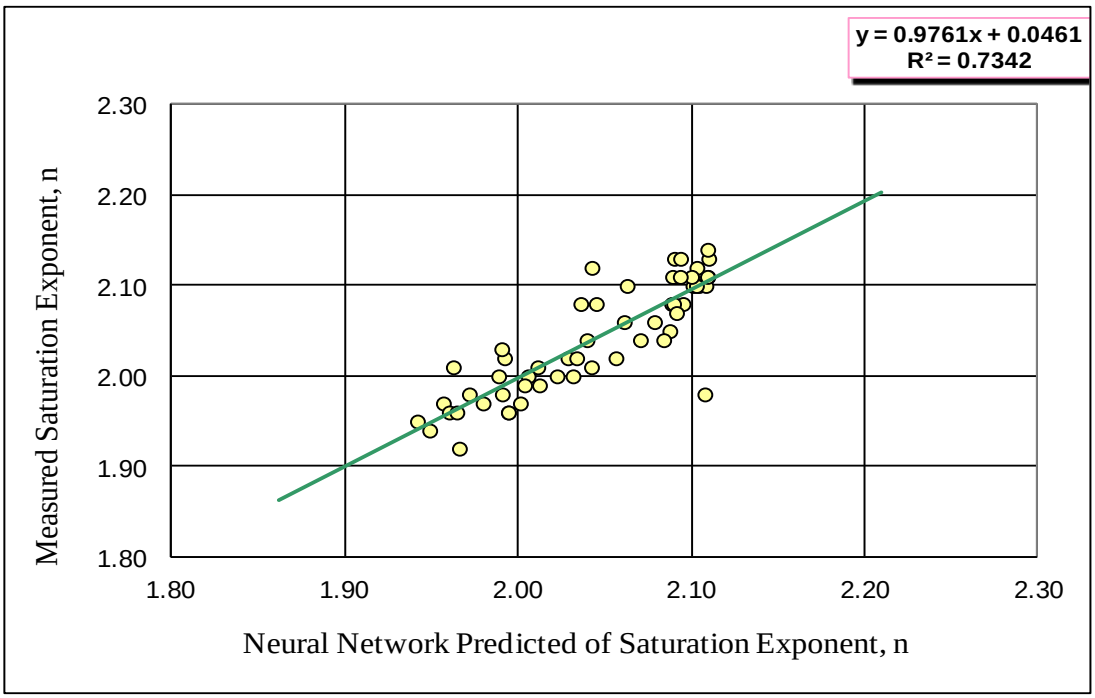

Figure 4.30. Crossplot of training data: measured saturation exponent (n) versus BPNN predicted saturation exponent for the case 3 predictor trained on the entire cored interval using 6 wireline logs for training well **A-02** at **0.5** ft spacing.

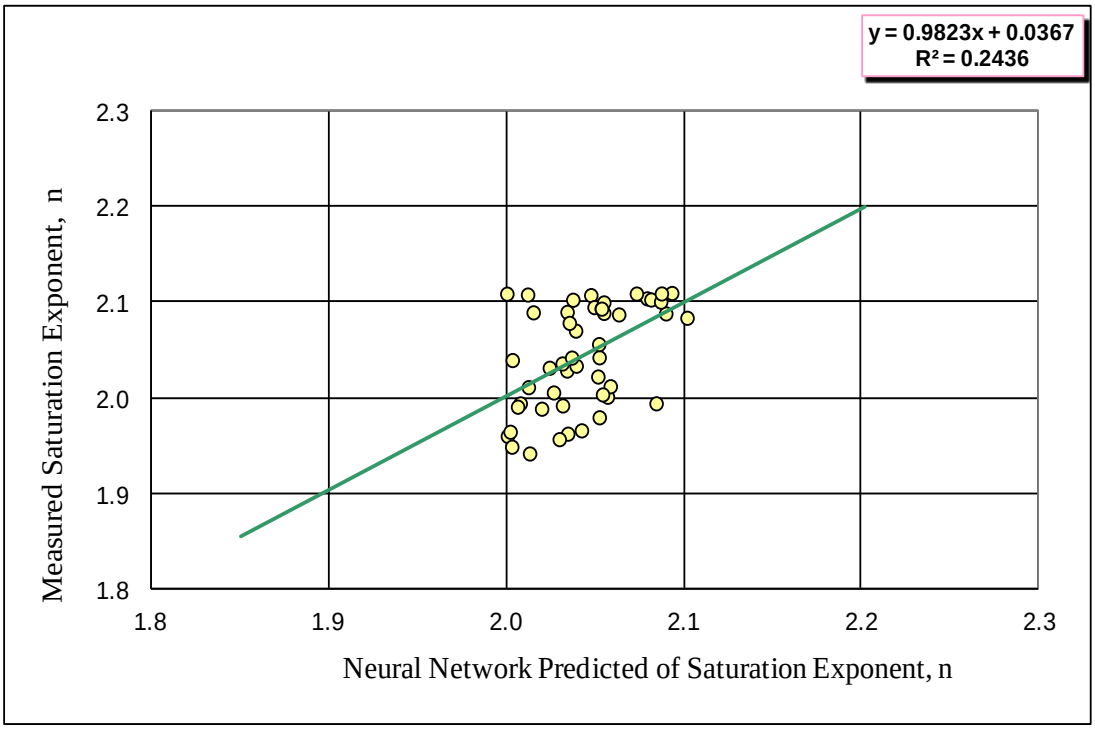

Figure 4.31. Crossplot of test data: measured saturation exponent (n) versus BPNN predicted saturation exponent when tested in adjacent well **A-01** for the case 3 predictor trained on the entire cored interval using 6 wireline logs from training well **A-02** at **0.5** ft spacing.

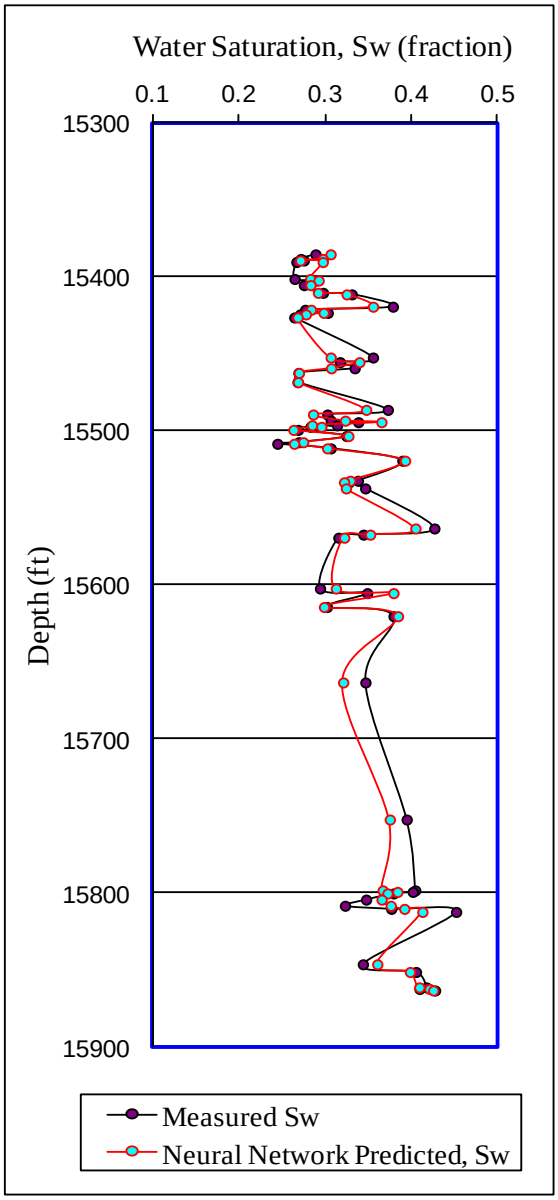

Figure 4.32. Measured S_w and BPNN predicted S_w along the depth in the training well **A-02** for case 3 using 6 conventional wireline logs at **0.5** ft spacing.

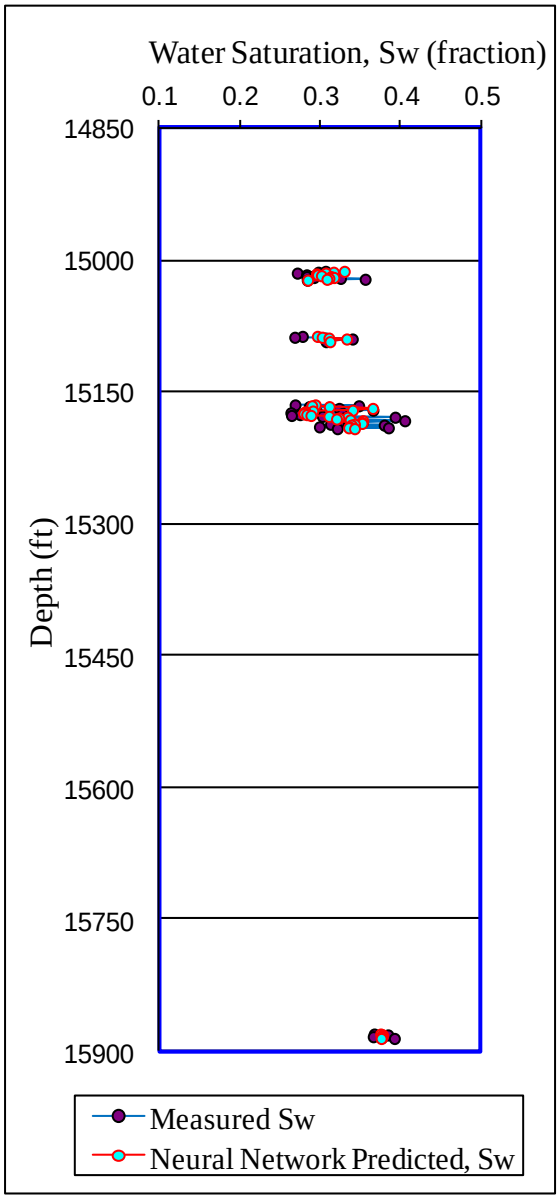

Figure 4.33. Measured S_w and BPNN predicted S_w along the depth in adjacent test well **A-01** for the case 3 predictor trained on the entire cored interval from training well **A-02** at **0.5** ft spacing.

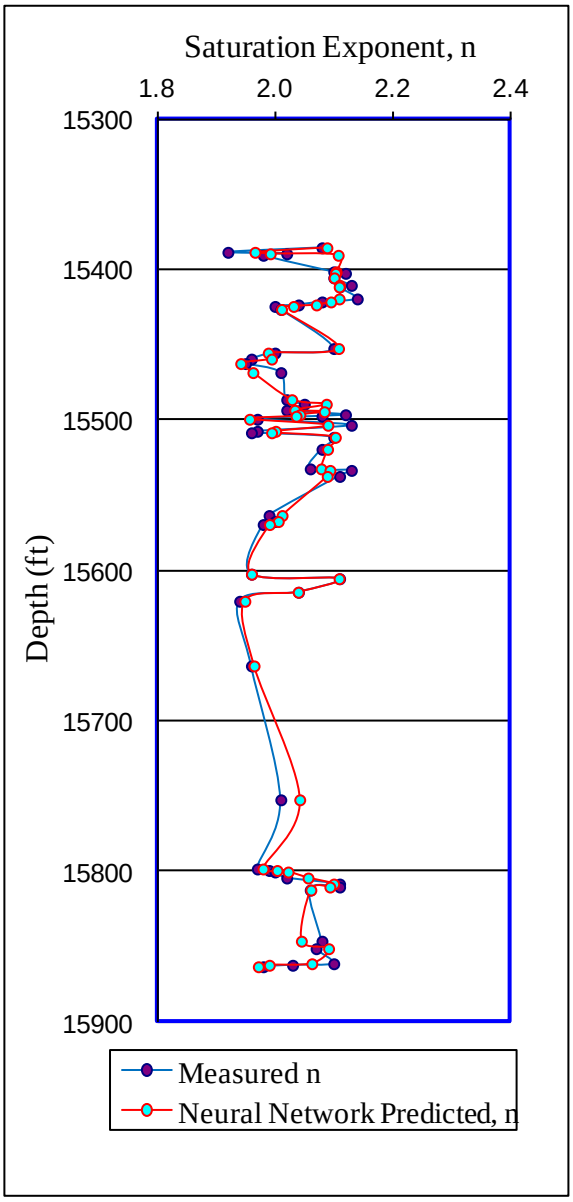

Figure 4.34. Measured n and neural network predicted n along the depth in the training well **A-02** for case 3 using 6 conventional wireline logs at **0.5** ft spacing

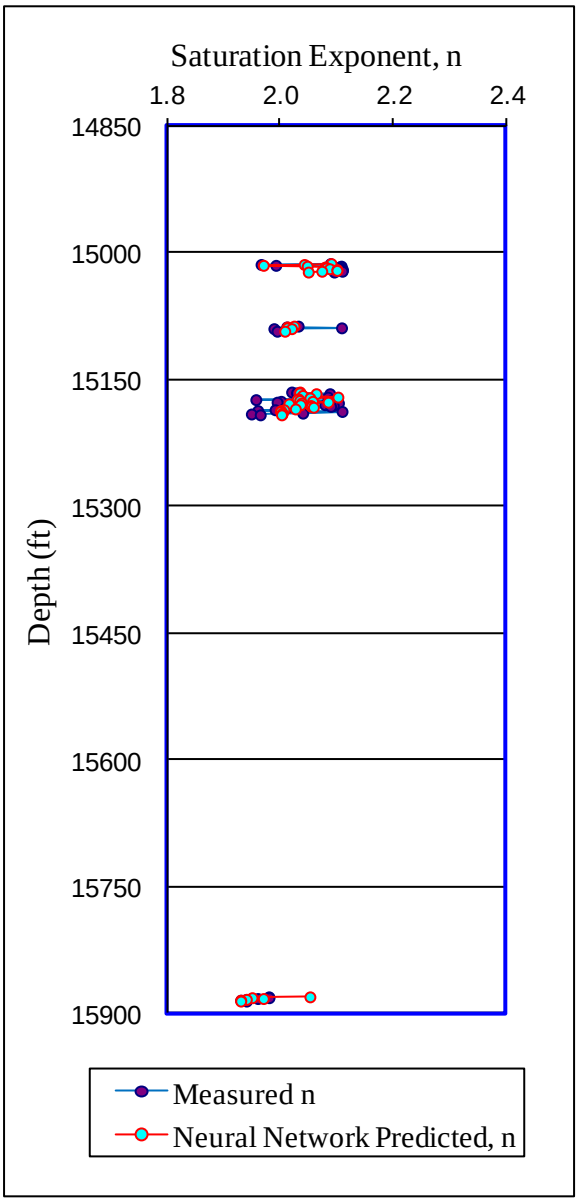

Figure 4.35. Measured n and neural network n predicted n along the depth in adjacent test well **A-01** for the case 3 predictor trained on the entire cored interval from training well **A-02** using 6 conventional wireline logs at **0.5** ft spacing.

4.7.3 *Test 4: testing predictions of water saturation and saturation exponent in another well (B-01) in a different oilfield using the training well (A-02) predictors*

The training well predictors for water saturation and saturation exponent were then tested on an interval in a different oil field in Field B – Libya. Tables 4.18 and 4.19 summarise the performance, in terms of the coefficient of determination (R^2) between the predicted and measured values, of various predictors based on different wireline log combinations at 0.5 ft depth spacing. Whilst the R^2 values are quite low, the regression lines for the crossplots of measured versus predicted water saturation (Figure 4.37) and saturation exponent (Figure 4.39) are still quite close to the 1:1 line, even though there is a spread of data points around this line. Figures 4.36 and 4.38 show the corresponding plots for the training data in each case.

Figures 4.41 and 4.43 show the water saturation and saturation exponent predictions in well B-01 trained on data at 0.5 ft spacing along the depth (the corresponding training data plots from well A-02 are shown in Figures 4.40 and 4.42). Despite the low R^2 values in Tables 4.18 and 4.19 the general profile along the depth of the predictions shown in Figures 4.41 and 4.43 follow the measured values reasonably well.

The results of predictions at 1.0 ft spacing are available in Appendix C. Tables C18 and C19 summarise the performance, in terms of the coefficient of determination (R^2) between the predicted and measured values, of various predictors based on different wireline log combinations. Crossplots of the measured versus predicted values are shown in Figures C12 and C13. The predictors were trained from well A-02 at 0.5 ft spacing and tested in another well B-01 at 1.0 ft spacing. These predictions were not quite as good as the predictions at 0.5 ft spacing.

The relationship between water saturation and resistivity index was then drawn to determine the slope (n). The results for the predicted and measured values were drawn for each test well. Figure 4.44 shows the predicted and measured results for case 4 for well A-01, and Figure 4.45 shows the results for case 4 for well B-01. The results for both test wells show that the predicted value of n is very close to the measured value.

Table 4.18. Summary results of water saturation (S_w) predictors (trained on the entire cored interval of well **A-02**) when applied in test well **B-01** in a different oil field at **0.5** ft spacing.

Input	Output	Coefficient of determination (R^2) in test well B-01
Case 2 (SGR,CGR,NPHI,ILD &ILM)	S_w	0.4320
Case 3 (SGR,CGR,RHOB,NPHI,ILD &ILM)	S_w	0.3407
Case 4 (SGR,CGR,RHOB,NPHI,ILD , ILM, & DT)	S_w	0.3308

Table 4.19. Summary results of saturation exponent (n) predictors (trained on all entire cored interval of well **A-02**) when applied in test well **B-01** in a different oil field at **0.5** ft spacing.

Input	Output	Coefficient of determination (R^2) in test well B-01
Case 2 (SGR,CGR,NPHI,ILD &ILM)	n	0.1951
Case 3 (SGR,CGR,RHOB,NPHI,ILD &ILM)	n	0.2966
Case 4 (SGR,CGR,RHOB,NPHI,ILD, ILM,& DT)	n	0.3825

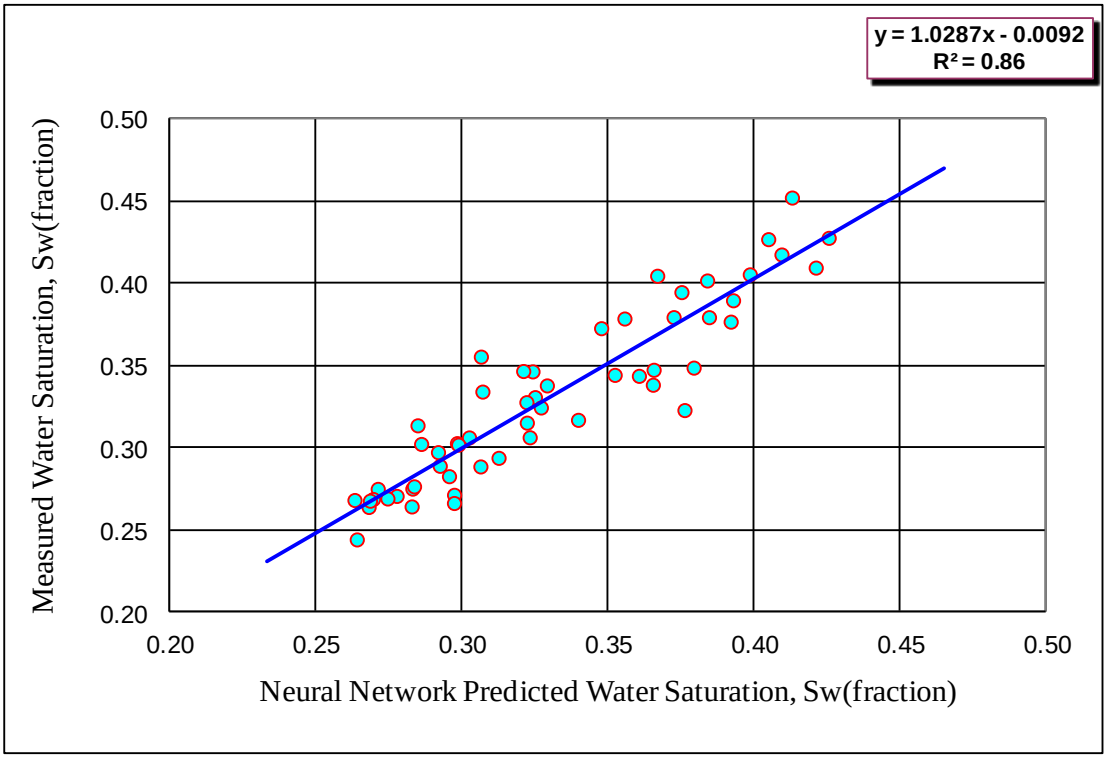

Figure 4.36. Crossplot of training data: measured water saturation (S_w) versus BPNN predicted water saturation for the case 3 predictor trained on the entire cored interval using 6 wireline logs for training well **A-02** at **0.5** ft spacing.

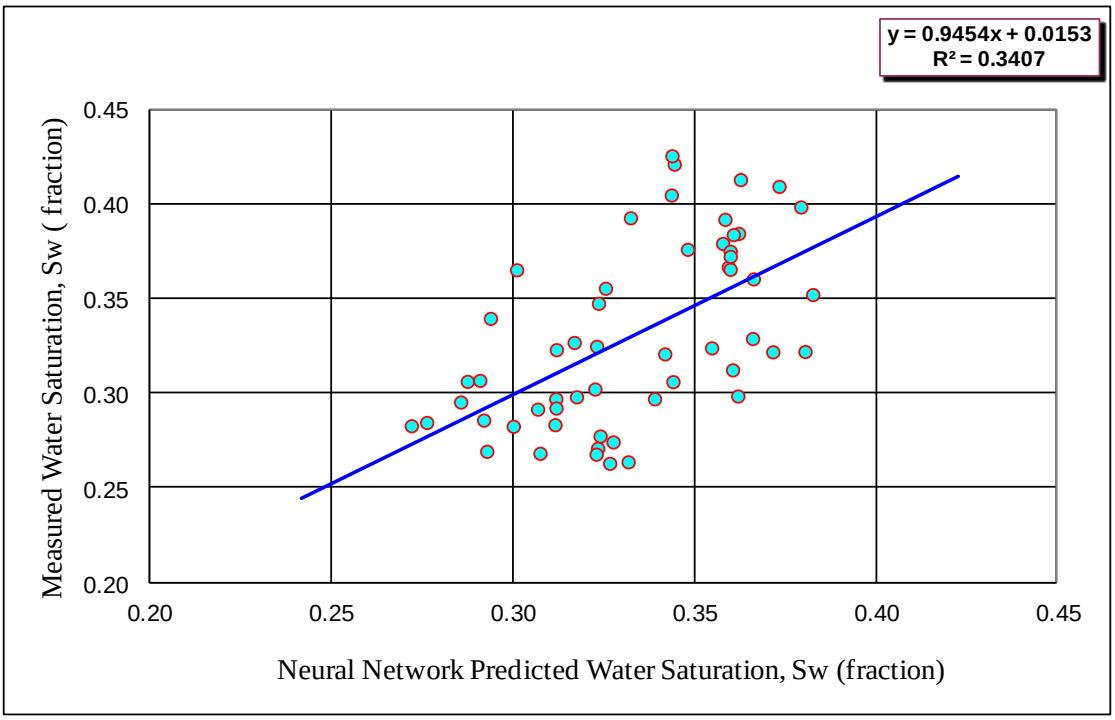

Figure 4.37. Crossplot of test data: measured water saturation (S_w) versus BPNN predicted water saturation when tested in well **B-01** in a different oil field for the case 3 predictor trained on the entire cored interval using 6 wireline logs from training well **A-02** at **0.5** ft spacing.

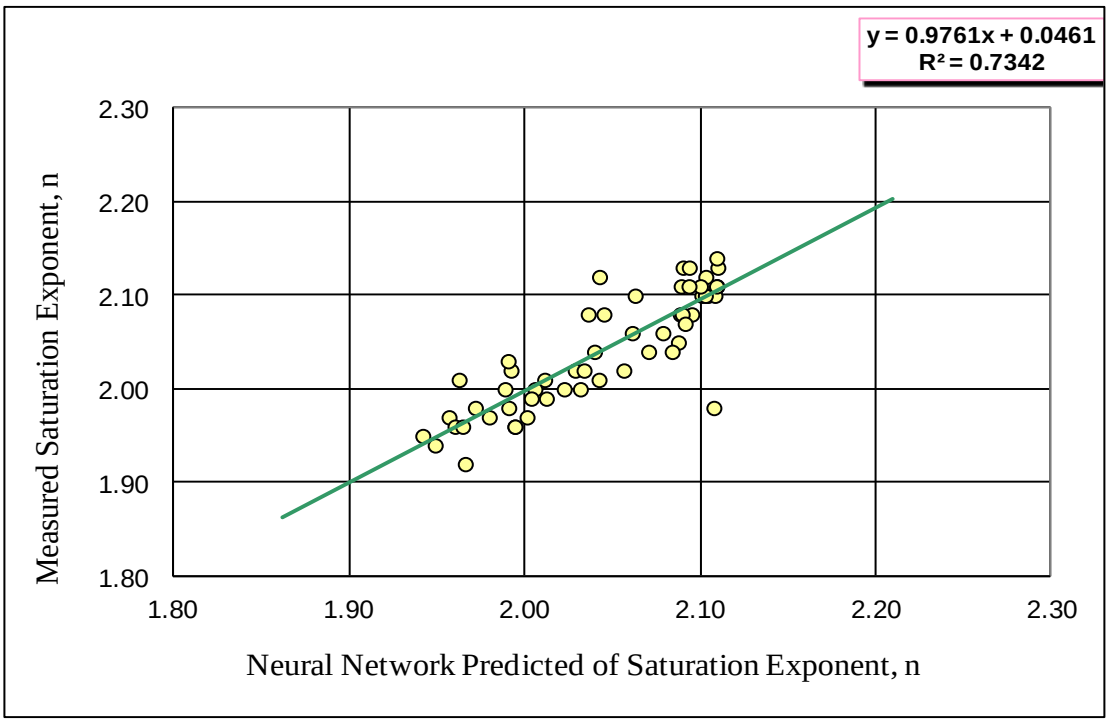

Figure 4.38. Crossplot of training data: measured saturation exponent (n) versus BPNN predicted saturation exponent for the case 3 predictor trained on the entire cored interval using 6 wireline logs for training well **A-02** every **0.5** ft spacing.

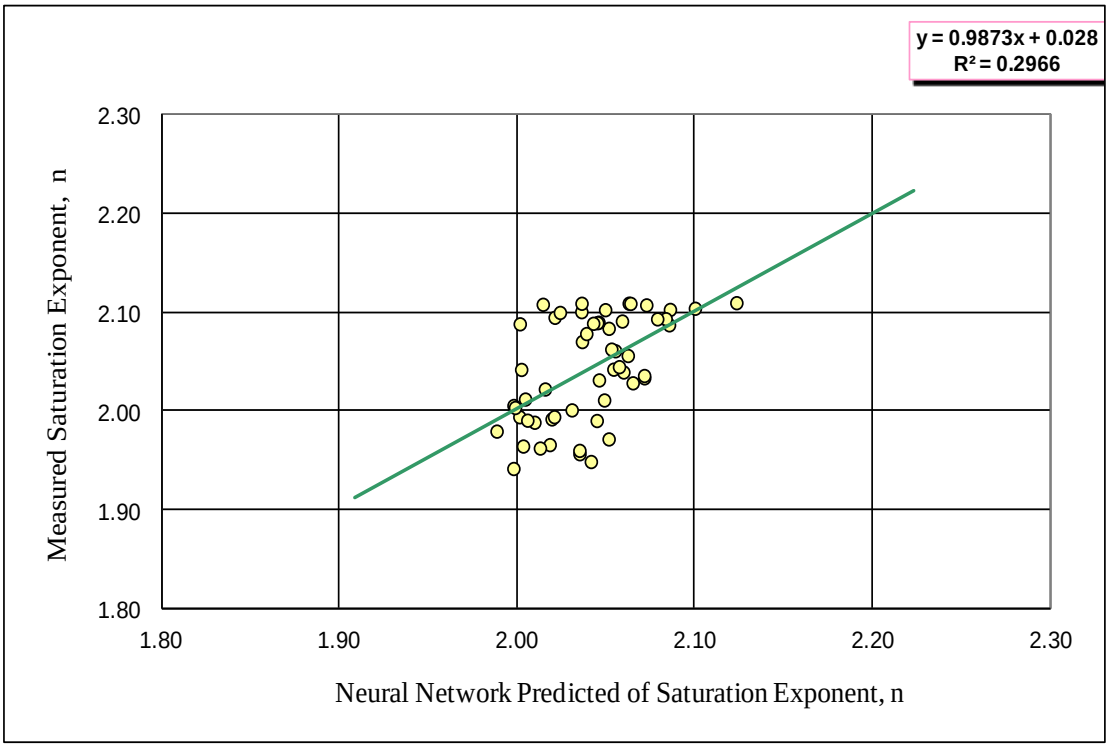

Figure 4.39. Crossplot of test data: measured saturation exponent (n) versus BPNN predicted saturation exponent when tested in well **B-01** in a different oil field for the case 3 predictor trained on the entire cored interval using 6 wireline logs from training well **A-02** at **0.5** ft spacing.

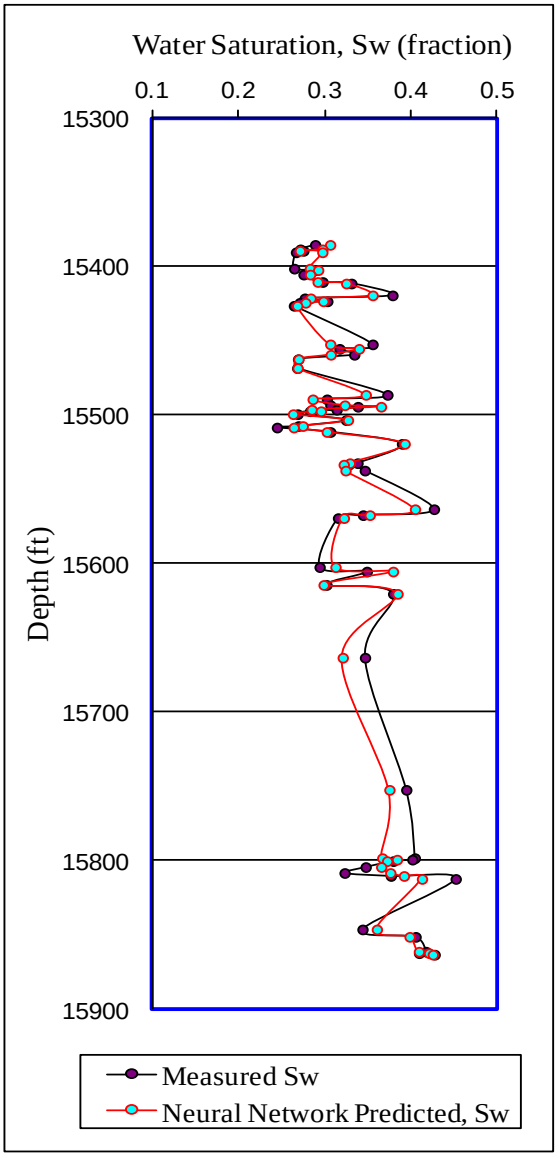

Figure 4.40. Measured S_w and BPNN predicted S_w along the depth in the training well **A-02** for case 3 using **6** conventional wireline logs at **0.5** ft spacing.

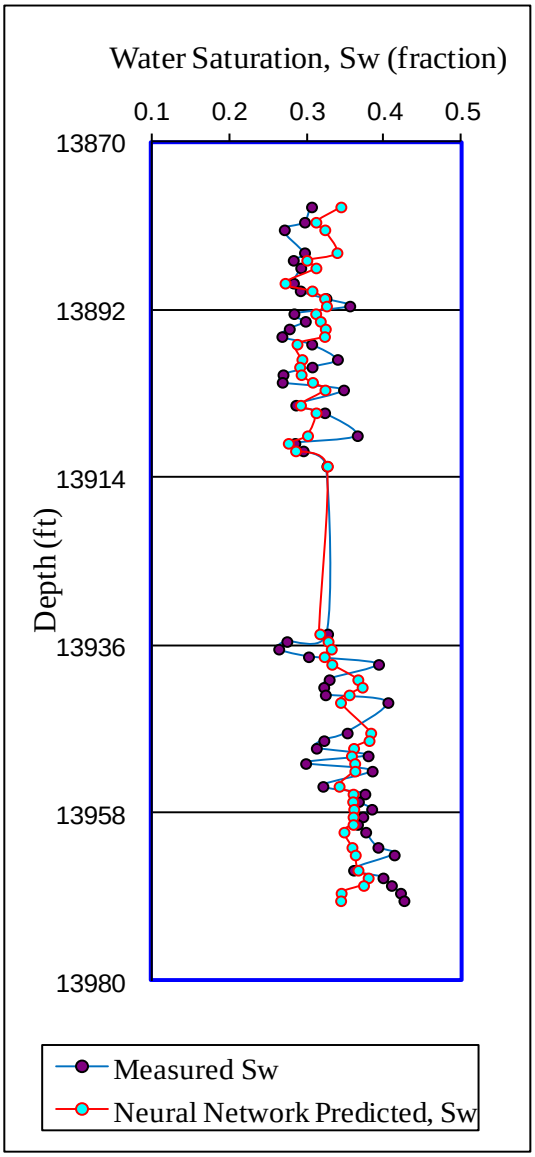

Figure 4.41. Measured S_w and BPNN predicted S_w along the depth in test well **B-01** in a different oil field for the case 3 predictor trained on the entire cored interval from the training well **A-02** at **0.5** ft spacing.

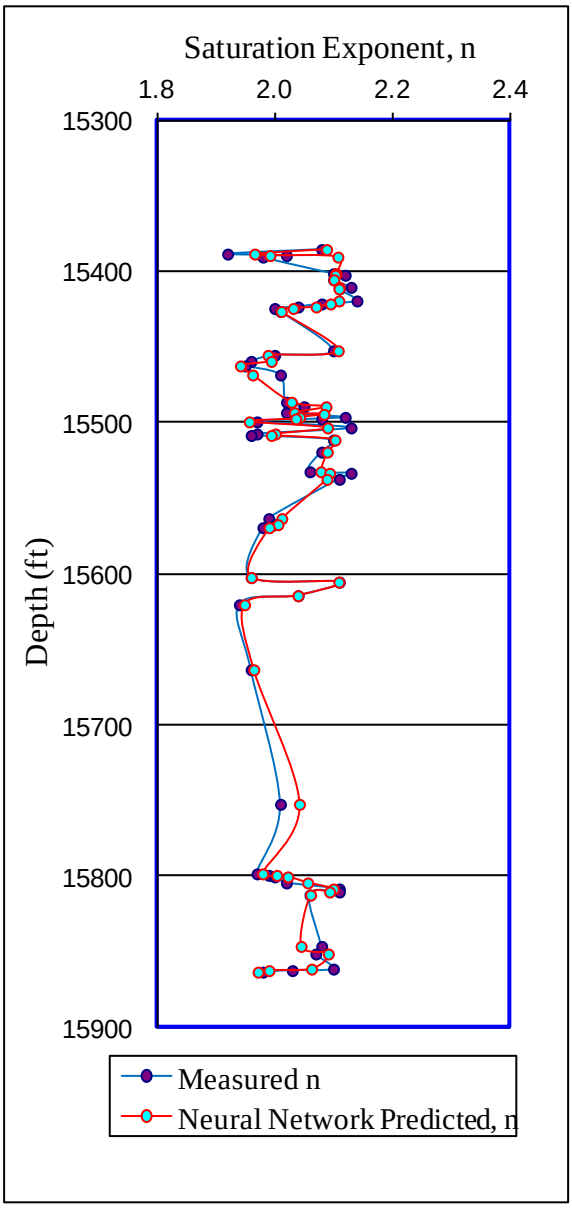

Figure 4.42. Measured n and BPNN predicted n along the depth in the training well **A-02** for case 3 using 6 conventional wireline logs at **0.5** ft spacing.

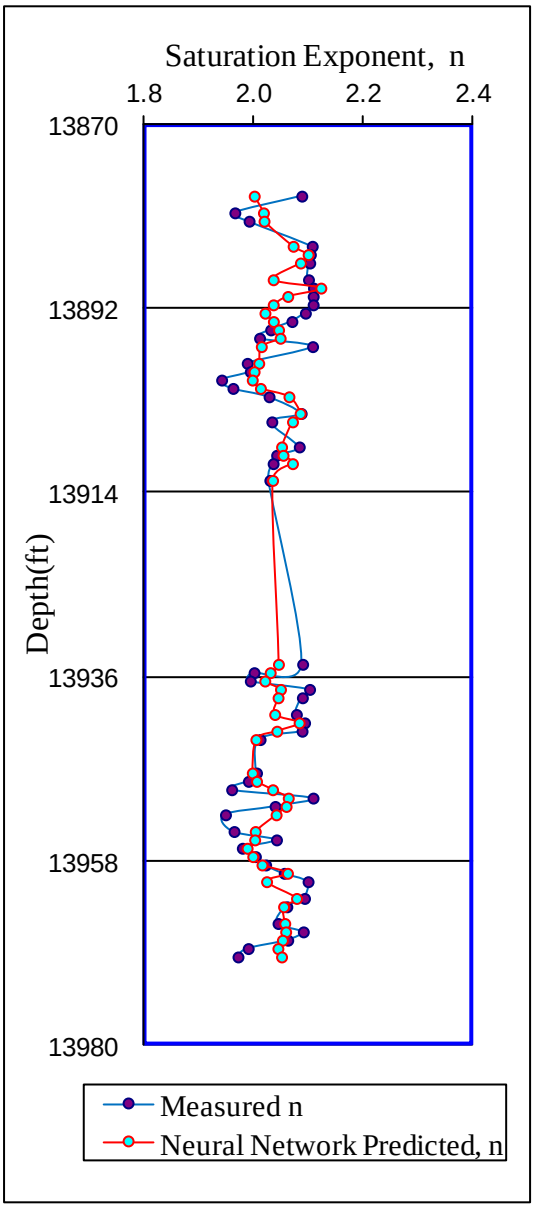

Figure 4.43. Measured n and BPNN predicted n along the depth in test well **B-01** in a different oil field for the predictor trained on the entire cored interval from well **A-02** using **6** conventional wireline logs at **0.5** ft spacing.

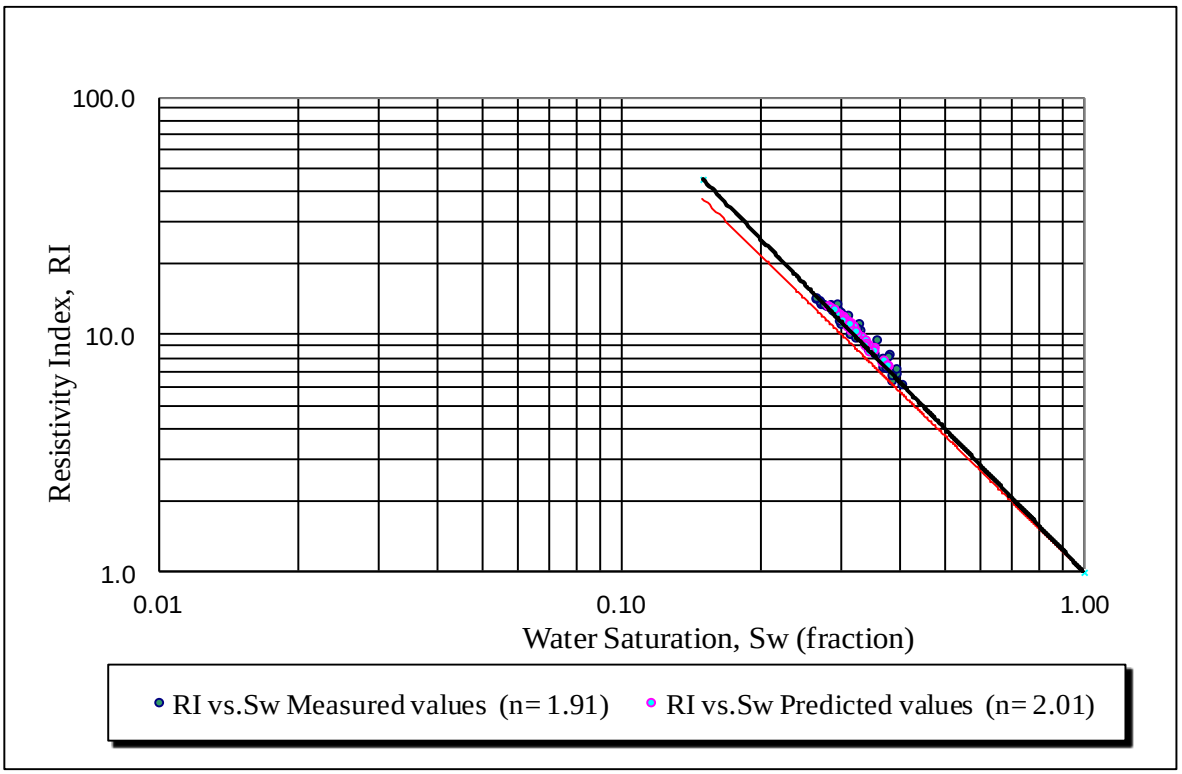

Figure 4.44. Measured and predicted values of water saturation versus resistivity index in the adjacent test well **A-01** for case **4**. The slope gives the value of the saturation exponent (n).

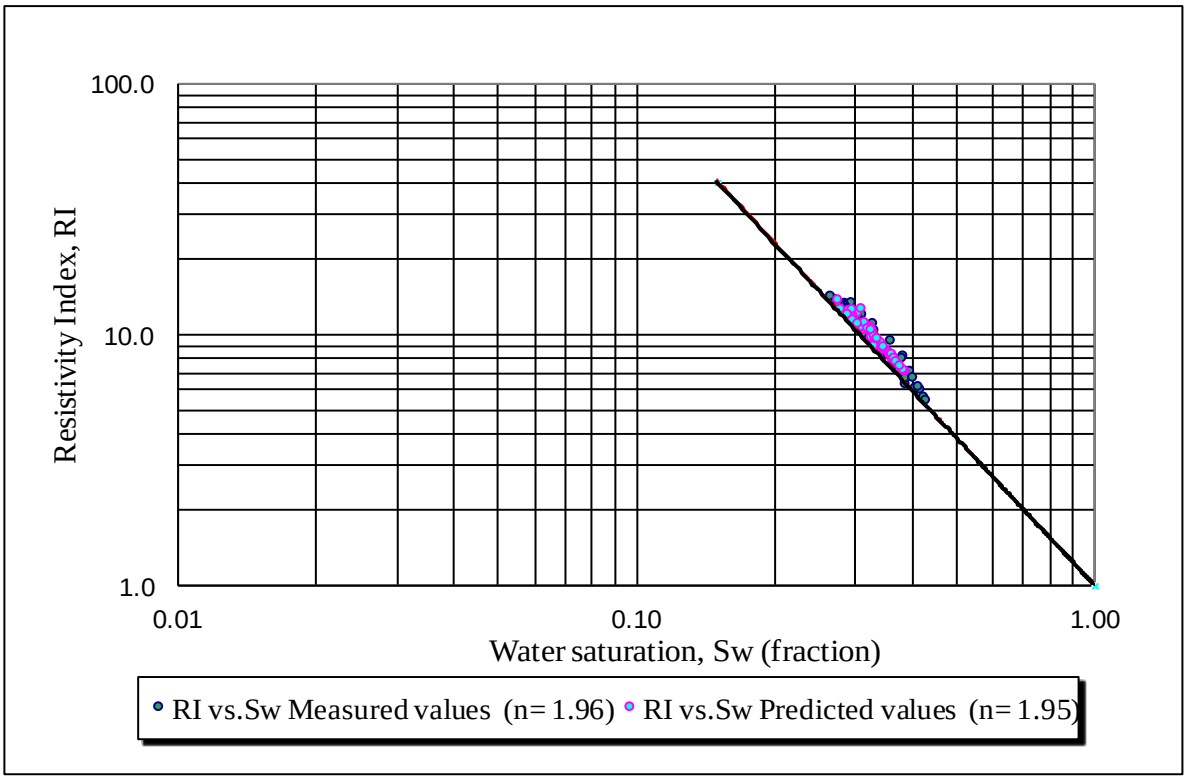

Figure 4.45. Measured and predicted values of water saturation versus resistivity index in the test well **B-01** for case **4**. The slope gives the value of the saturation exponent (n).

4.8 Introduction to Wettability

In hydrocarbon reservoirs there is always more than one fluid phase. The distribution of fluid within the rock pore space is not controlled by pore geometry alone. The interaction between the fluids and the rock surface has an important role too. When two immiscible fluids are in contact with the rock pore surface, one of them may spread onto the surface of the solid more likely than the other fluid. The fluid, which is more attracted to the solid surface, is known as the wetting phase, while the other fluid that is not attracted by the solid surface is known as the non-wetting phase. The wettability is defined as "the tendency of one fluid to spread on or adhere to a solid surface in the presence of other immiscible fluids." Wettability may change from place to place within the rock framework. In water-wet rocks, water occupies the smaller pores and spreads over the majority of the pore surface area of the grains which contact water, while oil is located in the middle of the pores. In oil-wet systems the rock is preferentially in contact with the oil, and the location of the two fluids is reversed from the water-wet case. Oil will occupy the small pores and contact the majority of the rock surface. The wettability of a system can range from strongly water-wet to strongly oil-wet. When the rock has no strong preference for either oil or water, the system is said to be of neutral (or intermediate wettability). The wettability of hydrocarbon bearing rocks can be altered from it is original water-wet state to oil-wet by adsorption of polar compounds or by adsorption of organic materials originally in the crude oil. Wettability is also easily altered as a result of coring fluid. In coring operations, the core is partially penetrated by the drilling fluid, which, if contains surface active materials, may change the wettability of the rock. Core handling during storage and testing (Anderson, 1986) may change the native wettability due to evaporation of fluids and exposure to surface active agents.

Anderson (1986, Part II) has reviewed the most common methods used to measure wettability. Quantitative measurement techniques include contact angle, Amott wettability (spontaneous imbibition and forced displacements) and United state Bureau of Mines (USBM). Amott wettability indices are presented as displacement by water ratios ranging from 1.0 to 0 (1 is strongly water-wet) or displacement by oil ratios ranging from 1.0 to 0 (1 is strongly oil-wet). Care should be taken in the interpretation of the data due to the fact that

sample wettability may be altered or reversed by a large number of factors (type of coring fluid, exposure to air, temperature, sample handling and plugging, cleaning, drying and preservation). The Amott-Harvey Wettability Index ($I_{A/H}$) is a single number that combines the displacement by water and oil ratios as

$$I_{w,AH} = I_w - I_o \quad \text{----------} \quad (4.10)$$

Where I_w and I_o are displacement by water and oil ratios respectively.

4.9 Amott-Harvey Wettability Index ($I_{A/H}$) Prediction Using Neural Networks

4.9.1 Available data

The predictors were trained using Amott-Harvey Wettability Index values, determined on the 55 SCAL plugs, in conjunction with the corresponding wireline log data at the same depths. The wireline log and core data were depth matched before training the neural networks. The wireline logs and Amott-Harvey Wettability Index values from all wells were normalised using Equation 4.7, and the values are shown in Tables 4.20-4.22. Most of the wireline logs were normalised based on the usual maximum and minimum values given in the log headers. The resistivity wireline log values were normalised based on the logarithm of their minimum and maximum values.

Table 4.20. The range of wireline log and Amott-Harvey Wettability Index ($I_{A/H}$) values for normalisation purposes in the BPNN for a training well A-02 at 1.0 ft spacing.

	SGR (API)	CGR (API)	CALI (in)	RHOB (g/cc)	NPHI (fraction)	Log ILD (Ohm.m)	Log ILM (Ohm.m)	DT (µs/ft)	$I_{A/H}$
Min.	11.85	4.50	5.78	2.36	0.042	0.127	0.29	59.4	-0.3875
Max	157.94	63.20	6.344	2.66	0.2109	1.95	2.07	78.6	-0.1763

Table 4.21. The range of wireline log and Amott-Harvey Wettability Index ($I_{A/H}$) values for normalisation purposes in the BPNN for adjacent test well A-01 in the same oil field at 0.5 ft spacing.

	SGR (API)	CGR (API)	CALI (in)	RHOB (g/cc)	NPHI (fraction)	Log ILD (Ohm.m)	Log ILM (Ohm.m)	DT (µs/ft)	$I_{A/H}$
Min.	10.09	7.21	5.53	2.38	0.035	0.238	0.302	56.8	-0.373
Max	121.25	86.47	7.17	2.75	0.239	1.78	1.85	73.6	-0.205

Table 4.22. The range of wireline log and Amott-Harvey Wettability Index ($I_{A/H}$) values for normalisation purposes in the BPNN for tested well B0-1 in a different oil field at 0.5 ft spacing.

	SGR (API)	CGR (API)	CALI (in)	RHOB (g/cc)	NPHI (fraction)	Log ILD (Ohm.m)	Log ILM (Ohm.m)	DT (µs/ft)	$I_{A/H}$
Min.	23.04	20.44	5.89	2.37	0.057	0.67	0.37	60.9	-0.373
Max	81.69	58.73	6.47	2.59	0.112	1.94	1.62	83.2	-0.205

4.10 Results

4.10.1 Amott-Harvey Wettability Index predictors from training well A-02

Table 4.23 shows the performance of the Amott-Harvey Wettability Index predictors trained in well A-02 from different combinations of wireline logs at 1.0 ft depth spacing in terms of the coefficient of determination (R^2) between the measured and predicted values. The predictors in Table 4.23 were trained on data at 1.0 ft spacing. Cases 1, 3 and 4 gave the best predictors in terms of the R^2 values, as was the case for the other SCAL parameters in sections 4.4 and 4.7. All these predictors contained the bulk density (RHOB) wireline log, whereas the case 2 predictors did not. Figure 4.46 shows the crossplot of predicted versus measured values for case 3 and the small scatter of points around the 1:1 regression line. Measured and predicted Amott-Harvey Wettability Index values are shown along the depth for case 3 and case 4 in Figures 4.47 and 4.48.

The results of the predictors from the training well that were trained on data at 0.5 ft depth spacing are shown in Appendix C. Table C23 shows the performance of various predictors (using different input wireline logs) in terms of the coefficient of determination (R^2) between the measured and predicted values of $I_{A/H}$ for the training well for prediction at 0.5 ft depth spacing. Crossplots of the measured versus predicted values are shown in Figure C14. The predictors at this smaller depth spacing were still very good, but their R^2 values were slightly lower that the predictors at 1.0 ft spacing.

.

Table 4.23. Summary results of the Amott-Harvey Wettability Index **($I_{A/H}$)** predictors trained on the entire cored interval in training well **A-02** at **1.0** ft spacing.

Input	Output	Coefficient of determination (R^2) in training well A-02
Case 1 (RHOB,NPHI,ILD &ILM)	$I_{A/H}$	0.8739
Case 2 (SGR,CGR,NPHI,ILD &ILM)	$I_{A/H}$	0.7851
Case 3 (SGR,CGR,RHOB,NPHI,ILD &ILM)	$I_{A/H}$	0.8753
Case 4 (SGR,CGR,RHOB,NPHI,ILD , ILM, & DT)	$I_{A/H}$	0.8777

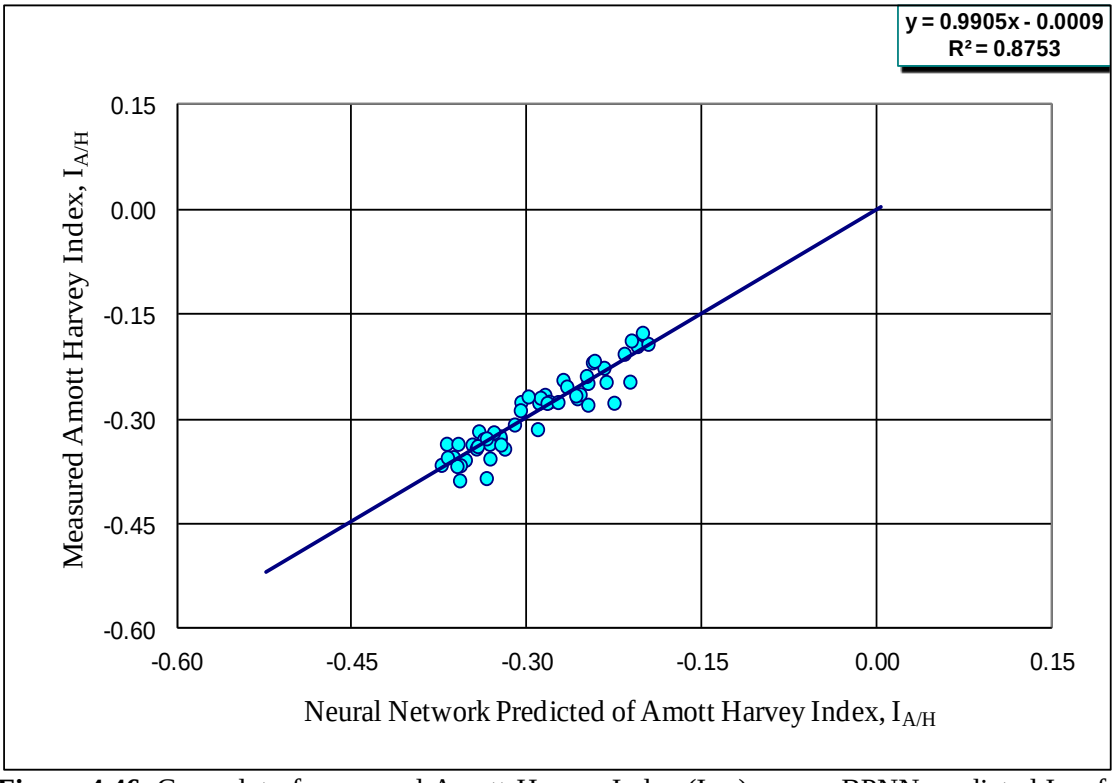

Figure 4.46. Crossplot of measured Amott-Harvey Index ($I_{A/H}$) versus BPNN predicted $I_{A/H}$ for the case 3 predictor trained on the entire cored interval using 6 wireline logs for training well **A-02** at **1.0** ft spacing.

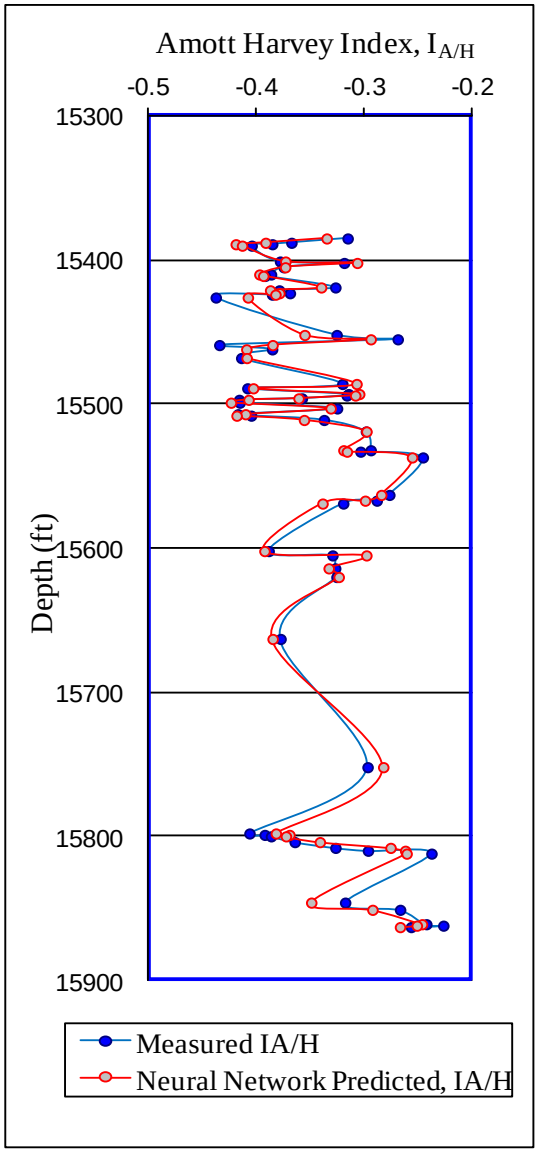

Figure 4.47. Measured $I_{A/H}$ and BPNN predicted $I_{A/H}$ along the depth in the training well **A-02** for case 3 using **6** conventional wireline logs at **1.0** ft spacing.

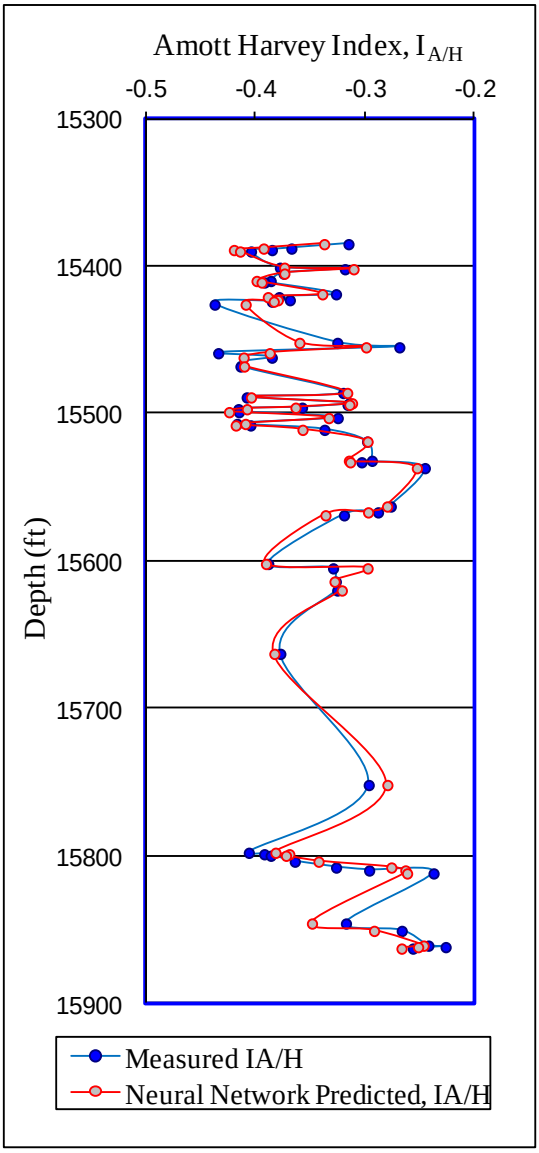

Figure 4.48 Measured $I_{A/H}$ and BPNN predicted $I_{A/H}$ along the depth in the training well **A-02** for case 4 using 7 conventional wireline logs at **1.0** ft spacing.

4.10.2 Test 5: testing predictions of Amott-Harvey Wettability Index in an adjacent well (A-01) in the same oilfield using the training well (A-02) predictors

After the training process in well A-02, the Amott-Harvey Wettability Index predictors were first tested on the cored interval in adjacent well A-01 in the same oil field. Table 4.24 summarises the performance, in terms of the coefficient of determination (R^2) between the predicted and measured values, of various predictors based on different wireline log combinations. The values of R^2 are reasonable for cases 3 and 4, but quite poor for cases 1 and 2. The greater number of wireline log inputs in cases 3 and 4 seem to make a difference here. The crossplot for case 3 (Figure 4.50 for the test data, along with the training data in Figure 4.49) shows that the regression line goes through the 1:1 line between the predicted and measured values.

Figure 4.52 shows the Amott-Harvey Wettability Index predictions in well A-01 from data trained at 0.5 ft spacing along the depth (the corresponding training data plots from well A-02 are shown in Figure 4.51). The predictions largely match the measured values. The results of predictions at 1.0 ft depth spacing are available in Appendix C. Tables C24 summarise the performance, in terms of the coefficient of determination (R^2) between the predicted and measured values, of various predictors. Crossplots of the measured versus predicted values are shown in Figure C15. These predictions were not quite as good as the predictions at 0.5 ft spacing.

5.10.3 Test 6: testing predictions of Amott-Harvey Wettability Index in another well (B-01) in a different oilfield using the training well (A-02) predictors

The training well predictors for Amott-Harvey Wettability Index were then tested on an interval in a different oil field in Field B – Libya. Table 4.25 summarises the performance, in terms of the coefficient of determination (R^2) between the predicted and measured values, of various predictors based on different wireline log combinations. Again the R^2 values are quite low, but the regression line for the crossplot of measured versus predicted Amott-Harvey Wettability Index (Figure 4.54) are still quite close to the 1:1 line, even

though there is a spread of data points around this line. Figure 4.52 shows the corresponding plots for the training data.

Figure 4.56 shows the Amott-Harvey Wettability Index predictions in well B-01 trained on data at 0.5 ft spacing along the depth (the corresponding training data plots from well A-02 are shown in Figure 4.55). Despite the low R^2 values in Table 4.25 the trend of the profile along the depth of the predictions shown in Figure 4.56 generally follows the measured values reasonably well.

The saturation exponent (n) was then plotted against Amott-Harvey Wettability Index. The results for the measured (Figure 4.57) and predicted (Figure 4.58) values are shown for case 4 for the training well A-02. Figures 4.57 and 4.58 show that the measured and predicted results for the relationship between saturation exponent and Amott-Harvey Wettability Index are very similar.

Table 4.24. Summary results of Amott-Harvey Index ($I_{A/H}$) predictors (trained on the entire cored interval in well **A-02**) when applied in adjacent test well **A-01** in the same oil field at **0.5** ft spacing.

Input	Output	Coefficient of determination (R^2) in adjacent well A-01
Case 1 (RHOB,NPHI,ILD, & ILM)	$I_{A/H}$	0.2355
Case 2 (SGR,CGR,NPHI,ILD &ILM)	$I_{A/H}$	0.3134
Case 3 (SGR,CGR,RHOB,NPHI,ILD &ILM)	$I_{A/H}$	0.4510
Case 4 (SGR,CGR,RHOB,NPHI,ILD , ILM, & DT)	$I_{A/H}$	0.4724

Table 4.25. Summary results of Amott-Harvey Index ($I_{A/H}$) predictors (trained on the entire cored interval in well **A-02**) when applied in test well **B-01** in a different oil field at **0.5** ft spacing.

Input	Output	Coefficient of determination (R^2) in test well B-01
Case 1 (RHOB,NPHI,ILD,& ILM)	$I_{A/H}$	0.1387
Case 2 (SGR,CGR,NPHI,ILD &ILM)	$I_{A/H}$	0.2586
Case 3 (SGR,CGR,RHOB,NPHI,ILD &ILM)	$I_{A/H}$	0.3706
Case 4 (SGR,CGR,RHOB,NPHI,ILD , ILM, & DT)	$I_{A/H}$	0.3740

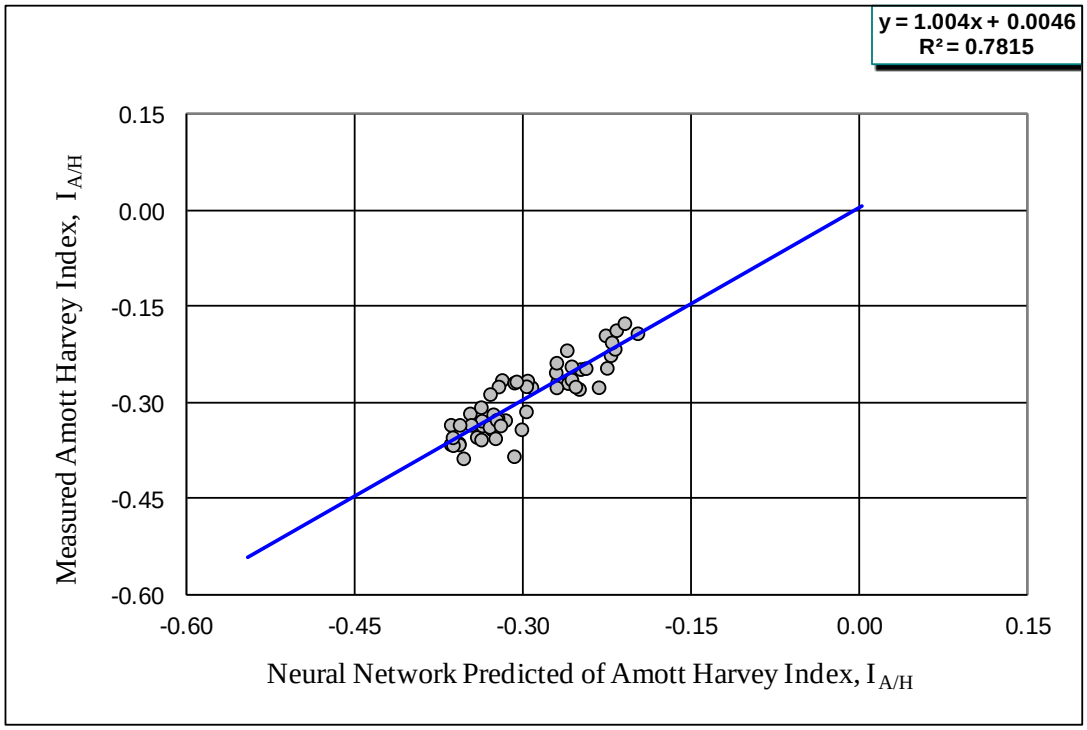

Figure 4.49. Crossplot of <u>training data</u>: measured Amott-Harvey Index ($I_{A/H}$) versus BPNN predicted $I_{A/H}$ for the case 3 predictor trained on the entire cored interval using 6 wireline logs for training well **A-02** at **0.5** ft spacing.

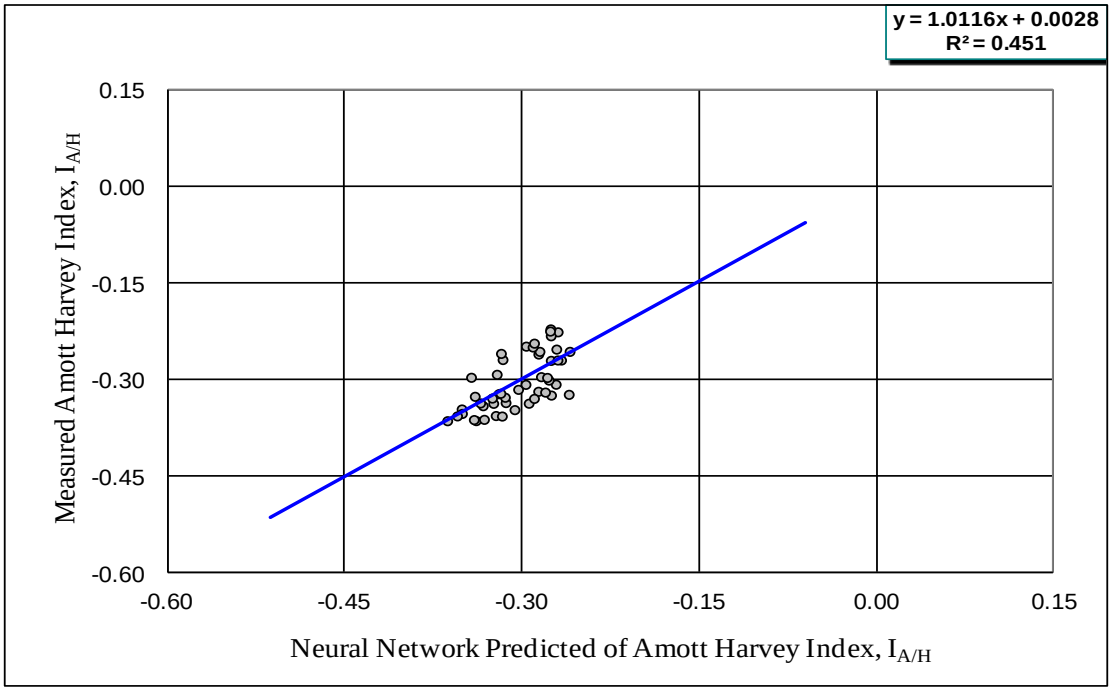

Figure 4.50. Crossplot of <u>test data</u>: measured Amott-Harvey Index ($I_{A/H}$) versus BPNN predicted $I_{A/H}$ in adjacent test well **A-01** for the case 3 predictor trained on the entire cored interval using 6 wireline logs from training well **A-02** at **0.5** ft spacing.

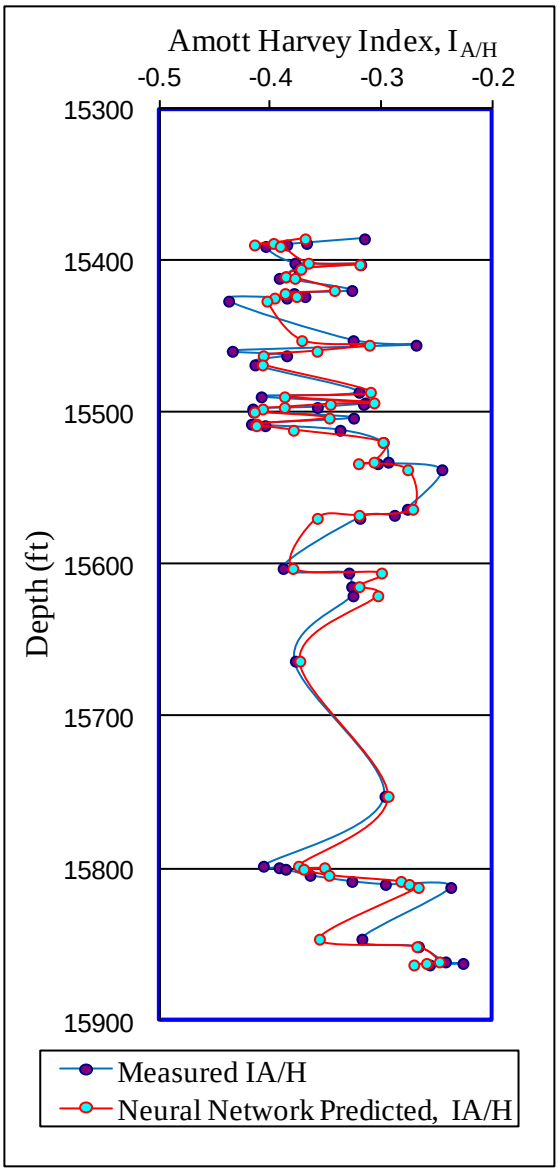

Figure 4.51. Measured $I_{A/H}$ and BPNN predicted $I_{A/H}$ along the depth in the training well **A-02** for case 3 using **6** conventional wireline logs at **0.5** ft spacing.

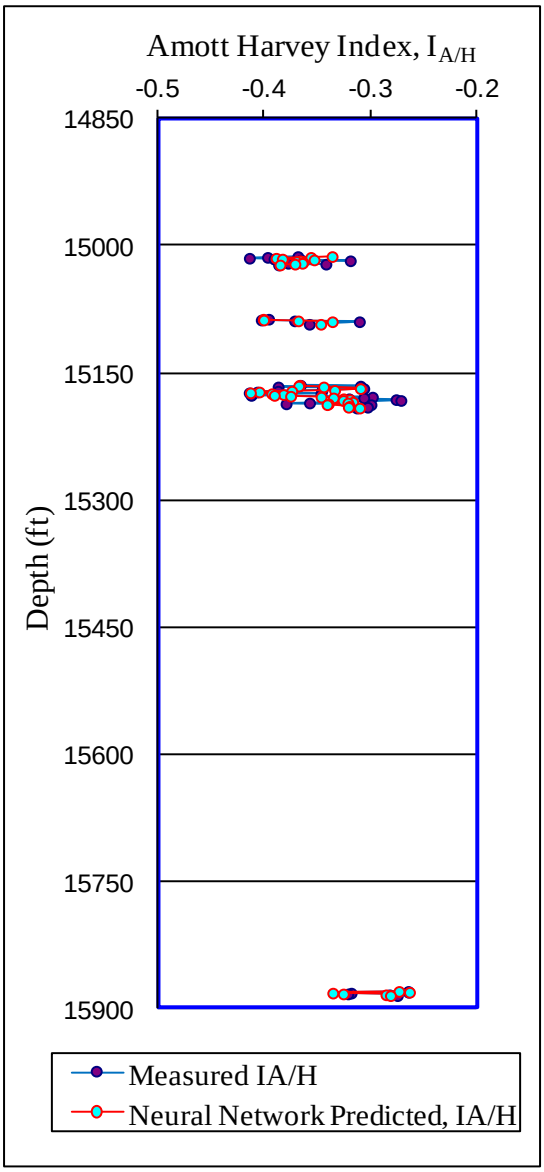

Figure 4.52. Measured $I_{A/H}$ and BPNN predicted $I_{A/H}$ along the depth in adjacent test well **A-01** for the case 3 predictor trained on the entire cored interval from training well **A-02** using **6** wireline logs at **0.5** ft spacing.

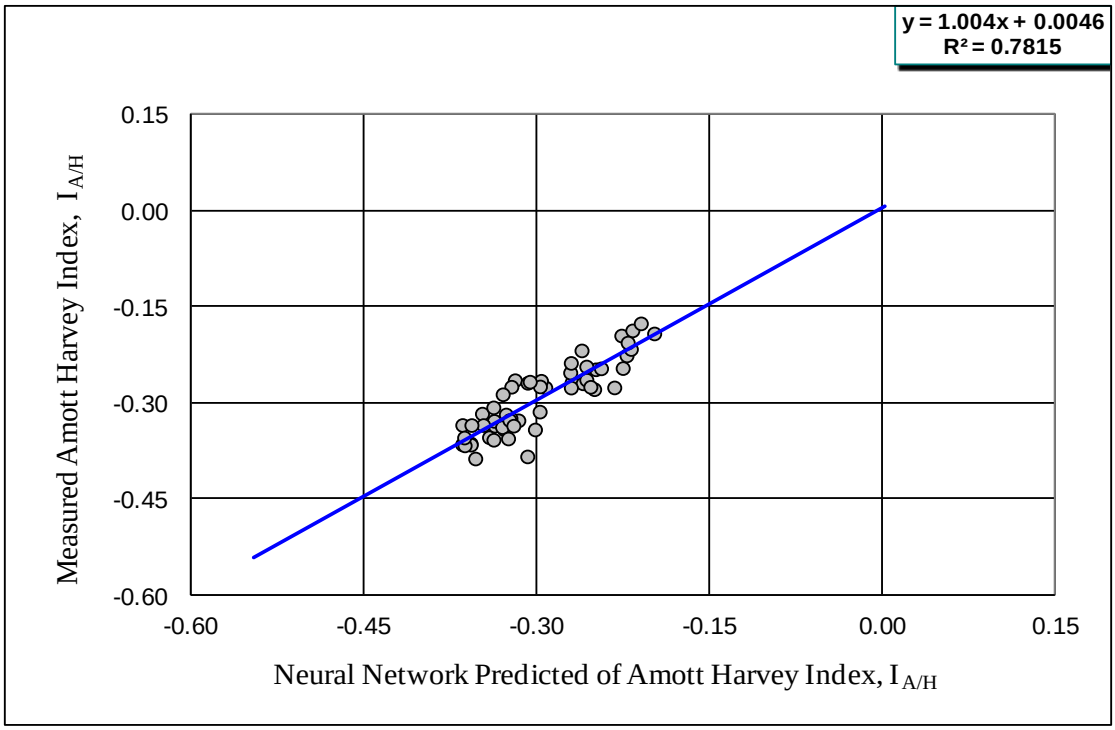

Figure 4.53. Cross plot of <u>training data</u>: measured Amott-Harvey Wettability Index ($I_{A/H}$) versus BPNN predicted ($I_{A/H}$) for the case 3 predictor trained on the entire cored interval using 6 wireline logs for training well **A-02** every **0.5** ft spacing.

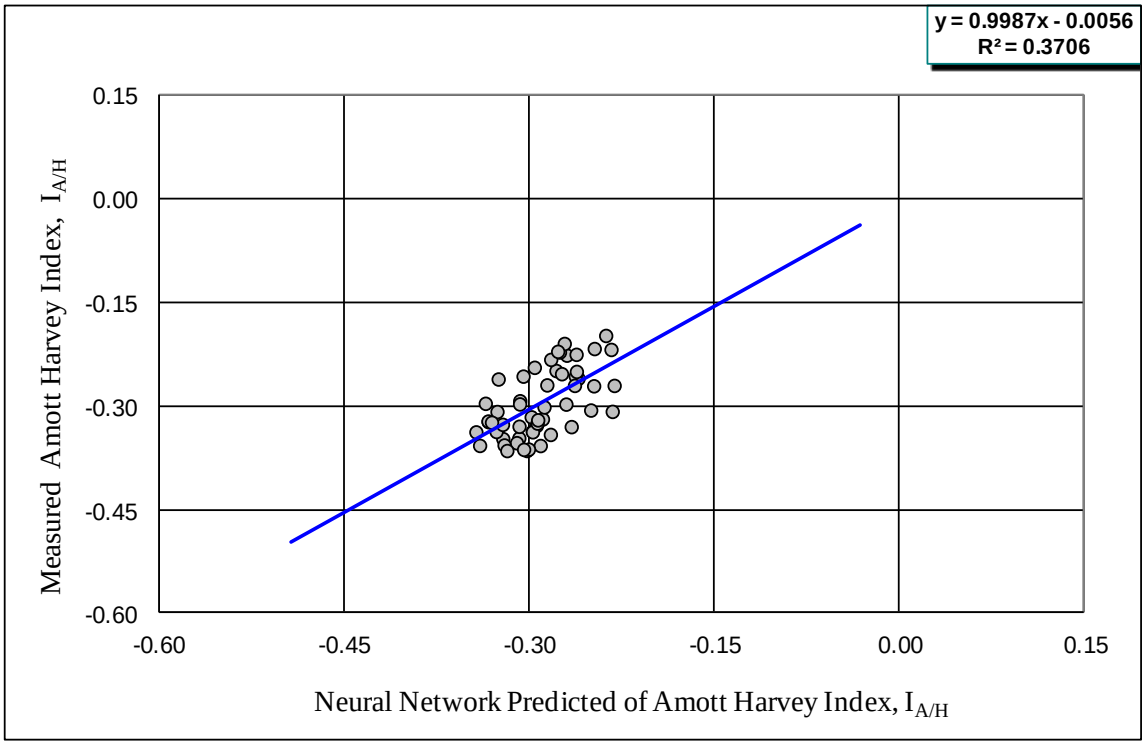

Figure 4.54. Crossplot of <u>test data</u>: measured Amott-Harvey Wettability Index ($I_{A/H}$) versus BPNN predicted $I_{A/H}$ in test well **B-01** in a different oil well for the case 3 predictor trained on the entire cored interval using **6** wireline logs from training well **A-02** at **0.5** ft spacing.

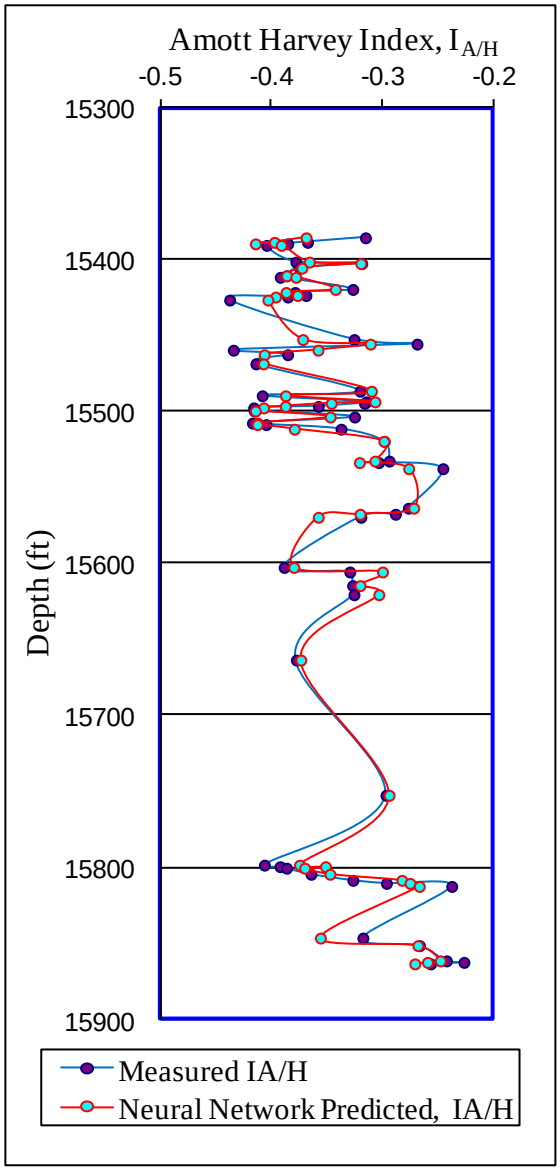

Figure 4.55. Measured $I_{A/H}$ and BPNN predicted $I_{A/H}$ along the depth in the training well **A-02** for case 3 using **6** conventional wireline logs at **0.5** ft spacing.

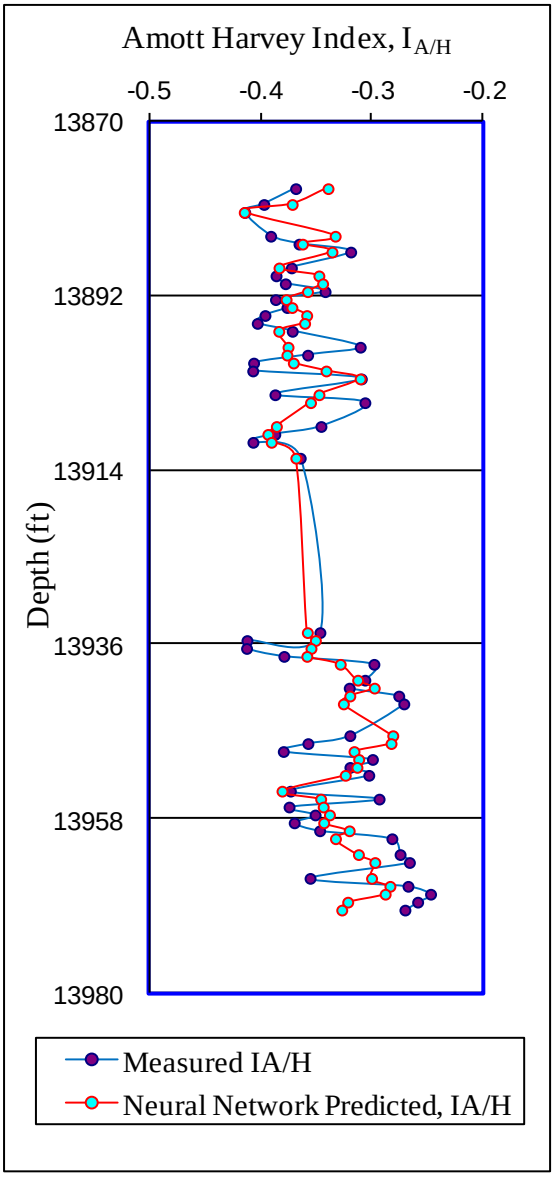

Figure 4.56. Measured $I_{A/H}$ and BPNN predicted $I_{A/H}$ along the depth in test well **B-01** in a different oil field for the case 3 predictor trained on the entire cored interval from training well **A-02** at **0.5** ft spacing.

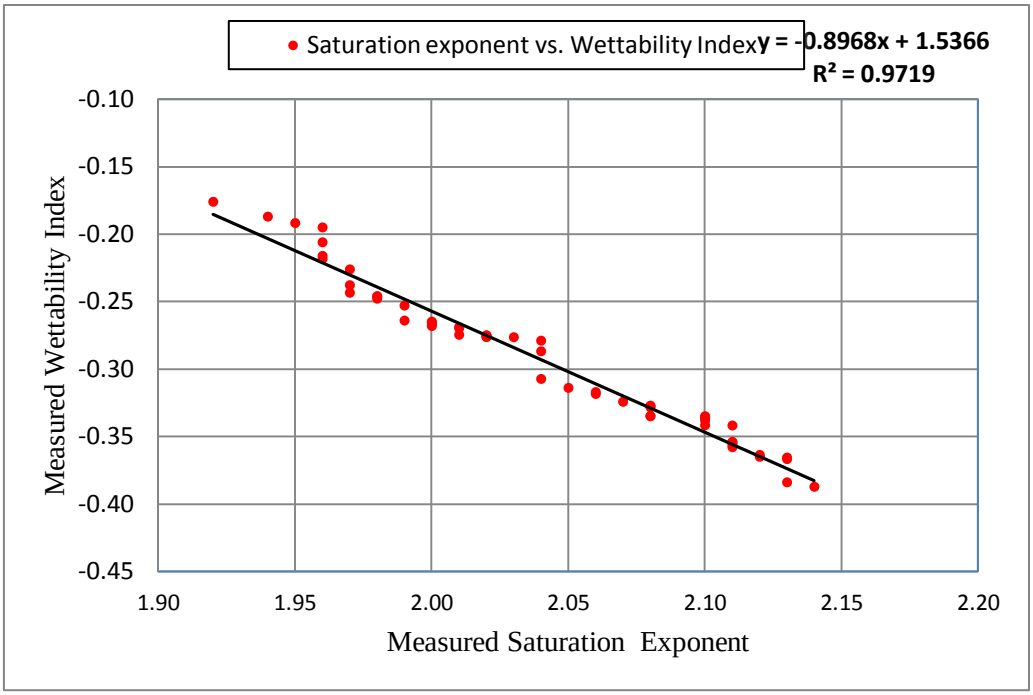

Figure 4.57. Crossplot of measured saturation exponent (n) versus measured Amott-Harvey Wettability Index ($I_{A/H}$) for case 4 for the training well **A-02**.

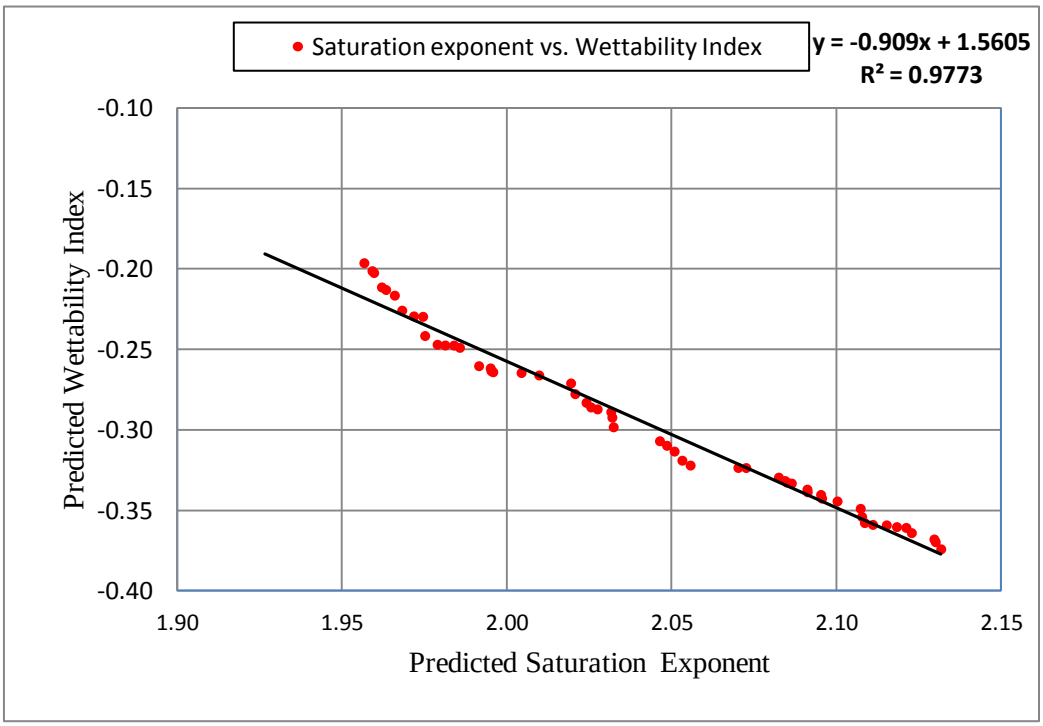

Figure 4.58. Crossplot of predicted saturation exponent (n) versus predicted Amott-Harvey Wettability Index ($I_{A/H}$) for case 4 for the training well **A-02.**

Table 4.26 Summary results of SCAL parameters trained on entire cored interval in the training well **A-02** at **1.0** ft spacing.

Output	**Input(Wireline logs)**			
	Case1 (RHOB, NPHI, ILD,ILM)	Case2 (SGR,CGR, NPHI, ILD, ILM)	Case3 (SGR,CGR, RHOB, NPHI, ILD, ILM)	Case4 SGR,CGR, RHOB, NPHI, ILD, ILM)
	R^2 (Coefficient of determination)			
R_t	0.8232	0.7507	0.8230	0.8320
RI	0.9061	0.8260	0.9070	0.9078
S_w	0.9040	0.8342	0.9056	0.9063
n	0.8535	0.8532	0.8525	0.8529
$I_{A/H}$	0.8739	0.7851	0.8753	0.8777

Table 4.27 Summary results of SCAL parameters (trained on entire cored interval in the well A-02) when tested in adjacent well **A-01** in the same oil field at **0.5** ft spacing.

Output	**Input(Wireline logs)**			
	Case1 (RHOB, NPHI, ILD,ILM	Case2 (SGR,CGR, NPHI, ILD, ILM)	Case3 (SGR,CGR, RHOB, NPHI, ILD, ILM)	Case4 SGR,CGR, RHOB, NPHI, ILD, ILM)
	R^2 (Coefficient of determination)			
R_t	-----	0.4232	0.4340	0.4580
RI	-----	0.5403	0.5875	0.5872
S_w	-----	0.4532	0.5595	0.5530
n	-----	0.2546	0.2436	0.2620
$I_{A/H}$	0.2355	0.3134	0.4510	0.4724

Table 4.28 Summary results of SCAL parameters (trained on entire cored interval in the well A-02) when tested in adjacent well **B-01** in different oil field at **0.5**ft spacing.

Output	**Input(Wireline logs)**			
	Case1 (RHOB, NPHI, ILD,ILM	Case2 (SGR,CGR, NPHI, ILD, ILM)	Case3 (SGR,CGR, RHOB, NPHI, ILD, ILM)	Case4 SGR,CGR, RHOB, NPHI, ILD, ILM)
	R^2 (Coefficient of determination)			
R_t	-----	0.2690	0.3150	0.3430
RI	-----	0.4223	0.3565	0.3589
S_w	-----	0.4320	0.3407	0.3308
n	-----	0.1951	0.2966	0.3825
$I_{A/H}$	0.1387	0.2586	0.3706	0.3740

4.11 Discussion of Results

4.11.1 Training well A-02

Predictors for the SCAL parameters (R_t, RI, Sw, n, and $I_{A/H}$) trained on data at 1.0 ft depth spacing agreed better with the measured data than predictors trained at 0.5 ft depth spacing. Firstly, this might be because the parameter values at 1.0 ft depth spacing represent the real value where the plug is taken, whereas half of the plug values at 0.5 ft spacing are interpolated values. Secondly, the 1.0 ft running data is closer to the vertical interval resolution over which most wireline logs do.

The case 1, 3 and 4 predictors were generally better than the case 2 predictors for most of the SCAL parameters studied. The case 2 predictors did not include a bulk density (RHOB) log input whereas all the other predictors did. Therefore the bulk density log appears to be an important input wireline log for prediction in the Nubian sandstone. The reason for this is not clear at present, but it may be due to natural cements within the sandstone that are picked up by the density log.

Experience with laboratory and field samples has generally established a value of 2 for the saturation exponent of clean water-wet quartz sands. In the training well the experimental results showed that n varies from 1.9 to 2.2 for a water-wet system. The variation may related to the distribution of GHEs in the reservoir, which has a significant control on saturation exponent and the other properties of reservoir rocks.

Figures 4.57 and 4.58 show that the saturation exponent increases linearly as the wettability of the core samples changes from water-wet to more oil-wet conditions. Figures 4.47 and 4.48 show that Amott-Harvey Wettability Index trends to be mixed-wet to water-wet in the lower part of the well. Donaldson and Siddiquie (1989) showed that an oil/water/rock system becomes more water-wet as the temperature (and therefore depth) increases.

4.11.2 Adjacent test well A-01in the same oil field

In the adjacent test well A-01 the SCAL parameters (R_T, RI, Sw, n, and $I_{A/H}$) trained on predictors from data at 0.5 ft depth spacing agreed better with the measured values than predictors trained from data at 1.0 ft depth spacing. The predictions also appeared to be better in the upper part of the well rather than in the lower part. The resistivity values at deeper depths are lower than at shallower depths, and the gamma ray is higher in the lower part. Also, with increasing water saturation with depth, the oil saturation decreases, and this matched with the measured values and neural network predicted values slightly better in the upper part than the lower part.

The predicted values of the Amott-Harvey Wettability Index ($I_{A/H}$) at deeper depths are higher than at shallower depths. With increasing depth the wettability tends to be water-wet near the oil-water contact. Our results matched those of Jerauld and Rathmell (1997). Jerauld and Rathmell (1997) documented the wettability of the Burdhoe Bay reservoir as a function of depth. Core samples were collected at different depths and their wettability was determined using the Amott test. A plot of the Amott indices of the cores versus their subsequent depths revealed the existence of water-wet rocks near the oil-water contact (down structure), and mixed-wet rocks near the oil-water contact (up structure). However, the samples taken at various depths above the oil-water contact clearly indicate progressively more oil-wet behaviour with height into the oil column. Figure 4.43 showed that the measured and predicted values of the saturation exponent (n), obtained from the slope of the relation between resistivity index and water saturation for test well A-01, were very similar. The values of n in Figure 5.44 show the wettability in this well is water-wet.

4. 11.3 Test well B-01 in a different oil field

In the test well B-01 the SCAL parameters (R_T, RI, Sw, n, and $I_{A/H}$) trained on predictors from data at 0.5 ft depth spacing agreed better with the measured values than predictors trained from data at 1.0 ft depth spacing. All the coefficients of determination (R^2) between measured and predicted values are relatively low compared to those in the training well. As mentioned before the coefficient of determination (R^2) values may not necessarily fully

reflect the true performance of the predictors. When the measured and predicted values of the SCAL parameters were plotted the slope of the regression line was equal or close to 1.0, and the points were well distributed around this line. This suggests that the performance of the predictors is still reasonably good. The relatively low R^2 values may merely be due to the measured core plug dataset being inadequate to validate the predictions. Also, the plots of the predictions with depth show that most of the predicted values gave comparable profiles to the measured values. Furthermore, Figure 4.45 showed that the measured and predicted values of the saturation exponent (n), obtained from the slope of the relation between resistivity index and water saturation for test well B-01, were very similar. The value of n also showed that the wettability in this well is water-wet. The Amott-Harvey Wettability Index tended to be mixed-wet to water–wet in the lower part of the well.

4.12 Conclusions

1. Several good neural network SCAL parameter predictors (for R_t, RI, water saturation, saturation exponent and Amott-Harvey Wettability Index) were generated using different combinations of standard wireline logs in the training well A-02. The best predictors were produced using the dataset from the entire 478 ft cored interval of the training well and all 7 available wireline logs.

2. Predictors that included the bulk density wireline log (cases 1, 3 and 4) in these Nubian Sandstone reservoirs generated potentially better predictors according to the training well data. This was subsequently proved by predictions in an adjacent test well and a further test well in a different oil field.

3. Predictors trained on data at 1.0 ft depth spacing appeared to be better in the training well. However, the prediction of resistivity parameters, water saturation, saturation exponent, and Amott-Harvey Wettability Index in an adjacent test well A-01 and a further test well B-01 in a different oil field gave slightly better results in general for predictors trained on data at 0.5ft depth spacing rather than at 1.0 ft depth spacing.

4. In a number of cases the coefficients of determination (R^2) between measured and predicted values were relatively low compared to those in the training well. However, the

R^2 values may not necessarily fully reflect the true performance of the predictors. When the measured and predicted values of the SCAL parameters were crossplotted the slope of the regression line was equal or close to 1.0, and the points were well distributed around the line suggesting that the predictors were still reasonably good. Also, the plots of the predictions along the depth show that most of the predicted values gave comparable profiles to the measured values.

5. Furthermore, plots of the water saturation versus resistivity index gave straight line results on a log-log crossplot, the slope of the line giving the saturation exponent (n). The predicted values of n matched the measured values extremely well in each of the test wells A-01 and B-01.

6. A linear relationship existed between wettability index and the saturation exponent for data in the training well A-02.

CHAPTER FIVE

Prediction of SCAL Parameters Using a Genetically Focused Neural Network (GFNN) Approach

5.1 Introduction

In Chapter 4 neural network SCAL parameter predictors were developed for the Nubian Sandstone Formation in the Sirt Basin in Fields A and B. In this chapter the same SCAL parameters are predicted using a different set of predictors. The main difference is that instead of using data from the whole interval to train the neural network, as in Chapter 4, a small representative training dataset is now used. This is a novel approach, which has been developed relatively recently (Potter et al., 2003) and termed Genetically Focused Neural Networks (GFNN). The advantages of this approach are that minimal representative core measurements are needed (saving time and expense), and computer processing time is also reduced. Most previous studies used much larger datasets. For instance, Zhang et al. (2000) used 143 core plug values and Bhatt and Helle (2001) used 185. However, Potter et al. (2003) demonstrated that 24 plugs from one representative genetic unit (RGU) were able to give excellent permeability predictions. Moreover, they also demonstrated that just 5 representative plugs (one plug from each GHE) also gave results of a comparable performance.

5.2 Genetic Petrophysics and Genetically Focused Neural Networks

The concept of Genetic Petrophysics was proposed by Corbett et al. (1998). They recognised that there are representative elements within reservoirs (genetic units) that may repeat several times (for example, shoreface coarsening upwards parasequences). These repeating units can be exploited for prediction purposes. By studying one of the representative genetic units (RGUs) in detail, the properties of the others in the rest of the well or in adjacent wells can be predicted. Le and Potter (2003) and Potter et al. (2003)

subsequently used this idea to train Genetically Focused Neural Nets (GFNNs) to predict permeability and other important petrophysical parameters. This involved training the neural net predictors merely on data from a short RGU instead of data from a larger interval. They showed that the GFNN predictors performed almost as well as predictors trained on the entire cored interval of a well.

The obvious advantage of the GFNN approach is that it provides a very cost effective (in terms of minimal core measurements and computer processing time) and rapid way of making predictions. A small RGU is first selected from the available wireline logs (Figure 5.1). This RGU is selected on the basis of geological criteria and representative of other units in the well and other wells in the same field. This RGU is then studied in detail and provides the training datasets for the GFNN predictors in other intervals and wells. Le and Potter (2003) have also used this approach to predict permeability from wireline logs using a back propagation algorithm in some North Sea reservoirs.

The present study applies the GFNN approach for the first time to the North African oil fields, and also for the first time uses this technique to predict some SCAL parameters such as true resistivity, resistivity index, saturation exponent, and Amott-Harvey Wettability Index. In this chapter the objective was to exploit the GFNN approach in conjunction with the genetic petrophysics approach for predicting the above parameters from wireline logs. In other words, the aim was to train neural networks only on data ideally from one RGU and then to predict SCAL parameters in other intervals.

5.3 Genetically Focused Neural Network Resistivity (R_t, RI) Prediction

The studied area was the same oil field in the Sirt Basin-Libya as that for Chapter 4. The conventional wireline logs and core data from 3 wells, A-02, well A-01, and well B-01, were available for this study. As before well A-02 was taken as the training well. The aim of the initial study was to develop a fast, reliable, and cost-effective reservoir SCAL predictor for these wells. One of the most important issues in neural net SCAL prediction has been the amount of core training data that is needed to produce a good and reliable

predictor. The aim of the GFNN approach was to produce a reliable predictor based on a small but representative training interval, an RGU.

5.3.1 Identification and description of the Representative Genetic Unit of well A-02

Shoreface reservoirs are characterized by coarsening up sequences of fine to medium grained sandstone. Single coarsening up parasequences are often easily recognizable within stacked shoreface sequences. These elements are the fundamental building blocks (representative genetic units) of such reservoirs. These geological criteria were identified in Nubian Sandstone oil fields.

(Corbett et al., 2001) provide a short review of the geological, petrophysical and statistical issues involved. The parasequence comprises lower middle and upper shoreface sandstones. Therefore, a parasequence was assigned as representative element (RGU) for the reservoir in this type of depositional environment. Figure 5.1 shows a schematic diagram indicating the essential elements prediction based on RGU. The measured RGU provides data that is used to train a genetically focused neural net (GFNN), which then used to predict a variety of properties in the other RGUs throughout the rest of the well and adjacent wells in the same oil field. There are several reasons for advocating this approach:

- The RGU sampled is selected on the basis of geological criteria mentioned earlier.
- The RGU is representative of the other units in the well, and adjacent wells in the same oil field.
- It is very cost effective in terms of core acquisition, core measurement and data processing.

An RGU of about 73 feet was identified in well A-02 from conventional wireline logs. The gamma ray log generally picked out the genetic unit boundaries and coarsening upwards sequences. This RGU and other similar genetic units in the same well A-02can be identified from the available wireline logs (Figure 5.2). This RGU charecterised by coarsening up muddy sand interval ranging in permeability from 2 mD to 772 mD and with average porosity of 11% , average water saturation of 25%. The RGU is mainly sandstone, brownish gray to light gray and greenish gray in colour, fine to medium to coarse grained.

The medium to coarse grained sandstone contains scattered granules and pebbles, moderately to well sorted. This RGU includes 14 core plugs. The different GHEs represented by all 14 core plugs in the RGU are shown in Figure 5.3.

5.3.2 Neural Network Training Datasets

The neural network processes were again carried out using commercially available neural network software called Java **NNS** version 1.1 with a back-propagation algorithm. The available database from training well A-02 that was used for the neural networks consisted of the wireline log and core data used in Chapter 4. The wireline log and core data was initially screened and the depth shifts were all applied before training the neural networks. To assess the performance of the GFNN approach, two main datasets were used to train the neural net predictors as follows:

- The first training dataset consisted of the wireline logs and core plug SCAL data (such as resistivity, water saturation, saturation exponent and wettability) within the entire cored interval of well A-02. This meant that 55 values of each wireline log and core plug SCAL were used. These predictors were called **entire core dataset predictors**. These were the predictors from Chapter 4.

- The second training dataset consisted of the wireline logs and horizontal core plug SCAL data only within the short 14 ft RGU of well A-02. In this case, only 14 values of each wireline log and SCAL core plug parameter were used. These predictors were called **GFNN predictors**.

For each of these two training datasets, the neural networks were trained with various combinations of the wireline logs as input, and the output was the SCAL parameter (R_t, RI, S_w, n and $I_{A/H}$). The data was normalised in a similar way to that described in Chapter 4 (section 4.3.2). The maximum and minimum values of each wireline log or core parameter are as given in Chapter 4.

5.4 Results of GFNN Prediction of R_t and RI

5.4.1 Results of GFNN predictors in training well A-02

Tables 5.1 and 5.2 summarise the various neural network true resistivity (R_t) and resistivity index (RI) predictors trained respectively from the entire cored interval dataset (55 training data points) and the GFNN predictors from the RGU dataset (14 training data points) at 1.0 ft spacing for all cases. The tables give details of which wireline logs were used as input, and also show the performance in terms of the coefficient of determination (R^2) between the measured and predicted values throughout the training well A-02 at 1.0 ft spacing.

The neural network predictors trained on the large dataset comprising the entire cored interval gave good results in terms of the R^2 values. Figures 5.4 and 5.6 show the measured and predicted true resistivity and resistivity index respectively along the depth for case 4 using all 7 conventional wireline logs as input at 1.0 ft spacing.

Significantly, the GFNN predictors trained from the RGU dataset gave comparable (generally slightly better) results for the R^2 values. Figures 5.5 and 5.7 show the predicted and measured true resistivity and resistivity index values along the depth for case 4 using all 7 conventional wireline logs as input at 1.0 ft spacing.

5.4.2 Results in adjacent test well A-01

After the training process in well A-02, the GFNN predictors were tested in the cored interval of adjacent well A-01 in the same oil field. Crossplots of measured versus predicted true resistivity (R_t) and resistivity index (RI) were drawn to obtain the linear regression coefficients of determination (R^2). Tables 5.3 and 5.4 summarise the performance of the R_t and RI predictors trained from the entire cored interval dataset and compare them with the GFNN predictors from the RGU dataset. All these predictors were trained at 0.5 ft spacing. The GFNN predictors gave better values of R^2 in almost every case than the equivalent predictors trained on the entire core dataset. Figures 5.8 and 5.10 show the results of measured and predicted R_t and RI along the depth in well A-01 using the case 3 predictor using 6 conventional wireline logs and trained on the entire cored

interval from well A-02 at 0.5 ft spacing. Figures 5.9 and 5.11 show the equivalent results using the GFNN predictor trained on the RGU dataset.

5.4.3 Results in test well B-01

Tables 5.5 and 5.6 summarise the performance of various neural network Rt and RI predictors trained from the entire cored interval dataset and the GFNN predictors trained from the RGU dataset. These predictors were trained at 0.5 ft spacing. The GFNN predictors again gave significantly better values of R^2 than the predictors trained on the entire core dataset. Figures 5.12 and 5.14 show the results of measured and predicted R_t and RI along the depth in well B-01 for case 4 predictor using 7 conventional wireline logs and trained on the entire cored interval from well A-02 at 0.5 ft spacing. Figures 5.13 and 5.15 show the equivalent results using the GFNN predictor trained on the RGU dataset.

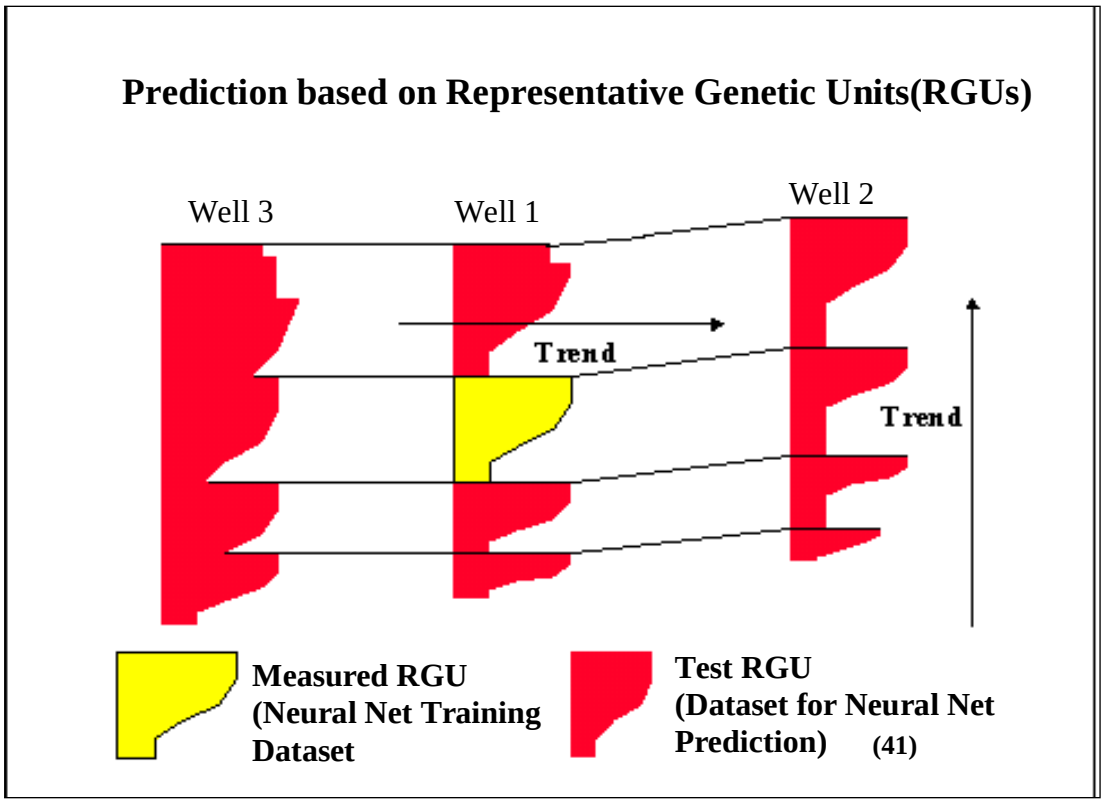

Figure 5.1. Schematic of coarsening upwards shoreface representative genetic units (RGU) in a shoreface environment (from Potter et al., 2003).

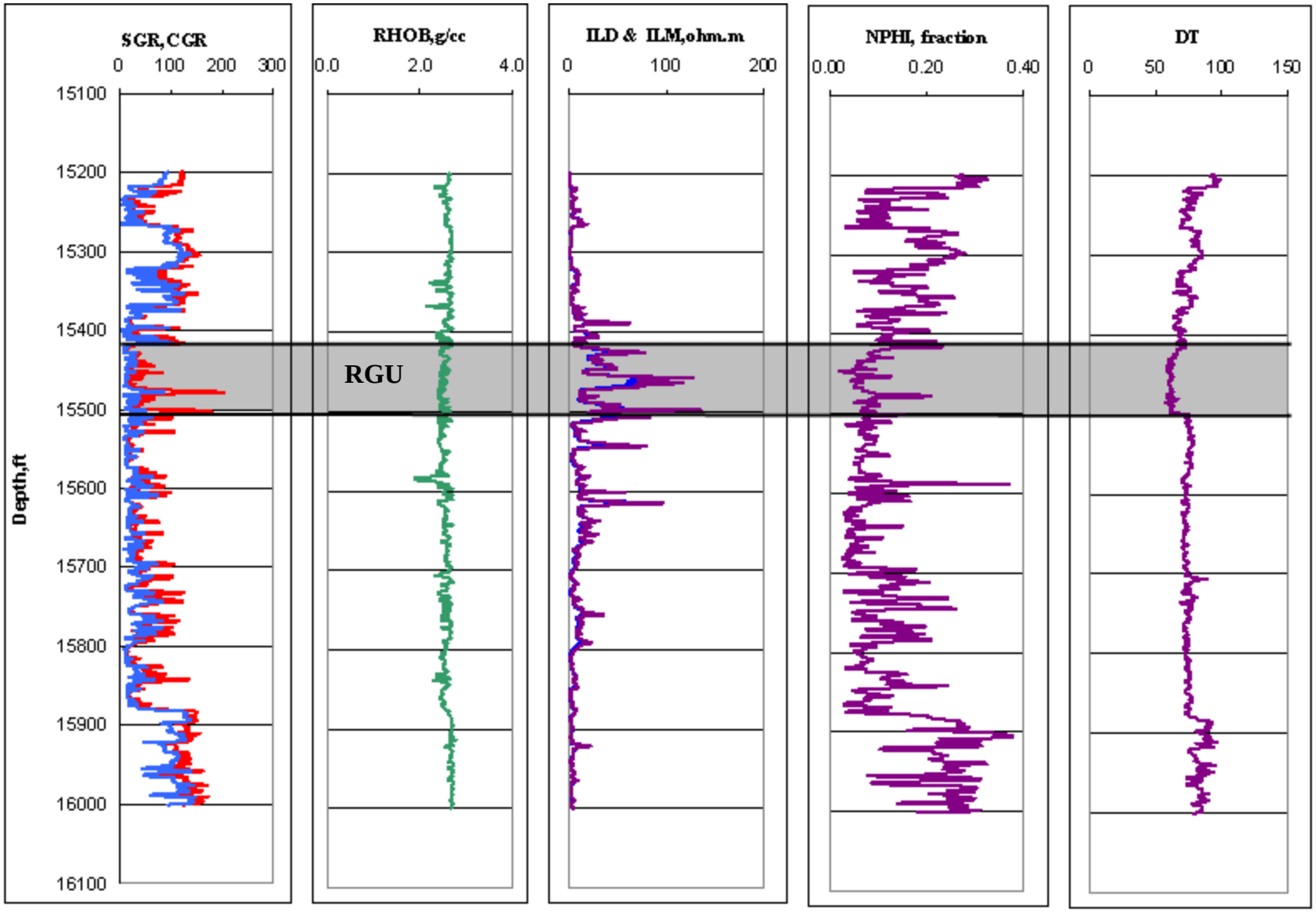

Figure 5.2. Conventional wireline logs for training well A-02. The shaded zone is the selected RGU used for training the GFNN predictors.

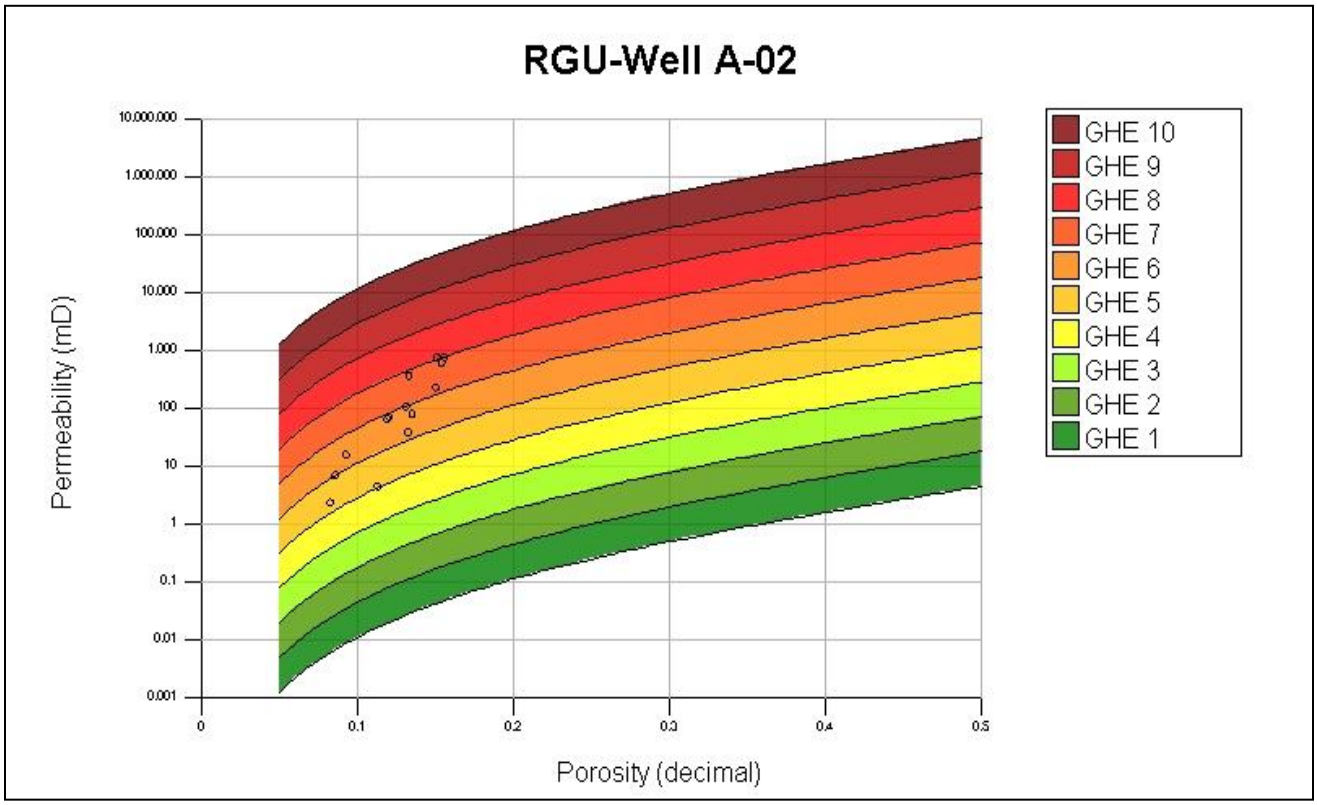

Figure 5.3. The 14 RGU plugs from well A-02 plotted on the Global Hydraulic Element (GHE) template.

Table 5.1. Summary of the performance in training well **A-02** of the R_t predictors trained from the entire core dataset and the GFNN predictors trained from the RGU dataset at **1.0** ft spacing.

Input Wireline logs	**Output**	**Coefficient of determination (R^2) for the predictors trained on the entire core dataset when tested throughout the cored interval**	**Coefficient of determination (R^2) for the GFNN predictors trained on the RGU dataset when tested throughout the cored interval**
Case 1 (RHOB,NPHI,ILD &ILM)	R_t	0.8232	0.8423
Case 2 (SGR,CGR,NPHI,ILD &ILM)	R_t	0.7507	0.7724
Case 3 (SGR,CGR,RHOB,NPHI,ILD &ILM)	R_t	0.8230	0.8724
Case 4 (SGR,CGR,RHOB,NPHI,ILD, ILM, & DT)	R_t	0.8320	0.8910

Table 5.2. Summary of the performance in training well **A-02** of the RI predictors trained from the entire core dataset and the GFNN predictors trained from the RGU dataset at **1.0** ft spacing.

Input Wireline logs	**Output**	**Coefficient of determination (R^2) for the predictors trained on the entire core dataset when tested throughout the cored interval**	**Coefficient of determination (R^2) for the GFNN predictors trained on the RGU dataset when tested throughout the cored interval**
Case 1 (RHOB,NPHI,ILD &ILM)	RI	0.9061	0.9163
Case 2 (SGR,CGR,NPHI,ILD &ILM)	RI	0.8260	0.8422
Case 3 (SGR,CGR,RHOB,NPHI,ILD &ILM)	RI	0.9070	0.9124
Case 4 (SGR,CGR,RHOB,NPHI,ILD , ILM, & DT)	RI	0.9078	0.9320

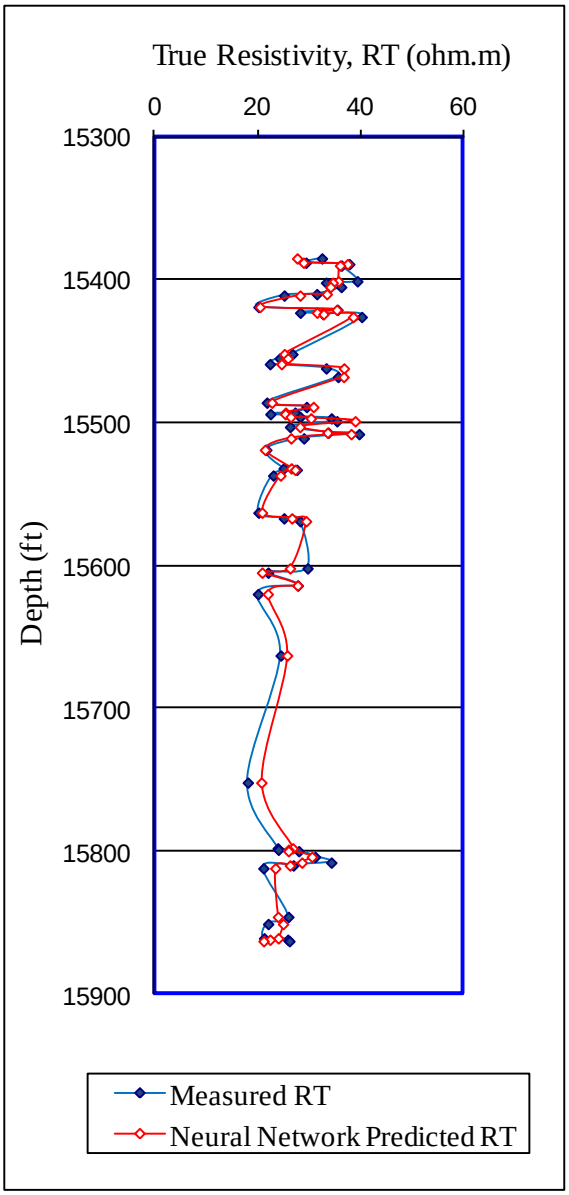

Figure 5.4. Measured and predicted true resistivity in the training well **A-02** for the predictor trained on the entire core dataset using 7 conventional wireline logs (case 4) at 1.0 ft spacing.

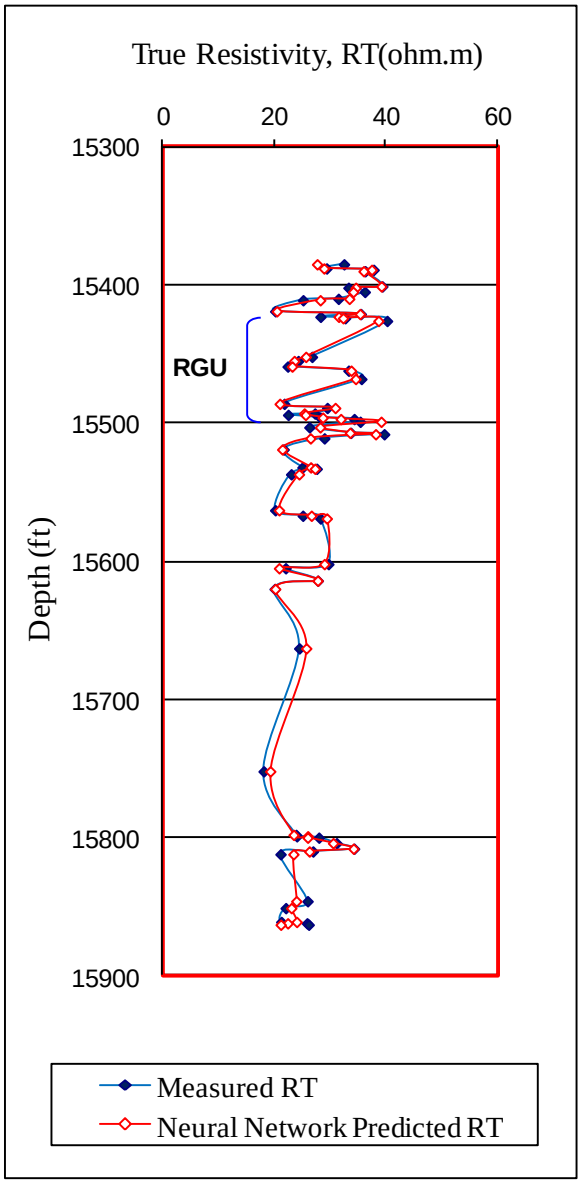

Figure 5.5. Measured and predicted true resistivity in training well **A-02** for the GFNN predictor trained on the **RGU** dataset using 7 conventional wireline logs (case 4) at 1.0 ft spacing.

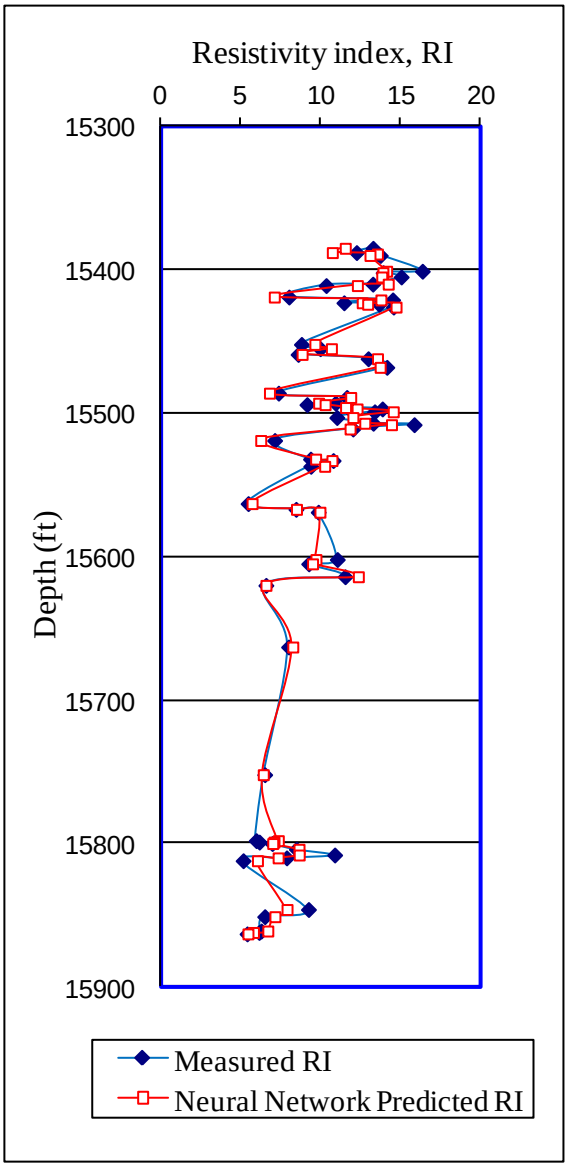

Figure 5.6. Measured and predicted resistivity index in the training well **A-02** for the predictor trained on the entire core dataset using **7** conventional wireline logs (case 4) at 1.0 ft spacing.

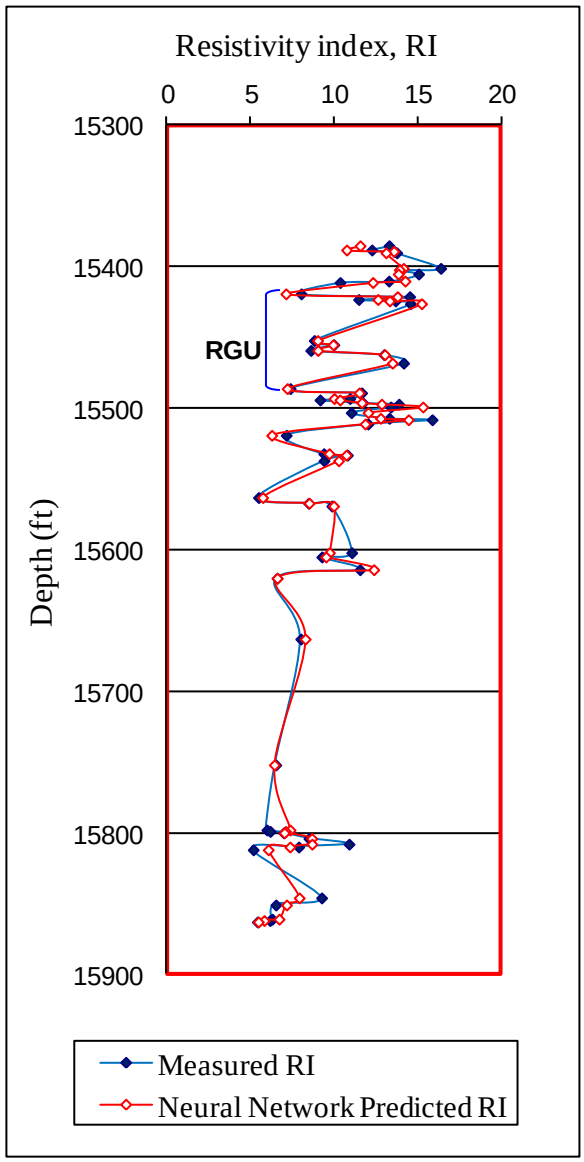

Figure 5.7. Measured and predicted resistivity index in the training well **A-02** for the GFNN predictor trained on the **RGU** dataset using **7** conventional wireline logs (case 4) at 1.0 ft spacing.

Table 5.3. Summary of the performance in adjacent well **A-01** of the R_t predictors trained from the entire core dataset and the GFNN predictors trained from the RGU dataset at **0.5** ft spacing.

Input Wireline logs	**Output**	**Coefficient of determination (R^2) for the predictors trained on the entire core dataset when tested throughout the cored interval of well A-01**	**Coefficient of determination (R^2) for the GFNN predictors trained on the RGU dataset when tested throughout the cored interval of well A-01**
Case 2 (SGR,CGR,NPHI,ILD &ILM)	R_t	0.4232	0.4842
Case 3 (SGR,CGR,RHOB,NPHI,ILD &ILM)	R_t	0.4340	0.4999
Case 4 (SGR,CGR,RHOB,NPHI,ILD , ILM, & DT)	R_t	0.4580	0.5407

Table 5.4. Summary of the performance in adjacent well **A-01** of the RI predictors trained from the entire core dataset and the GFNN predictors trained from the RGU dataset at **0.5** ft spacing.

Input Wireline logs	**Output**	**Coefficient of determination (R^2) for the predictors trained on the entire core dataset when tested throughout the cored interval of well A-01**	**Coefficient of determination (R^2) for the GFNN predictors trained on the RGU dataset when tested throughout the cored interval of well A-01**
Case 2 (SGR,CGR,NPHI,ILD &ILM)	RI	0.5403	0.5247
Case 3 (SGR,CGR,RHOB,NPHI,ILD &ILM)	RI	0.5875	0.6121
Case 4 (SGR,CGR,RHOB,NPHI,ILD , ILM, & DT)	RI	0.5872	0.6119

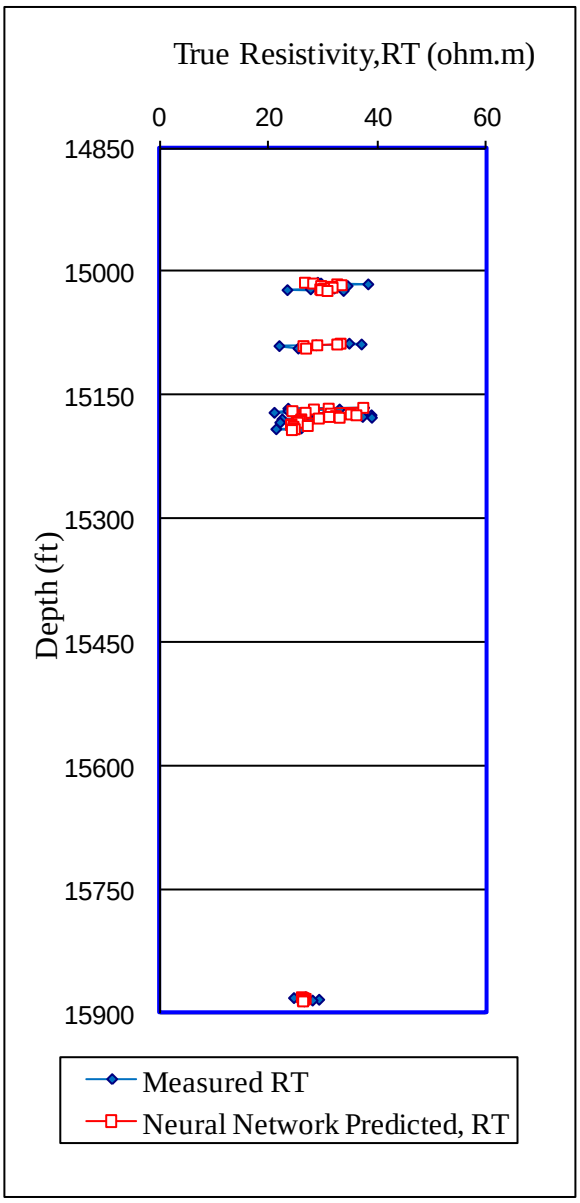

Figure 5.8. Measured and predicted true resistivity in adjacent well **A-01** for the predictor trained on the entire core dataset using 6 conventional wireline logs (case 3) from well **A-02** at 0.5 ft spacing.

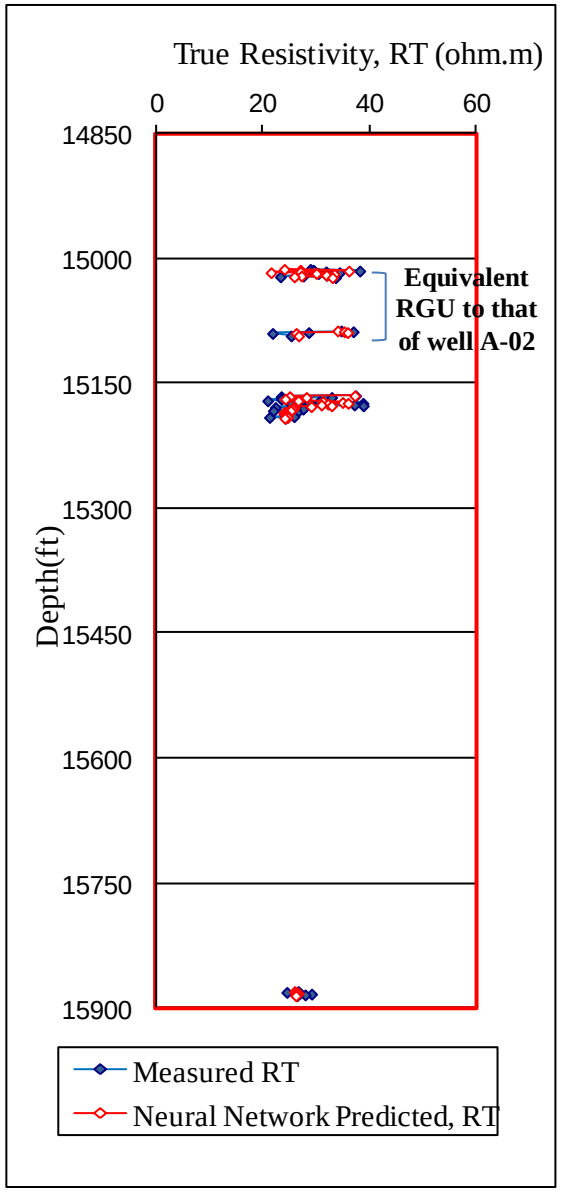

Figure 5.9. Measured and predicted true resistivity in adjacent well **A-01** for the GFNN predictor trained on the **RGU** dataset using **6** conventional wireline logs (case 3) from well **A-02** at 0.5 ft spacing.

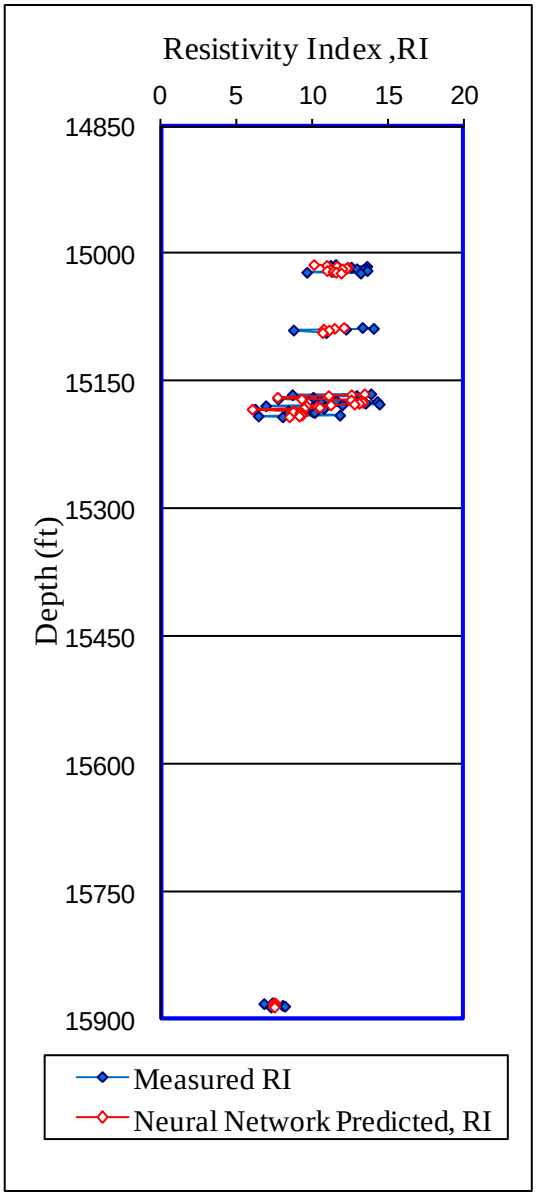

Figure 5.10. Measured and predicted resistivity index in adjacent well **A-01** for the predictor trained on the entire core dataset using **6** conventional wireline logs (case 3) from well **A-02** at 0.5 ft spacing.

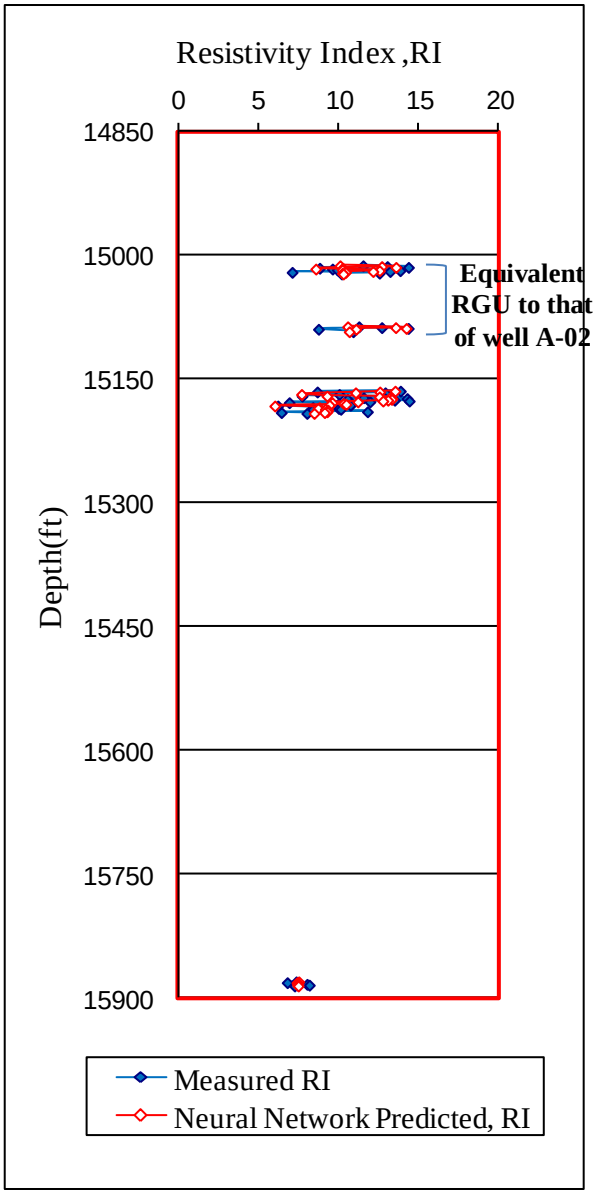

Figure 5.11. Measured and predicted resistivity index in adjacent well **A-01** for the GFNN predictor trained on the **RGU** dataset using **6** conventional wireline logs (case 3) from well **A-02** at 0.5 ft spacing.

Table 5.5. Summary of the performance in test well **B-01** of the R_t predictors trained from the entire core dataset and the GFNN predictors trained from the RGU dataset at **0.5** ft spacing.

Input Wireline logs	**Output**	**Coefficient of determination (R^2) for the predictors trained on the entire core dataset when tested throughout the cored interval of well B-01**	**Coefficient of determination (R^2) for the GFNN predictors trained on the RGU dataset when tested throughout the cored interval of well B-01**
Case 2 (SGR,CGR,NPHI,ILD &ILM)	R_t	0.269	0.4916
Case 3 (SGR,CGR,RHOB,NPHI,ILD &ILM)	R_t	0.315	0.5823
Case 4 (SGR,CGR,RHOB,NPHI,ILD , ILM, & DT)	R_t	0.343	0.5497

Table 5.6. Summary of the performance in test well **B-01** of the RI predictors trained from the entire core dataset and the GFNN predictors trained from the RGU dataset at **0.5** ft spacing.

Input Wireline logs	**Output**	**Coefficient of determination (R^2) for the predictors trained on the entire core dataset when tested throughout the cored interval**	**Coefficient of determination (R^2) for the GFNN predictors trained on the RGU dataset when tested throughout the cored interval**
Case 2 (SGR,CGR,NPHI,ILD &ILM)	RI	0.4223	0.5320
Case 3 (SGR,CGR,RHOB,NPHI,ILD &ILM)	RI	0.3565	0.5423
Case 4 (SGR,CGR,RHOB,NPHI,ILD , ILM, & DT)	RI	0.3589	0.6191

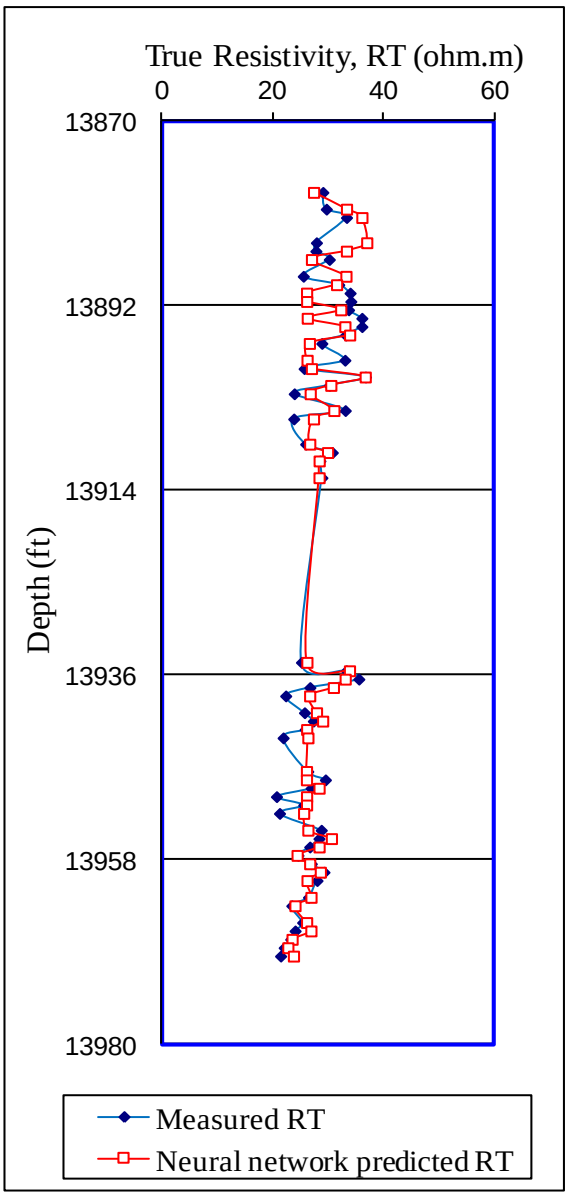

Figure 5.12. Measured and predicted true resistivity in test well **B-01** for the predictor trained on the entire core dataset using **7** conventional wireline logs (case 4) from well **A-02** at 0.5 ft spacing.

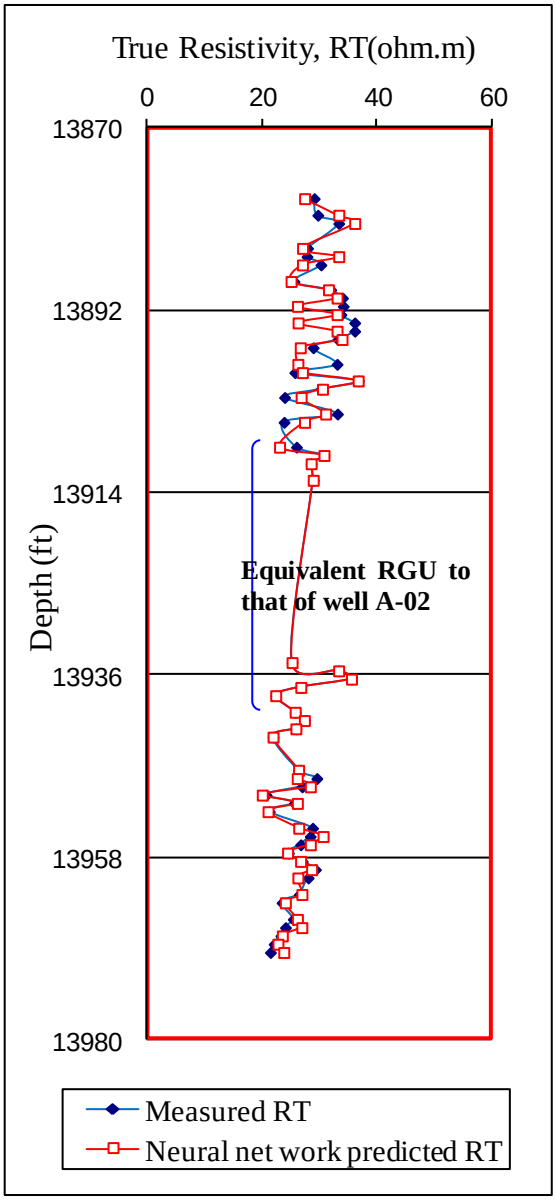

Figure 5.13. Measured and predicted true resistivity in test well **B-01** for the GFNN predictor trained on the **RGU** dataset using **7** conventional wireline logs (case 4) from well **A-02** at 0.5 ft spacing.

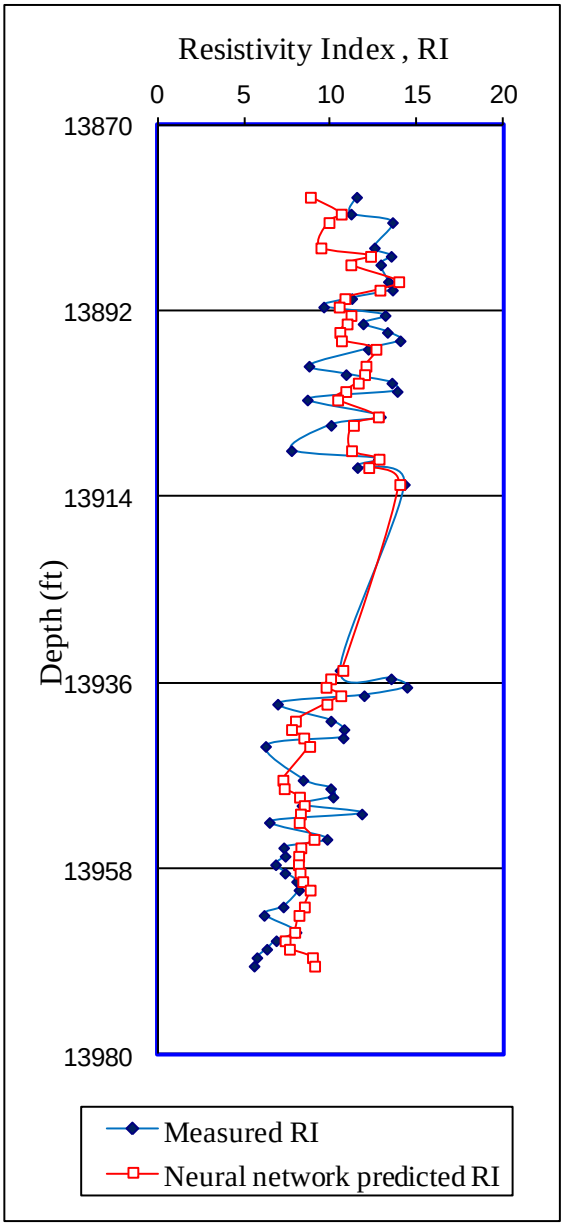

Figure 5.14. Measured and predicted resistivity index in test well **B-01** for the predictor trained on the entire core dataset using **7** conventional wireline logs (case 4) from well **A-02** at 0.5 ft spacing.

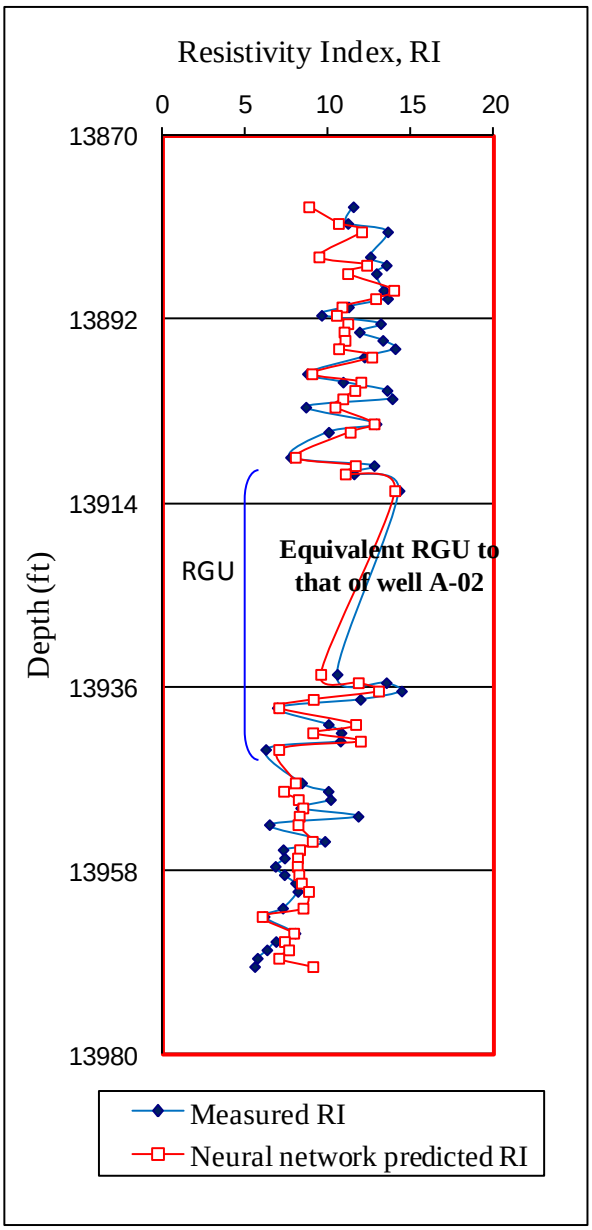

Figure 5.15. Measured and predicted resistivity index in test well **B-01** for the GFNN predictor trained on RGU dataset using **7** conventional wireline logs (case 4) from well **A-02** at 0.5 ft spacing.

5.5 Genetically Focused Neural Network (GFNN) Prediction of Water Saturation (S_w) and Saturation Exponent (n)

Helle and Bhatt (2002) established a neural network predictor for fluid saturation using wireline logs without relying on the functions that explicitly depend on porosity and auxiliary parameters derived from the laboratory. Azizi (2003) and Azizi and Potter (2004) trained GFNN water saturation predictors using residual water saturation from core plug laboratory measurements in the chosen RGU interval to predict the residual S_w in the rest of the training well and in other wells in the same field by neural networks with a standard back propagation algorithm. Following this case study Al Towijri (2004) trained GFNNs to predict residual three phase saturations (water, oil and gas). Goda et al. (2005) have also used neural networks to predict irreducible water saturation using data from a number of onshore and offshore Australian hydrocarbon basins. The present study further develops GFNN water saturation predictors for two fields in North Africa.

5.6 Results of GFNN Prediction of S_w and n

5.6.1 Results of GFNN predictors in training well A-02

Tables 5.7 and 5.8 summarise the performance of the various neural network water saturation (S_w) and saturation exponent (n) predictors trained from the entire cored interval dataset (55 training data points) and the GFNN predictors from the RGU dataset (14 training data points) at 1.0 ft spacing. The coefficient of determination (R^2) between the measured and predicted values throughout the training well A-02 show that the GFNN predictors give comparable results to the predictors trained on the entire core dataset. The GFNN predictors give slightly better R^2 values in all cases, particularly for the saturation exponent (Table 5.8).

Figures 5.16 and 5.18 show the measured and predicted water saturation and saturation exponent respectively along the depth for the case 3 predictor using 6 conventional wireline logs trained on the entire core dataset at 1.0 ft spacing. Figures 5.17 and 5.19 show that the equivalent GFNN predictor gives very similar results.

5.6.2 Results in adjacent test well A-01

After the training process in well A-02, the GFNN predictors were tested in the cored interval of adjacent well A-01 in the same oil field. Crossplots of measured versus predicted S_w and n were drawn to obtain the linear regression coefficients of determination (R^2). Tables 5.9 and 5.10 summarise the performance of the S_w and n predictors trained from the entire cored interval dataset and compared with the GFNN predictors from the RGU dataset. All these predictors were trained at 0.5 ft spacing. The GFNN predictors gave better values of R^2 in almost every case than the equivalent predictors trained on the entire core dataset. Figures 5.20 and 5.22 show the results of the measured and predicted S_w and n values along the depth using the case 3 predictor trained on the all entire cored interval, while Figures 5.21 and 5.23 show the results using the equivalent GFNN predictor trained on the RGU dataset.

5.6.3 Results in test well B-01

The case 3 GFNN predictor trained using 6 wireline logs was also tested in test well B-01 in a different oil field. Tables 5.11 and 5.12 summarise the various neural network water saturation and saturation exponent predictors trained from the entire cored interval dataset and the GFNN predictors trained from the RGU dataset at 0.5 ft spacing. In well B-01 the GFNN predictors give significantly better R^2 values than the predictors trained on the entire cored interval from the training well. Figures 5.24 and 5.26 show the results of measured and predicted S_w and n values along the depth in test well B-01 using the case 3 predictor trained on the all entire cored interval, while Figures 5.25 and 5.27 show the results using the equivalent GFNN predictor trained on the RGU dataset.

Table 5.7. Summary of the performance in training well **A-02** of the S_w predictors trained from the entire core dataset and the GFNN predictors trained from the RGU dataset at **1.0** ft spacing.

Input Wireline logs	**Output**	**Coefficient of determination (R^2) for the entire core dataset predictors**	**Coefficient of determination (R^2) for the GFNN (RGU dataset) predictors**
Case 1 (RHOB,NPHI,ILD &ILM)	S_w	0.9040	0.9124
Case 2 (SGR,CGR,NPHI,ILD &ILM)	S_w	0.8342	0.8531
Case 3 (SGR,CGR,RHOB,NPHI,ILD &ILM)	S_w	0.9056	0.9272
Case 4 (SGR,CGR,RHOB,NPHI,ILD , ILM, & DT)	S_w	0.9063	0.9281

Table 5.8. Summary of the performance in training well **A-02** of the saturation exponent (n) predictors trained from the entire core dataset and the GFNN predictors trained from the RGU dataset at **1.0** ft spacing.

Input Wireline logs	**Output**	**Coefficient of determination (R^2) for the entire core dataset predictors**	**Coefficient of determination (R^2) for the GFNN (RGU dataset) predictors**
Case 1 (RHOB,NPHI,ILD &ILM)	n	0.8535	0.9163
Case 2 (SGR,CGR,NPHI,ILD &ILM)	n	0.8532	0.9182
Case 3 (SGR,CGR,RHOB,NPHI,ILD &ILM)	n	0.8525	0.9225
Case 4 (SGR,CGR,RHOB,NPHI,ILD , ILM, & DT)	n	0.8529	0.9287

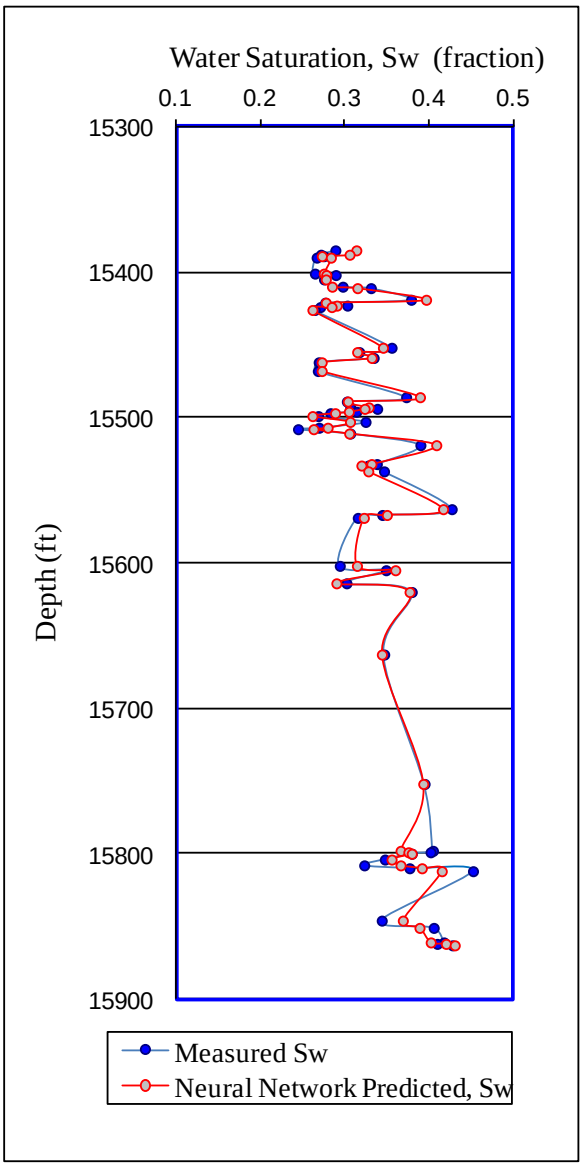

Figure 5.16. Measured and predicted S_w in training well **A-02** for the predictor trained on the entire core dataset using **6** conventional wireline logs (case 3) at 1.0 ft spacing.

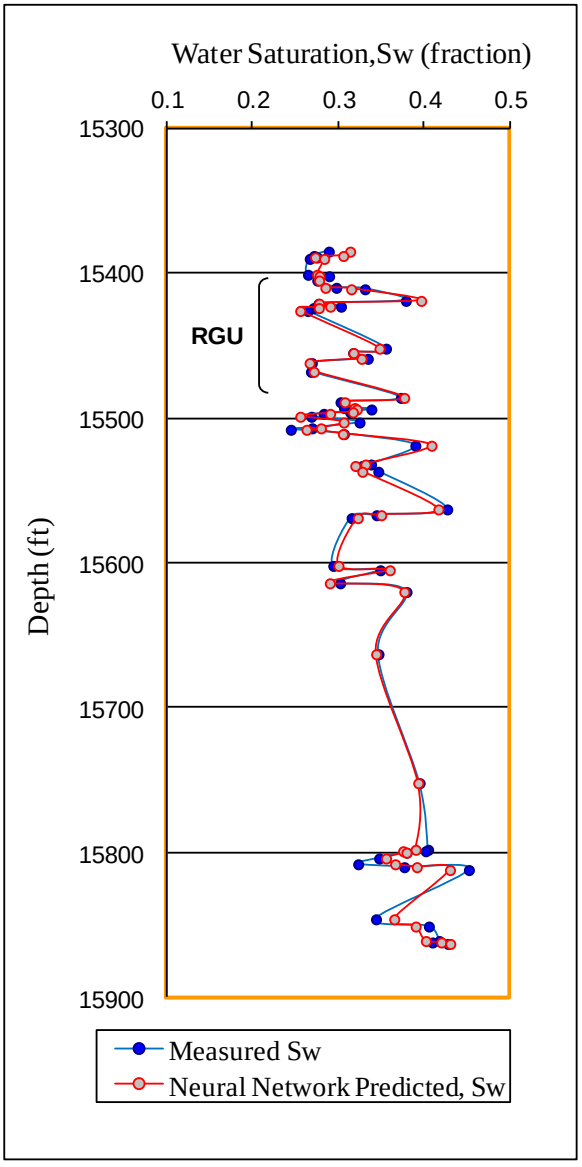

Figure 5.17. Measured and predicted S_w in training well **A-02** for the GFNN predictor trained on the RGU dataset using **6** conventional wireline logs (case 3) at 1.0 ft spacing.

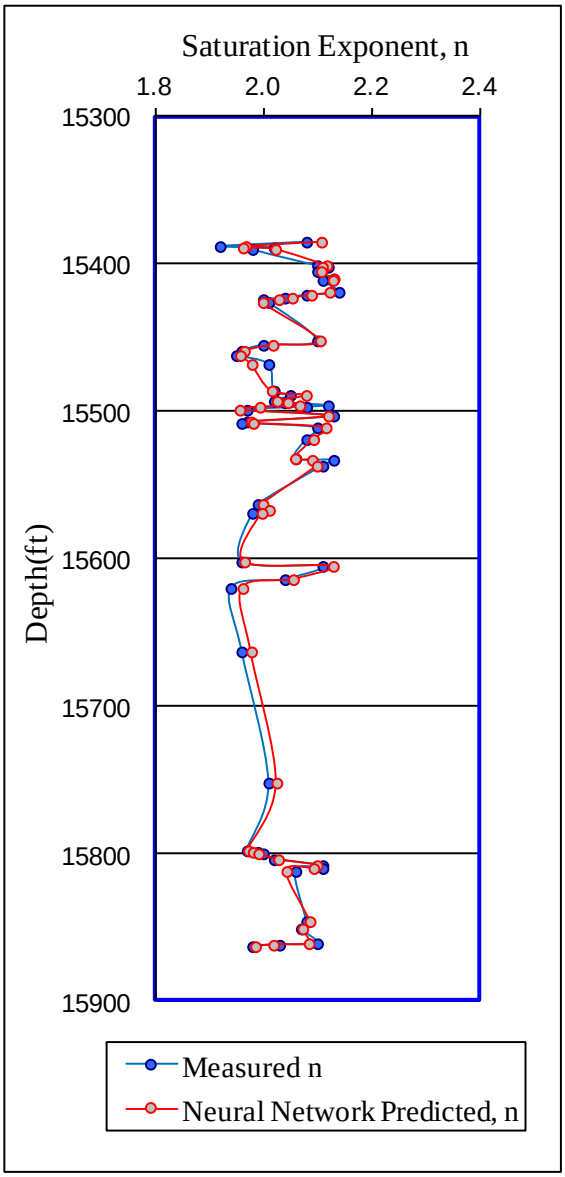

Figure 5.18. Measured and predicted saturation exponent (n) in training well **A-02** for the predictor trained on the entire core dataset using **6** conventional wireline logs (case 3) at 1.0 ft spacing.

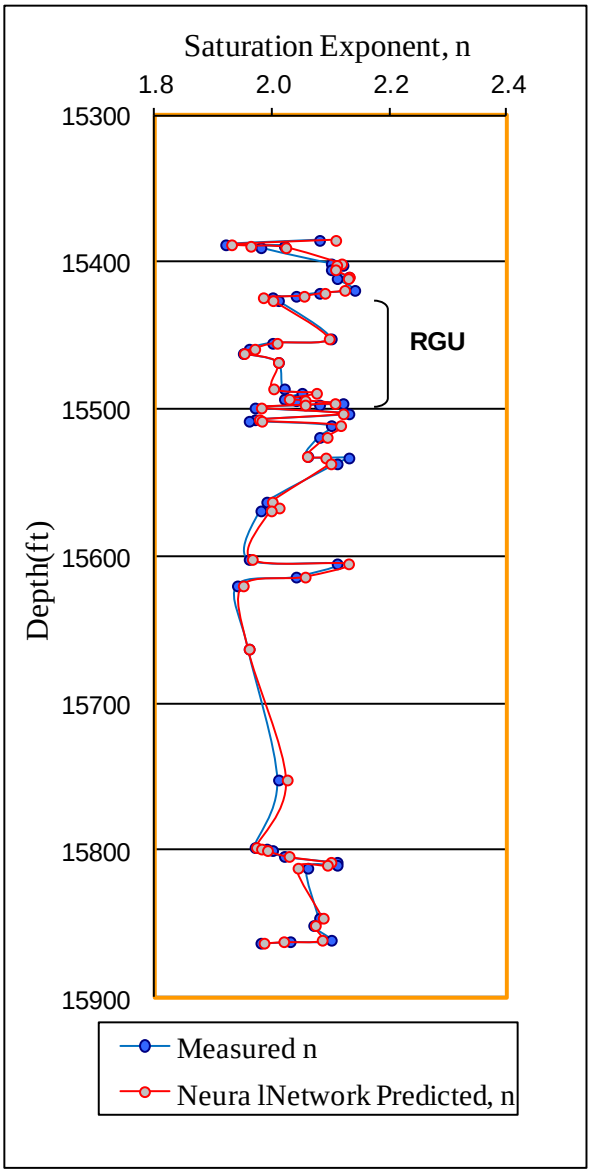

Figure 5.19. Measured and predicted saturation exponent (n) in training well **A-02** for the GFNN predictor trained on the RGU dataset using **6** conventional wireline logs (case 3) at 1.0 ft spacing.

Table 5.9. Summary of the performance in adjacent well **A-01** of the S_w predictors trained from the entire core dataset and the GFNN predictors trained from the RGU dataset at **0.5** ft spacing.

Input Wireline logs	**Output**	**Coefficient of determination (R^2) for the entire core dataset predictors**	**Coefficient of determination (R^2) for the GFNN (RGU dataset) predictors**
Case 2 (SGR,CGR,NPHI,ILD &ILM)	S_w	0.4532	0.4580
Case 3 (SGR,CGR,RHOB,NPHI,ILD &ILM)	S_w	0.5595	0.5776
Case 4 (SGR,CGR,RHOB,NPHI,ILD , ILM, & DT)	S_w	0.5530	0.5737

Table 5.10. Summary of the performance in adjacent well **A-01** of the n predictors trained from the entire core dataset and the GFNN predictors trained from the RGU dataset at **0.5** ft spacing.

Input Wireline logs	**Output**	**Coefficient of determination (R^2) for the entire core dataset predictors**	**Coefficient of determination (R^2) for the GFNN (RGU dataset) predictors**
Case 2 (SGR,CGR,NPHI,ILD &ILM)	n	0.2546	0.2368
Case 3 (SGR,CGR,RHOB,NPHI,ILD &ILM)	n	0.2436	0.3417
Case 4 (SGR,CGR,RHOB,NPHI,ILD , ILM, & DT)	n	0.262	0.2741

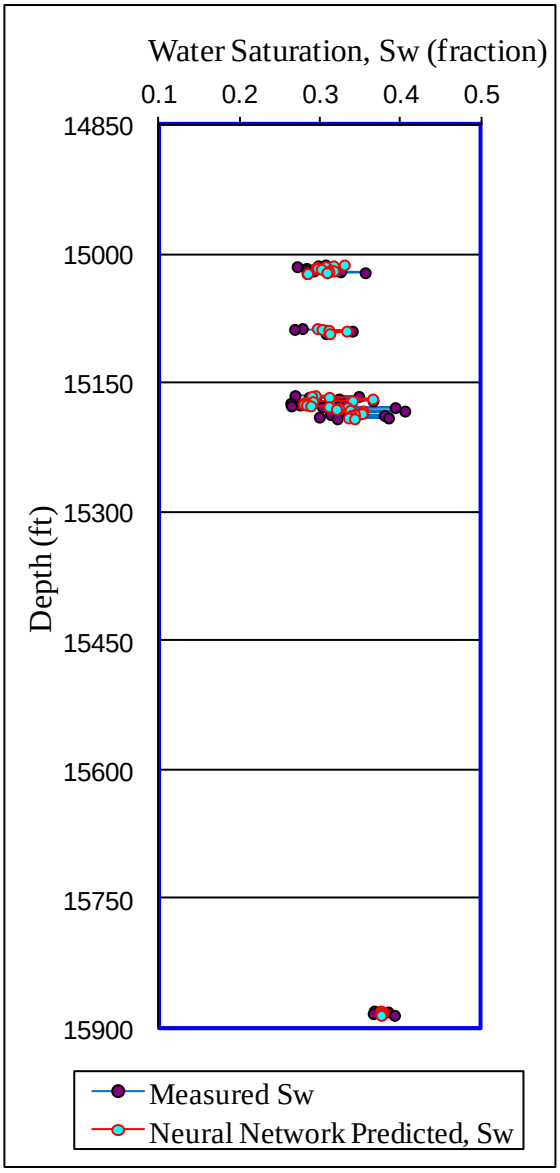

Figure 5.20. Measured and predicted S_w in adjacent well **A-01** for the predictor trained on the entire core dataset using **6** conventional wireline logs (case 3) from well **A-02** at 0.5 ft spacing.

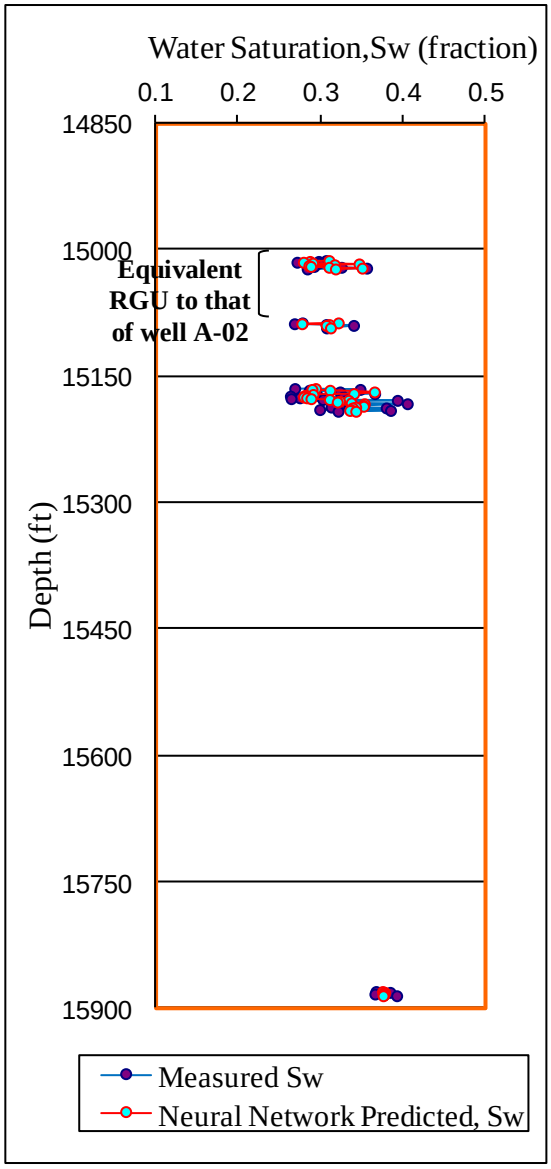

Figure 5.21. Measured and predicted S_w in adjacent well **A-01** for the GFNN predictor trained on the RGU dataset using **6** conventional wireline logs (case 3) from well **A-02** at 0.5 ft spacing.

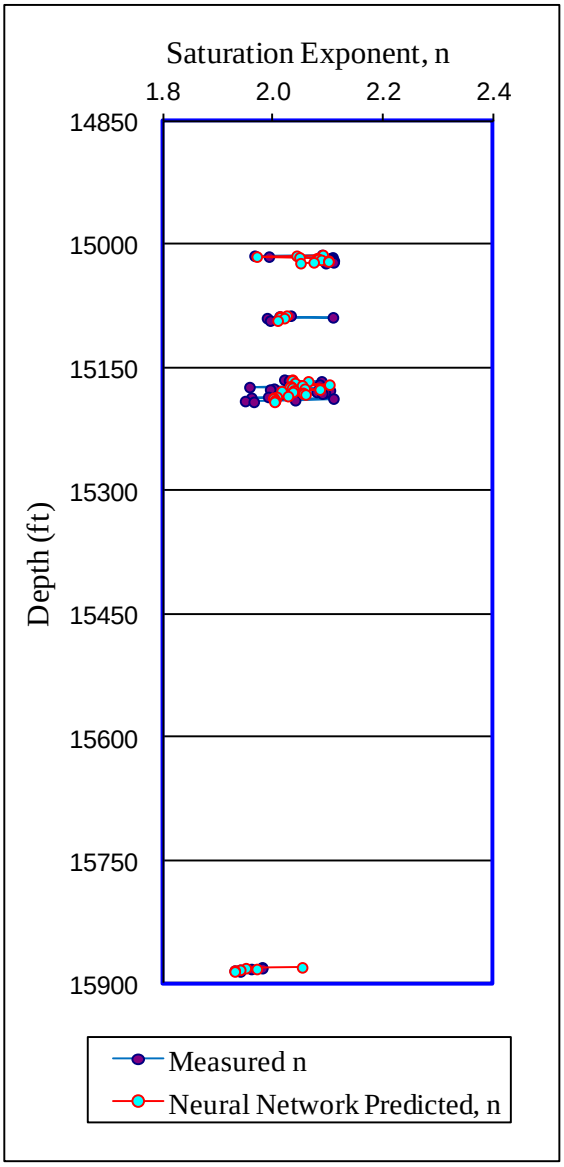

Figure 5.22. Measured and predicted saturation exponent (n) in adjacent well **A-01** for the predictor trained on the entire core dataset using **6** conventional wireline logs (case 3) from well **A-02** at 0.5 ft spacing.

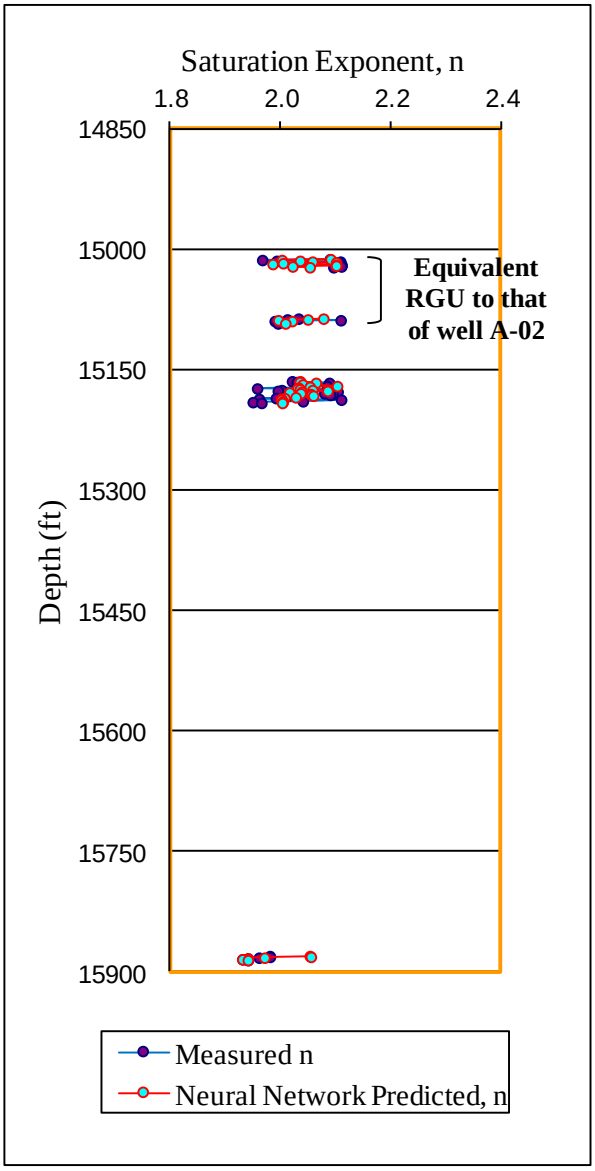

Figure 5.23. Measured and predicted saturation exponent (n) in adjacent well **A-01** for the GFNN predictor trained on the RGU dataset using **6** conventional wireline logs (case 3) from well **A-02** at 0.5 ft spacing.

Table 5.11. Summary of the performance in test well **B-01** of the S_w predictors trained from the entire core dataset and the GFNN predictors trained from the RGU dataset at **0.5** ft spacing.

Input Wireline logs	**Output**	**Coefficient of determination (R^2) for the entire core dataset predictors**	**Coefficient of determination (R^2) for the GFNN (RGU dataset) predictors**
Case 2 (SGR,CGR,NPHI,ILD &ILM)	S_w	0.432	0.5326
Case 3 (SGR,CGR,RHOB,NPHI,ILD &ILM)	S_w	0.3407	0.5214
Case 4 (SGR,CGR,RHOB,NPHI,ILD , ILM, & DT)	S_w	0.3308	0.5319

Table 5.12. Summary of the performance in test well **B-01** of the n predictors trained from the entire core dataset and the GFNN predictors trained from the RGU dataset at **0.5** ft spacing.

Input Wireline logs	**Output**	**Coefficient of determination (R^2) for the entire core dataset predictors**	**Coefficient of determination (R^2) for the GFNN (RGU dataset) predictors**
Case 2 (SGR,CGR,NPHI,ILD &ILM)	n	0.1951	0.3427
Case3 (SGR,CGR,RHOB,NPHI,ILD &ILM)	n	0.2966	0.3871
Case 4 (SGR,CGR,RHOB,NPHI,ILD , ILM, & DT)	n	0.3825	0.4402

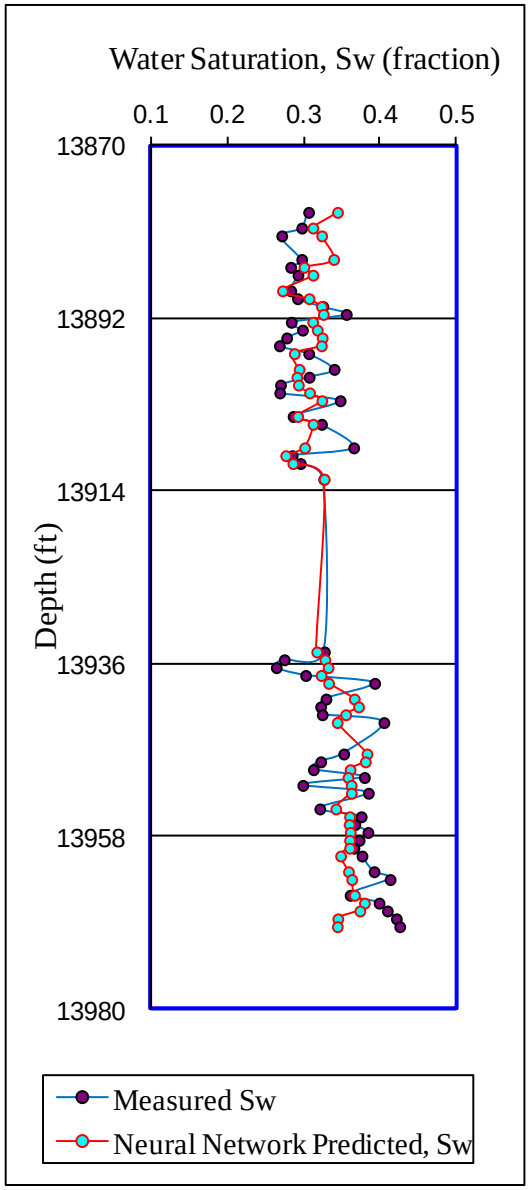

Figure 5.24. Measured and predicted S_w in test well **B-01** for the predictor trained on the entire core dataset using **6** conventional wireline logs (case 3) from well **A-02** at 0.5 ft spacing.

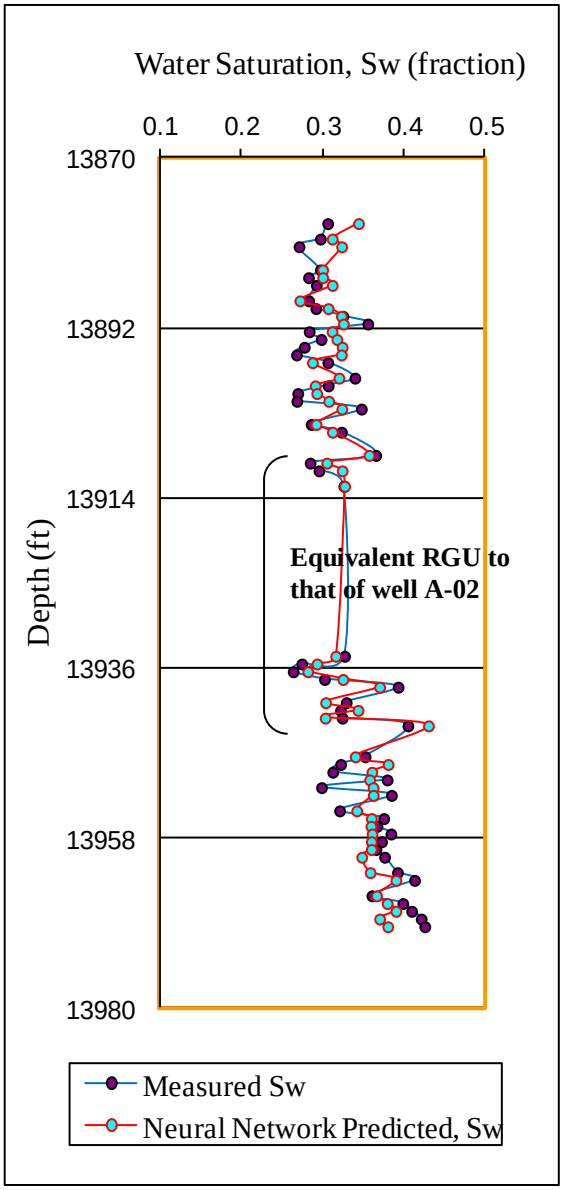

Figure 5.25. Measured and predicted S_w in test well **B-01** for the GFNN predictor trained on the RGU dataset using **6** conventional wireline logs (case 3) from well **A-02** at 0.5 ft spacing.

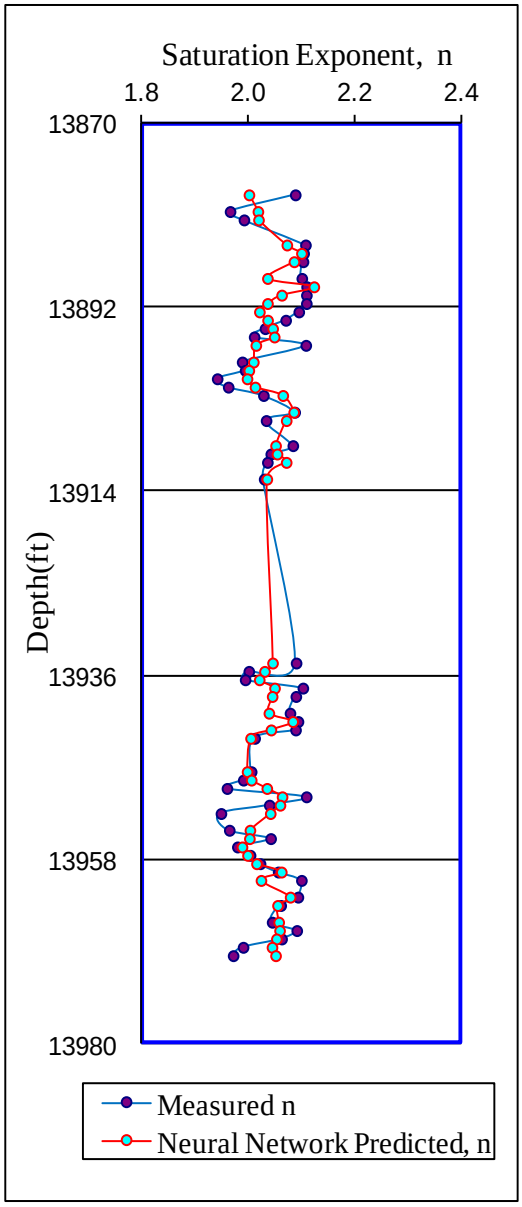

Figure 5.26. Measured and predicted saturation exponent (n) in test well **B-01** for the predictor trained on the entire core dataset using **6** conventional wireline logs (case 3) from well **A-02** at 0.5 ft spacing.

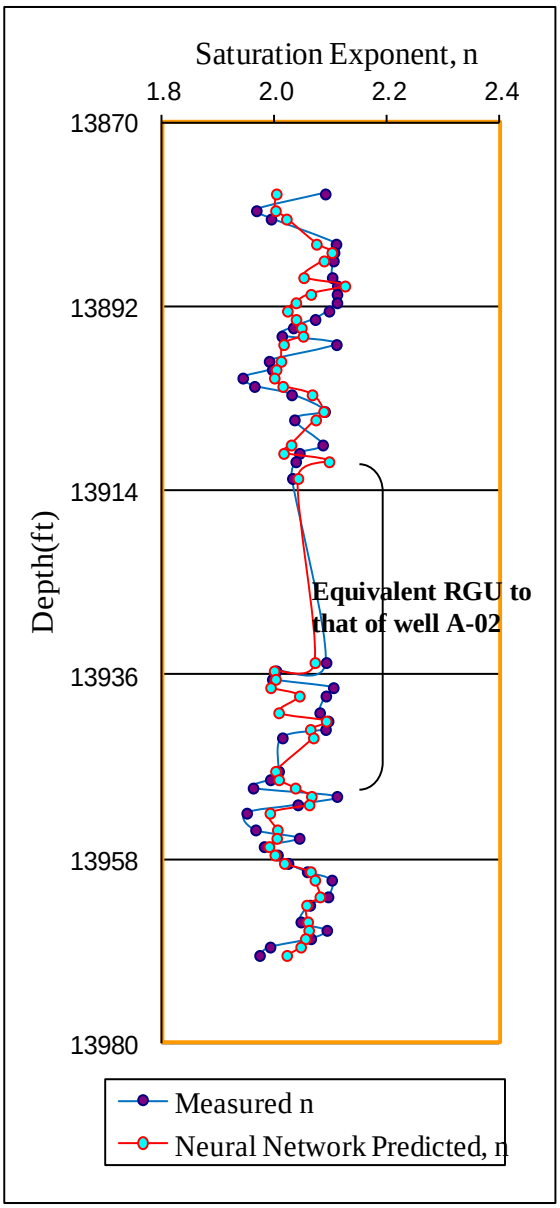

Figure 5.27. Measured and predicted saturation exponent (n) in test well **B-01** for the GFNN predictor trained on the RGU dataset using **6** conventional wireline logs (case 3) from well **A-02** at 0.5 ft spacing.

5.7 Genetically Focused Neural Network Amott-Harvey Wettability Index ($I_{A/H}$) Prediction

This section develops GFNN Amott-Harvey Wettability Index predictors for two oil fields in North Africa (in the Sirt Basin, Libya). Again the conventional wireline logs and core data from wells A-02, A-01, and B-01 were used for this study. Well A-02 was taken as the training well. The aim of the GFNN approach was to produce a reliable predictor based on a small but representative training interval.

5.8 Results of GFNN Prediction of ($I_{A/H}$)

5.8.1 Results of GFNN predictors in training well A-02

Table 5.13 summarises the performance of various neural network Amott-Harvey Wettability Index ($I_{A/H}$) predictors trained from the entire cored interval dataset (55 training data points) and the GFNN predictors from the RGU dataset (14 training data points) at 1.0 ft spacing. The GFNN predictors and the predictors trained on the entire core dataset gave very similar good results in terms of high values of R^2 between measured and predicted results. The GFNN predictors gave slightly better R^2 values in each case. Figure 5.28 shows the measured and predicted Amott-Harvey Wettability Index ($I_{A/H}$) along the depth for the case 3 predictor using 6 conventional wireline logs trained on the entire cored interval dataset at 1.0 ft spacing. Figure 5.29 shows the plot for the equivalent GFNN predictor.

5.8.2 Results in adjacent test well A-01

After the training process in well A-02, the GFNN $I_{A/H}$ predictors were tested in the cored interval of adjacent well A-01 in the same oil field. Crossplots of measured versus predicted $I_{A/H}$ were drawn to obtain the linear regression coefficients of determination (R^2). Table 5.14 summarises the performance of the $I_{A/H}$ predictors trained from the entire cored interval dataset and compared with the GFNN predictors from the RGU dataset. All these predictors were trained at 0.5 ft spacing. The GFNN predictors gave better values of R^2 in every case than the equivalent predictors trained on the entire core dataset.

Figure 5.30 shows the results of measured and predicted ($I_{A/H}$) along the depth for the case 3 predictor using 6 wireline logs and trained on the entire cored interval, while Figure 5.31 shows the equivalent results using the GFNN predictor trained on the RGU dataset.

5.8.3 Results in test well B-01

The predictors were also tested in well B-01 in a different oil field. Table 5.15 summarises the performance of the various neural network Amott-Harvey Wettability Index ($I_{A/H}$) predictors trained from the entire cored interval dataset and the GFNN predictors trained from the RGU dataset at 0.5 ft spacing. Again the GFNN predictors gave better results in terms of the R^2 values. Figure 5.32 shows the results of measured and predicted ($I_{A/H}$) with depth for the case 3 predictor using 6 wireline logs and trained on the entire cored interval, while Figure 5.33 shows the equivalent results using the GFNN predictor trained on the RGU dataset.

Table 5.13. Summary of the performance in training well **A-02** of the Amott-Harvey Wettability Index ($I_{A/H}$) predictors trained from the entire core dataset and the GFNN predictors trained from the RGU dataset at **1.0** ft spacing.

Input Wireline logs	**Output**	**Coefficient of determination (R^2) for the entire core dataset predictors**	**Coefficient of determination (R^2) for the GFNN (RGU dataset) predictors**
Case 1(RHOB,NPHI,ILD &ILM)	$I_{A/H}$	0.8739	0.9012
Case 2(SGR,CGR,NPHI,ILD &ILM)	$I_{A/H}$	0.7851	0.8462
Case 3 (SGR,CGR,RHOB,NPHI,ILD &ILM)	$I_{A/H}$	0.8753	0.9074
Case 4 (SGR,CGR,RHOB,NPHI,ILD, ILM, & DT)	$I_{A/H}$	0.8777	0.9124

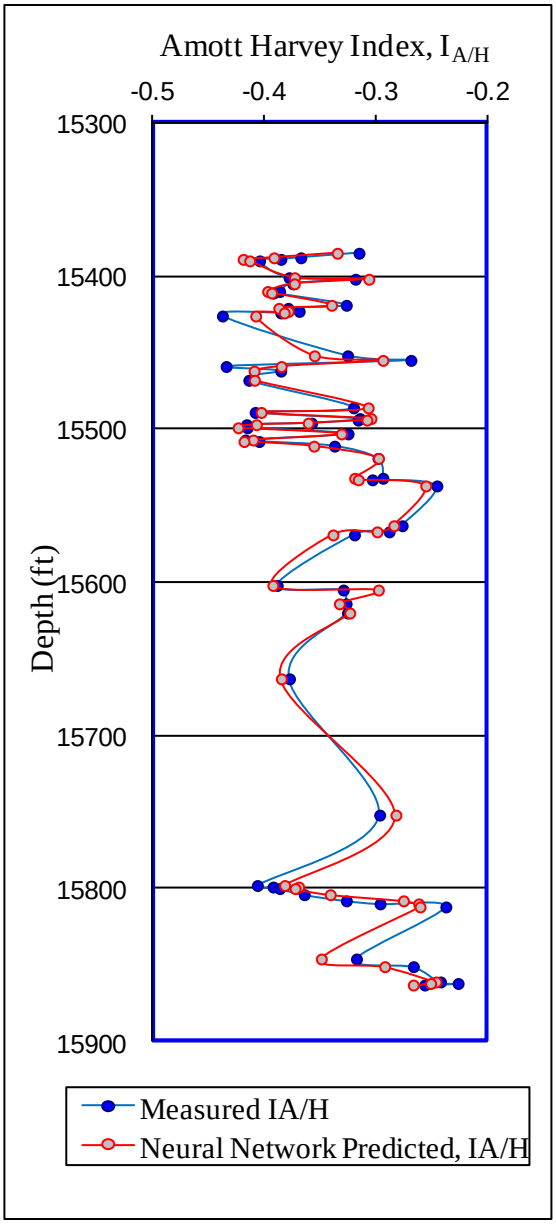

Figure 5.28. Measured and predicted Amott-Harvey Wettability Index ($I_{A/H}$) in training well **A-02** for the predictor trained on the entire core dataset using **6** conventional wireline logs (case 3) at 1.0 ft spacing.

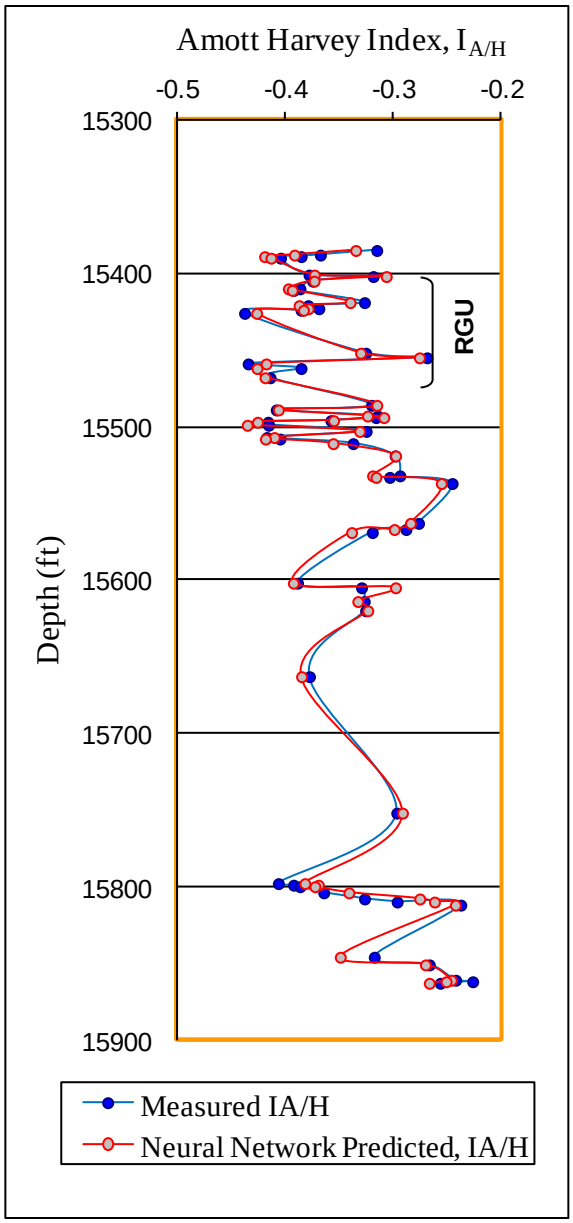

Figure 5.29. Measured and predicted Amott-Harvey Wettability Index ($I_{A/H}$) in training well **A-02** for the GFNN predictor trained on the RGU dataset using **6** conventional wireline logs (case 3) at 1.0 ft spacing.

Table 5.14. Summary of the performance in adjacent well **A-01** of the Amott-Harvey Wettability Index ($I_{A/H}$) predictors trained from the entire core dataset and the GFNN predictors trained from the RGU dataset at **0.5** ft spacing.

Input Wireline logs	**Output**	**Coefficient of determination (R^2) for the entire core dataset predictors**	**Coefficient of determination (R^2) for the GFNN (RGU dataset) predictors**
Case 1 (RHOB,NPHI,ILD &ILM)	$I_{A/H}$	0.2355	0.3557
Case 2 (SGR,CGR,NPHI,ILD &ILM)	$I_{A/H}$	0.3134	0.5086
Case 3 (SGR,CGR,RHOB,NPHI,ILD &ILM)	$I_{A/H}$	0.451	0.5817
Case 4 (SGR,CGR,RHOB,NPHI,ILD, ILM, & DT)	$I_{A/H}$	0.4724	0.5572

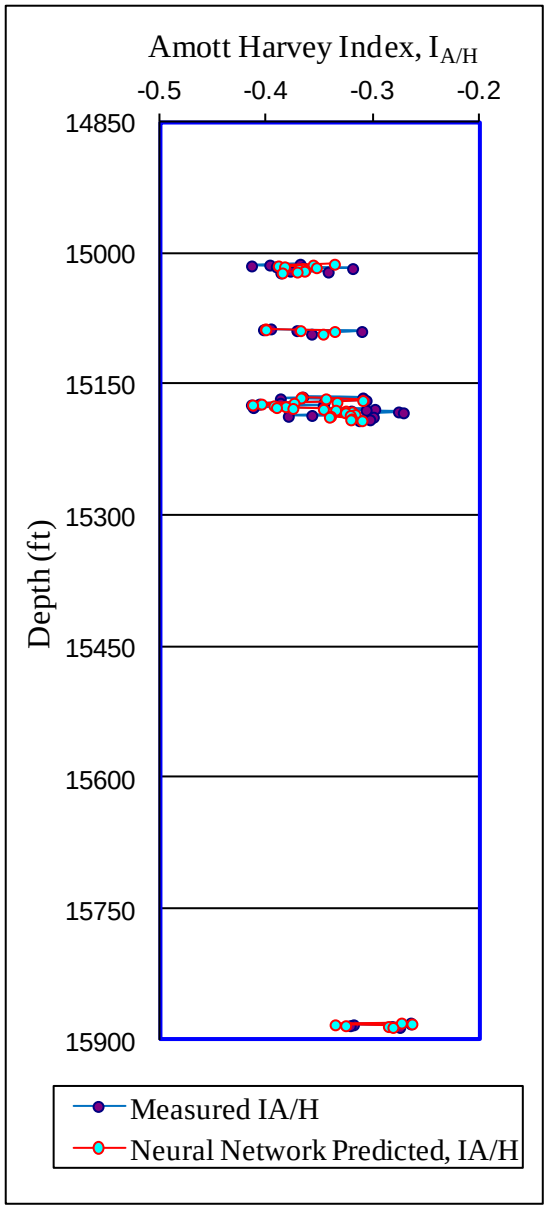

Figure 5.30. Measured and predicted Amott-Harvey Wettability Index ($I_{A/H}$) in adjacent well **A-01** for the predictor trained on the entire core dataset using **6** conventional wireline logs (case 3) from well **A-02** at 0.5 ft spacing.

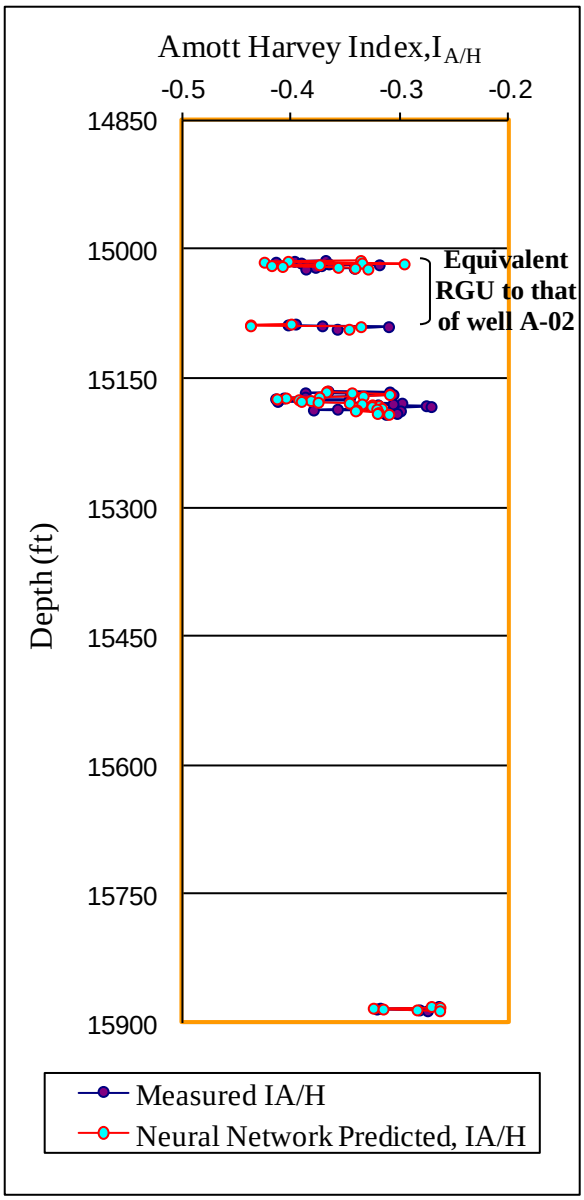

Figure 5.31. Measured and predicted Amott-Harvey Wettability Index ($I_{A/H}$) in adjacent well **A-01** for the GFNN predictor trained on the RGU dataset using **6** conventional wireline logs (case 3) from well **A-02** at 0.5 ft spacing.

Table 5.15. Summary of the performance in test well **B-01** of the Amott-Harvey Wettability Index ($I_{A/H}$) predictors trained from the entire core dataset and the GFNN predictors trained from the RGU dataset at **0.5** ft spacing.

Input Wireline logs	**Output**	**Coefficient of determination (R^2) for the entire core dataset predictors**	**Coefficient of determination (R^2) for the GFNN (RGU dataset) predictors**
Case 1 (RHOB,NPHI,ILD &ILM)	$I_{A/H}$	0.1387	0.4621
Case 2 (SGR,CGR,NPHI,ILD &ILM)	$I_{A/H}$	0.2586	0.5383
Case 3 (SGR,CGR,RHOB,NPHI,ILD &ILM)	$I_{A/H}$	0.3706	0.5926
Case 4 (SGR,CGR,RHOB,NPHI,ILD, ILM, & DT)	$I_{A/H}$	0.3740	0.5972

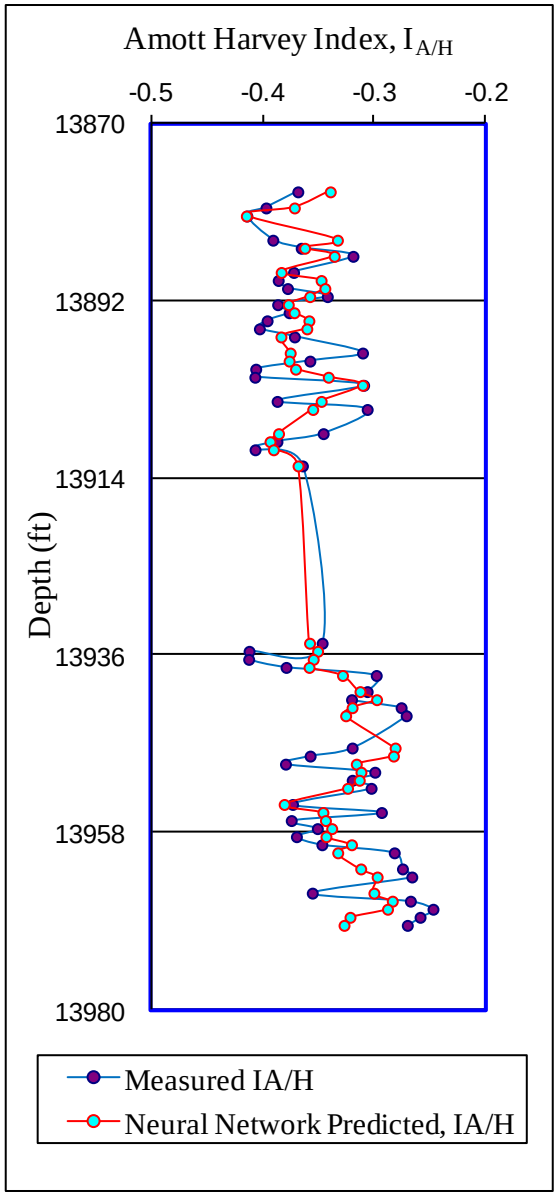

Figure 5.32. Measured and predicted Amott-Harvey Wettability Index ($I_{A/H}$) in test well **B-01** for the predictor trained on the entire core dataset using **6** conventional wireline logs (case 3) from well **A-02** at 0.5 ft spacing.

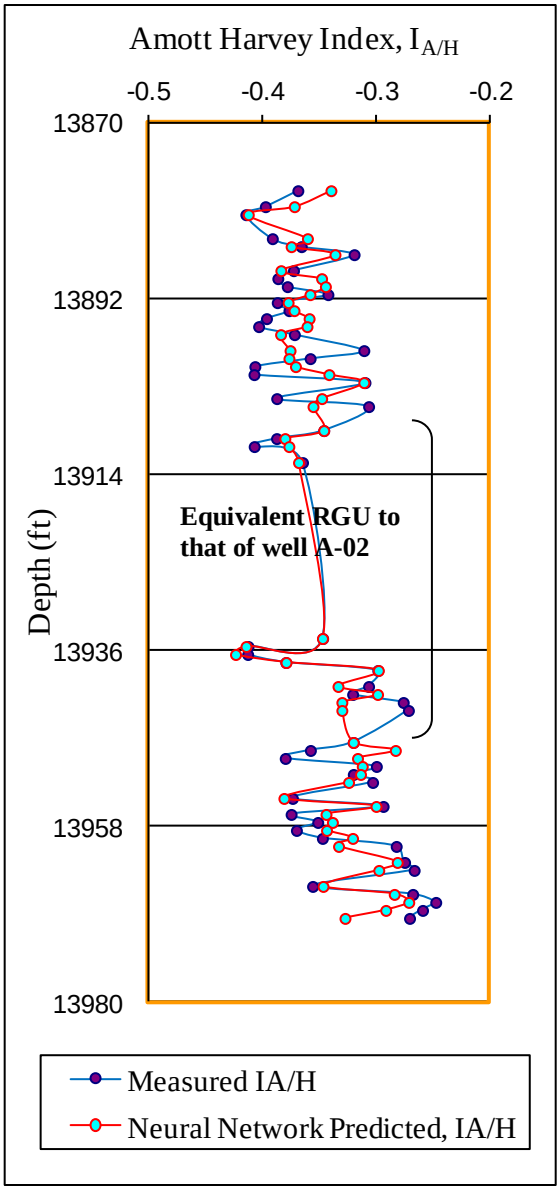

Figure 5.33. Measured and predicted Amott-Harvey Wettability Index ($I_{A/H}$) in test well **B-01** for the GFNN predictor trained on the RGU dataset using **6** conventional wireline logs (case 3) from well **A-02** at 0.5 ft spacing.

5.9 Using the GFNN predictors trained in the well A-02 RGU to predict SCAL parameters in the equivalent RGU intervals of wells A-01 and B-01

The GFNN predictors trained from the RGU dataset of well A-02 were also tested in just the equivalent RGU intervals of wells A-01 and B-01 (rather than throughout the entire cored intervals of the test wells). These equivalent RGU intervals were identified by core and wireline log data and have been indicated in the previous figures that showed the predictions along the depth. Tables 5.16 and 5.17 summarise the performance of the GFNN case 3 predictors trained at 0.5 ft spacing in the equivalent RGUs of wells A-01 and B-01 respectively. The R^2 values in many cases are quite high, and higher than those for the GFNN predictions made throughout the cored intervals of these two wells. Figures 5.34 – 5.43 show the associated crossplots for all the cases shown in Tables 5.16 and 5.17. Figures 5.34-5.38 refer to well A-01, whilst Figures 5.39-5.43 refer to well B-01. The crossplots show that the regression lines are very close in each case to the 1:1 line, and in most cases there is a relatively small scatter of the points around this regression line.

Table 5.16. Summary of the performance of some GFNN SCAL parameter predictors trained in well **A-02** (using the RGU training dataset) when tested in the equivalent RGU in adjacent test well **A-01** at **0.5** ft spacing.

Input Wireline Logs	**Output**	**Coefficient of determination (R^2) for the GFNN predictors when tested in the equivalent RGU in well A-01**
Case 3 (SGR,CGR,NPHI,ILD & ILM)	R_t	0.7743
Case 3 (SGR,CGR,NPHI,ILD & ILM)	RI	0.6399
Case 3 (SGR,CGR,NPHI,ILD & ILM)	S_w	0.5344
Case 3 (SGR,CGR,NPHI,ILD & ILM)	n	0.5166
Case 3 (SGR,CGR,NPHI,ILD & ILM)	$I_{A/H}$	0.8862

Table 5.17. Summary of the performance of some GFNN SCAL parameter predictors trained in well **A-02** (using the RGU training dataset) when tested in the equivalent RGU in the test well **B-01** in a different oil field at **0.5** ft spacing.

Input Wireline Logs	**Output**	**Coefficient of determination (R^2) for the GFNN predictors when tested in the equivalent RGU in well B-01**
Case 3 (SGR,CGR,NPHI,ILD & ILM)	R_t	0.6990
Case 3 (SGR,CGR,NPHI,ILD & ILM)	RI	0.4366
Case 3 (SGR,CGR,NPHI,ILD & ILM)	S_w	0.4135
Case 3 (SGR,CGR,NPHI,ILD & ILM)	n	0.7428
Case 3 (SGR,CGR,NPHI,ILD & ILM)	$I_{A/H}$	0.7476

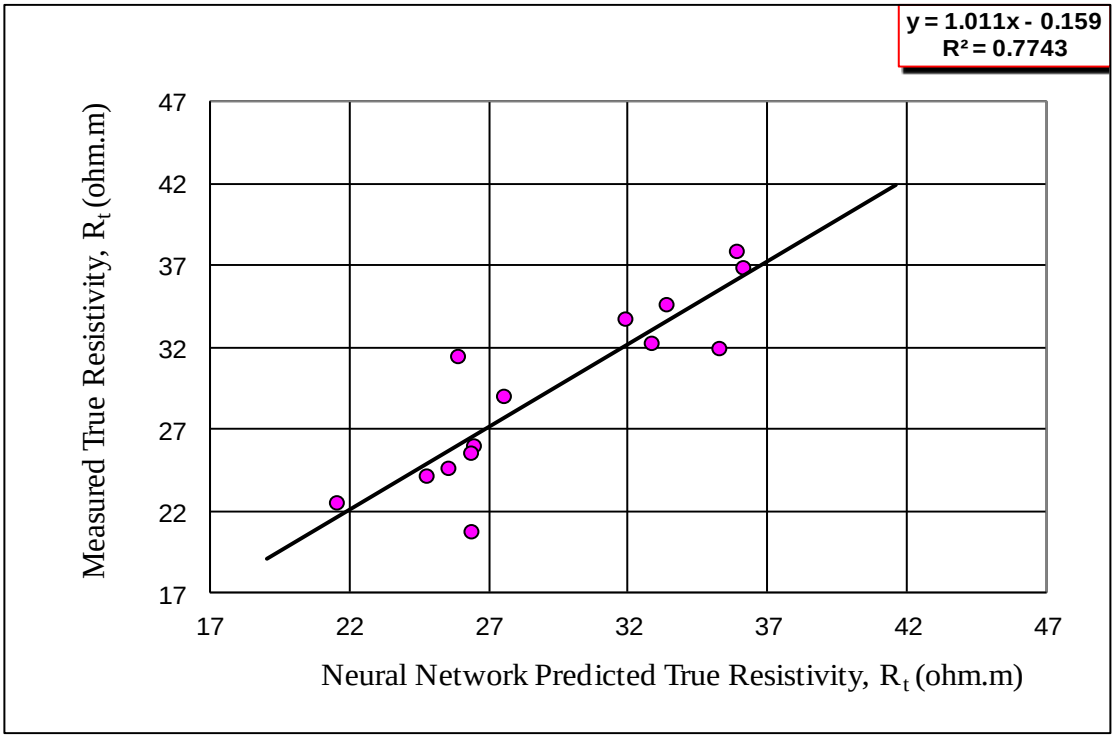

Figure 5.34. Measured versus predicted true resistivity for the case 3 GFNN predictor trained on the RGU dataset at 0.5 ft spacing when tested in the equivalent RGU in well **A-01**.

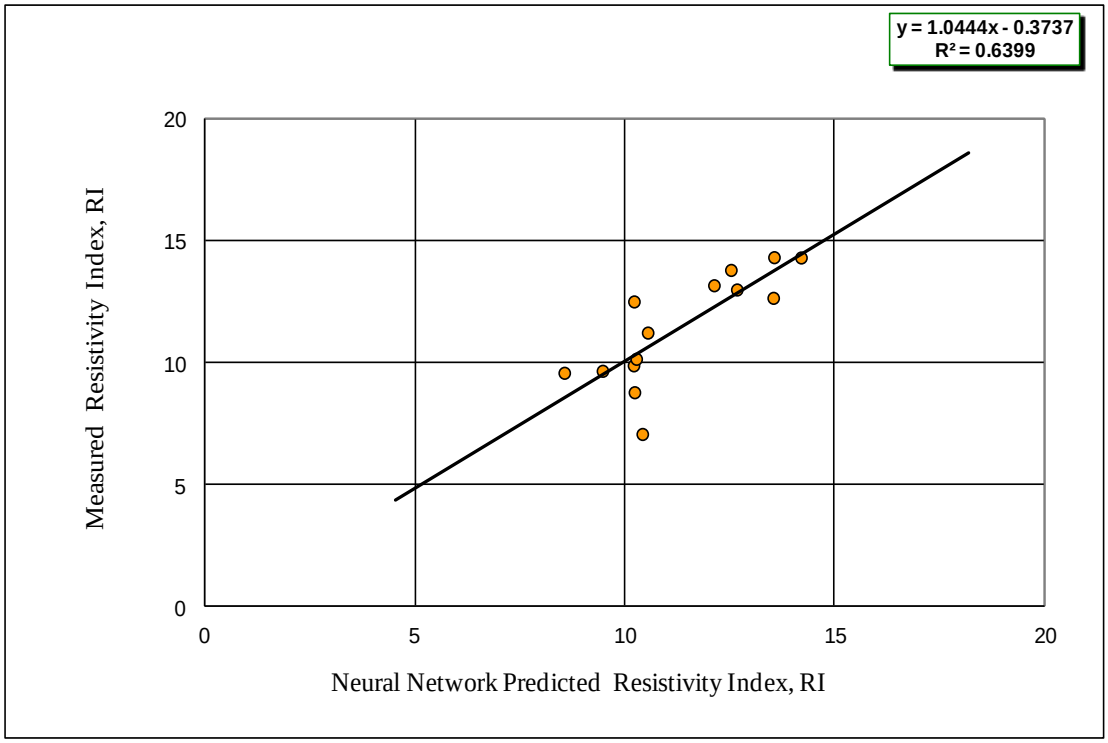

Figure 5.35. Measured versus predicted resistivity index for the case 3 GFNN predictor trained on the RGU dataset at 0.5 ft spacing when tested in the equivalent RGU in well **A-01**.

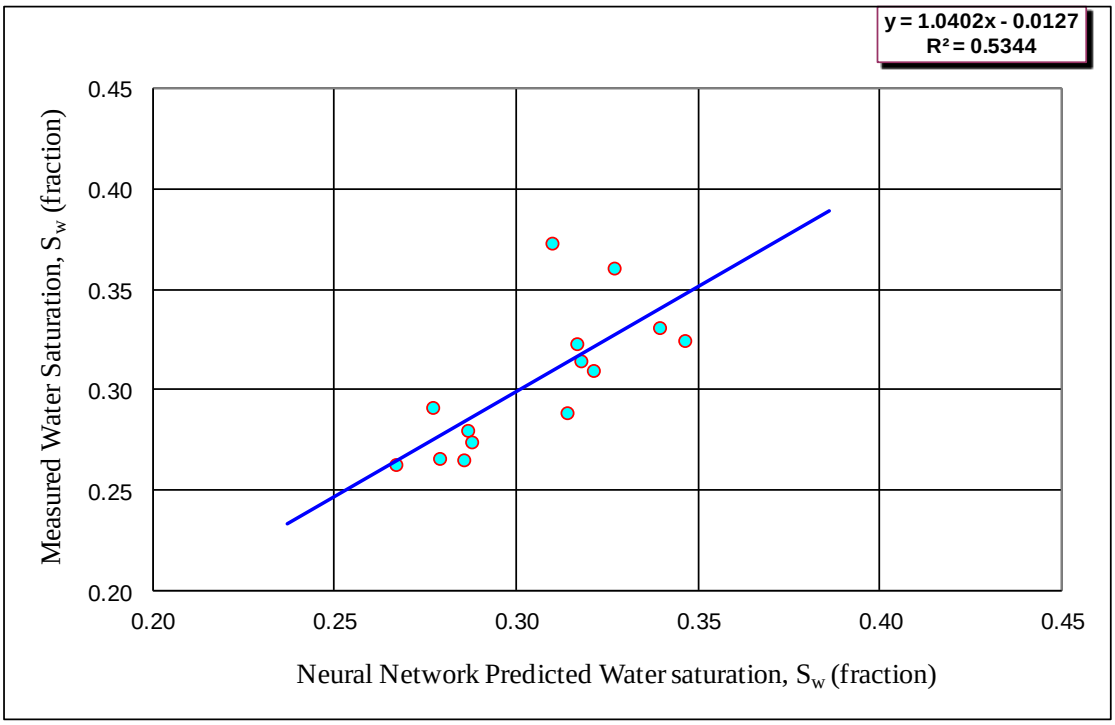

Figure 5.36. Measured versus predicted water saturation for the case 3 GFNN predictor trained on the RGU dataset at 0.5 ft spacing when tested in the equivalent RGU in well **A-01.**

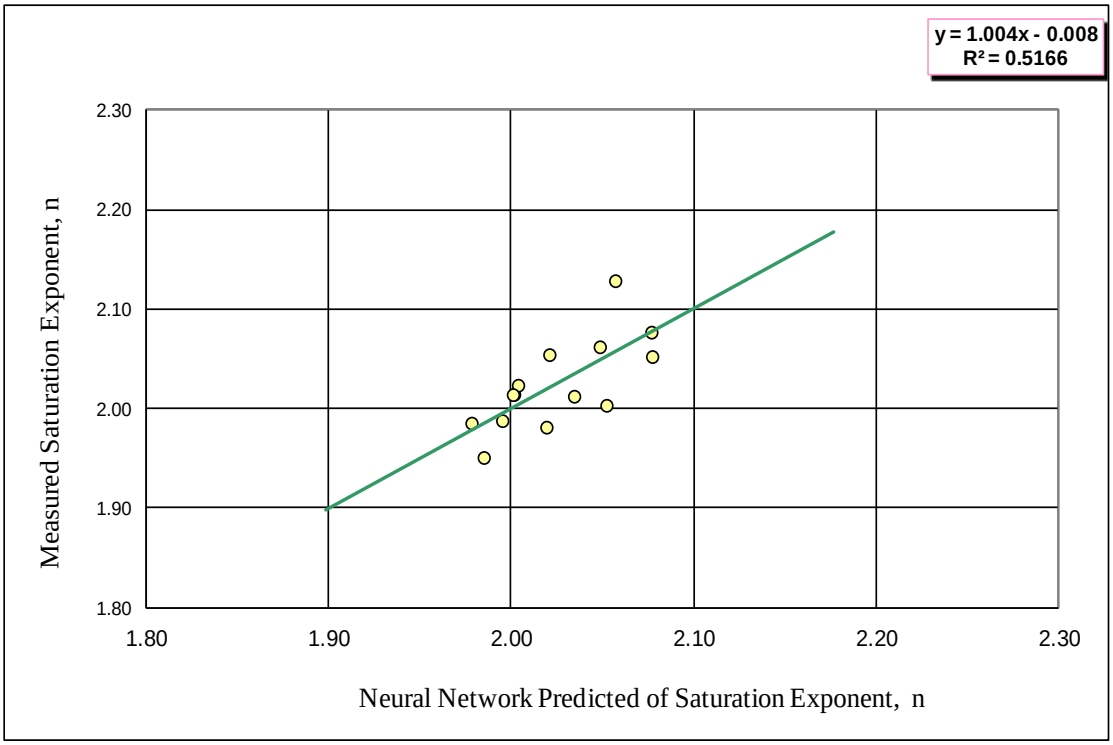

Figure 5.37. Measured versus predicted saturation exponent (n) for the case 3 GFNN predictor trained on the RGU dataset at 0.5 ft spacing when tested in the equivalent RGU in well **A-01.**

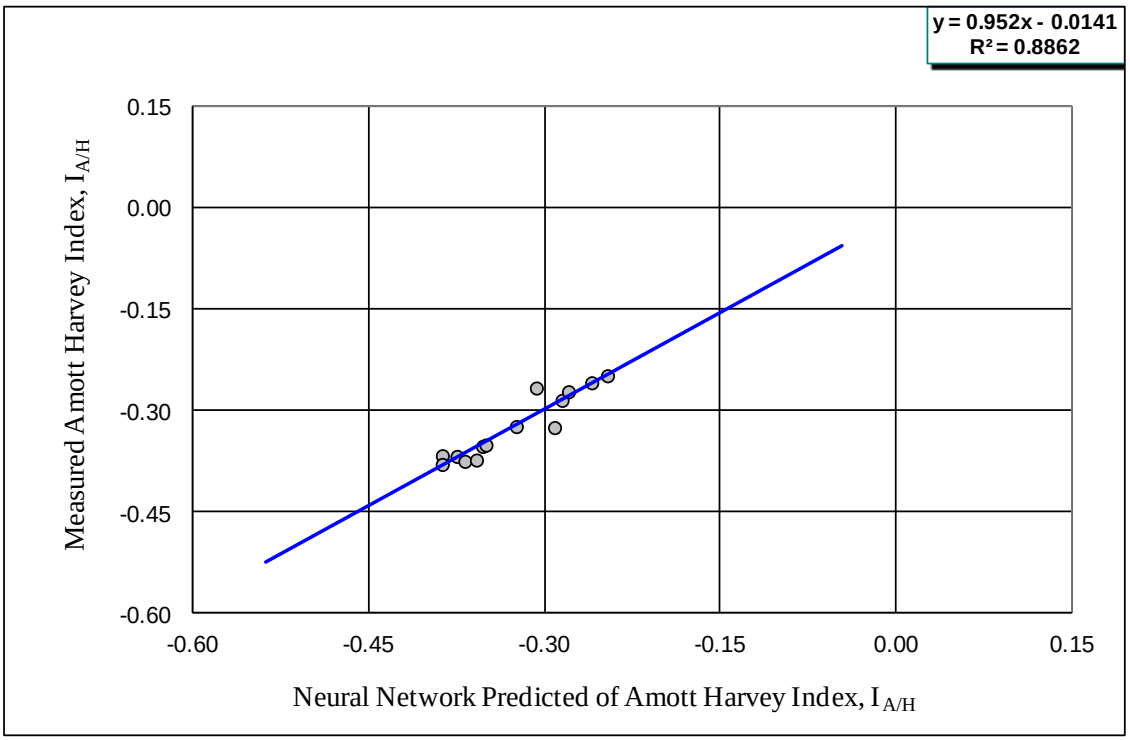

Figure 5.38. Measured versus predicted Amott-Harvey Wettability Index ($I_{A/H}$) for the case 3 GFNN predictor trained on the RGU dataset at 0.5 ft spacing when tested in the equivalent RGU in well **A-01**.

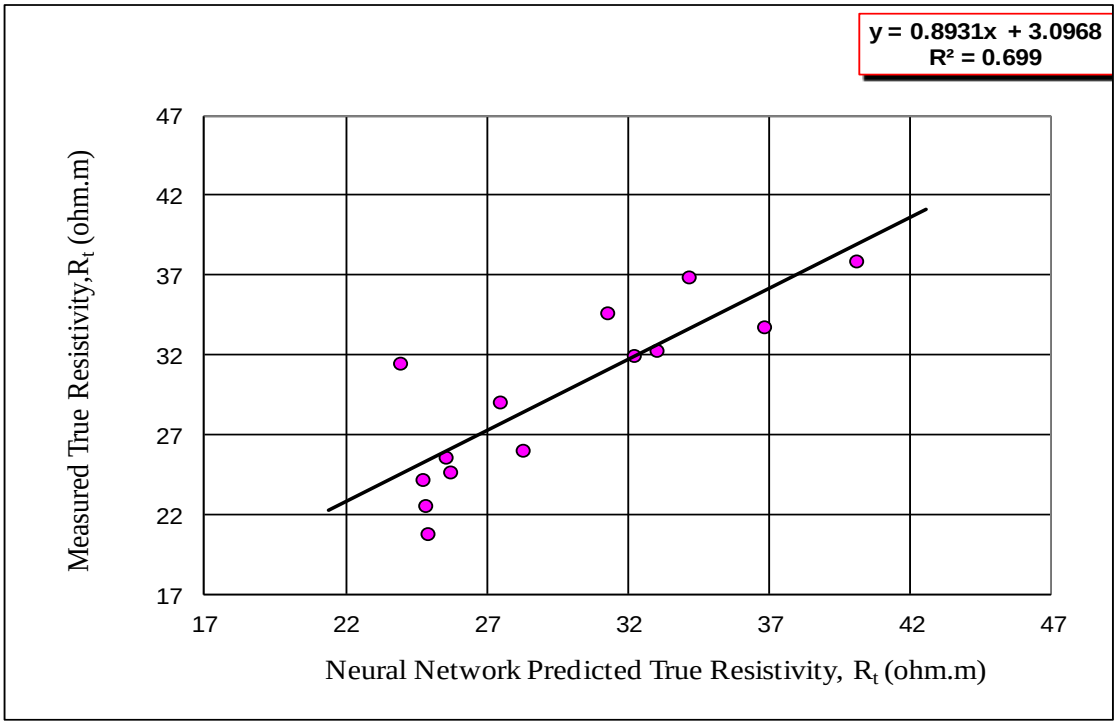

Figure 5.39. Measured versus predicted true resistivity for the case 3 GFNN predictor trained on the RGU dataset at 0.5 ft spacing when tested in the equivalent RGU in well **B-01**.

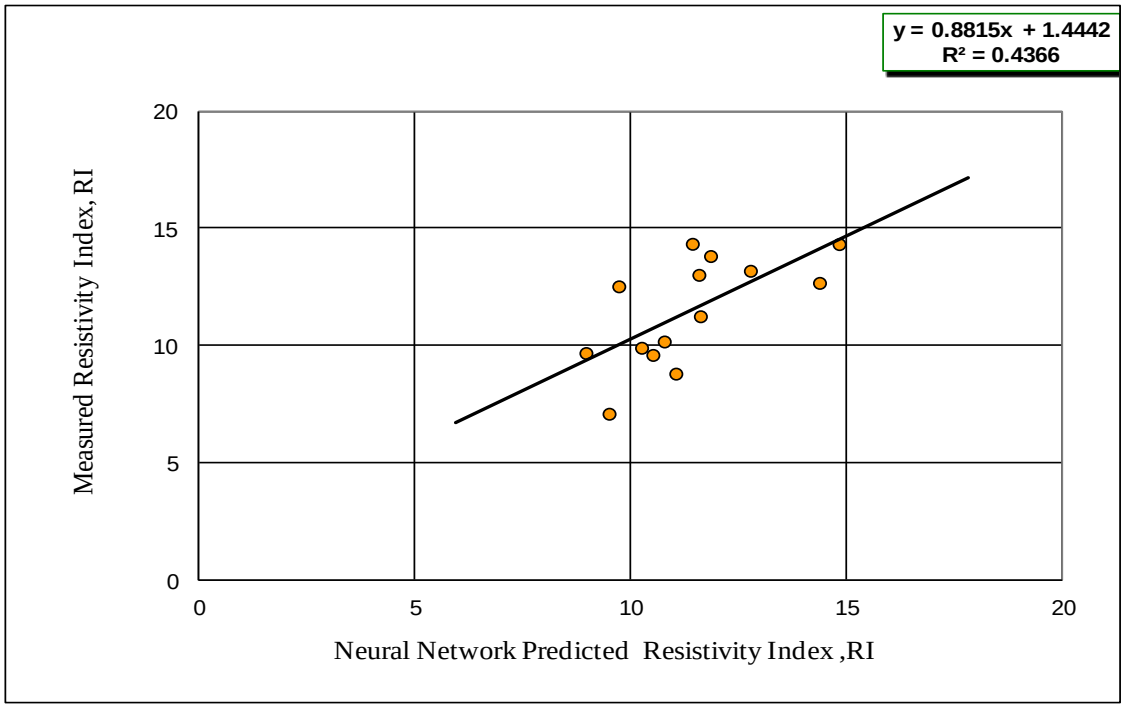

Figure 5.40. Measured versus predicted resistivity index for the case 3 GFNN predictor trained on the RGU dataset at 0.5 ft spacing when tested in the equivalent RGU in well **B-01.**

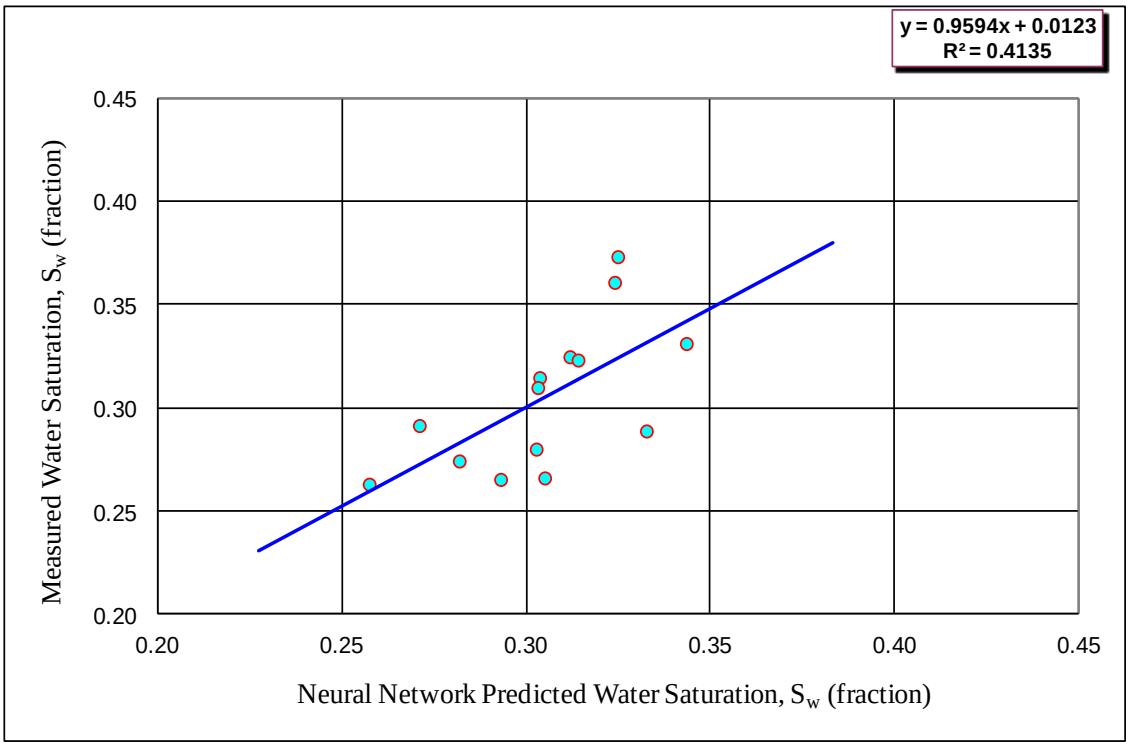

Figure 5.41. Measured versus predicted water saturation (S_w) for the case 3 GFNN predictor trained on the RGU dataset at 0.5 ft spacing when tested in the equivalent RGU in well **B-01**.

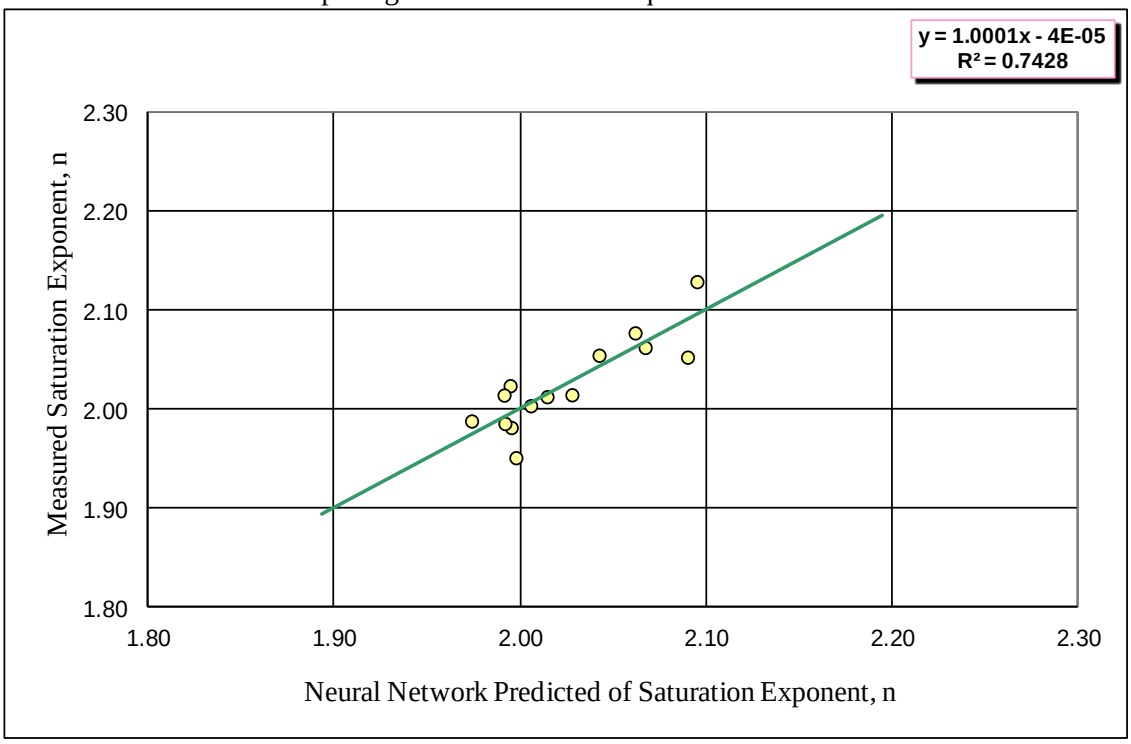

Figure 5.42. Measured versus predicted saturation exponent (n) for the case 3 GFNN predictor trained on the RGU dataset at 0.5 ft spacing when tested in the equivalent RGU in well **B-01** .

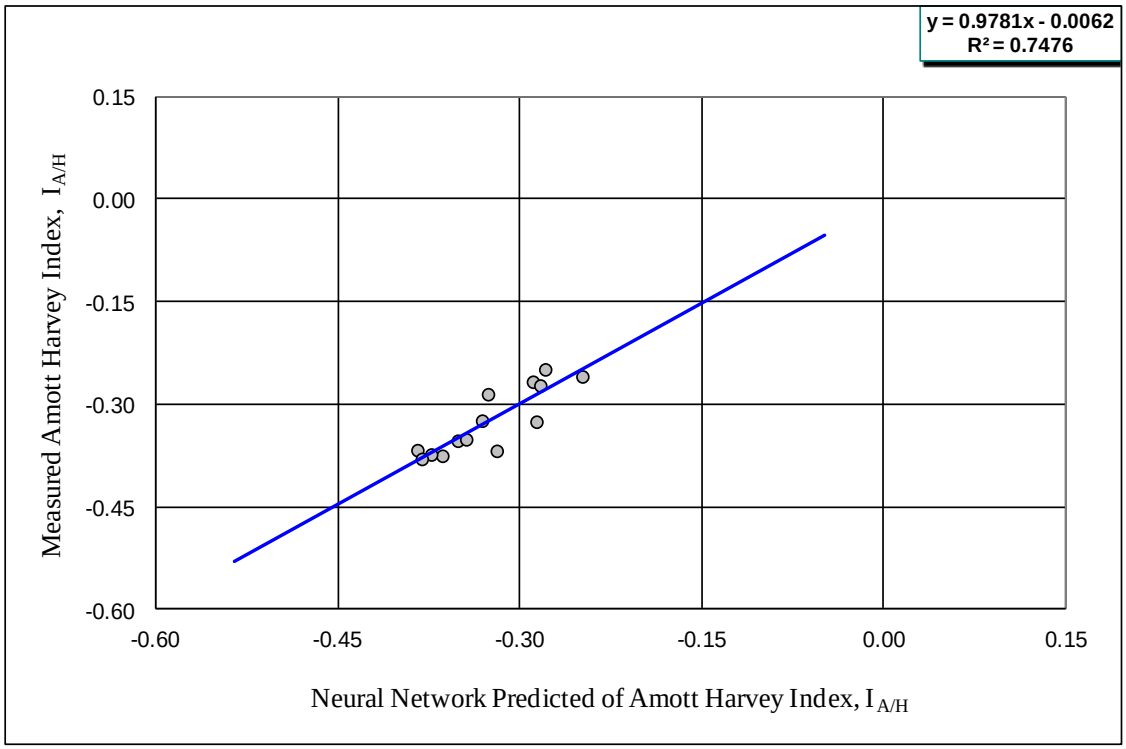

Figure 5.43. Measured versus predicted Amott-Harvey Wettability Index ($I_{A/H}$) for the case 3 GFNN predictor trained on the RGU dataset at 0.5 ft spacing when tested in the equivalent RGU in well **B-01**.

Table 5.18. Summary of the performance in training well **A-02** of SCAL predictors trained from the entire dataset and GFNN predictors trained from RGU dataset at 1.0 ft spacing.

Output	**Input(Wireline logs)**			
	Case1 (RHOB, NPHI, ILD,ILM	Case2 (SGR,CGR, NPHI, ILD, ILM)	Case3 (SGR,CGR, RHOB, NPHI, ILD, ILM)	Case4 SGR,CGR, RHOB, NPHI, ILD, ILM)
	R^2 (Coefficient of determination for all entire core dataset)			
R_t	0.8232	0.7507	0.8230	0.8320
RI	0.9061	0.8260	0.9070	0.9078
S_w	0.9040	0.8342	0.9056	0.9063
n	0.8535	0.8532	0.8525	0.8529
$I_{A/H}$	0.8739	0.7851	0.8753	0.8777
R^2 (Coefficient of determination for GFNN, RGU dataset)				
R_t	0.8423	0.7724	0.8724	0.8910
RI	0.9163	0.8422	0.9124	0.9320
S_w	0.9124	0.8531	0.9272	0.9281
n	0.9163	0.9182	0.9225	0.9287
$I_{A/H}$	0.9012	0.8462	0.9074	0.9124

Table 5.19. Summary of the performance in adjacent well **A-01** of SCAL predictors trained from the entire dataset and GFNN predictors trained from RGU dataset at **0.5** ft spacing.

Output	**Input(Wireline logs)**			
	Case1 (RHOB, NPHI, ILD,ILM	Case2 (SGR,CGR, NPHI, ILD, ILM)	Case3 (SGR,CGR, RHOB, NPHI, ILD, ILM)	Case4 SGR,CGR, RHOB, NPHI, ILD, ILM)
	R^2 (Coefficient of determination for all entire core dataset)			
R_t	-----	0.4232	0.4340	0.4580
RI	-----	0.5403	0.5875	0.5872
S_w	-----	0.4532	0.5595	0.5530
n	-----	0.2546	0.2436	0.2620
$I_{A/H}$	0.2355	0.3134	0.4510	0.4724
R^2 (Coefficient of determination for GFNN, RGU dataset)				
R_t	------	0.4842	0.4999	0.5407
RI	-----	0.5247	0.6121	0.6119
S_w	-----	0.4580	0.5776	0.5737
n	-----	0.2368	0.3417	0.2741
$I_{A/H}$	0.3557	0.5086	0.5817	0.5572

Table 5.20. Summary of the performance in test well **B-01** of SCAL predictors trained from the entire dataset and GFNN predictors trained from RGU dataset at **0.5** ft spacing.

Output	**Input(Wireline logs)**			
	Case1 (RHOB, NPHI, ILD,ILM	Case2 (SGR,CGR, NPHI, ILD, ILM)	Case3 (SGR,CGR, RHOB, NPHI, ILD, ILM)	Case4 SGR,CGR, RHOB, NPHI, ILD, ILM)
	R^2 (Coefficient of determination for all entire core dataset)			
R_t	-----	0.2690	0.3150	0.3430
RI	-----	0.4223	0.3565	0.3589
S_w	-----	0.4320	0.3407	0.3308
n	-----	0.1951	0.2966	0.3825
$I_{A/H}$	0.1387	0.2586	0.3706	0.3740
R^2 (Coefficient of determination for GFNN, RGU dataset)				
R_t	------	0.4916	0.5823	0.5497
RI	-----	0.5320	0.5423	0.6191
S_w	-----	0.5326	0.5214	0.5319
n	-----	0.4962	0.5136	0.5247
$I_{A/H}$	0.4621	0.5383	0.5926	0.5972

5.10 Conclusions

1. GFNN predictors trained only on the small RGU dataset (consisting of 14 SCAL core plugs and associated wireline log data) were comparable, in terms of their R^2 values between predicted and measured SCAL parameters, to equivalent predictors that were trained on the entire core dataset (consisting of 55 SCAL core plugs and associated wireline log data). In most cases the GFNN predictors in the training well had slightly higher R^2 values than the predictors trained on the entire core dataset.

2. When the GFNN predictors were tested throughout the cored intervals of an adjacent well in the same field (well A-01) and another well in a different oil field (well B-01) their performance was again better (in terms of the R^2 values) than the equivalent predictors trained on the entire core dataset in the training well.

3. When the GFNN predictors were tested only in the equivalent RGU intervals in the test wells A-01 and B-01 their performance was generally even better than when tested throughout the cored intervals of those wells, and showed some significantly higher R^2 values.

4. The conclusions above demonstrate that the GFNN approach is potentially very useful for making predictions of SCAL parameters in large intervals without the need to cut large sections of core, since the GFNN predictors were as good (generally better) than the predictors trained on the much larger entire cored interval dataset from the training well. This is very cost effective in terms of the minimal, but representative core material that is required, as well as the much reduced computer processing time.

CHAPTER SIX

Summary of New Aspects, Conclusions and Recommendations

6.1 Summary of New Aspects

The thesis contributed the following novel aspects:

- In this study the Global Hydraulic Elements (GHEs) have been used for the first time in the Nubian Sandstone reservoirs in six representative wells in Field A, B, and C in North Africa, and then was used to select minimal representative core plugs to train genetically focused neural network(GFNN) predictors.

- Using experimental measurements of routine and special core analysis with integrating by capillary pressure curves, a non linear relationship between resistivity index versus water saturation and mercury capillary pressure curves was obtained. These experiments were made for the first time to obtain a relation between pore size distribution and saturation exponent (n). The experimental results indicate that there is a good relation between resistivity and pore type depending on the pore size.

- Predicting diverse (SCAL) parameters using Neural network instead of collecting extensive core or performing SCAL measurements in all wells. Neural network predictors are potentially very useful in the present study due to the limited SCAL data for the studied well. The number of SCAL parameters were predicted using neural networks based on different combinations of wireline logs. The procedure firstly involved training the neural network predictors using data in a training well. These predictors were then applied to an adjacent test well in the same oil field, and to another test well in a different oil field.

- The present study developing a new methodology, termed genetically focused neural network (GFNN) approach and applies for the first time to the North African oil fields, and also for the first time uses this technique to predict some SCAL parameters such as true resistivity, resistivity index, saturation exponent,

and Amott-Harvey Wettability Index. The objective was to exploit the GFNN approach in conjunction with the genetic petrophysics approach for predicting the above parameters from wireline logs. In other words, the aim was to train neural networks only on data ideally from one RGU and then to predict SCAL parameters in other intervals.

6.2 Conclusions

The main conclusions drawn from the area investigated throughout the course of this study are summarized below.

6.2.1 Hydraulic Units (HUs) and Global Hydraulic Elements (GHEs) approach

Reservoir heterogeneity measurements by coefficient of variation, C_v, the Dykstra-Parsons coefficient,V_{DP}, and the Lorenz coefficient, Lc are consistent in all six wells A-01, A-02, A-03, B-01, C-01, and C-02 in the Nubian Sandstone Formation. Despite the most popular heterogeneity measure, V_{dp} (Lake,1989), the Lorenze plot not rely on best-fit procedures and the calculation error in Lc is less than in V_{DP}.The Lorenz plots from all the wells showed that 75-90% of the total flow is coming from global hydraulic elements (GHEs) 7 and 8, whilst most of the storage is in GHEs 2-6.

- A comparative study of six wells in the Nubian Sandstone Formation in three North African fields showed that for each well the number of global hydraulic elements (GHEs), using the template from Corbett and Potter (2004), was almost the same as the number of hydraulic units (HUs) using the classical methodology of Amaefule et al. (1993). Hence it appears that the arbitrary number of GHEs proposed by Corbett and Potter (2004) on the pre-determined template is about right for this particular study area. This reinforces the usefulness of the GHE approach, which rapidly allows one to compare porosity-permeability data from any reservoir on the same template without the need to make any calculations.

6.2.2 Measurements of routine and special core analysis

- Changes were observed in the formation resistivity factor (FF) and cementation exponent (m) due to ambient conditions and overburden pressure. The cementation exponent also decreased from GHE 5 to GHE 8. Changes were also observed in the saturation exponent (n) and water saturation (S_w) before and

after wettability measurements. Samples with an oil-wet tendency have a higher Archie saturation exponent values than samples with a uniform water-wet surface.

- By integrating capillary pressure curves with other routine and special core analysis (wettability test), the pores and porosity types (macro- and micro-porosity were quantified. A non linear relationship between resistivity index versus water saturation and mercury capillary pressure curves, and a good relation between resistivity after wettability test and type of pores, was observed for the Nubian sandstone samples.

- It's more accurate to applying wettability test in resistivity index relationship to identifying type of pores instead of using overburden pressure as Swanson (1985) was used.

- 4. High pressure mercury porosimeter is useful in determining the relative proportion of microporosity in reservoir rocks.

- Petrophysical characteristics such as porosity, recovery efficiency, water saturation, pore-throat size, pore-throat size distribution and threshold pressure are determined using mercury porosimetry. These characteristics determine the shape, slopes and plateau of the capillary-pressure curve. Analysis of the MICP curve is, therefore, important for various phases of reservoir production, especially secondary and tertiary recovery. These data may be evaluated in conjunction with additional SCAL and routine core petrophysical data in order to provide an accurate assessment of reservoir and/or seal potential.

6.2.3 Prediction of SCAL Parameters using Neural Network

a) Training well (A-02)

- Several good neural network SCAL parameter predictors (for true resistivity, R_t, resistivity index, RI, water saturation, S_w, saturation exponent, n, and Amott-Harvey Wettability Index, $I_{A/H}$) were generated using different combinations of standard wireline logs in the training well A-02. Predictors that included the bulk density wireline log (cases 1, 3 and 4) in these Nubian Sandstone reservoirs generated potentially better predictors according to the training well data. This

was subsequently proved by predictions in an adjacent test well and a further test well in a different oil field. Predictors trained on data at 1.0 ft depth spacing appeared to be better in the training well.

- A linear relationship existed between wettability index and the saturation exponent for data in the training well A-02.

b) Adjacent well A-01 and test well B-01

- The prediction the above SCAL parameters in an adjacent test well (A-01) and a further test well B-01 in a different oil field of Nubian Sandstone reservoirs of North Africa gave slightly better results in general for predictors trained on data at 0.5ft depth spacing than at 1.0 ft depth spacing.
- Plots of the water saturation versus resistivity index gave straight line results on a log-log crossplot, the slope of the line giving the saturation exponent (n). The predicted values of n matched the measured values extremely well in each of the test wells A-01 and B-01.

6.2.4 Prediction of SCAL parameters using (GFNN) approach

a) Training well (A-02)

- Genetically focused neural network (GFNN) predictors trained only on the short RGU dataset (consisting of 14 SCAL core plugs and associated wireline log data) from the training well A-02 were comparable, in terms of their R^2 values between predicted and measured SCAL parameters, to equivalent predictors that were trained on the entire core dataset (consisting of 55 SCAL core plugs and associated wireline log data). In most cases the GFNN predictors in the training well had slightly higher R^2 values than the predictors trained on the entire core dataset.

b) Adjacent well A-01 and test well B-01

- When the GFNN predictors were tested throughout the cored intervals of an adjacent well in the same field (well A-01) and another well in a different oil field (well B-01) their performance was again slightly better (in terms of the R^2 values) than the equivalent predictors trained on the entire core dataset in the training well. When the GFNN predictors were tested only in the equivalent RGU intervals in the test wells A-01 and B-01 their performance was generally

even better than when tested throughout the cored intervals of those wells, and showed some significantly higher R^2 values.

- This study demonstrated that the GFNN approach (which is very cost effective in terms of minimal, representative, core and reduced computer processing time) is potentially very useful for making predictions of SCAL parameters in large intervals without the need to cut large sections of core.

6.3 Recommendations

Following the successful GHE technique and GFNN approach further studies should be considered:

- The results of this study showing that the Global Hydraulic Elements (GHE) approach is useful for understanding the variation in petrophysical properties and it is important to extend this approach in the other fields (Abuttiful and Sarir oil field in the Sirt Basin, Libya and other new concessions in Kofra Basin which is still version).

- Three core plug sample has been selected from each Global Hydraulic Elements (GHEs) in this study for the laboratory work, special core analysis, porous plate to measure the saturation exponent, cementation factor and mercury injection to measure the capillary pressure, pore size distribution. Involving more than three core plugs sample will help to avoid the laboratory errors.

- Resistivity measurements were made at ambient conditions. It is recommended to perform these measurements at reservoir conditions. It is possible that significant errors might be introduced when resistivity measurements are not performed at reservoir conditions.

- Extending the prediction of SCAL parameters to in-situ reservoir conditions. Predictions could be made from a few representative SCAL measurements at reservoir pressures.

- Integration of more than one genetic unit in the training dataset either from one well or several different wells (i.e. a multiple representative genetic units

approach) within the field, to cover the whole range of possible lithologies and global hydraulic elements, should be considered.

- Potentially other SCAL parameters of interested could be predicted from the GFNN methodology.

REFERENCES

Abbaszadeh, M., Fujji, H. and Fujimoto F., 1996:"Permeability prediction by Hydraulic Flow Units – Theory and Applications", SPE 30158. SPE Formation Evaluation, December, pp.263-271

Abousraf E. M., 2000. "Petrophysics and Rock Mechanics: Effect of Different Sress States on Resistivity", Mphill thesis, Heriot Watt University, Edinburgh.

Ahmed, T., 2001. "Reservoir Engineering Handbook" Gulf Proffesional Publishing Company. ISBN 0-8841-57709.

AL-Towijri, A. H., 2004. prediction of residual three phase saturation using neural networks and minimal representative data. MSc. Thesis, Heriot- Watt University.

Ali, J.K., British Gas PLC. Neural Network: "Anew Tool for the petroleum Industry" SPE 27561. pp217-231

Amaeful, J.O, Altunbay, M., Tiab, D, Kersey, D.G., and Keelan, D.K., 1993. Enhanced Reservoir Description: Using Core and Log data to identify Hydraulic (Flow) Units and Predict permeability in uncored intervals/wells. SPE 26436, paper presented at 16th Ann. Teac. Conf. And Exhibition, Houston, TX.

Amyx, W. A., Daniel M. B., and Robert, L. W., 1960: "Petroleum Reservoir Engineering" McGraw-Hill Book Company, ISBN: 07-001600-3, p.610.

Aminian, K., SPE, Billgesu, I. H., SPE, Ameri, S., SPE, and Gil, E., SPE, West Virginia University. "A New Approach for Reservoir Characterisation" SPE 78710

Anderson, W.G., 1986 "wettability Literature survey-Part 2: Wettability Measurement" JPT, Nov., pp.1246-1262

Anderson, W.G., 1986 "wettability Literature survey-Part 3: The effect of wettability on elecrtical properties of porous media" JPT, Dec., pp.1371-1378

Archie, G.E., 1942 " The electrical resistivity log as an aid in determining some reservoir characterstics" Trans.AIME, vol.146, pp.54-62

Arpat, G.B., Gumrah, F., and Yeten, B., 1998. The neighborhood approach to prediction of permeability from wireline logs and linited core plugs analysis data using back-propagation artificial neural networks. Journal of Petroleum Science & Engineering, 20, 1-8.

Atkins, E. R. and Smith, G. H., March,1961, "The significance of Particle Shape in Formation Resistivity Factor –Porosity Relationships" Trans. AIME., p.285-291

Azizi M. I., 2003 Prediction of Residual Water Saturation Using Genetically Focused Neural Nets. Msc Thesis, Heriot Watt University, Edinburgh, p.70

Azizi M. I., and Potter D. K., 2004 Prediction of residual water saturation Using Genetically Focused Neural Nets. SPE 88457. SPE Asia Pacific Oil and Gas Conference and Exhibition, Austalia, October 2004.

Barr, F.T. and Weegar, A. A. 1972**:** Stratigraphic Nomenclature of the Sirte Basin, Libya, Petrol. Explor. Soc. Libya, p.1-179

Beard, D., and Weyl, P., 1973**:** Influence of Texture on porosity and permeability of Unconsolidated Sand, AAPG Bulletin, 57, pp. 349 -369.

Bennion, D., B., Thomas, F., B. and Bietz, R., F., 1996: "Determination of initial Fluid Saturations Using Traced Drilling Media" Hycal Energy Research Laboratory Ltd.99-8, pp2-11.

Bhatt, A., 2002: Reservoir properties from wireline logs using neural network. PhD Thesis, Norwegian Institute of science and Technology, p.3-5

Carman, P. C., 1937: Fluid Flow trough Granular Beds. Trans. Inst, Chem. Engrs., 15, pp150-166.

Corbett, P. W. M., Ellabad, Y., Mohammed, K., and Pososyaev, A., 2003. Global Hydraulic Elements – elementary petrophysics for reduced reservoir modeling. European Association of Geoscienist and Wngineers 65th Conference, Paper F-26 EAGE meeting, stavanger,June2-June 5.

Corbett, P. W. M., Jensen, J. L., and sorbi, K. S., 1998. A review of up-scaling and cross-scaling issues in core and log data interpretation and prediction: In Harvey, P. K. and Lovell, M. A., eds., Core-log integration: Geological Society Special Publication,136, 9-12.

Corbett, P. W. M., and Potter, D. K., 2004 Petrotyping- A basemap and atlas for Navigating Through Permeability and Porosity Data foe reservoir Comparison and permeability prediction. Proceedings of the 2004 International Symposium of the Society of Core Analysis, Abu Dhabi, United Arab Emirates (5-9 October, 2004), Paper SCA2004-30.

Corbett, P. W. M., and J. L., Jensen, " A Comparison of Small-Scale Permeability Measurements Methods for Reservoir Characterisation," presented at the PSTI Advances in Reservoir Technology Conference, Edinburgh, February 21-22, 1991.

Cosentino., L., 2001: " Integrated Reservoir Studies" Editions Technip, Paris, ISBN 2-7108-0797-1, p.310

Donaldson, E. C. and Siddiqui, T. K., 1989,"Relationship Between the Archie Saturation Exponent and Wettability" SPE, 16790-PA Formation Evaluation, Sept., pp.359-362

Du, Y., Weiss, W. W., Xu J., Balch R. S., 2003. Obtain an Optimum Artificial Neural Network Model for reservoir studies. SPE 84445 paper presented at the SPE Annual Technical Conference and Exhibition held in Denver, Colorado, U.S.A., 5-8 October 2003.

Dykstra, H. and R. L. Parsons, "The Prediction of Oil Recovery by Waterflood," Secondary Recovery of Oil in the United State, 2nd ed., New York: American Petroleum Institute, 1950, pp.160-174

Ellabad, Y. R., 2003**:** "A Method for Reservoirs Modelling Incorporating Geostatistical Models of Flow-Storage Elements Calibrated by Dynamic Tools. Nakhla oil field, Sirt Basin" PhD Thesis, Heriot-Watt University-Edinburgh, 290 p.

Elhakimi, I. F., 2006: "Petrophysical Parameter Prediction using Neural networks Trained on Wireline Logs, Core Probe and Core Plug Data" Mphi Thesis, Heriot Watt University-Edinburgh.112p.

Glanville, C. R., 1959 "Laboratory Study indicates significant effects of pressure on resistivity of reservoir rocks"JPT, Apr., pp.20-26.

Goda, H. M., Maier, H. R. and Behrenbruch, P., 2005. The Development of an Optimal Artificial Neural Network Model for Estimating Irreducible water saturation – Australian Reservoirs.SPE 93307.

Gunter, G. W. , SPE, Amoco EPTG; Finneran, J.M., Amoco EPTG, Hartman, D.J., and Miller, J. D., 1997**:** Early Determination of Reservoir flow Units Using an Integrated petrophysical Method, SPE 38679; pp. 1-8

Helle, H.B., Bhatt, A., and Ursin, B., 2001. Porosity and Permeability Prediction from wireline Logs Using ANN : A North sea Case Study. Geophysical Prospecting, 49, 431-444.

Helle, H. B. and Bhatt. A., 2002. Fluid Saturation from Well Logs Using Committe Neural Networks. Petroleum Geoscience, Vol. 8, 109-118.

Huang, Z., Shimeld, J., Williamson, M., and Katsube, J., 1996. Permeability Prediction With Artificial Neural Network Modeling in Venture gas Field, Offshore Eastern Canada. Geophysics, 61, 422-436.

Jamialahmadi, M., and Javadpour F. G., 2000. "Relationship of Permeability, Porosity and Depth Using an Artificial Neural Network". Journal of Petroleum Science & Engineering,26, 235-239.

Jensen, J. L.; Lake, L.W., Corbett, P. W. M. and Goggin, D. J., 2000: "Statistics for Petroleum Engineers and Geoscientists" Elsevier, ISBN: 0-444-50552-1, p127-136.

Jerauld, G.R.,SPE, Rathmell, J. J.,SPE,(1997) "Wettability and Relative Permeability of Brodhone Bay: A case Study in Mixed Wet Reservoirs" Arco E&p SPE 28576, Reservoir Engineering February, 1997. Technology pp.1-8.

John Shafer1 & John Neasham2, Mercury Porosimetry Protocol for Rapid Determination of Petrophysical and Reservoir Quality Properties, SCA 2000-21.

Khalifa, S. A., 2006: Identification of Global Hydraulic Elements in the Ordovician of H-field, Libya and Implication for Oil in place. H-field, Murzuq Basin NC 115. Unpublished MPhil Thesis, Heriot Watt University-Edinburgh, 116-120 p.

Killer G.V., 1953, "Effect of Wettability on Electrical Resistivity of Sand" Oil and Gas Journal, January,pp.62-65.

Killer G. V., 1989, "Electrical Properties" Practical Handbook of Physical Properties of Rocks and Minerals.

Kozeny, J., 1927: Uber kapillare letung des wassers im Boden. Sitzungsber Akad., Wiss, Wein, Math-Naturwiss, KL, 136, pp 271-306.

Lake, L. W. and Jenson J. L., 1991: "A Review of Heterogeneity Measures used in Reservoir Characterisation" SPE 20156 pp.1-25

Lake, L. W., 1989: "Enhanced Oil Recovery" Englewood Cliffs, N. J: Prentice Hall, pp.411-416.

Lamber, M. E., 1981: "A Statistical Study of Reservoir Heterogeneity," M. S. Thesis, The University of Texas at Austin.

Le, A. H. and Potter, D. K., 2003. "Genetically Focused Neural Nets for Permebility Prediction from Wireline Logs". European Association of Geoscientists and Enginners 65th Conference, Extended Abstract, Volume 1, paper F-28, EAGE meeting, Stavanger, June2-5

Le. A. H., 2004. Innovative Neural Network Approaches For Petrophysical Parameter Prediction. Ph.D. thesis, Heriot-Watt University, Edinburgh, p.30.

Longeron. D. G., Argand, M. J., and Feraud, J. P., 1986, "Effect of overburden pressure and the nature and microscopic distribution of fluids on electrical properties of

rock samples" SPE 15383, 61st Annual Technical Conference and Exhibition, New Orleans, October 5-8.

Lorenz, M. O., 1905: "Methods of Measuring the Concentration of wealth", J. Amer. Statistics Ass. (N.S), No. 70, pp.209-219.

Malki, H. A., Baldwin, J. L., and Kwari, M. A., 1996. Estimating permeability by use of Neural Networks in Thinly Bedded Shaly Gas Sands. SPE Computer Applications SPE31010.

Massa, D., and Delort, T., 1984, Evolution du Bassin de Syrte (Libya) du Cambrien au Cretace Basal: Bulletin Société Géologique de France, Series 7, v. 26, no. 6, p. 1087–1096

Mohaghegh, S., "Neural Network: What it Can Do For Petroleum Engineers," SPE 29219, JPT, pp42 Jan. 1995.

Mohaghegh, S., Arefl, R., Bilgesu L., Amerl S. and Rose D. 1995. Design and Development of an artificial Neural Network for Estimation of Formation Permeability. SPE 28237.p.151-154

Moissis, D.E. and Wheeler, M.F. 1990. Effect of the structure of the Porous Medium on Unstable Miscible Displacement, ed. J.H. Cushman, Dynamics of Fluids in Hirerarchical Porous Media, 243-271, San Diego, CA: Academic Press.

Moss, K. A., and Jing, D. X., Centre for Petroleum Studies.TH Huxley School of Environment, Earth Sciences and Engineering Imperial College of Science, Technology and Medicine London SW7 2BP "Resistivity Index and Capillary Pressure Characteristics of reservoir Sandstone in different wettability Conditions"SCA-9945p.1-13

Mungan, N. And Moore, E. J., 1968, "Certain wettability effects on electrical resistivity in porous media" The Journal of Canadian Petroleum Technology, January-February.p20-25

Noreddin Issaa A. Mousa " Identification of Global Hydraulic Elements in the Lower Cretaceous of 3V Area, Sirt Basin Libya and Implication for Saturation Exponent Distribution in the Nubian Sandstone Formation." Mphil degree, Heriot Watt University, June 2008

Osborne, D. A., 1992. Neural Networks provide more accurate reservoir permeability. Oil & Gas Journal, Sep.,p.80-83

Pittman, E. D., 1971, "Microporosity in Carbonate Rocks" AAPG Bull., Vol. 55, No.10 (October,1971), pp.1873-1881.

Potter, D. K., Le, A. H., Corbett, P. W. M., McCann, C., Assefa, S., Astin, T., Sothcott, J., Bennett, B., Larter, S., and Lager, L., 2003. Genetic petrophysics approach to core analysis – application to shoreface sandstone reservoirs. Proceedings of the 2003 International Symposium of the society of Core Analysts, paper SCA2003, 421-433.

Potter, D. K., Wright, J. M., and Corbett, W. M., 1999. "Agenetic petrophysics approach to facies and permeability prediction in a PEGASUS well". European Association of Geoscientists and Engineers 61st Conference, Extended abstract, Volume 1, Paper 2-53, EAGE meeting, Helsinki, June 8-11.

Pnisetti, M., 2000: "Integrated Numerical well Test Modelling in Fluvial Reservoir", PhD Thesis. Heriot Watt University, Edinburgh.

Rasmus, J. C., 1987, "A Summary of The Effects of Various Pore Geometries and Their Wettabilities on Measured and In-Situ Values of Cementation and Saturation Exponents" The log Analyst, March-April,pp.151-164

Rathmell, J. J., Braun, P. H. and Perkins, R. K. "Reservoir Waterflood Residual Oil Saturation from Laboratory tests." Soc.Petrol. Eng. JPT, Vol. 25, feb. 1973

Ringen J. K., Halvorsen C., Lehne K. A., and Holand, 1999. "Reservoir Water Saturation Measured On Cores; Cases Histories and Recommendations" Proceedings of the 1999 International Symposium of the Society of Core Analysts, Colorado, U.S.A, SCA paper 9906.

Schmalz, J. P. And H. S. Rahme, " The Variation of Waterflood Performance with Variation in Permeability Profile," Producers Monthly, 14 (July1950), p.9-12

Schon, J. H., 1996, "Physical Properties of Rocks: Fundamentals and Principles of petrophysics" Volume 18, Pergamon, ISBN: 0-0804-1008-1

Serra, O., 1984. Fundamentals of Well-Log Interpretation (Vol. 1): The Acquisition of Logging Data*:* Dev. Pet. Sci., 15A: Amsterdam (Elsevier).

Spearing, M., Allen, T., McAuley, G., 2001. Review of the Winland R35 Method for net pay definition and its application in low permeability sands. *Proceedings of the 2001 International Symposium of the Society of Core Analysts*, paper SCA 2001-63.

Swanson, B. F., 1985, "Microporosity in Reservoir Rocks: Itis Measurements and Influence on Electrical Resistivity" Trans. SPWLA,26th Ann.Logg.Symp., June,17-20.p42-52.

Sweeny, S. A. and Jenning, H. Y., 1960 "The Electrical Resistivity of Prefentially water-Wet and Prefentially Oil-Wet carbonate Rock" Producers Monthly,may,pp.29-32

Tiab, J., and Donaldson, E. C., 1996. Petrophysics- Theory and Practice of Measuring Reservoir Rock anf Fluid Transport Properties. Gulf Publishing Company, Huston, Texas, U.S.A. p.286

Toomarian, N. B., "Oil Reservoir Properties Estimation Using Neural Network" centre for Integrated Microsystems, California Institute of Technology. CONF-970348

Van Houten, F.B., 1980**:** Latest Jurassic Early Cretaceous regressive facies, North East Africa craton. Bull. Am. Assoc. Petrol. Geol., 64 (6), pp. 857-867.

Washburn, E.W. (1921) : "Note on a method of determining the distribution of pore size in a porous material" Proceedings of the National Academy of Science, v. 7, p.115-116

Winsaur, W. O., Shearin, H. M., Masson, P. H., and Williams, W., 1952, "Resistivity of Brine-saturated Sands in Relation to Pore Geometry" AAPG, Vol.36, No. 2, Feb., pp.253-277

Wong, P. M., Henderson, D. J., and Brooks, L. J., 1997. Reservoir permeability determination from well logs data using artificial neural networks: an example from the Ravva field, offshore India. SPE 38034.

Wong, P. M., Jian, F. X., and Taggat, I. J., 1995. A eritical Comparison of neural networks and discriminant analysis in lithofacies, porosity and permeability predictions. Journal of Petroleum Geology, 18, 191-206.

Wyble, D. O., 1958, "effect of Applied Pressure on the Conductivity, Porosity, and Permeability of Sandstones" Trans. AIME, Vol.213, pp.430-432.

Zhang, Y., Salisch, H. A., and Arns., C., 2000. Permeability evaluation in the glauconiterich formation in the Carnarvon basin, western Australia. Geophysics, 65, 46-53

Table A-1. Conventional data for 94 samples of Nubian Sandstone Formation.

Sample #	Porosity (%)	Grain density (g/cc)	Permeability (mD)	Well Name
3	10.39	2.67	337.51	A-01
6	10.01	2.65	62.96	A-01
8	11.11	2.65	129.32	A-01
10	9.01	2.65	34.11	A-01
11	9.12	2.65	61.11	A-01
14	11.20	2.66	35.87	A-01
46	12.52	2.65	187.27	A-01
47	9.30	2.65	69.64	A-01
48	12.29	2.65	151.24	A-01
49	9.69	2.65	88.63	A-01
50	11.10	2.65	228.74	A-01
51	9.39	2.65	41.86	A-01
52	11.26	2.64	196.95	A-01
53	11.16	2.65	297.71	A-01
54	11.22	2.65	111.80	A-01
55	12.41	2.65	321.25	A-01
31	11.12	2.67	24.34	A-02
81	11.01	2.65	10.24	A-02
83	9.56	2.65	27.73	A-02
93	12.35	2.65	126.41	A-02
94	12.32	2.65	107.46	A-02
119	13.95	2.65	87.00	A-02
123	12.76	2.65	118.09	A-02
127	14.98	2.66	277.50	A-02
128	14.23	2.65	244.8	A-02
162	10.97	2.60	7.997	A-02
165	10.39	2.60	33.26	A-02
232	12.35	2.60	31.28	A-02

Sample #	Porosity (%)	Grain density (g/cc)	Permeability (mD)	Well Name
233	12.54	2.58	75.65	A-02
239	10.48	2.65	10.64	A-02
356	15.60	2.66	283.57	A-02
357	11.86	2.72	58.65	A-02
401	11.43	2.66	54.02	A-02
12	10.44	2.64	13.44	A-03
15	12.17	2.65	12.55	A-03
18	9.65	2.65	22.49	A-03
20	11.19	2.65	23.26	A-03
24	8.01	2.65	9.91	A-03
30	11.86	2.65	21.35	A-03
37	12.70	2.66	489.64	A-03
38	12.36	2.65	488.83	A-03
40	14.26	2.66	883.96	A-03
42	11.71	2.65	4.90	A-03
57	12.17	2.65	29.29	A-03
68	12.39	2.65	73.72	A-03
72	13.94	2.65	340.57	A-03
14	15.18	2.64	320.16	B-01
18	14.59	2.65	1146	B-01
52	18.15	2.65	569.64	B-01
61	15.74	2.64	373.56	B-01
75	9.08	2.64	3.182	B-01
126	15.73	2.65	310.60	B-01
39	15.85	2.65	575.3	C-01
40	14.89	2.65	881.5	C-01
41	15.34	2.65	666.7	C-01
42	12.98	2.64	579.6	C-01
45	14.27	2.66	376.5	C-01
26	18.98	2.65	1519.5	C-02
27	9.65	2.64	2.364	C-02
28	9.72	2.65	2.413	C-02
29	16.28	2.65	76.25	C-02
47	16.24	2.64	318.83	C-02
48	11.87	2.64	73.445	C-02

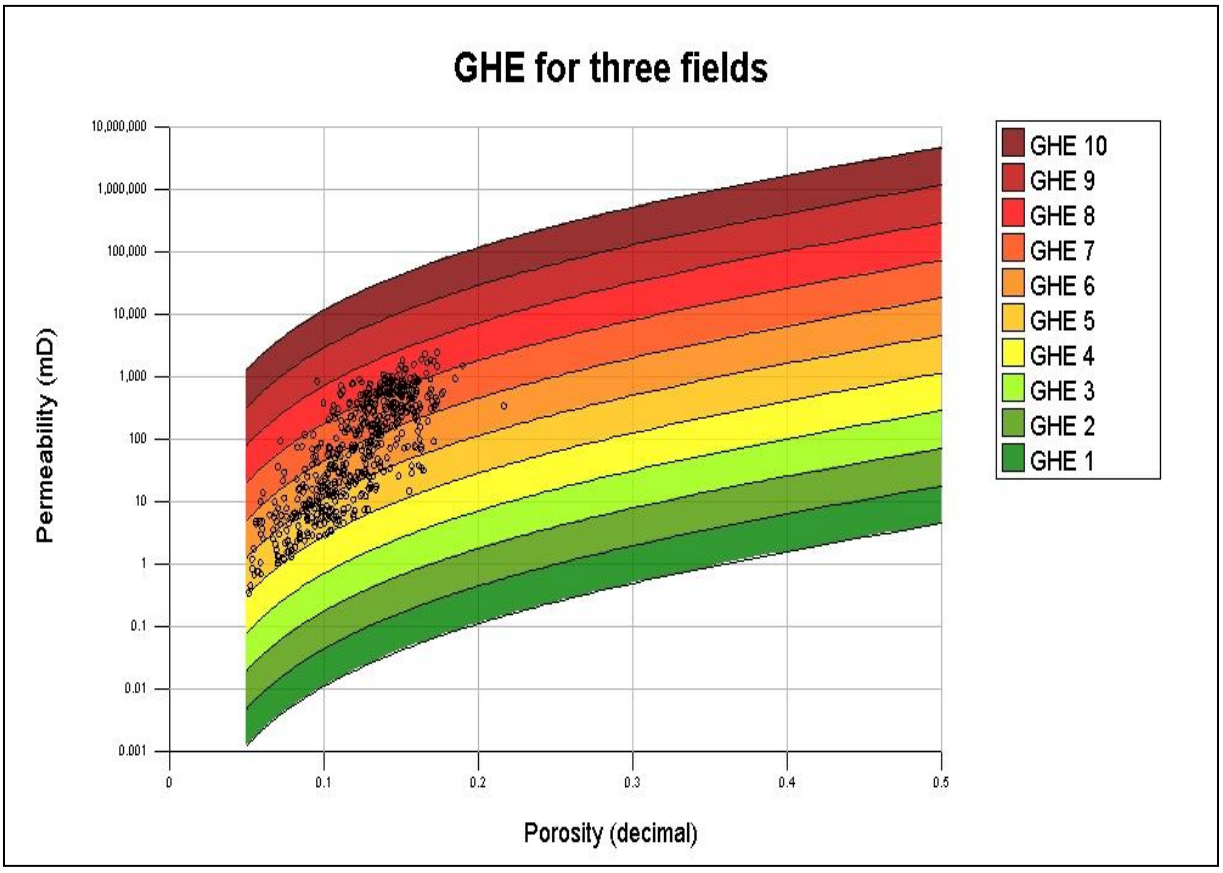

Figure A1. Global hydraulic element porosity-permeabilty crossplot for conventional core analysis from three different wells.

Table A2. Porosity, Permeability values of selected Samples from the studied wells.

Sample No.	Well Name	Ø (%)	K(mD)
15	A-03	12.17	12.55
29	C-02	17.38	69.86
42	A-03	11.71	4.90
24	A-03	8.01	9.91
47	C-02	17.91	279.72
83	A-02	9.56	27.73
10	A-01	9.01	34.11
41	C-01	15.34	660.45
123	A-02	12.76	118.09
3	A-01	10.39	337.51
18	B-01	14.59	1146.0
53	A-01	11.16	297.71

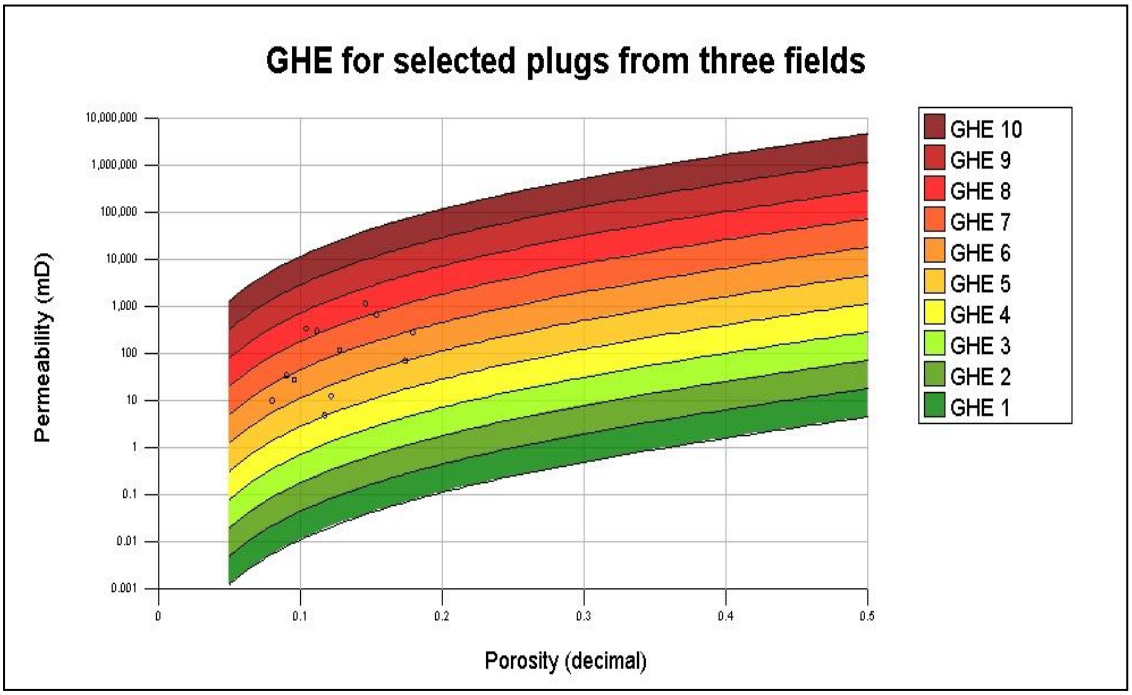

Figure A2. Global hydraulic element porosity-permeability crossplot for the twelve selected representative samples.

Table A3. Summary of resistivity index data for sample # 10.

Sample # 10 (Before wettability)		Sample #10 (After wettability)	
RI	**Sw**	**RI**	**Sw**
1.0000	1.0000	1.0000	1.0000
1.1976	0.9227	1.3639	0.9100
2.5298	0.6018	4.4340	0.6524
6.9144	0.3247	7.4847	0.5700
8.0369	0.3014	13.7617	0.3814
8.4556	0.2857	15.0369	0.3300
11.1344	0.2500	18.8258	0.2987
12.4389	0.2350	19.7097	0.2847
14.3279	0.2258	22.2617	0.2741

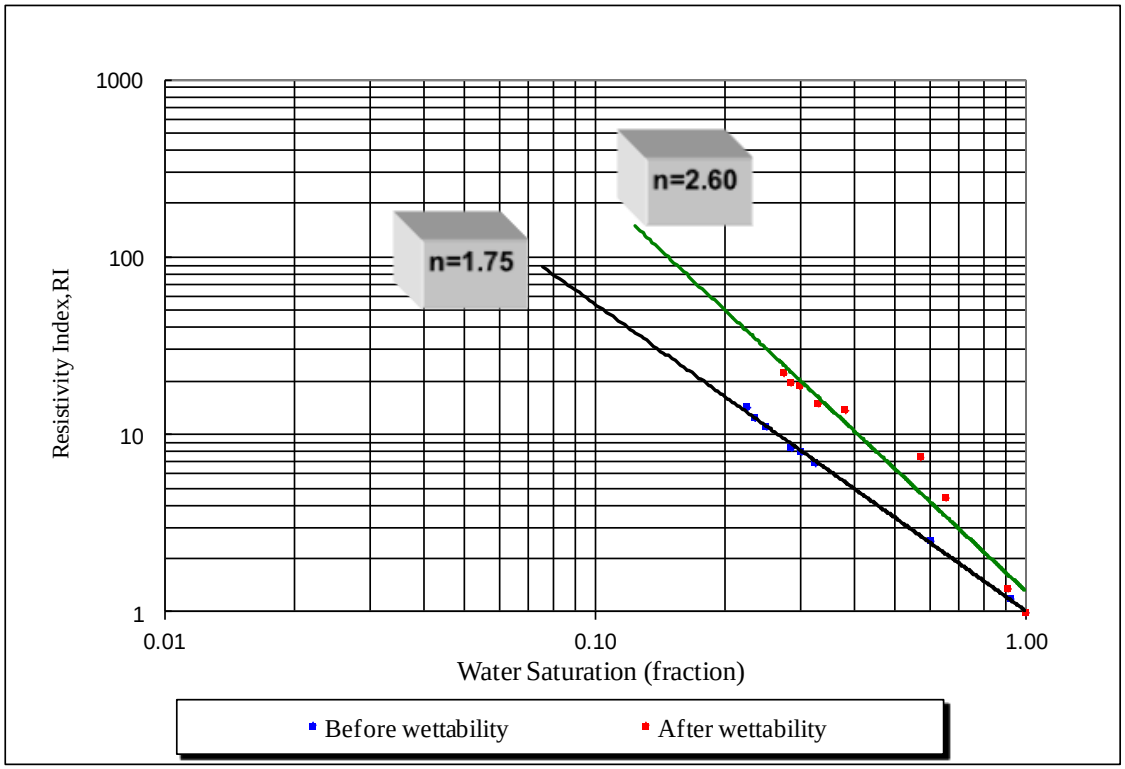

Figure A3. Resistivity index vs. water saturation for sample #10 before and after wettability measurement.

Table A4. Summary of resistivity index data for sample #15.

Sample # 15 (Before wettability)		Sample # 15 (After wettability)	
RI	**Sw**	**RI**	**Sw**
1.0000	1.0000	1.0000	1.0000
1.4282	0.8647	1.5234	0.8731
1.7518	0.7580	2.1897	0.7700
2.1014	0.6974	2.7543	0.7100
4.1860	0.5024	5.1328	0.5723
5.9193	0.4215	7.5428	0.4815
8.0589	0.3587	16.0771	0.3800
8.8546	0.3325	20.0453	0.3345
12.7923	0.3002	21.8815	0.3100

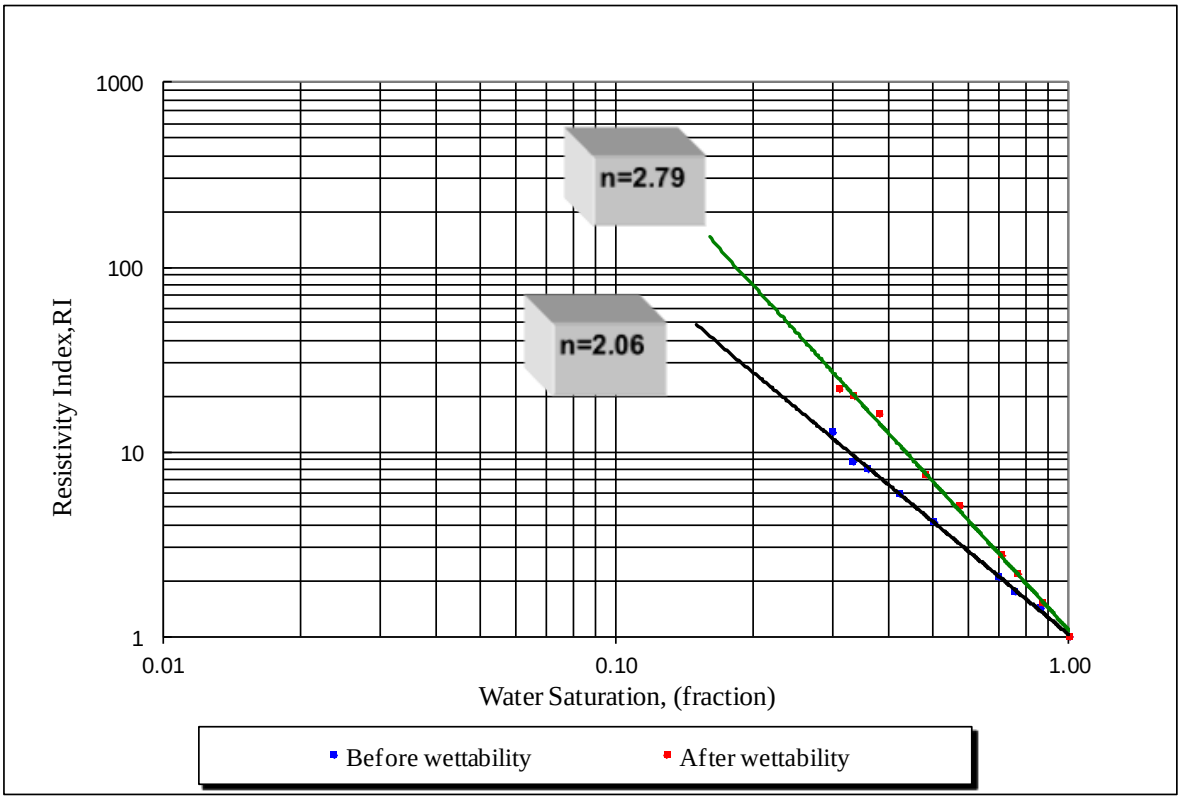

Figure A4. Resistivity index versus water saturation for sample #15 before and after wettability measurement .

Table A 5. Summary of resistivity index data for sample #24

Sample # 24 (Before wettability)		Sample # 24 (After wettability)	
RI	**Sw**	**RI**	**Sw**
1.0000	1.0000	1.0000	1.0000
1.6122	0.8100	1.7196	0.8210
1.8310	0.7500	1.9775	0.7631
2.2954	0.6500	2.4566	0.6823
4.0052	0.4869	4.4253	0.5300
5.5018	0.4125	6.3365	0.4200
8.6365	0.3200	10.0875	0.3300
10.8244	0.2837	12.7283	0.3000
11.9990	0.2731	14.8164	0.2800

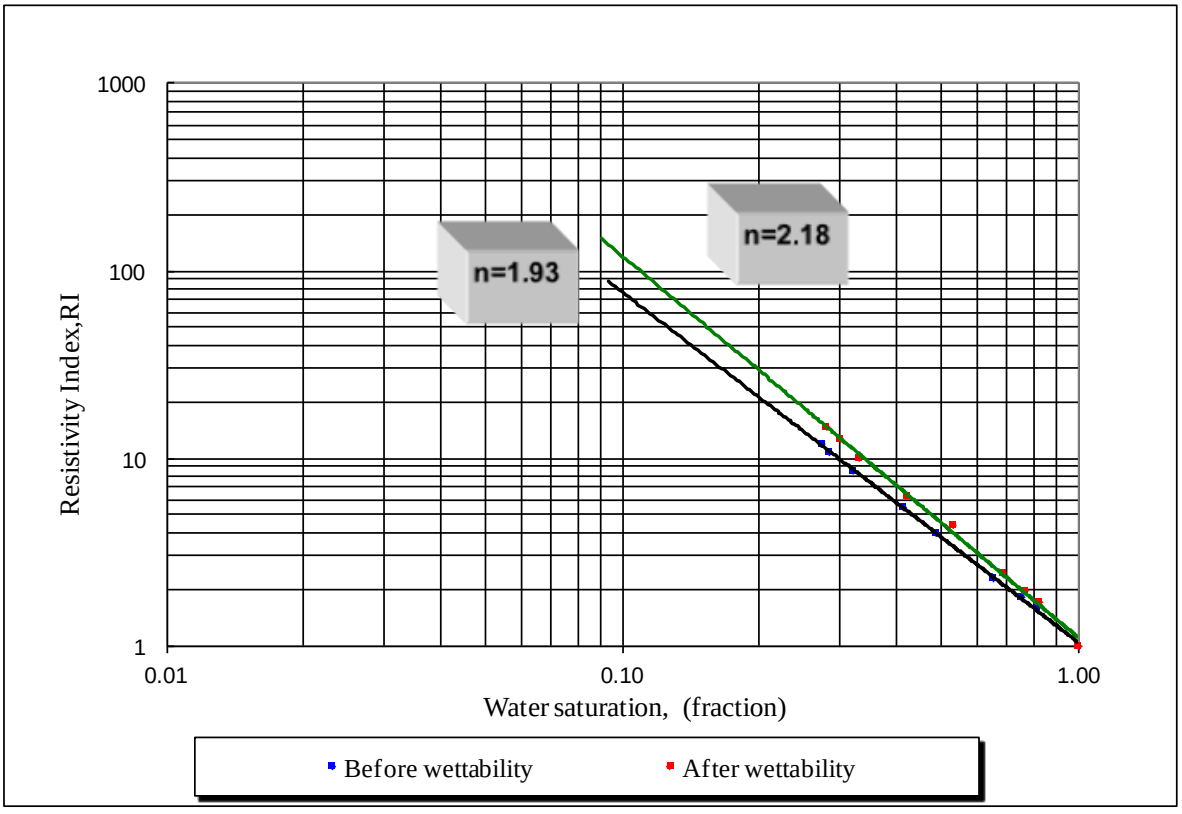

Figure A5. Resistivity index vs.water saturation for sample #24 before and after wettability measurement

Table A6. Summary of resistivity index data for sample# 29

Sample # 29 (Before wettability)		Sample # 29 (After wettability)	
RI	**Sw**	**RI**	**Sw**
1.0000	1.0000	1.0000	1.0000
1.3315	0.8913	1.4240	0.8621
1.7580	0.7324	1.6635	0.8300
2.0805	0.6524	2.2192	0.7540
4.8783	0.4200	12.4862	0.4325
9.4013	0.2854	15.6297	0.3584
14.0678	0.2201	18.9421	0.3000
17.1786	0.2000	22.0528	0.2876
19.3780	0.1964	25.2825	0.2710

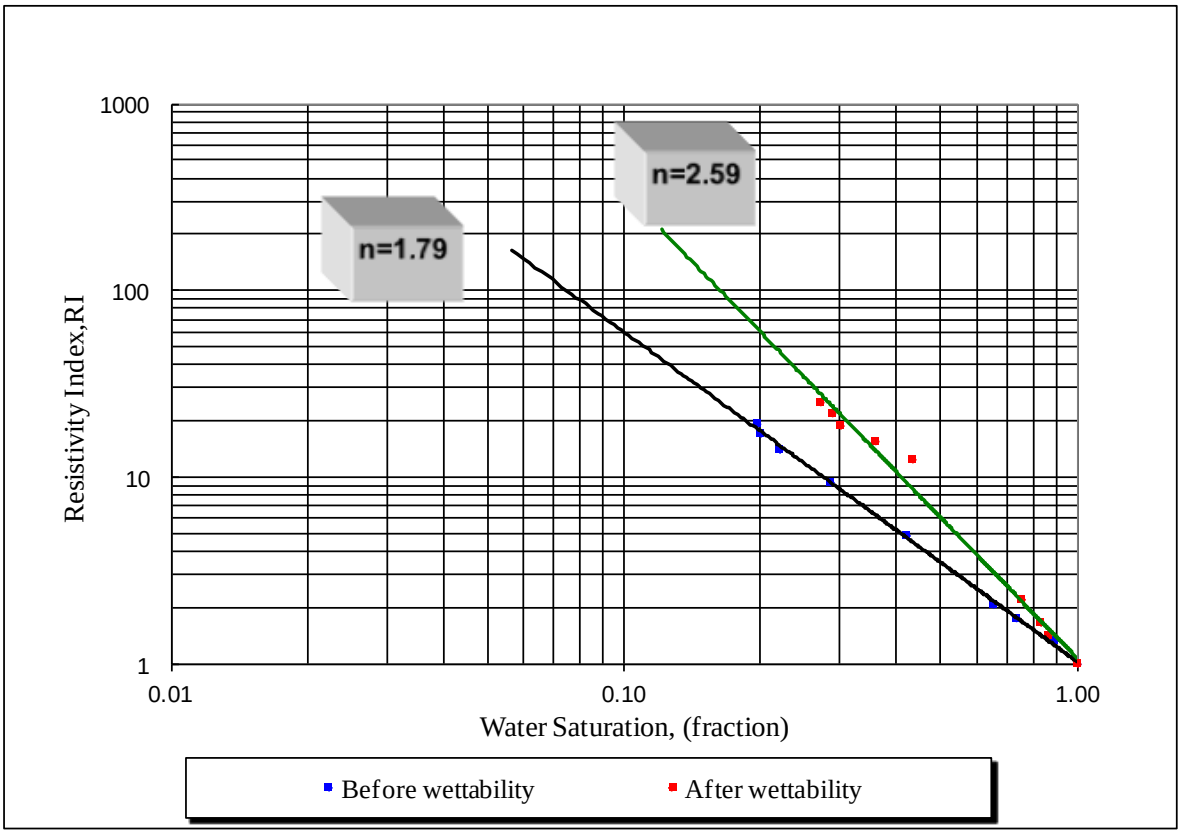

Figure A6 . Resistivity index versus water saturation for sample #29 before and after wettability measurement

Table A7. Summary of resistivity index data for sample #41

Sample # 41 (Before wettability)		Sample # 41 (After wettability)	
RI	**Sw**	**RI**	**Sw**
1.0000	1.0000	1.0000	1.0000
1.3525	0.8457	1.4769	0.8500
3.1305	0.5587	3.4960	0.6300
7.6287	0.3458	9.0445	0.4521
13.1817	0.2547	18.6659	0.3400
20.4168	0.1935	32.1729	0.2547
42.4244	0.1362	48.8705	0.2014
52.3850	0.1200	57.0155	0.1874
68.2920	0.1025	63.2951	0.1754

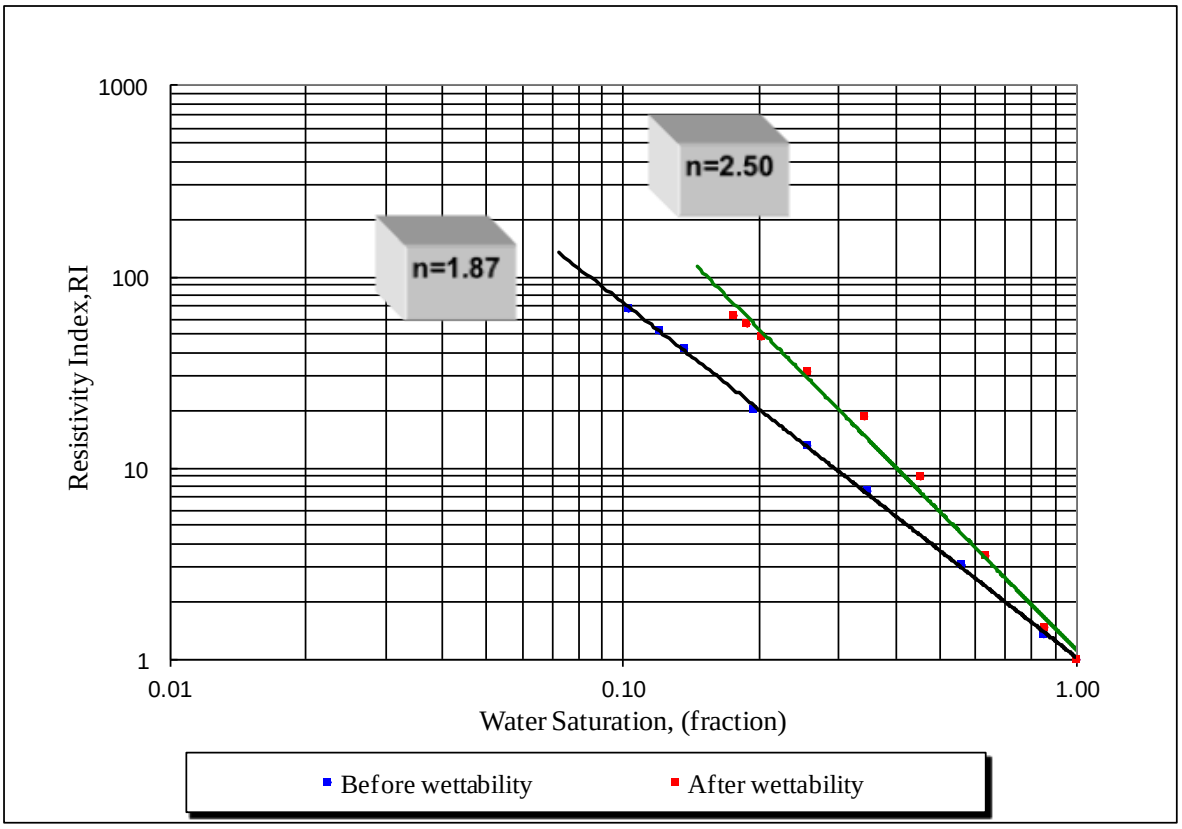

Figure A7. Resistivity index versus water saturation for sample # 41 before and after wettability measurement.

Table A 8. Summary of resistivity index measurement for sample # 42.

Sample # 42 (Before wettability)		Sample # 42 (After wettability)	
RI	**Sw**	**RI**	**Sw**
1.0000	1.0000	1.0000	1.0000
1.4465	0.8500	1.5953	0.8400
2.2286	0.6814	2.7179	0.7000
2.4500	0.6524	3.3047	0.6600
4.0637	0.5321	4.5647	0.5800
4.9563	0.4796	6.9839	0.5180
6.4612	0.4235	9.2872	0.4568
7.2019	0.4025	11.1674	0.4315
7.8628	0.3936	13.0705	0.4120

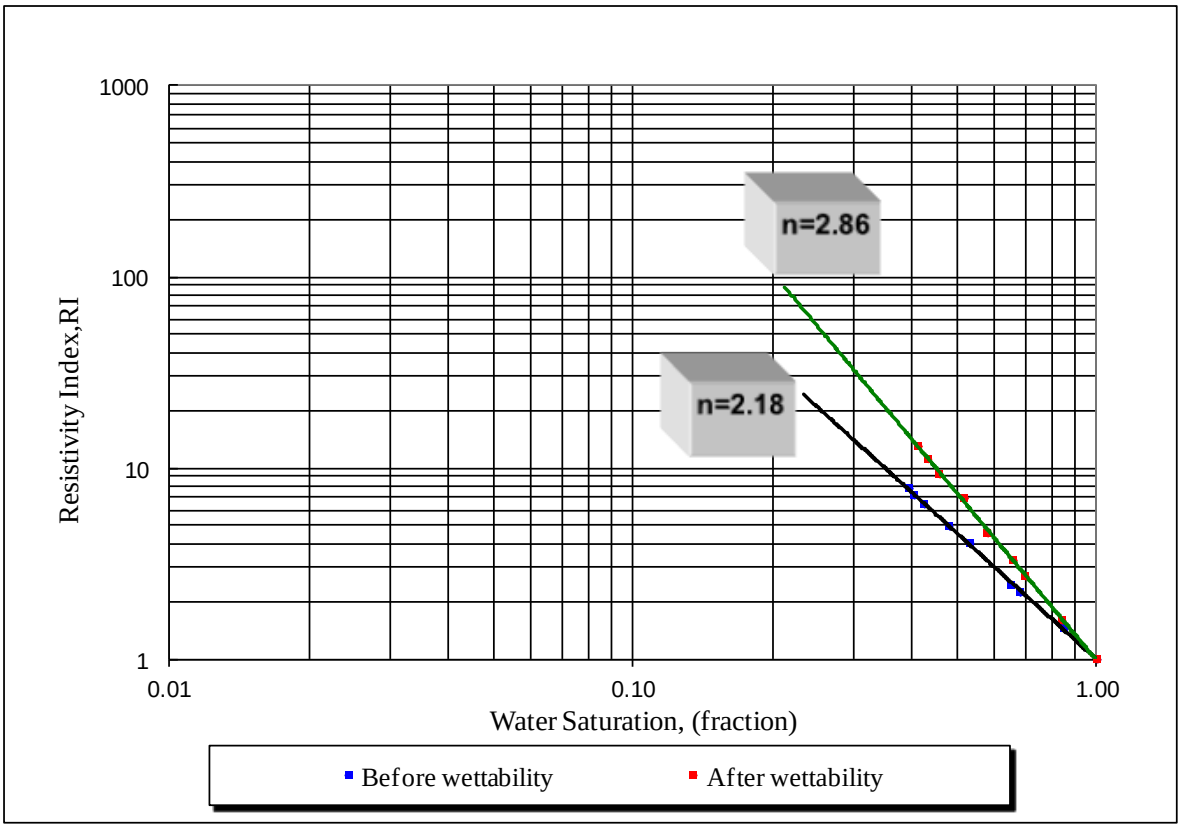

Figure A8. Resistivity index versus water saturation for sample# 42 before and after wettability measurement.

Table A9 Summary of resistivity index measurement for sample #47.

Sample # 47(Before wettability)		Sample # 47(After wettability)	
RI	**Sw**	**RI**	**Sw**
1.0000	1.0000	1.0000	1.0000
1.3727	0.8630	1.5467	0.8900
2.3715	0.6233	2.7667	0.6750
5.0543	0.4269	6.4215	0.5102
11.9406	0.2715	16.5954	0.3556
25.3908	0.1896	23.4865	0.3025
40.6626	0.1438	47.9334	0.2314
45.5720	0.1311	55.6599	0.2105
55.5978	0.1243	70.7815	0.1934

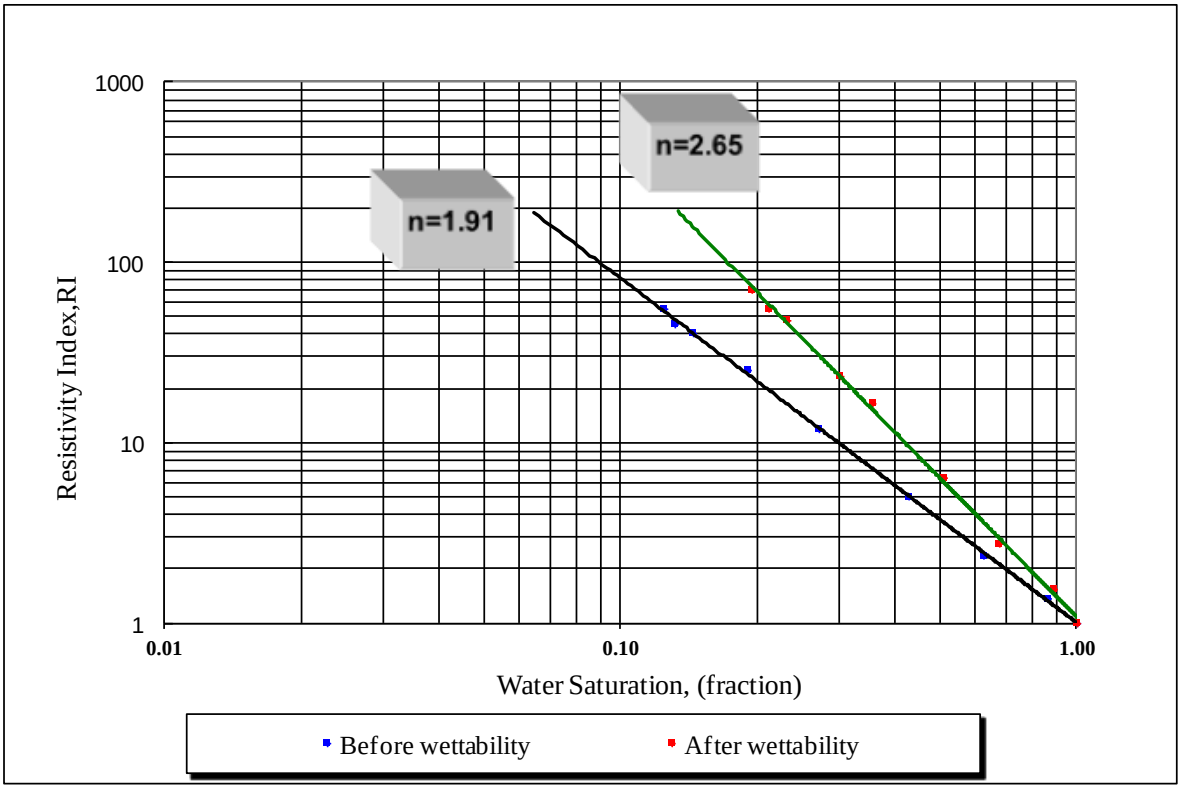

Figure A9. Resistivity index versuss. water saturation for sample # 47 before and after wettability measurement.

Table A10. Summary of resistivity index measurement for sample #53.

Sample # 53(Before wettability)		Sample # 53(After wettability)	
RI	**Sw**	**RI**	**Sw**
1.0000	1.0000	1.0000	1.0000
1.5577	0.7725	1.7308	0.8124
3.5936	0.4875	4.5887	0.5628
8.6346	0.2975	10.3151	0.4200
12.7277	0.2365	19.9861	0.2967
19.3620	0.1857	24.5977	0.2587
35.4654	0.1354	36.3926	0.2135
42.6280	0.1238	45.3633	0.2001
43.8682	0.1200	54.3224	0.1879

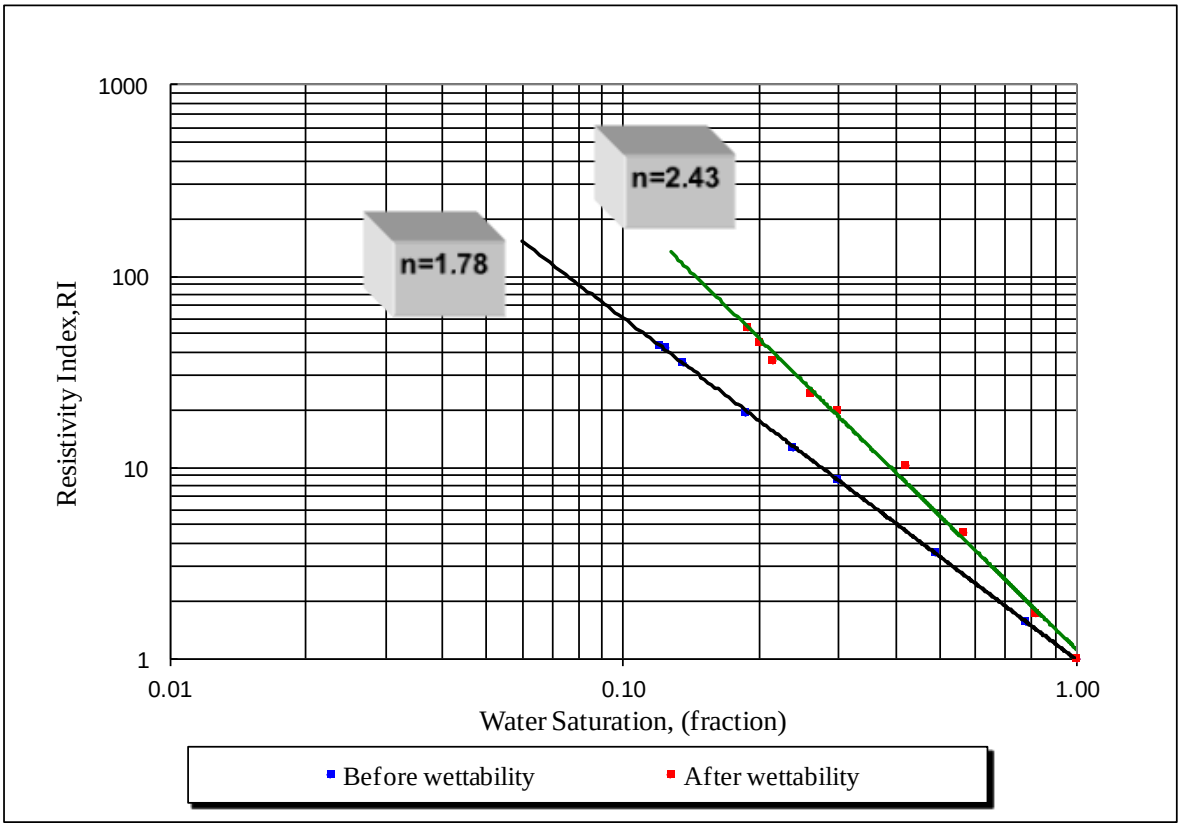

Figure A10. Resistivity index versus water saturation for sample# 53 before and after wettability measurement.

Table A11. Summary of resistivity index measurement for sample # 83.

Sample # 83 (Before wettability)		Sample # 83(After wettability)	
RI	**Sw**	**RI**	**Sw**
1.0000	1.0000	1.0000	1.0000
1.2552	0.9095	2.1367	0.7852
2.8524	0.5874	4.2488	0.6214
4.8101	0.4587	5.3355	0.5320
6.8689	0.3825	7.1195	0.4521
8.4584	0.3365	8.9345	0.4089
10.6209	0.2931	12.2910	0.3514
12.4473	0.2715	14.7116	0.3214
14.7929	0.2568	17.9892	0.2987

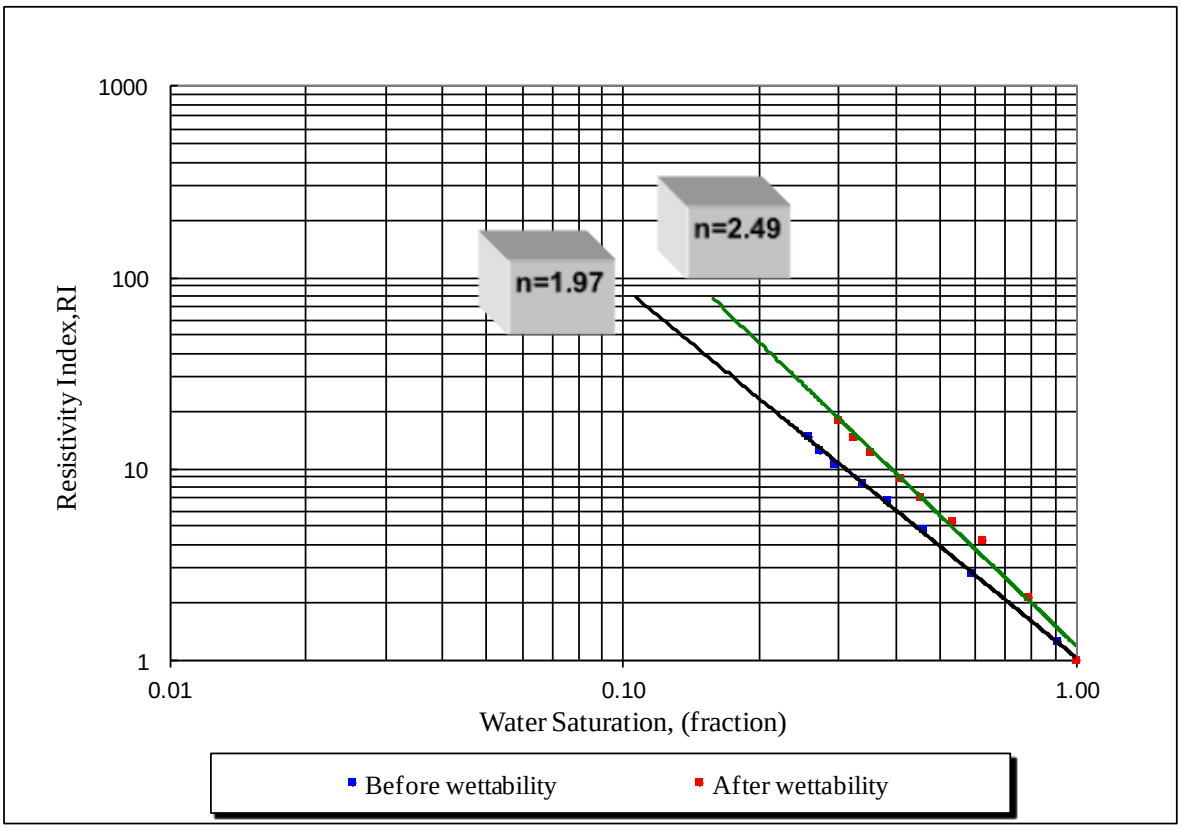

Figure A11. Resistivity index versus water saturation for sample # 83 before and after wettability measurement.

Table A12. Summarise resistivity index data for sample #123.

Sample # 123(After wettability)		Sample # 123(Before wettability)	
RI	**Sw**	**RI**	**Sw**
1.0000	1.0000	1.0000	1.0000
1.5504	0.7845	2.5840	0.6817
2.6413	0.5586	3.3330	0.6120
5.5371	0.3765	5.8404	0.4587
9.4801	0.2758	8.4239	0.3915
14.3353	0.2147	11.4422	0.3325
23.0714	0.1625	18.9185	0.2610
28.3053	0.1436	25.8927	0.2200
32.0494	0.1368	32.3790	0.2012

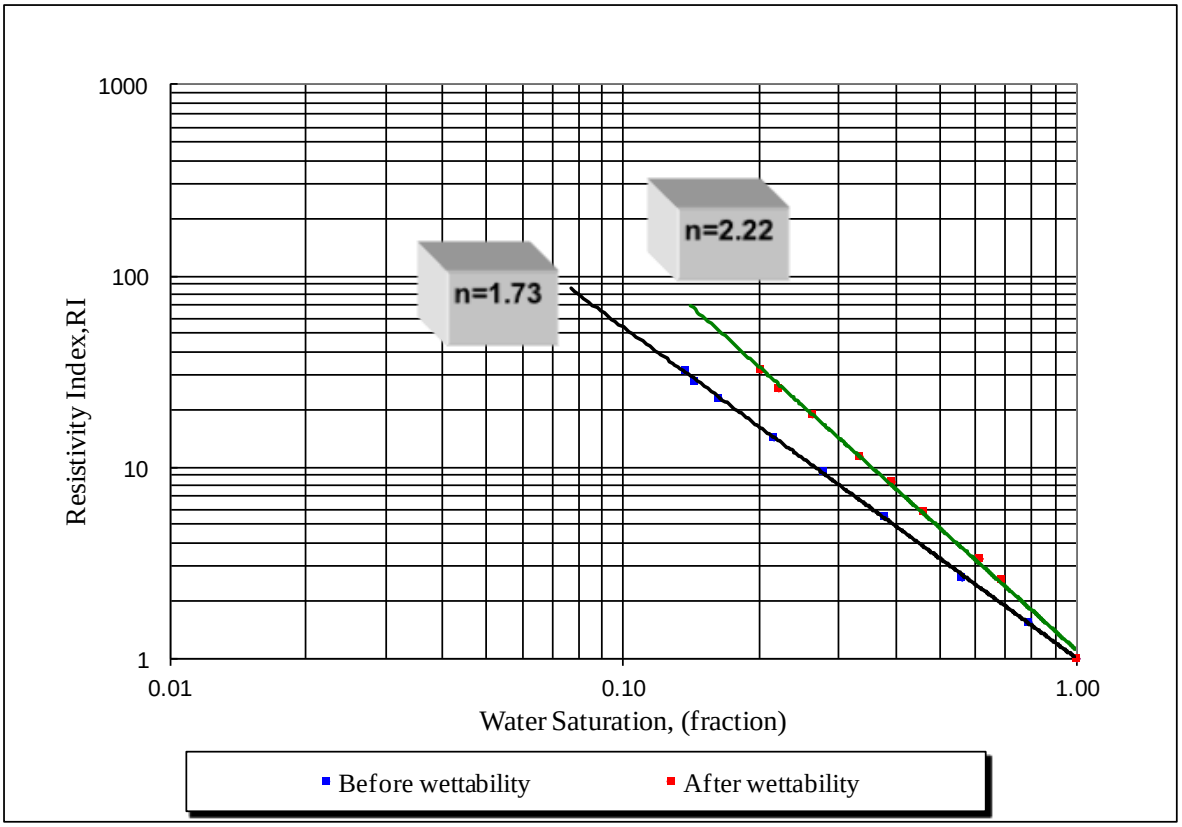

Figure A12. Resistivity index versus water saturation for sample # 123 before and after wettability measurement.

Table A13 . Wettability measurements results (Amott Method).

Sample #	Iw	Io	IA/H =Iw-Io	Type of wettability
03	0.0750	0.2000	-0.1250	Strongly Intermediate wettability
10	0.0320	0.4010	-0.3690	Oil-Wet
15	0.1510	0.3540	-0.2030	Strongly intermediate Wettability
18	0.2105	0.1466	0.0639	Intermediate Wettability
24	0.2220	0.3157	-0.0937	Intermediate Wettability
29	0.2850	0.1430	0.1420	Intermediate Wettability
41	0.1000	0.1300	-0.0300	Intermediate Wettability
42	0.0530	0.2560	-0.2030	Strongly intermediate Wettability
47	0.1700	0.2000	-0.0300	Strongly intermediate Wettability
53	0.0950	0.2000	-0.1050	Strongly intermediate Wettability
83	0.0340	0.3100	-0.2760	Strongly intermediate Wettability
123	0.1070	0.2120	-0.1050	Strongly intermediate Wettability

Mercury Injection Capillary Pressure and Pore Size Distribution

Table A14. MICP results of sample # 10**.**

Well :	**A1-Libya**
Sample # :	**10**

Core Sample Data	
Pore vol. (cc)	0.154
Porosity (%)	8.8
Air Perm. (mD)	34.11

Experimental Values	
Threshold Pressure (psi)	10.483
Dry Weight (gm)	4.211
Sample Depth (ft)	15019

Pressure Psia	Cycle	Cum. Hg Sat. Pore Vol., %	Wetting Phase (Sw) Pore Vol., %	Incr. Hg Sat. Pore Vol., %	rp microns
10.4835	D	0.000	100.000	0.000	10.174
12.9759	D	9.597	90.403	9.597	8.220
15.9713	D	18.242	81.758	8.645	6.678
20.0179	D	26.386	73.614	8.144	5.328
25.9937	D	32.918	67.082	6.532	4.103
35.9698	D	38.071	61.929	5.153	2.965
39.2712	D	39.061	60.939	0.991	2.716
44.2156	D	39.918	60.082	0.857	2.412
52.3657	D	42.599	57.401	2.681	2.037
71.2496	D	45.046	54.954	2.447	1.497
86.9137	D	47.094	52.906	2.048	1.227
111.2993	D	49.308	50.692	2.213	0.958
136.3898	D	51.094	48.906	1.787	0.782
172.2394	D	52.876	47.124	1.782	0.619
217.1787	D	54.960	45.040	2.084	0.491
267.2498	D	56.748	43.252	1.788	0.399
326.6384	D	58.240	41.760	1.492	0.327
415.6652	D	59.570	40.430	1.330	0.257
516.5950	D	60.430	39.570	0.860	0.206
635.9481	D	61.134	.866	0.704	0.168
800.5975	D	61.866	3838.134	0.733	0.133
986.5861	D	62.554	37.446	0.687	0.108
1197.6113	D	63.073	36.927	0.519	0.089
1496.3926	D	63.696	36.304	0.623	0.071
1895.8596	D	64.347	35.653	0.651	0.056

Pressure Psia	Cycle	Cum. Hg Sat. Pore Vol., %	Wetting Phase (Sw) Pore Vol., %	Incr. Hg Sat. Pore Vol., %	rp microns
2343.8408	D	64.953	35.047	0.606	0.0455
2894.4695	D	65.546	34.454	0.594	0.0369
3593.2529	D	66.116	33.884	0.570	0.0297
4484.1294	D	66.116	33.884	0.000	0.0238
5582.3975	D	66.507	33.493	0.391	0.0191
6883.0942	D	66.709	33.291	0.202	0.0155
8584.2500	D	67.027	32.973	0.318	0.0124
10581.6436	D	67.214	32.786	0.187	0.0101
13183.2295	D	67.260	32.740	0.046	0.0081
14782.0908	D	67.330	32.670	0.070	0.0072
16379.5244	D	67.396	32.604	0.066	0.0065
19981.4590	D	67.525	32.475	0.129	0.0053
24991.5703	D	67.701	32.299	0.176	0.0043
29991.4043	D	67.701	32.299	0.000	0.0036
34988.2461	D	67.715	32.285	0.014	0.0030
39988.9141	D	67.715	32.285	0.000	0.0027
44990.3359	D	67.715	32.285	0.000	0.0024
49986.3906	D	67.766	32.234	0.051	0.0021
54993.6016	D	67.766	32.234	0.000	0.0019
59853.5938	D	67.766	32.234	0.000	0.0018
46097.3008	I	66.959	33.041		
35508.0234	I	66.959	33.041		
27307.9531	I	66.959	33.041		
21010.9063	I	66.959	33.041		
16007.0928	I	66.959	33.041		
12411.96	I	66.959	33.041		
9611.19629	I	66.959	33.041		
7313.36719	I	66.959	33.041		
5716.21631	I	66.959	33.041		
4029.02441	I	63.695	36.305		
3301.15015	I	63.346	36.654		
2591.625	I	63.205	36.795		
1995.72119	I	63.014	36.986		
1502.30603	I	62.738	37.262		
1204.31067	I	62.490	37.510		
903.416931	I	62.490	37.510		
701.609924	I	62.490	37.510		
500.307404	I	62.490	37.510		
399.082214	I	62.490	37.510		
301.014801	I	62.490	37.510		

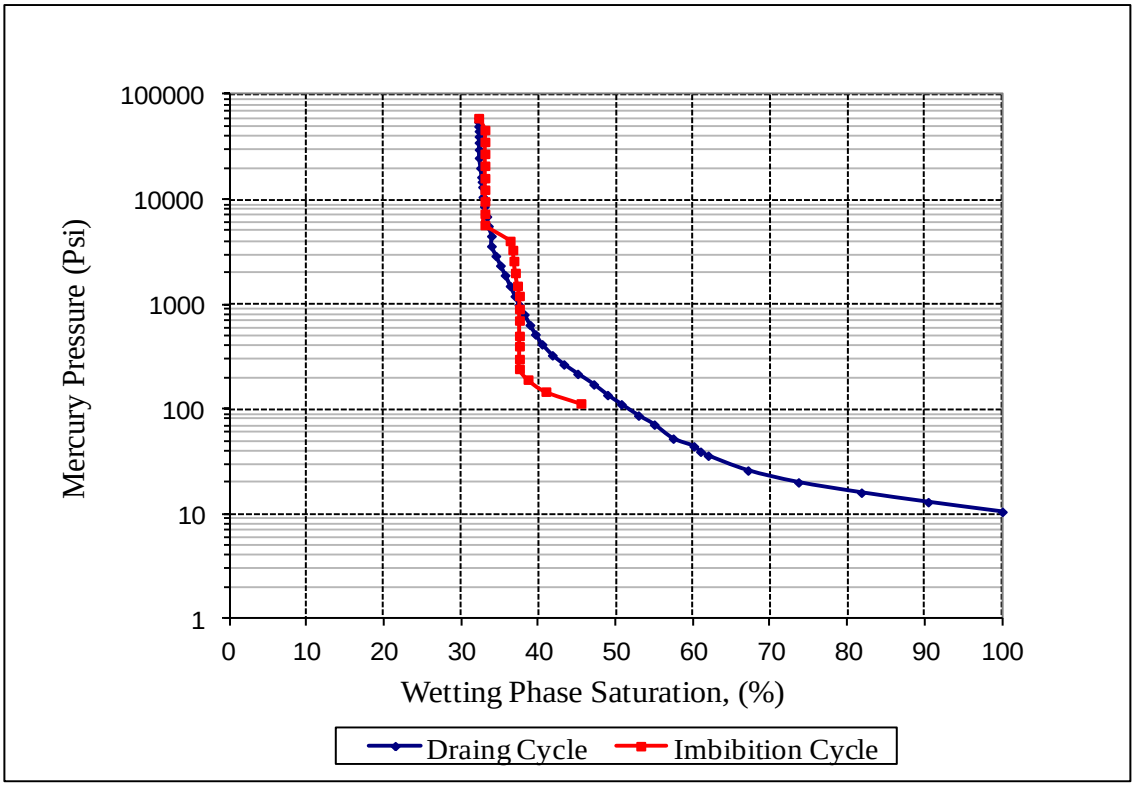

Figure A13. MICP curves (Drainage and imbibtion cycles) for sample # 10.

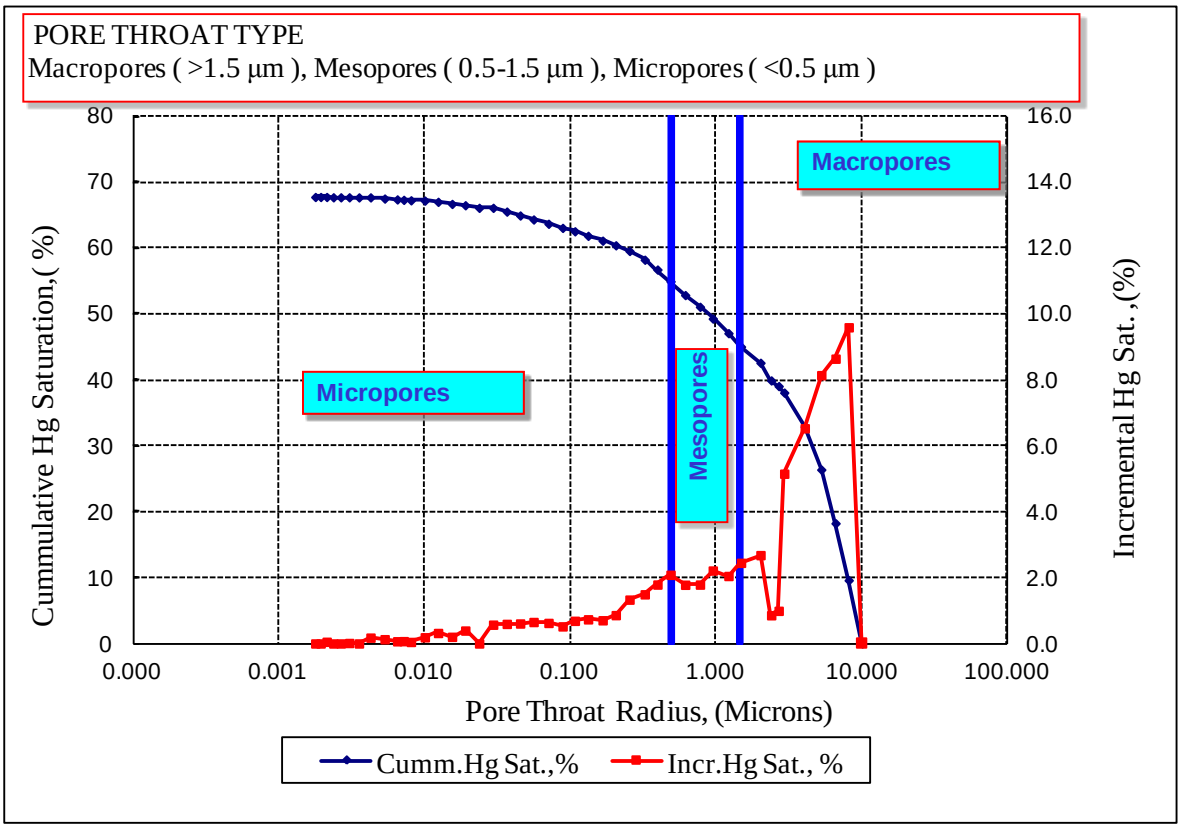

Figure A14. Pore size distribution for sample # 10 using mercury injection capillary pressure.

Mercury Injection Capillary Pressure and Pore Size Distribution

Table A15. MICP results of sample # 15.

Well :	**A3-Libya**
Sample # :	**15**

Core Sample Data	
Pore vol. (cc)	0.279
Porosity (%)	11.85
Air Perm. (mD)	12.55

Experimental Values	
Threshold Pressure (psi)	19.951
Dry Weight (gm)	5.472
Sample Depth (ft)	15240

Pressure Psia	Cycle	Cum. Hg Sat. Pore Vol., %	Wetting Phase (Sw) Pore Vol., %	Incr. Hg Sat. Pore Vol., %	rp microns
19.9509	D	0.000	100.000	0.000	5.346
24.9884	D	8.816	91.184	8.816	4.268
29.9702	D	17.987	82.013	9.171	3.559
33.2544	D	21.244	78.756	3.257	3.207
44.1754	D	29.269	70.731	8.025	2.415
55.5412	D	34.956	65.044	5.688	1.920
71.7072	D	40.872	59.128	5.915	1.487
87.0914	D	45.305	54.695	4.434	1.225
112.3988	D	50.504	49.496	5.199	0.949
136.6413	D	53.720	46.280	3.216	0.781
171.1099	D	56.691	43.309	2.971	0.623
219.4102	D	59.267	40.733	2.576	0.486
269.4115	D	61.115	38.885	1.848	0.396
326.3907	D	62.709	37.291	1.594	0.327
419.7991	D	64.553	35.447	1.844	0.254
516.6651	D	66.240	33.760	1.688	0.206
637.3146	D	68.156	31.844	1.915	0.167
796.7532	D	70.269	29.731	2.113	0.134
985.2423	D	71.938	28.062	1.669	0.108
1198.8870	D	73.103	26.897	1.165	0.089
1498.1414	D	73.965	26.035	0.861	0.0712
1895.5714	D	74.700	25.300	0.735	0.0563
2345.7690	D	75.232	24.768	0.533	0.0455
2893.6230	D	75.555	24.445	0.323	0.0369
3594.4619	D	76.503	23.497	0.948	0.0297

Pressure Psia	Cycle	Cum. Hg Sat. Pore Vol., %	Wetting Phase (Sw) Pore Vol., %	Incr. Hg Sat. Pore Vol., %	rp microns
4487.2495	D	76.503	23.497	0.000	0.0238
5581.9053	D	76.503	23.497	0.000	0.0191
6883.6836	D	76.503	23.497	0.000	0.0155
8584.5039	D	76.503	23.497	0.000	0.0124
10580.5215	D	77.148	22.852	0.645	0.0101
13181.0186	D	77.148	22.852	0.000	0.0081
14780.4121	D	77.148	22.852	0.000	0.0072
16381.7646	D	77.350	22.650	0.202	0.0065
19978.7285	D	77.350	22.650	0.000	0.0053
24991.8184	D	77.350	22.650	0.000	0.0043
29990.0137	D	78.386	21.614	1.036	0.0036
34988.0820	D	78.386	21.614	0.000	0.0030
39988.9531	D	78.386	21.614	0.000	0.0027
44988.0898	D	78.386	21.614	0.000	0.0024
49989.4180	D	78.386	21.614	0.000	0.0021
54992.8008	D	78.386	21.614	0.000	0.0019
59895.0430	D	78.386	21.614	0.000	0.0018
46099.9102	I	74.341	25.659		
35507.1719	I	74.341	25.659		
27300.9063	I	74.341	25.659		
21008.8555	I	74.341	25.659		
16007.7715	I	74.341	25.659		
12412.2744	I	74.341	25.659		
9613.36816	I	74.341	25.659		
7311.01221	I	74.341	25.659		
5708.21729	I	74.341	25.659		
4306.92578	I	74.341	25.659		
3303.48462	I	74.341	25.659		
2609.82007	I	74.341	25.659		
2000.65918	I	74.341	25.659		
1501.43066	I	74.341	25.659		
704.618347	I	74.341	25.659		
501.908691	I	74.341	25.659		
404.433319	I	74.341	25.659		
299.692047	I	73.341	26.659		
242.495163	I	72.193	27.807		
192.545685	I	70.772	29.228		
147.410263	I	68.827	31.173		
111.48613	I	66.531	33.469		
87.4215698	I	63.968	36.032		
68.1553802	I	61.065	38.935		
52.7037201	I	57.274	42.726		
33.1465111	I	47.739	52.261		

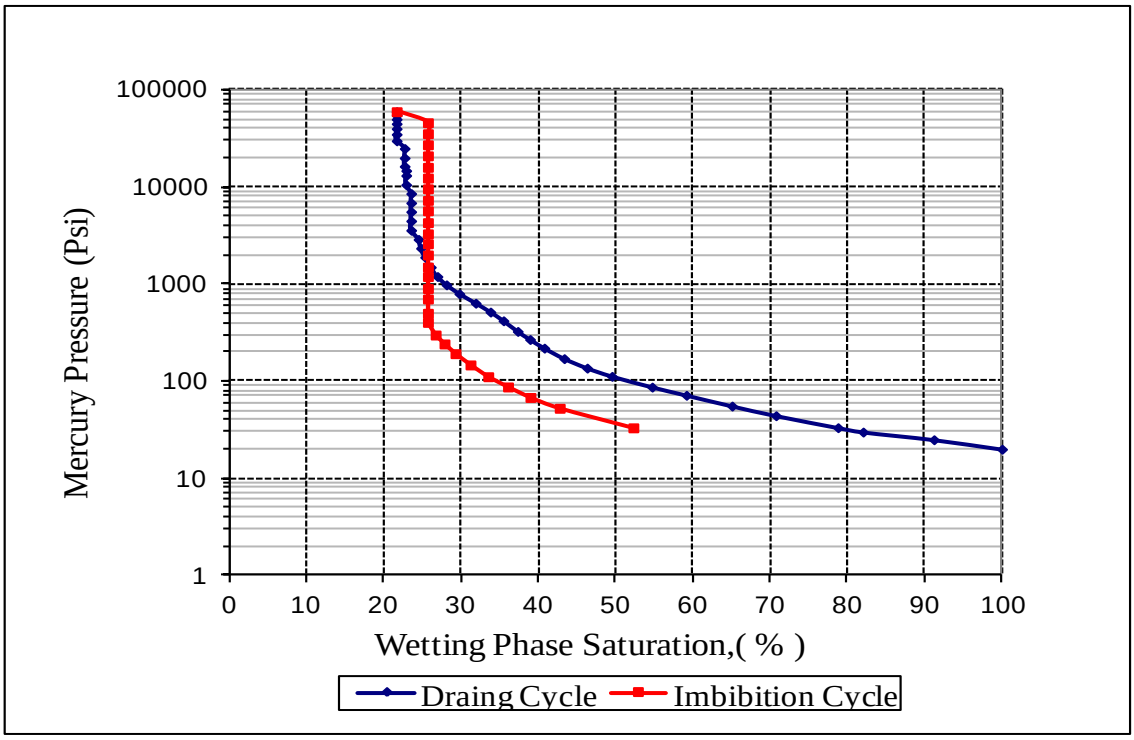

Figure A15. MICP curves (Drainage and imbibtion cycles) for sample # 15.

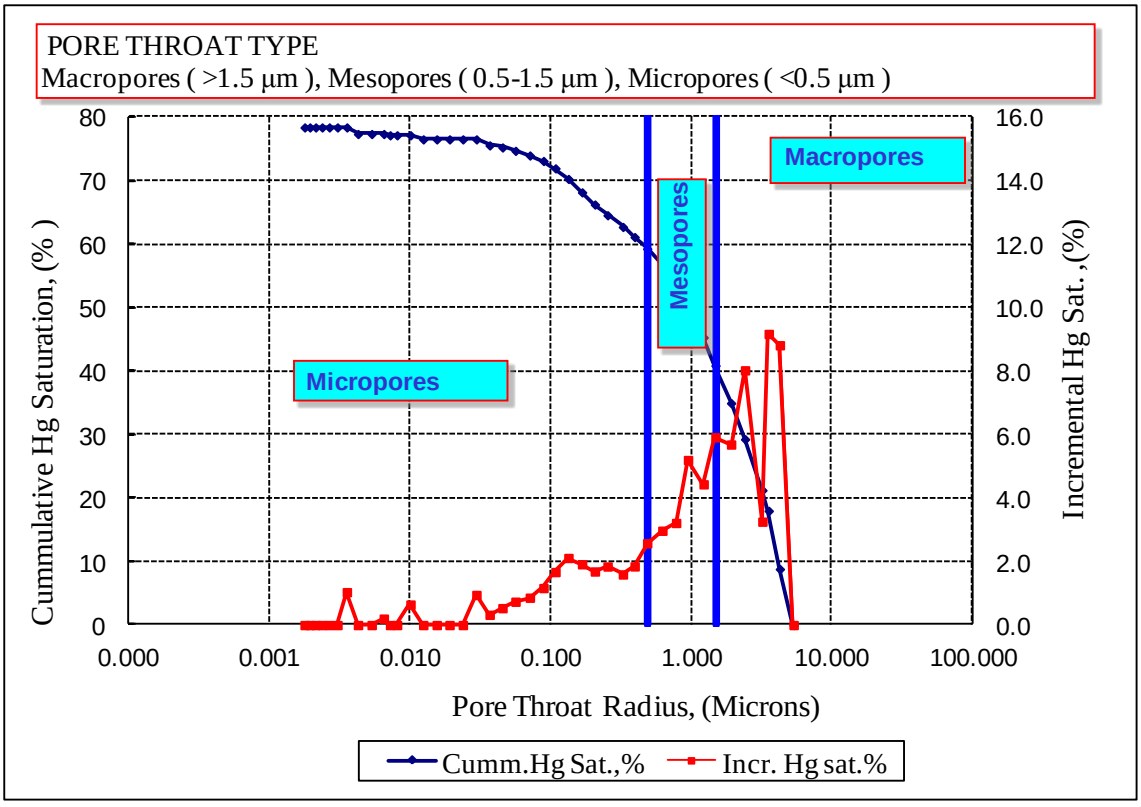

Figure A16. Pore size distribution of sample # 15 using mercury injection capillary pressure.

Mercury Injection Capillary Pressure and Pore Size Distribution

Table A16. MICP results of sample # 18.

Well :	**B1-Libya**
Sample # :	**18**

Core Sample Data	
Pore vol. (cc)	0.294
Porosity (%)	14.42
Air Perm. (mD)	1146

Experimental Values	
Threshold Pressure (psi)	5.495
Dry Weight (gm)	4.652
Sample Depth (ft)	13894

Pressure Psia	Cycle	Cum. Hg Sat. Pore Vol., %	Wetting Phase (Sw) Pore Vol., %	Incr. Hg Sat. Pore Vol., %	rp microns
5.4955	D	0.000	100.000	0.000	19.409
5.9981	D	7.398	92.602	7.398	17.783
7.4888	D	23.842	76.158	16.444	14.243
8.4914	D	30.734	69.266	6.892	12.561
10.4829	D	37.730	62.270	6.996	10.175
12.9842	D	41.896	58.104	4.166	8.215
15.9689	D	44.531	55.469	2.635	6.679
19.9507	D	46.672	53.328	2.142	5.346
24.9829	D	48.450	51.550	1.778	4.269
29.9699	D	49.852	50.148	1.402	3.559
36.8067	D	50.794	49.206	0.942	2.898
46.5821	D	51.926	48.074	1.133	2.290
57.1378	D	52.589	47.411	0.663	1.867
71.6207	D	53.723	46.277	1.134	1.489
87.2981	D	54.702	45.298	0.980	1.222
112.3827	D	55.918	44.082	1.215	0.949
138.5413	D	56.973	43.027	1.055	0.770
171.6716	D	57.707	42.293	0.733	0.621
215.8710	D	58.611	41.389	0.904	0.494
266.1542	D	58.846	41.154	0.235	0.401
326.2492	D	59.600	40.400	0.754	0.327
415.3791	D	60.137	39.863	0.538	0.257
518.1566	D	60.476	39.524	0.338	0.206
636.2901	D	60.647	39.353	0.172	0.168
797.5998	D	60.763	39.237	0.116	0.134

Pressure Psia	Cycle	Cum. Hg Sat. Pore Vol., %	Wetting Phase (Sw) Pore Vol., %	Incr. Hg Sat. Pore Vol., %	rp microns
986.5137	D	60.825	39.175	0.061	0.108
1199.8822	D	60.910	39.090	0.086	0.089
1496.1877	D	60.931	39.069	0.020	0.0713
1895.3978	D	60.933	39.067	0.003	0.0563
2343.8223	D	60.933	39.067	0.000	0.0455
2895.5396	D	60.933	39.067	0.000	0.0368
3592.2053	D	60.933	39.067	0.000	0.0297
4482.0117	D	60.933	39.067	0.000	0.0238
5581.2930	D	60.933	39.067	0.000	0.0191
6883.3589	D	60.933	39.067	0.000	0.0155
8584.3105	D	60.933	39.067	0.000	0.0124
10584.5977	D	60.933	39.067	0.000	0.0101
13182.3076	D	60.933	39.067	0.000	0.0081
14782.7236	D	60.933	39.067	0.000	0.0072
16378.7529	D	60.933	39.067	0.000	0.0065
19979.6445	D	60.933	39.067	0.000	0.0053
24992.5703	D	60.933	39.067	0.000	0.0043
29990.3516	D	60.933	39.067	0.000	0.0036
34989.4844	D	60.933	39.067	0.000	0.0030
39990.0234	D	60.933	39.067	0.000	0.0027
44991.6211	D	60.933	39.067	0.000	0.0024
49987.3672	D	60.933	39.067	0.000	0.0021
54991.7422	D	60.933	39.067	0.000	0.0019
59820.7969	D	60.933	39.067	0.000	0.0018
46099.7891	I	57.675	42.325		
35500.3320	I	57.675	42.325		
27308.0605	I	57.675	42.325		
21010.2227	I	57.675	42.325		
7311.96289	I	57.675	42.325		
2597.65625	I	57.675	42.325		
2005.53857	I	57.675	42.325		
1506.71436	I	57.675	42.325		
1205.33655	I	57.675	42.325		
900.453979	I	57.675	42.325		
699.179993	I	57.675	42.325		
503.18158	I	57.675	42.325		
400.924225	I	57.675	42.325		
301.92569	I	57.675	42.325		
241.032669	I	57.675	42.325		
193.467667	I	57.675	42.325		
148.476547	I	57.110	42.890		
113.563675	I	56.415	43.585		

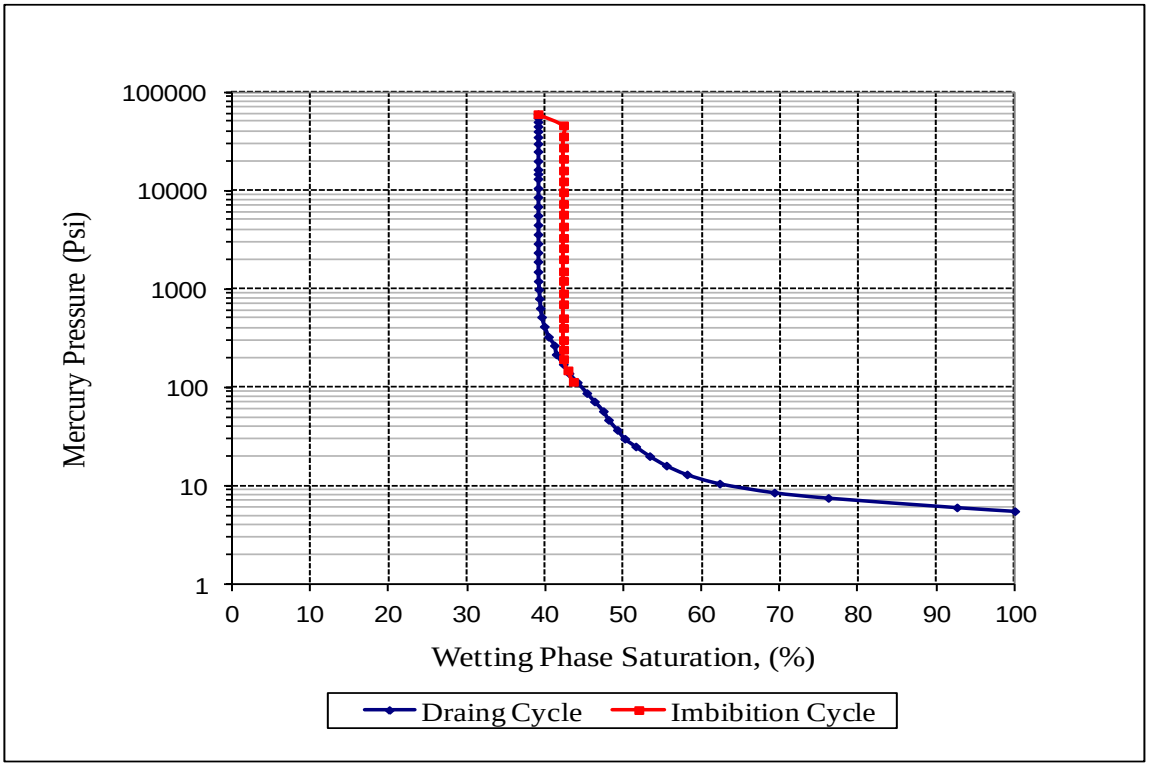

Figure A17. MICP curves (Drainage and imbibtion cycles) for sample # 18.

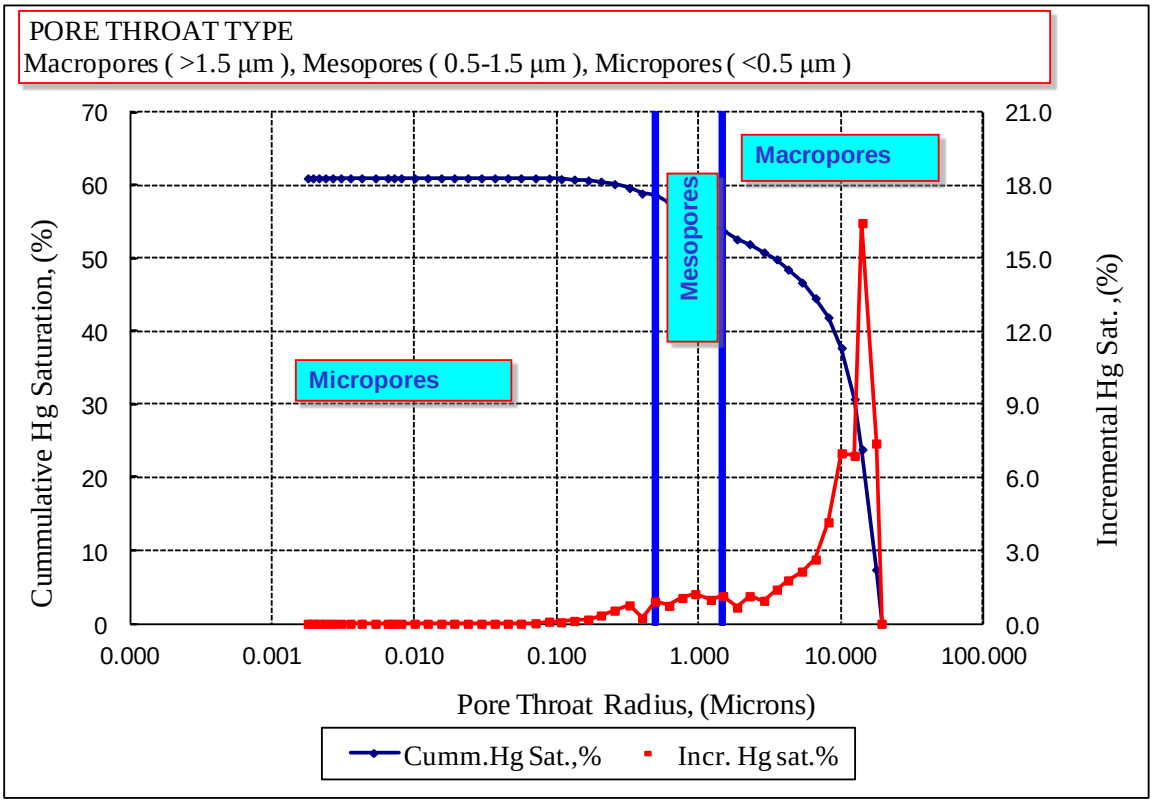

Figure A18. Pore size distribution for sample # 18 using mercury injection capillary pressure.

Mercury Injection Capillary Pressure and Pore Size Distribution

Table A17. MICP results of sample # 24.

Well :	**A3-Libya**
Sample # :	**24**

Core Sample Data	
Pore vol. (cc)	0.139
Porosity (%)	7.1
Air Perm. (mD)	9.91

Experimental Values	
Threshold Pressure (psi)	47.634
Dry Weight (gm)	4.794
Sample Depth (ft)	15249

Pressure Psia	Cycle	Cum. Hg Sat. Pore Vol., %	Wetting Phase (Sw) Pore Vol., %	Incr. Hg Sat. Pore Vol., %	rp microns
47.6337	D	0.000	100.000	0.000	2.239
56.3711	D	4.167	95.833	4.167	1.892
72.9620	D	10.926	89.074	6.759	1.462
87.1393	D	16.554	83.446	5.628	1.224
112.2718	D	24.574	75.426	8.020	0.950
138.5887	D	32.521	67.479	7.946	0.770
172.5341	D	39.880	60.120	7.359	0.618
230.7032	D	47.311	52.689	7.431	0.462
269.6449	D	52.000	48.000	4.689	0.396
329.4263	D	55.935	44.065	3.935	0.324
415.4030	D	59.760	40.240	3.825	0.257
517.2204	D	62.865	37.135	3.105	0.206
635.9337	D	65.513	34.487	2.648	0.168
798.2017	D	68.022	31.978	2.508	0.134
987.7503	D	69.840	30.160	1.818	0.108
1205.2545	D	71.176	28.824	1.336	0.088
1495.0732	D	72.338	27.662	1.163	0.0713
1895.6301	D	73.317	26.683	0.978	0.0563
2345.9568	D	73.944	26.056	0.628	0.0455
2892.9468	D	74.723	25.277	0.779	0.0369
3594.1533	D	74.723	25.277	0.000	0.0297
4484.4751	D	75.019	24.981	0.297	0.0238
5585.6572	D	75.155	24.845	0.136	0.0191
6881.7300	D	75.483	24.517	0.328	0.0155
8586.6348	D	75.513	24.487	0.030	0.0124

Pressure Psia	Cycle	Cum. Hg Sat. Pore Vol., %	Wetting Phase (Sw) Pore Vol., %	Incr. Hg Sat. Pore Vol., %	rp microns
10583.6191	D	75.513	24.487	0.000	0.0101
13181.0303	D	75.513	24.487	0.000	0.0081
14779.7041	D	75.513	24.487	0.000	0.0072
16379.9521	D	75.513	24.487	0.000	0.0065
19978.9258	D	75.541	24.459	0.029	0.0053
24991.5977	D	75.638	24.362	0.097	0.0043
29992.9492	D	75.649	24.351	0.011	0.0036
34990.6094	D	75.784	24.216	0.135	0.0030
39993.3047	D	75.784	24.216	0.000	0.0027
44990.3008	D	75.971	24.029	0.187	0.0024
49989.5938	D	76.004	23.996	0.033	0.0021
54994.4023	D	76.004	23.996	0.000	0.0019
59876.6055	D	76.004	23.996	0.000	0.0018
46099.5977	I	75.370	24.630		
35500.8125	I	75.370	24.630		
27308.3926	I	75.370	24.630		
21009.4570	I	75.370	24.630		
16008.1475	I	75.370	24.630		
12403.1465	I	75.370	24.630		
9611.89258	I	75.370	24.630		
7311.61621	I	75.370	24.630		
5712.47949	I	75.370	24.630		
4305.4043	I	75.370	24.630		
3308.30591	I	75.370	24.630		
2606.29639	I	75.370	24.630		
1999.24854	I	75.370	24.630		
1502.39917	I	75.370	24.630		
1204.63953	I	74.799	25.201		
901.801514	I	73.866	26.134		
701.336853	I	73.866	26.134		
503.328064	I	73.866	26.134		
398.062683	I	73.393	26.607		
299.969452	I	72.359	27.641		
243.883377	I	71.073	28.927		
192.570969	I	69.639	30.361		
145.95784	I	67.684	32.316		
111.453819	I	65.451	34.549		
88.9560242	I	63.198	36.802		
67.4477463	I	60.290	39.710		

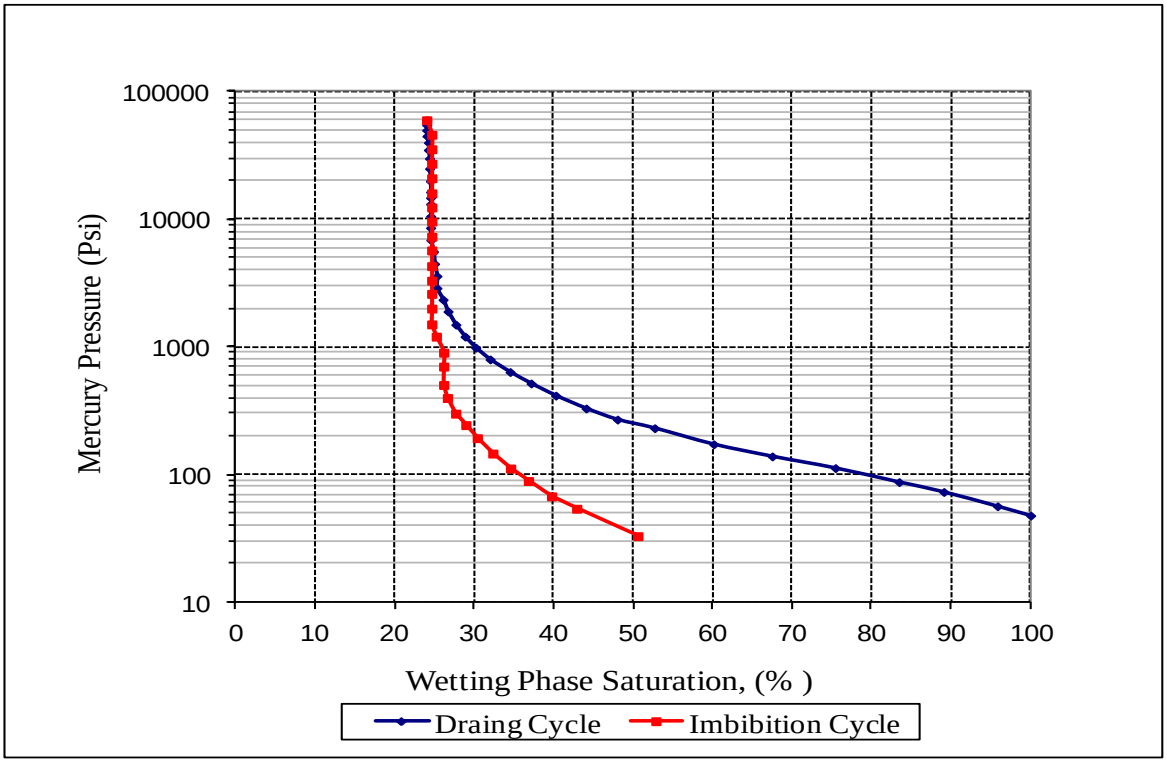

Figure A19. MICP curves (Drainage and imbibtion cycles) for sample # 24.

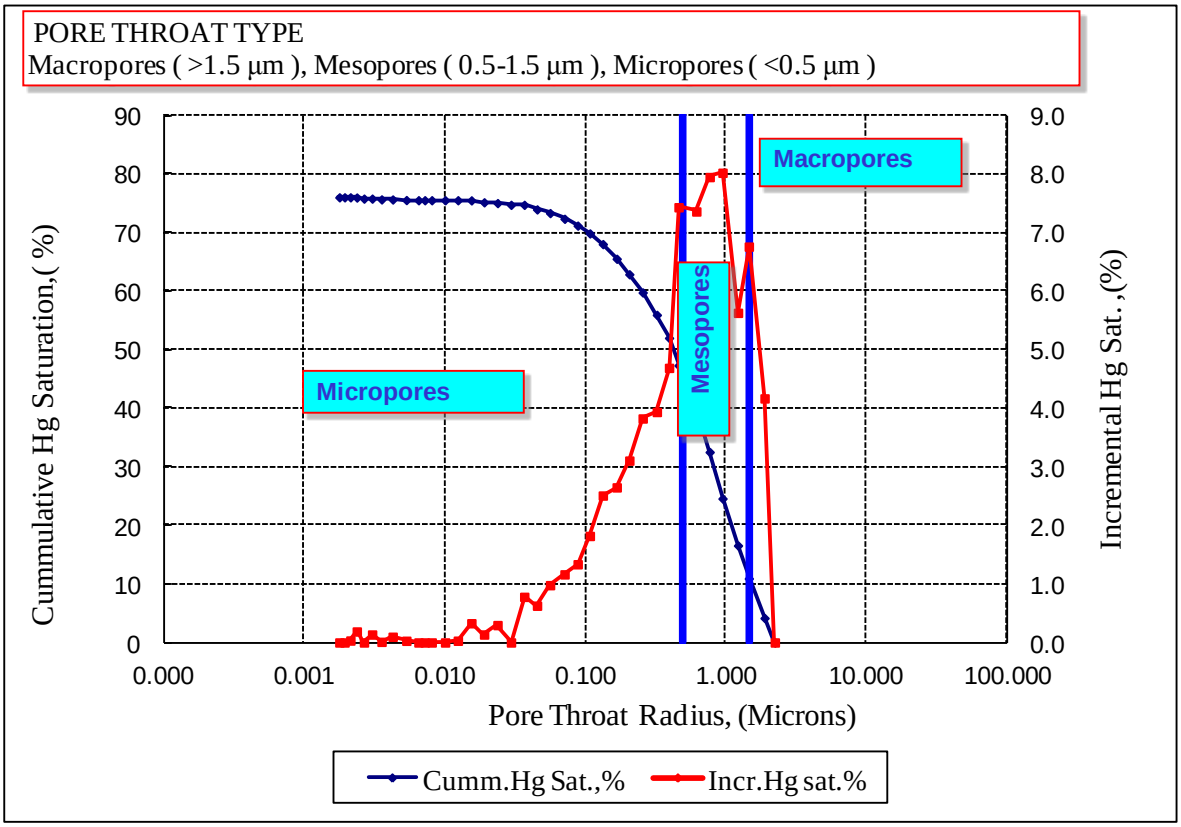

Figure A20. Pore size distribution for sample # 24 using mercury injection capillary pressure.

Mercury Injection Capillary Pressure and Pore Size Distribution

Table A18.MICP results of sample # 29

Well :	**C2-Libya**
Sample # :	**29**

Core Sample Data	
Pore vol. (cc)	0.386
Porosity (%)	17.29
Air Perm. (mD)	69.86

Experimental Values	
Threshold Pressure (psi)	15.961
Dry Weight (gm)	4.875
Sample Depth (ft)	11544

Pressure Psia	Cycle	Cum. Hg Sat. Pore Vol., %	Wetting Phase (Sw) Pore Vol., %	Incr. Hg Sat. Pore Vol., %	rp microns
15.9613	D	0.000	100.000	0.000	6.683
20.0144	D	8.089	91.911	8.089	5.329
24.9875	D	17.573	82.427	9.484	4.269
29.9686	D	24.644	75.356	7.071	3.559
36.9294	D	29.470	70.530	4.826	2.888
46.7738	D	37.177	62.823	7.707	2.280
57.4699	D	42.378	57.622	5.202	1.856
71.6051	D	47.838	52.162	5.460	1.490
86.8684	D	52.206	47.794	4.367	1.228
112.8912	D	57.428	42.572	5.222	0.945
136.1896	D	61.279	38.721	3.851	0.783
171.5764	D	65.221	34.779	3.942	0.622
217.1224	D	68.321	31.679	3.100	0.491
265.9098	D	70.612	29.388	2.291	0.401
326.3781	D	72.531	27.469	1.919	0.327
415.7185	D	74.222	25.778	1.691	0.257
516.2141	D	75.452	24.548	1.230	0.207
636.1778	D	76.283	23.717	0.831	0.168
796.2495	D	77.022	22.978	0.739	0.134
989.7847	D	77.429	22.571	0.407	0.108
1198.6354	D	77.856	22.144	0.427	0.089
1495.9160	D	78.246	21.754	0.390	0.0713
1898.3046	D	78.443	21.557	0.197	0.0562
2346.5610	D	78.487	21.513	0.044	0.0455
2894.3870	D	78.570	21.430	0.083	0.0369

Pressure Psia	Cycle	Cum. Hg Sat. Pore Vol., %	Wetting Phase (Sw) Pore Vol., %	Incr. Hg Sat. Pore Vol., %	rp microns
3592.1257	D	78.570	21.430	0.000	0.0297
4483.8027	D	78.570	21.430	0.000	0.0238
5583.0684	D	78.570	21.430	0.000	0.0191
6884.4326	D	78.570	21.430	0.000	0.0155
8583.6582	D	78.570	21.430	0.000	0.0124
10581.0488	D	78.570	21.430	0.000	0.0101
13182.0957	D	78.570	21.430	0.000	0.0081
14779.9492	D	78.570	21.430	0.000	0.0072
16380.0557	D	78.570	21.430	0.000	0.0065
19980.7324	D	78.570	21.430	0.000	0.0053
24990.6055	D	78.570	21.430	0.000	0.0043
29990.6348	D	78.570	21.430	0.000	0.0036
34991.8867	D	78.570	21.430	0.000	0.0030
39990.1250	D	78.570	21.430	0.000	0.0027
44990.6758	D	78.570	21.430	0.000	0.0024
49990.8594	D	78.570	21.430	0.000	0.0021
54984.4336	D	78.570	21.430	0.000	0.0019
59752.4922	D	78.570	21.430	0.000	0.0018
46103.1719	I	76.043	23.957		
35510.6250	I	76.043	23.957		
27296.6738	I	76.043	23.957		
21009.4844	I	76.043	23.957		
16005.8057	I	76.043	23.957		
12411.7598	I	76.043	23.957		
9607.51367	I	76.043	23.957		
7311.87354	I	76.043	23.957		
5715.44287	I	76.043	23.957		
3985.63574	I	76.043	23.957		
3300.97852	I	76.043	23.957		
2602.49561	I	76.043	23.957		
2006.95947	I	76.043	23.957		
1498.26636	I	76.043	23.957		
1202.45752	I	76.043	23.957		
903.709045	I	76.043	23.957		
703.35553	I	76.043	23.957		
504.678131	I	76.043	23.957		
401.789673	I	76.043	23.957		
300.124786	I	76.043	23.957		
242.531937	I	75.721	24.279		

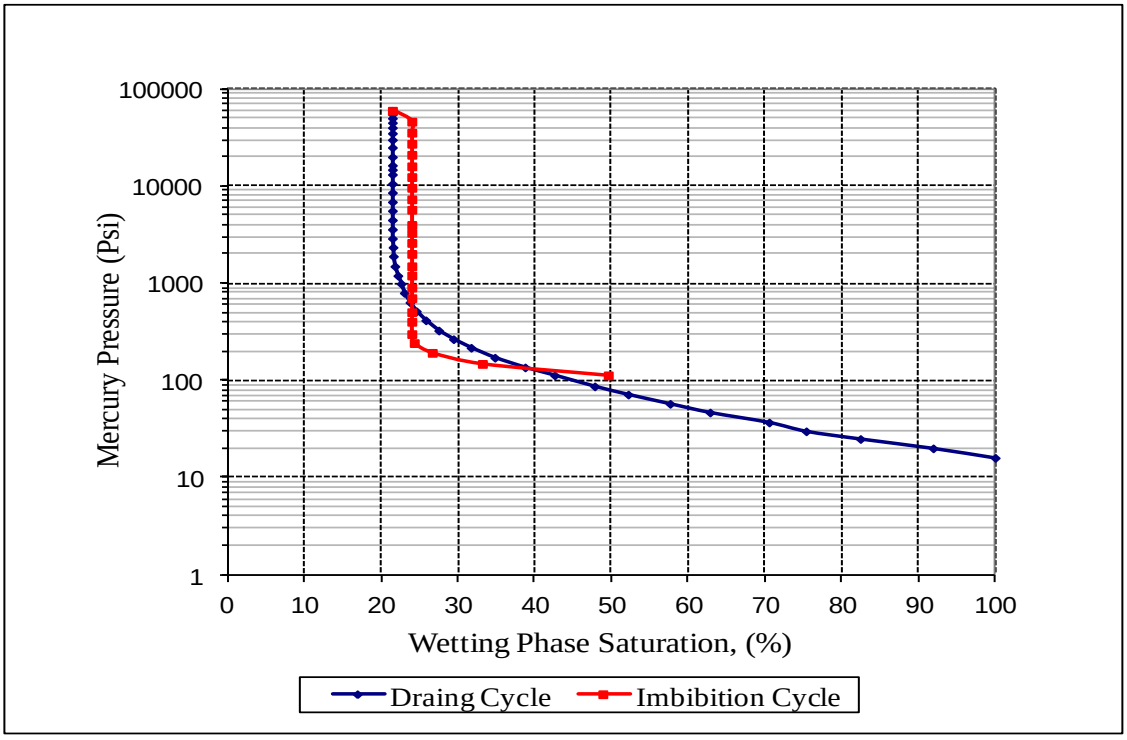

Figure A21. MICP curves (Drainage and imbibtion cycles) for sample # 29.

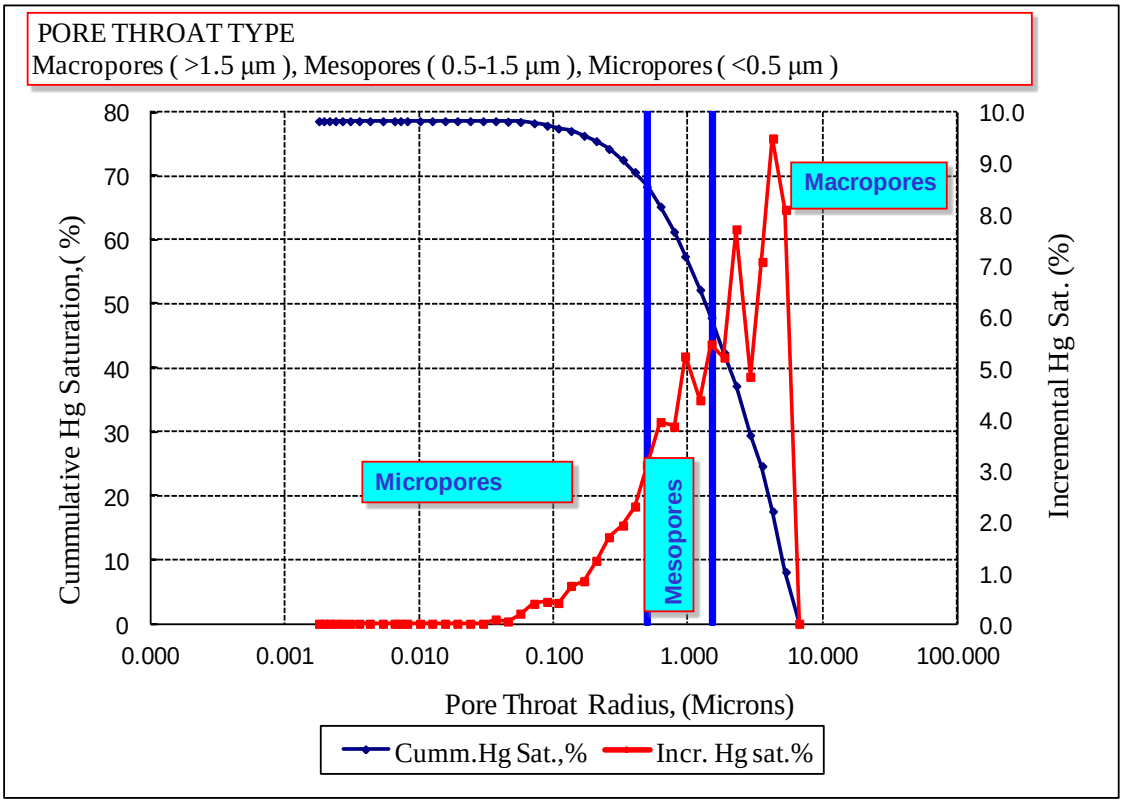

Figure A22. Pore size distribution for sample # 29 using mercury injection capillary pressure.

Mercury Injection Capillary Pressure and Pore Size Distribution

Table A19. MICP results of sample # 41.

Well :	**C1-Libya**
Sample # :	**41**

Core Sample Data	
Pore vol. (cc)	0.287
Porosity (%)	15.35
Air Perm. (mD)	660.5

Experimental Values	
Threshold Pressure (psi)	7.489
Dry Weight (gm)	4.189
Sample Depth (ft)	12225

Pressure Psia	Cycle	Cum. Hg Sat. Pore Vol., %	Wetting Phase (Sw) Pore Vol., %	Incr. Hg Sat. Pore Vol., %	rp microns
7.4893	D	0.000	100.000	0.000	14.242
8.4913	D	18.253	81.747	18.253	12.561
10.4868	D	40.608	59.392	22.356	10.171
12.9823	D	56.841	43.159	16.232	8.216
15.9617	D	61.311	38.689	4.470	6.682
19.9510	D	64.442	35.558	3.131	5.346
24.9869	D	66.829	33.171	2.388	4.269
29.9767	D	68.434	31.566	1.605	3.558
36.2970	D	69.534	30.466	1.100	2.939
47.2357	D	70.766	29.234	1.232	2.258
56.1448	D	71.684	28.316	0.918	1.900
70.7006	D	72.778	27.222	1.094	1.509
85.8671	D	73.504	26.496	0.726	1.242
112.2828	D	74.422	25.578	0.918	0.950
136.2031	D	75.071	24.929	0.650	0.783
173.4282	D	75.695	24.305	0.624	0.615
216.1870	D	77.071	22.929	1.376	0.493
267.8377	D	77.834	22.166	0.763	0.398
326.1405	D	78.187	21.813	0.353	0.327
416.6283	D	78.214	21.786	0.026	0.256
516.8196	D	78.597	21.403	0.383	0.206
637.8608	D	78.597	21.403	0.000	0.167
795.0106	D	78.597	21.403	0.000	0.134
986.1746	D	78.604	21.396	0.007	0.108
1194.2732	D	78.604	21.396	0.000	0.089

Pressure Psia	Cycle	Cum. Hg Sat. Pore Vol., %	Wetting Phase (Sw) Pore Vol., %	Incr. Hg Sat. Pore Vol., %	rp microns
1496.1393	D	78.604	21.396	0.000	0.0713
1897.9318	D	78.604	21.396	0.000	0.0562
2344.0032	D	78.604	21.396	0.000	0.0455
2897.7957	D	78.604	21.396	0.000	0.0368
3595.4971	D	78.604	21.396	0.000	0.0297
4483.8740	D	78.604	21.396	0.000	0.0238
5583.6050	D	78.604	21.396	0.000	0.0191
6883.1138	D	78.604	21.396	0.000	0.0155
8585.2070	D	78.604	21.396	0.000	0.0124
10582.9268	D	78.604	21.396	0.000	0.0101
13178.7051	D	78.604	21.396	0.000	0.0081
14780.1660	D	78.604	21.396	0.000	0.0072
16379.8623	D	78.604	21.396	0.000	0.0065
19978.3047	D	78.604	21.396	0.000	0.0053
24992.0586	D	78.604	21.396	0.000	0.0043
29992.9277	D	78.604	21.396	0.000	0.0036
34992.5352	D	78.604	21.396	0.000	0.0030
39990.8516	D	78.604	21.396	0.000	0.0027
44990.5117	D	78.604	21.396	0.000	0.0024
49988.7422	D	78.604	21.396	0.000	0.0021
54987.8945	D	78.604	21.396	0.000	0.0019
59839.2383	D	78.604	21.396	0.000	0.0018
46102.1250	I	75.479	24.521		
35505.9727	I	75.479	24.521		
27308.5195	I	75.093	24.907		
21007.8164	I	75.093	24.907		
16007.6289	I	75.093	24.907		
4073.48853	I	75.093	24.907		
3304.25586	I	75.093	24.907		
2595.1311	I	75.093	24.907		
2001.81738	I	75.093	24.907		
1506.19641	I	75.093	24.907		
1199.24951	I	75.093	24.907		

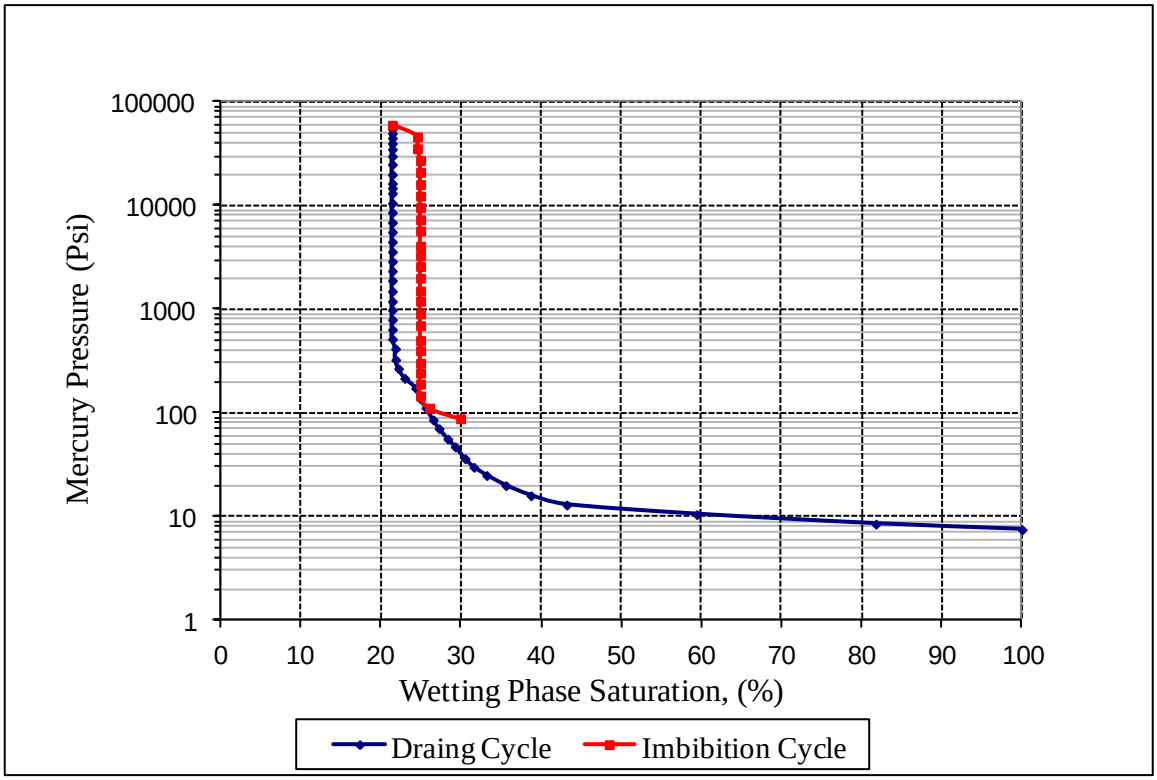

Figure A23. MICP curves (Drainage and imbibtion cycles) for sample # 41.

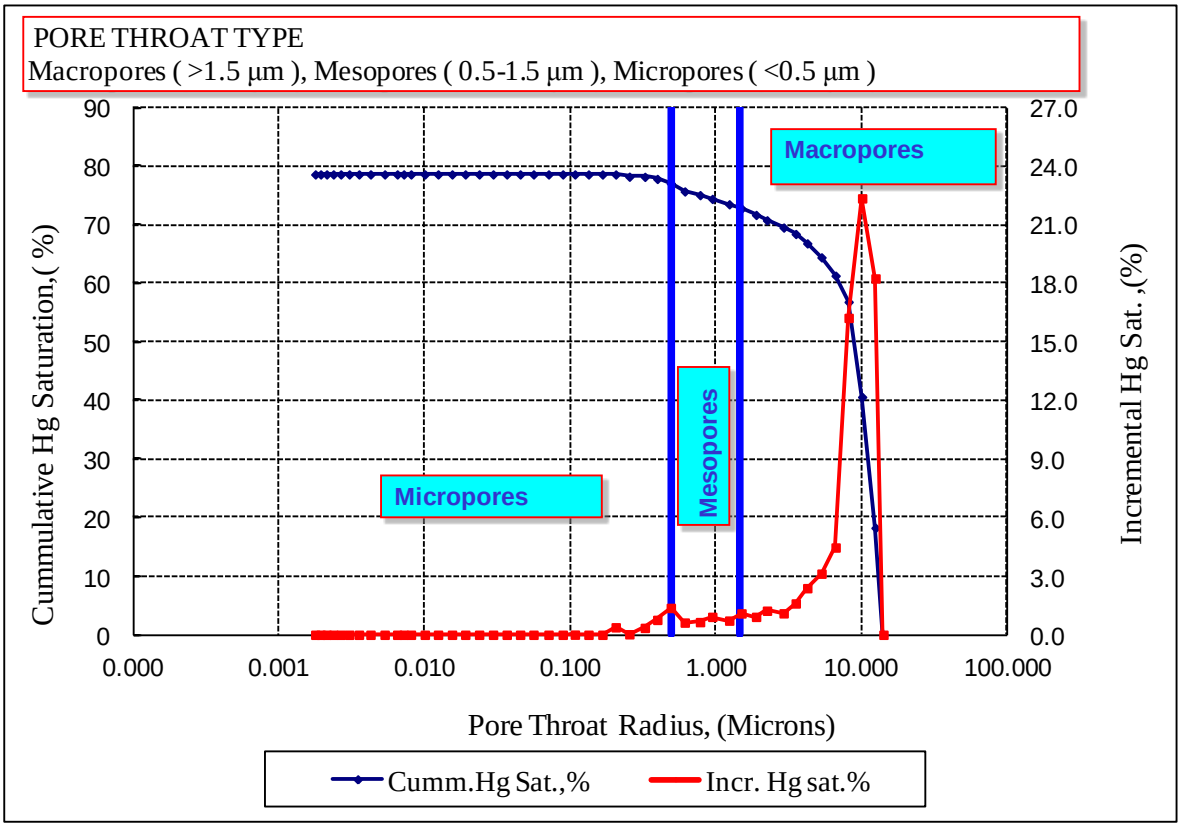

Figure A24. Pore size distribution for sample # 41 using mercury injection capillary pressure.

Mercury Injection Capillary Pressure and Pore Size Distribution

Table A20. MICP results of sample # 42.

Well :	**A3-Libya**
Sample # :	**42**

Core Sample Data	
Pore vol. (cc)	0.188
Porosity (%)	9.26
Air Perm. (mD)	4.90

Experimental Values	
Threshold Pressure (psi)	24.995
Dry Weight (gm)	4.855
Sample Depth (ft)	15268

Pressure Psia	Cycle	Cum. Hg Sat. Pore Vol., %	Wetting Phase (Sw) Pore Vol., %	Incr. Hg Sat. Pore Vol., %	rp microns
24.9945	D	0.000	100.000	0.000	4.267
29.9771	D	2.553	97.447	2.553	3.558
36.6215	D	3.553	96.447	1.000	2.913
46.7595	D	6.019	93.981	2.466	2.281
56.0390	D	7.421	92.579	1.403	1.903
71.2392	D	10.031	89.969	2.610	1.497
86.8824	D	12.874	87.126	2.843	1.228
112.6080	D	18.275	81.725	5.401	0.947
136.5288	D	22.094	77.906	3.819	0.781
172.9312	D	26.745	73.255	4.651	0.617
216.9527	D	30.718	69.282	3.973	0.492
268.8844	D	34.201	65.799	3.483	0.397
329.0758	D	36.777	63.223	2.575	0.324
417.3931	D	40.398	59.602	3.621	0.256
515.0226	D	43.536	56.464	3.138	0.207
635.1263	D	47.078	52.922	3.542	0.168
797.7714	D	51.546	48.454	4.467	0.134
987.1682	D	56.405	43.595	4.860	0.108
1197.3392	D	59.708	40.292	3.303	0.089
1499.7233	D	62.748	37.252	3.039	0.0711
1893.9144	D	64.955	35.045	2.207	0.0563
2344.8713	D	66.512	33.488	1.557	0.0455
2895.7700	D	67.385	32.615	0.874	0.0368
3592.2158	D	68.098	31.902	0.713	0.0297
4485.8789	D	68.544	31.456	0.445	0.0238

Pressure Psia	Cycle	Cum. Hg Sat. Pore Vol., %	Wetting Phase (Sw) Pore Vol., %	Incr. Hg Sat. Pore Vol., %	rp microns
5581.8579	D	68.863	31.137	0.320	0.0191
6883.6045	D	68.863	31.137	0.000	0.0155
8584.7041	D	68.863	31.137	0.000	0.0124
10583.3486	D	68.863	31.137	0.000	0.0101
13182.6240	D	68.863	31.137	0.000	0.0081
14783.5273	D	68.863	31.137	0.000	0.0072
16380.1494	D	68.863	31.137	0.000	0.0065
19980.7441	D	68.863	31.137	0.000	0.0053
24992.4219	D	68.863	31.137	0.000	0.0043
29992.2207	D	68.863	31.137	0.000	0.0036
34992.2266	D	68.863	31.137	0.000	0.0030
39991.4805	D	68.863	31.137	0.000	0.0027
44990.4766	D	68.863	31.137	0.000	0.0024
49988.3516	D	68.863	31.137	0.000	0.0021
54993.5000	D	68.863	31.137	0.000	0.0019
59908.0195	D	68.863	31.137	0.000	0.0018
46108.5664	I	65.643	34.357		
35498.4961	I	65.643	34.357		
27307.3984	I	65.643	34.357		
21009.6602	I	65.643	34.357		
16008.3818	I	65.643	34.357		
12410.7969	I	65.643	34.357		
9615.20117	I	65.643	34.357		
7312.76172	I	65.643	34.357		
5711.56201	I	65.643	34.357		
4307.28271	I	65.643	34.357		
3304.7395	I	65.643	34.357		
2602.27148	I	65.643	34.357		
1998.51221	I	65.643	34.357		
1496.229	I	65.643	34.357		
1203.47778	I	65.643	34.357		
899.550537	I	65.643	34.357		
698.38269	I	65.579	34.421		
504.701263	I	64.603	35.397		
402.047913	I	63.281	36.719		
299.436523	I	61.797	38.203		
239.731812	I	59.884	40.116		
190.820129	I	57.630	42.370		
146.569443	I	54.895	45.105		

113.219704	I	51.737	48.263		
87.4197998	I	47.126	52.874		
68.0344543	I	44.214	55.786		
53.0329742	I	41.041	58.959		
32.9238472	I	33.580	66.420		
21.1242161	I	27.106	72.894		

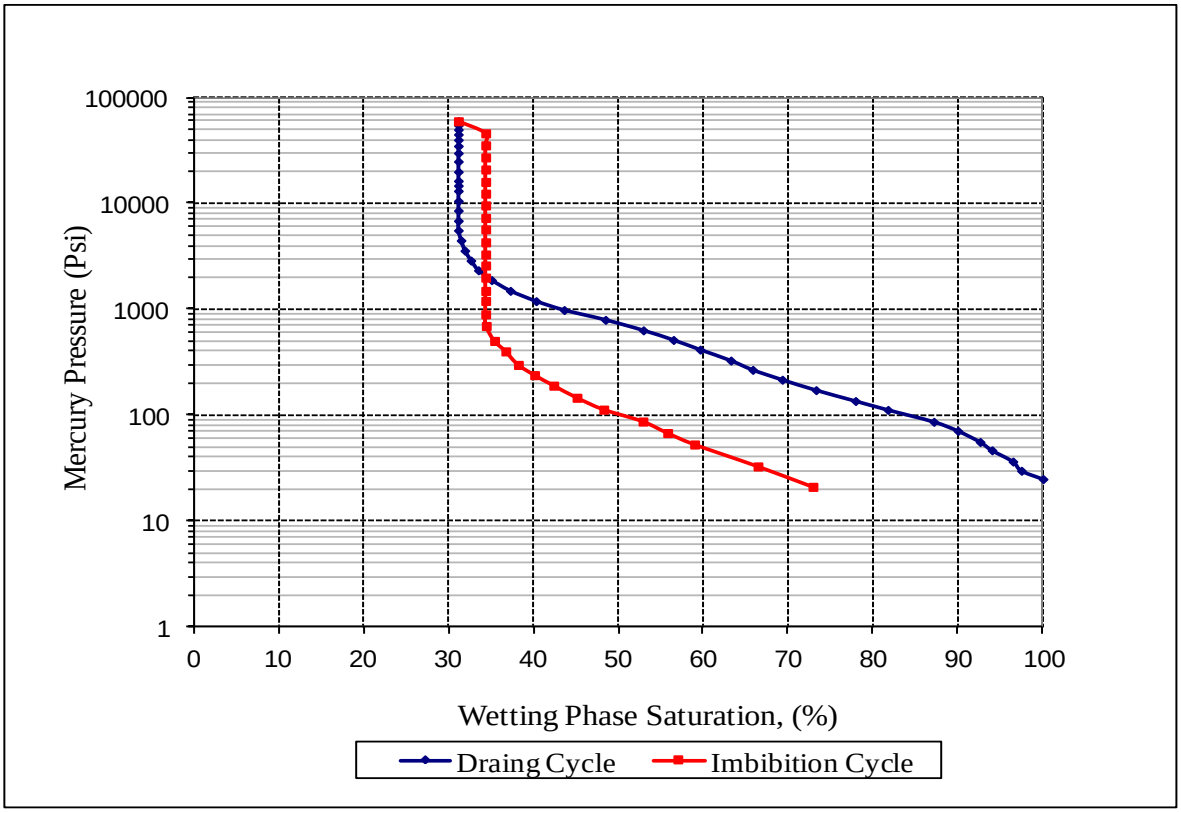

Figure A25. MICP curves (Drainage and imbibtion cycles) for sample # 42.

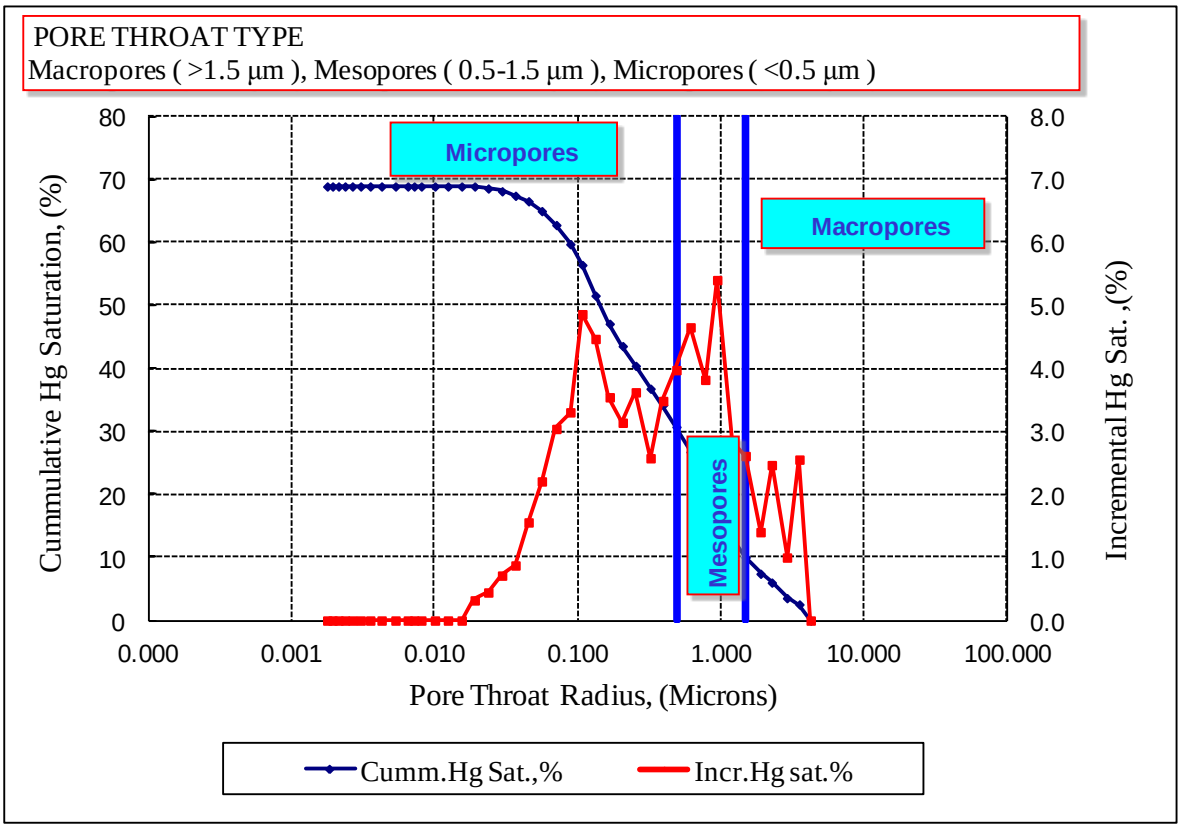

Figure A26. Pore size distribution for sample # 42 using mercury injection capillary pressure.

Mercury Injection Capillary Pressure and Pore Size Distribution

Table A21. MICP results of sample # 47.

Well :	**C2-Libya**
Sample # :	**47**

Core Sample Data	
Pore vol. (cc)	0.375
Porosity (%)	16.14
Air Perm. (mD)	279.72

Experimental Values	
Threshold Pressure (psi)	7.489
Dry Weight (gm)	5.145
Sample Depth (ft)	11562

Pressure Psia	Cycle	Cum. Hg Sat. Pore Vol., %	Wetting Phase (Sw) Pore Vol., %	Incr. Hg Sat. Pore Vol., %	rp microns
7.4886	D	0.000	100.000	0.000	14.243
8.4911	D	4.156	95.844	4.156	12.562
10.4826	D	12.142	87.858	7.987	10.175
12.9785	D	19.387	80.613	7.245	8.218
15.9719	D	25.047	74.953	5.660	6.678
19.9525	D	30.503	69.497	5.456	5.346
24.9955	D	35.950	64.050	5.446	4.267
29.9744	D	40.309	59.691	4.359	3.558
36.5198	D	43.224	56.776	2.915	2.921
47.0719	D	46.608	53.392	3.384	2.266
56.4595	D	49.937	50.063	3.329	1.889
71.8638	D	55.843	44.157	5.906	1.484
87.2740	D	58.360	41.640	2.517	1.222
111.5954	D	62.638	37.362	4.278	0.956
136.5958	D	65.988	34.012	3.350	0.781
171.4628	D	69.100	30.900	3.112	0.622
215.5402	D	71.863	28.137	2.763	0.495
267.7250	D	73.867	26.133	2.004	0.398
327.1107	D	75.254	24.746	1.387	0.326
416.3082	D	76.549	23.451	1.295	0.256
515.5229	D	77.426	22.574	0.878	0.207
637.2040	D	78.083	21.917	0.657	0.167
797.0695	D	78.589	21.411	0.506	0.134
990.8516	D	78.929	21.071	0.340	0.108
1200.1208	D	79.207	20.793	0.278	0.089

Pressure Psia	Cycle	Cum. Hg Sat. Pore Vol., %	Wetting Phase (Sw) Pore Vol., %	Incr. Hg Sat. Pore Vol., %	rp microns
1499.8829	D	79.429	20.571	0.222	0.0711
1898.0858	D	79.537	20.463	0.108	0.0562
2346.6697	D	79.637	20.363	0.100	0.0455
2893.9719	D	79.637	20.363	0.000	0.0369
3594.8916	D	79.637	20.363	0.000	0.0297
4487.4946	D	79.637	20.363	0.000	0.0238
5581.3140	D	79.637	20.363	0.000	0.0191
6881.5840	D	79.637	20.363	0.000	0.0155
8583.7412	D	79.637	20.363	0.000	0.0124
10583.1855	D	79.637	20.363	0.000	0.0101
13183.4766	D	79.637	20.363	0.000	0.0081
14780.3066	D	79.637	20.363	0.000	0.0072
16380.0703	D	79.637	20.363	0.000	0.0065
19978.8105	D	79.637	20.363	0.000	0.0053
24990.4121	D	79.637	20.363	0.000	0.0043
29992.1602	D	79.637	20.363	0.000	0.0036
34988.8867	D	79.637	20.363	0.000	0.0030
39990.8281	D	79.637	20.363	0.000	0.0027
44988.2813	D	79.637	20.363	0.000	0.0024
49990.9141	D	79.637	20.363	0.000	0.0021
54991.8516	D	79.637	20.363	0.000	0.0019
59905.2070	D	79.637	20.363	0.000	0.0018
46104.1836	I	77.049	22.951		
35506.8945	I	77.049	22.951		
27302.2832	I	77.049	22.951		
20999.0176	I	77.049	22.951		
16010.9941	I	77.049	22.951		
12406.3408	I	77.049	22.951		
9611.81738	I	77.049	22.951		
7313.08008	I	77.049	22.951		
5705.63525	I	77.049	22.951		
4173.7627	I	76.804	23.196		
3304.81763	I	76.804	23.196		
2603.10229	I	76.804	23.196		
1996.67603	I	76.804	23.196		
1498.18127	I	76.804	23.196		
1199.98584	I	76.804	23.196		
904.649841	I	76.804	23.196		
702.538635	I	76.804	23.196		

501.185028	I	76.804	23.196		
398.827393	I	76.804	23.196		
299.656647	I	76.804	23.196		
242.62735	I	76.172	23.828		
193.438812	I	75.158	24.842		
148.778656	I	73.405	26.595		
114.143959	I	70.447	29.553		
87.7312469	I	65.974	34.026		
67.3911972	I	58.742	41.258		
53.2774811	I	48.689	51.311		

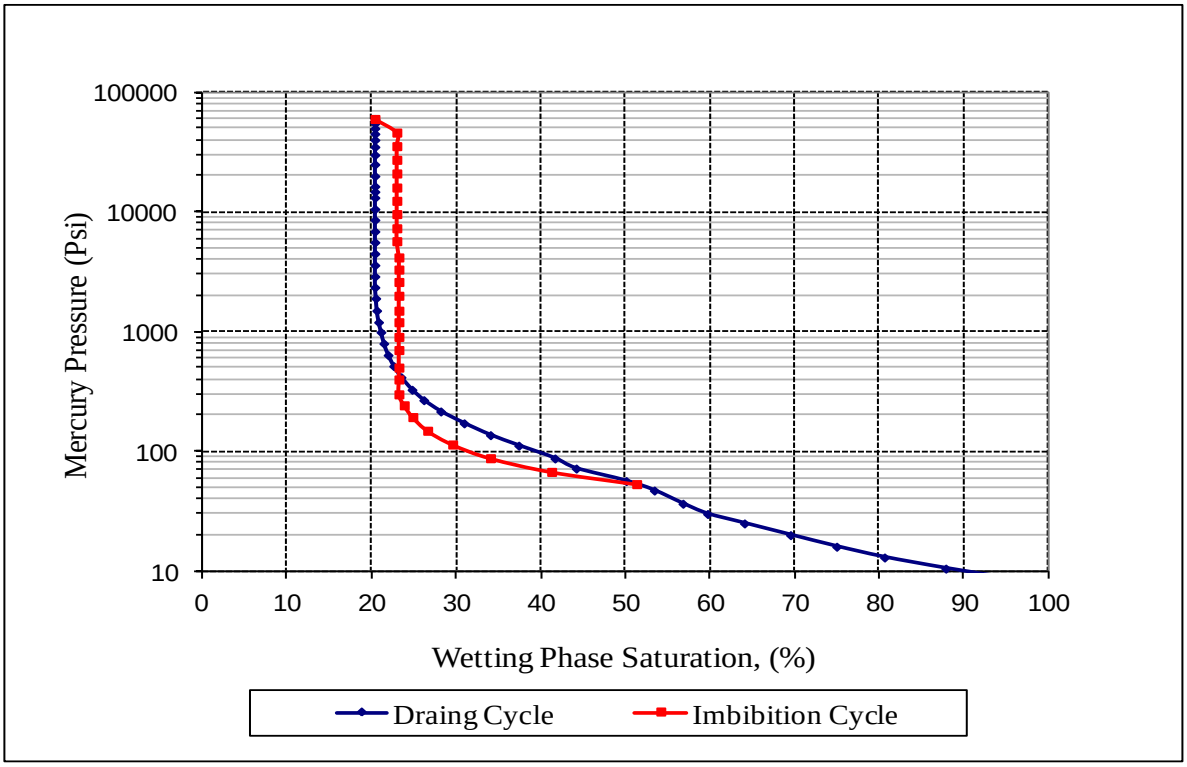

Figure A27. MICP curves (Drainage and imbibtion cycles) for sample # 47.

.

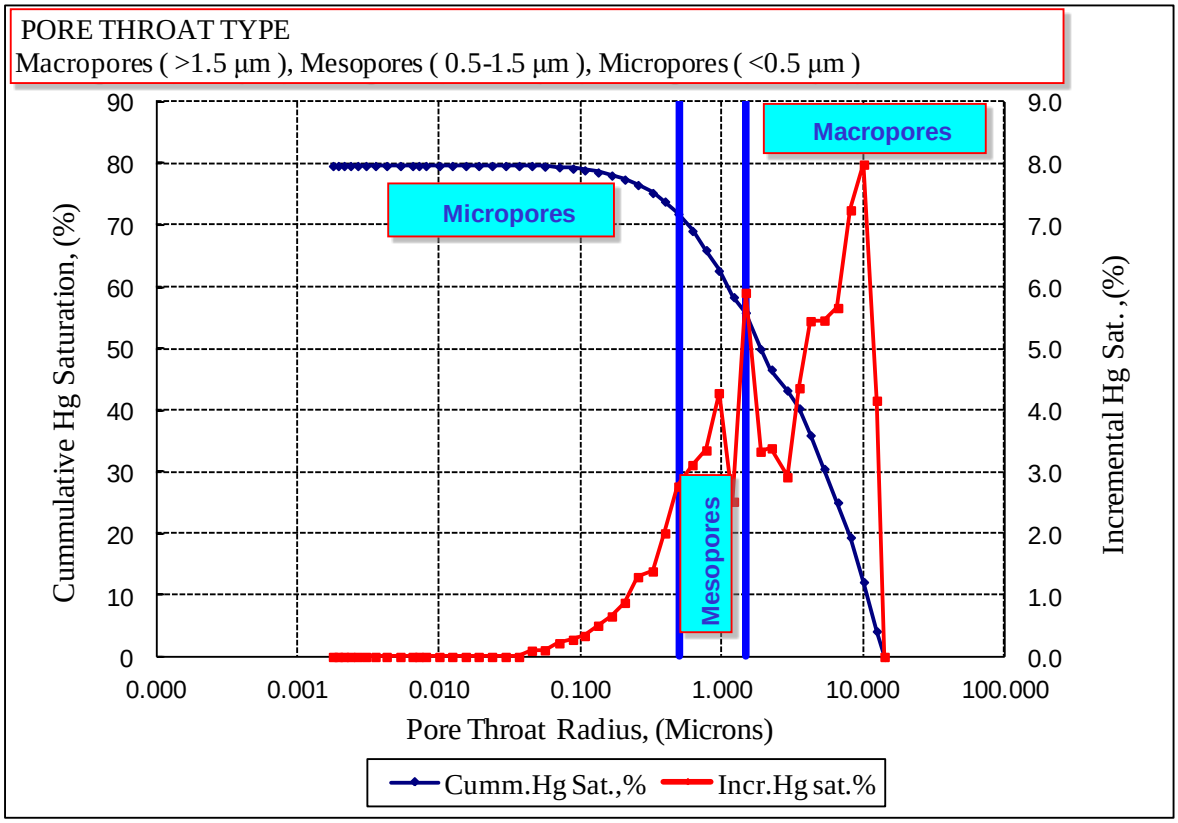

Figure A28. Pore size distribution for sample # 47 using mercury injection capillary pressure.

Mercury Injection Capillary Pressure and Pore Size Distribution

Table A.22. MICP results of sample # 53.

Well :	**A1-Libya**
Sample # :	**53**

Core Sample Data	
Pore vol. (cc)	0.295
Porosity (%)	12.43
Air Perm. (mD)	297.71

Experimental Values	
Threshold Pressure (psi)	5.501
Dry Weight (gm)	5.487
Sample Depth (ft)	15880

Pressure Psia	Cycle	Cum. Hg Sat. Pore Vol., %	Wetting Phase (Sw) Pore Vol., %	Incr. Hg Sat. Pore Vol., %	rp microns
5.5007	D	0.000	100.000	0.000	19.390
5.9977	D	3.669	96.331	3.669	17.784
7.4876	D	19.223	80.777	15.554	14.245
8.4946	D	27.129	72.871	7.906	12.556
10.4810	D	35.979	64.021	8.849	10.177
12.9817	D	41.547	58.453	5.568	8.216
15.9644	D	45.306	54.694	3.759	6.681
19.9501	D	48.381	51.619	3.075	5.346
24.9883	D	51.068	48.932	2.687	4.268
29.9754	D	53.070	46.930	2.002	3.558
36.5549	D	54.732	45.268	1.662	2.918
46.5389	D	56.746	43.254	2.014	2.292
57.4176	D	58.427	41.573	1.681	1.858
71.7285	D	60.252	39.748	1.826	1.487
85.6692	D	61.569	38.431	1.317	1.245
112.3114	D	63.271	36.729	1.702	0.950
138.1392	D	64.453	35.547	1.182	0.772
171.6116	D	65.541	34.459	1.089	0.622
217.7383	D	66.600	33.400	1.059	0.490
266.8052	D	67.421	32.579	0.822	0.400
326.5880	D	68.171	31.829	0.749	0.327
416.2935	D	68.906	31.094	0.736	0.256
517.2520	D	69.357	30.643	0.451	0.206
636.7900	D	69.865	30.135	0.509	0.167
797.6531	D	70.234	29.766	0.369	0.134

Pressure Psia	Cycle	Cum. Hg Sat. Pore Vol., %	Wetting Phase (Sw) Pore Vol., %	Incr. Hg Sat. Pore Vol., %	rp microns
989.9167	D	70.358	29.642	0.124	0.108
1200.5979	D	70.505	29.495	0.147	0.089
1498.1100	D	70.711	29.289	0.207	0.0712
1895.2352	D	70.740	29.260	0.029	0.0563
2343.3411	D	70.740	29.260	0.000	0.0455
2895.7878	D	70.877	29.123	0.137	0.0368
3594.2344	D	70.877	29.123	0.000	0.0297
4487.3555	D	70.877	29.123	0.000	0.0238
5582.0269	D	70.877	29.123	0.000	0.0191
6886.0586	D	70.993	29.007	0.116	0.0155
8586.0967	D	70.993	29.007	0.000	0.0124
10583.4463	D	71.592	28.408	0.599	0.0101
13183.7842	D	71.592	28.408	0.000	0.0081
14781.5195	D	71.592	28.408	0.000	0.0072
16381.7305	D	71.592	28.408	0.000	0.0065
19980.0820	D	71.592	28.408	0.000	0.0053
24991.1504	D	71.592	28.408	0.000	0.0043
29994.1152	D	71.592	28.408	0.000	0.0036
34996.2461	D	71.592	28.408	0.000	0.0030
39988.8242	D	71.592	28.408	0.000	0.0027
44988.1836	D	71.592	28.408	0.000	0.0024
49988.1641	D	71.592	28.408	0.000	0.0021
54990.8633	D	71.592	28.408	0.000	0.0019
59907.2695	D	71.592	28.408	0.000	0.0018
46097.8047	I	66.801	33.199		
35499.1914	I	66.801	33.199		
27294.2910	I	66.801	33.199		
21006.2949	I	66.801	33.199		
16011.2334	I	66.801	33.199		
12407.8398	I	66.801	33.199		
9612.99414	I	66.801	33.199		
7307.89844	I	66.801	33.199		
5699.62207	I	66.801	33.199		
4312.84814	I	66.801	33.199		
3302.41333	I	66.801	33.199		
2607.60449	I	66.801	33.199		
2007.448	I	66.801	33.199		
1502.69678	I	66.801	33.199		
1201.74658	I	66.801	33.199		

902.536438	I	66.801	33.199		
703.036011	I	66.801	33.199		
503.054504	I	66.801	33.199		
401.670105	I	66.801	33.199		
304.803345	I	66.801	33.199		
241.686111	I	66.801	33.199		
193.364792	I	66.801	33.199		
147.012527	I	66.801	33.199		
112.447166	I	66.801	33.199		
88.6106033	I	66.801	33.199		
68.8514709	I	66.585	33.415		
52.4409447	I	65.597	34.403		
33.3937988	I	63.260	36.740		

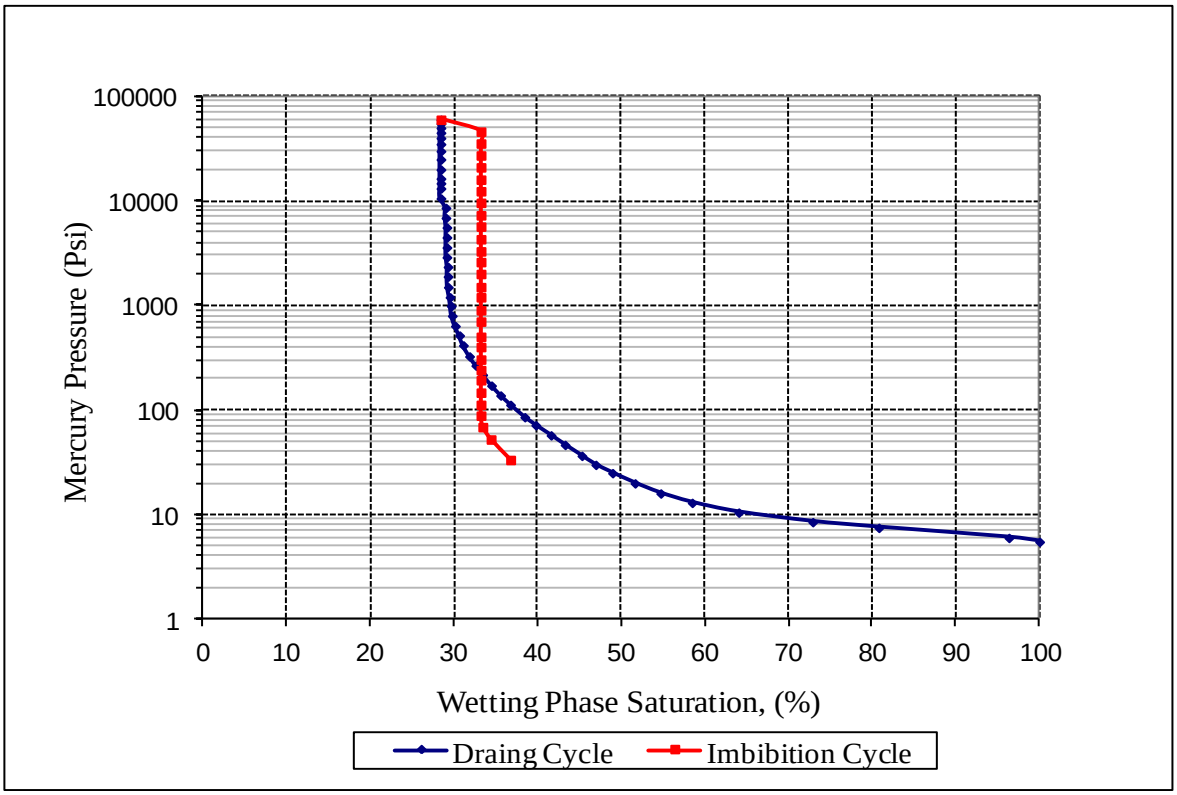

Figure A29. MICP curves (Drainage and imbibtion cycles) for sample # 53.

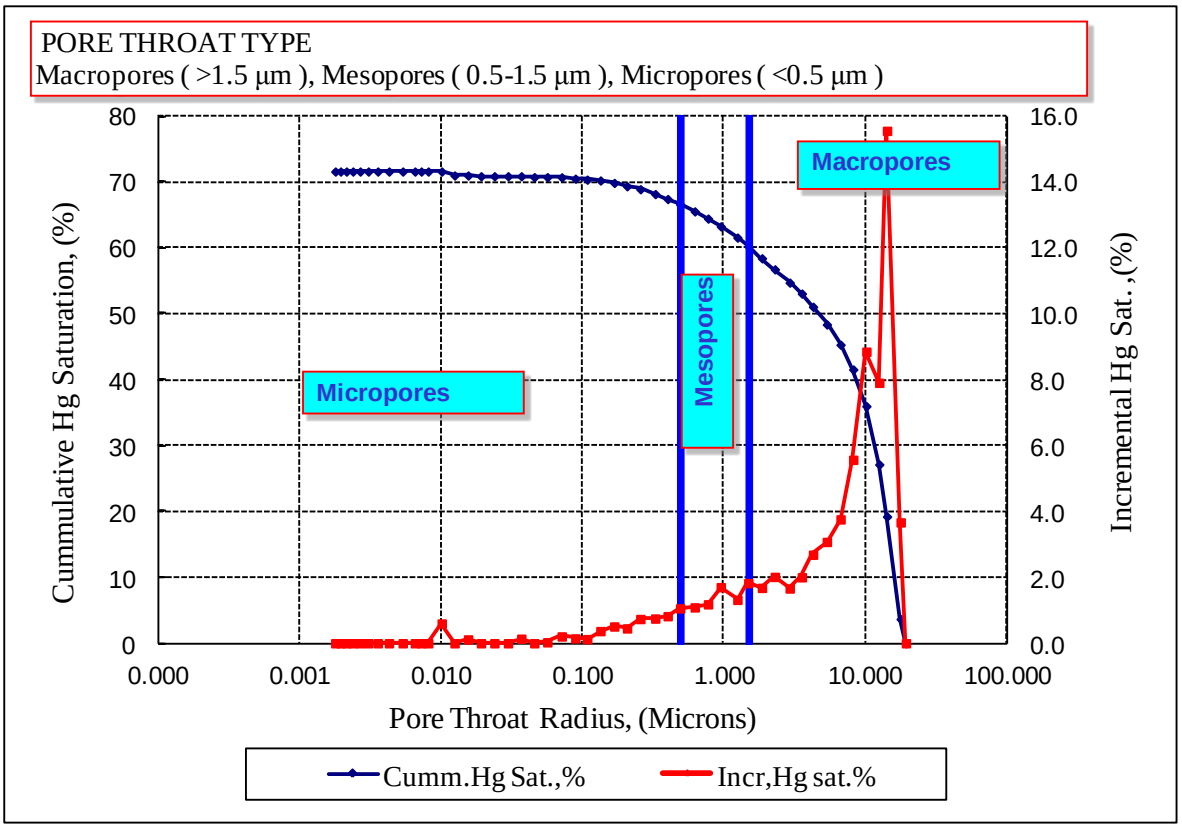

Figure A30. Pore size distribution of sample # 53 using mercury injection capillary pressure.

Table B1. Statistical analysis of horizontal permeability for well A-01.

Permeability Range	Sample in Range	Mean permeability		Frequency (%)	Cumulative Frequency (%)
		Arithm.	Geom.		
0.02-0.04	1	0.020	0.020	1.9	1.9
0.08-0.16	2	0.119	0.115	3.7	5.6
0.16-0.32	3	0.218	0.214	5.6	11.1
0.32-0.64	2	0.451	0.442	3.7	14.8
0.64-1.25	4	0.978	0.956	7.4	22.2
1.25-2.50	7	1.767	1.741	13.0	35.2
2.50-5.00	6	4.005	3.888	11.1	46.3
5- 10	3	7.188	7.176	5.6	51.9
10- 20	4	13.54	13.28	7.4	59.3
20- 40	4	31.42	30.98	7.4	66.7
40- 80	5	58.61	56.8	9.3	75.9
80- 160	5	118.3	116.6	9.3	85.2
160- 320	5	236.6	231.2	9.3	94.4
320- 640	2	439.3	429.8	3.7	98.1
640-1280	1	838.0	838.0	1.9	100.0

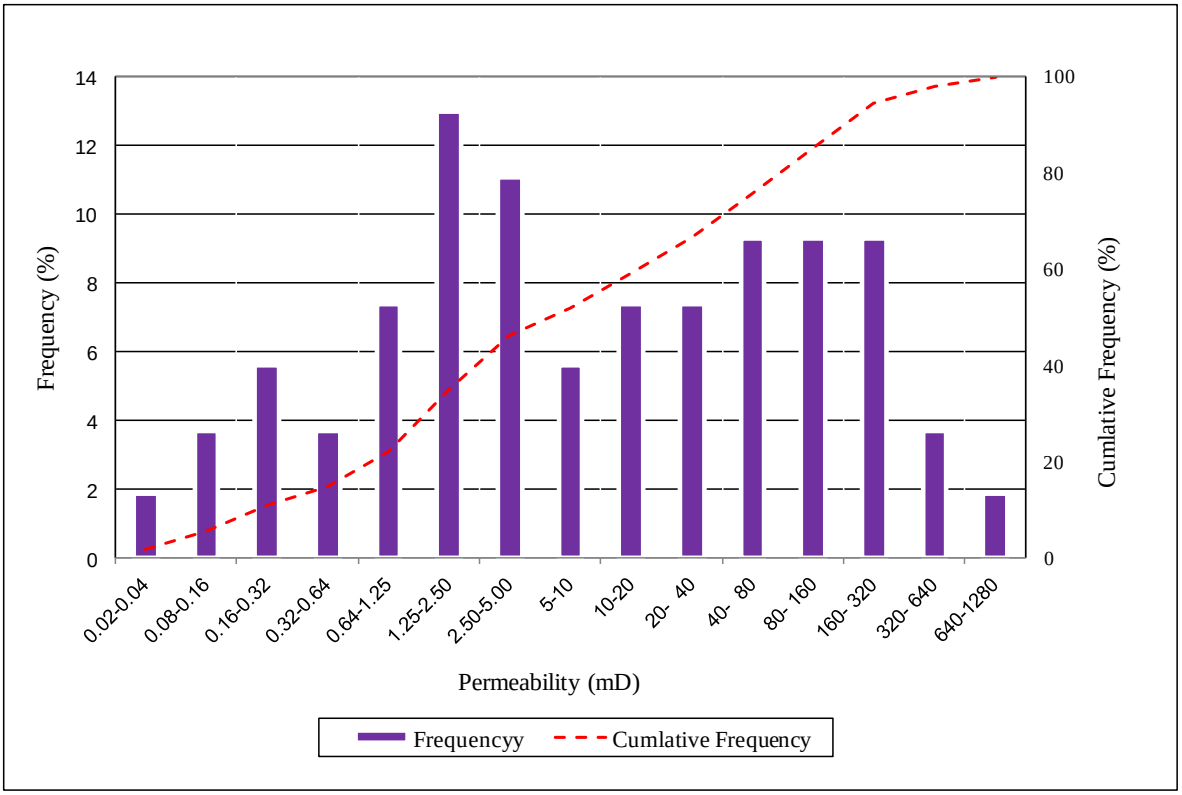

Figure B1. Horizontal permeability frequency distribution for well A-01.

Table B2. Statistical analysis of porosity for well A-01.

Porosity Range	Samples in Range	Mean Porosity	Frequency (%)	Cumulative Frequency (%)
0-2	2	0.73	3.70	3.70
2-4	6	3.16	11.11	14.81
4-6	13	5.16	24.07	38.89
6-8	6	7.04	11.11	50.00
8-10	9	9.47	16.67	66.67
10-12	11	10.86	20.37	87.04
12-14	6	12.77	11.11	98.15
16-18	1	16.00	1.85	100.00

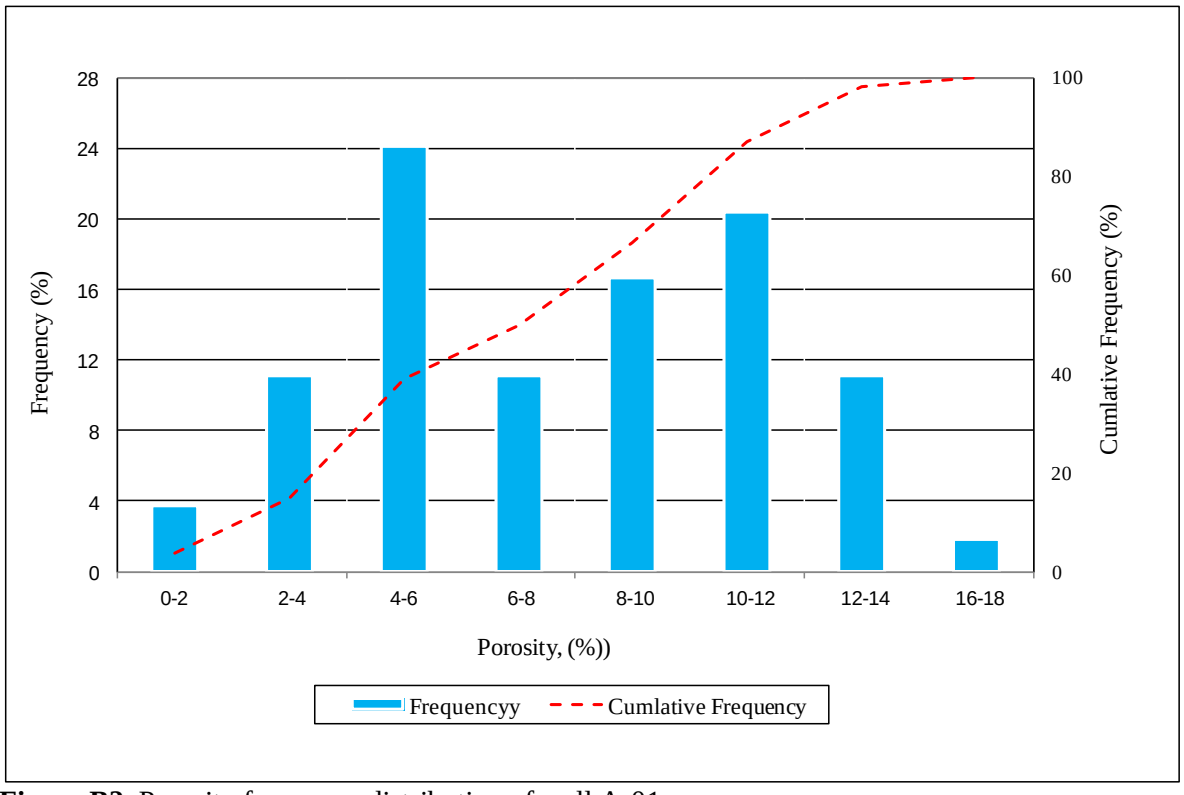

Figure B2. Porosity frequency distribution of well A-01.

Table B3. Statistical analysis of horizontal permeability for well A-03.

Permeability Range	Samples in Range	Mean permeability		Frequency (%)	Cumulative Frequency (%)
		Arithm.	Geom.		
0.01-0.02	1	0.015	0.015	1.2	1.2
0.02-0.04	3	0.026	0.026	3.5	4.7
0.04-0.08	1	0.040	0.040	1.2	5.8
0.08-0.16	4	0.146	0.146	4.7	10.5
0.16-0.32	5	0.225	0.222	5.8	16.3
0.32-0.64	8	0.414	0.406	9.3	25.6
0.64-1.25	5	0.957	0.937	5.8	31.4
1.25-2.50	11	1.813	1.785	12.8	44.2
2.50-5.00	5	3.388	3.338	5.8	50.0
5- 10	6	7.135	6.977	7.0	57.0
10- 20	9	14.29	14.02	10.5	67.4
20- 40	9	30.27	29.80	10.5	77.9
40- 80	7	54.69	53.4	8.1	86.0
80- 160	2	125.0	125.0	2.3	88.4
160- 320	4	257.7	251.1	4.7	93.0
320- 640	5	474.6	468.2	5.8	98.8
640-1280	1	991.0	991.0	1.2	100.0

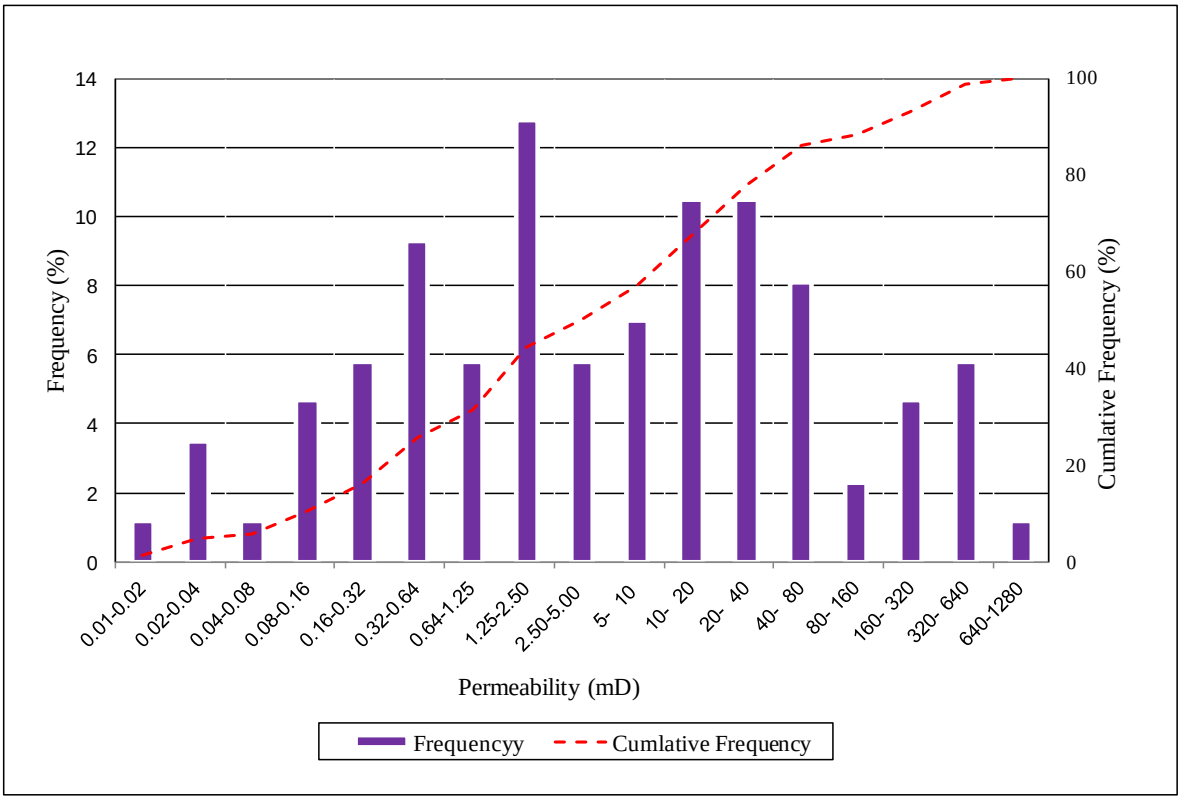

Figure B3. Horizontal permeability frequency distribution of well A-03.

Table B4. Statistical analysis of porosity for well A-03.

Porosity Range	Samples in Range	Mean Porosity	Frequency (%)	Cumulative Frequency (%)
0-2	3	0.95	3.26	3.26
2-4	9	2.84	9.78	13.04
4-6	1	4.45	1.09	14.13
6-8	9	7.09	9.78	23.91
8-10	14	9.25	15.22	39.13
10-12	20	10.79	21.74	60.87
12-14	29	12.73	31.52	92.39
14-16	6	14.82	6.52	98.91
16-18	1	16.93	1.09	100.00

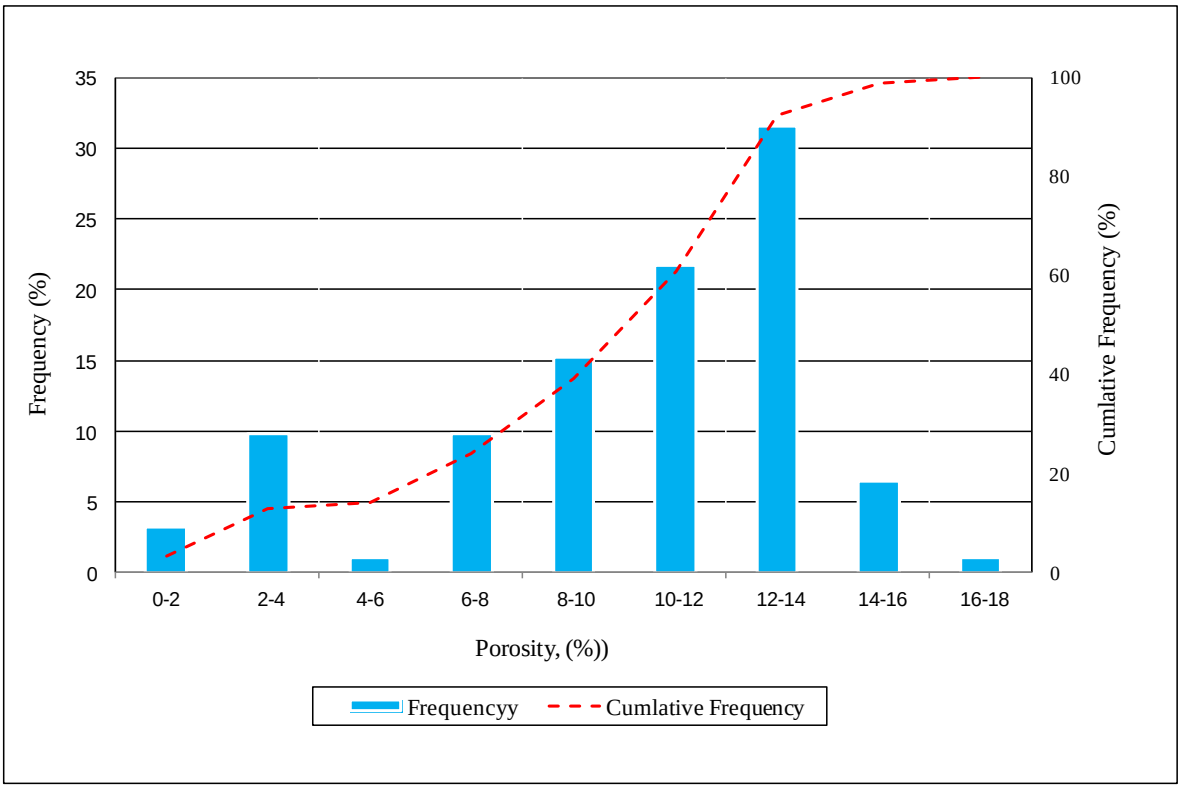

Figure B4. Porosity frequency distribution for well A-03.

Table B5. Statistical analysis of Horizontal permeability for well B-01.

Permeability Range	Samples in Range	Mean permeability		Frequency (%)	Cumulative Frequency (%)
		Arithm.	Geom.		
0.04-0.08	0	0.000	0.00	0.00	0.00
0.08-0.16	1	0.113	0.113	0.45	0.45
0.16-0.32	3	0.200	0.199	1.35	1.79
0.32-0.64	2	0.501	0.494	0.90	2.69
0.64-1.25	5	0.902	0.877	2.24	4.93
1.25-2.5	2	1.735	1.702	0.90	5.83
2.5 - 5	12	3.468	3.398	5.38	11.21
5 - 10	20	6.884	6.763	8.97	20.18
10 - 20	7	14.29	14.15	3.14	23.32
20 - 40	10	27.95	27.55	4.48	27.80
40 - 80	10	64.58	63.57	4.48	32.29
80 - 160	18	118.90	116	8.07	40.36
160 -320	36	233.64	228	16.14	56.50
320 -640	56	477.3	467.24	25.11	81.6
640-1280	28	861.89	851.52	12.56	94.17
1280-2500	13	1722.69	1690.46	5.83	100.00

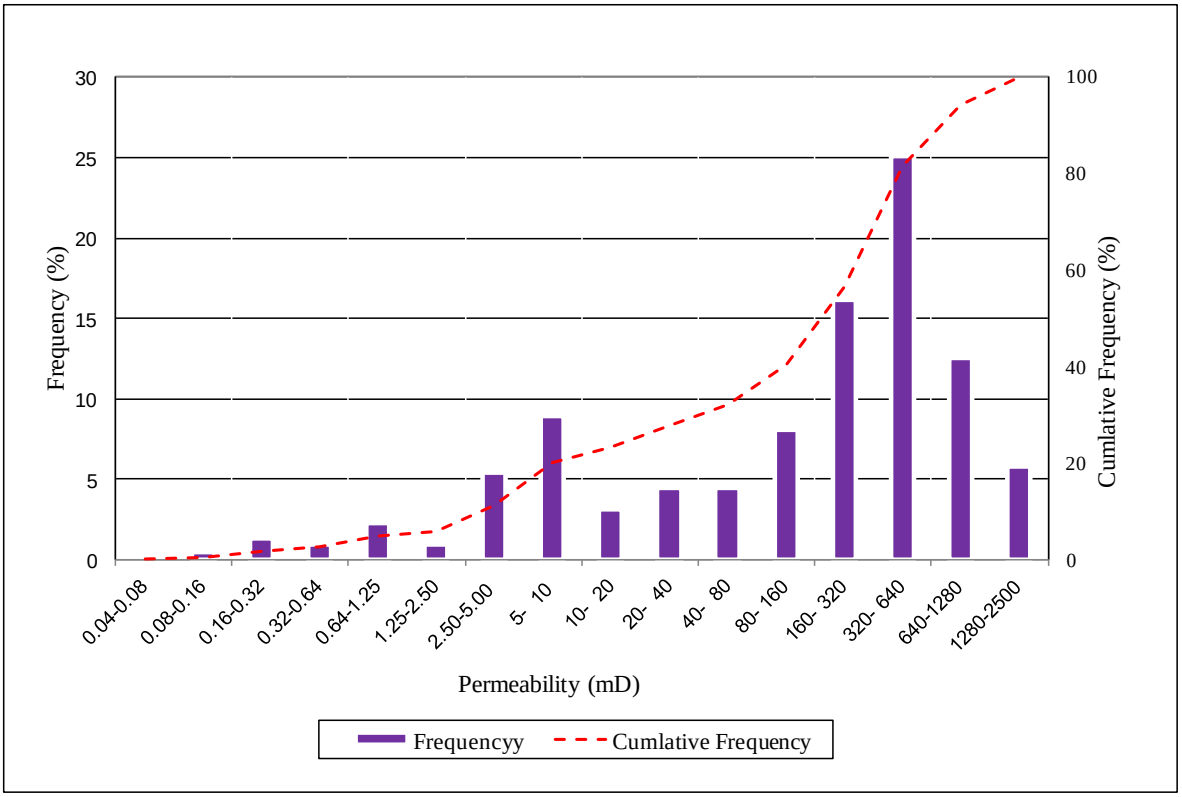

Figure B5. Horizontal permeability frequency distribution of well B-01.

Table B6. Statistical analysis of porosity for well B-01.

Porosity Range	Samples in Range	Mean Porosity	Frequency (%)	Cumulative Frequency (%)
2-4	0	0.00	0.00	0.00
4-6	6	5.64	2.69	2.69
6-8	8	6.79	3.59	6.28
8-10	25	8.99	11.21	17.49
10-12	27	11.03	12.11	29.60
12-14	47	13.21	21.08	50.67
14-16	84	14.93	37.67	88.34
16-18	25	16.69	11.21	99.55
18-20	0	0.00	0.00	99.55
20-22	1	21.65	0.45	100.00

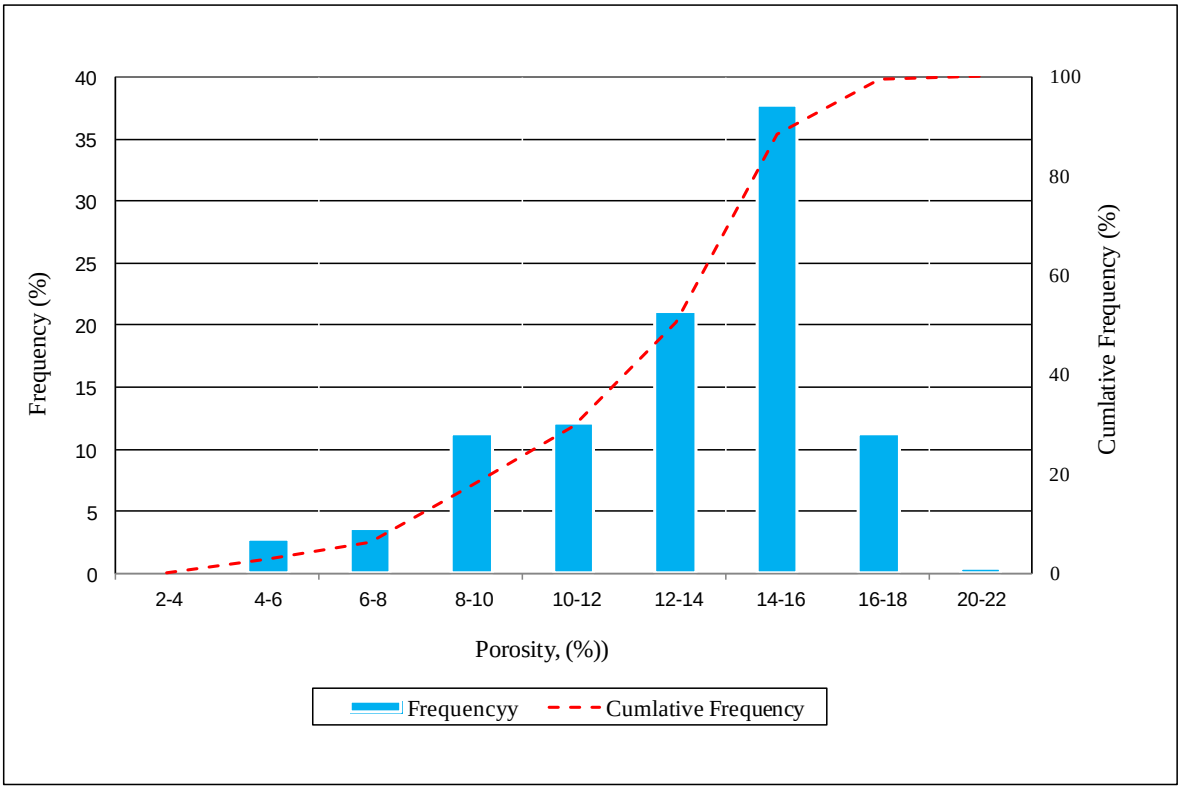

Figure B6. Porosity frequency distribution for well B-01.

Table B7. Statistical analysis of Horizontal permeability for well C-01.

Permeability Range	Samples in Range	Mean permeability		Frequency (%)	Cumulative Frequency (%)
		Arithm.	Geom.		
10 - 20	0	0.00	0.00	0.00	0.00
20 - 40	4	35.33	35.22	2.94	2.94
40 - 80	7	62.00	61.03	5.15	8.09
80 - 160	12	119.58	117.0	8.82	16.91
160 -320	26	255.85	252.0	19.12	36.03
320 -640	50	482.4	473.9	36.76	72.8
640-1280	32	877.75	862.9	23.53	96.32
1280-2500	5	1724.32	1714.2	3.68	100.00

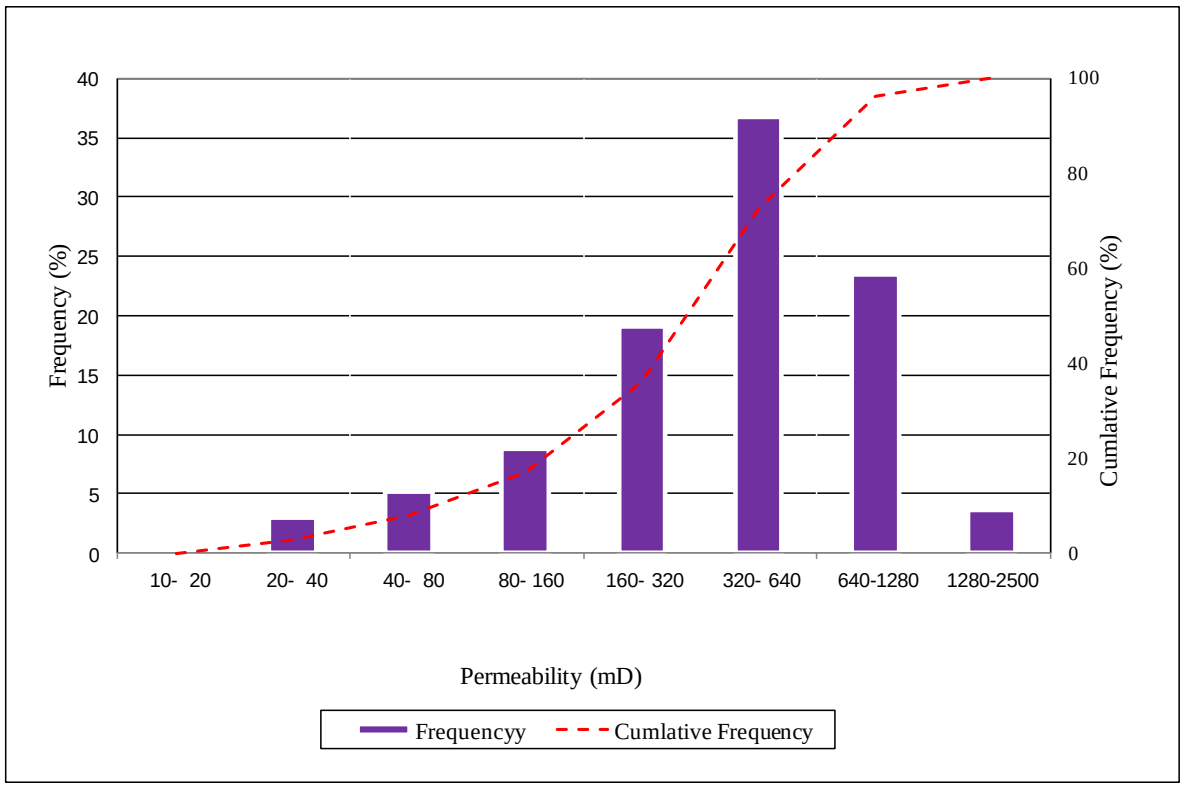

Figure B7. Horizontal permeability frequency distribution of well C-01.

Porosity Range	Samples in Range	Mean Porosity	Frequency (%)	Cumulative Frequency (%)
8-10	0	0.00	0.00	0.00
10-12	7	11.74	5.15	5.15
12-14	46	13.34	33.82	38.97
14-16	75	14.75	55.15	94.12
16-18	8	16.53	5.88	100.00

Table B8. Statistical analysis of porosity for well C-01.

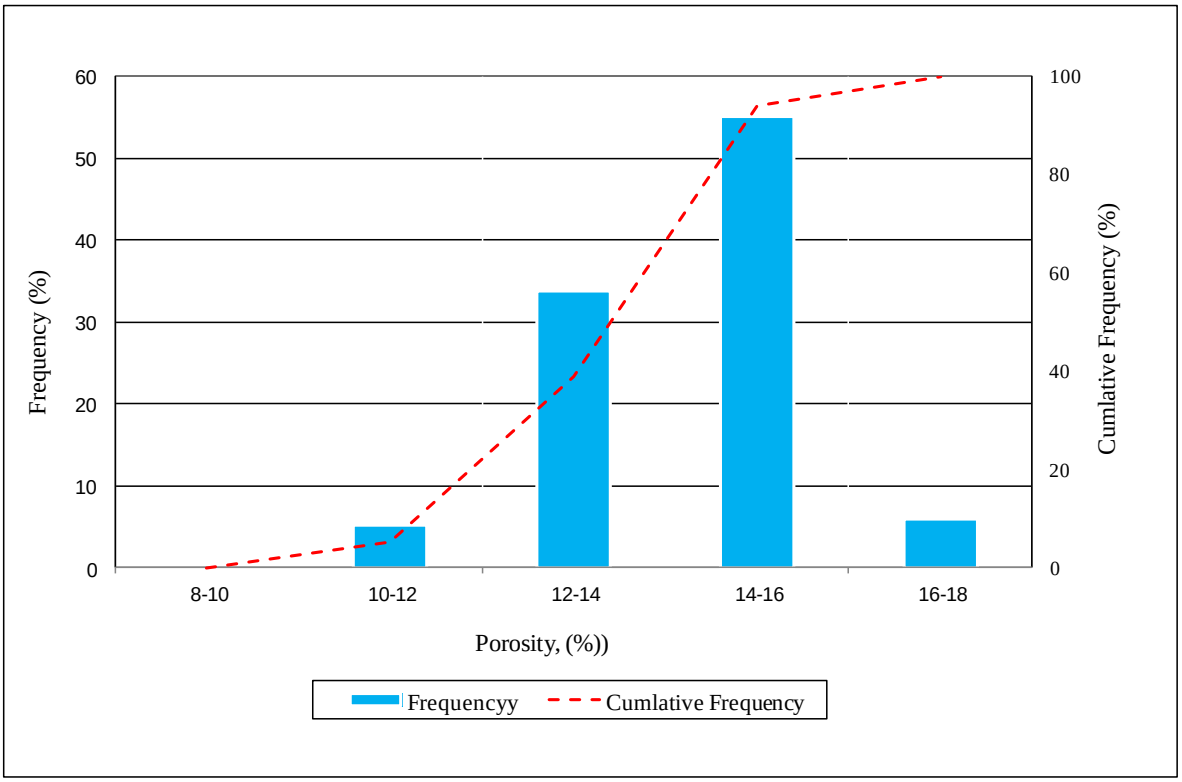

Figure B8. Porosity frequency distribution for well C-01.

Permeability Range	Samples in Range	Mean permeability		Frequency (%)	Cumulative Frequency (%)
		Arithm.	Geom.		
0.08-0.16	0	0.000	0.000	0.00	0.00
0.16-0.32	1	0.241	0.241	1.06	1.06
0.32-0.64	4	0.472	0.452	4.26	5.32
0.64-1.25	7	0.890	0.875	7.45	12.77
1.25-2.5	7	2.129	2.098	7.45	20.21
2.5 - 5	4	3.201	3.144	4.26	24.47
5 - 10	4	6.672	6.583	4.26	28.72
10 - 20	4	16.96	16.86	4.26	32.98
20 - 40	12	30.63	30.27	12.77	45.74
40 - 80	7	74.25	74.21	7.45	53.19
80 - 160	6	109.80	106	6.38	59.57
160-320	8	253.41	249	8.51	68.09
320-640	17	444.5	437.56	18.09	86.2
640-1280	12	822.09	816.09	12.77	98.94
1280-2500	1	1519.50	1519.50	1.06	100.00

Table B9. Statistical analysis of horizontal permeability for well C-02.

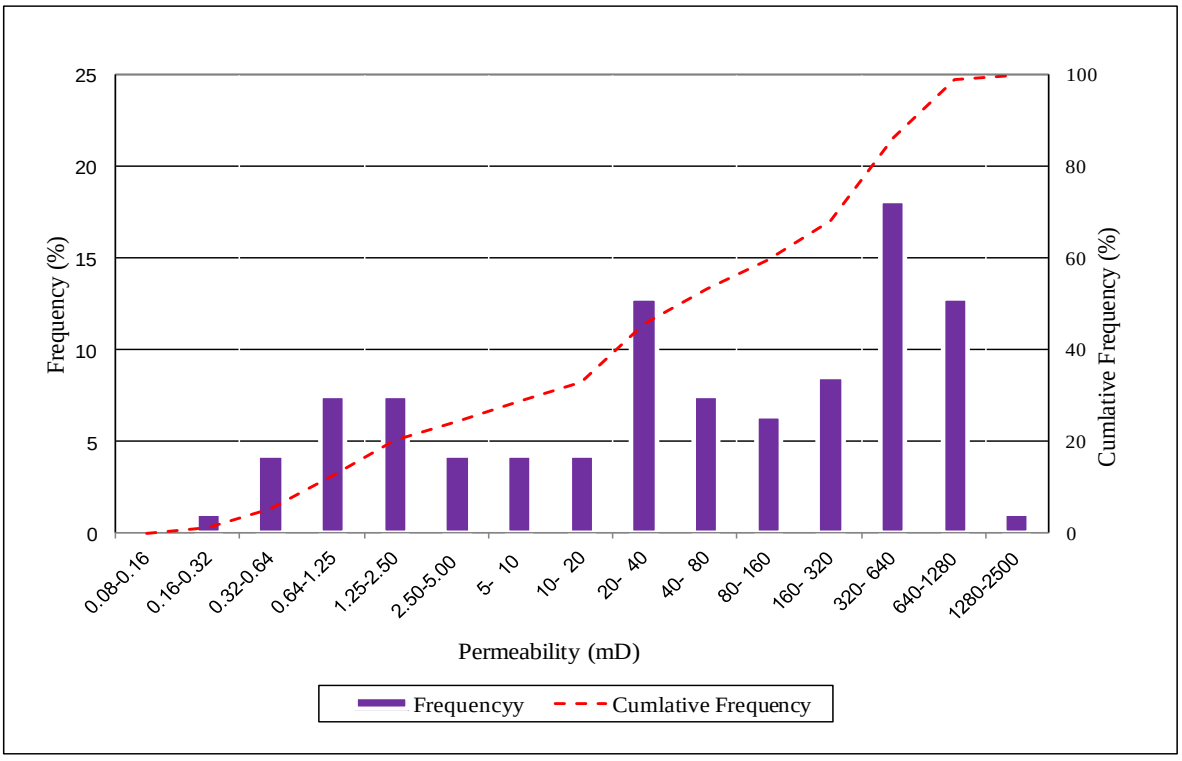

Figure B9. Horizontal permeability frequency distribution for well C-02.

Permeability Range	Samples in Range	Mean Porosity	Frequency (%)	Cumulative Frequency (%)
0 - 2	0	0.00	0.00	0.0
2 - 4	1	3.11	1.06	1.06
4 - 6	1	4.02	1.06	2.13
6 - 8	3	7.63	3.19	5.32
8-10	14	9.27	14.89	20.21
10-12	25	11.16	26.60	46.81
12-14	27	12.76	28.72	75.53
14-16	10	15.15	10.64	86.17
16-18	11	16.61	11.70	97.87
18-20	2	18.73	2.13	100.00

Table B10. Statistical analysis of porosity for well C-02.

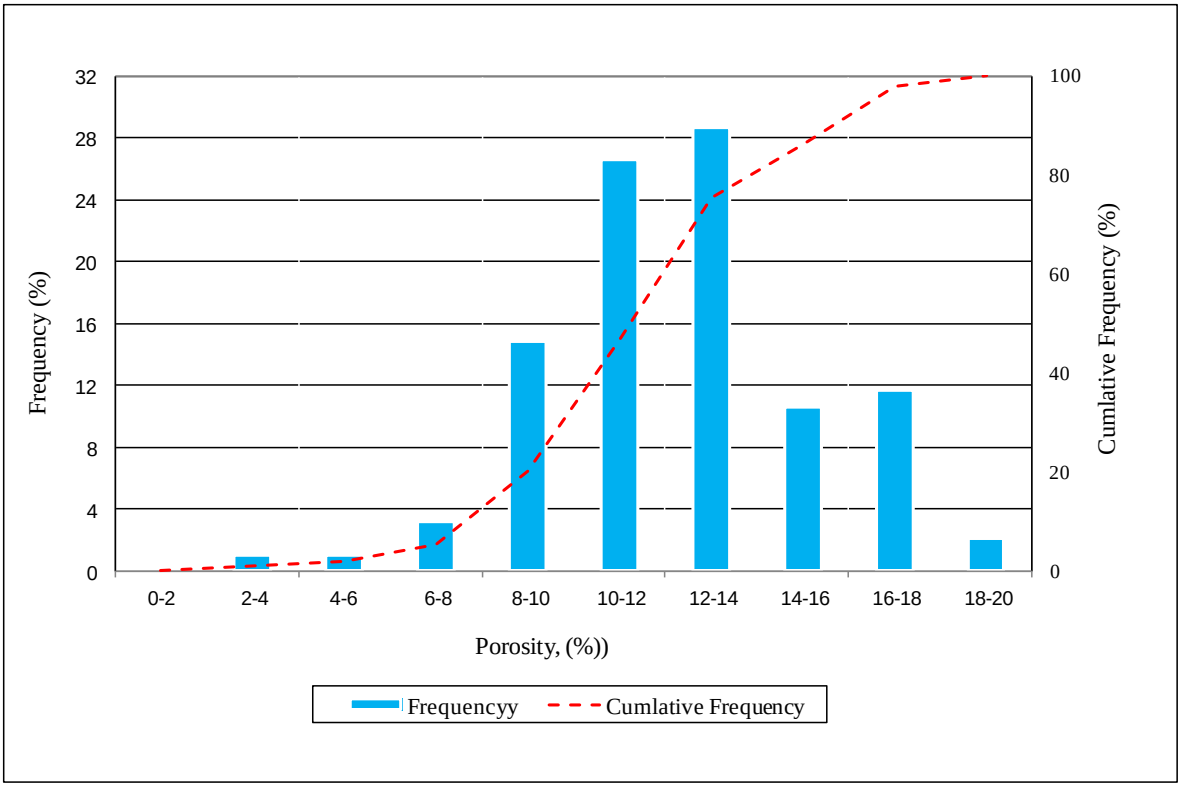

Figure B10. Porosity frequency distribution for well C-02.

Table C1. The range of wireline log and resistivity values for normalisation purposes in the BPNN for training well **A-02** at **0.5** ft spacing.

	SGR (API)	CGR (API)	CALI in	RHOB g/cc	NPHI fraction	Log ILD Ohm.m	Log ILM Ohm.m	DT µs/ft	Log RT Ohm.m	Log RI Ohm.m
Min.	11.36	6.17	5.76	2.38	0.038	0.129	0.30	59.9	1.256	0.71
Max.	112.96	60.88	6.30	2.69	0.182	2.013	2.09	78.6	1.60	1.21

Table C2. The range of wireline log and resistivity values for normalisation purposes in the BPNN for adjacent test well **A-01** in the same oil field at **1.0** ft spacing.

	SGR (API)	CGR (API)	CALI in	RHOB g/cc	NPHI fraction	Log ILD Ohm.m	Log ILM Ohm.m	DT µs/ft	Log RT Ohm.m	Log RI Ohm.m
Min.	9.51	6.301	5.51	2.41	0.037	0.237	0.31	56.8	1.31	0.76
Max.	118.01	85.15	7.63	2.76	0.243	1.79	1.91	72	1.59	1.16

Table C3. The range of wireline log and resistivity values for normalisation purposes in the BPNN for tested well **B0-1** in different oil field at **1.0** ft spacing.

	SGR (API)	CGR (API)	CALI (in)	RHOB (g/cc)	NPHI fraction	Log ILD Ohm.m	Log ILM Ohm.m	DT µs/ft	Log RT Ohm.m	Log RI Ohm.m
Min.	23.21	20.24	5.89	2.36	0.059	0.636	0.411	60.9	1.31	0.76
Max.	98.11	67.38	6.51	2.64	0.117	2.63	1.53	82.4	1.59	1.16

Table C4. Summary of the petrophysical parameters used in study area from training well A-02 and its GHEs.

Sample#	Log depth (ft)	Core depth (ft)	K(mD)	Ø (fraction)	RQI	$Ø_z$	FZI	GHE
30	15385	15373	3.01	0.0842	0.1877	0.0919	2.0420	5
33	15388	15376	76.3	0.0856	0.9375	0.0936	10.0142	7
34	15389	15377	117	0.0930	1.1137	0.1025	10.8619	7
35	15390	15378	118	0.0874	1.1538	0.0958	12.0471	7
44	15401	15389	34.2	0.1428	0.4859	0.1666	2.9170	5
45	15402	15390	74.1	0.0826	0.9405	0.0900	10.4455	7
48	15405	15393	19.6	0.1202	0.4010	0.1366	2.9348	5
51	15410	15398	455	0.1551	1.7007	0.1836	9.2645	7
52	15411	15399	221	0.1193	1.3515	0.1355	9.9768	7
57	15419	15407	56.5	0.1159	0.6933	0.1311	5.2885	6
59	15421	15409	524	0.1448	1.8889	0.1693	11.1560	7
61	15423	15411	960	0.1391	2.6086	0.1616	16.1446	8
62	15424	15412	771	0.1588	2.1879	0.1888	11.5899	8
64	15426	15414	4.53	0.1127	0.1991	0.1270	1.5673	5
80	15452	15439	108.54	0.1311	0.9035	0.1509	5.9881	6
83	15455	15442	15.913	0.0924	0.4121	0.1018	4.0475	6
86	15459	15446	2.341	0.0825	0.1673	0.0899	1.8602	5
89	15462	15449	38.362	0.1324	0.5345	0.1526	3.5024	6
95	15468	15455	72.833	0.1200	0.7736	0.1364	5.6729	6
111	15486	15473	772.31	0.1507	2.2479	0.1774	12.6683	8
114	15489	15476	607.125	0.1537	1.9735	0.1816	10.8663	7
118	15493	15480	66.43	0.1190	0.7419	0.1351	5.4925	6
119	15494	15481	79.873	0.1349	0.7641	0.1559	4.8998	6
121	15496	15483	371.063	0.1328	1.6598	0.1531	10.8387	7
122	15497	15484	7.001	0.0856	0.2840	0.0936	3.0334	6
124	15499	15486	231.88	0.1502	1.2337	0.1767	6.9803	7
127	15503	15490	274.752	0.1451	1.3664	0.1697	8.0503	7

Sample#	Log depth (ft)	Core depth (ft)	K(mD)	Ø (fraction)	RQI	$Ø_z$	FZI	GHE
131	15507	15494	68.044	0.1320	0.7129	0.1521	4.6880	6
132	15508	15495	61.771	0.1288	0.6876	0.1478	4.6512	6
134	15511	15498	31.068	0.1088	0.5306	0.1221	4.3463	6
142	15519	15506	70.956	0.1102	0.7968	0.1238	6.4335	7
155	15532	15519	16.833	0.1303	0.3569	0.1498	2.3821	5
156	15533	15520	7.493	0.1125	0.2563	0.1268	2.0216	5
160	15537	15524	15.932	0.1334	0.3432	0.1539	2.2292	5
186	15563	15550	13.583	0.1076	0.3528	0.1206	2.9260	5
190	15567	15554	31.916	0.1127	0.5284	0.1270	4.1602	6
192	15569	15556	4.953	0.0894	0.2337	0.0982	2.3806	5
223	15602	15589	20.291	0.1098	0.4269	0.1233	3.4607	6
226	15605	15592	5.829	0.0756	0.2757	0.0818	3.3714	6
235	15614	15601	5.728	0.0819	0.2626	0.0892	2.9437	5
241	15620	15607	149.809	0.1339	1.0503	0.1546	6.7935	7
279	15663	15650	51.44	0.0931	0.7381	0.1027	7.1897	7
353	15752	15738	36.166	0.1074	0.5762	0.1203	4.7888	6
394	15798	15784	11.46	0.0743	0.3899	0.0803	4.8575	6
395	15799	15785	16.51	0.0976	0.4084	0.1082	3.7760	6
396	15800	15786	10.81	0.0905	0.3432	0.0995	3.4490	6
400	15804	15790	21.83	0.0734	0.5415	0.0792	6.8365	7
404	15808	15794	157.27	0.1112	1.1808	0.1251	9.4383	7
406	15810	15796	81.02	0.1118	0.8453	0.1259	6.7153	7
408	15812	15798	8.94	0.0906	0.3119	0.0996	3.1308	6
439	15846	15832	6.86	0.1078	0.2504	0.1208	2.0728	5
444	15851	15837	12.32	0.1238	0.3132	0.1413	2.2167	5
454	15861	15847	18.57	0.0864	0.4604	0.0946	4.8682	6
455	15862	15848	25.19	0.0893	0.5273	0.0981	5.3777	6
456	15863	15849	14.33	0.0865	0.4041	0.0947	4.2680	6

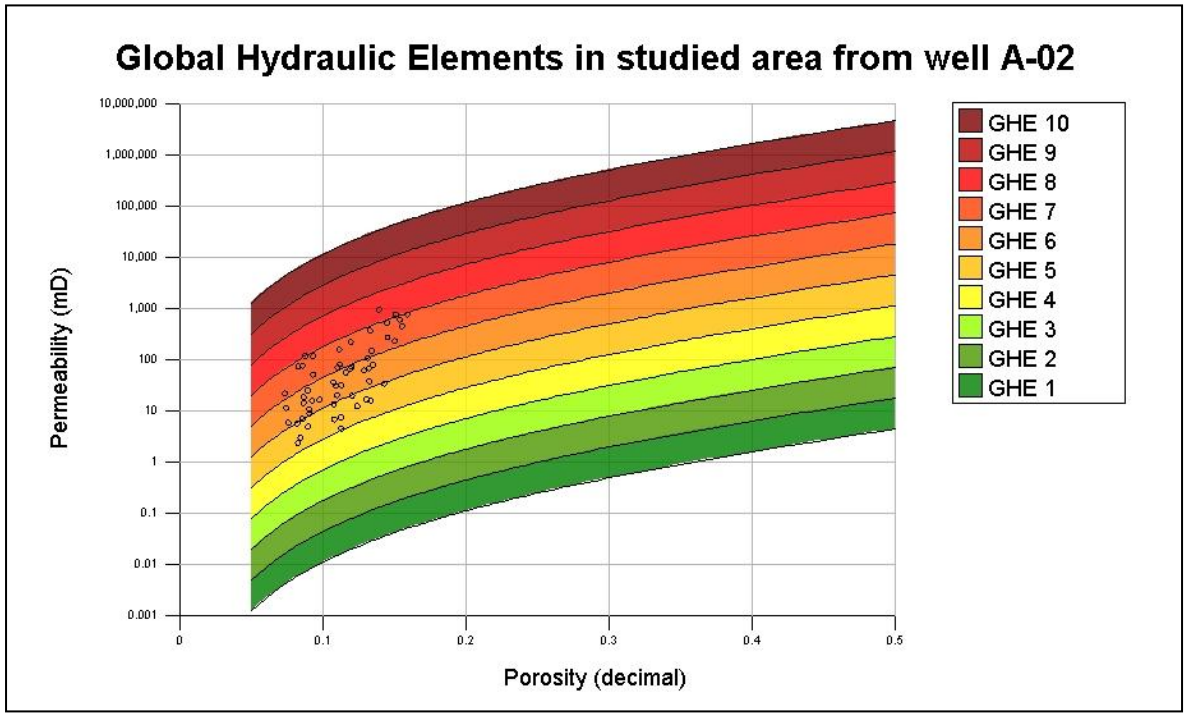

Figure C1. Global hydraulic element porosity-permeability crossplot for the 55 SCAL samples.

Table C5. Summary results of true resistivity (R_t) predictors trained on the entire cored interval (containing 55 SCAL plugs) in training well **A-02** at **0.5 ft** spacing.

Input	**Output**	**Coefficient of determination (R^2)in training well A-02**
Case 1 (RHOB,NPHI,ILD &ILM)	R_t	0.7654
Case 2 (SGR,CGR,NPHI,ILD &ILM)	R_t	0.7369
Case 3 (SGR,CGR,RHOB,NPHI,ILD &ILM)	R_t	0.7698
Case 4 (SGR,CGR,RHOB,NPHI,ILD , ILM,& DT)	R_t	0.7697

Table C6. Summary results of resistivity index (RI) predictors trained on the entire cored interval (containing 55 SCAL plugs) in training well **A-02** at **0.5 ft** spacing.

Input	**Output**	**Coefficient of determination (R^2)in training well A-02**
Case 1 (RHOB,NPHI,ILD &ILM)	RI	0.8426
Case 2 (SGR,CGR,NPHI,ILD &ILM)	RI	0.8088
Case 3 (SGR,CGR,RHOB,NPHI,ILD &ILM)	RI	0.8452
Case 4 (SGR,CGR,RHOB,NPHI,ILD , ILM,& DT)	RI	0.8455

Table C7. Summary results of true resistivity predictors (trained on the entire cored interval in well **A-02**) when tested in adjacent well **A-01** in the same oil field at **1.0** ft spacing.

Input	**Output**	**Coefficient of determination (R^2)in adjacent well A-01**
Case 2 (SGR,CGR,NPHI,ILD &ILM)	R_t	0.2575
Case 3 (SGR,CGR,RHOB,NPHI,ILD &ILM)	R_t	0.3101
Case 4 (SGR,CGR,RHOB,NPHI,ILD, ILM,& DT)	R_t	0.3296

Table C8. Summary results of resistivity index (RI) predictors (trained on the entire cored interval in well **A-02**) when tested in adjacent well **A-01** in the same oil field at **1.0** ft spacing.

Input	**Output**	**Coefficient of determination (R^2) in adjacent well A-01**
Case 2 (SGR,CGR,NPHI,ILD &ILM)	RI	0.4262
Case 3 (SGR,CGR,RHOB,NPHI,ILD &ILM)	RI	0.5379
Case 4 (SGR,CGR,RHOB,NPHI,ILD ,ILM,& DT)	RI	0.5482

Table C9. Summary results of true resistivity predictors (trained on the entire cored interval in well **A-02**) when tested in adjacent well **B-01** in the different oil field at **1.0** ft spacing.

Input	**Output**	**Coefficient of determination (R^2)in test well B-01**
Case 2 (SGR,CGR,NPHI,ILD &ILM)	R_t	0.1555
Case 3 (SGR,CGR,RHOB,NPHI,ILD &ILM)	R_t	0.1946
Case 4 (SGR,CGR,RHOB,NPHI,ILD ,ILM,& DT)	R_t	0.2474

Table C10. Summary results of resistivity index predictors (trained on the entire cored interval in well **A-02**) when tested in adjacent well **B-01** in the different oil field at **1.0** ft spacing.

Input	**Output**	**Coefficient of determination (R^2)in test well B-01**
Case 2 (SGR,CGR,NPHI,ILD &ILM)	RI	0.3649
Case 3 (SGR,CGR,RHOB,NPHI,ILD &ILM)	RI	0.3164
Case 4 (SGR,CGR,RHOB,NPHI,ILD,ILM, & DT)	RI	0.3422

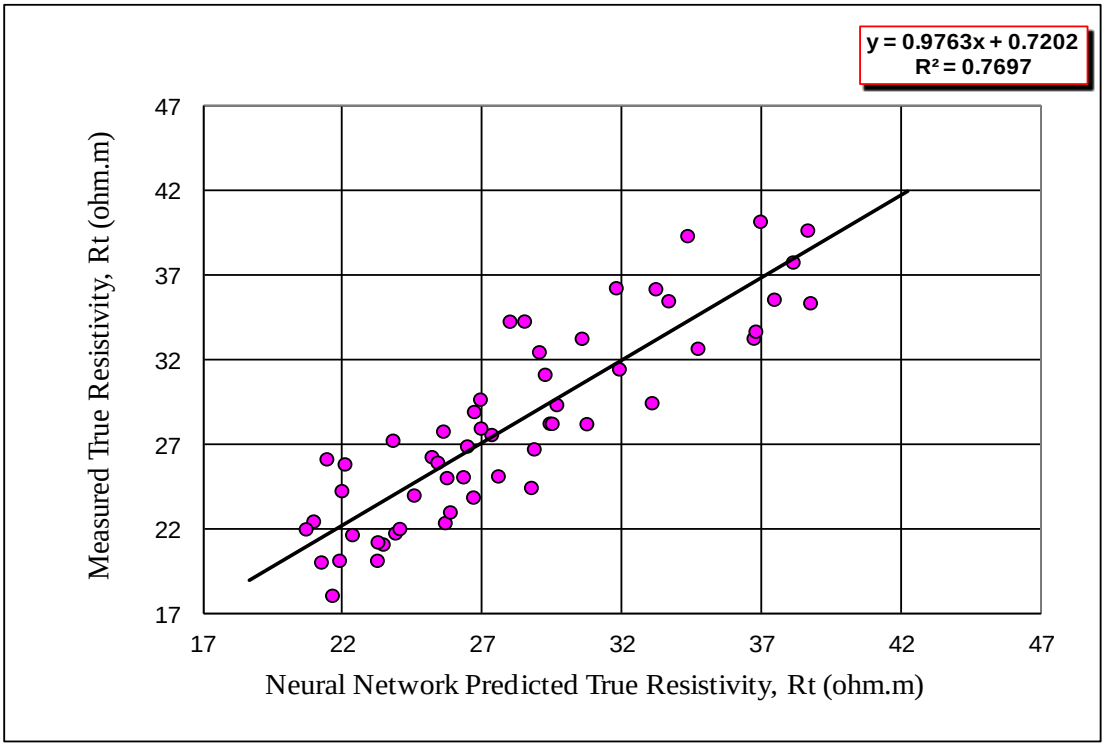

Figure C2. Crossplot of measured true resistivity versus BPNN predicted true resistivity for the case **4** predictor trained on the entire cored interval using **7** wireline logs for training well **A-02** at **0.5** ft spacing.

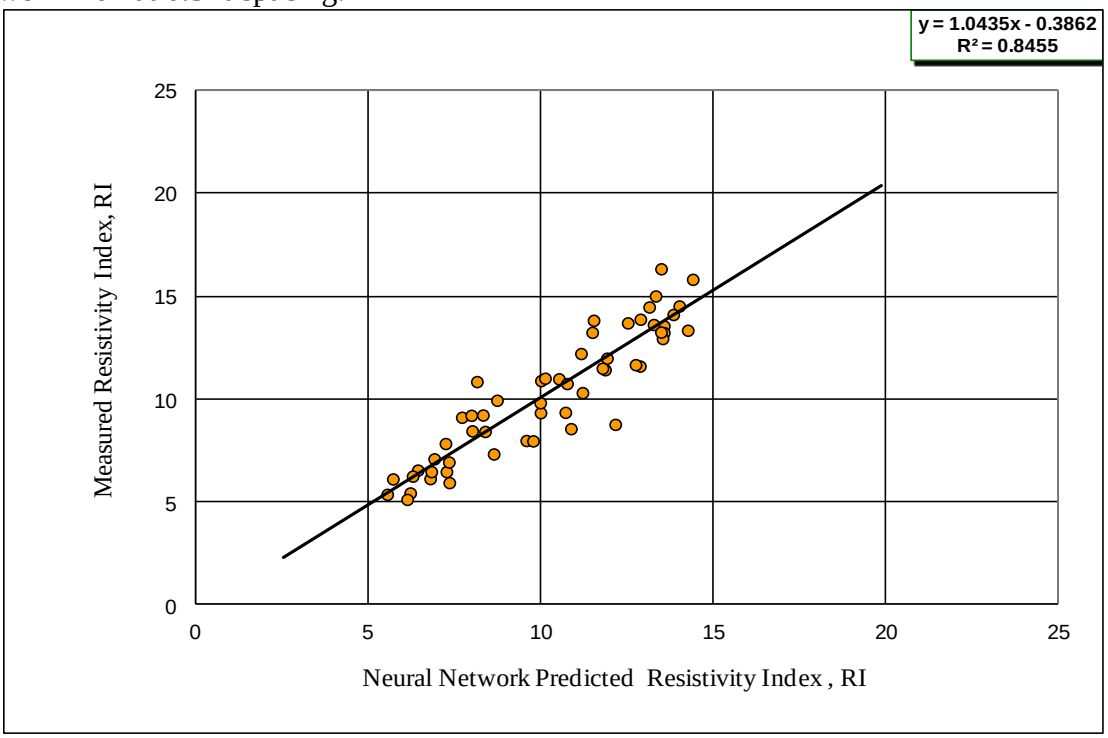

Figure C3. Crossplot of measured true resistivity versus BPNN predicted true resistivity for the case **4** predictor trained on the entire cored interval using **7** wireline logs for training well **A-02** at **0.5** ft spacing.

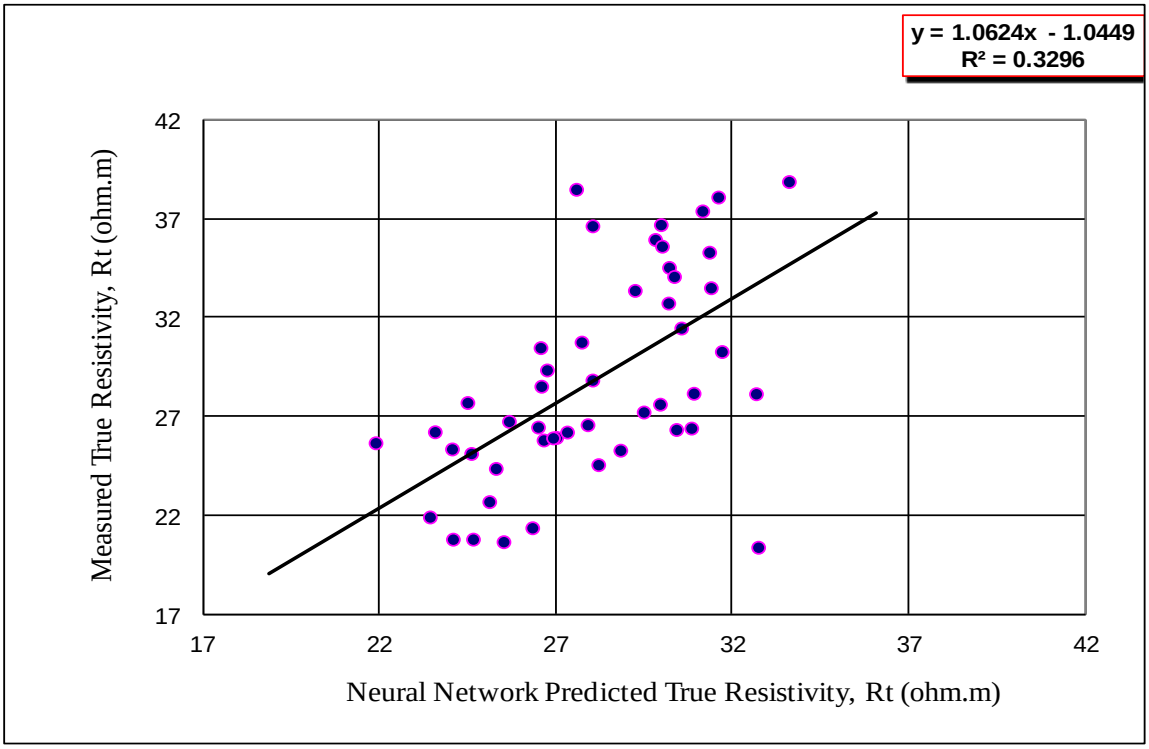

Figure C4. Crossplot of test data: measured true resistivity versus BPNN predicted true resistivity when tested in adjacent well **A-01** for the case **4** predictor trained on the entire cored interval using **7** wireline logs from training well **A-02** at **1.0** ft spacing.

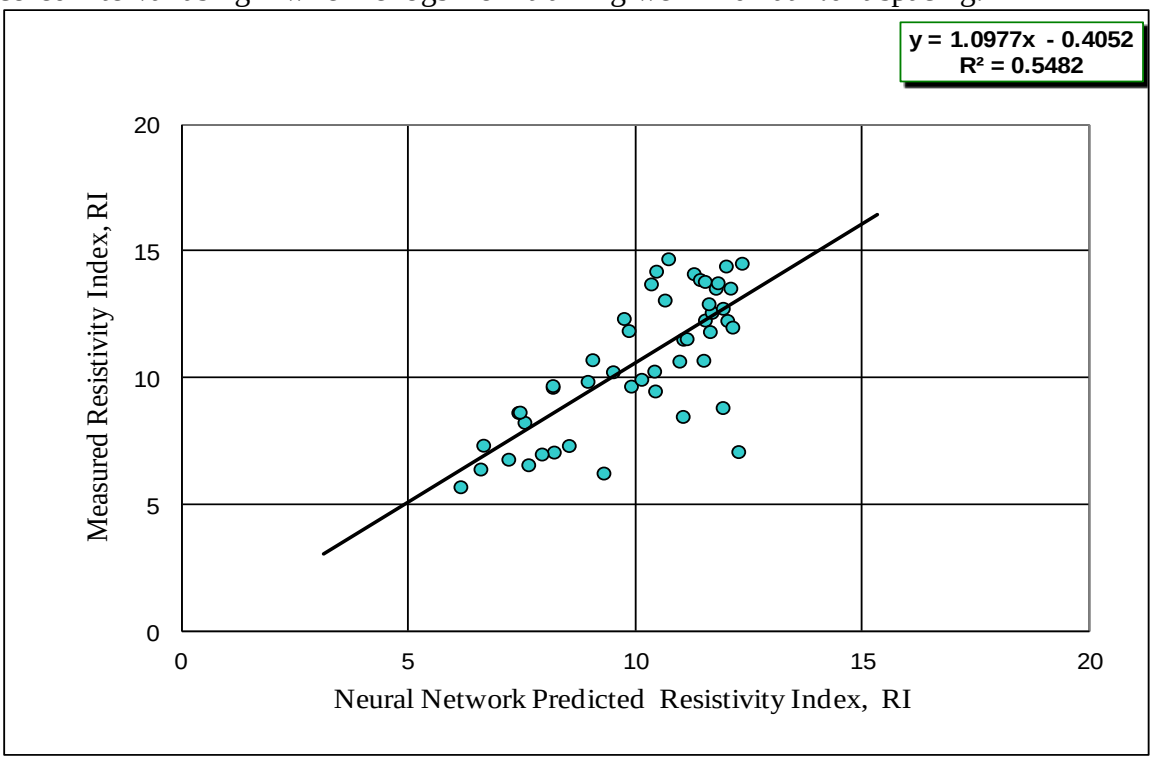

Figure C5. Crossplot of test data: measured resistivity index versus BPNN predicted resistivity index when tested in adjacent well **A-01** for the case **4** predictor trained on the entire cored interval using **7** wireline logs from training well **A-02** at **1.0** ft spacing.

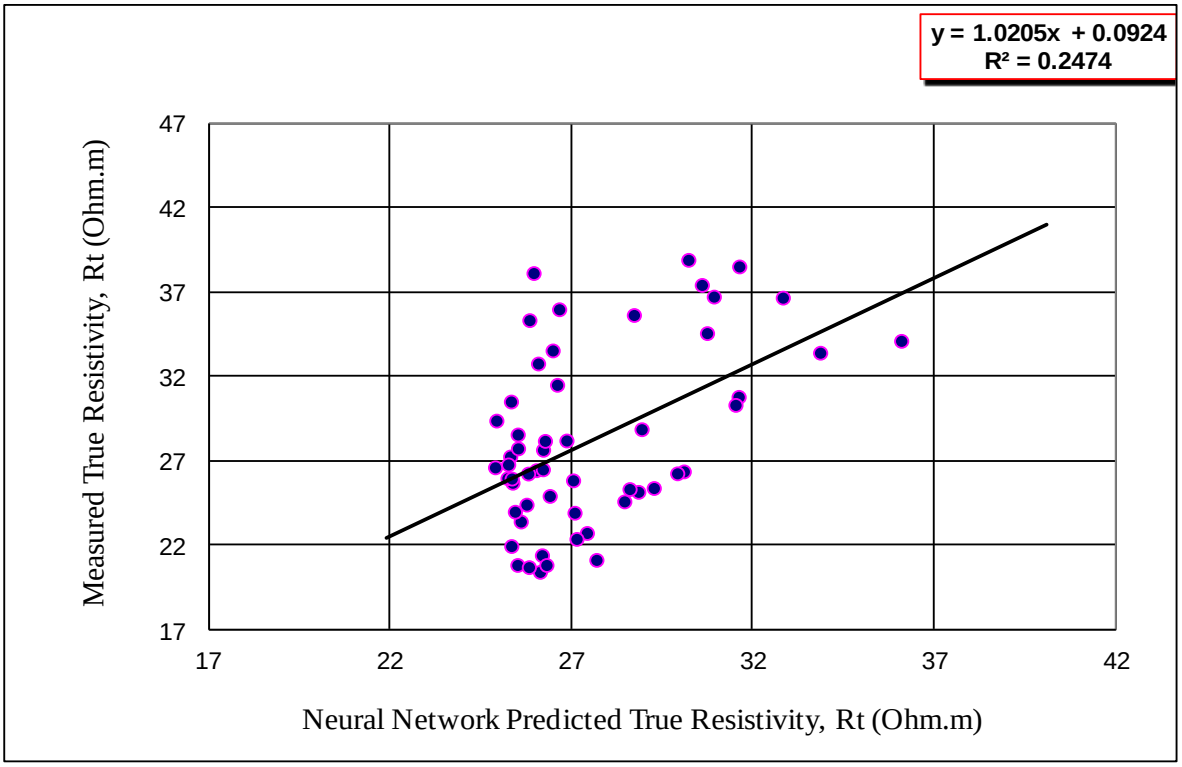

Figure C6. Crossplot of test data: measured true resistivity versus BPNN predicted true resistivity when tested in adjacent well **B-01** for the case **4** predictor trained on the entire cored interval using **7** wireline logs from training well **A-02** at **1.0** ft spacing.

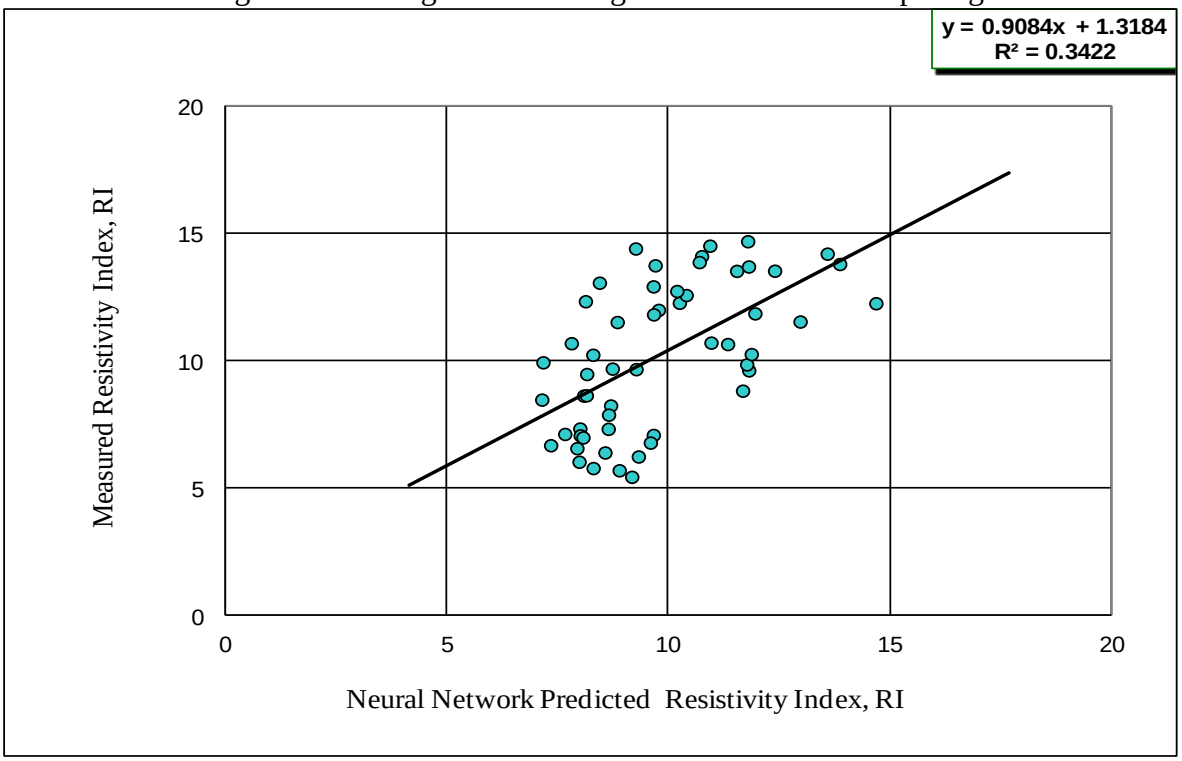

Figure C7. Crossplot of test data: measured resistivity index versus BPNN predicted resistivity index when tested in adjacent well **B-01** for the case **4** predictor trained on the entire cored interval using **7** wireline logs from training well **A-02** at **1.0** ft spacing.

Table C11. The range of wireline log and water saturation and saturation exponent values for normalisation purposes in the BPNN for a training well **A-02** at **0.5** ft spacing.

	SGR (API)	CGR (API)	CALI in	RHOB g/cc	NPHI fraction	Log ILD Ohm.m	Log ILM Ohm.m	DT µs/ft	S_w	n
Min.	11.36	6.17	5.76	2.38	0.038	0.129	0.30	59.9	0.2444	1.92
Max.	112.96	60.88	6.30	2.69	0.182	2.013	2.09	78.6	0.4521	2.14

Table C12. The range of wireline log and water saturation and saturation exponent values for normalisation purposes in the BPNN for adjacent test well **A-01** in the same oil field at **1.0** ft spacing.

	SGR (API)	CGR (API)	CALI in	RHOB g/cc	NPHI fraction	Log ILD Ohm.m	Log ILM Ohm.m	DT µs/ft	S_w	n
Min.	9.51	6.301	5.51	2.41	0.037	0.237	0.31	56.8	0.2576	1.95
Max.	118.01	85.15	7.63	2.76	0.243	1.79	1.91	72	0.4178	2.13

Table C13. The range of wireline log and water saturation and saturation exponent values for normalisation purposes in the BPNN for adjacent test well **B-01** in the different oil field at **1.0** ft spacing.

	SGR (API)	CGR (API)	CALI (in)	RHOB (g/cc)	NPHI fraction	Log ILD Ohm.m	Log ILM Ohm.m	DT µs/ft	S_w	n
Min.	23.21	20.24	5.89	2.36	0.059	0.636	0.411	60.9	0.2576	1.95
Max.	98.11	67.38	6.51	2.64	0.117	2.63	1.53	82.4	0.4178	2.13

Table C14. Summary results of water saturation (S_w) predictors trained on the entire cored interval in the training well **A-02** at **0.5** ft spacing.

input	**Output**	**Coefficient of determination (R^2)in training well A-02**
Case 1 (RHOB,NPHI,ILD &ILM)	S_w	0.8574
Case 2 (SGR,CGR,NPHI,ILD &ILM)	S_w	0.8251
Case 3 (SGR,CGR,RHOB,NPHI,ILD &ILM)	S_w	0.8600
Case 4 (SGR,CGR,RHOB,NPHI,ILD , ILM,& DT)	S_w	0.8602

Table C15. Summary results of saturation exponent (n) predictors trained on the entire cored interval in the training well **A-02** at **0.5** ft spacing.

Input	**Output**	**Coefficient of determination (R^2)in training well A-02**
Case 1 (RHOB,NPHI,ILD &ILM)	n	0.7069
Case 2 (SGR,CGR,NPHI,ILD &ILM)	n	0.7082
Case 3 (SGR,CGR,RHOB,NPHI,ILD &ILM)	n	0.7342
Case 4 (SGR,CGR,RHOB,NPHI,ILD , ILM,& DT)	n	0.7377

Table C16. Summary results of, water saturation (S_w) predictors (trained on the entire cored interval of well **A-02**) when tested in adjacent well **A-01** in the same oil field at **1.0** ft spacing.

Input	**Output**	**Coefficient of determination (R^2) in adjacent well A-01**
Case 2 (SGR,CGR,NPHI,ILD &ILM)	S_w	0.3250
Case 3 (SGR,CGR,RHOB,NPHI,ILD &ILM)	S_w	0.4875
Case 4 (SGR,CGR,RHOB,NPHI,ILD, ILM,& DT)	S_w	0.5157

Table C17. Summary results of, saturation exponent (n) predictors (trained on the entire cored interval of well **A-02**) when tested in adjacent well **A-01** in the same oil field at **1.0** ft spacing.

Input	Output	Coefficient of determination (R^2) in adjacent well A-01
Case 2 (SGR,CGR,NPHI,ILD &ILM)	n	0.216
Case 3 (SGR,CGR,RHOB,NPHI,ILD &ILM)	n	0.237
Case 4 (SGR,CGR,RHOB,NPHI,ILD , ILM, & DT)	n	0.252

Table C18. Summary results of, water saturation (S_w) predictors (trained on the entire cored interval of well **A-02**) when tested in adjacent well **B-01** in the same oil field at **1.0** ft spacing

Input	Output	Coefficient of determination (R^2) in test well B-01
Case 2 (SGR,CGR,NPHI,ILD &ILM)	S_w	0.3878
Case 3 (SGR,CGR,RHOB,NPHI,ILD &ILM)	S_w	0.3288
Case 4 (SGR,CGR,RHOB,NPHI,ILD, ILM,& DT)	S_w	0.3455

Table C19. Summary results of, saturation exponent (n) predictors (trained on the entire cored interval of well **A-02**) when tested in adjacent well **B-01** in the same oil field at **1.0** ft spacing.

Input	Output	Coefficient of determination (R^2) in test well B-01
Case 2 (SGR,CGR,NPHI,ILD &ILM)	n	0.2360
Case 3 (SGR,CGR,RHOB,NPHI,ILD &ILM)	n	0.2869
Case 4 (SGR,CGR,RHOB,NPHI,ILD,ILM,& DT)	n	0.2904

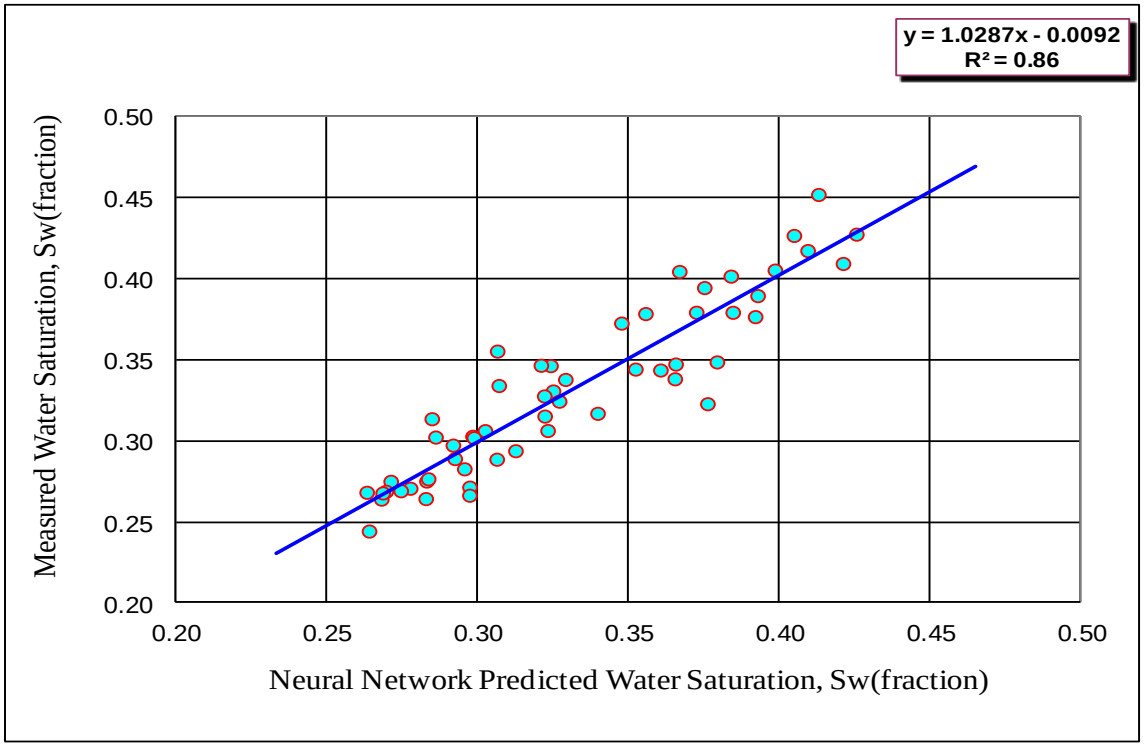

Figure C8. Crossplot of measured water saturation (S_w) versus BPNN predicted water saturation for the case **3** predictor trained on the entire cored interval using **6** wireline logs for training well **A-02** at **0.5** ft spacing.

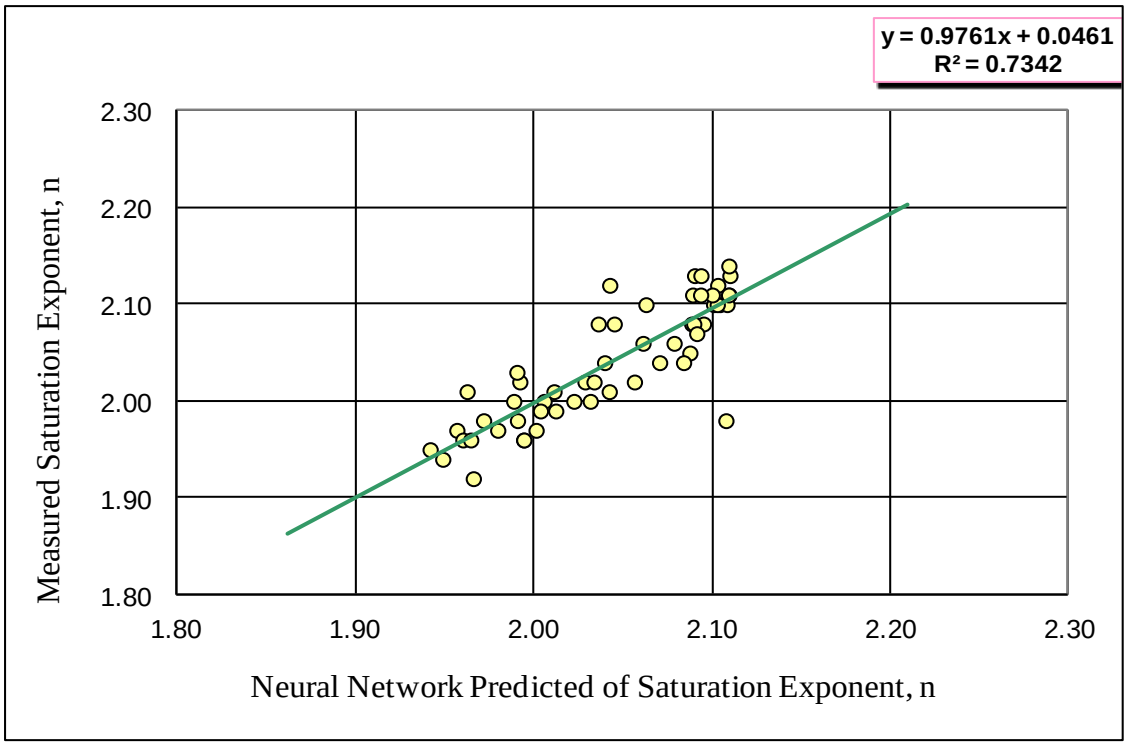

Figure C9. Crossplot of measured saturation exponent (n) versus BPNN predicted saturation exponent for the case **3** predictor trained on the entire cored interval using **6** wireline logs for training well **A-02** at **0.5** ft spacing.

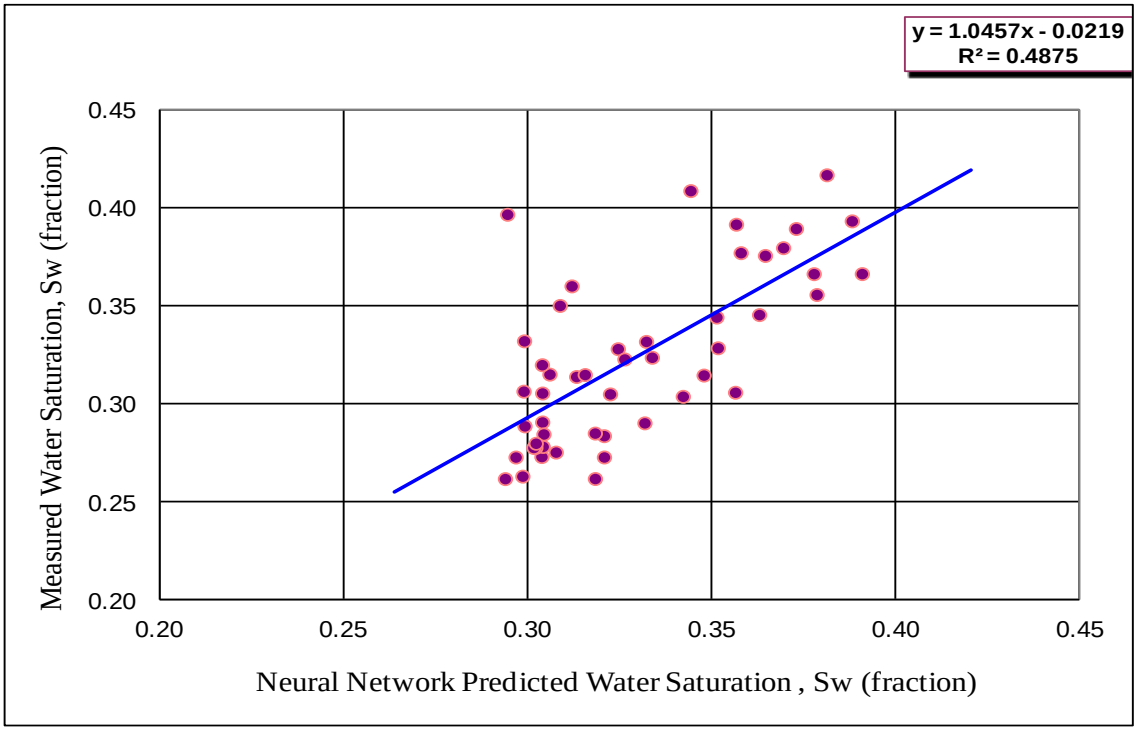

Figure C10. Crossplot of test data: measured water saturation (S_w) versus BPNN predicted water saturation when tested in adjacent well **A-01** for the case **3** predictor trained on the entire cored interval using **6** wireline logs from training well **A-02** at **1.0** ft spacing.

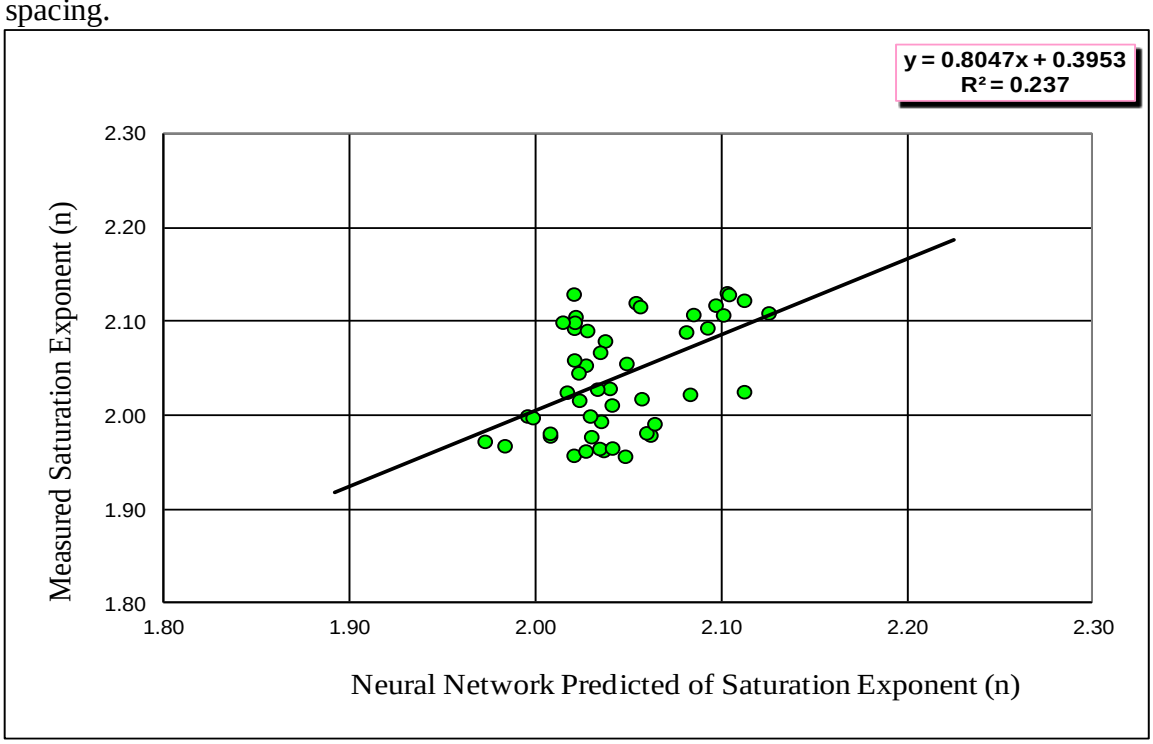

Figure C11. Crossplot of test data: measured saturation exponent (n) versus BPNN predicted saturation exponent when tested in adjacent well **A-01** for the case **3** predictor trained on the entire cored interval using **6** wireline logs from training well **A-02** at **1.0** ft spacing.

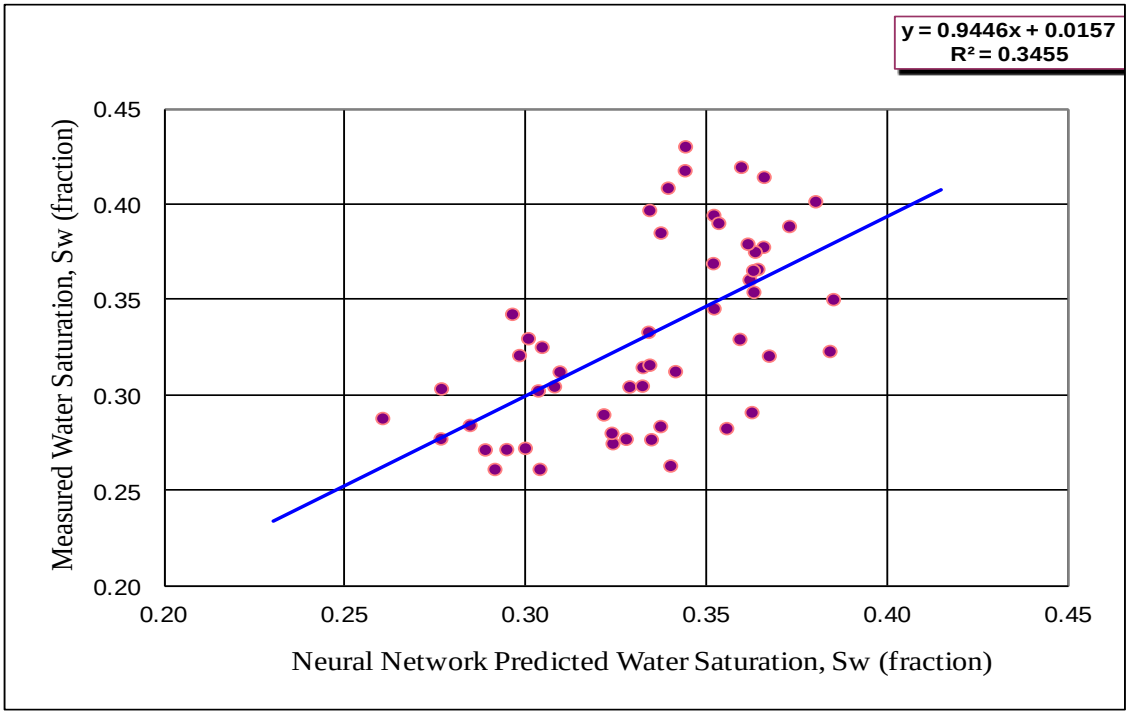

Figure C12. Crossplot of test data: measured water saturation (S_w) versus BPNN predicted water saturation when tested in adjacent well **B-01** for the case **4** predictor trained on the entire cored interval using **7** wireline logs from training well **A-02** at **1.0** ft spacing.

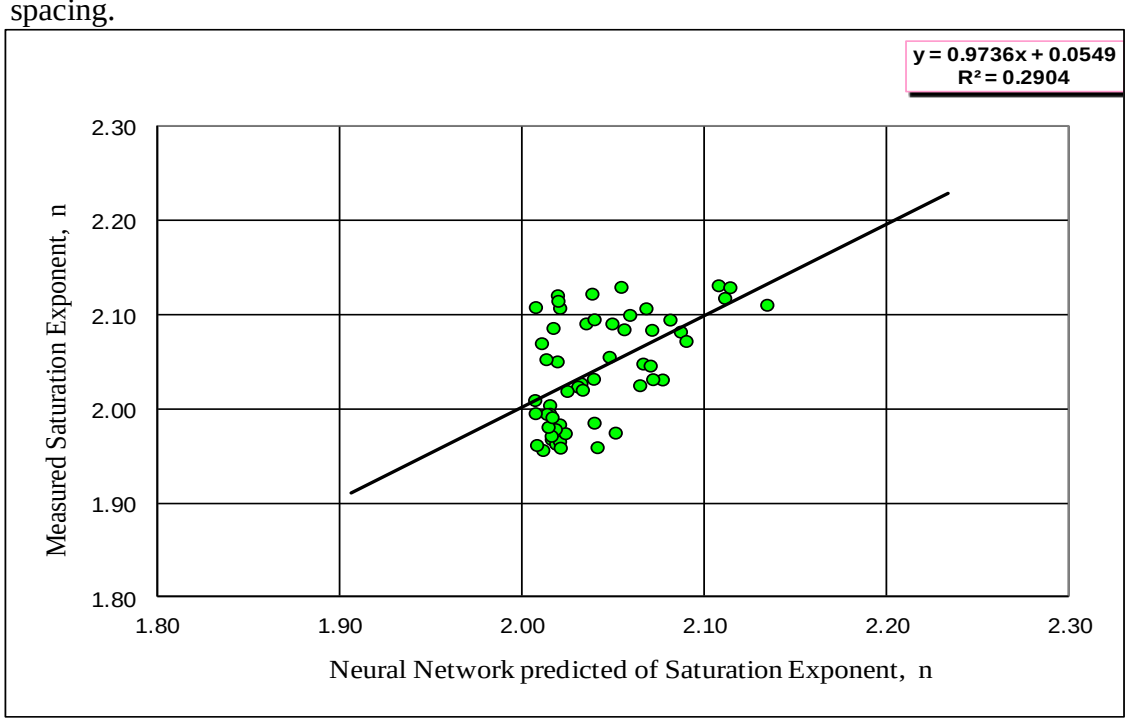

Figure C13. Crossplot of test data: measured saturation exponent (n) versus BPNN predicted saturation exponent when tested in adjacent well **B-01** for the case **4** predictor trained on the entire cored interval using **7** wireline logs from training well **A-02** at **1.0** ft spacing.

Table C20. The range of wireline log, Amott- Harvey wettability Index ($I_{A/H}$) values for normal Purposes in the BPNN for a training well **A-02** at **0.5** ft spacing.

	SGR (API)	CGR (API)	CALI in	RHOB g/cc	NPHI fraction	Log ILD Ohm.m	Log ILM Ohm.m	DT µs/ft	$I_{A/H}$
Min.	11.36	6.17	5.76	2.38	0.038	0.129	0.30	59.9	-0.3875
Max.	112.96	60.88	6.30	2.69	0.182	2.013	2.09	78.6	-0.1763

Table C21. The range of wireline log, Amott- Harvey wettability Index ($I_{A/H}$) values for normalisation Purposes in the BPNN for adjacent test well **A-01** in the same oil field at **1.0** ft spacing.

	SGR (API)	CGR (API)	CALI in	RHOB g/cc	NPHI fraction	Log ILD Ohm.m	Log ILM Ohm.m	DT µs/ft	$I_{A/H}$
Min.	9.51	6.301	5.51	2.41	0.037	0.237	0.31	56.8	-0.373
Max.	118.01	85.15	7.63	2.76	0.243	1.79	1.91	72	-0.205

Table C22. The range of wireline log Amott- Harvey wettability Index ($I_{A/H}$) values for normalisation Purposes in the BPNN for adjacent test well **B-01** in the different oil field at **1.0** ft spacing.

	SGR (API)	CGR (API)	CALI (in)	RHOB (g/cc)	NPHI fraction	Log ILD Ohm.m	Log ILM Ohm.m	DT µs/ft	$I_{A/H}$
Min.	23.21	20.24	5.89	2.36	0.059	0.636	0.411	60.9	-0.373
Max.	98.11	67.38	6.51	2.64	0.117	2.63	1.53	82.4	-0.205

Table C23. Summary results of the Amott-Harvey Wettability Index **($I_{A/H}$)** predictors trained on the entire cored interval in training well **A-02** at **0.5** ft spacing.

Input	Output	Coefficient of determination (R^2)in training well A-02
Case 1 (RHOB,NPHI,ILD &ILM)	$I_{A/H}$	0.7744
Case 2 (SGR,CGR,NPHI,ILD &ILM)	$I_{A/H}$	0.7177
Case 3 (SGR,CGR,RHOB,NPHI,ILD &ILM)	$I_{A/H}$	0.7815
Case 4 (SGR,CGR,RHOB,NPHI,ILD , ILM,& DT)	$I_{A/H}$	0.7811

Table C24. Summary results of Amott-Harvey Index ($I_{A/H}$) predictors (trained on the entire cored interval in well **A-02**) when tested in adjacent well **A-01** in the same oil field at **1.0** ft spacing.

Input	Output	Coefficient of determination (R^2) in adjacent well A-01
Case 1 (RHOB,NPHI,ILD, & ILM)	$I_{A/H}$	0.161
Case 2 (SGR,CGR,NPHI,ILD &ILM)	$I_{A/H}$	0.1982
Case 3 (SGR,CGR,RHOB,NPHI,ILD &ILM)	$I_{A/H}$	0.254
Case 4 (SGR,CGR,RHOB,NPHI,ILD , ILM,& DT)	$I_{A/H}$	0.307

Table C25. Summary results of Amott-Harvey Index ($I_{A/H}$) predictors (trained on the entire cored interval in well **A-02**) when tested in adjacent test well **B-01** in the different oil field at **1.0** ft spacing.

Input	Output	Coefficient of determination (R^2) in test well B-01
Case 1 (RHOB,NPHI,ILD,& ILM)	$I_{A/H}$	0.1694
Case 2 (SGR,CGR,NPHI,ILD &ILM)	$I_{A/H}$	0.2045
Case 3 (SGR,CGR,RHOB,NPHI,ILD &ILM)	$I_{A/H}$	0.3516
Case 4 (SGR,CGR,RHOB,NPHI,ILD , ILM, & DT)	$I_{A/H}$	0.3639

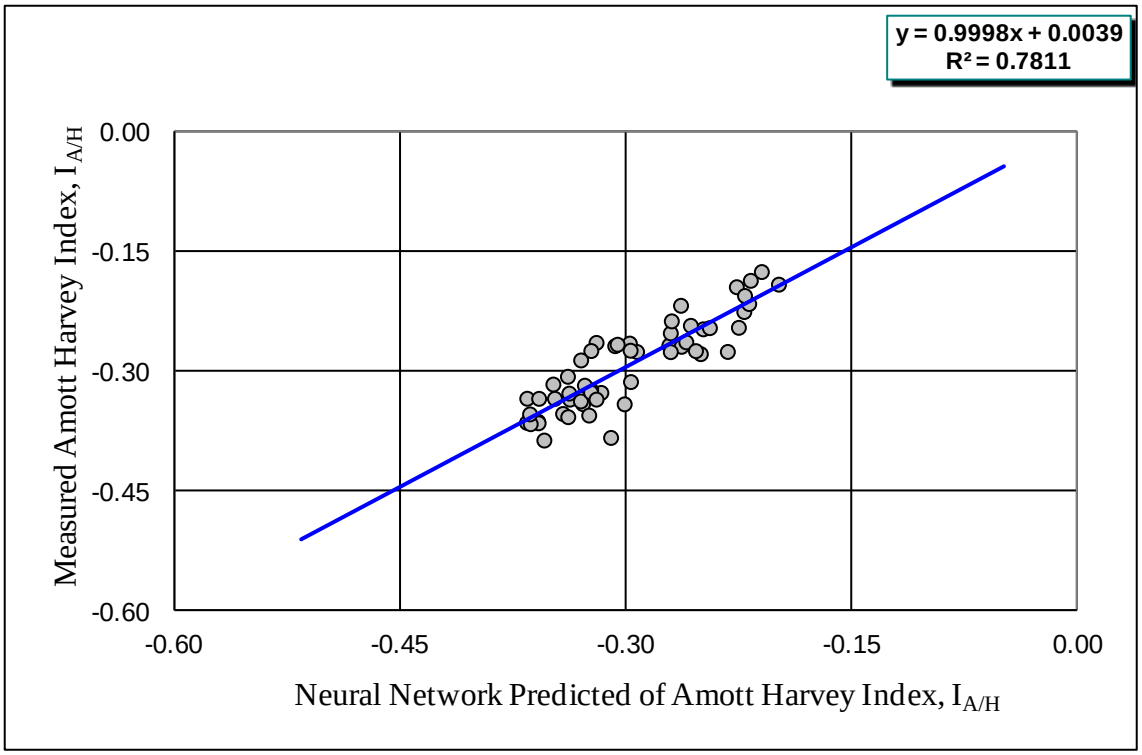

Figure C14. Crossplot of measured Amott-Harvey Index ($I_{A/H}$) versus BPNN predicted $I_{A/H}$ for the case **4** predictor trained on the entire cored interval using **7** wireline logs for training well **A-02** at **0.5** ft spacing.

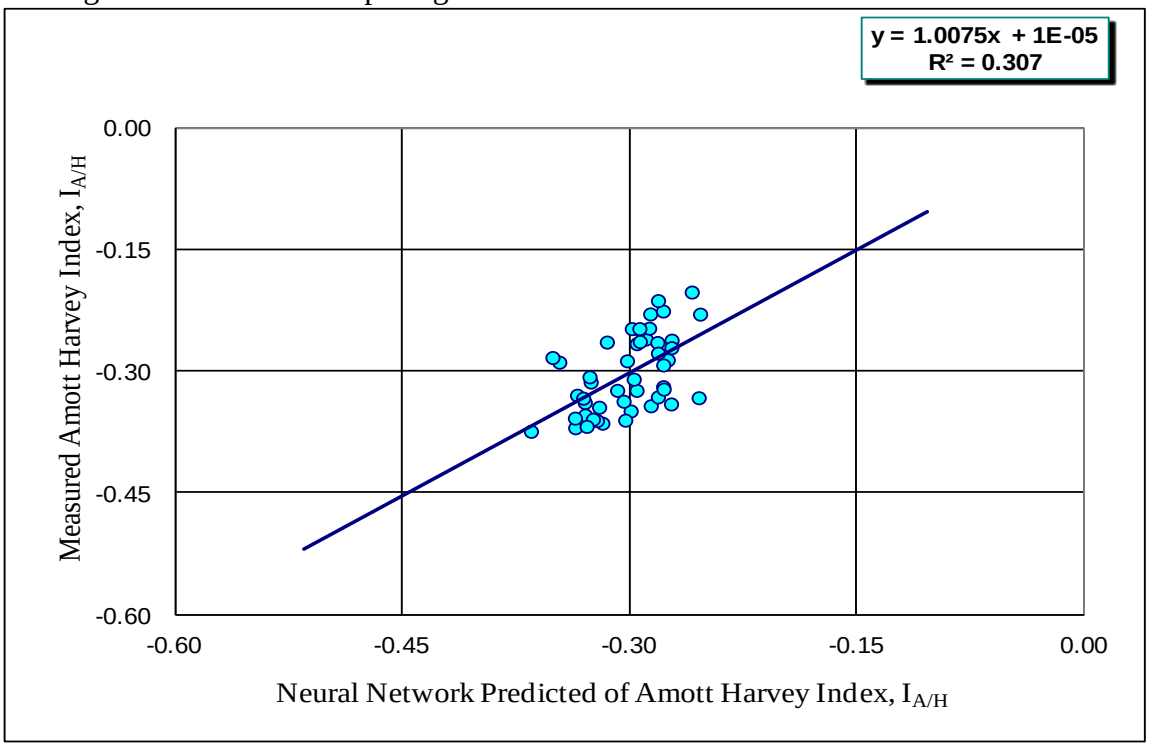

Figure C15. Crossplot of test data: measured Amott-Harvey Index ($I_{A/H}$) versus BPNN predicted $I_{A/H}$ in adjacent test well **A-01** for the case **4** predictor trained on the entire cored interval using **7** wireline logs from training well **A-02** at **1.0** ft spacing.

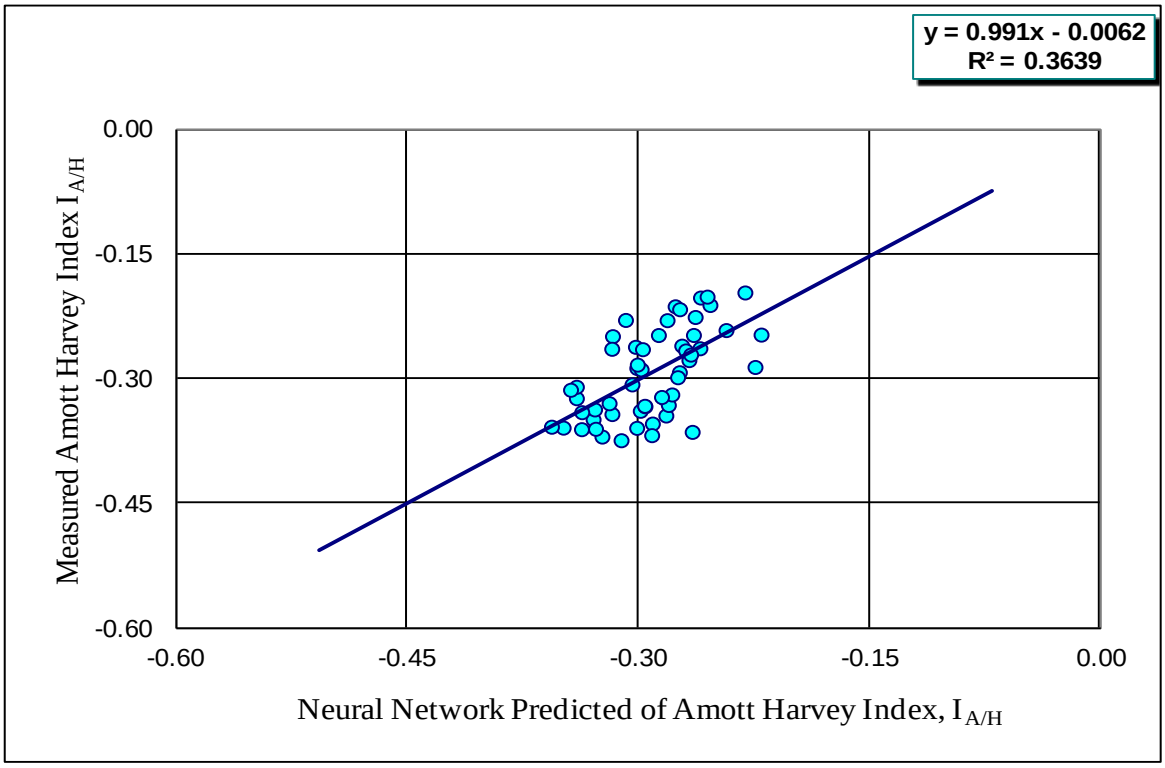

Figure C16. Crossplot of <u>test data</u>: measured Amott-Harvey Index ($I_{A/H}$) versus BPNN predicted $I_{A/H}$ in test well **B-01** in a different oil well for the case **4** predictor trained on the entire cored interval using **7** wireline logs from training well **A-02** at **1.0** ft spacing.

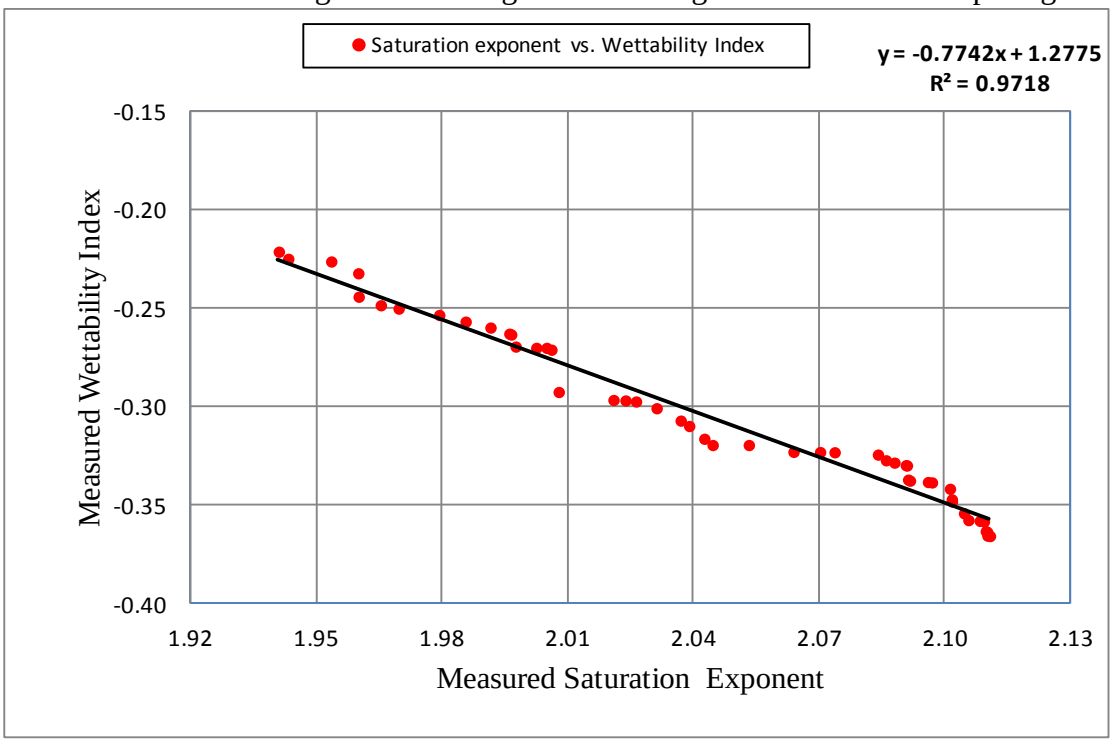

Figure C17. Crossplot of measured saturation exponent (n) versus measured Amott-Harvey Wettability Index ($I_{A/H}$) for case 4 for adjacent well **A-01** at **1.0** ft spacing.

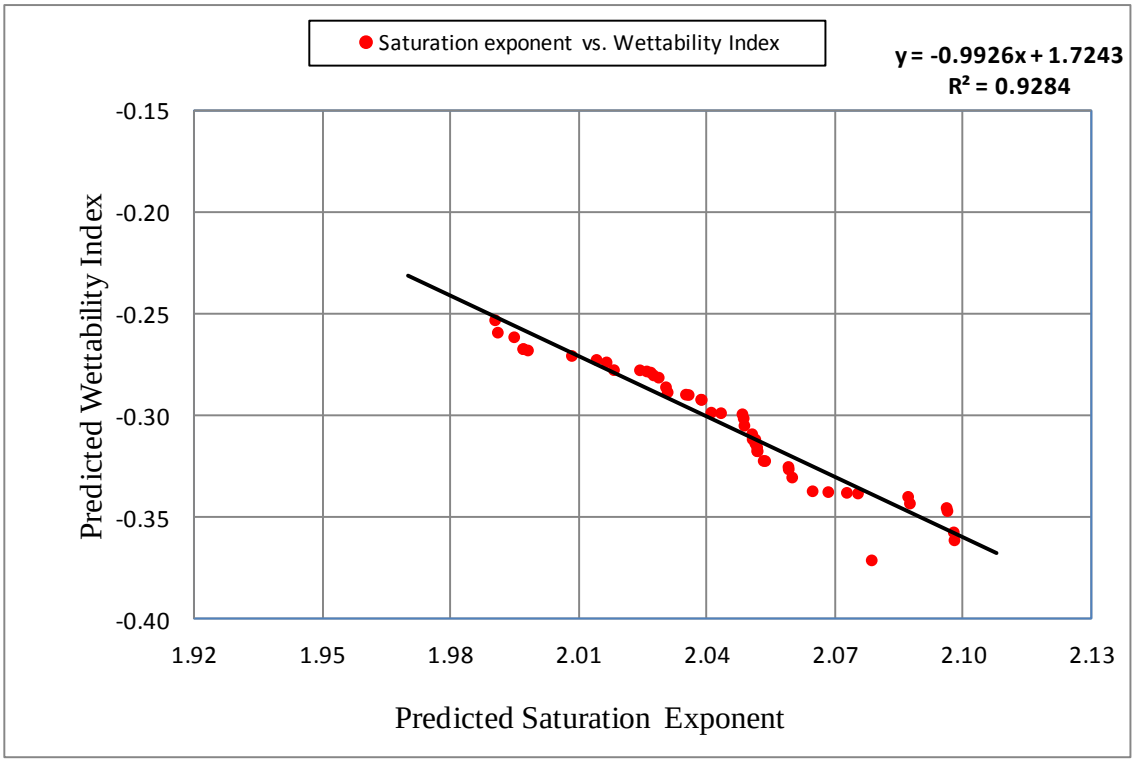

Figure C18. Crossplot of measured saturation exponent (n) versus measured Amott-Harvey Wettability Index ($I_{A/H}$) for case 4 for the training well **A-01**at **1.0** ft spacing.

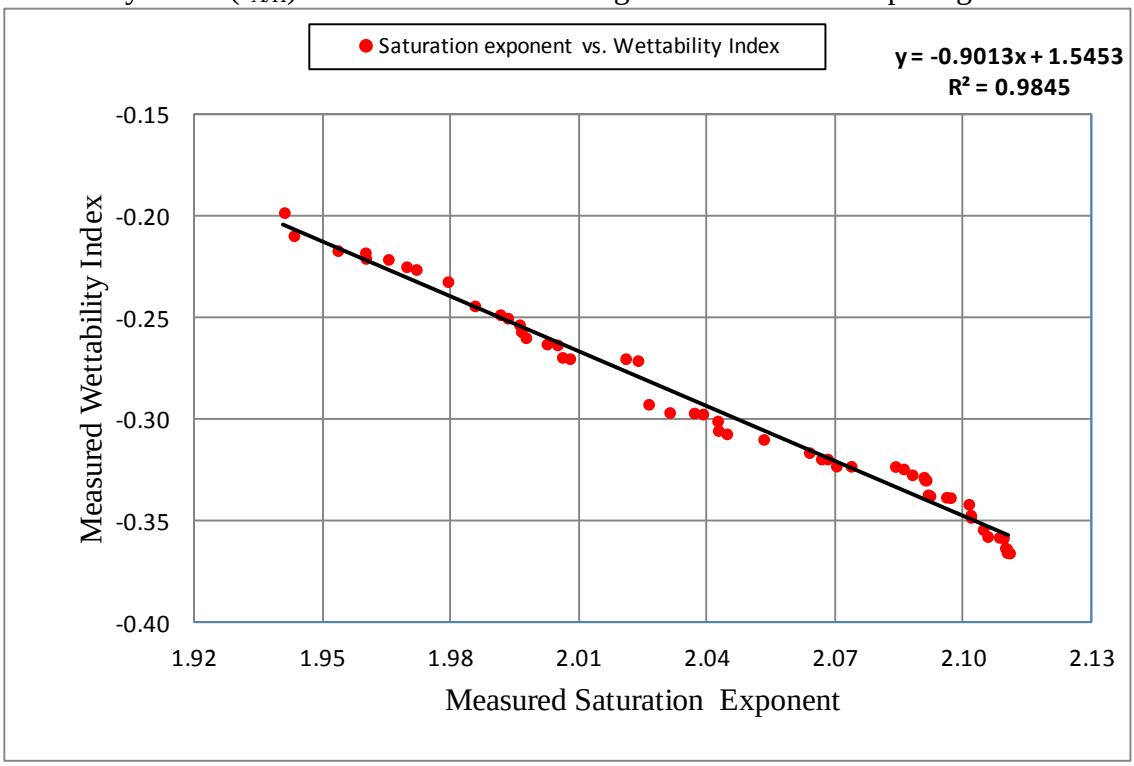

Figure C19. Crossplot of measured saturation exponent (n) versus measured Amott-Harvey Wettability Index ($I_{A/H}$) for case 4 for the training well **B-01**at **1.0** ft spacing.

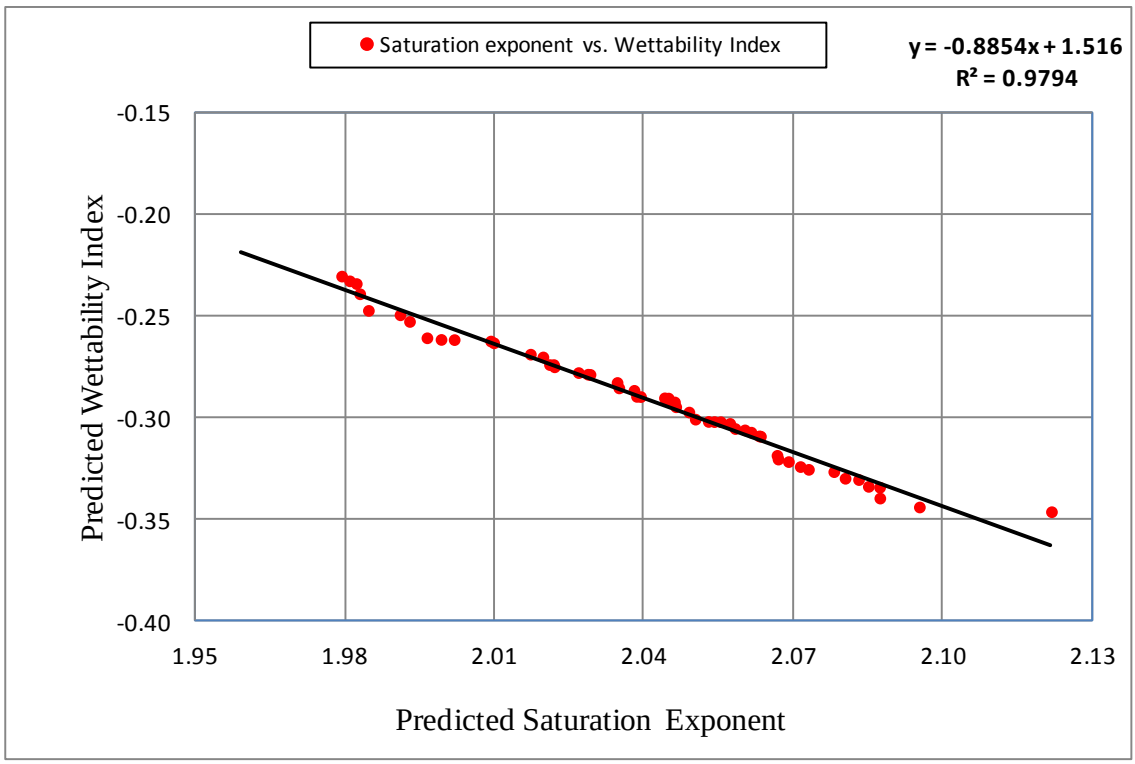

Figure C20. Crossplot of measured saturation exponent (n) versus measured Amott-Harvey Wettability Index ($I_{A/H}$) for case 4 for the training well **B-01**at **1.0** ft spacing.

Experimental Techniques and Equipment

D.1 Introduction and core preparation in the laboratory

This chapter details the laboratory experimental techniques that employed and the equipment that used to make the special core analysis (SCAL) measurements at the Libyan Petroleum Institute (LPI).

D.1.1 Core cutting and Trimming

The measurement of the physical properties of a cored formation in the laboratory requires the preparation of representative samples, either plug or whole core. A plug is a right cylinder of core, usually cut either parallel (horizontal) or perpendicular (vertical) to the bedding, with a hollow cylindrical diamond core bit mounted on a heavy-duty drill press. The horizontal and vertical plugs should be drilled from the same depth to avoid excessive core damage and to allow for a comparative dataset (to avoid differences due to heterogeneity and anisotropy). A variety of bit lubricants are used depending on the fluid content of the rock, rock mineralogy and type of drilling fluid. Common lubricants include brines, oils, kerosene or liquid nitrogen. For conglomeratic sections, the extreme heterogeneity will often demand the use of a whole core sample. This is particularly true also in vuggy and fractured rock. However, for conventional core analysis, it is normally sufficient, in the majority of cores, to take plug samples only. In the present study 94 plug samples with 1.5 inch diameter were cut from full diameter core in the horizontal direction (from 6 wells and 3 fields in the Sirt Basin, Libya) using a diamond core bit with water as the bit coolant and lubricant.

.

Figure D.1. 1.5 inch diameter SCAL plug samples.

D.1.2 Core cleaning

The measurement of core permeability, porosity and grain density requires the removal of all residual fluids, including mud filtrate, formation water and hydrocarbons from the pore space. Sample cleaning can be achieved using several techniques. This cleaning can be achieved in hot or cool refluxing equipments, which use a range of solvents, such as toluene or xylene to remove hydrocarbons and methanol to remove salts. Cores that have been cut with non damaging mud or low invasion core bits may allow the analysis of 'fresh state' samples. However, most plugs are cleaned as the first phase of testing. The selection of the cleaning procedure and the solvents to be used will be dependent upon the rock type and the fluids (particularly the hydrocarbon) in place. Geochemical analysis of the oil can be useful in the identification of the solvents that will remove oil. In the present study the plug samples were extracted to remove hydrocarbons using toluene, and leached of salt using methanol.

Core cleaning tends to create water-wet samples. However, if restoration of wettability by core ageing in crude oil is to be undertaken the cleaning has to be thorough with the aim of producing a water-wet sample. This of course has to be achieved without damaging the fabric of the sample, and sensitive samples may require cleaning by low rate miscible solvent displacement.

D1.3 Core drying

Various drying methods are used for drying core samples. Core drying can be achieved using a vacuum or humidity oven. Critical point drying may also be used for special drying such as drying of rocks containing special minerals, which are sensitive to conventional drying methods. The dry oven (Figure D.2) was used in the present experiments to remove solvents left in the rock pore space after cleaning. Temperatures ranging from 80-120° C must be used to remove solvents and ensure there is no mineral alteration. In the present study the plug samples were oven dried at 80° C for a period of 48 to 72 hours, then they were left to cool at room temperature before the core analysis commenced.

Figure D.2. Core drying in the dry oven.

Figure D.3. Core preservation after drying for subsequent Routine core analysis (RCAL) and special core analysis (SCAL).

D.2 Porosity, Permeability, and Grain Density Measurements

The 94 clean and dry plug samples were subjected to various analyses to determine porosity, permeability and grain density values where possible. The experimental procedures and equipment specifications are discussed below.

D.2.1 Helium gas expansion porosimeter

The core analysis laboratory of the Libyan Petroleum Institute uses a twin cell helium expansion gas porosimeter (Figure D.4) for the plug sample grain volume measurement. The porosimeter operates using the principle of Boyle's Law. A sealed reference chamber in the instrument is filled with helium gas at ambient temperature to a pressure of 100 psi. A sample is placed in another sealed chamber, connected to the reference chamber by a two way valve. This valve when opened allows the gas in the reference chamber to expand into the combined volume of the two chambers. From Boyle's Law, the volume of the sample chamber can be calculated when the volume of the reference chamber, the initial pressure and the final pressure are known. The instrument must be calibrated beforehand. This is done by running a series of stainless steel blanks of known volumes, to build up a graph of blank volume versus the inverse of the final pressure. The resulting calibration graph has to be entered into a computer program which performs a linear regression, producing an equation relating the grain volume of any sample run to the final pressure reading. The porosity and the grain density are then calculated by determining the bulk volume, and the weight of the sample. As a quality check, a suite of standard samples of known porosities and grain densities are measured every 20 samples.

The instrument used by our laboratory has the following specifications

Pressure indicator with remote pressure transducer

1- Range	:	0-100 psi
2- Resolution		0.01 psi
3- Accuracy	:	$\pm$ 0.1% of the full scale

Precision Pressure Controller

1- Range	:	0-100 psi
2- Resolution	:	0.01 psi
3- Repeatability	:	Better than 0.02 psi

Figure D.4. Helium gas expansion porosimeter.

D.2.2. Positive displacement pump

The positive displacement mercury pump is used to determine the bulk volume of each sample. The unit consists of a stainless steel high pressure pycnometer (sample container); it is attached to the volumetric pump cylinder. As the hand wheel connected to the pump is wound in or out, mercury is charged or withdrawn from the sample chamber. The volume of mercury displaced is measured linearly by a digital transducer connected to the pump. In practice, mercury is allowed into the pycnometer to a set reference mark, and the transducer was set to zero. This process should be repeated several times to ensure accuracy. The mercury is subsequently released back into the pump and the sample is placed and sealed in the pycnometer. After that mercury is allowed back into the pycnometer up to the previously determined reference mark, and the display shown on the digital transducer is noted. This value is later converted to the actual volume by using a simple correction factor derived from calibration volumes. The mercury is cleaned and the pump is reset to zero at least once every four samples, depending on the sample type.

D.2.3. Calculation of Porosity

The porosity of a plug sample is calculated by using the following equations

Pore volume (ft^3) = Bulk volume - Grain volume ---------- (D.1)

$$\text{Porosity (\%)} = \frac{\text{Pore volume}}{\text{Bulk volume}} \times 100 \quad \text{---------- (D.2)}$$

$$\text{Grain density } (lb/ft^3) = \frac{\text{Sample weight}}{\text{Grain volume}} \quad \text{---------- (D.3)}$$

D.2.4 Nitrogen gas Permeability

A clean, dry sample is placed in the Hassler-type core holder (Figure D.5) and an overburden pressure of 200 psi (industry standard practice to sample) is applied to the cell, compressing the rubber sleeve around the sample. Nitrogen gas pressure is applied to one end face of the sample, whilst the other end face is open to atmospheric pressure, causing the gas to flow through the sample. The flow of gas is measured at the low pressure (downstream) end face of the sample. The flow rate is measured by passing the gas through one of three laminar flow orifices and the differential pressure developed across the orifice is also measured. The transducers and flow orifices are calibrated using a dead weight tester and soap film meter at least once every three months, or when any component is altered or replaced. The equipment specifications are as follows

High pressure precision regulator

1- Range : 0-30 psi
2- Resolution : Better than 0.01 psi

High pressure transducer and readout (upstream)

1- Range : 0-100 psi
2- Resolution : 0.01 psi
3- Accuracy : $\pm$ 0.1 % of the full range

Low pressure transducer and readout (upstream)

1- Range : 0-15 psi
2- Resolution : 0.001 psi
3- Accuracy : ± 0.1 % of full scale

The length of the sample, upstream and downstream pressures, flow rate, viscosity of nitrogen, barometric pressure and temperature are entered into Darcy's equation for gas permeability, and the permeability of the sample calculated as follows:

$$Kg = \frac{2.2 \times P_b \times Q_g \times \mu_g \times L}{(P_1^2 - P_2^2) \times A} \quad \text{---------- (D.4)}$$

where:

Kg = Gas permeability, mD
Pb = Barometric pressure, Psi
P_1 = Upstream pressure, Psi
P_2 = Downstream pressure, Psi
Qg = Gas flow rate, ft^3/sec
μg = Gas viscosity, cp
L = Sample length ,ft
A = Cross-sectional area, ft^2

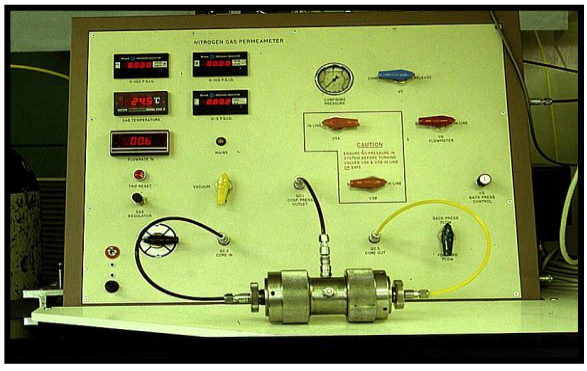

Figure D.5. Nitrogen gas permeameter.

The generated data of porosity and permeability are presented in Tables A-1 and A-2 and Figures A-1 and A-2 in Appendix A.

D.3 Formation Resistivity Factor at ambient and Overburden Pressures

The formation resistivity factor was measured for twelve of the SCAL samples. The clean and dry samples were loaded in a stainless steel saturator and evacuated for 12 hours. A solution of 135,000 ppm sodium chloride was introduced at the end of this period, followed by pressurizing the system at 2000 psi for 12 hours to assist penetration. The brine saturated plugs were placed in turn between electrodes (Figure D.6) at 1 KHz frequency and their electrical resistance were measured on consecutive days until ionic equilibrium was achieved between the fluid and rock sample. Formation resistivity factor measurements were made on 100 percent brine saturated core samples at ambient conditions and the elevated reservoir overburden pressure. The sample resistance was measured and converted to resistivity using the sample cross-sectional area and length. Formation resistivity factor is calculated as the ratio of the sample resistivity to the resistivity of the water saturating it. The formation resistivity factors of a group of samples are plotted versus their porosities on log-log graph paper. The slope of the best fit line is the value of the cementation factor, "m", and the intercept is the value of "a".

$$FF = \frac{a}{\phi^m} \quad \text{---------- (D.5)}$$

where:

a Rock consolidation factor

FF Formation resistivity factor

Ø Fractional porosity

m Cementation factor

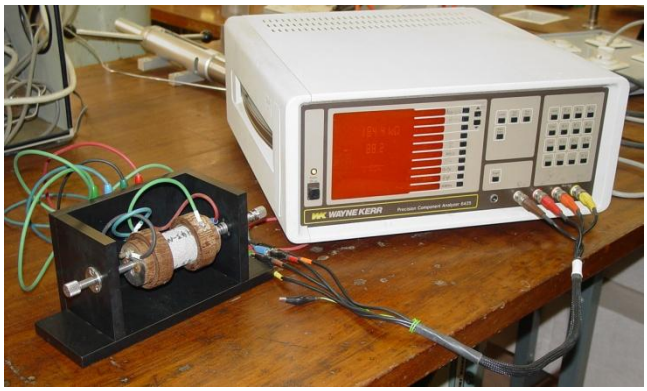

Figure D.6. Resistivity measurement set up at ambient conditions.

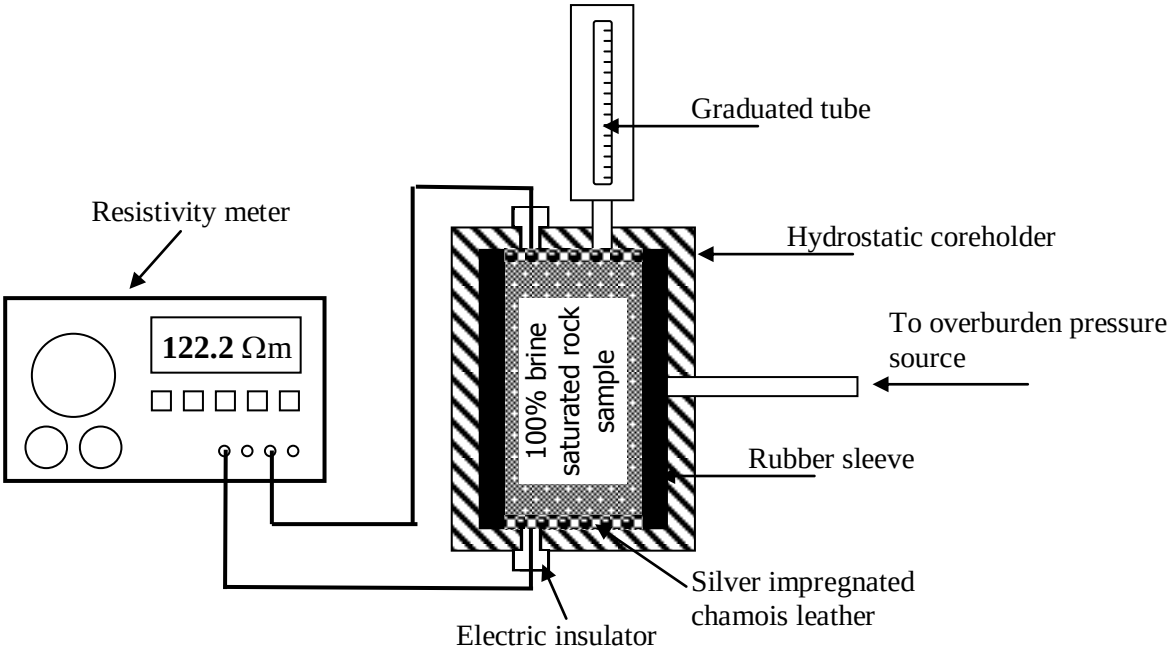

Figure D.7. Formation resistivity factor measurement set up at overburden pressure.

For the overburden pressure the fully saturated samples were individually placed between stainless steel end pieces. All connecting pipe work and contact surfaces were fully saturated with simulated formation brine to ensure electrical continuity. The overburden pressure applied to the cores was from 1000-5000 psi, and the samples were allowed to stabilize before their resistance were measured. On achieving equilibrium, the samples' resistances were measured using two electrode systems at 1 KHz frequency.

D.4 Resistivity Index (RI)

Resistivity index measurements were conducted for the twelve SCAL samples from the Nubian sandstone in the Sirt Basin. These tests were conducted after the formation resistivity factor tests. The fully saturated samples were placed on a semi-permeable porous plate cell (Figure D.8) in a capillary pressure apparatus, to bring the samples to lower saturation. Air humidified by water was admitted at a controlled pressure to the apparatus and the volume expelled was monitored. When equilibrium saturation had been attained, the samples were removed from the cell, and their weight and electrical resistance were

measured. The sample dry weight, the fully saturated weight and the weight after each desaturation step were used to calculate the average saturation of the sample. The resistance was used to calculate the true sample resistivity and the resistivity was divided by the sample resistivity at 100% liquid saturation which yield the resistivity index (RI).

In the laboratory it is necessary to firstly determine the resisitivity at 100% water saturation (R_o) of the sample. Once this value has been established, the air as the non-conducting fluid is forced into the sample over a range of designated pressures to displace an increasing portion of the brine phase. At each stage, when the saturation is in equilibrium relative to the pressure, the true formation resistivity (R_t) is measured.

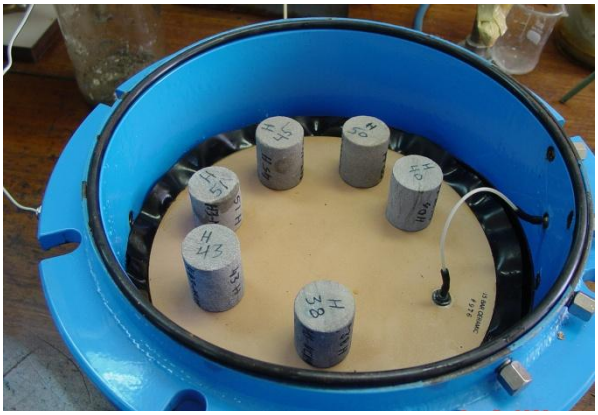

Figure D.8. Porous plate cell for rock desaturation and air-brine capillary pressure measurement.

The water saturation in hydrocarbon reservoirs is generally estimated from resistivity well logs. The interpretation of these logs is based on two empirical equations by Archie. In clean formations (those containing little or no clay) Archie (1942) defined the resistivity index as the ratio of the resistivity of the formation (R_t), which is partially saturated to the resistivity of the same formation when it is entirely saturated with water (R_o). Therefore, the resistivity index can be expressed in terms of rock resistivities and water saturation as follows:

$$RI = \frac{R_t}{R_o} = S_w^{-n} \quad \text{---------- (D.6)}$$

The generated data of resistivity index before and after wettability measurement are presented in Tables A3-A12 and in Figures A3-A12 in Appendix A.

D.5 Wettability Measurement (Amott method)

Wettability measurements were performed for the twelve SCAL samples using the Amott method (Figure D.9). This involves a static imbibition phase followed by forced displacement in a flow cell. With a core sample saturated with oil and water at irreducible water saturation, it was placed in an Amott cell under water for 1000 hours. The oil displaced by spontaneous water imbibition is monitored daily until a stable oil measurement was obtained (Vw, s). The rock sample was then placed in a flow cell and the oil is flushed with water down to residual oil saturation (Sor) and the oil displaced dynamically (approximately equal to the volume of water dynamically imbibed) is measured (Vw, d). Following brine displacement, the rock sample is placed in an Amott cell under oil for 1000 hours. The water displaced by spontaneous imbibition of oil was monitored daily until a stable water measurement was obtained (Vo,s). The core is then removed and placed in a flow cell and flushed with oil down to irreducible water saturation (Swirr) and the amount of water dynamically displaced (approximately equal to the volume of oil dynamically imbibed) was measured (Vo, d).

$$I_w = \frac{V_{w,s}}{V_{w,s} + V_{w,d}} \quad \text{---------- (D.7)}$$

$$I_o = \frac{V_{o,s}}{V_{o,s} + V_{o,d}} \quad \text{---------- (D.8)}$$

where I_w and I_o are the displacement ratios by water and oil ratios respectively. Care should be taken in the interpretation of this data due to the fact that sample wettability may be altered or reversed by a large number of factors (type of coring fluid, exposure to air, temperature, sample handling and plugging, cleaning, drying and preservation). The Amott-Harvey wettability index ($I_{w,AH}$) is a single number that combines the displacement by water and oil ratios :

$$I_{w,AH} = I_w - I_o \quad \text{---------- (D.9)}$$

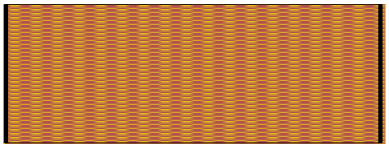

Rock sample at irreducible water saturation

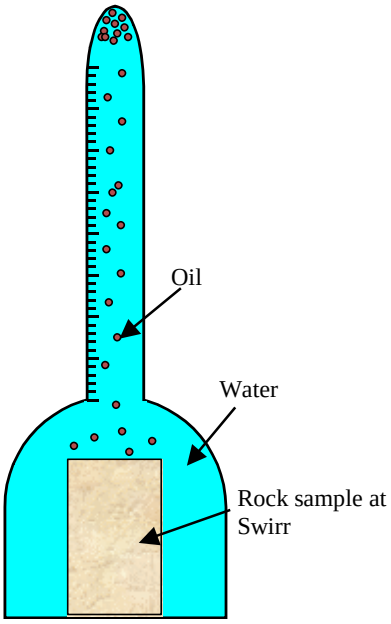

b) Spontaneous imbibition of water

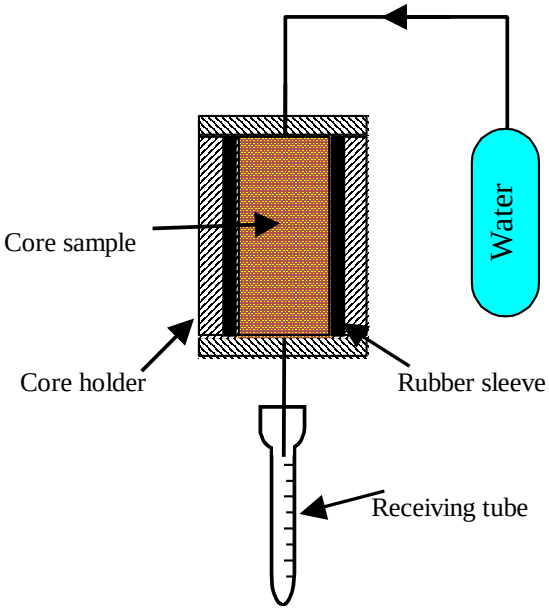

a) Forced displacement of oil

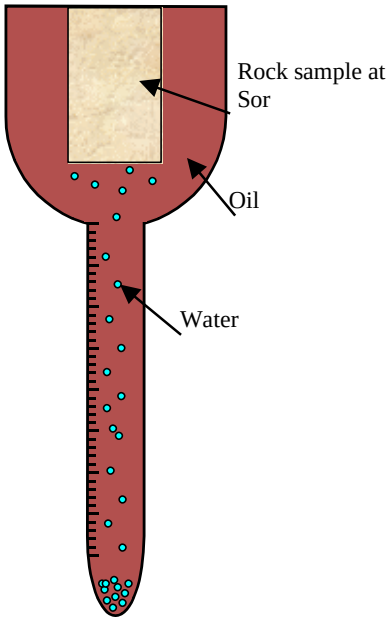

d) Spontaneous imbibition of oil

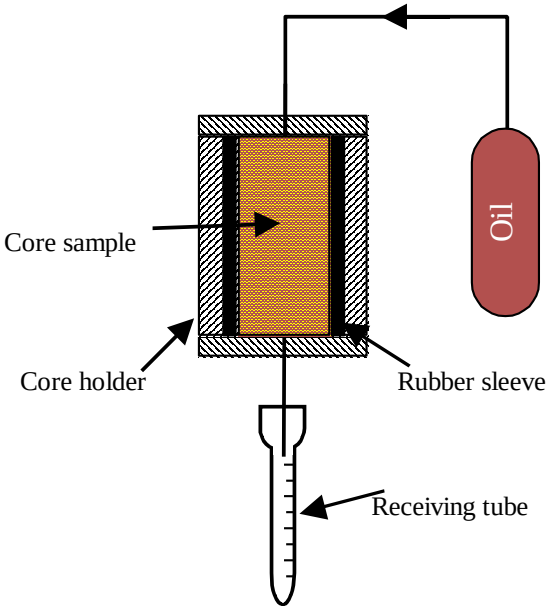

b) Forced displacement of water

Figure D.9. Amott wettability measurement sequence.

D.6 Mercury Injection Capillary Pressure (MICP) Measurement

Modern mercury injection capillary pressure apparatus (Figure D.10) enables one to inject mercury into a rock sample at high pressure. An injection pressure of up to 60,000 psi can be achieved. This high pressure injection can penetrate pores down to 0.003 microns in diameter, which enables one to obtain a detailed pore size distribution. Using the core pore volume, injection pressure and mercury volume, pressure is plotted versus mercury saturation to generate a capillary pressure curve. The analysis is very rapid allowing up to 8 samples to be analysed in 24 hours. The analysis can provide high resolution data. Irregular and small samples can be used. However, the test is destructive. Samples cannot be used for subsequent core testing and samples cannot be confined. Delicate mineralogy may be damaged by the advancing mercury and the air/mercury system is not a true wetting/non-wetting system.

Figure D.10. High-pressure (0-60,000 psi) mercury injections capillary pressure setup.

Twelve SCAL samples underwent capillary pressure measurements using the Micromeritics Auto Pore IV 9510 Mercury Porosimeter with windows software. Prior to testing, the routine petrophysical properties of porosity, grain density and permeability to air were re-measured. Each sample was individually weighed and a sample information file that describes the sample and gives the analysis conditions and other parameters was created. The instrument performs semi-automatically injection of mercury at programmed pressure steps from less than 1 psi to 60,000 psi.

To begin the test, each sample was individually loaded into a calibrated glass penetrometer. The penetrometer consists of a sample chamber and precision-bore glass capillary whose volume was selected to be just larger than the measured routine pore volume. The outside of the glass capillary was plated with metal which acts as one plate of a capacitor. The mercury within the capillary acts as the other capacitance plate and then installs the loads penetrometer into the low pressure port. The first phase of the low pressure analysis is the evacuation of gases from the penetrometer for 20-30 minutes, and then the penetrometer is backfilled automatically with mercury. For pressures up to 30 psi air pressure is used. When the low pressure analysis is complete, the penetrometer is removed from the low pressure port and installed in a high pressure port in which hydraulic pressured oil is used. The pore volume data are calculated by determining the volume of mercury remaining in the penetrometer. As the pressure increases, mercury moves into the sample's pores, vacating the stem (Drainage or Intrusion). The greater the pressure, the smaller the pore diameter into which the mercury can be forced. Then the pressure is decreased gradually in steps to withdraw the mercury from the pores in pressure steps from 60,000 psi to 14 psi (Imbibition or Extrusion).

The generated data are presented in Tables A14-A23, and in Figures A13-A30 in Appendix A.